Ph.D. Dissertation of Engineering

Cyclic Lateral Tests and Strength Prediction for Composite Walls with Steel U-Section Boundary Element

U형 강재단부요소를 지닌 합성벽체에 대한 반복가력실험 및 강도예측모델

August 2022

Graduate School of Engineering
Seoul National University
Architecture and Architectural Engineering

Hyeon-Jin Kim

Cyclic Lateral Tests and Strength Prediction for Composite Walls with Steel U-Section Boundary Element

Advisor: Hong-Gun Park

Submitting a Ph.D. Dissertation of Architecture and Architectural Engineering

August 2022

Graduate School of Engineering
Seoul National University
Architecture and Architectural Engineering

Hyeon-Jin Kim

Confirming the Ph.D. Dissertation written by Hyeon-Jin Kim

August 2022

Chair	Sung-Gul Hong	(Seal)
Vice Chair	Hong-Gun Park	(Seal)
Examiner	Cheol-Ho Lee	(Seal)
Examiner	Thomas Kang	(Seal)
Examiner	Tae-Sung Eom	(Seal)
Examiner	Yail Jimmy Kim	(Seal)

Abstract

Cyclic Lateral Tests and Strength Prediction for Composite Walls with Steel U-Section Boundary Element

Kim, Hyeon Jin
Department of Architecture and Architectural Engineering
College of Engineering
Seoul National University

Generally, RC walls are used as the primary lateral load-resisting system in buildings. On the other hand, in high-rise buildings and large industrial buildings (e.g., factories and power plants), high structural performance is required to satisfy the high safety and serviceability demands (e.g., story drift ratio, floor vibration). For such high structural performance, a steel-concrete composite wall with boundary element of steel U-section (SUB-C wall) was developed. In the proposed method, large steel area is concentrated at the wall ends to maximize flexural strength and stiffness, and to minimize steel connection and weld length. The structural integrity and constructability can be improved by using an open section of U-shaped steel element; by concrete pouring, boundary steel element and reinforced concrete are integrated with conventional headed studs. Further, the U-shaped element can provide lateral confinement to the boundary zone, and increase the shear strength of walls. Thus, labor works related to vertical reinforcement and hoop reinforcement can be reduced.

Cyclic lateral loading tests were performed on the proposed walls to investigate the flexural and shear performances. As the steel U-sections provided high confinement to the boundary concrete, crushing of the boundary concrete was restrained, which developed strain hardening of the steel U-section in tension. Thus, the flexural strength of the SUB-C wall was 37% greater than that of the counterpart RC wall. Further, the steel U-sections restrained shear cracking and shear sliding. Thus, the deformation capacity and energy dissipation were increased by 38%-53% and 99%-173%, respectively. The SUB-C walls exhibited ultimate drift ratios over 3%, and failed due to web crushing in the plastic hinge zone (i.e., post-yield shear failure). On the other hand, the shear strength of the SUB-C walls was 13%–54% greater than that of the counterpart RC walls. This is because the steel U-sections not only resisted shear transferred from the diagonal struts, but also restrained diagonal tension cracking in the web and crack penetration into the boundary zone. For this reason, the shear strength of the SUB-C walls was determined by web crushing, without diagonal tension failure and crushing of the boundary concrete. The increase in flexural and shear strengths was more pronounced when steel U-sections with greater area were used.

Nonlinear finite element analysis was performed for the walls that failed in elastic web crushing (before flexural yielding). The analysis results reveal that the compressive strength of the diagonal struts is significantly degraded due to large horizontal tensile deformation in the mid-height of the walls, which ultimately leads to web crushing. Such mechanism is named “horizontal elongation mechanism”, and an empirical equation to predict the maximum horizontal elongation was developed based on the parametric analysis. The horizontal elongation is greatly affected by shear reinforcement ratio and aspect ratio of walls. However, the boundary steel area has little effect on the maximum horizontal elongation.

For the shear strength model, two shear failure mechanisms were defined: elastic and inelastic web crushing failures. Those mechanisms were implemented by the traditional truss analogy, and the model improvement was achieved by considering distinctive features of SUB-C walls: For the elastic web crushing strength (shear strength), the horizontal elongation mechanism was implemented, but the contribution of boundary elements was neglected for conservatism and simplicity in design. On the other hand, for the inelastic web crushing strength (i.e., post-yield shear strength), the vertical elongation and frame action of boundary elements in the plastic hinge zone were considered. In particular, since the vertical elongation is defined as a function of deformation demand, the post-yield shear strength can be calculated at every deformation levels of walls. The accuracy of the proposed model was validated from the comparison with the test results. For an advanced design of the shear strength (elastic web crushing strength), an equivalent elastic analysis method using commercial analysis programs was developed.

The deformation-based design method for SUB-C walls was developed using the proposed shear strength model. The deformation capacity was defined at the intersection of the shear demand and inelastic web crushing strength. In general, the predicted deformation capacities, in terms of overall lateral drift ratio and normalized plastic hinge deformation, agree with the test results.

Based on the test results and existing design methods, allowable material strengths and detailing requirements for SUB-C walls were provided. Note that the proposed design strengths are valid only when the design requirements are satisfied. The detailing methods outside the scope of the requirements should be applied after in-depth verification through further experimental and analytical studies.

Keywords : Steel-concrete composite wall, Composite Boundary element, Steel U-section end plate, Flexural strength, Web crushing shear strength, Vertical elongation, Horizontal elongation, Post-yield shear degradation.
Student ID : 2014-22627

Contents

List of Tables

List of Figures

List of Symbols

a : Shear span ratio = l_s/l_w

$A_{b,w}$: Total section area of two web plates in a steel U-section

A_b : Cross-sectional area of a steel U-section

A_b : Area of gross wall section

A_{bc} : Area of infilled concrete in the boundary zone

$A_{b,w}$: total section area of two web plates in a steel U-section

A_r : Cross-sectional area of a vertical reinforcing bar or a boundary hoop bar

A_s : Cross-sectional area of vertical steel reinforcement

A_{sc} : Total cross-sectional area of headed studs and tie bars within their vertical spacing

A_{sh} : Cross-section area of a horizontal reinforcing bar

A_{sc1} : Area of a steel connector

A_w : Total section area of two steel faceplates in the wall web

b_c : Dimension of the confined core measured to the outside edges of the confinement hoop bars

b_{uf} : Largest unsupported length of the flange plate in a steel U-section between steel anchors or between steel anchors and the plate edge

b_{uw} : Largest unsupported length of the web plate in a steel U-section between steel anchors or between steel anchors and the plate edge

C_v : Coefficient to represent the level of shear degradation of concrete ($\leq$ 1.0)

d : Distance from the extreme compression fiber to the centroid of tension reinforcement

e_h : Horizontal elongation in the mid-height of walls

e_v : Vertical elongation in plastic hinge zone

E_D : Dissipated energy within a load cycle in the lateral-displacement relationship

E_P : Dissipated energy based on idealized elastic-perfectly plastic cyclic curve

E_c : Elastic modulus of concrete

E_s : Elastic modulus of steel

f_c' : Compressive strength of concrete measured from cylinder tests

f_{sh} : Average tensile stress of horizontal reinforcement

f_{sv} : Average stress of vertical web reinforcement

f_u : Ultimate tensile strength of reinforcing bar

f_y : Yield strength of reinforcing bar

f_{yh} : Yield strength of shear reinforcement

$F_{u,sc}$: Ttensile strength of shear connector

F_u : Ultimate tensile strength of steel plate

F_y : Yield strength of steel plate

h_w : Wall height

I_b : Moment of inertia of steel U-section with respect to the center of the boundary element

I_{bc} : Moment of inertia of boundary infill concrete with respect to the center of the boundary element

I_g : Moment of inertia of gross wall section

I_s : Moment of inertia of steel section

K_f : Flexural yield stiffness

K_s : Shear yield stiffness

K_y : Lateral yield stiffness of wall

l_{be} : Horizontal length of boundary zone

l_c : Moment of inertia of concrete section

l_{dp} : Development length of the steel U-section

l_e : Effective moment-arm length or effective shear section

l_p : Plastic hinge zone length

l_s : Shear span length

l_w : Wall length

l_{web} : Depth of web region = $l_w - 2l_{be}$

M_{bp} : Plastic moment capacity of steel U-sections subjected to pure bending

M_n : Nominal flexural strength

M_p : Tested flexural strength

M_y : Flexural yield moment

n_a : Axial force ratio $= N/A_g f_c'$

Q_{cv} : Shear strength of shear connectors

R_h : Reduced stiffness factor for horizontal ties in the strip model

s_h : Vertical spacing of horizontal shear reinforcement

s_c : Spacing of steel anchors (headed studs or tie bars)

s_v : Horizontal spacing of vertical web reinforcement

t_p : Thickness of faceplate

t_{uf} : Thickness of the flange plate in a steel U-section

t_{uw} : Thickness of the web plate in a steel U-section

t_w : Wall thickness

V_{RC} : Contribution of RC wall to the overall shear strength of SUB-C walls

V_b : Contribution of steel U-sections to the shear strength of walls

V_c : Contribution of concrete to the shear strength of walls.

V_f : Shear demand resulting from flexural strength

V_y : Shear demand resulting from flexural yield strength

$V_{n,max}$: Maximum shear strength corresponding to web crushing failure

V_n : Nominal shear strength

V_s : Contribution of horizontal shear reinforcement to the shear strength of walls

V_{test} : Tested peak strength of walls

V_v : Contribution of vertical web reinforcement to the shear strength of walls

V_w : Contribution of steel web faceplates to the shear strength of walls

$V_{wc,m}$: Maximum contribution of concrete to the inelastic web crushing strength

V_{wc} : Contribution of concrete to web crushing strength

w_s : Width of strips in the strip model

$(EI)_{eff}$: Effective flexural stiffness

$\alpha_{h,max}$: Maximum horizontal elongation ratio

α_f : Reduction factor for the elastic flexural stiffness

α_v : Index to represent the stress levels of the steel U-section in compression

γ_p : Average shear strain in the plastic hinge zone

γ_m : Maximum average shear distortion measured within the mid-height panel zone

γ_s : Shear deformation measured in the wall web

Δ : Lateral displacement measured at the top of a cantilever wall

Δ_f : Lateral displacement contributed by flexural deformation

Δ_s : Lateral displacement contributed by shear deformation

Δ_{sl} : Horizontal sliding displacement

Δ_p : Lateral displacement at the top of the plastic hinge zone

Δ_θ : Lateral displacement of elastic zone due to rigid body rotation

Δ_e : Lateral displacement of the elastic zone due to flexural and shear deformations

δ_o : Drift ratio at the peak strength

δ_u : Ultimate drift ratio

δ_{pl} : Plastic drift ratio

δ_{pu} : Ultimate drift ratio in plastic hinge zone

δ_y : Yield drift ratio

δ_{py} : Yield drift ratio in plastic hinge zone

ε_2 : Principal compressive strain

ε_h : Average horizontal strain

ε_o : Axial strain at peak compressive stress of concrete

ε_v : Average vertical strain

ε_y : Yield strain of steel reinforcements

ε_{yh} : Yield strain of shear reinforcement

η_c : Shear degradation factor for concrete

θ_c : Average inclination angle of diagonal cracks with respect to vertical axis of walls

θ_f : Rotation measured at the top of the plastic hinge zone

θ_p : Plastic hinge rotation

ρ_h : Horizontal web reinforcement ratio

ρ_{be} : Boundary reinforcement (steel) ratio

ρ_c : Area ratio of confinement reinforcement to the boundary zone

ρ_s : Area ratio of overall vertical steel sections to the gross wall section

ρ_v : Vertical web reinforcement ratio

μ : Lateral drift ductility

Ω : Over-strength factor for flexural strength of walls

T : Flexural tension force of walls

k : Effective average strength factor for concrete

δ : Ratio of lateral displacement to the shear span (lateral drift ratio)

η : Coefficient to take into account the Bauschinger effect for a steel plate subjected to reversed cyclic loading

θ	: Inclination angle of diagonal struts with respect to vertical axis of walls
κ	: Energy dissipation ratio
ϕ	: Average flexural curvature in the plastic hinge zone
ω_h	: Mechanical shear reinforcement ratio

Chapter 1. Introduction

1.1 General

Traditionally, reinforced concrete (RC) walls have been used as a lateral load-resisting system, due to their good structural performance and economy. On the other hand, in super high-rise buildings and nuclear power plants (NPP), high-performance walls are required to satisfy the high safety and serviceability demands:

1) For high-rise buildings, high <u>lateral stiffness and damping</u> are required to control lateral displacement and vibration.

2) For the NPP, high <u>flexural and shear strengths</u> are required to achieve good seismic performance.

Under such high demand conditions, large-diameter (> 57 mm) reinforcing bars and large wall thickness (= 1100–2000 mm for high-rise buildings taller than 450 meters; 500–1500 mm for NPP) are required, which decrease constructability and economy, due to the high cost of materials, labor, and formwork (**Fig. 1-1**).

Labor-intensive rebar construction for High-rise buildings

Typical containment walls in NPP

Fig. 1-1 High-performance RC walls in high-rise buildings and NPPs.

For high-performance walls, steel–concrete (SC) composite walls can be considered. A common method is to use boundary elements of concrete-encased steel columns (the RC-CES wall, **Fig. 1-2**(a)), or concrete-filled steel tube columns (the RC-CFT wall, **Fig. 1-2**(b)). The steel sections in the boundary elements not only increase flexural resistance of walls, but also provide strong connections to steel beams.

In the cyclic lateral loading tests of Dan et al. (2011), Ji et al. (2014), and Ren et al. (2018), the boundary CES and CFT columns were effective in increasing the flexural strength and displacement ductility of walls. However, the displacement capacity is closely related to the boundary details: to achieve a large inelastic deformation, early spalling and crushing of concrete (CES columns) and early local buckling of steel plates (CFT columns) need to be restrained. For this reason, in JGJ 138 (2016) and AISC 341 (2016), highly dense confining reinforcement is required in the boundary CES sections; and in AISC 360 (2016), the compressive strength of CFT section is limited according to the width-to-thickness ratio of the steel plates. Further, to prevent separation between boundary elements and web concrete, horizontal reinforcing bars are penetrated or welded to boundary CES or CFT sections, which may decrease constructability.

For better axial and shear capacities, concrete-encased steel plate (CESP) walls (**Fig. 1-2**(c)) can be used: a steel plate is encased in the web of RC wall, and the plate ends are connected to boundary steel sections. The concrete encasement provides fire-proofing and buckling restraint for the web steel plate, ensuring structural stability under high compression force. Thus, CESP walls have been studied primarily for use in high-rise buildings (e.g., Xiao et al. 2012; Wang et al. 2018; Jiang et al. 2019). In concrete-filled steel plate (CFSP) walls (**Fig. 1-2**(d)), concrete is filled between two steel faceplates, and the faceplates provide forms for concrete casting. Since the 1990s, extensive experimental and analytical studies have been conducted on CFSP walls for use in NPP facilities (e.g., Takeuchi et al. 1998; Ozaki et al. 2004; Varma et al. 2014; Epackachi et al. 2014), and in high-rise buildings (e.g., Eom et al. 2009; Nie et al. 2013; Yan et al. 2018;

Zhao et al. 2020). The existing studies on CESP and CFSP walls showed that although the steel web plates significantly contributed to the shear strength of walls, their contribution to flexural strength was less than that of the boundary elements. Further, the displacement ductility was limited by the local buckling of steel web plates, even with concrete encasement or filling. Thus, relatively thick steel plates and steel anchors (or stiffeners) are required for the web plates (JGJ 138, 2016; AISC N690, 2018), which increases the overall construction cost. Further, elaborate on-site welding or bolting is required for the joints between the steel plate modules.

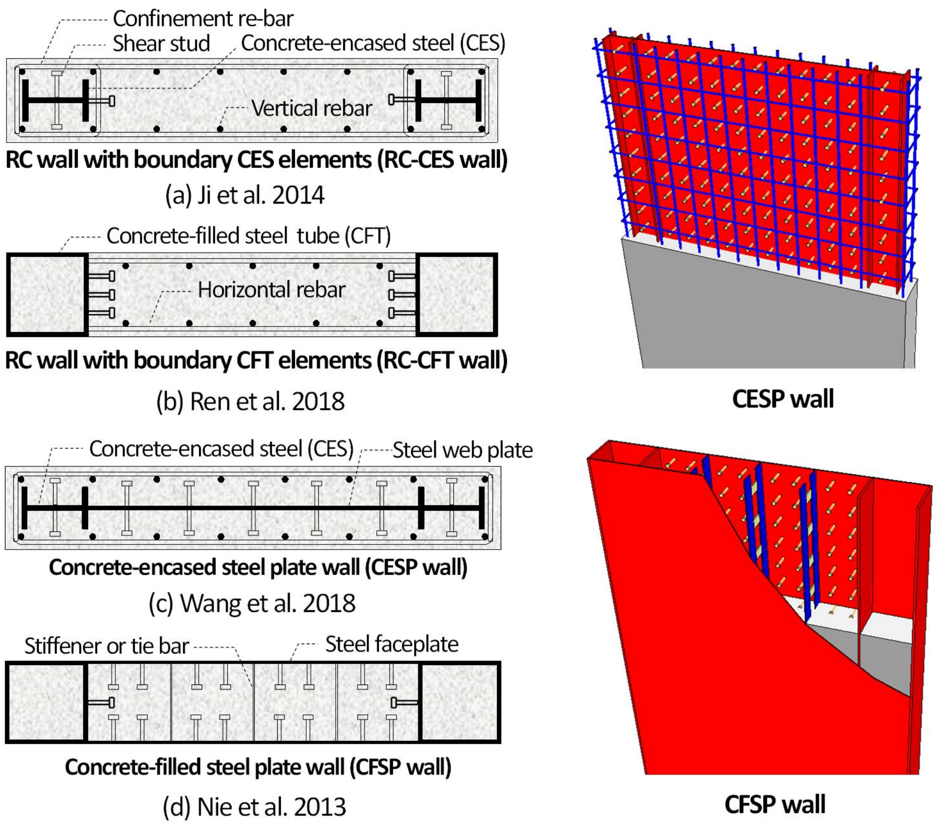

Fig. 1-2 Existing steel–concrete composite walls with (a) concrete-encased steel (CES) end column; (b) concrete-filled steel tube (CFT) end column; (c) CES section and steel web plate; and (d) CFT section and concrete-filled steel faceplate.

In the present study, for high structural performance and constructability, a composite wall with boundary elements of steel U-section (U-shaped steel boundary element-composite wall = SUB-C wall) was developed (**Fig. 1-3**). In the proposed method, large steel area is concentrated at the wall ends to maximize flexural strength and stiffness, and to minimize steel connection and weld length. The structural integrity and constructability can be improved by using an open section of U-shaped steel element; by concrete pouring, boundary steel element and reinforced concrete are integrated with conventional headed studs. Further, the U-shaped element can provide lateral confinement to the boundary zone, and increase the shear strength of walls. Thus, labor works related to vertical reinforcement and hoop reinforcement can be reduced. If necessary, steel plate beams and faceplates can be used for web reinforcement, forming steel-framed concrete walls or CFSP walls, but the web steel area can be minimized (**Fig. 1-3**).

For such advantages, the proposed SUB-C walls have good potential for use in high-rise buildings and NPPs (**Fig. 1-4**): 1) In core walls of high-rise buildings, steel U-sections are used for boundary columns of the exterior wall segments, providing strong reinforcement to an opening and direct connections to coupling beams; and 2) in NPPs, labyrinth walls are designed as steel-framed concrete walls, providing fast construction, light reinforcement, and clean construction environment.

As a fundamental research, the present study focused on the in-plane flexural and shear behaviors of SUB-C walls. Cyclic lateral loading test was performed to investigate the effect of boundary steel U-sections on the strength and deformation capacity. The tested strengths were compared with the predictions of existing design methods and nonlinear finite element (FE) analysis. Based on the test and FE analysis results, an analytical model, to predict the shear strength and post-yield shear strength of the proposed composite walls, was developed using a modified truss analogy (i.e., truss-beam model). Further, the proposed shear strength was defined as a function of deformation demand, so that the lateral load-displacement relationship was fully established. For reasonable design of SUB-C walls, recommendations for materials and structural detailing were provided.

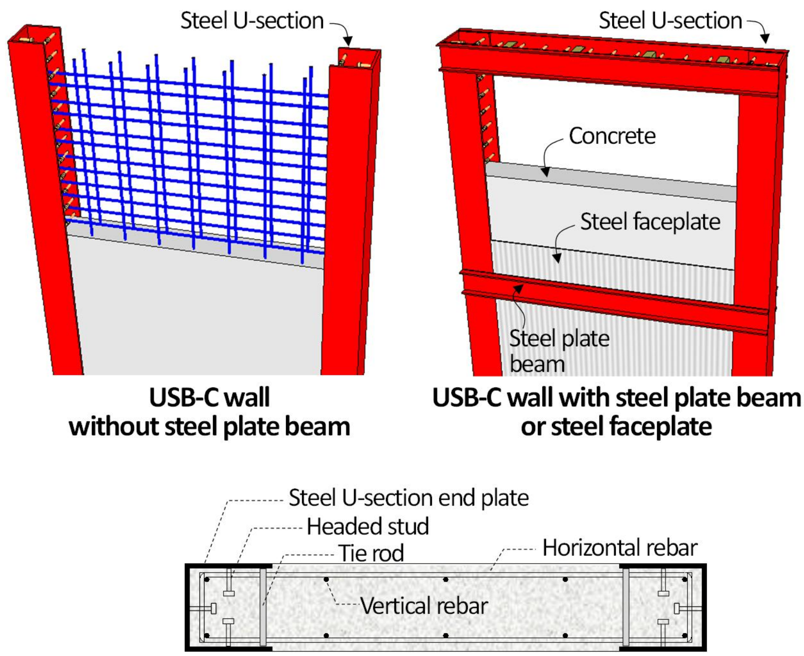

Fig. 1-3 Steel U-section boundary element-Composite (SUB-C) Walls.

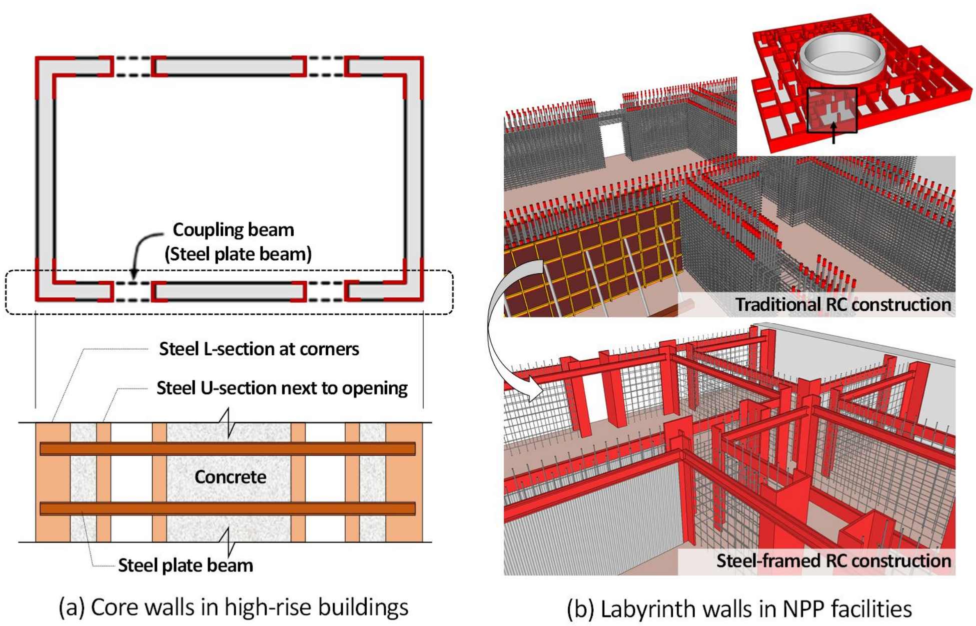

Fig. 1-4 Potential use of SUB-C walls to high-rise buildings and NPPs.

1.2 Scope and Objectives

For high structural performance and constructability, a composite wall with boundary elements of steel U-section (SUB-C Wall) was developed. As a fundamental and comprehensive study, the major objectives of this dissertation are:

1) to verify the in-plane flexural and shear performances of the novel composite walls subjected to cyclic lateral loading.

2) to identify the effect of boundary steel U-sections on the flexural and shear strengths, deformation capacity, and failure mode of SUB-C walls.

3) to develop an analytical model to predict the shear strength and post-yield shear strength of SUB-C walls.

4) to provide design strengths and recommendations for use in practice.

For the first two objectives, a total of 23 wall specimens, consisting of 17 SUB-C specimens and 6 equivalent RC specimens, were experimentally tested under cyclic lateral loading. Note that, for high structural performance, the boundary reinforcement ratio was intentionally increased, which is even greater than the maximum ratio (= 8% in ACI 318, 2019) of RC columns. From the test results, the flexural and shear strengths, lateral stiffness, deformation capacity/ductility, ultimate failure mode, and energy dissipation capacity of SUB-C walls were evaluated. The tested properties of the major design parameters included:

- Arrangement of vertical reinforcement (uniform distribution or concentration at boundary element)

- Type of boundary reinforcement (reinforcing bar or steel U-section)

- Sectional area of steel U-section (boundary reinforcement ratio = 9.3%–19.0%; web plate thickness = 9, 12, 16 mm; web plate length = 200, 300, 320, 450 mm)

- Yield strength of steel U-section (= *379–596 MPa*)

- Type of web reinforcement (horizontal reinforcing bar or steel plate beam or vertical steel faceplate)

- Spacing and diameter of horizontal reinforcements (*shear reinforcement ratio = 0.24%–1.06%*)

- Yield strength of horizontal reinforcements (445–514 MPa for reinforcing bars; 456 MPa for steel plate beams; and 321 MPa for steel web faceplates)

- Aspect ratio of walls (*1.0, 2.0, or 2.5*)

- Concrete strength (*44.7–68.3 MPa*)

- Axial force ratio (= *0, not implemented*).

Further, partly for the second objective, nonlinear finite element (FE) analysis was performed for the test specimens. The results of FE analysis were compared with the test results, to confirm the main cause of elastic shear failure (horizontal elongation mechanism) and to verify the contribution of steel U-sections to the elastic shear strength. Using the proposed FE model, the parametric analysis was performed to investigate the effect of various design parameters (boundary reinforcement ratio, shear reinforcement ratio, aspect ratio of walls) on the horizontal elongation. Based on the parametric analysis, an empirical equation to predict the horizontal elongation was developed.

For the third objective, two shear failure mechanisms were defined based on the tested failure modes: elastic and inelastic web crushing failures. The observed mechanisms were implemented using the traditional truss analogy, and the model improvement was achieved by considering distinctive features of SUB-C walls: For the elastic web crushing strength (shear strength), the effect of horizontal elongation on the shear deformation was considered based on the FE analysis results; On the other hand, for the inelastic web crushing strength (i.e., post-yield shear strength), the vertical elongation and frame action of boundary elements in the plastic hinge zone were considered. Since the vertical elongation is a function of deformation demand, the post-yield shear strength was evaluated at every deformation level of walls. The accuracy of the proposed model was validated from the comparison with the test results. For the elastic web crushing strength, a simpler equation was derived based on the available range of major design parameters. Further, for advanced design of elastic web crushing strength, an equivalent elastic analysis method using commercial analysis programs was developed.

For the last objective, the deformation-based design approach was adopted considering all possible failure modes of SUB-C walls subjected to cyclic lateral loading. That is, the design strengths and deformation capacity were provided to define overall lateral load-displacement relationship of SUB-C walls. To ensure the proposed design strengths, allowable material strengths (for concrete, steel plates, reinforcing bars, steel anchors) and detailing requirements (for steel U-section, horizontal reinforcement, vertical web reinforcement) were provided.

The scope and objectives of this study are illustrated in **Fig. 1-5**.

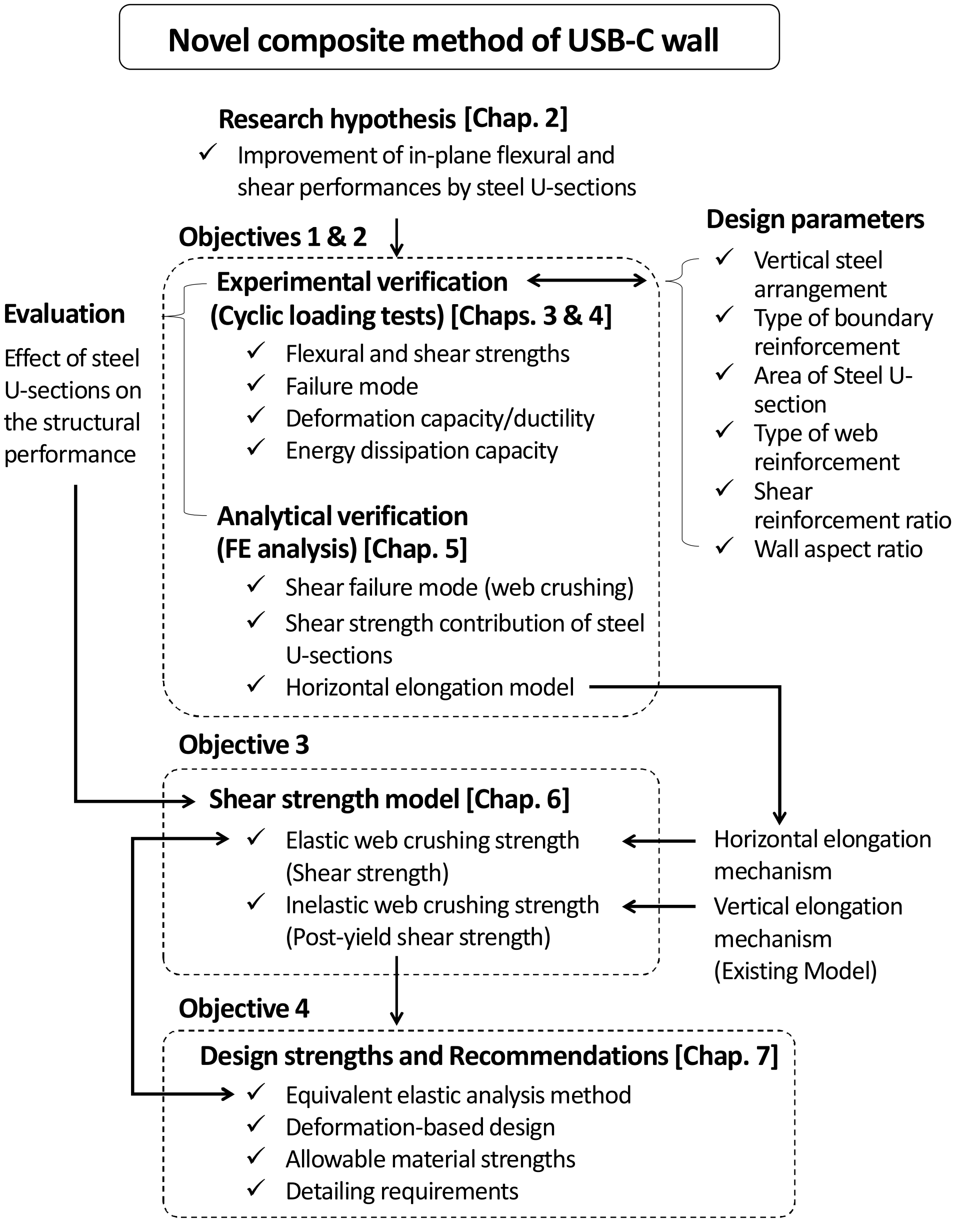

Fig. 1-5 Outlines of dissertation: scope and objectives.

1.3 Outline of dissertation

In Chapter 2, the existing shear strength models for RC walls and steel-concrete composite walls are reviewed. Then, the historical research trends for steel-concrete composite walls are introduced. From the discussion on the existing studies, the research hypothesis for verification is established.

In Chapters 3 and 4, the experimental test results of SUB-C walls are reported. The test parameters, design method, and test setup for cyclic lateral loading and measurement are described in detail.

Chapter 3 focuses on the flexural performance of SUB-C walls. Thus, the test results, including the load-displacement behavior, failure mode, flexural and shear deformations, energy dissipation capacity, and local behavior measured from strain gauges, are thoroughly reported. The tested flexural strength, stiffness, and displacement ductility are compared with the existing design methods and the test results of existing composite wall specimens.

Chapter 4 focuses on the shear performance of SUB-C walls. Thus, the test results, including diagonal cracking mode and the shear strength contributions of each structural components are further reported. The tested shear strengths are compared with the existing design methods.

In Chapter 5, nonlinear FE modeling methods and analysis results for SUB-C wall are reported. The model adequacy is verified by comparing the tested strengths with the FE analysis results. Then, the predicted damage patterns of concrete are compared with the actual failure modes, for clear understanding of shear failure mechanism. The shear strength contribution of steel U-sections is reevaluated at every cross section along the wall height. Lastly, the horizontal elongation model calibrated from the parametric analysis is introduced.

In Chapter 6, the shear strength models developed based on two shear failure mechanisms are introduced. The theoretical base, model assumptions, and detailed derivations of the models are provided. For verification, the shear strengths calculated from the proposed model are compared with the test results. Lastly, the effect of axial force on the shear strength prediction is discussed.

In Chapter 7, the equivalent elastic analysis method to predict the elastic web crushing strength is introduced first. For understanding of readers, the detailed analysis procedure and its application are provided. Secondly, for deformation-based design, the design equations to calculate the flexural and shear strengths, and deformation capacity are presented. Lastly, the allowable material strengths and detailing requirements for SUB-C walls are provided.

In Chapter 8, final conclusions and summary are presented.

The outline of the dissertation is illustrated in **Fig. 1-5**.

Chapter 2. Literature Review

In this chapter, 1) Sections 2.1 introduces the existing design methods to predict the shear strength of walls. 2) Section 2.2 introduces the existing models to predict the web crushing strength according to deformation demand. 3) Section 2.3 provides the literature reviews of existing experimental and analytical studies on various steel-concrete composite walls. 4) Section 2.4 provides the discussion on 1), 2), and 3), and defines the major hypotheses for subsequent verification studies.

2.1 Code-Based Shear Strength

2.1.1 ACI 318 (ACI Committee 318, 2019)

In the general provisions of ACI 318-19 (Chapter 11), the shear strength of a non-prestressed RC wall is calculated as the sum of the contributions of concrete (V_c) and shear reinforcement (V_s), assuming 45° truss mechanism:

$$V_n = V_c + V_s \leq V_{n,max} \tag{2-1}$$

where,

$$V_c = \alpha_c \sqrt{f_c'} A_{cv} \tag{2-2}$$

$$V_s = \rho_h f_{yh} A_{cv} \tag{2-3}$$

$$V_{n,max} = 0.66\sqrt{f_c'} A_{cv} \tag{2-4}$$

where, α_c = 0.25 for h_w / l_w (h_w = wall height and l_w = wall length) $\leq$ 1.5, α_c = 0.167 for h_w / l_w $\geq$ 2.0, and α_c varies linearly between 0.25 and 0.167 for 1.5 < h_w / l_w < 2.0; A_{cv} = net shear area in the cross section, which is defined as the gross section area for a rectangular wall; and ρ_h = horizontal shear reinforcement ratio. The nominal shear strength is limited by the maximum shear strength $V_{n,max}$ corresponding to web crushing failure. Until the mid-1950s, the ACI Standard limited $V_{n,max}$ according to compressive strength f_c' of concrete. However, after the diagonal tension failure of girders at the Wilkins Airforce Depot Warehouse, the average shear stresses were limited absolutely to 2.48 MPa. The 1963 ACI provisions proposed the dependence of web crushing strength on $\sqrt{f_c'}$, which is still in use today. The coefficient in Eq. (2-4) has been reduced from a value of 5/6 in ACI 318-14 to a value of 2/3 in ACI 318-19 because the effective shear area was increased to entire wall area (= $t_w l_w$, t_w and l_w = thickness and length of rectangular wall section) from the effective area based on the flexural depth

(=$t_w d$, d = distance from the extreme compression fiber to the centroid of tension reinforcement) in prior editions of the Code. Seismic provisions of ACI 318 (Chapter 18) provides the same web crushing strength as shown in Eq. (2-4).

In Chapter 22, the general shear strength for a RC member is provided considering the effect of member depth (i.e., size effect) and the effect of longitudinal reinforcement ratio. Here, the concrete contribution is defined according to the level of horizontal reinforcement ratio, as follows:

When $\rho_h \geq \rho_{h,min}$

$$V_c = \left(0.17\sqrt{f_c'} + \frac{N_u}{6A_g}\right) b_w d$$

$$\text{or} \tag{2-5a}$$

$$V_c = \left(0.66\rho_s^{1/3}\sqrt{f_c'} + \frac{N_u}{6A_g}\right) b_w d$$

When $\rho_h < \rho_{h,min}$

$$V_c = \left(0.66\rho_s^{1/3}\lambda_s\sqrt{f_c'} + \frac{N_u}{6A_g}\right) b_w d \tag{2-5b}$$

where, $\rho_{h,min}$ = minimum transverse reinforcement ratio (= $0.062 f_c'/f_y$), respectively; N_u = demand axial force (positive for compression and negative for tension); A_g = gross sectional area of cross section; b_w = width of cross section (= t_w); d = effective depth of cross section (= $0.8l_w$); ρ_s = longitudinal reinforcement ratio; and λ_s = size effect modification factor = $\sqrt{2/(1+0.1d)} \leq 1$. The contribution of transverse shear reinforcement V_s and the maximum shear strength $V_{n,max}$ are calculated as Eqs. (2-3) and (2-4), respectively.

2.1.2 Eurocode 2 & 8 (British Standards Institution, 2004)

Eurocode 2 provides the shear strength of a RC member with or without shear reinforcement. When shear reinforcement is unnecessary (i.e., shear demand < V_c), the shear strength is calculated based on the contribution of concrete, as follows:

$$\begin{aligned} V_n = V_c &= \left[C_{Rd,c}k(100\rho_l f_c')^{\frac{1}{3}} + k_1\sigma_{cp}\right]b_w d \\ &\geq \left[v_{min} + k_1\sigma_{cp}\right]b_w d \end{aligned} \tag{2-6}$$

where, $C_{Rd,c}$ = 0.18/λ_c (λ_c = partial factor for concrete = 1.5), k = size effect modification factor = $1+\sqrt{200/d} \leq 2$; ρ_l = area ratio of longitudinal tensile reinforcement to the gross section; k_1 = 0.15; σ_{cp} = axial force demand = N_u/A_g < $0.2f_c'$ (N_u > 0 for compression); and $v_{min} = 0.035k^{3/2}f_c'^{1/2}$.

When shear reinforcement is required, the shear strength is calculated only based on the contribution of shear reinforcement, using a variable angle truss mechanism.

$$V_n = V_s = \frac{A_{sh}}{s_h} z f_{yh} \cot\theta \leq V_{n,max} \tag{2-7}$$

where, A_{sh} = total sectional area of shear reinforcement within a spacing s_h of shear reinforcement; z = length of the inner lever arm (= 0.9d); f_{yh} = yield strength of shear reinforcement; and θ = inclination angle of diagonal struts with respect to the longitudinal axis of members. Here, the inclination angle θ can be chosen between the limiting values for design (22° $\leq \theta \leq$ 45°).

The maximum shear strength corresponding to web crushing failure is calculated as follows:

$$V_{n,max} = \alpha_{cw} b_w \nu_1 z f_c' / (\cot\theta + \tan\theta) \tag{2-8}$$

where, α_{cw} = coefficient taking account of the state of the stress in the compression chord (= 1.0 for non-prestressed members); and v_1 = strength reduction factor for concrete cracked in shear = $0.6(1 - 0.004f_c')$.

In Eurocode 8, which provides the provisions for seismic design, the provisions of Eurocode 2 are applied to the walls with shear span ratio greater than 2.0 (a = $M_u/(V_u l_w)$ = 2.0), with the values of z = $0.8l_w$ and $\tan\theta$ = 1.0. If a < 2.0, the following equation is used.

$$V_n = V_c + 0.75a\rho_h f_{yh} b_w l_w \quad (2\text{-}9)$$

In the outside critical region, the maximum shear strength is calculated as Eq. (2-8). On the other hand, in the critical region, 40% of the value outside the critical region is used.

2.1.3 fib MC 2010

In fib MC, the shear strength of a RC member without shear reinforcement is calculated as follows:

$$V_n = V_c = k_v \frac{\sqrt{f_c'}}{\gamma_c} b_w z \qquad \text{(2-10)}$$

For members with no significant axial load, with $f_y \leq$ 600 MPa, $f_c' \leq$ 70 MPa, and with a minimum aggregate size of not less than 10 mm,

$$k_v = \frac{180}{1000 + 1.25z} \qquad \text{(2-11)}$$

For more general case,

$$k_v = \frac{0.4}{1 + 1500\varepsilon_z} \cdot \frac{1300}{1000 + k_{dg} z} \qquad \text{(2-12)}$$

where, γ_c = strength reduction factor for concrete = 1.5; ε_z = longitudinal strain at the mid-depth of the effective shear depth; and k_{dg} = 32 / (16+d_g) $\geq$ 0.75, in which d_g = maximum size of the aggregate. Here, k_{dg} can be taken as 1.0, provided that the size of the maximum aggregate particles, d_g, is not less than 16 mm. Eq. (2-11) is derived assuming the longitudinal strain is equal to ε_z = 0.00125. In general case, ε_z is calculated by performing section analysis or by the following equation.

$$\varepsilon_z = \frac{1}{2E_s A_{sl}} \left(\frac{M_u}{z} + V_u + N_u \left(\frac{1}{2} \mp \frac{\Delta e}{z} \right) \right) < 0.003 \qquad \text{(2-13)}$$

where, E_s = elastic modulus of steel; A_{sl} = area of longitudinal reinforcement in the tension chord; M_u = demand flexural moment; V_u = demand shear force; and Δe = eccentric distance of axial load (positive in the compression chord).

For members with shear reinforcement, the shear strength can be predicted based on the following approximation levels: Level I. Variable angle truss approach, Level II. Generalized stress field approach, and Level III. Simplified modified compression field theory. In level I and II approximations, only the contribution of shear reinforcement V_s is considered ($V_n = V_s$), and the equation for V_s is the same as that of Eurocode 2 (Eq. (2-7)). However, the minimum strut angle is defined as $\theta_{\min} = 30°$ (for RC members) for level I approximation, and $\theta_{\min} = 20° + 10{,}000\varepsilon_z$ for level II approximation. ε_z is calculated as Eq. (2-13). In level III approximation, the concrete contribution V_c is also considered using Eq. (2-10) ($V_n = V_c + V_s$). However, k_v is calculated using the following equation:

$$k_v = \frac{0.4}{1 + 1500\varepsilon_z}\left(1 - \frac{V_u}{V_{n,max}(\theta_{min})}\right) \tag{2-14}$$

where, $\theta_{\min}$ is calculated according to level II approximation ($\theta_{\min} = 20° + 10{,}000\varepsilon_z$).

For all approximations, the maximum shear strength $V_{n,max}$ corresponding to web crushing is calculated as follows:

$$V_{n,max} = k_\varepsilon \eta_{fc} b_w z f_c' \sin\theta\cos\theta \tag{2-15}$$

where, $k_\varepsilon = 0.55$ (for level I approximation) or $k_\varepsilon = 1/(1.2 + 55\varepsilon_1) \leq 0.65$ (for level II approximation); and $\eta_{fc} = (30/f_c')^{1/3} \leq 1.0$. Here, the principal tensile strain ε_1 is obtained from Mohr's circle for strain, as follows:

$$\varepsilon_1 = \varepsilon_z + (\varepsilon_z + 0.002)\cot^2\theta \tag{2-16}$$

For seismic walls with plastic hinges, the maximum shear strength $V_{n,max}$ is calculated according to Eq. (2-15), but using the value of $k_\varepsilon = 0.25$.

2.1.4 JGJ 138 (China Building & Construction Standards, 2016)

JGJ 138 provides the shear strengths of steel-concrete composite walls with the section configurations shown in **Fig. 2-1**.

For conventional SC composite walls, the shear strength is provided by concrete (V_c), shear reinforcement (V_s), boundary steel plates (V_b), and web steel plates (V_w), as follows:

$$V_n = V_c + V_s + V_b + V_w \leq V_{n,max} \tag{2-17}$$

For the walls without web steel plates (**Fig. 2-1**(a) and (b)), the shear strength contributions shown in Eq. (2-17) are calculated as follows:

$$V_c = \frac{1}{\lambda - 0.5}\left(0.5 f_t b_w h_{w0} + 0.13N\frac{A_w}{A}\right) \tag{2-18}$$

$$V_s = f_{yh}\frac{A_{sh}}{s_h}h_{w0} \tag{2-19}$$

$$V_b = \frac{0.4}{\lambda}F_{yb}A_b \tag{2-20}$$

$$V_w = \frac{0.6}{\lambda - 0.5}F_{yp}A_p \tag{2-21}$$

where, λ = shear span ratio (if λ < 1.5, λ = 1.5; and if λ > 2.2, λ = 2.2); f_t = tensile strength of concrete = $0.395 f_{cu,m}^{0.55}$ ($f_{cu,m}$ = average compressive strength of concrete cube); b_w = width of concrete infill; h_{w0} = effective depth of the wall section (= $h_w - l_a$, in which l_a = distance from the extreme tension fiber to the centroid of tensile reinforcement); N = applied axial force; A_w = area of wall web section; A = gross wall area including flange section; A_{sh} = area of horizontal web reinforcement within spacing s_h; F_{yb} = yield strength of boundary steel column; A_b = area of boundary steel column (smaller of each column in both ends); F_{yp} = yield strength of web steel plate; and A_p = area of web steel plate.

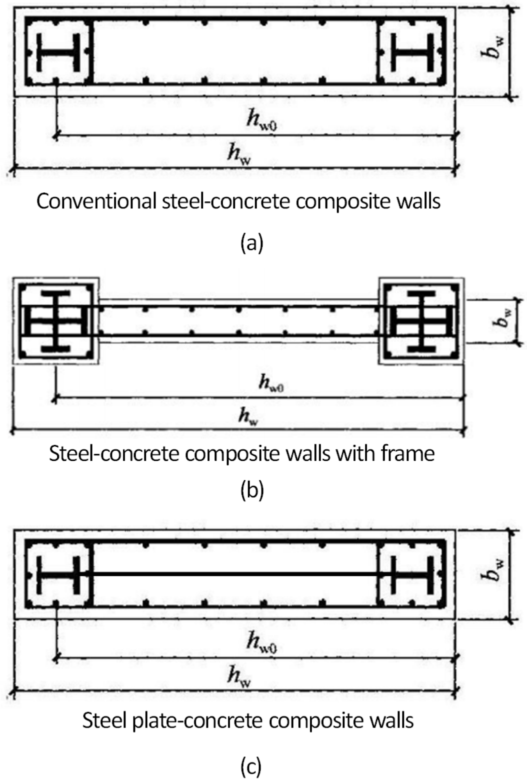

Fig. 2-1 Section configurations of SC composite walls in JGJ 138 (2016)

For the walls using web steel plates (**Fig. 2-1**(c)), the contribution V_b of boundary steel plates is decreased as follows:

$$V_b = \frac{0.3}{\lambda} F_{yb} A_b \tag{2-22}$$

When the walls are subjected to longitudinal tension, the minimum shear strength is calculated as follows:

$$V_n \geq V_s + V_b + V_w \tag{2-23}$$

For seismic design, the shear strength of Eq. (2-17) is reduced by 20%.

For the composite walls without web steel plates, the maximum shear strength $V_{n,max}$ corresponding to web crushing failure is calculated as follows:

For general design case,

$$V_{n,max} = 0.25 f_c' b_w h_{w0} + \frac{0.4}{\lambda} F_{yb} A_b \quad (2\text{-}24)$$

For seismic design case,

$$V_{n,max} = 0.2 f_c' b_w h_{w0} + \frac{0.32}{\lambda} F_{yb} A_b \qquad \text{for } \lambda > 2.5 \quad (2\text{-}25a)$$

$$V_{n,max} = 0.15 f_c' b_w h_{w0} + \frac{0.32}{\lambda} F_{yb} A_b \qquad \text{for } \lambda \leq 2.5 \quad (2\text{-}25b)$$

For the composite walls using web steel plates, the maximum shear strength $V_{n,max}$ corresponding to web crushing failure is calculated as follows:

For general design case,

$$V_{n,max} = 0.25 f_c' b_w h_{w0} + \frac{0.3}{\lambda} F_{yb} A_b + \frac{0.6}{\lambda - 0.5} F_{yp} A_p \quad (2\text{-}26)$$

For seismic design case,

$$V_{n,max} = 0.2 f_c' b_w h_{w0} + \frac{0.25}{\lambda} F_{yb} A_b + \frac{0.5}{\lambda - 0.5} F_{yp} A_p \qquad \text{for } \lambda > 2.5 \quad (2\text{-}27a)$$

$$V_{n,max} = 0.15 f_c' b_w h_{w0} + \frac{0.25}{\lambda} F_{yb} A_b + \frac{0.5}{\lambda - 0.5} F_{yp} A_p \qquad \text{for } \lambda \leq 2.5 \quad (2\text{-}27b)$$

2.1.5 ANSI/AISC 341 (2016)

AISC 341, seismic provisions for steel or composite structures, provides the shear strength of walls with composite boundary elements, concrete-encased steel plates (CESP), and concrete-filled steel plate (CFSP).

For RC walls with steel-concrete composite boundary elements, the shear strength is calculated assuming that the shear forces are carried by the reinforced concrete walls and the entire gravity and overturning forces are carried by the boundary elements in conjunction with the shear wall.

For CESP walls, the shear strength is calculated as follows:

$$V_n = 0.6A_pF_p \tag{2-28}$$

For use of Eq. (2-28), the following requirements should be satisfied:

The concrete thickness shall be a minimum of 100 mm on each side when concrete is provided on both sides of the steel plate and 200 mm when concrete is provided on one side of the steel plate. Steel headed stud anchors or other mechanical connectors shall be provided to prevent local buckling and separation of the plate and reinforced concrete. Horizontal and vertical reinforcement shall be provided in the concrete encasement to meet or exceed the requirements in ACI 318 Sections 11.6 and 11.7. The reinforcement ratio in both directions shall not be less than 0.0025. The maximum spacing between bars shall not exceed 450 mm.

Otherwise, the shear strength of CESP walls shall be calculated as follows:

$$V_n = 0.42A_pF_p\sin 2\alpha_w \tag{2-29}$$

where, α_w = angle of web yielding in degrees, measured with respect to the vertical. The angle of inclination, α_w, is permitted to be taken as 40°.

For CFSP walls with boundary elements, the shear strength is calculated

$$V_n = \kappa A_{fp} F_p \tag{2-30}$$

Where,

$$\kappa = 1.11 - 5.16\bar{\rho} \leq 1.0 \tag{2-31}$$

where, $\bar{\rho}$ = strength adjusted reinforcement ratio, which is calculated as

$$\bar{\rho} = \frac{A_{fp} F_p}{83 A_{cw} \sqrt{f_c'}} \tag{2-32}$$

where, A_{fp} = area of two faceplates on both sides of web section; and A_{cw} = area of infill concrete between faceplates. Note that for most cases, 0.9 $\leq \kappa \leq$ 1.0.

For CFSP walls without boundary elements, the shear strength is calculated for the steel plates alone, in accordance with Eq. (2-28).

2.1.6 AISC N 690 (2018)

AISC N 690, which is special design provisions for safety-related nuclear facilities (NPP), provides the shear strength of CFSP walls, based on Von-Mises yielding of two faceplates and orthotropic properties of cracked infill concrete. Since AISC 341 refers to AISC N 690, the shear strength of CFSP walls is calculated as Eq. (2-29).

2.2 Existing Models for Web Crushing Capacity

Existing design codes, described in the previous section, permits the use of their shear strength equations only for strength-based design, depending on the design cases: general and seismic. However, there has been researches on the web crushing capacity of RC walls correlated with the deformation demand, which enables deformation-based design. Some of the researches are presented here, as follows:

2.2.1 Oesterle et al. (1984)

Oesterle et al. suggest an analytical model to correlate web crushing strength with deformation demand, based on the experiments conducted by Portland Cement Association (PCA) (Oesterle et al. 1979). The tested walls with flanged and barbell cross section all failed due to web crushing after significant shear and flexural yielding; significant inelastic deformation with fan-shaped shear cracking was attained in the plastic hinge zone, prior to any degradation of load-carrying capacity.

Based on the traditional truss analogy, the web crushing strength is defined as a function of the diagonal strut angle θ and effective average strut compressive strength kf_c', of which the equation form is similar to the expressions for the maximum shear strengths of Eurocode 2 and fib MC.

$$\frac{V_{wc}}{t_w d} = v_{wc} = kf_c' cos\theta sin\theta \tag{2-33}$$

This also indicates that, although the fanning crack pattern produce higher peak stresses in the plastic hinge zone, the model assumes the average stress distribution in the effective shear section and thus adopts the effective average strength factor k which is calibrated from the test results (0.16 – 0.49 from the PCA wall tests). The measured k is related to strain condition, as suggested by Collins (1978), and the following relationship for k is provided:

$$k = \frac{3.6}{1 + \frac{2\gamma_m}{\varepsilon_o}} \tag{2-34}$$

where, γ_m = maximum average shear distortion measured within the plastic hinge zone prior to web crushing; and ε_o = axial strain at peak compressive stress of concrete.

The relationship between total drift ratio δ_p (= flexural rotation plus shear distortion) and shear distortion γ within the plastic hinge zone (i.e., inter-story drift ratio) is determined from a linear regression analysis of test data.

$$\gamma = \left(0.76 - 2.6\frac{N}{A_g f_c'}\right)\delta_p \qquad \text{for } 0 < N/A_g f_c' \leq 0.09 \tag{2-35a}$$

$$\gamma = 0.52\delta_p \qquad \text{for } N/A_g f_c' > 0.09 \tag{2-35b}$$

By substituting Eq. (2-35) into Eq. (2-33) and (2-34), the relationship between web crushing strength and drift ratio within the plastic hinge zone is developed, in which the concrete strain ε_o at peak compressive stress is assumed to be 0.0025.

$$v_{wc} = \frac{1.8 f_c'}{1 + \left(600 - 2000\frac{N}{A_g f_c'}\right)\delta_p} \qquad \text{for } 0 < n_a \leq 0.09 \tag{2-36a}$$

$$v_{wc} = \frac{1.8 f_c'}{1 + 420\delta_p} \qquad \text{for } n_a > 0.09 \tag{2-36b}$$

For design of web crushing strength, Eq. (2-36a) and (2-36b) are simplified assuming inter-story drift limit of 2.0 %.

$$v_{wc} = 0.14 f_c' + \frac{N}{2 l_w t_w} \leq 0.18 f_c' \tag{2-37}$$

2.2.2 Paulay and Priestley (1992)

To prevent premature web crushing failure of walls, Paulay and Priestley recommend that the shear stress demand be limited to $v_{wc} \leq 0.16f_c'$. However, the tests conducted by PCA (Oesterle et al. 1979) and the University of California at Berkeley (Vallenas et al. 1979) reveals that, despite the limitation on maximum shear stress above, web crushing in the plastic hinge zone could occur at displacement ductility ratios of 4 or more. Only in the walls with ductility demand of 3 or less, the shear strength equal to or greater than $0.16f_c'$ could be attained. In particular, it is noticed that highly confined boundary elements could resist significant shear after the failure of the concrete web, due to their short column effect or dowel action. Nevertheless, to prevent web crushing failure, it is recommended to rely more on the shear resistance of the wall web, rather than on the second defense of boundary elements. To ensure this, the shear stress demand, used as a measure of diagonal compression, is limited by the following relationship, where the web crushing strength is proportional to concrete strength, f_c', but degrades with the increased displacement ductility, μ:

$$v_{wc} = \left(\frac{0.22}{\mu} + 0.03\right) f_c' \leq 0.16 f_c' \leq 6MPa \tag{2-38}$$

2.2.3 Hines and Seible (2004)

To assess the web crushing behavior of RC walls, Hines and Seible clearly distinguish between elastic and inelastic web crushing failure mechanisms (**Fig. 2-2**). The elastic zone, which is the remaining region other than the plastic hinge zone, is stressed mainly under in-plane shear stress while the effect of flexural strain is not significant. Thus, elastic struts with parallel shear cracking are formed in the wall web that have not experienced significant tensile strains along both the vertical and horizontal directions. On the other hand, in plastic hinge zone, large flexural strains with horizontal flexural cracks prohibit shear transfer into the wall base at any location except for the flexural compression zone, thus the struts should fan upward until they are able to carry the full inelastic shear force. These inelastic fanning struts are denoted as inelastic or flexure-shear struts.

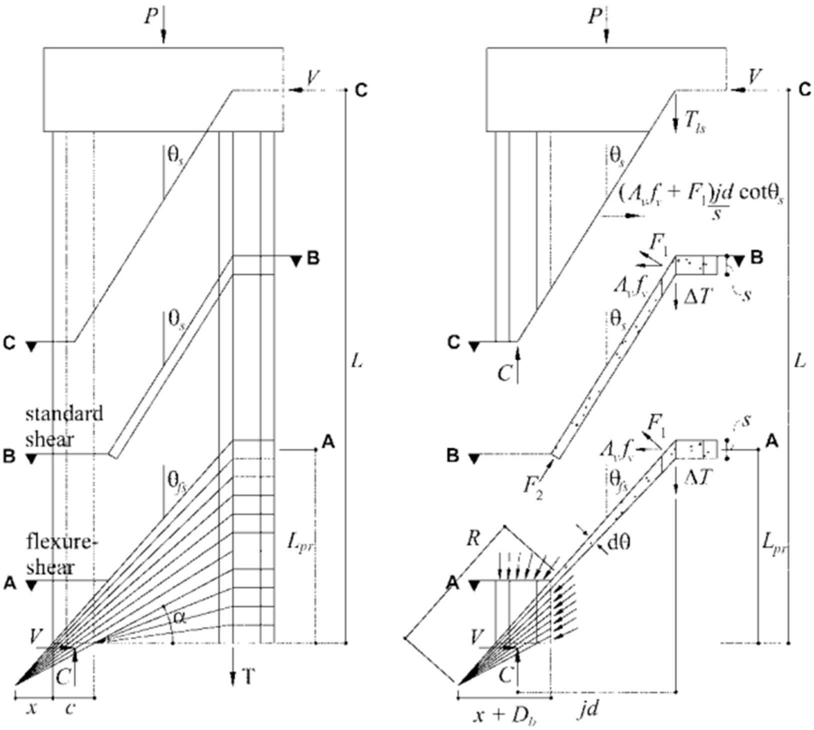

Fig. 2-2 Free body diagrams used for assessing inelastic web crushing capacity of structural wall with confined boundary elements.

The approach to web crushing capacity is based on the assessment of capacity and demand on individual struts inside the elastic zone and plastic hinge zone. The force demand on the elastic strut (N_{Ds}) is calculated from equilibrium analysis of its free body diagram, assuming that the depth of the individual elastic strut is proportional to the vertical spacing s_h of horizontal shear reinforcement. The capacity of the elastic strut (N_{Cs}) is calculated according to the web crushing equation proposed by Oesterle et al. (1984) and Paulay and Priestley (1992).

$$N_{Cs} = kf_c' t_w s \sin\theta_s \tag{2-39}$$

$$N_{Ds} = \frac{\Delta T}{cos\theta_s} - f_1 s t_w \sin\theta_s \tag{2-40}$$

where, k = compression softening factor for concrete; ΔT = net flexural tension force applied to the elastic strut (= Vs_h/jd) ; f_1 = principal tensile stress in the concrete; and θ_s = inclination angle of elastic struts.

The demand and capacity of the inelastic struts depend on the geometry of the plastic hinge zone where fanning cracks are formed. Among the fanning cracks, the top-most strut with the smallest inclination angle from the vertical is regarded as the critical inelastic strut to assess the inelastic web crushing strength (shear transfer through the struts near the wall base is less effective due to the greater strut angle). Further, it is assumed that web crushing occurs at the tip of the critical strut that meets the compression boundary elements. From these assumptions, the demand (N_{Dfs}) and capacity (N_{Cfs}) on the critical strut are provided as follows:

$$N_{Cfs} = kf_c' t_w R d\theta \tag{2-41}$$

$$N_{Dfs} = \frac{\Delta T}{cos\theta_{fs}} - f_1 s t_w \sin\theta_{fs} \tag{2-42}$$

where, $R\mathrm{d}\theta$ = depth of the critical inelastic strut; and θ_{fs} = inclination angle of the critical inelastic strut. In calculating θ_{fs}, the determination of plastic hinge zone length L_{pr} is required (refer to **Fig. 2-2**), which is calculated assuming θ_{fs}

$= \theta_s$.

The relevant variables are determined based on a moment-curvature analysis of the cross section and the strut geometry. The compression softening factor k for concrete is calculated according to modified compression field theory (MCFT), with an empirical approach for determining the principal tensile strain ε_1. The prediction of overall web crushing behavior is conducted by monitoring the capacity-to-demand ratios for both the elastic and inelastic struts.

2.2.4 Eom and Park (2013)

The analytical model of Eom and Park considers the effect of cyclic loading on the web crushing capacity of walls, on the basis of longitudinal elongation mechanism: After flexural yielding, longitudinal elongation occurs in the plastic hinge zone due to the plastic strains of flexural reinforcement, which is accumulated under repeated cyclic loading. This elongation mechanism increases diagonal tension cracking, and thus decreases the effective compressive strength of the web concrete, ultimately causing premature web concrete crushing. For a cantilever wall, the longitudinal elongation in the plastic hinge zone is derived based on truss analogy for the plastic hinge region and hysteretic stress-strain relationship of longitudinal flexural reinforcement. By using displacement compatibility, the longitudinal elongation within the plastic hinge zone is related with the overall lateral displacement of walls, for both the cases under monotonic loading and cyclic loading.

For cyclic loading and low compression force,

$$e_l = \frac{(\Delta_t - \Delta_{ef})\frac{h_s}{l_s}\left(1 + \eta\frac{\sigma_{lc}}{2f_y}\right) - \left(1 - \frac{l_p}{2l_s}\right)}{1 - \left(1 + \eta\frac{\sigma_{lc}}{f_y}\right)\left(1 - \frac{l_p}{l_s}\right)} \tag{2-43a}$$

For monotonic loading and high compression force,

$$e_l = (\Delta_t - \Delta_{ef})\frac{h_s}{2l_s} \tag{2-43b}$$

Where,

$$\sigma_{lc} = -f_y\left(\frac{A_b}{A'_b}\right)\left(1 - \frac{l_p}{l_s}\right) + \left[\frac{N}{A'_b} - f_{yw}\left(\frac{A_w}{A'_b}\right)\right]\left(1 - \frac{l_p}{2l_s}\right) \tag{2-44}$$

where, Δ_t = lateral displacement at the top of cantilever walls; Δ_{ef} = lateral displacement at flexural yielding; h_s = distance between the centers of the vertical flexural rebars at wall boundaries; l_s = shear span of walls; l_p = plastic hinge zone length (= d); σ_{lc} = compressive stress of boundary flexural rebars; f_y = yield stress of flexural rebars; η = coefficient to consider the Bauschinger effect (= 0.6); N (< 0 for compression) = axial compression force on walls; A_b and A'_b = areas of the tensile and compressive rebars at the wall boundaries; and f_{yw} and A_w = yield strength and area of longitudinal rebars in the web.

The web crushing strength model suggested follows the traditional form of truss model, as shown in Eq. (2-45), except that the effective shear section is limited to the web region (= h_w). Here, the effective compressive strength f_{ce} (= kf'_c) of concrete is defined according to MCFT, relating the longitudinal elongation with the principal tensile strain in the cracked web concrete. As the longitudinal elongation is the function of the lateral displacement (Eq. (2-43a) and (2-43b)), the web crushing strength is calculated for a given lateral displacement, as follows:

$$v_{wc} = \frac{1}{2}\left(\frac{f'_c}{1.48 + 170(e_l/d)}\right)\left(\frac{h_w}{d}\right) \le \frac{1}{2}f'_c\left(\frac{h_w}{d}\right) \qquad (2\text{-}45)$$

2.3 Literature Reviews on Existing Composite Walls

2.3.1 RC walls with composite boundary elements

This sections introduces the experimental and analytical studies on RC walls with boundary elements of CES columns or CFT columns. Most of studies have been conducted by Chinese researchers, because high-rise buildings have been constructed at an increasing rate in China. In high-rise buildings, the shear walls at the lower stories can be subjected to large axial compressive forces and flexural moments. To control the axial force ratio and provide adequate load-carrying capacity, thick concrete walls and large amounts of reinforcement are often required, which reduces the architectural floor area and decreases the overall constructability. Because of these potential deficiencies of RC shear walls for use in high-rise buildings, steel–concrete composite walls have gained popularity in engineering practice. Some of the researches are presented here, as follows:

1) Dan et al. (2011)

Dan et al. (2011) tested six RC web walls (1:3 scale) with concrete-encased steel (CES) columns, under cyclic lateral load and constant axial force (axial force ratio = 1.5–2.1%) (**Fig. 2-3**). The arrangement and cross section type of the embedded steel columns were considered as major test parameters.

The tested wall behavior was governed by flexure, with no major influence of the shear effects. The failure mode is the crushing of the compressed concrete and the tearing of the tensioned steel. The vertical reinforcing bars, placed in tension side yielded, but it never failed. On the compression side after concrete crushing, local buckling occurred.

By using high-strength concrete, the failure in compression was prevented before the steel yielding, providing good ductility. The tested strengths and deformation capacities were slightly greater that the counterpart RC walls. A higher confinement of boundary elements using more dense stirrups could improve the results by reducing the concrete degradation. For the specimen using partially-encased steel sections, local buckling of the steel flange appeared and developed quickly in the failure. The cross section type of the CES had little effect on the load-displacement behavior.

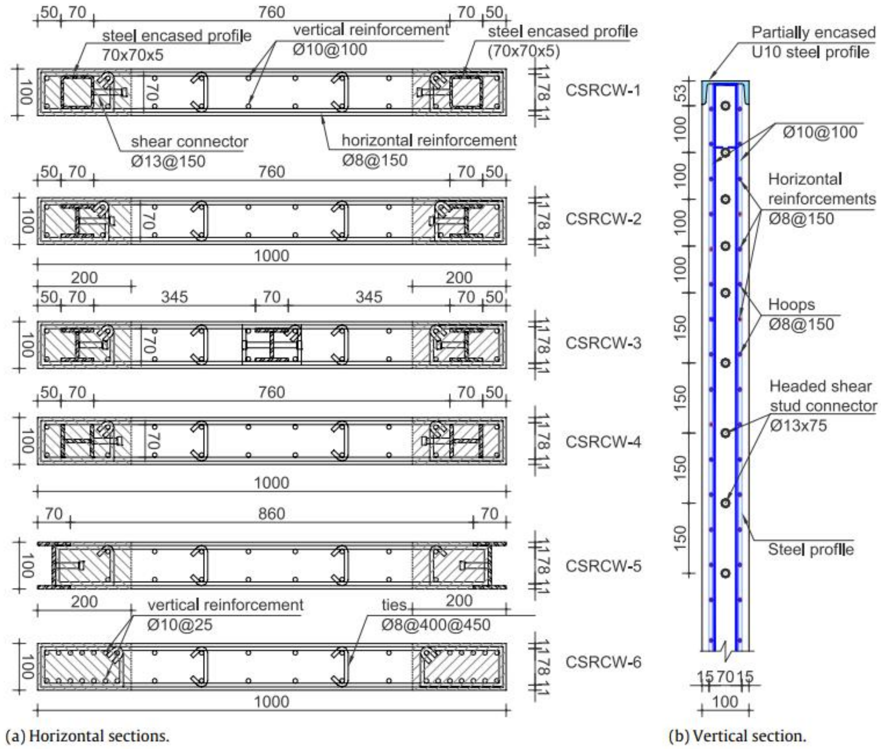

Fig. 2-3 Details of wall specimens in Dan et al. (2011).

2) Ji et al. (2015)

Similar testing and design parameters as those of Dan et al. (2011) were used for the test specimens, but much higher axial force ratio (= 32–34%) was used. The flexural strength and deformation capacity were greater than those of counterpart RC wall. The flexural strength of the walls increased with increasing area ratio of embedded steel section, while the section type of the steel did not affect the flexural strength. The walls under high axial force ratio had an ultimate lateral drift ratio of approximately 1.4%.

They developed a multi-layer shell element model using OpenSees program. The numerical model was validated through comparison with the test data. The model was able to predict the lateral stiffness, strength and deformation capacities of composite walls with a reasonable level of accuracy. The effective flexural stiffness of composite walls was highly dependent on the applied axial force ratio. They reported that the effective flexural stiffness of RC walls suggested by Adebar et al. (2007) appeared to be appropriate for use in estimating the effective flexural stiffness of composite walls under high axial force ratios.

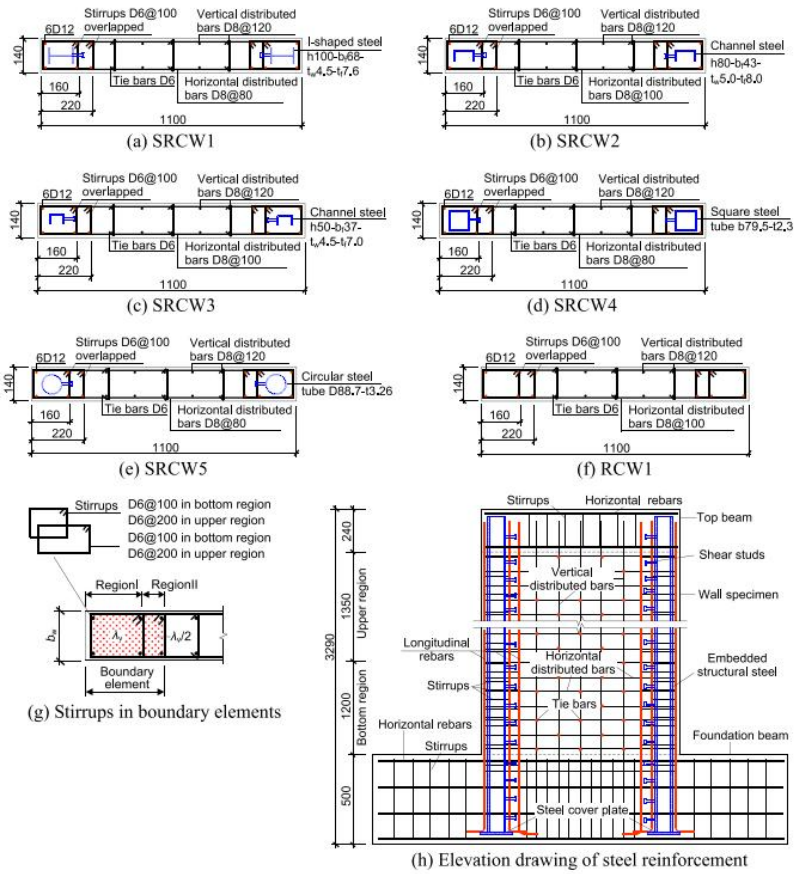

Fig. 2-4 Details of wall specimens in Ji et al. (2015).

3) Ren et al. (2018)

Ren et al. adopted a carbon fiber–reinforced polymer (CFRP) to confine the core concrete of boundary elements (**Fig. 2-5**). Furthermore, the confined concrete core with CFRP was encased in steel tubes, providing high levels of confinement and safety under large axial stresses.

To evaluate its seismic performance, the proposed wall was tested under constant axial compression force and lateral cyclic loading. Three additional shear walls with different boundary column configurations were also tested: (1) an ordinary shear wall, (2) a shear wall with CFT boundary columns, and (3) a shear wall with double-skin CFT boundary columns. All the walls showed flexure-dominated behavior.

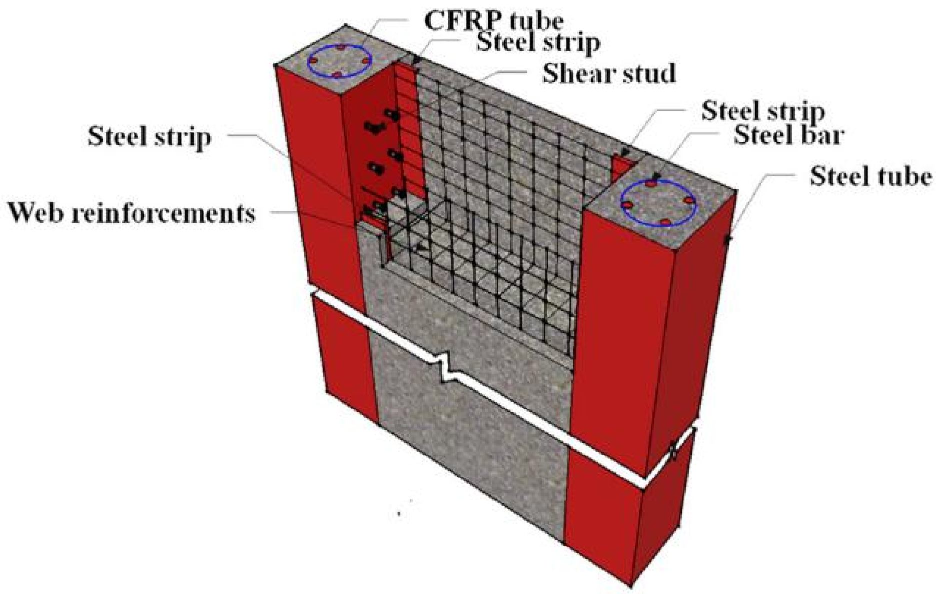

Fig. 2-5 CFRP-reinforced CFT boundary elements (Ren et al. 2018).

The seismic performance of the proposed wall was superior to that of the ordinary shear wall and the shear wall with boundary CFT columns. The proposed wall had the similar load-carrying capacity as that of the shear wall with double-skin CFT columns, but the post-peak strength degradation was less brittle, thus increasing displacement ductility and larger dissipation capacity.

Despite the effort to provide high confinement to boundary concrete, the displacement ductility of the proposed wall was also limited by local buckling of the steel tubes and subsequent crushing of concrete confined by the steel tube. Further, spalling and delamination of concrete was concentrated at the interface between the boundary elements and the web, deteriorating their structural integrity (**Fig. 2-6**). Diagonal tension cracking and crushing were also severe at the center of the web.

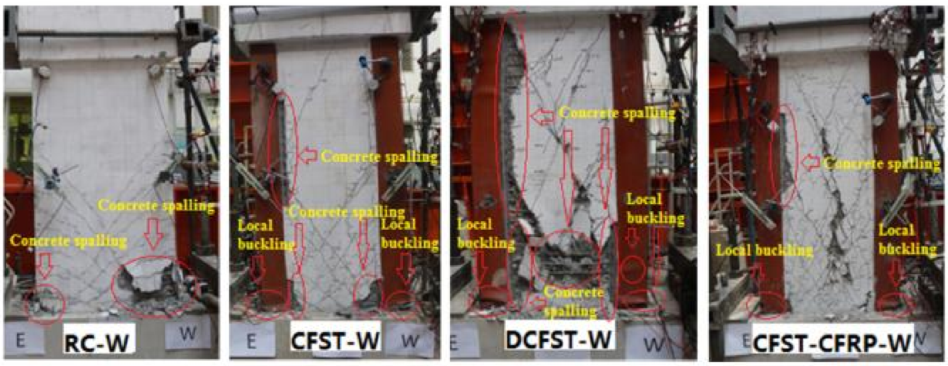

(c)Ultimate state.

Fig. 2-6 Ultimate failure mode of test specimens in Ren et al. (2018).

4) Zhang et al. (2021)

Zhang et al. used high-strength concrete (65–88 MPa) and steel (yield strength = 602–739 MPa for rebars and 364–481 MPa for steel plates) for RC walls with CFT boundary elements. Five specimens were tested to investigate the influences of the concrete strength, steel tube type, steel fiber volume ratio (for steel fiber-reinforced concrete), and double-skin bottom plates (for strengthening of plastic hinge zone) on the cyclic performance of the composite walls. In particular, for connection of steel boundary elements and concrete web, specially manufactured shear connectors were used (**Fig. 2-7**).

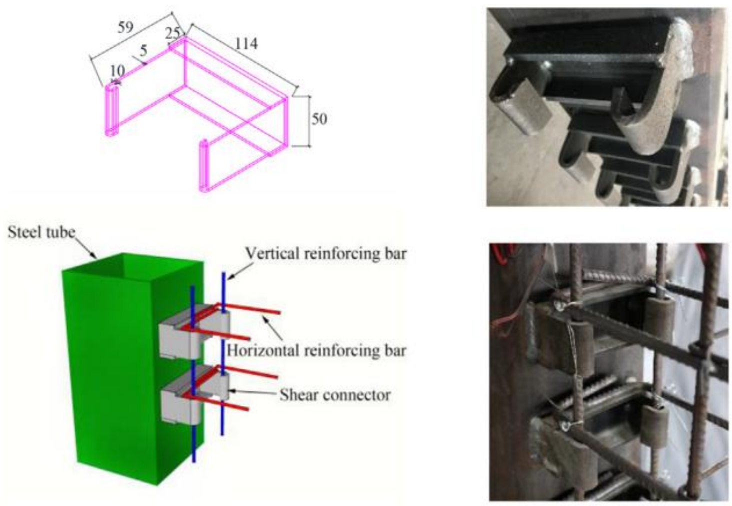

(a) Schematic diagram (b) Photos of the specimen production

Fig. 2-7 Steel shear connectors used for wall specimens of Zhang et al. (2021).

All specimens exhibited flexural-dominated failure modes, where the shear connectors reliably linked the boundary CFT columns to the wall web. By increasing the concrete strength, the load-carrying capacity (flexural strength), deformation and energy dissipation capacities were improved. In particular, steel fibers effectively restrained crack development and increased the flexural deformation capacity, thereby increasing the hysteretic performance of the walls.

The strengthening of plastic hinge zone using double-skin steel plates (i.e., faceplates) effectively confined the non-fiber-reinforced web concrete, thus increasing the load-carrying capacity and deformation capacity of the composite wall. Furthermore, the stiffness degradation was alleviated. Based on the test results, an analytical model for section analysis was proposed to predict the flexural strength of the composite walls.

5) Tupper 1999

Tupper evaluated the cyclic performance of RC walls with three types of boundary elements: hollow steel stub section, steel channel section, and conventional RC section. Among them, the specimen using steel channel boundary elements (**Fig. 2-8**) exhibited better energy dissipation capacity than the other two specimens. However, significant separation occurred between the steel channel and RC web. The failure mode of the composite wall was determined by local buckling of the steel boundary elements.

The steel channel method of Tupper was similar to the proposed SUB-C walls. However, due to the short web length of the conventional channel section, the area of steel section and confined boundary zone was limited.

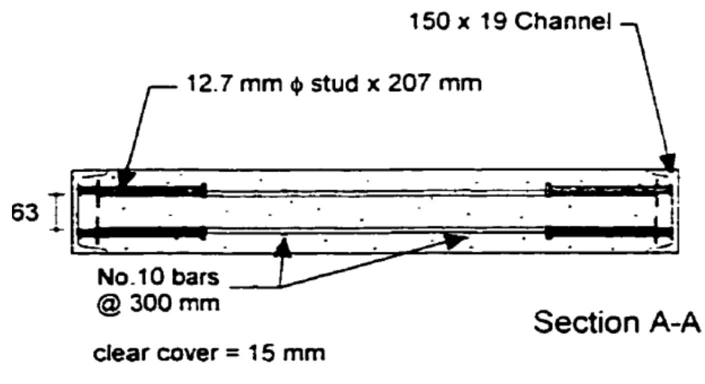

Fig. 2-8 RC wall specimen with boundary elements of steel channel section (Tupper, 1999).

2.3.2 Concrete-encased steel plate walls

For better applicability in high-rise buildings, many researchers and engineers studied the use of the composite walls with a web steel plate with RC ensacement on one or both sides (CESP walls). In super high-rise walls, the RC shear walls at the bottom becomes more thicker and less ductile due to the increased shear and gravity load demands. Further, due to the thick walls, architectural usable area is reduced, and the relevant construction becomes more challenging. For such structural and architectural demands, the use of CESP walls is increasing for the following reasons: 1) for the same shear capacity, the thickness and weight of concrete walls are reduced, which provides larger usable space and smaller foundations. 2) ductility is improved by the potential yielding of steel plates both in the web and boundary elements, which is more pronounced due to the concrete encasement that provides lateral restraint for plate buckling. 3) Further, the concrete encasement provides strong insultation against high temperature, which reduces the extra cost for fire-proofing. Some of the researches on CESP walls are presented here, as follows:

1) Astanel-Asl (2002) & Zhao and Astaneh-Asl (2004)

Both studies provides the experimental tests on the same composite wall system consisting of a steel plate panel and RC encasement bolted to each other. The test results showed that the composite steel plate walls provided excellent lateral resistance and deformation capacity exceeding inter-story drift ratios of 4% without degradation of load-carrying capacity.

Further, they proposed a more innovative composite system using a gap between RC walls and the boundary steel columns and beams (**Fig. 2-9**): due to the gap, the RC wall is not engaged with the frame and thus not involved in resisting lateral loads under relatively small lateral displacements. Thus, at small displacements, the system behaves as "stiffened steel shear wall", developing stable yielding behavior of the embedded steel plates. When the large displacement is developed, the RC panel begins to resist against the wall shear, and provide extra stiffness in compensation for the stiffness loss of the steel plates due to yielding.

The test results revealed that, due to the presence of the gap in the innovative system, damage to the concrete wall under relatively large cycles was much less than the damage to the concrete wall in a traditional system.

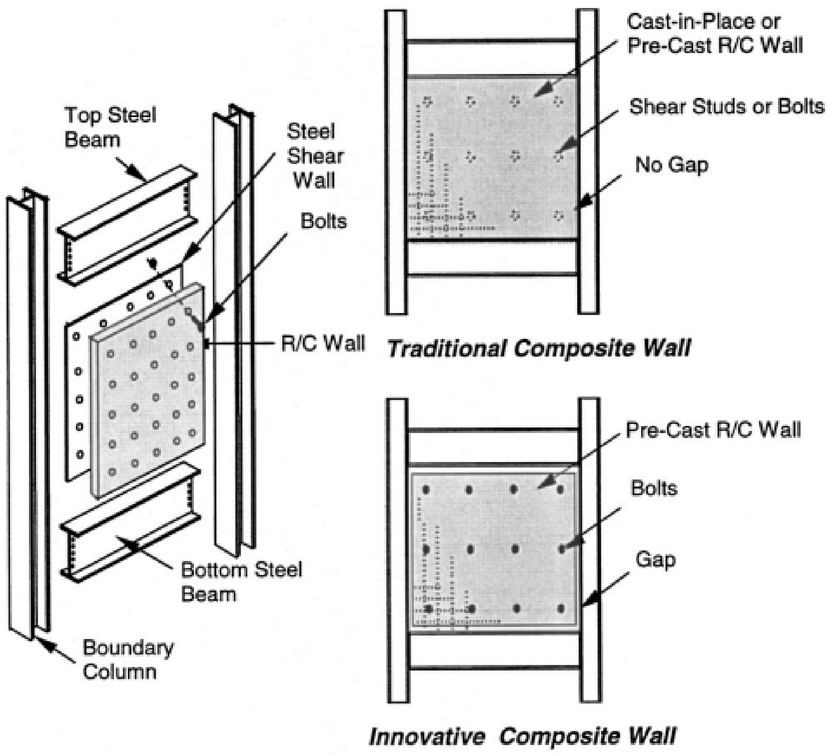

Fig. 2-9 Composite shear walls with boundary frame studied in Zhao and Astaneh-Asl (2004)

2) Xiao et al. (2012)

They prepared six CESP wall specimens for testing, and tested the effect of concrete strength (47.7 MPa to 84.1 MPa) and axial fore ratio (0.36 to 0.58) on the lateral load-carrying capacity and deformation capacity of the walls. They also prepared the same number of counterpart RC wall specimens for comparison. They reported that the CESP specimens showed lighter damage and better hysteretic characteristics than those of traditional RC specimens under the same axial compression force. As the axial compression force increased, the ultimate loading capacity increased but the displacement ductility of the test specimens decreased significantly.

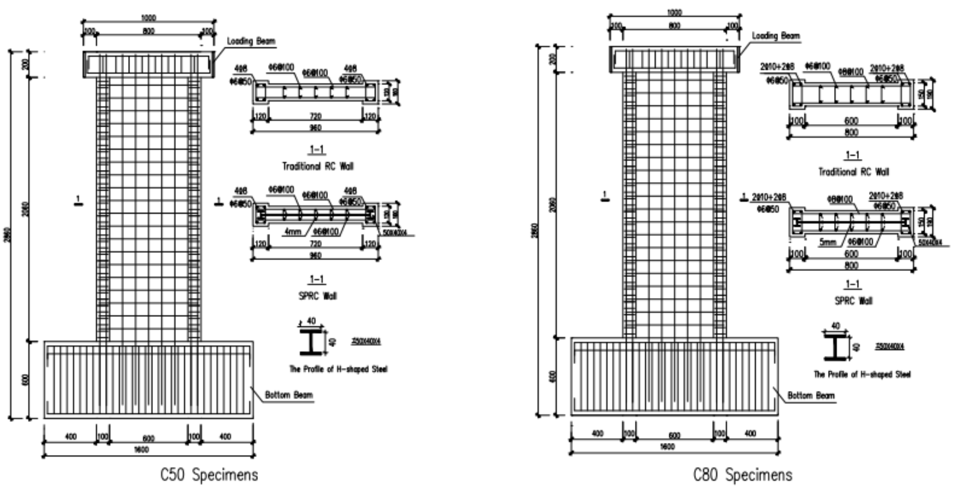

Fig. 2-10 CESP and RC specimens of Xiao et al. (2012)

3) Wang et al. (2018)

They performed extensive experimental tests on a total of 16 CESP wall specimens and 3 traditional RC wall specimens. They considered the design parameters including the aspect ratio, wall thickness, steel plate ratio, concrete strength, detailing between steel plates and concrete (e.g., lateral ties, shear studs, both, or none). Among them, the test results showed that the thickness of the wall is the most important parameter to increase deformation capacity, ductility and energy dissipation capacity, followed by detailing and thickness of the steel plate. They reported that, compared with lateral ties, the structural detailing of shear studs on steel plates was more effective.

In the walls with aspect ratio of 2.0, their failure mode was determined by flexural damage: damage and yielding of boundary elements, followed by crushing of concrete at the entire region of the wall base. On the other hand, in the wall with lower aspect ratio of 1.5. their behavior is controlled by horizontal crack at the bottom of the concrete, despite the use of web steel plates. Ultimately, combined flexure-shear failures appeared. Further, local buckling occurred across the entire cross section of the embedded web plate (**Fig. 2-11**).

Fig. 2-11 Failure modes of flexure-shear walls in Wang et al. (2018)

4) Ziang et al. (2019)

They conducted an experimental investigation to study both shear and flexure behavior of CESP walls using high-strength concrete. Two different aspect ratios (1.5 and 2.7) were considered to develop different failure modes. Embedment of steel plates and axial force ratio were also considered as test parameters.

For the CESP specimens, the ultimate drift is larger than 1.0% and the ductility was around 4 when the axial force ratio is lower than 0.5. A more severe strength and stiffness degradations were observed in flexural yielding-specimens with the axial force ratio higher than 0.5. When the axial force ratio increases to 0.58, the ductility factor substantially decreased to 2.61 and the ultimate drift ratio is lower than 1.0%.

Due to the small wall thickness, a relatively weak confinement was provided to the embedded steel plate, which resulted in severe buckling and subsequent spalling of the cover concrete (**Fig. 2-12**). Thus, the authors recommended that a higher transverse reinforcement ratio be used to improve the concrete confinement effect.

They measured the strains of the steel plates during the tests, to evaluate their shear strength contributions. The shear strength contribution of the embedded steel plates were almost 50% of the design shear strength, and gradually increased until failure. On the other hand, the RC contribution began to decrease before the load-carrying capacity reached its peak value. The reason was related to the premature damage of the cover concrete due to buckling of the embedded steel plates.

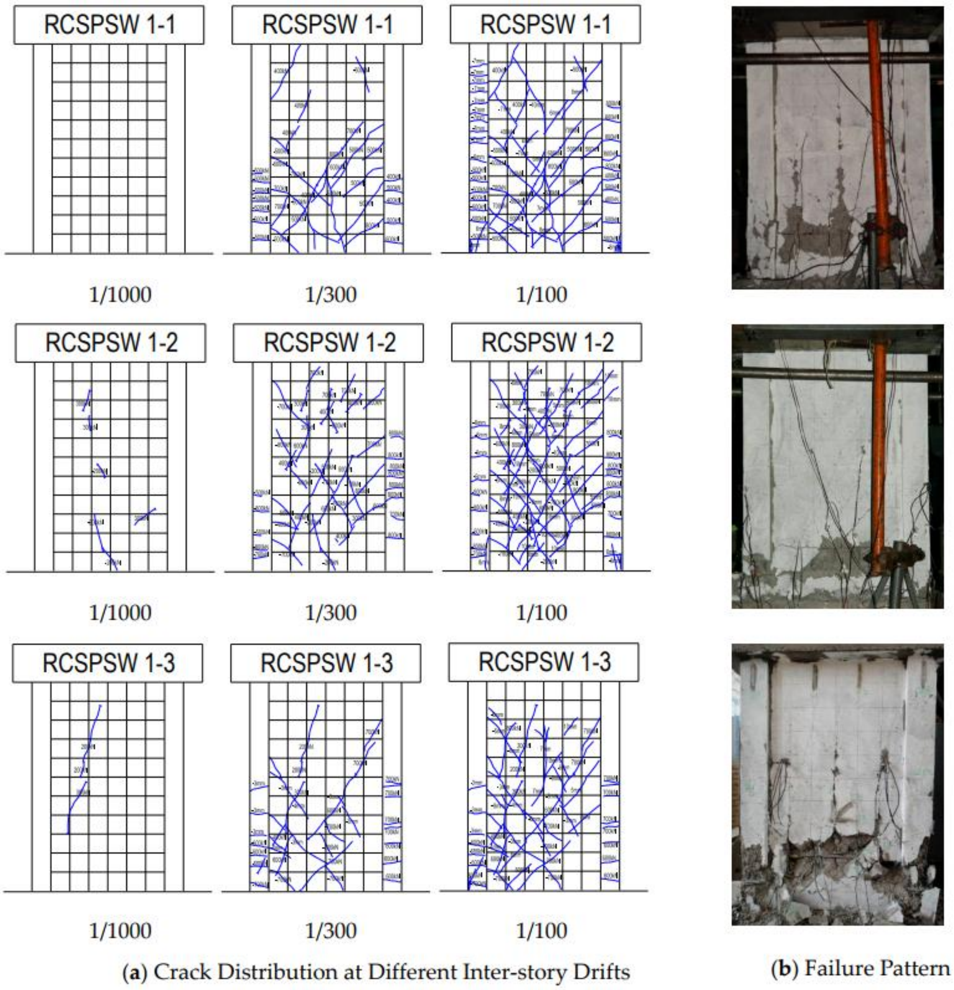

Fig. 2-12 Crack patterns and failure mode of CESP walls that failed in shear (Ziang et al. 2019)

2.3.3 Concrete-filled steel plate walls

Concrete-filled steel plate (CFSP) walls were conceived initially from the idea to eliminate concrete formwork and to provide strong shields against impact loading. Recently, they are also being considered for future small modular reactor (SMR) plants. Because of such usefulness, CFSP walls have long been studied for their use in safety-related facilities such as nuclear power plants and containment structures. Since the 1980s, extensive studies on the behavior, analysis, and design of CFSP walls have been done in Japan, to establish design guidelines (JEAG 4618, 2005) for CFSP walls in nuclear facilities. Similar guidelines (KEPIC-SNG, 2010) were also developed by researchers in South Korea. CFSP walls were also studied for use in high-rise buildings, because of their good constructability and structural performance. Some of the researches on CFSP walls are presented here, as follows:

1) Ozaki et al. 2001

They focused on the fundamental flexural and shear performances of CFSP walls, by testing under lateral loading. Further, the effect of an opening on the structural performance was investigated. From the tests, they found similarity in design for shear and flexural strengths of CFSP walls with those of RC walls. The influence of an opening to the strength was also be evaluated using the method for RC walls.

2) Varma et al. (2011)

Varma et al. made a significant contribution to the development of design strengths and relevant guidelines for CFSP walls in nuclear facilities. Extensive experimental and analytical studies have been conducted by him and his research team, for CFSP walls subjected to in-plane shear loading, out-of-plane shear and flexure loading, biaxial lateral loading, and blast loading.

For in-plane shear loading, they developed mechanics-based model simulating the composite action of two steel faceplates and cracked orthotropic concrete. From the model, a tri-linear shear force-shear strain relationship was developed. The model explicitly accounts for the composite section behavior before cracking and the cracked orthotropic composite behavior after cracking. The reliability of the model was verified by comparing the model prediction with the experimental results from tests conducted in Japan. Currently, the simplified version of the mechanics-based shear strength was adopted for AISC design provisions for CFSP walls in nuclear facilities (AISC N690, 2018).

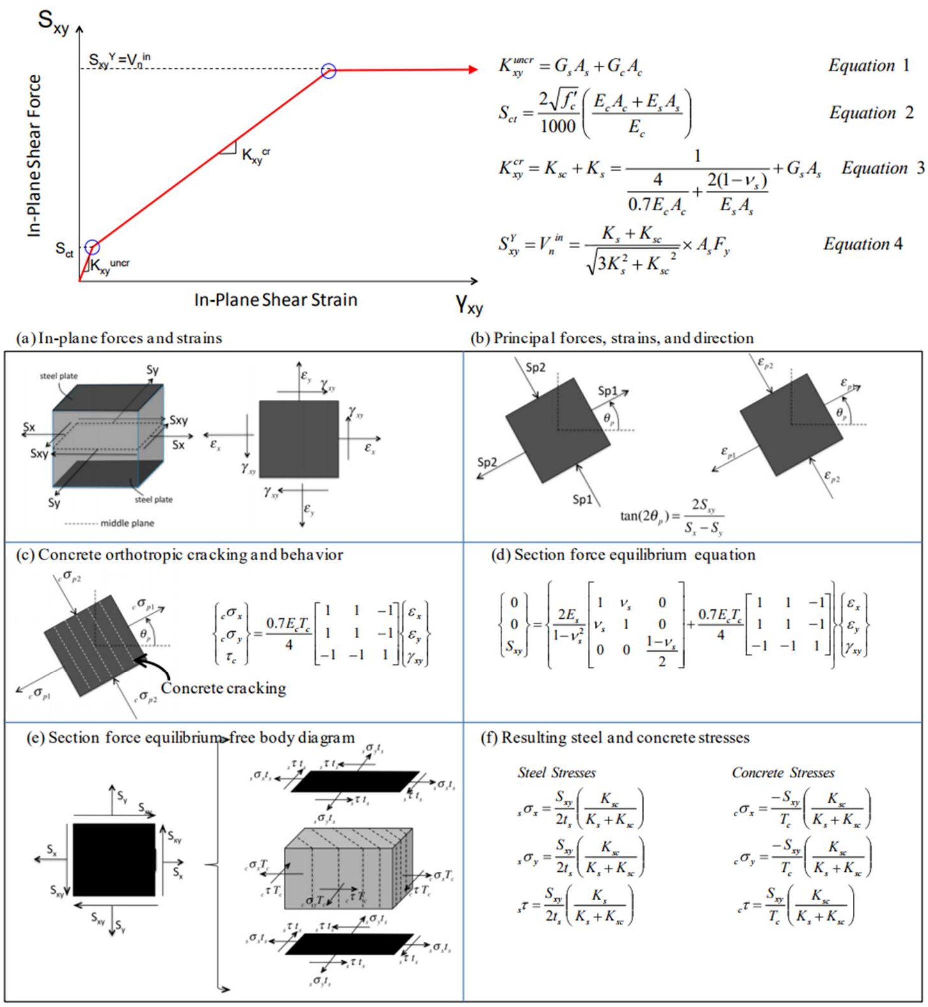

Fig. 2-13 Summary of in-plane composite shear behavior (Varma et al. 2011)

3) Zhang et al. (2014)

They focused on the buckling behavior of faceplates in CFSP walls depending on the details of shear connectors. Steel headed shear studs are often used to prevent local buckling of steel faceplates and to provide composite action between steel plates and concrete infill of CFSP walls. From the experimental and numerical parametric studies, they developed the design requirements (for stud spacing and plate slenderness ratio) to develop yielding of faceplates and to prevent their buckling. Further, those requirements were adopted in AISC design provisions for CFSP walls in nuclear facilities (AISC N690, 2018).

4) Booth et al. (2020)

They advanced the shear strength proposed by Varma et al. (2011), by considering final compression failure of the concrete infill. The previous model was based on Von-Mises yielding of faceplates. They assumed that, as load levels increase beyond the faceplate yielding limit state, the diagonal compression in the cracked concrete infill is anchored and resisted by the boundary elements. Thus, the ultimate strength of CFSP walls then depends on the yield strength of the steel faceplates and the diagonal compression capacity of the cracked concrete infill.

From nonlinear finite element models, they revealed that the reduced concrete strength converged to a specific value of 50% of original concrete strength. The proposed, calibrated analytical approach was verified using the existing database of tests conducted on SC shear walls with flanges or boundary elements. Consequently, they proposed an analytical model to predict the entire in-plane shear force-shear strain relationship of CFSP walls.

5) Nie et al. (2013)

They studied CFSP walls with boundary CFT columns (**Fig. 2-14**). Twelve CFSP wall specimens were experimentally tested under large axial compressive force and reversed cyclic lateral load. No evident buckling of surface steel plates was observed due to reasonable width-to-thickness ratios of steel plates and properly arranged batten plates, so that the surface steel plates and infill high-strength concrete could work compatibly in the whole loading process. The typical failure modes were local buckling of steel plates and vertical weld fracture with slight horizontal fracture at the boundary CFT columns.

Based on the test results, they proposed that the width-to-thickness ratio of CFT boundary elements be equivalent to those for CFT columns. Finally, a strength prediction approach based on the section analysis method was presented

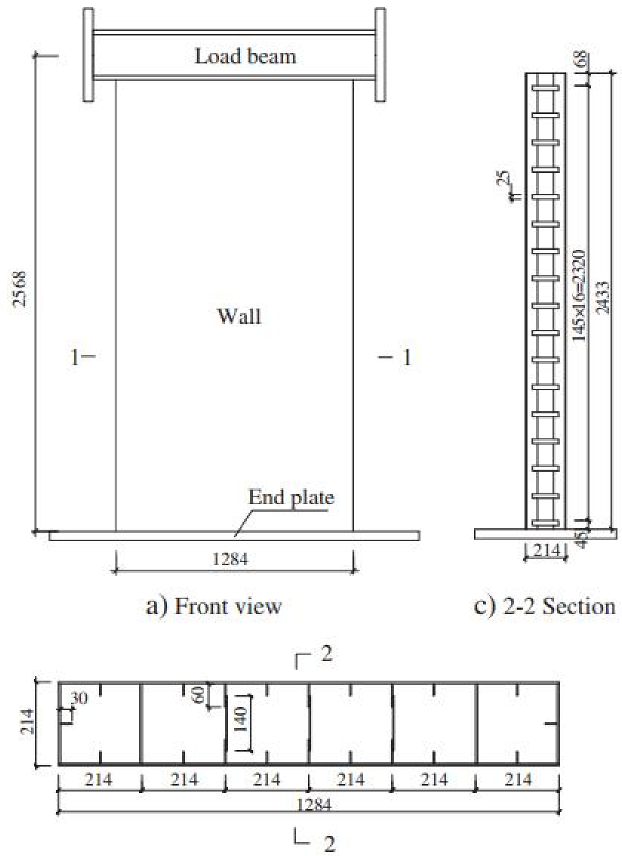

Fig. 2-14 Details of CFSP specimens in Nie et al. (2013).

6) Yan et al. (2018)

Yan et al. primarily investigated the effect of overlapped headed studs on the composite behavior of CFSP walls (**Fig. 2-15**). Thus, the major test parameters included the height of overlapped headed studs, axial force ratio, introducing steel tubes in boundary columns, and aspect ratio of CFSP walls. The tested seven specimens all failed in flexure mode that is characterized by local buckling occurred to the steel face plates at wall base of the specimen, tensile facture of the boundary steel column, and crushing of concrete in the boundary column.

Increasing the height of overlapped headed studs in the CFSP walls improved the seismic behavior of the CFSP walls. Increasing the height of the headed studs from 50 mm to 90 mm increased the pullout resistance of headed studs from the infilled concrete, which resulted in higher confinement to the concrete and larger buckling resistance of steel faceplates under compression. These improvements increased the deformation capacity and energy dissipation capacity of the CFSP wall, and it also delayed the local buckling of the steel faceplate, rigidity and strength degradation of the CFSP wall. Thus, they recommended that the height of headed studs be crossing through the cross section for the CFSP walls.

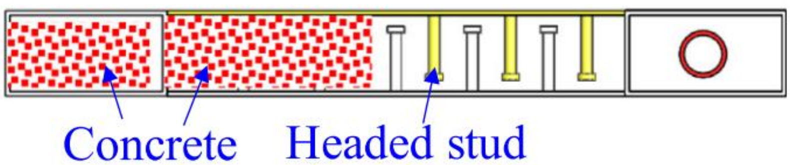

Fig. 2-15 Details of overlapped headed studs (Yan et al. 2018).

7) Eom et al. (2009)

Eom et al. performed cyclic lateral loading tests to investigate the seismic behavior of isolated and coupled CFSP walls with rectangular and T-shaped cross sections. The wall specimens failed mainly by tensile fracture of the welded joints at the wall base and coupling beams, or by local buckling of the steel plates. In particular, they emphasized the concerns about premature fracture of the welded joints at the wall base, where high stress concentration is developed by the welded joints and large plastic strain demand arising from the large depth of the walls.

In preventing early fracture of the welded connection at the wall base, the cover plate strengthening method, which uniformly increased the steel plate thickness near the connection region, was superior to the rib plate strengthening method (refer to **Fig. 2-16**). Thus, they recommended that the redundant strengthening scheme, such as the cover plates used in this study, be used to make the wall base stronger than the wall.

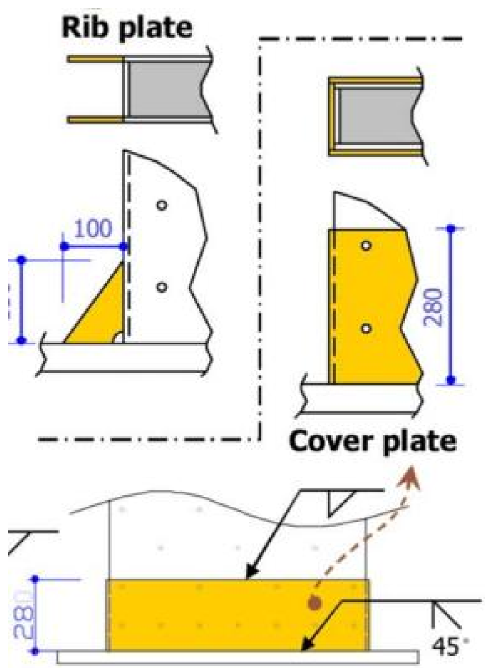

Fig. 2-16 Base-strengthening methods proposed by Eom et al. (2009).

8) Zhao et al. (2020)

Zhao et al. tested the cyclic lateral loading behavior of four CFSP wall specimens with CFT boundary elements, two with flat faceplates and two with corrugated faceplates. All specimens failed in flexure with a progression of steel tube fracture, steel faceplate buckling, and concrete crushing at wall bottom.

The corrugated CFSP walls and the flat CFSP wall with standard bolt spacing exhibited an ultimate drift ratio around 3.4% and a ductility ratio greater than 5.4, while the flat CFSP wall with bolt spacing 50% over code limit presented early faceplate buckling and undesired seismic performance.

The use of corrugated faceplates significantly increased the stiffness, ductility and energy dissipation. This advantage was more pronounced when faceplates with denser corrugation was used. Even with a sparse corrugation and 50% reduction in the number of tie bolts, the corrugation still eliminated elastic local buckling of faceplates.

The steel faceplates contributed to 5-15% of the total base moment and approximately 50% of the total base shear. Corrugated faceplates resisted more flexural moment than flat faceplates, particularly with denser corrugation. However, corrugated and flat faceplates resisted approximately same amount of shear.

The boundary CFT columns not only resisted 50-60% of total base moment also resisted approximately 40% of shear. The concrete infill provided 25-40% of total base moment and approximately 10% of shear.

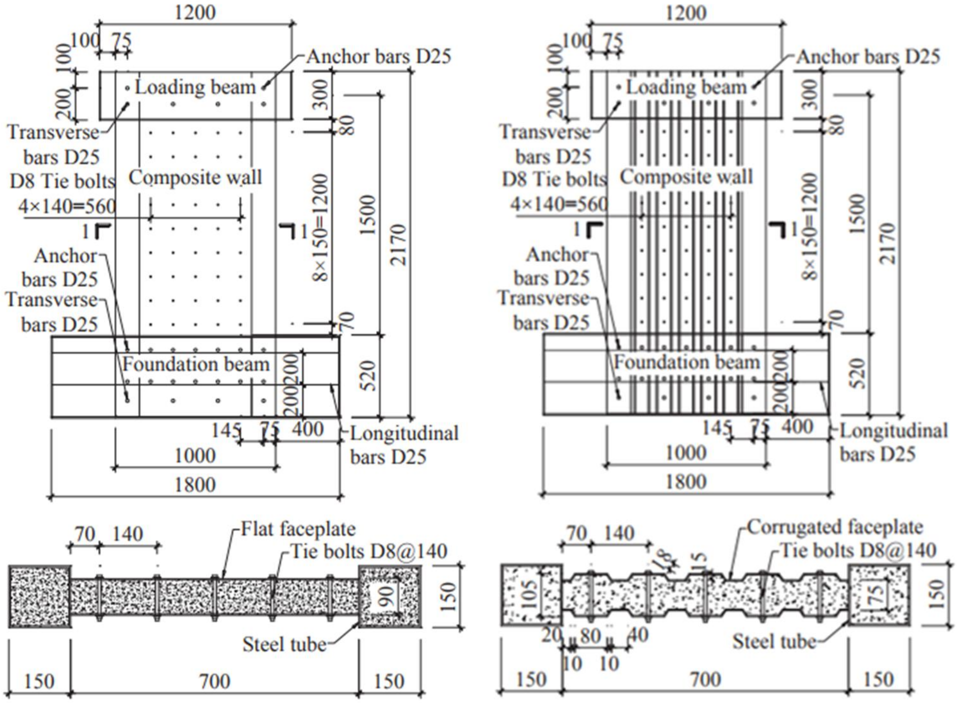

Fig. 2-17 CFSP wall specimens with flat faceplates and corrugated faceplates

(Zhao et al. 2020)

2.4 Discussion and Research Hypothesis

In Sections 2.1, the existing shear strength models for RC walls and steel-concrete composite walls were reviewed, for their application to the proposed SUB-C walls. The RC design methods of ACI 318 (2019), Eurocode 2 & 8 (2004), and fib MC (2010) provide the shear strength of RC walls, based on the truss mechanism of concrete and shear reinforcement. In these methods, the shear contribution of boundary elements is not directly accounted. Similarly, AISC 341 (2016) recommends that the shear force on walls be resisted solely by RC walls, even with composite boundary elements. Only JGJ 138 (2016) considers the contribution of boundary steel sections in calculating the shear strength of composite walls. However, its application is limited to the boundary CES elements.

On the other hand, the existing studies on composite walls revealed that the boundary elements fairly contributed to the shear strength of walls (e.g., Zhao et al. 2020), even though they primarily resisted flexural moments on the walls. Further, there was some statement in the existing studies that the increased strength of boundary elements made the concrete in the wall web more susceptible to damage, because the stiffness ratio of the boundary frame to the wall web increased (Ren et al. 2018). From these observations, it can be presumed that the use of steel boundary elements with large area may provide notable shear resistance to walls.

In the flexural tests on composite walls, the existing studies commonly stated that the use of composite boundary elements highly increased the flexural strength and deformation capacity of walls. Further, it was revealed that the use of CFT boundary columns was more effective than CES boundary columns. However, the use of CFT boundary columns had a shortcoming that the wall becomes susceptible to separation between the boundary elements and wall web, especially in the large deformation of walls. This is because the structural integrity between the CFT columns and concrete web depends only on the steel anchors attached to the steel sections, and their anchoring resistance can be significantly degraded under spalling and crushing of web concrete. Further, for all cases, the deformation capacity of the walls was limited by local buckling of the steel sections in the boundary elements, even with concrete encasement.

In the proposed SUB-C walls, large steel area is concentrated at wall boundaries, for high-performance walls. Thus, based on the observations from the existing studies, the following advantages are expected:

1) The steel U-sections with headed studs may provide adequate confinement to the infill concrete, because the studs act as confinement reinforcement and their confining behavior with steel U-sections becomes similar to that of CFT columns.

2) The steel U-sections with large sectional area may provide adequate shear resistance to the walls, because the shear force is more attracted in the boundary steel U-sections with high lateral stiffness.

3) Due the open steel section, the structural integrity between the boundary elements and wall web may be superior to that of the wall with boundary CFT elements, even though no special anchors are used.

4) The steel U-sections designed as compact section may delay the occurrence of local buckling, which increases the deformation capacity of walls.

These effects, mentioned above, were used as major hypotheses for subsequent verification studies.

Chapter 3. Cyclic Lateral Test of Flexural Specimens

3.1 Overview

In the proposed composite (SUB-C) walls, by using steel U-sections, large steel area can be concentrated at wall boundaries, which significantly increases the flexural strength and stiffness. Further, the deformation capacity can also be increased as the steel U-sections confined the boundary zone: crushing and spalling of the boundary concrete can be restrained in the large inelastic deformation of walls.

In this chapter, cyclic lateral loading tests were performed to investigate the flexural performance and failure mode of SUB-C walls. In particular, to verify the applicability on high-performance walls, a very large steel area was used for boundary elements, although the steel ratio exceeds the requirement of current design codes. The tested strength and stiffness were compared with the predictions of existing design methods. Further, the flexural strength and displacement ductility of SUB-C walls were compared with the test results of existing composite walls.

3.2 Design Strengths

3.2.1 Nominal flexural strength

The nominal flexural strength M_n of the composite specimens was calculated based on strain compatibility and the limit state of concrete crushing (ACI 318, 2019): linear strain distribution across the cross section and crushing strain of 0.003. In the present study, the distribution of concrete stress was approximated using uniform compressive stress of $0.85f_c'$ (f_c' = compressive strength of concrete), and neglecting tensile stress and confinement effect on concrete strength and ductility. For steel sections, the stress–strain relationships were idealized to be elastic–perfectly plastic. The predicted flexural strengths were compared with the test results, to investigate the effect of boundary steel U-sections on the flexural strength of the proposed composite walls.

3.2.2 Nominal shear strength

The nominal shear strength V_n of the specimens was calculated as the sum of the contributions of concrete and horizontal reinforcement, using 45-degree truss mechanism (ACI 318, 2019). When steel faceplates were used, V_n was calculated as the sum of the shear contributions of the cracked web concrete and steel faceplates (Varma et al. 2011; AISC N690, 2018). For all specimens, to assure flexural yielding before shear failure, the nominal shear strength was conservatively estimated, neglecting the contribution of boundary elements. Section 2.3 presents the detailed calculations of existing design methods to predict the shear strength.

3.2.3 Design of failure mode

The design of test specimens was intended to show ductile behavior after flexural yielding. Thus, to prevent premature shear failure, the nominal shear strengths V_n of the test specimens (= 2,842–2,864 kN for specimens with aspect ratio 2.5; 1,169–3,053 kN for specimens with aspect ratio 2.0, **Table 3-4**) were designed to be greater than the shear demands V_f (= M_n / l_s = 1,290–2,000 kN for specimens with aspect ratio 2.5, 828–1,421 kN for specimens with aspect ratio 2.0) resulting from the nominal flexural strengths M_n (**Table 3-4**).

3.3 Test Plan

3.3.1 Test parameters and specimens

Nine flexural wall specimens were prepared for testing. **Table 3-1** and **Table 3-2** shows the major design parameters (i.e., material and geometric properties) of the specimens with aspect ratio of 2.5 and 2.0, respectively. The dimensions of the specimens were length (l_w) × thickness (t_w) × height (h_w) = 1,800 mm × 300 mm × 4,500 mm for the specimens with aspect ratio of 2.5; and 1,600 mm × 200 mm × 3,200 mm for the specimens with aspect ratio of 2.0. In the names of the specimens, the first character indicates the structure type: **R** = reinforced concrete wall and **C** = composite wall using steel U-sections. The second character indicates the intended failure mode of specimens: **F** = flexural yielding and **S** = shear failure (the shear failure-mode specimens are discussed in Chapter 4). The third character (number) indicates the aspect ratio (wall height h_w-to-length l_w ratio) of wall specimens. In some specimens, additional characters are provided at the end of the specimen name, to represent their intrinsic properties: **S**: ductile boundary detailing for special structural wall; **VH**: steel U-sections with greater area; **SB**: steel plate beams for horizontal web reinforcement; and **SF**: steel faceplates for web reinforcement.

Fig. 3-1 and **Fig. 3-2** show the details of the specimens with aspect ratio of 2.5. Two RC wall specimens were prepared for control specimens: **RF2.5** with uniformly distributed vertical rebars (i.e., an ordinary wall without boundary elements) and **RF2.5S** with concentrated vertical rebars at the boundary elements. In **RF2.5** (**Fig. 3-1**(a)), eighteen vertical D35 bars (bar diameter = 34.9 mm, cross-sectional area A_r = 957 mm^2 each, yield strength f_y = 499 MPa) were uniformly placed in two layers along the wall length. In **RF2.5S** (**Fig. 3-1**(b)), to maximize the flexural strength and stiffness, nine vertical D35 bars (f_y = 499 MPa) were placed at each boundary element (length of boundary element l_{be} = 300 mm, boundary steel ratio $\rho_{be} = \sum A_s / (l_{be} \cdot t_w)$ = 9.6 %), which exceeded the maximum ratio (8 % for column) of ACI 318 (2019). On the other hand, for vertical web reinforcement, four D16 bars (diameter = 15.9 mm, A_r = 199 mm^2 each, f_y = 445 MPa, the area ratio of web reinforcement to the web section $\rho_v = 2A_r / (s_v \cdot t_w)$ = 0.32 %, s_v = horizontal spacing of vertical web reinforcement) were used, which was close to the minimum reinforcement ratio (= 0.0025, ACI 318, 2019). For **RF2.5**, special details for boundary confinement were not used. On the other hand in **RF2.5S**, lateral confinement detailing was applied to the boundary element, in accordance with the requirement of special structural walls (for design drift ratio of 1.5 %) in ACI 318 (2019): horizontal hoops of D13 bars with 135° hooks (diameter = 12.7 mm, A_r = 127 mm^2 each, f_y = 444 MPa) were placed at a vertical spacing of 75 mm in the lower part of the wall (within 2,050 mm distance above the wall base), and at a vertical spacing of 150 mm in the remaining upper part of the wall.

In flexure-mode composite wall **CF2.5** (**Fig. 3-2**(a)), a steel U-section of U-300×300×9×9 (flange length × web length × web plate thickness × flange plate thickness (in millimeters), cross-section area A_b = 7,938 mm^2 each, l_{be} = 300 mm, yield strength F_y = 379 MPa) was placed at each wall end. For vertical web reinforcement, two layers of ten D16 bars were uniformly placed (ρ_v = 0.32 %). Including steel end plates and vertical rebars, the boundary steel ratio ρ_{be} was 9.3 %, which was similar to that of the counterpart specimen **RF2.5** (ρ_{be} = 9.6 %). In **RF2.5**, **RF2.5S**, and **CF2.5**, the overall area ratio ρ_s of vertical steel (rebars and steel plates) to the gross wall section was designed to be similar, to investigate the effect of vertical steel configuration on the flexural strength of the walls (ρ_s = 3.2% for **RF2.5** and 3.3% for **RF2.5S** and **CF2.5**). However, the yield strength of U-300×300×9×9 plate (F_y = 379 MPa) in **CF2.5** was 24 % less than that of vertical D35 bars (f_y = 499 MPa) in **RF2.5** and **RF2.5S**. Thus, in **CF2.5**, the mechanical steel ratio (= $\rho_s F_y / f_c'$ = 0.18), which is an influence factor for flexural strength, was 26 % less than that of **RF2.5** and **RF2.5S** (= $\rho_s f_y / f_c'$ = 0.25 for both). In **CF2.5VH** (**Fig. 3-2**(b)), to investigate the effect of the steel U-section on the flexural strength, the thickness of steel plates was increased by 78 % (U-300×300×16×16, A_b = 13,888 mm^2 each, l_{be} = 300 mm, ρ_{be} = 15.9 %), while the details of web reinforcement were the same as that of **CF2.5**. Thus, the overall steel ratio and mechanical steel ratio were increased to ρ_s = 5.5 % and $\rho_s F_y / f_c'$ = 0.33, respectively. In all flexure-mode specimens with aspect ratio of 2.5, D16 bars (cross-section area A_{sh} = 199 mm^2 each) were used for horizontal web reinforcement at a vertical spacing of s_h = 150 mm (horizontal reinforcement ratio $\rho_h = 2A_{sh} / (s_h \cdot t_w)$ = 0.88 %).

Table 3-1 Design parameters of flexural yielding specimens (aspect ratio = 2.5)

Specimens	**RF2.5**	**RF2.5S**	**CF2.5**	**CF2.5VH**
Structural type	RC	RC	SUB-C[a]	SUB-C[a]
Wall height h_w, mm	4,500	4,500	4,500	4,500
Wall length l_w, mm	1,800	1,800	1,800	1,800
Wall thickness t_w, mm	300	300	300	300
Concrete strength f_c', MPa	64.6	68.3	68.3	64.3
Vertical boundary steel	-	D35	U-300×300×9×9[b]	U-300×300×16×16[b]
Boundary length l_{be}, mm	-	300	300	300
Steel ratio ρ_{be}[c], %	-	9.6	9.3	15.9
Confinement ratio ρ_c[d], %	-	1.34	0.89	0.89
Total area, mm^2	-	17,219	16,672	28,572
f_y (or F_y), MPa	-	499	379	388
f_u (or F_u), MPa	-	609	543	546
Vertical web steel	D35	D16	D16	D16
Horizontal spacing s_v, mm	210	420	412.5	412.5
Reinforcement ratio ρ_v[e], %	3.2	0.32	0.32	0.32
f_y, MPa	499	445	445	445
f_u, MPa	609	597	597	597
Vertical steel ratio ρ_s[f], %	3.2	3.3	3.3	5.5
Horizontal web steel	D16	D16	D16	D16
Vertical spacing s_h, mm	150	150	150	150
Reinforcement ratio ρ_h[g], %	0.88	0.88	0.88	0.88
f_y, MPa	445	445	445	445
f_u, MPa	597	597	597	597

[a]Steel–concrete composite wall with boundary elements of steel U-section.
[b]Steel U-section: U-flange length × web length × web thickness × plate thickness.
[c]Area ratio of vertical boundary steel reinforcement to boundary concrete section = $\sum A_r / (l_{be} \cdot t_w)$ for RC; $A_b / (l_{be} \cdot t_w)$ for SUB-C.
[d]Area ratio of transverse confinement reinforcement (headed studs for composite walls) to the boundary confined concrete section = $A_{sc} / (s_c \cdot b_c)$.
[e]Area ratio of vertical web steel reinforcement to web concrete section = $2A_r / (s_v \cdot t_w)$.
[f]Total area ratio of vertical steel sections to gross wall section = $\sum A_s / (l_w \cdot t_w)$.
[g]Area ratio of horizontal web steel reinforcement to web concrete section = $2A_{sh} / (s_h \cdot t_w)$.

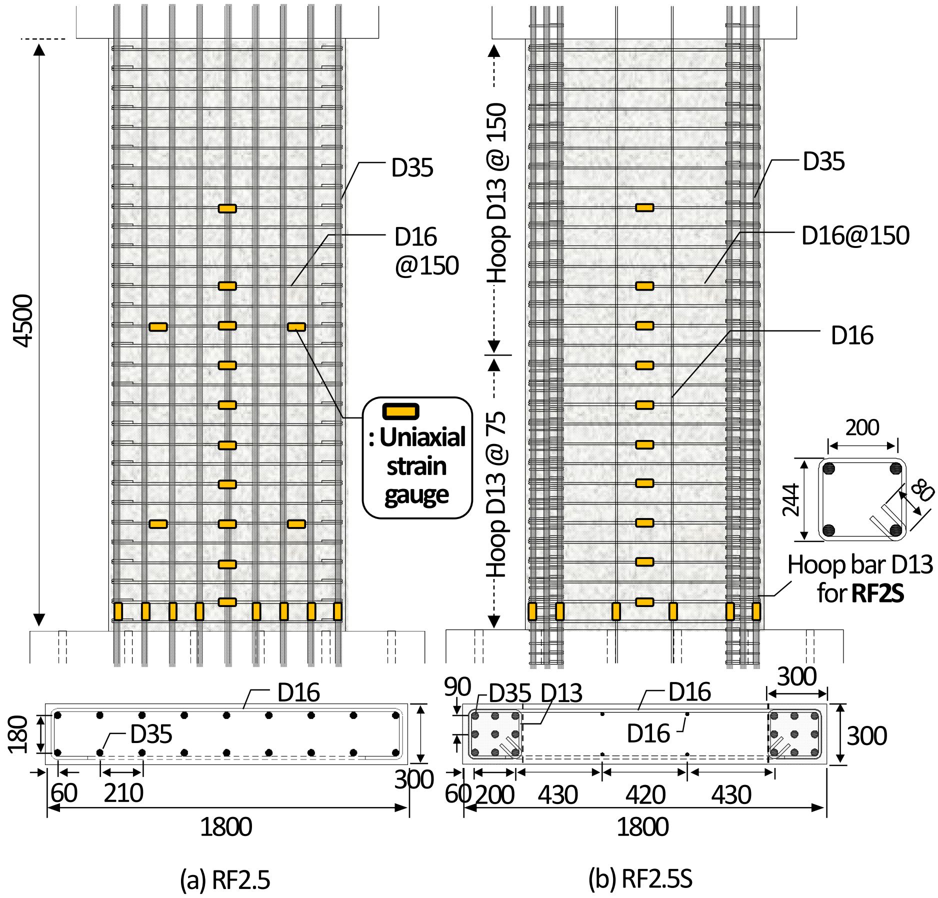

Fig. 3-1 Details of flexural yielding specimens: (a) RF2.5; (b) RF2.5S.

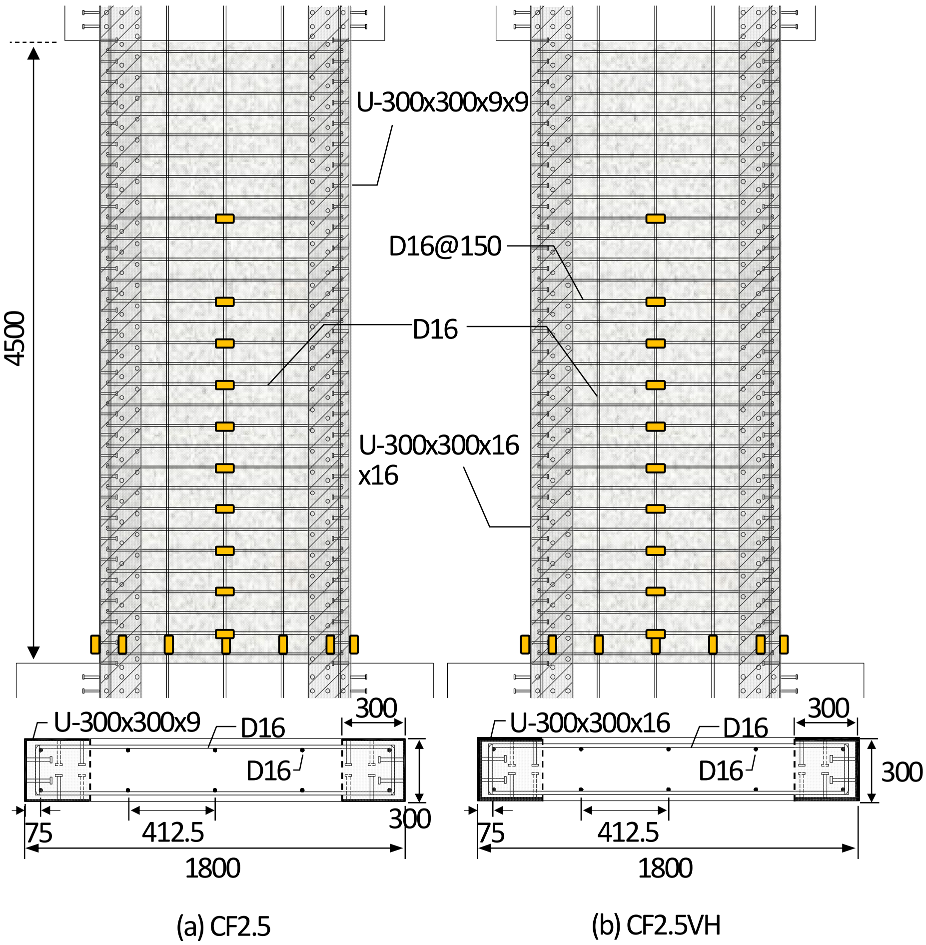

Fig. 3-2 Details of flexural yielding specimens: (a) CF2.5; (b) CF2.5VH.

Fig. 3-3 and **Fig. 3-4** show the flexural yielding specimens with aspect ratio of 2.0. In RC wall **RF2S** (**Fig. 3-3**(a)), four vertical D35 bars (A_r = 957 mm^2 each, f_y = 466 MPa) were used for the boundary elements (length of boundary element l_{be} = 220 mm, ρ_{be} = 9.6 %), and horizontal hoops of D10 bars (A_r = 71 mm^2 each, f_y = 514 MPa, vertical spacing = 75 mm) were used for boundary confinement reinforcement along the entire height of the wall. The vertical web reinforcement ratio (ρ_v = 0.39 %) was close to the minimum ratio (= 0.0025 + 0.5(2.5 – h_w/l_w)(ρ_h – 0.0025) = 0.33 %) of ACI 318 (2019): Fourteen D10 bars (A_r = 71 mm^2 each, f_y = 514 MPa) were uniformly placed in two layers along the web length. For horizontal web reinforcement, D13 bars (A_{sh} = 127 mm^2 each, f_y = 445 MPa) were placed at a vertical spacing of s_h = 225 mm (ρ_h = 0.56 %).

In **CF2** (**Fig. 3-3**(b)), a steel U-section of U-200×200×9×9 (A_b = 5,238 mm^2 each, l_{be} = 200 mm, ρ_{be} = 13.1 %) was used for each boundary element, while the other details were the same as those of **RF2S**. The yield strength of the steel plates (F_y = 404 MPa) was 13 % less than that of vertical boundary D35 bars (f_y = 466 MPa) in **RF2S**. For fair comparison, the area of the steel plates was designed to be greater than that of the vertical boundary rebars in **RF2S**, showing similar mechanical steel ratio ($\rho_s F_y / f_c'$ = 0.29 for **RF2S** and 0.30 for **CF2**).

In **CF2VH** (**Fig. 3-3**(c)), the web plate length of steel U-sections (U-200×320×9×9, A_b = 7,398 mm^2 each, l_{be} = 320 mm, ρ_{be} = 11.6%, F_y = 404 MPa) was increased by 60 %, to investigate the effect of the increased steel plate area on the flexural performance. Due to the increased shear demand (i.e., flexural strength), a smaller spacing of horizontal D13 bars (s_h = 120 mm, f_y = 445 MPa) was used. The vertical web reinforcement was the same as that of **CF2.**

For better constructability and connectivity to steel frames, a framed composite wall was considered for **CS2SB** (**Fig. 3-4**(a)): steel plate beams (i.e., horizontal batten plates) of PL-105×6 (width × thickness, length = 1,500 mm) were used at a vertical spacing of s_h = 750 mm (ρ_h = 0.84 %). The steel plate beams were connected to boundary steel elements that were the same as that of **CF2**. For the connection between the steel beams and boundary elements, fillet welding (weld size = 6 mm, effective throat > 4 mm) was used. The nominal weld strength (= 490 kN, AISC 360, 2016) was greater than the yield strength of the steel beams (= 287 kN). Neither horizontal nor vertical web reinforcements was used. However, for actual construction, minimum reinforcement may be required to restrain concrete cracking due to creep and shrinkage.

In **CF2SF** (**Fig. 3-4**(b)), the specimen was designed to be similar to the existing concrete-filled steel plate walls. However, using steel U-section, a large steel area was concentrated at the boundary elements, and the web steel area was minimized: Steel faceplates of PL-1200×4 (ρ_v and ρ_h = $2t_p$ / t_w = 4.0 %, in which t_p = thickness of faceplate) were placed at both sides of the web concrete, and the boundary steel U-section was the same as that of **CF2**. As the faceplates provides high shear resistance and lateral confinement to the web concrete, the ductility of the composite wall was expected to increase, even under high shear demand. However, for the vertical connection between faceplates, long welding is required, which decreases on-site constructability. Further, the weld joints near the critical section are vulnerable to brittle fracture (Eom et al. 2009). Thus, in **CF2SF**, the boundary steel elements and web faceplates were intentionally unconnected, though this practice violates the requirement of AISC 341 (2016). Instead, for shear connection, shear-friction D19 bars with a vertical spacing of 250 mm (length = 500 mm) were placed between the boundary elements and web concrete. In actual construction, steel mesh reinforcement could be used for better constructability.

Table 3-2 Design parameters of flexural yielding specimens (aspect ratio = 2.0)

Specimens	RF2S	CF2	CF2VH	CF2SB	CF2SF
Structural type	RC	SUB-C[a]	SUB-C[a]	SUB-C[a]	SUB-C[a]
Wall height h_w, mm	3,200	3,200	3,200	3,200	3,200
Wall length l_w, mm	1,600	1,600	1,600	1,600	1,600
Wall thickness t_w, mm	200	200	200	200	200
Concrete strength f_c', MPa	47.4	48.2	44.7	44.7	48.7
Vertical boundary steel	D35	U-200×200×9×9[b]	U-200×320×9×9[b]	U-200×200×9×9[b]	U-200×200×9×9[b]
Boundary length l_{be}, mm	200	200	200	200	200
Steel ratio ρ_{be}[c], %	9.6	13.1	13.1	11.6	13.1
Confinement ratio ρ_c[d], %	1.22	2.01	1.57	2.01	2.41
Total area, mm^2	7,653	10,476	10,476	14,796	10,476
f_y (or F_y), MPa	466	404	404	404	404
f_u (or F_u), MPa	584	571	571	571	571
Vertical web steel	D10	D10	D10	-	PL-1200×4[g]
Horizontal spacing s_v, mm	180	420	412.5	-	-
Reinforcement ratio ρ_v[e], %	0.39	0.32	0.32	-	4.0
f_y, MPa	514	445	445	-	321
f_u, MPa	600	597	597	-	473
Vertical steel ratio ρ_s[f], %	2.7	3.6	4.9	3.3	5.6
Horizontal web steel	D13	D13	D13	PL-105×6[h]	-
Vertical spacing s_h, mm	225	225	120	750	-
Reinforcement ratio ρ_h[g], %	0.56	0.56	1.06	0.84	-
f_y, MPa	445	445	445	456	-
f_u, MPa	584	584	584	597	-

[a]Steel–concrete composite wall with boundary elements of steel U-section.
[b]Steel U-section: U-flange length × web length × web thickness × plate thickness.
[c]Area ratio of vertical boundary steel reinforcement to boundary concrete section = $\sum A_r / (l_{be} \cdot t_w)$ for RC; $A_b / (l_{be} \cdot t_w)$ for SUB-C.
[d]Area ratio of transverse confinement reinforcement (headed studs for composite walls) to the boundary confined concrete section = $A_{sc} / (s_c \cdot b_c)$.
[e]Area ratio of vertical web steel reinforcement to web concrete section = $2A_r / (s_v \cdot t_w)$.
[f]Total area ratio of vertical steel sections to gross wall section = $\sum A_s / (l_w \cdot t_w)$.
[g]Area ratio of horizontal web steel reinforcement to web concrete section = $2A_{sh} / (s_h \cdot t_w)$.
[h]Flat plate section: PL-width × thickness.

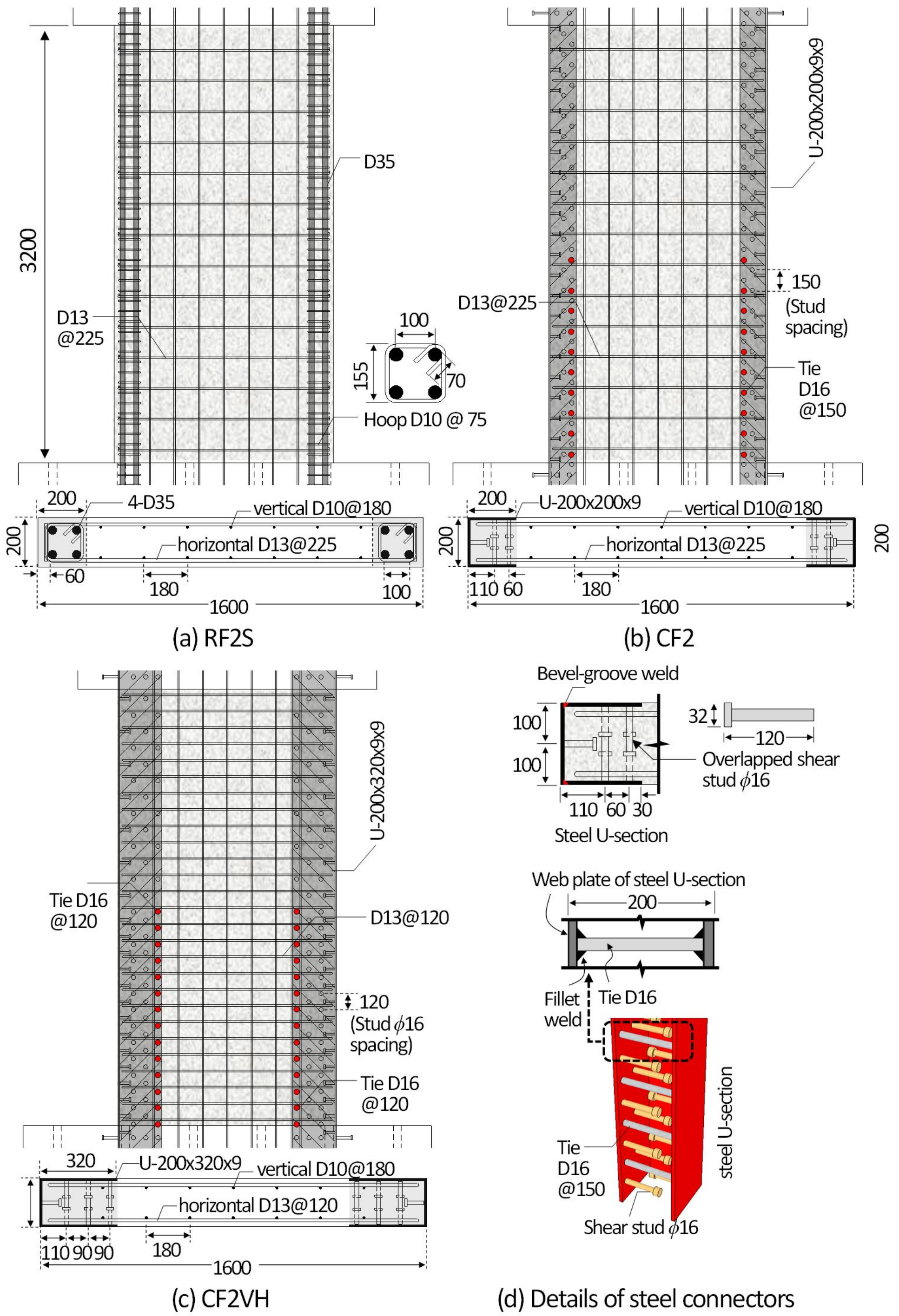

Fig. 3-3 Details of flexural yielding specimens: (a) RF2; (b) CF2; (c) CF2VH; and (d) details of steel connectors.

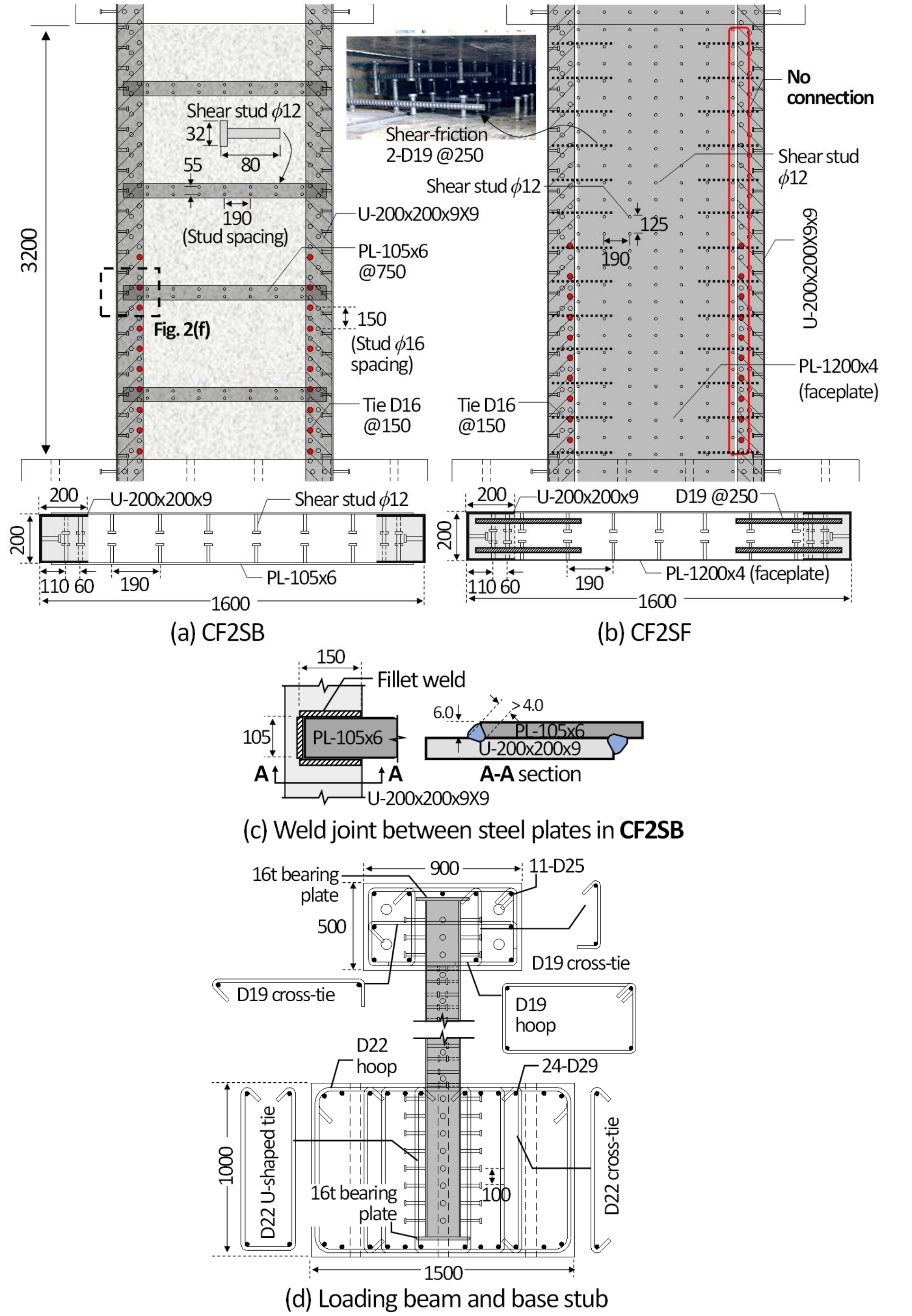

Fig. 3-4 Details of flexural yielding specimens: (a) CF2SB; (b) CF2SF; (c) weld joint between steel plates in CF2SB; and (d) loading beam and base stub.

In all flexural yielding-mode composite specimens, the steel U-section with a flange and two web plates was designed as compact section according to AISC 360 (2016). The flange and web plates were connected using Bevel-groove welding along the wall height (**Fig. 3-4**(d)). For composite action between the steel and concrete, headed studs (diameter = 16 mm, height = 120 mm, nominal tensile strength = 500 MPa) were welded to the flange plate and web plate along the entire length of the steel U-sections. In the specimens with aspect ratio of 2.5, only headed studs were used for the plates, without lateral ties. On the other hand, in the specimens with lower aspect ratio of 2.0, lateral tie bars (diameter = 16 mm, length = 180 mm, yield strength = 445 MPa) were also used between the web plates in plastic hinge zone (within 1,600 mm above the wall base). Note that the present study focused on the effect of steel U-sections and their area on the flexural performance of walls. Thus, unexpected early failure of steel plates should be avoided. For this reason, the strength and spacing of the studs and ties were designed according to AISC N690 (2018), to develop the yield strength of the plates and to minimize inelastic local buckling of the plates.

Since the wall length was relatively short, end hooks were used to assure the anchorage of horizontal web reinforcement. In the RC wall specimens, a 180-degree hook was used for anchorage, while in the composite wall specimens, a 90-degree hook was used.

3.3.2 Material strengths

Table 3-1 and **Table 3-2** shows the strengths of the materials used for flexural yielding-mode specimens. The compressive strength of concrete f_c' indicates the average strength of three concrete cylinders (diameter × height = 100 mm × 200 mm) tested on the day of each wall test (f_c' = 64.3–68.3 MPa for specimens with aspect ratio 2.5; 44.7–48.7 MPa for specimens with aspect ratio 2.0). For steel plates and reinforcing bars, tension tests were performed using three coupon specimens corresponding to each steel section (KS B 0802, 2018) (**Fig. 3-5**). The yield strengths of the coupon specimens were determined by using the 0.2 % offset method (AISC 360, 2016). In **Table 3-1** and **Table 3-2**, f_y (f_u) and F_y (F_u) indicates the average of the measured yield strengths (ultimate tensile strengths) of steel sections. In the specimens with aspect ratio 2.5, the steel strengths were f_y = 445–499 MPa (f_u = 597–609 MPa) for reinforcing bars; and F_y = 379–388 MPa (F_u = 543–546 MPa) for steel plates. In the specimens with aspect ratio 2.0, the steel strengths were f_y = 445–514 MPa (f_u = 584–600 MPa) for reinforcing bars; and F_y = 321–456 MPa (F_u = 473–597 MPa) for steel plates. The measured material strengths were used to predict the nominal strengths of the wall specimens.

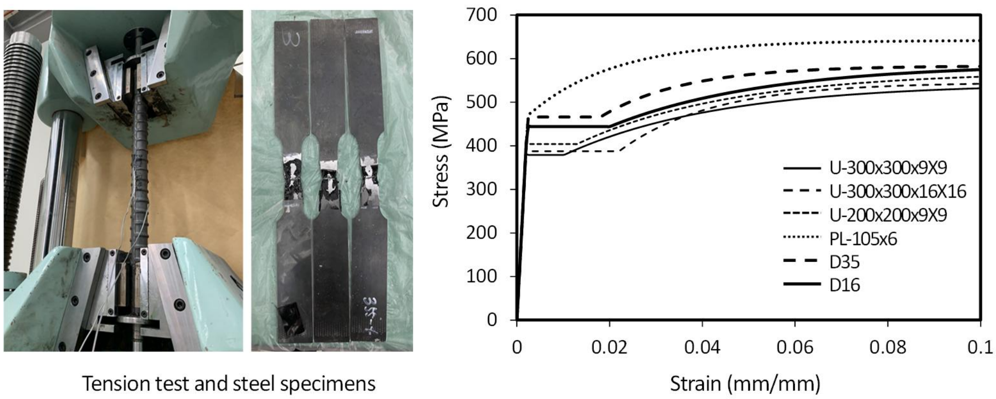

Fig. 3-5 Stress-strain relationships of steel specimens.

3.3.3 Lateral confinement to wall boundary

The deformation capacity of walls depends on the amount of lateral confinement reinforcement at wall boundaries (Massone et al. 2017). In RC specimens **RF2.5S** and **RF2S** with boundary confinement detailing, the boundary confinement ratio in the lower part of the wall was $\rho_c = 2A_{sc} / (s_c \cdot b_c) = 1.34\%$ and 1.22%, respectively (A_{sc} = total cross-sectional area of confining reinforcement within its vertical spacing s_c and perpendicular to b_c, in which b_c = dimension of the confined core measured to the outside edges of the confinement hoop bars = 244 mm for **RF2.5S**, 155 mm for **RF2S**), which were close to or greater than the requirements (1.38% for **RF 2.5S**, 0.96% for **RF2S**) for rectilinear boundary confining hoops of special structural walls in ACI 318 (2019) (**Table 3-1**).

In the composite specimens, the steel U-section with open shape cannot provide adequate lateral confinement if steel anchors or lateral ties are not used: the headed studs or lateral tie bars in the web plates resist lateral expansion of the boundary concrete. Thus, the boundary confinement ratio ρ_c was calculated from the amount of headed studs and tie bars, using A_{sc} = total cross-sectional area of headed studs and tie bars within their vertical spacing (= s_c) in a web plate of steel U-sections, and b_c = the boundary length (l_{be} = 300 mm). In composite specimens **CF2.5** and **CF2.5VH** with aspect ratio of 2.5, only headed studs were used for the web plates, without lateral ties. Here, the boundary confinement ratio was $\rho_c = 0.89\%$, which was less than that of **RF2.5S** ($\rho_c = 1.34\%$) and the requirement (= 1.3%) of special structural walls in ACI 318 (2019) (**Table 3-1**). Note that in the boundary element, the vertical steel area of **CF2.5** was the same as that of counterpart specimen **RF2.5S**.

In the composite specimens with lower aspect ratio of 2.0, lateral tie D16 bars were also used between the web plates. The confinement ratio was $\rho_c = 2.01\%$ for **CF2**, 1.57% for **CF2VH**, 2.01% for **CF2SB** and 2.41% for **CF2SF**, respectively, which was greater than that of **RF2S** ($\rho_c = 1.22\%$) and the requirement (= 0.88%–1.37%) of seismic provisions in ACI 318 (2019) (**Table 3-2**).

3.3.4 Test setup for loading and measurement

Fig 3-6 shows the test setup for loading and measurement. A lateral load V was applied by a displacement-controlled loading actuator located at the top of the specimens. The distance from the loading point to the wall base (= shear span l_s) was 4,750 mm for specimens with aspect ratio 2.5, and 3,450 mm for specimens with aspect ratio 2.0. At the top of the specimens, lateral supports were provided to prevent out-of-plane displacement of the wall specimens. Reversed cyclic loading was planned according to ACI 374.2R (2013): three cycles of loading at lateral drift ratios of $\delta = \pm 0.06\%$, 0.12%, 0.25%, 0.5%, 0.75%, 1.0%, 1.5%, and 2.0%; and two cycles at $\delta = \pm 3.0\%$ and 4.0%. In the present test, axial load was not applied to the wall specimens, to focus on their pure flexural and shear strengths. However, for reliable use in buildings subjected to high compression (e.g., high-rise buildings), further study is required for the proposed composite walls subjected to axial load.

Lateral displacement at the loading point was measured using a draw-wire displacement sensor (denoted as M1). Linear variable differential transformers (LVDTs) were used to measure the flexural deformation at the plastic hinge zone (R1–R4 for specimens with aspect ratio 2.5; R1 and R2 for specimens with aspect ratio 2.0), shear deformation at the web wall (D1–D6 for specimens with aspect ratio 2.5; D1–D4 for specimens with aspect ratio 2.0), sliding and rotational displacements of the base stub (S1–S3), and sliding displacement above the wall base (S4). Strain gauges were used to measure the strains of steel reinforcements (**Figs. 3-1** to **3-4**).

From existing predictive equations, the plastic hinge zone length was estimated to be 1,200–1,600 mm for the present RC specimens with aspect ratio of 2.5 [1,195 mm for Bohl and Adebar (2011); 1,385 mm for Paulay and Priestley (1992); and 1,625 mm for Kazaz (2013)]; and 1,000–1,300 mm for the RC specimen with aspect ratio of 2.0 [985 mm for Bohl and Adebar (2011); 1,123 mm for Paulay and Priestley (1992); and 1,336 mm for Kazaz (2013)]. In the present study, the greatest value (1,600 mm) of the predictions was assumed for the plastic hinge length l_p, to measure all possible inelastic rotation in the plastic hinge zone. The same length was also assumed for the proposed composite walls (to accurately estimate the actual plastic hinge zone length, further studies are required).

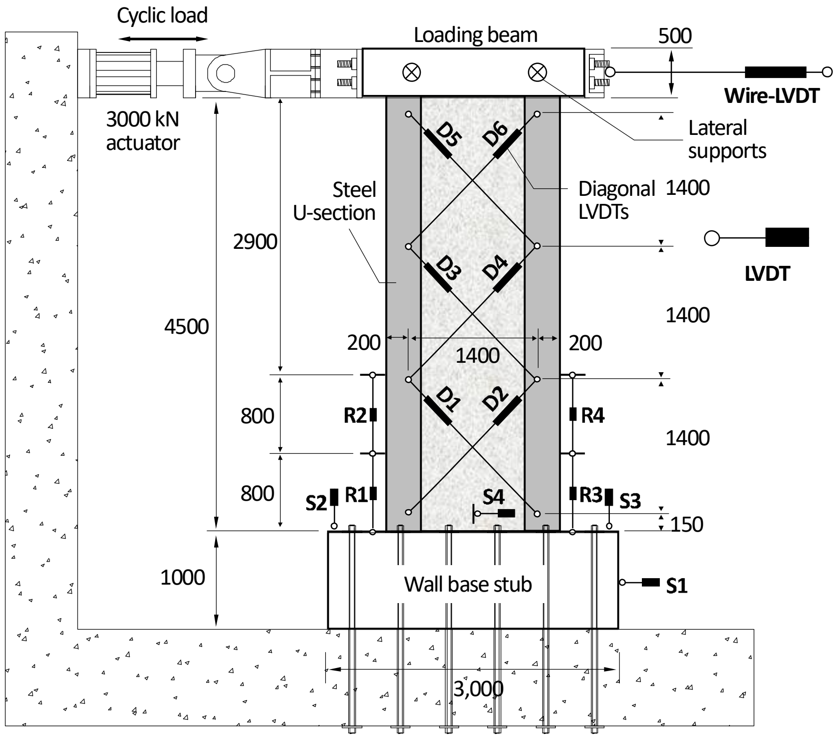

2.5-aspect ratio wall testing

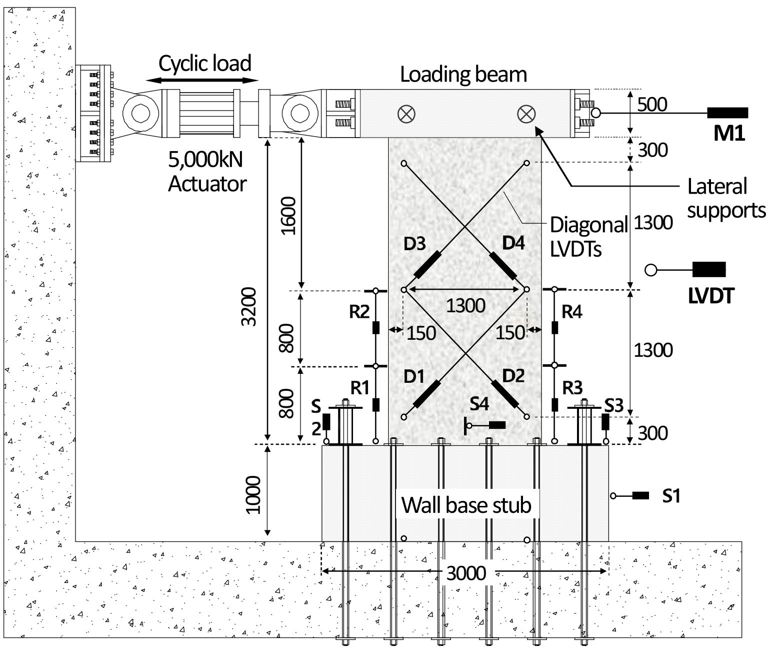

2.0-aspect ratio wall testing

Fig. 3-6 Test setup for wall specimens with aspect ratios of 2.5 and 2.0.

3.4 Test Results

3.4.1 Lateral load-displacement relationship

Fig. 3-7 and **Fig. 3-8** show the lateral load–drift ratio (V–δ) relationships of the flexural yielding-mode specimens with aspect ratios of 2.5 and 2.0, respectively. The drift ratio δ (= Δ / l_s) was calculated by dividing the lateral displacement Δ by the shear span l_s, in which Δ represents the net lateral displacement excluding the sliding and rotational displacements of the base stub. **Fig. 3-9** and **Fig. 3-10** show the damage of concrete and steel in the specimens. **Table 3-3** shows the peak strength V_{test}, drift ratio at the peak strength δ_o, and ultimate drift ratio δ_u. The ultimate drift ratio was defined as the maximum drift ratio in the load cycle where the post-peak strength decreased to 80% of V_{test}. All test specimens showed ductile behavior of flexural yielding. Ultimately, because of the high flexural capacity, post-yield shear failure occurred in the web concrete.

1) Wall specimens with aspect ratio 2.5

In **RF2.5** with uniformly distributed vertical rebars (**Fig. 3-7**(a)), the peak strengths of V_{test} = +1,299 and –1,273 kN occurred at δ_o = +1.60% and –1.29%, respectively, as flexural crushing of boundary concrete was initiated at the wall base due to the high reinforcement ratio (**Fig. 3-9**(a)). The ultimate drift ratios in the positive and negative loading directions were δ_u = +2.63% and –2.81%, respectively.

In **RF2.5S** with boundary reinforcement and confinement detailing (**Fig. 3-7**(b)), the average of V_{test} = +1,466 and –1,445 kN (at δ_o = +1.11% and –1.78%) was 13% greater than that of **RF2.5**. However, after V_{test}, a large horizontal crack extended over the entire cross section at 200 mm above the wall base, followed by shear sliding along the horizontal crack, dowel action of the vertical bars, spalling of cover concrete, and eventual strength degradation (**Fig. 3-9**(b)). In the design of **RF2.5S**, the nominal shear sliding strength (i.e., shear-friction strength = 4,730 kN) calculated according to ACI 318 (2019) was three times the nominal flexural strength, when all vertical rebars were considered as shear-friction reinforcement. Nevertheless, shear sliding occurred after flexural yielding, for the following reason: since vertical steel area was concentrated at boundary elements, large plastic strains and subsequent elongation occurred in most of the vertical boundary reinforcement, which significantly degraded the shear-friction strength. Thus, despite the boundary ductile detailing, the average of δ_u = +2.80% and –2.29% was 6% less than that of **RF2.5**.

In composite wall **CF2.5** with steel U-sections (**Fig. 3-7**(c)), the load-carrying capacity gradually increased after flexural yielding. Unlike **RF2.5S**, shear sliding did not occur as the steel U-sections provided good shear-sliding resistance. At δ = +1.25%, local buckling was initiated in the flange of steel U-sections at the wall base (point F). During the second load cycle of δ = $\pm$3.0%, local buckling became severe in both web plates and flange plates of the steel U-sections, which caused stiffness degradation (point G). However, the local buckling did not decrease the load-carrying capacity, because concrete in the boundary region confined by the steel U-sections was able to provide flexural compression resistance. Thus, although the yield strength of the steel U-sections (= 379 MPa) was 24% less than that of the boundary D35 bars (= 499 MPa) in **RF2.5S**, the peak strengths of V_{test} = +1,413 and –1,411 kN (at δ_o = +2.65% and –2.70%, respectively) were close to those of **RF2.5S**. At δ = –3.30%, the post-peak strength was degraded due to unexpected tensile weld-fracture at the horizontal construction joint for the steel U-sections (**Fig. 3-9**(c)) (only **CF2.5** had the horizontal joint using a partial penetration weld at 2,000 mm above the wall base). Nevertheless, the ultimate drift ratios of δ_u = +3.70% and –3.72% were greater than those of **RF2.5** and **RF2.5S**, as shear sliding and flexural crushing were restrained at the wall base.

In **CF2.5VH** with thicker steel plates (**Fig. 3-7**(d)), the overall behavior was similar to that of **CF2.5**. However, the average of V_{test} = +2,106 and –2,181 kN (at δ_o = +2.71% and –2.88%) was 52% greater than that of **CF2.5**, due to the greater area of steel U-sections. Unlike **CF2.5**, local buckling of the steel U-section did not occur. Ultimately, crushing and spalling of web concrete (point H) occurred in the plastic hinge zone (**Fig. 3-9**(d)), which decreased the load-carrying capacity. Despite the higher strength, the deformation capacity (δ_u = +3.80% and –3.97%) was slightly greater than that of **CF2.5**.

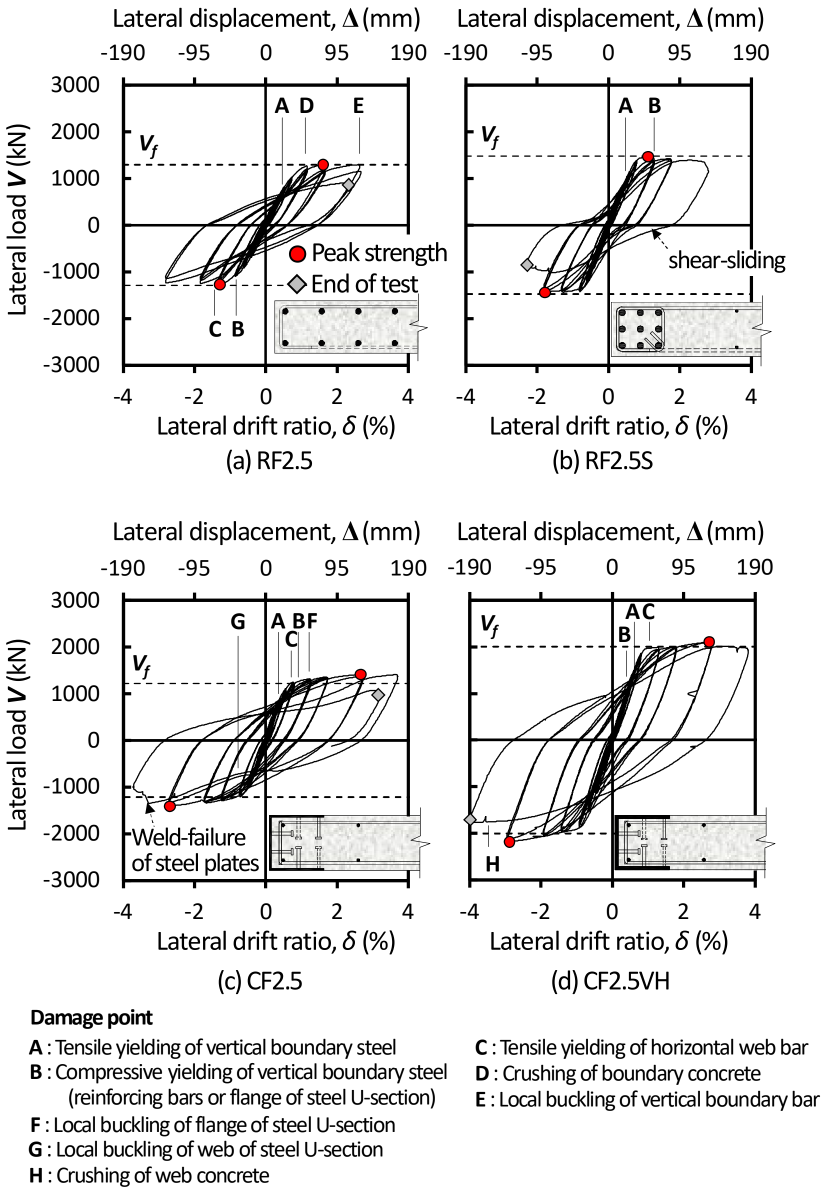

Fig. 3-7 Lateral load-drift ratio relationships of flexural yielding specimens with aspect ratio of 2.5.

2) Wall specimens with aspect ratio 2.0

In RC specimen **RF2S** with boundary elements of vertical rebars (**Fig. 3-8**(a)), the peak strengths of V_{test} = +888 and –872 kN occurred at drift ratios of δ_o = +0.93% and –1.5%, respectively. After δ = ±1.5%, the post-peak strength degradation was similar to that of **RF2.5S** that showed shear sliding: the load-carrying capacity began to decrease as horizontal flexural cracks penetrated into the entire cross section at the wall bottom, and subsequent shear sliding occurred along the horizontal cracks (**Fig. 3-10**(a)). As the shear sliding increased, the wall failed at δ_u = +1.96% and –2.01%, due to significant spalling of concrete.

In composite specimen **CF2** with boundary steel U-sections (**Fig. 3-8**(b)), after flexural yielding, the load-carrying capacity gradually increased until δ = ±2.0 %. Thus, the average of V_{test} = +1,227 and –1,192 kN (at δ_o = +2.58% and –1.99%) was 37% greater than that of the counterpart **RF2S**. This is because the steel U-sections experienced large strain hardening stress, providing good lateral confinement to the boundary concrete. The post-yield strength was degraded due to the crushing of web concrete at the wall bottom (i.e., plastic hinge zone), showing δ_u = +3.02% and –3.06%.

In **CF2VH** with the greater web plate length of steel U-sections (**Fig. 3-8**(c)), the average of V_{test} = +1,594 and –1,650 kN (at δ_o = +3.10% and –2.85%) was 34% greater than that of counterpart **CF2**. During the load cycle of δ = ±4.0%, crushing of web concrete occurred at the wall bottom, which decreased the load-carrying capacity. Nevertheless, the ultimate drift ratios of δ_u = +3.95% and –4.04% were on average 31% greater than those of **CF2**.

In **CF2SB** with steel plate beams (**Fig. 3-8**(d)), the average of V_{test} = +1,168 and –1,218 kN (at δ_o = +2.70% and –2.87%) was similar to that of **CF2** without steel beams. This result indicates that, until flexural yielding, the steel plate beams provided adequate shear resistance to the wall. The post-yield strength was degraded due to crushing of web concrete (**Fig. 3-10**(d)). However, the ultimate drift ratio increased to δ_u = ±4.03 %.

In **CF2SF** with steel web faceplates (**Fig. 3-10**(e)), the peak strengths of V_{test} = +1,622 and –1,671 kN (at δ_o = +1.94% and –1.97%) were the greatest in the specimens. However, the V_{test} was not significantly greater than that of **CF2VH**, due to the lesser steel area in the boundary elements. Further, the ultimate drift ratios of δ_u = +2.94% and –3.08% were less than those of **CF2VH** and **CF2SF**, as local buckling of web faceplates and crushing of web concrete occurred in a brittle manner.

Table 3-3 Summary of tested lateral load-drift ratio relationships of flexural yielding specimens

Specimens		Peak strength V_{test} [kN]			Drift ratio δ_o at V_{test} [%]			Yield drift ratio δ_y [%]			Ultimate drift ratio δ_u [%]			Drift ductility μ (= δ_u / δ_y)		
		+ve	–ve	Avg.	+ve	–ve	Avg.	+ve	–ve	Avg.	+ve	–ve	Avg.	+ve	–ve	Avg.
Aspect ratio = 2.5	RF2.5	1,299	-1,273	1,286	1.60	-1.29	1.45	0.93	-0.94	0.93	2.63	-2.81	2.72	2.83	3.00	2.91
	RF2.5S	1,466	-1,445	1,455	1.11	-1.78	1.44	0.79	-0.73	0.76	2.80	-2.29	2.55	3.53	3.16	3.34
	CF2.5	1,413	-1,411	1,412	2.65	-2.70	2.67	0.77	-0.84	0.80	3.70	-3.72	3.71	4.83	4.42	4.63
	CF2.5VH	2,106	-2,181	2,143	2.71	-2.88	2.80	0.88	-1.06	0.97	3.80	-3.97	3.89	4.31	3.76	4.04
Aspect ratio = 2.0	RF2S	888	-872	880	0.93	-1.50	1.22	0.63	-0.62	0.63	1.96	-2.01	1.99	3.11	3.24	3.18
	CF2	1,227	-1,192	1,210	2.58	-1.99	2.29	0.79	-0.74	0.76	3.02	-3.06	3.04	3.83	4.15	3.99
	CF2VH	1,594	-1,650	1,622	3.10	-2.85	2.97	0.92	-0.97	0.94	3.95	-4.04	4.00	4.30	4.19	4.24
	CF2SB	1,168	-1,218	1,193	2.70	-2.87	2.78	0.77	-0.85	0.81	4.03	-4.03	4.03	5.23	4.76	5.00
	CF2SF	1,622	-1,671	1,646	1.94	-1.97	1.95	0.90	-0.86	0.88	2.94	-3.08	3.01	3.28	3.58	3.43

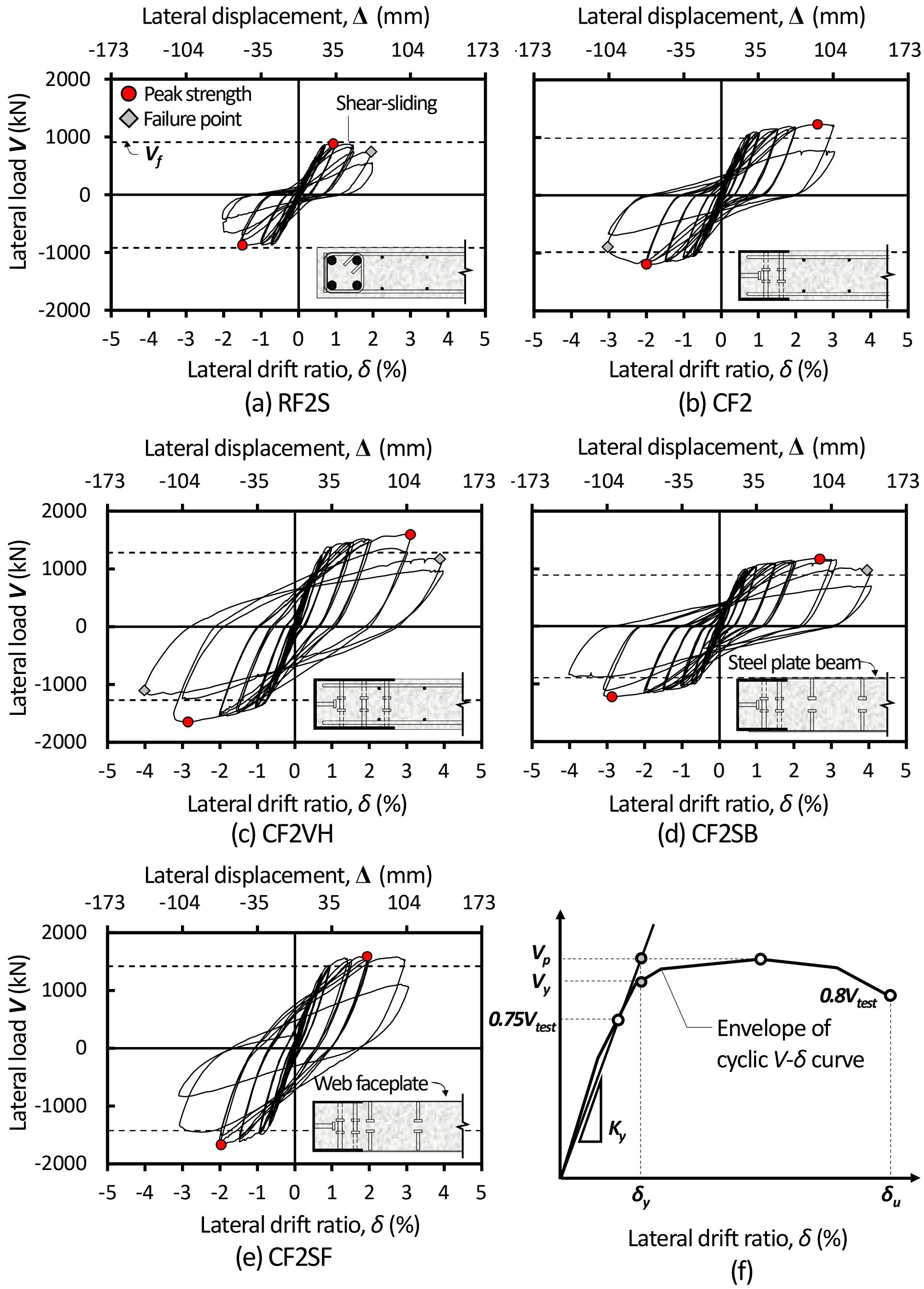

Fig. 3-8 Lateral load-drift ratio relationships of flexural yielding specimens with aspect ratio of 2.0.

3.4.2 Failure mode

Fig. 3-9 shows the damage of concrete and steel at the end of tests, for the specimens with aspect ratio of 2.5. In **RF2.5** (**Fig. 3-9**(a)), horizontal flexural cracks occurred at the wall boundary region, and the cracks propagated to the web region forming X-shaped diagonal tension cracks. Crushing and spalling of concrete due to flexural action were concentrated at the wall boundary region, in the plastic hinge zone. Local buckling of the vertical bars and anchorage loosening of horizontal bars occurred after spalling of the cover concrete in the boundary region. In **RF2S** (**Fig. 3-9**(b)) showing post-yield shear sliding failure, spalling of concrete and dowel deformation of vertical rebars were concentrated at the wall base, without severe damage in the remaining region.

On the other hand, in **CF2.5** (**Fig. 3-9**(c)), boundary steel U-sections restrained shear sliding. Further, lateral confinement of the steel U-sections restrained crushing of the boundary concrete. Thus, concrete spalling was not significant, though flexure–shear cracks were distributed at the wall bottom. However, in **CF2.5VH** (**Fig. 3-9**(d)) with the greater shear demand, post-yield web concrete spalling occurred in the plastic hinge zone, as the shear strength was degraded by inelastic deformation; Compression softening occurred at the web concrete cracked in diagonal tension (Vecchio and Collins 1986), and the softening effect was pronounced due to spalling of concrete subjected to cyclic loading. In the test specimens with aspect ratio of 2.5, local buckling of steel U-sections (with headed studs only) occurred only in **CF2.5** with the thinner plates, and its effect on displacement ductility was marginal. However, in actual walls subjected to axial force, greater stresses and strains occur in the steel U-sections, which can cause early buckling of steel plates and subsequent crushing of the boundary concrete.

Fig. 3-10 shows the damage of concrete and steel according to the drift level of δ = 1.0% – 4.0%, for the specimens with aspect ratio of 2.0. For the specimens except **CF2SF**, diagonal cracking in the web concrete was initiated at δ = 0.1% – 0.2% (In **CF2SF**, concrete cracking was not observed due to the faceplates). In

RF2S (**Fig. 3-10**(a)), crack patterns of concrete (e.g., horizontal flexural cracks at wall boundaries and diagonal tension cracks in wall web) were similar to those of **RF2.5S** with the greater aspect ratio. Further, after $\delta = \pm 1.5\%$, the post-yield shear-sliding failure mode was also similar: horizontal flexural cracks penetrated into the entire cross section at the wall bottom, and subsequent spalling of concrete occurred along the horizontal cracks. In the composite specimens except **CF2SF**, the ultimate failure mode was the same: post-yield web concrete crushing in the plastic hinge zone. In **CF2** (**Fig. 3-10**(b)), the number and spacing of diagonal tension cracks were similar to those of **RF2S**. On the other hand, in the boundary elements, damage of concrete was moderate, due to the confinement of steel U-sections. Local buckling of the steel U-sections was not significant. In **CF2VH** (**Fig. 3-10**(c)), the number of diagonal tension cracks increased in the web concrete showing smaller spacing, but spalling and crushing of the concrete were less severe due to the closely spaced horizontal rebars (see $\delta = 1.0\%$ in **Figs. 3-10**(b) and (c)). However, due to the greater inelastic deformation ($\delta_u = +3.10\%$ and -2.85% for **CF2**; and +3.95% and –4.04% for **CF2VH**), local buckling occurred at the flange plate of steel U-sections. In **CF2SB** (**Fig. 3-10**(d)), the number of diagonal cracks (with greater spacing) decreased, and spalling of the web concrete decreased, despite the absence of web reinforcing bars (see $\delta = 3.0\%$ in **Figs. 3-10**(b) and (d)). This is because the greater spacing of concrete cracks alleviated compression softening of the diagonal concrete struts due to diagonal cracking. In **CF2SF** (**Fig. 3-10**(e)), at $\delta = \pm 1.5\%$, local buckling of the faceplates was initiated at the edges of the plates. At $\delta = \pm 3.0\%$, plate buckling became severe, followed by crushing of the web concrete, and vertical sliding between the web and boundary elements. No notable separation occurred between the web and boundary elements.

In RC specimens **RF2.5S** and **RF2S** with the large area of boundary reinforcement (overall vertical steel ratio was the same as that of composite specimens), post-yield shear sliding occurred at the wall bottom, while in **RF2.5** with uniformly distributed vertical reinforcement, shear sliding failure did not occur. At the critical section for shear sliding, it is generally assumed that the applied shear is resisted by 1) friction between cracks, 2) adhesive bond/interlocking, and 3) dowel action of shear-transfer reinforcement perpendicular to the assumed shear plane (fib MC, 2010). In the test specimens, horizontal cracks penetrated the entire cross section at the wall base, due to large flexural tension zone and due to the effect of reversed cyclic loading. Further, after flexural yielding, the crack widths in the flexural tension zone significantly increased due to the elongation of vertical reinforcement experiencing large plastic strains, and the cracks in the compression zone were not completely closed due to the residual tensile strains of vertical rebars (i.e., longitudinal elongation mechanism, Eom and Park 2010). In such condition, shear sliding is resisted primarily by the dowel action of vertical web reinforcement, as the resistances for shear-friction and adhesive bond/interlocking disappear in the overall cross section, and the dowel resistance of boundary rebars degrade due to the large plastic strains. Particularly in **RF2.5S** and **RF2S**, vertical steel area was concentrated at the wall boundary (flexural tension zone), while the use of vertical web reinforcement was minimized. Thus, after flexural yielding, large plastic strains and elongation occurred in most of vertical rebars at the wall base, which significantly degraded the overall resistance against shear sliding. On the other hand, **in RF2.5**, in which vertical steel area is distributed in the cross section, vertical web reinforcement remained elastic even after flexural yielding (see the tested vertical strains in **Fig. 3-23** in Section 3.4.9). In this case, the web region can provide adequate resistance for shear sliding. For this reason, shear sliding did not occur in **RF2.5**.

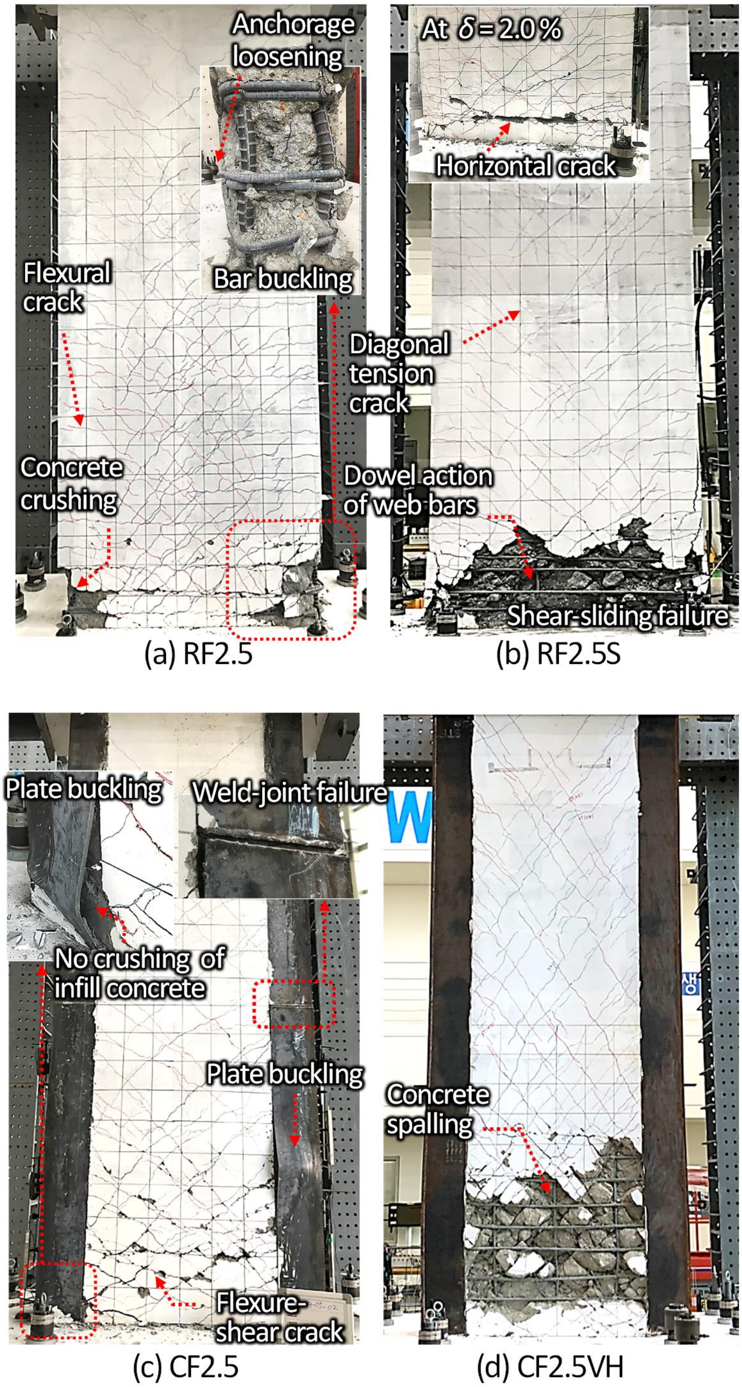

Fig. 3-9 Failure mode of flexural yielding specimens with aspect ratio of 2.5.

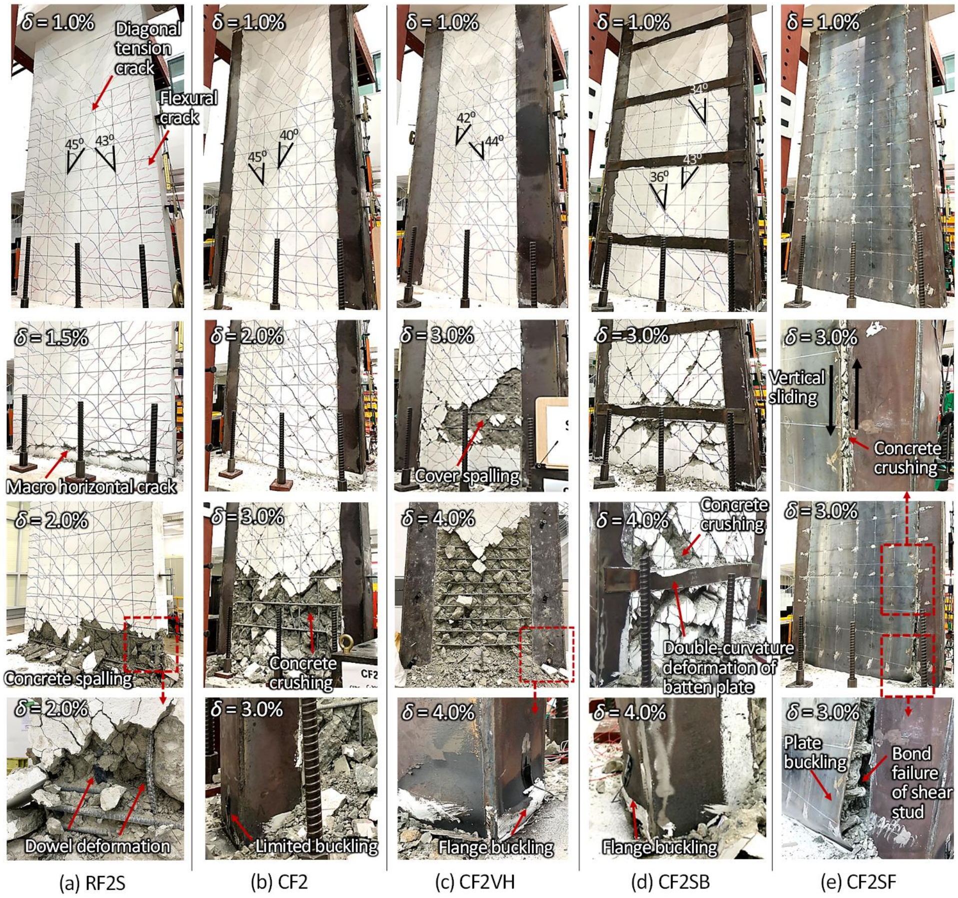

Fig. 3-10 Failure mode of flexural yielding specimens with aspect ratio of 2.0.

Fig. 3-11 shows the plastic hinge zone of the composite specimens subjected to large inelastic deformation. As damage of web concrete (i.e., diagonal strut) became severe in the plastic hinge zone, the steel U-sections resisted shear force by moment-resisting frame action (boundary elements in the plastic hinge zone acted as short columns), showing double-curvature flexural deformation. Further, in **CF2SB**, the steel plate beams in the plastic hinge zone also showed double-curvature deformation, developing plastic hinges at the ends of the steel plate beam.

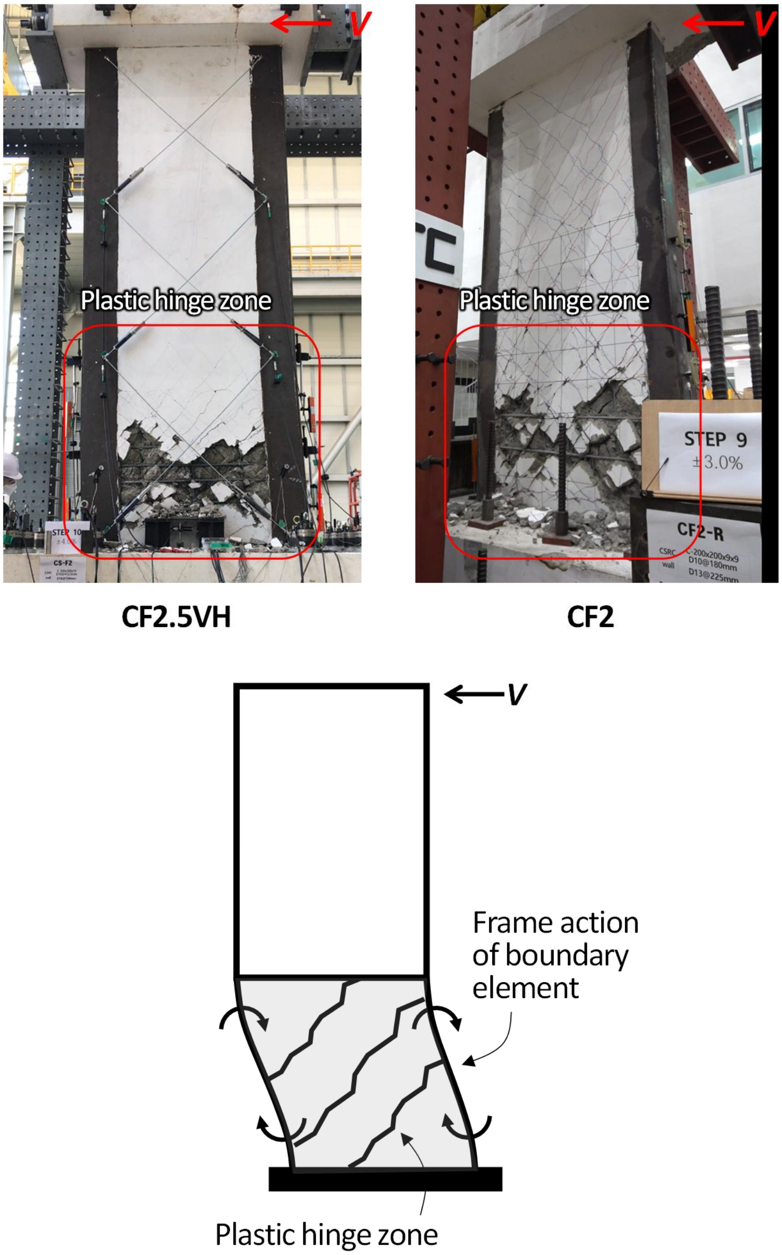

Fig. 3-11 Failure mode and deformation of plastic hinge zone.

3.4.3 Flexural rotation in plastic hinge zone

In flexural walls, plastic hinge rotation capacity is generally used to assess the nonlinear seismic performance (ASCE 41, 2017). Thus, for the test specimens, the overall flexural rotation θ_f within the plastic hinge length l_p was calculated based on the LVDT measurement, as follows:

$$\theta_f = \theta_{f1} + \theta_{f2} \tag{3-1}$$

$$\theta_{f1} = (r_1 - r_3)/b_f \tag{3-2}$$

$$\theta_{f2} = (r_2 - r_4)/b_f \tag{3-3}$$

where, θ_{f1} and θ_{f2} = rotations over the two consecutive panels (with a height of $0.5l_p$ = 800 mm) at the wall bottom, respectively; r_1, r_2, r_3, and r_4 = displacements measured from the vertical LVDTs of R1, R2, R3, and R4; and b_f = distance between the vertical LVDTs (see **Fig. 3-6**).

Fig. 3-12 and **Fig. 3-13** show the lateral load-flexural rotation (V– θ_f) relationships of the specimens with aspect ratios of 2.5 and 2.0, respectively. Compared to the V–δ relationships, the V–θ_f relationships showed relatively fat hysteresis hoops, which implies the majority of energy was dissipated by flexural deformation in the plastic hinge zone. However, at the load cycles where wall failure occurred (almost at δ_u), the increase in flexural deformation decreased, particularly in the specimens showing post-yield shear failure (**CF2.5VH**, **CF2**, **CF2VH**, **CF2SB** showing web concrete spalling; and **RF2.5S** and **RF2S** showing excessive shear sliding). This result indicates that the strength degradation in plastic hinge zone was greater in shear, rather than in flexure.

Table 3-4 shows the yield rotation θ_{fy}, ultimate rotation θ_{fu}, and plastic hinge rotation θ_p (= θ_{fu} − θ_{fy}), in which θ_{fy} and θ_{fu} were determined from envelopes of the V– θ_f relationships, according to **Fig. 3-8**(f) (The detailed calculation was explained in section 3.5: “Effect of Design Parameters”). In the composite specimens with aspect ratio of 2.5 (**Fig. 3-12**), the plastic hinge rotations θ_p (= 0.0255 rad for **CF2.5**; 0.0208 rad for **CF2.5VH**) were greater than those of RC specimens (= 0.0193 rad for **RF2.5**; 0.0094 rad for **RF2.5S**). In **RF2.5S**, the θ_p was the lowest due to post-yield shear sliding. Similar trend was also seen in the specimens with the lower aspect ratio of 2.0 (**Fig. 3-13**): θ_p of the composite specimens (= 0.0144 – 0.0224 rad) were greater than that of RC specimen **RF2S** showing shear sliding (θ_p = 0.0069 rad). Further, for all composite specimens, θ_p was greater than the requirement of 0.015 rad for the performance level of “Collapse Prevention” of ASCE 41 (2017).

Table 3-4 Flexural rotation and shear deformation measured in plastic hinge zone

Specimens		Flexural rotation			Shear deformation		
		yield θ_y [rad]	ultimate θ_y [rad]	plastic θ_p [rad]	yield $\gamma_{s1,y}$ [rad]	ultimate $\gamma_{s1,u}$ [rad]	plastic $\gamma_{s1,p}$ [rad]
Aspect ratio = 2.5	RF2.5	0.0070	0.0263	0.0193	0.0013	0.0075	0.0062
	RF2.5S	0.0051	0.0144	0.0094	0.0014	0.0288	0.0274
	CF2.5	0.0047	0.0303	0.0255	0.0019	0.0355	0.0336
	CF2.5VH	0.0058	0.0266	0.0208	0.0026	0.0420	0.0394
Aspect ratio = 2.0	RF2S	0.0046	0.0115	0.0069	0.0020	0.0097	0.0077
	CF2	0.0051	0.0197	0.0146	0.0033	0.0280	0.0247
	CF2VH	0.0060	0.0284	0.0224	0.0032	0.0319	0.0287
	CF2SB	0.0059	0.0256	0.0197	0.0034	0.0326	0.0292
	CF2SF	0.0059	0.0202	0.0144	0.0016	0.0225	0.0209

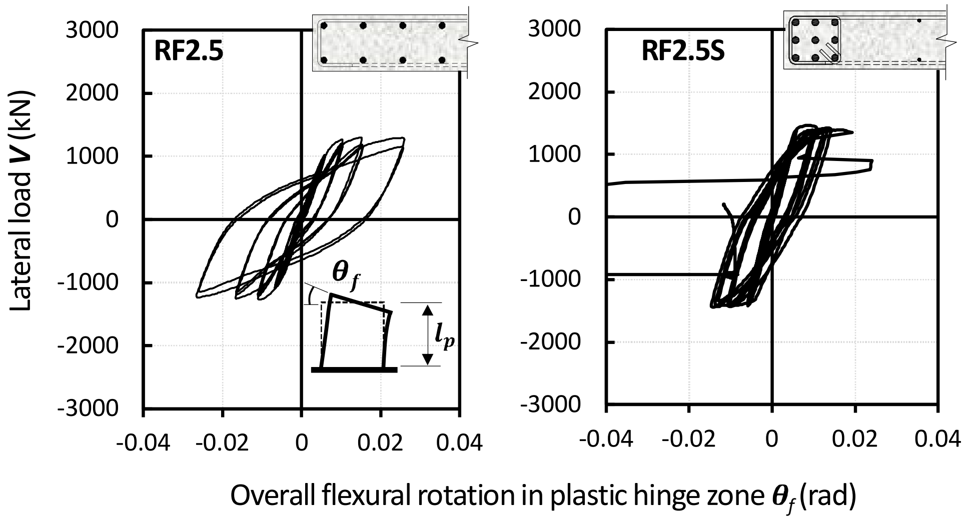

Fig. 3-12 Lateral load-plastic hinge rotation relationships of flexural yielding specimens with aspect ratio of 2.5.

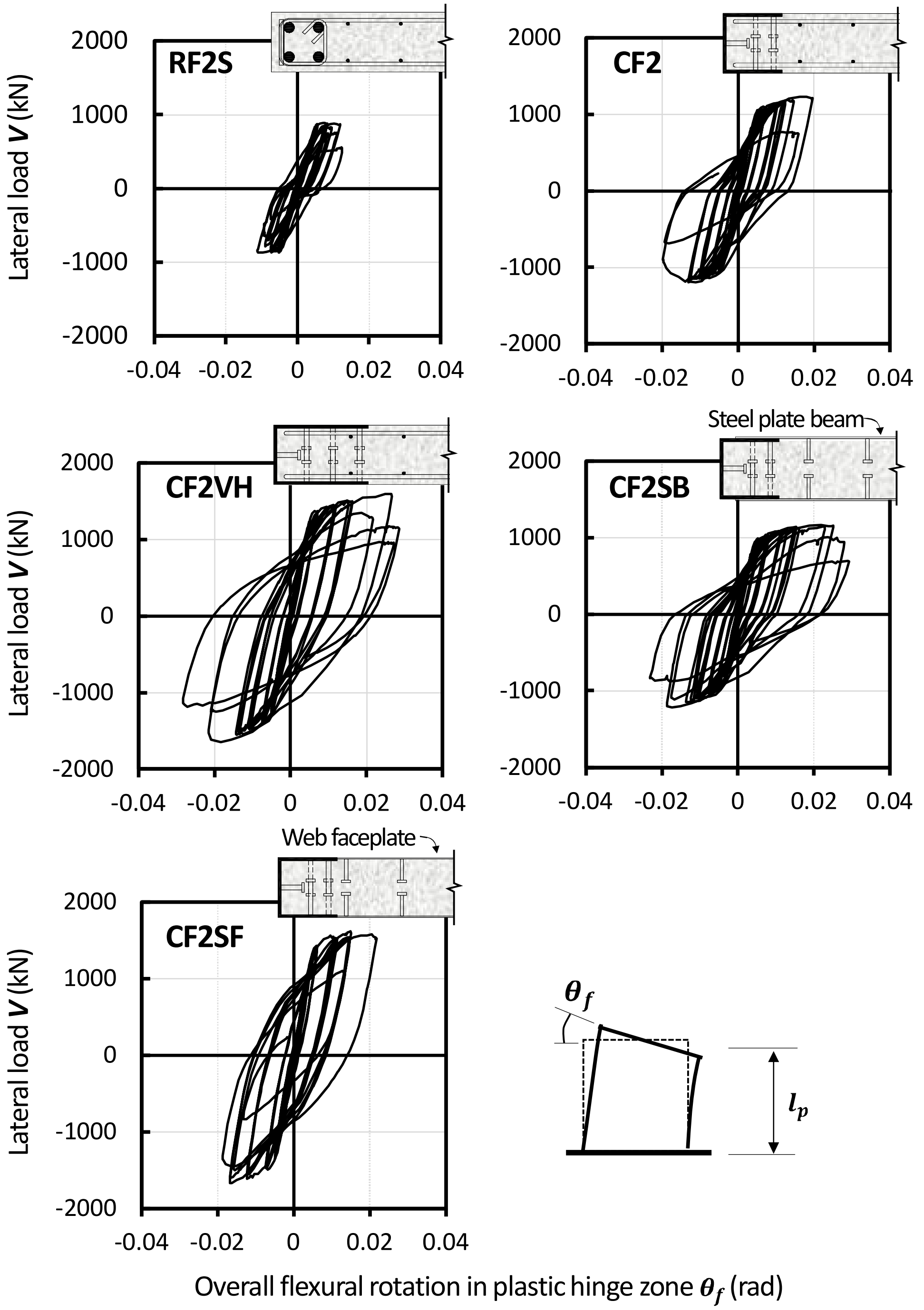

Fig. 3-13 Lateral load-plastic hinge rotation relationships of flexural yielding specimens with aspect ratio of 2.0.

Fig. 3-14 and **Fig. 3-15** shows the two consecutive flexural rotations θ_{f1} and θ_{f2}, according to the lateral drift ratio. For all specimens, θ_{f1} was greater than θ_{f2}, due to greater flexural moment (i.e., curvature) at the wall bottom. As the lateral drift increased, the two rotations increased in the same direction until δ = 2.0%. However, in the composite specimens showing post-yield web concrete spalling (**CF2.5VH**, **CF2S**, **CF2VH**, **CF2SB**), the direction of θ_{f2} became reversed in the large inelastic deformation (after δ = 2.0%), opposite to the direction of θ_{f1}. This is because, due to the post-yield shear degradation of web concrete, boundary steel U-sections within the plastic hinge zone resisted shear by frame action, showing double-curvature flexural deformation. In this case, the direction of θ_{f1} may not be coincide with that of θ_{f2} (see Fig. **3-14**). Such reversal did not occur in the RC specimens and the composite specimens **CF2.5** and **CF2SF**. In **CF2.5**, the damage of web concrete in the plastic hinge zone was relatively insignificant due to the early weld fracture (**Fig. 3-9**(c)). In **CF2SF**, the post-yield shear degradation of web concrete was alleviated due to the high shear contribution of web faceplates.

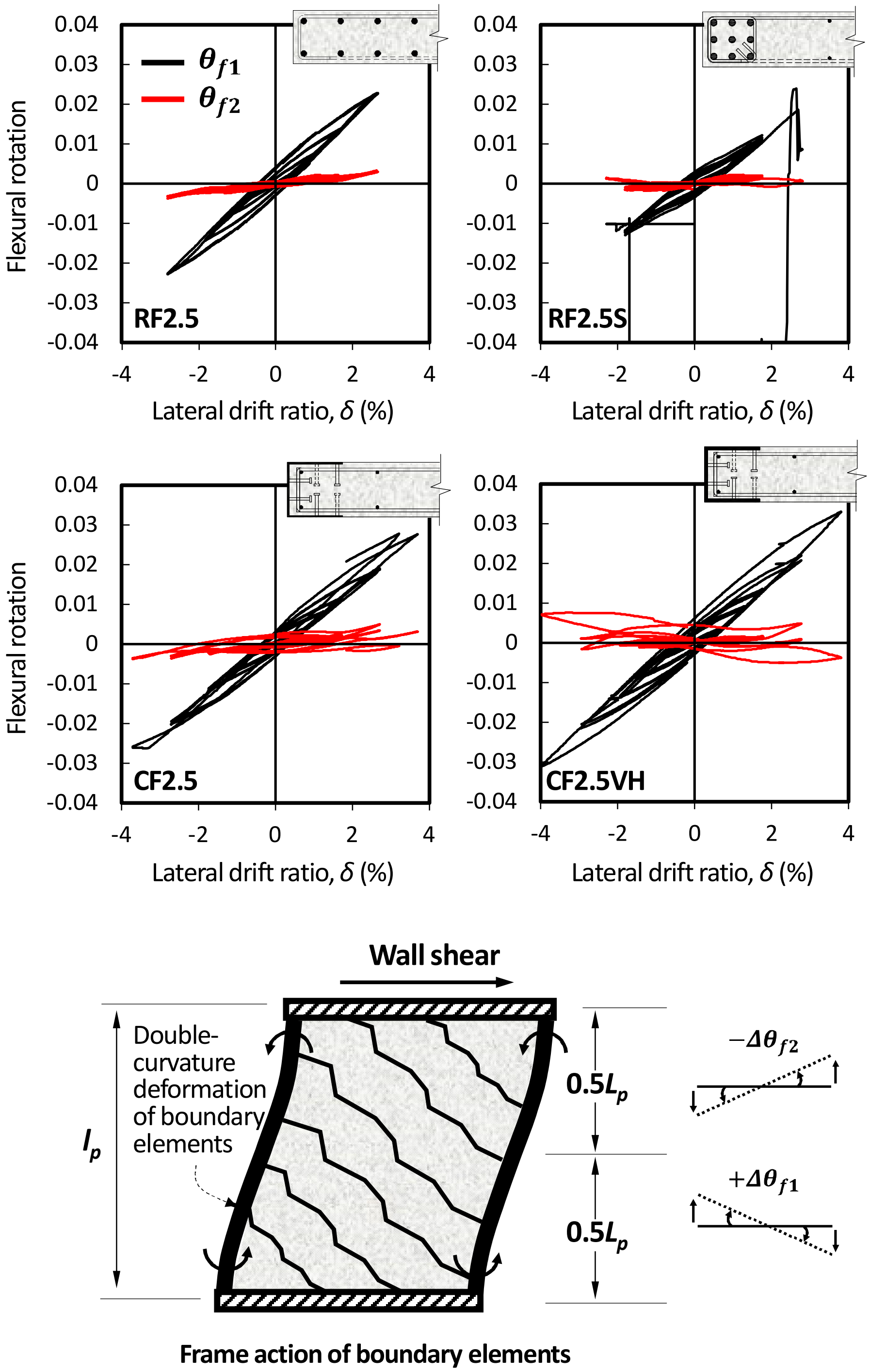

Fig. 3-14 Flexural rotation-drift ratio relationships of flexural yielding specimens with aspect ratio of 2.5.

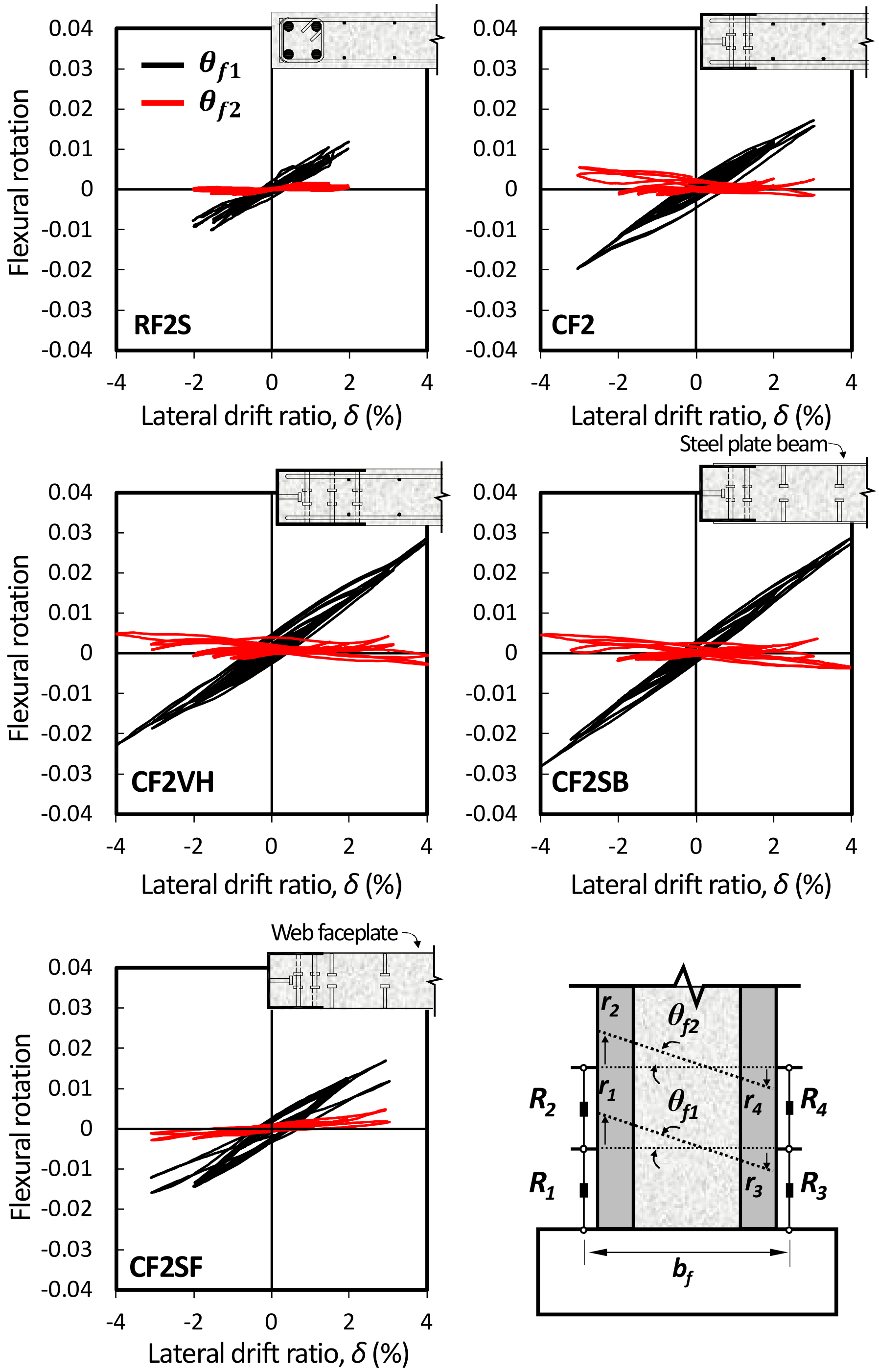

Fig. 3-15 Flexural rotation-drift ratio relationships of flexural yielding specimens with aspect ratio of 2.0.

3.4.4 Shear deformation

The shear deformation in the wall web was calculated from the measurement of diagonal LVDTs (see **Fig. 3-6**), as follows:

$$\gamma_{s,j} = \frac{d_o}{2b_s h_s}\left[\left(d_{2j} - d_o\right) - \left(d_{2j-1} - d_o\right)\right] \tag{3-4}$$

where, b_s, h_s and d_o = original lengths of width, height, and diagonals of a square shear panel (b_s = h_s = 1,400 mm and d_o = 1,980 mm for specimens with aspect ratio 2.5; b_s = h_s = 1,300 mm and d_o = 1,690 mm for specimens with aspect ratio 2.0); and d_{2j-1} and d_{2j} = deformed lengths of diagonal LVDTs at j^{th} shear panel (j = index number of shear panels = 1, 2, 3 for the specimens with aspect ratio 2.5; and j = 1, 2 for the specimens with aspect ratio 2.0).

Fig. 3-16 and **Fig. 3-17** show the lateral load–shear deformation (V–γ_s) relationships of the specimens with the aspect ratios of 2.5 and 2.0, respectively. In the figures, $\gamma_{s,1}$, $\gamma_{s,2}$, and $\gamma_{s,3}$ indicate the shear deformations measured at the upper, central, and lower panels of the walls (in the 2.0-aspect ratio specimens, $\gamma_{s,2}$ indicates the shear deformation in the upper panel of the walls, **Fig. 3-17**). For all specimens, as the lateral load increased, the shear deformation increased. However, after flexural yielding, the increase in shear deformation was concentrated at the lower panel (i.e., plastic hinge zone, see $\gamma_{s,1}$) where the damage of web concrete was significant (Note that the increase in flexural deformation relatively decreased in the plastic hinge zone, see **Fig**. **3-12** and **Fig. 3-13**). Such phenomenon was more pronounced in the specimens showing post-yield shear failure (all specimens except **RF2.5**, **CF2.5**, and **CF2SF**). On the other hand, in **CF2SF** with web faceplates, both the shear deformations in the upper and lower panel significantly increased after web concrete crushing. Compared to the V–θ relationships shown in **Fig. 3-7** and **Fig. 3-8**, the V–γ_s relationships showed narrow hysteresis loops (i.e., a pinched curve), due to diagonal tension cracking and subsequent shear sliding. Nevertheless, the composite specimens with steel U-sections showed relatively large hysteresis loop area. In the composite specimens, the maximum shear deformation $\gamma_{s1,u}$ in the plastic hinge zone was 0.036 – 0.042 rad for the specimens with aspect ratio 2.5; and 0.023 – 0.033 rad for the specimens with aspect ratio 2.0 (**Table 3-4**). Those $\gamma_{s1,u}$ values were greater than those of the counterpart RC specimens ($\gamma_{s1,u}$ = 0.0075 – 0.029 rad). In the composite specimens **CF2.5VH** and **CF2VH** (with greater area of steel U-sections), the $\gamma_{s1,u}$ values were greater than those of **CF2.5** and **CF2**, respectively. These results indicates that the frame action of boundary steel U-sections increased the shear deformation capacity in the plastic hinge zone, particularly when steel U-sections with greater area were used.

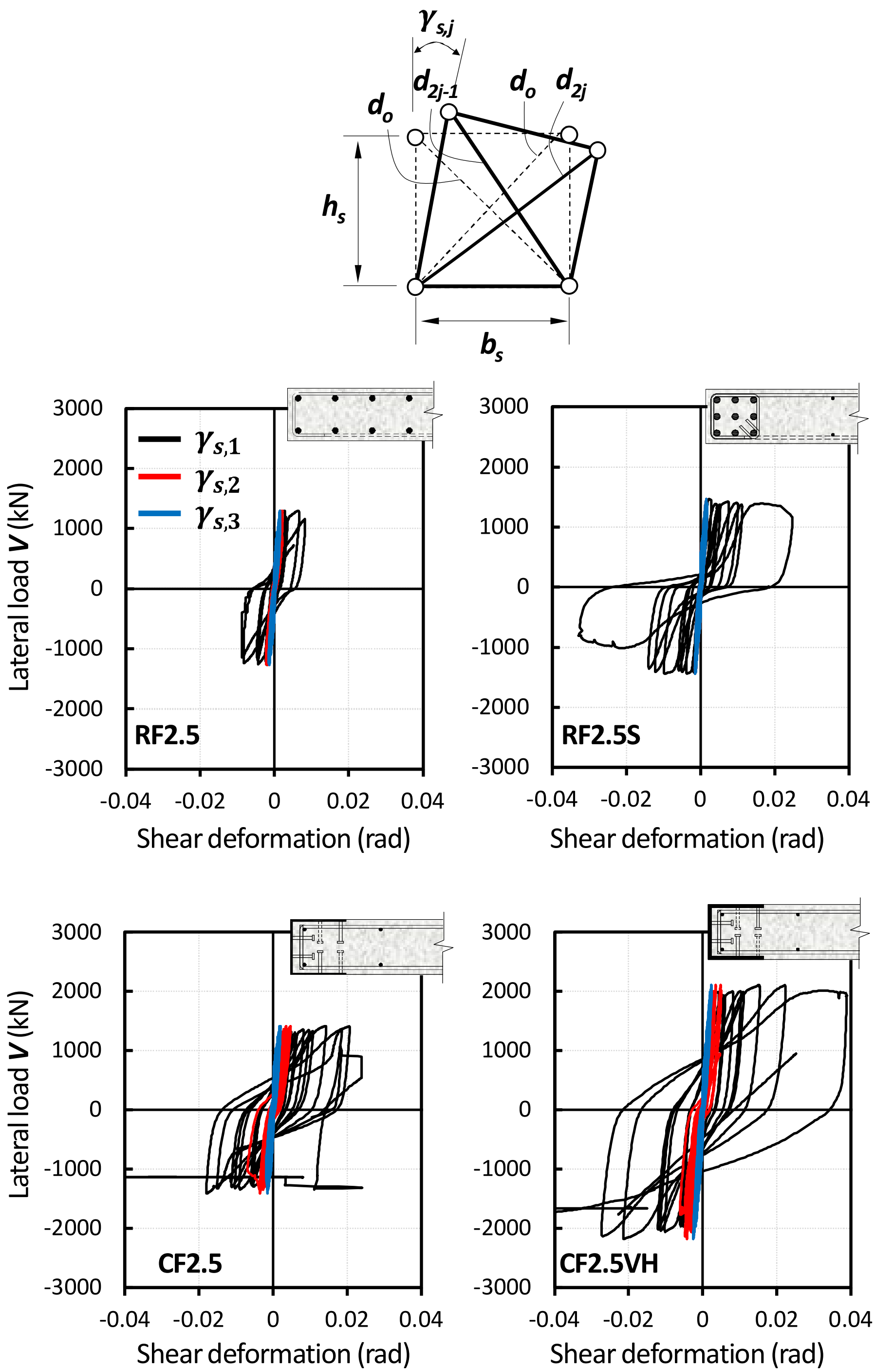

Fig. 3-16 Lateral load-shear deformation relationships of flexural yielding specimens with aspect ratio of 2.5.

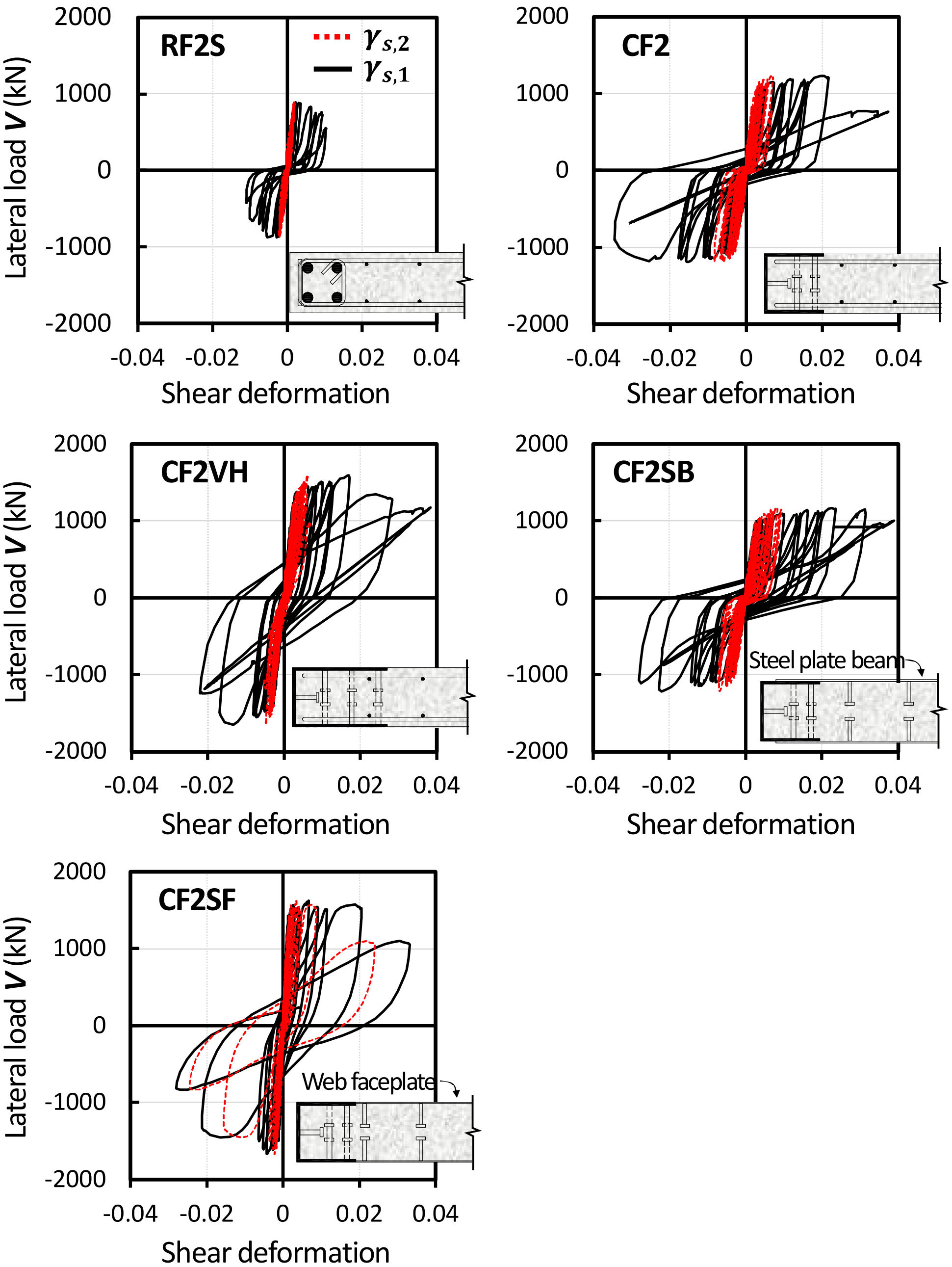

Fig. 3-17 Lateral load-shear deformation relationships of flexural yielding specimens with aspect ratio of 2.0.

3.4.5 Displacement contributions

The overall lateral displacement Δ of a cantilever wall is defined as the sum of flexural (Δ_f), shear (Δ_s), and sliding (Δ_{sl}) deformations, as follows:

$$\Delta = \Delta_f + \Delta_s + \Delta_{sl} \tag{3-5}$$

In the present study, the flexural contribution Δ_f was calculated as the sum of contributions $\Delta_{f,L}$ and $\Delta_{f,U}$, in which $\Delta_{f,L}$ and $\Delta_{f,U}$ indicate the flexural deformations contributed by the plastic hinge zone (with a height of l_p) and the upper panel (with a height of $l_s - l_p$) of the wall, respectively (**Fig. 3-18** and **Fig. 3-19**). Here, $\Delta_{f,L}$ was calculated based on the flexural rotations θ_{f1} and θ_{f2} measured from the vertical LVDTs, considering inelastic curvature distribution in the plastic hinge zone of walls (Massone and Wallace 2004, see **Appendix I**). $\Delta_{f,U}$ was calculated using the effective flexural stiffness $(EI)_{eff}$ (= $0.35E_cI_g + E_sI_s$, in which E_c and E_s = elastic moduli of concrete (= $4{,}700\sqrt{f_c'}$) and steel (= 200 GPa), respectively; and I_g and I_s = moments of inertia of the gross wall section and boundary steel sections, respectively, ACI 318, 2019). In the specimens with aspect ratio of 2.5, the shear contribution Δ_s was estimated as the sum of the contributions $\Delta_{s,1}$, $\Delta_{s,2}$, and $\Delta_{s,3}$ measured in the bottom, middle, and top shear panels with equal height h_s (**Fig. 3-18**). In the specimens with aspect ratio of 2.0, only $\Delta_{s,1}$ and $\Delta_{s,2}$ were considered (**Fig. 3-19**). **Appendix I** presents the detailed calculations of $\Delta_{f,L}$, $\Delta_{f,U}$, $\Delta_{s,1}$, $\Delta_{s,2}$, and $\Delta_{s,3}$. The sliding deformation Δ_{sl} was directly measured from a horizontal LVDT installed at 150 mm above the wall base (see the LVDT of S4 in **Fig. 4**).

Fig. 3-18 shows the ratios of the displacement contributions $\Delta_{f,L}$, $\Delta_{f,U}$, Δ_s, and Δ_{sl} to the overall lateral displacement Δ measured from the test specimens with aspect ratio of 2.5. In general, the sum of the contributions agreed with the measured overall lateral displacement, except for a case (at δ = 2.5 %) shown in **RF2.5S**. In **RF2.5S** showing excessive shear sliding, the sliding displacement Δ_{sl}

was not properly measured due to spalling of concrete at the wall base. Thus, the sum of displacement contributions was 20 % less than the overall lateral displacement Δ. In all specimens, the contribution of flexural deformation ($\Delta_{f,L}$ + $\Delta_{f,U}$) was greater than that of shear deformation. The flexural contribution in the lower part ($\Delta_{f,L}$) showed the greatest ratio: $\Delta_{f,L}$ / Δ = 78% for **RF2.5**, 69% for **RF2.5S**, 70% for **CF2.5**, and 67% for **CF2.5VH**, on average. After flexural yielding (δ = 0.8% – 0.9%), $\Delta_{f,L}$ / Δ gradually increased, and $\Delta_{f,U}$ / Δ decreased. This result indicates that plastic deformation was concentrated at the lower part. In **RF2.5S**, **CF2.5**, and **CF2.5VH** with boundary reinforcement, $\Delta_{f,L}$ / Δ was less than that of **RF2.5**, but the shear contribution was greater (Δ_s / Δ = 13 % for **RF2.5**; 24 % for **RF2.5S**; 23 % for **CF2.5**; and 27 % for **CF2.5VH**, on average). This is because the contribution of boundary reinforcement was greater in the flexural stiffness, and less in the shear stiffness. In **RF2.5S**, at δ_u = 2.5 %, Δ_s / Δ significantly increased due to shear sliding.

Fig. 3-18(e) shows the contribution of each panel $\Delta_{s,1}$, $\Delta_{s,2}$, and $\Delta_{s,3}$ to the overall shear deformation Δ_s measured in **CF2.5**. Until flexural yielding (δ < 0.9%), $\Delta_{s,1}$, $\Delta_{s,2}$, and $\Delta_{s,3}$ were similar each other. However, after flexural yielding, the shear deformation significantly increased at the lower panel (i.e., plastic hinge zone). This result indicates that the post-yield shear degradation was concentrated in the plastic hinge zone.

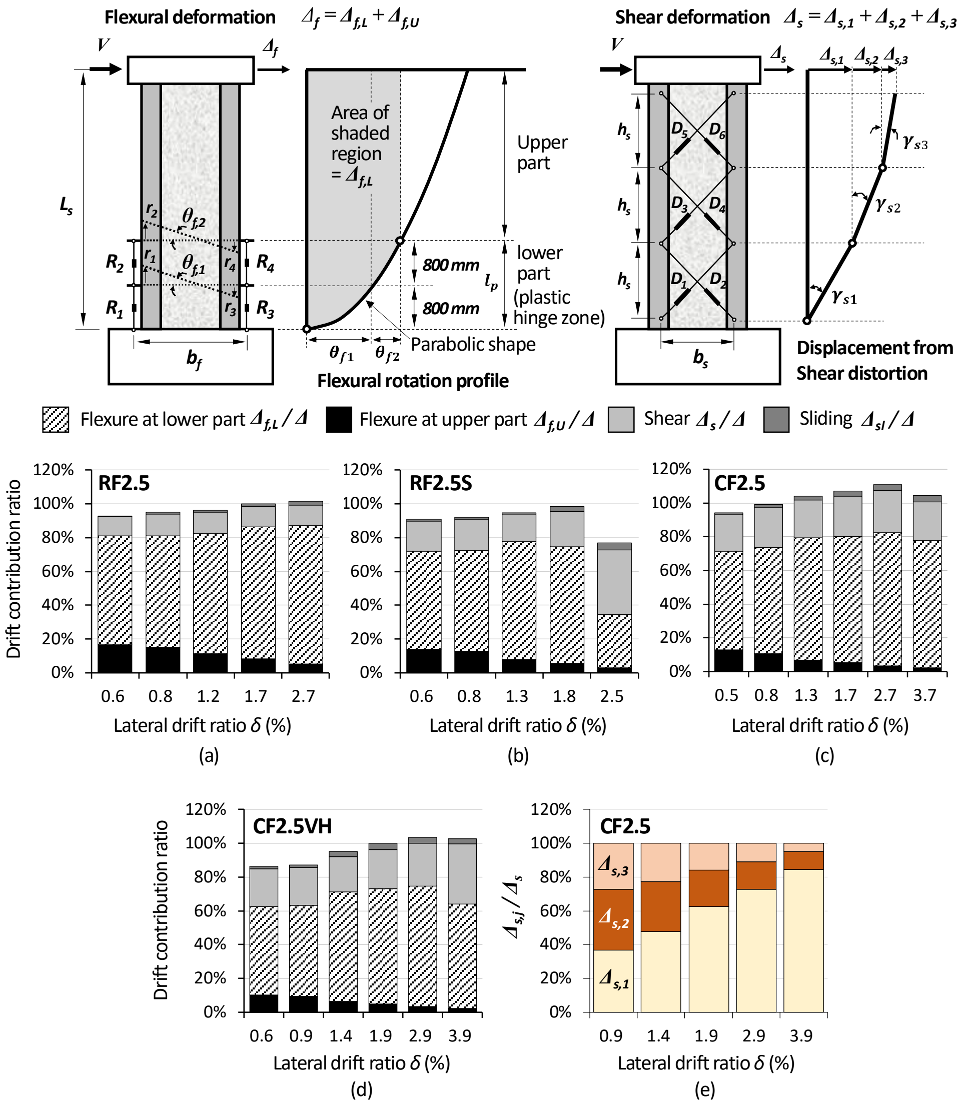

Fig. 3-18 Lateral displacement contributions measured in flexural yielding specimens with aspect ratio of 2.5.

In the specimens with the aspect ratio of 2.0 (**Fig. 3-19**), the difference between the measured overall lateral displacement Δ and the sum of the calculated contributions was 8% on average. The flexural deformation in the plastic hinge zone was $\Delta_{f,L} / \Delta$ = 62%–67%, which was slightly less than that of the specimens with greater aspect ratio of 2.5 (= 67%–78%). On the other hand, the overall shear deformation was increased to 20%–36% of Δ (Δ_s / Δ = 20% for **RF2S**, 32% for **CF2**, 28% for **CF2VH**, 36% for **SF2SB**, and 14% for **CF2SF**, respectively). These results indicate that the walls, including 2.5-aspect ratio walls, basically showed flexural deformation behavior. Nevertheless, the contribution of shear deformation to the overall deformation is not negligible. In 2.0-aspect ratio specimens except **CF2SF**, Δ_s / Δ was slightly greater than that of RC specimen **RF2S**, due to the greater shear demand. On the other hand, Δ_s / Δ of **CF2SF** was the smallest until failure (δ = 3.0 %), due to the contribution of steel faceplates to the shear stiffness. In **RF2S**, the sliding contribution ratio Δ_{sl} / Δ (= 26 %) significantly increased at the ultimate drift ratio. On the other hand, in the composite specimens, as the steel U-sections restrained shear sliding, the sliding contribution was only 4%–7% of Δ.

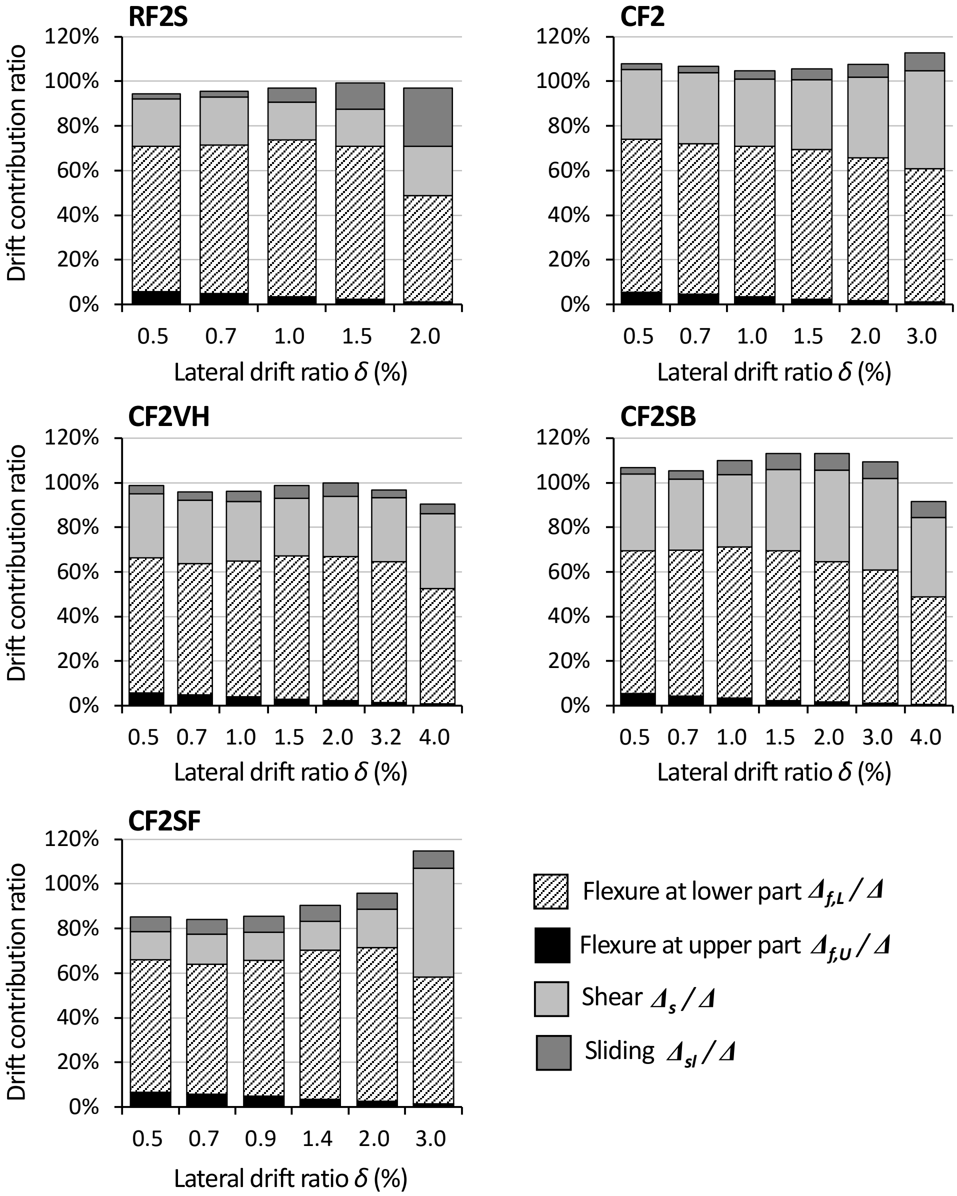

Fig. 3-19 Lateral displacement contributions measured in flexural yielding specimens with aspect ratio of 2.0.

3.4.6 Flexural and shear stiffness

Fig. 3-20 shows the relationships (V–Δ_f and V–Δ_s) between the lateral load and the two lateral displacement contributions from the flexural deformation (Δ_f) and shear deformation (Δ_s) (average for positive and negative loading direction). From the relationships, the respective secant stiffness was calculated at each drift level as shown in **Fig. 3-21**, and the respective yield stiffness was calculated according to **Fig. 3-10**(f): flexural yield stiffness K_f, and shear yield stiffness K_s (**Table 3-5**). For all specimens, the shear stiffness was much greater than the flexural stiffness. Thus, the specimens showed flexure-dominant deformation behavior. However, the shear secant stiffness was more rapidly degraded (**Fig. 3-21**). Thus, as the inelastic deformation increased, the shear secant stiffness became close to the flexural secant stiffness. For this reason, in **Fig. 3-18** and **Fig. 3-19**, as the lateral drift increased, the contribution of shear deformation to the lateral displacement (Δ_s / Δ) gradually increased.

In **CF2.5** with steel U-sections, the flexural yield stiffness was K_f = 56.1 kN/mm, which was similar to that of **RF2.5S** (with the same steel area of boundary reinforcement) (**Table 3-5**). In **CF2.5VH** (with the greater area of steel U-sections), the flexural yield stiffness was increased to 71.8 kN/mm. In **RF2.5** (with uniformly distributed vertical reinforcement), the flexural yield stiffness (K_f = 34.8 kN/mm) was the smallest. In the composite specimens with aspect ratio of 2.0, the average of K_f (= 63.7 – 87.2 kN/mm) was slightly increased due to the lower aspect ratio, which was 28% greater than that of counterpart RC specimen **RF2S** with vertical boundary rebars (K_f = 59.1 kN/mm). Further, in **CF2VH** (with greater area of steel U-sections), K_f was 11% and 24% greater than that of **CF2** and **CF2SB**, respectively. In **CS2SF**, K_f (= 87.2 kN/mm) was the greatest due to the large steel area of boundary steel U-sections and web faceplates.

On the other hand, in the composite specimens **CF2.5** and **CF2.5VH** with aspect ratio of 2.5, the shear yield stiffness K_s (= 194.6 – 202.5 kN/mm) was even less than that of counter RC specimen **RF2.5S** (K_s = 233.5 kN/mm). Such trend was also seen in the specimens with the lower aspect ratio (except **CF2SF**): K_s =198.1 kN/mm for **RF2S** and K_s =134.3 – 177.5 kN/mm for **CF2**, **CF2VH**, and **CF2SB** (**Table 3-5**). This result indicates that the contribution of steel U-sections to the flexural yield stiffness was pronounced, but the contribution to the shear yield stiffness was not significant. However, after flexural yielding, the contribution of steel U-sections to the shear stiffness increased, due to severe damage of the web concrete. Thus, in **Fig. 3-21**, the post-yield shear stiffness of the composite specimens was greater than that of the RC specimens. Specimen **CF2SB** with steel plate beams showed the smallest K_s (= 134.3 kN/mm). This result indicates that, compared to uniformly distributed reinforcing bars, the use of steel plate beams with relatively large spacing was less effective in the shear yield stiffness of the wall web. In **CF2SF**, K_s (= 420.2 kN/mm) was significantly greater than that of other specimens, due to the contribution of steel faceplates.

Table 3-5 Flexural yield stiffness and shear yield stiffness

Specimens		Flexural yield stiffness K_f [kN/mm]	Shear yield stiffness K_s [kN/mm]
Aspect ratio = 2.5	RF2.5	34.8	233.7
	RF2.5S	53.9	233.5
	CF2.5	56.1	194.6
	CF2.5VH	71.8	202.5
Aspect ratio = 2.0	RF2S	59.1	198.1
	CF2	71.2	147.1
	CF2VH	63.7	134.3
	CF2SB	79.0	177.5
	CF2SF	87.2	420.2

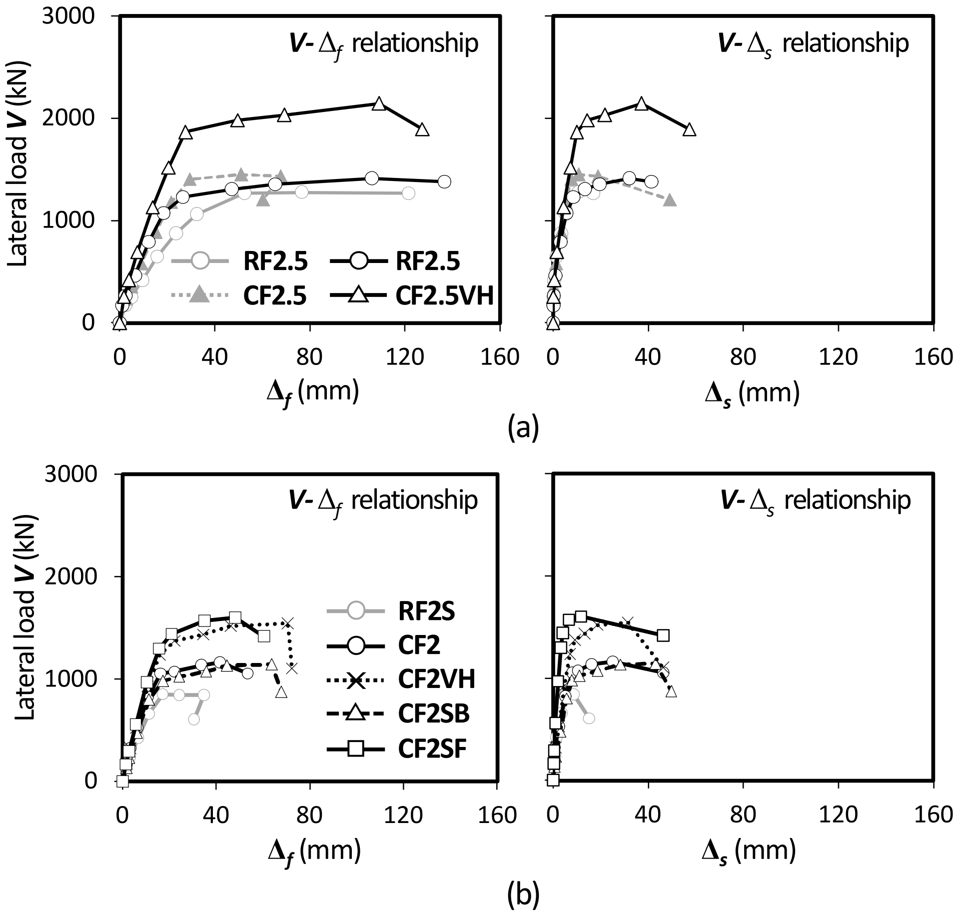

Fig. 3-20 Relationships between lateral load and two displacement contributions from flexural and shear deformations measured in flexural yielding specimens with: (a) 2.5-aspect ratio; (b) 2.0-aspect ratio.

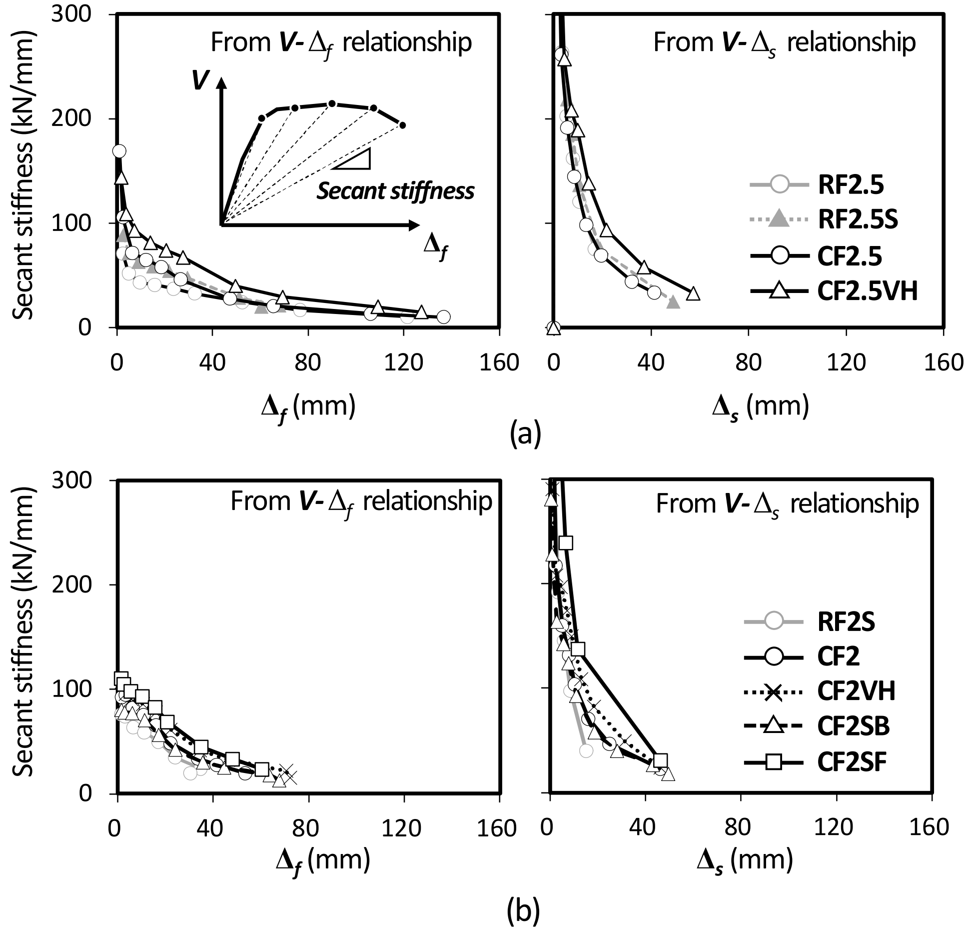

Fig. 3-21 Flexural secant stiffness and shear secant stiffness measured in flexural yielding specimens with: (a) 2.5-aspect ratio; (b) 2.0-aspect ratio.

3.4.7 Deformation capacity

In the composite specimens with aspect ratio of 2.5, the boundary reinforcement ratio (ρ_c = 0.89 %) was designed to be 33 % less than that of counterpart RC specimen **RF2.5S** (ρ_c = 1.34%) (**Table 3-1**). However, in the tests, its contribution to deformation capacity (i.e., ultimate drift ratio δ_u) was not clear, as the load-carrying capacity of **RF2.5S** was degraded by shear sliding before flexural crushing; the boundary confinement detailing did not work properly in the large deformation of the wall. Nevertheless, the greater deformation capacity of **CF2.5** (see **Table 3-3**) indicates that the steel U-sections provided good resistance for shear sliding as well as lateral confinement. In **CF2.5VH** with the greater area of steel U-sections, the deformation capacity was similar to that of **CF2.5**, due to the post-yield web concrete spalling. Further, in **CF2.5** and **CF2.5VH**, the steel U-sections restrained crack penetration (into the boundary zone), and crushing and spalling of the boundary concrete. Thus, although ρ_c was less than the requirement of ACI 318 seismic provisions (ACI 2019), the ultimate drift ratio (close to 4.0 %) was much greater than the design drift ratio of 1.5 %, and was similar to those of existing composite walls (Massone et al. 2017) with boundary confinement detailing of ACI 318. This result indicates that ductility of the proposed composite wall can be significantly increased by using the steel U-section if closely spaced headed studs are provided.

In the composite specimens with aspect ratio of 2.0, their test results were similar to those of the specimens with aspect ratio of 2.5: due to the boundary steel U-sections, the shear demand (i.e., flexural strength) increased, and post-yield shear failure occurred in the web concrete, before crushing of boundary zone. For this reason, the effect of boundary confinement on the deformation capacity could not be properly evaluated. In **CF2SB**, the deformation capacity was greater than that of **CF2**, because the use of steel plate beams alleviated post-yield shear degradation in the web concrete. In **CF2VH** with the greater area of steel U-sections, the deformation capacity was greater than that of **CF2**, despite the higher strength (i.e., higher shear demand). This is because, during the post-yield shear degradation of web concrete, the steel U-sections with greater area provided better contribution to shear resistance of plastic hinge zone (i.e., greater flexural strength of steel U-sections for frame action, refer to subfigure in **Fig. 3-14**). In **CF2SF** with steel web faceplates, despite the higher strength, the deformation capacity was similar to that of **CF2** with conventional web reinforcement. However, it was slightly less than the deformation capacity of **CF2VH**, due to more brittle failure mode of the composite web.

3.4.8 Energy dissipation

The energy dissipation corresponding to the overall deformation per load cycle (E_D) was defined as the area enclosed by a load cycle in the tested V–Δ curve. **Fig. 3-22**(a) shows the variation of $\sum E_D$ accumulated during all load cycles. **Fig. 3-22**(b) shows the energy dissipation ratio κ (= E_D / E_P), in which E_P indicates the energy dissipation based on the idealized elastic–perfectly plastic cyclic curve. After δ = 1.0 %, as the plastic deformation increased after flexural yielding, $\sum E_D$ began to increase, while κ decreased as shear cracking and sliding degraded the strength and stiffness of walls.

In the specimens with aspect ratio of 2.5, at δ = 3.0%, $\sum E_D$ (= 1,428 kN·m) of **CF2.5** was 46%–57% greater than that of **RF2.5** ($\sum E_D$ = 980 kN·m) and **RF2.5S** ($\sum E_D$ = 911 kN·m), despite the similar peak strength. Further, in **CF2.5**, the energy dissipation ratio (κ = 0.66) was 25% greater than that of **RF2.5** and **RF2.5S** (κ = 0.53 for both). This is because the boundary steel U-sections alleviated the degradation of strength and stiffness, restraining flexural and shear cracks. For this reason, the steel plates experienced larger plastic strains, which increased energy dissipation. In **CF2.5VH** with the greater area of steel U-sections, the maximum $\sum E_D$ (= 2,616 kN·m) was 34% greater than that of **CF1** (= 1,947 kN·m), and 166%–187% greater than that of the RC specimens, due to the greater strength, stiffness, and deformation capacity. However, at the ultimate drift ratio of δ_u, κ was slightly less than that of **CF1**, due to more severe damage in the web concrete.

In the composite specimens with the lower aspect ratio of 2.0, at δ = 2.0 %, $\sum E_D$ and κ were 80%–156% and 30%–86% greater than those of counterpart **RF2S**, respectively. For the energy dissipation ratio, at $\delta = \delta_u$, κ (= 0.46–0.57) was 28%–58% greater than that of **RF2S** (κ = 0.36). **CF2SF** (with steel web faceplates) showed the greatest κ (= 0.68 on average), due to the highest steel ratio. Nevertheless, for all specimens with aspect ratio of 2.0, the energy dissipation ratio was slightly less than that of the specimens with aspect ratio of 2.5. This is because, due to the lower aspect ratio, the shear demand increased, which caused more shear cracking and sliding in the plastic hinge zone (the maximum shear demand V_{test}/A_g = 2.38 – 3.97 MPa for specimens with aspect ratio of 2.5; and 2.75– 5.14 MPa for specimens with aspect ratio of 2.0).

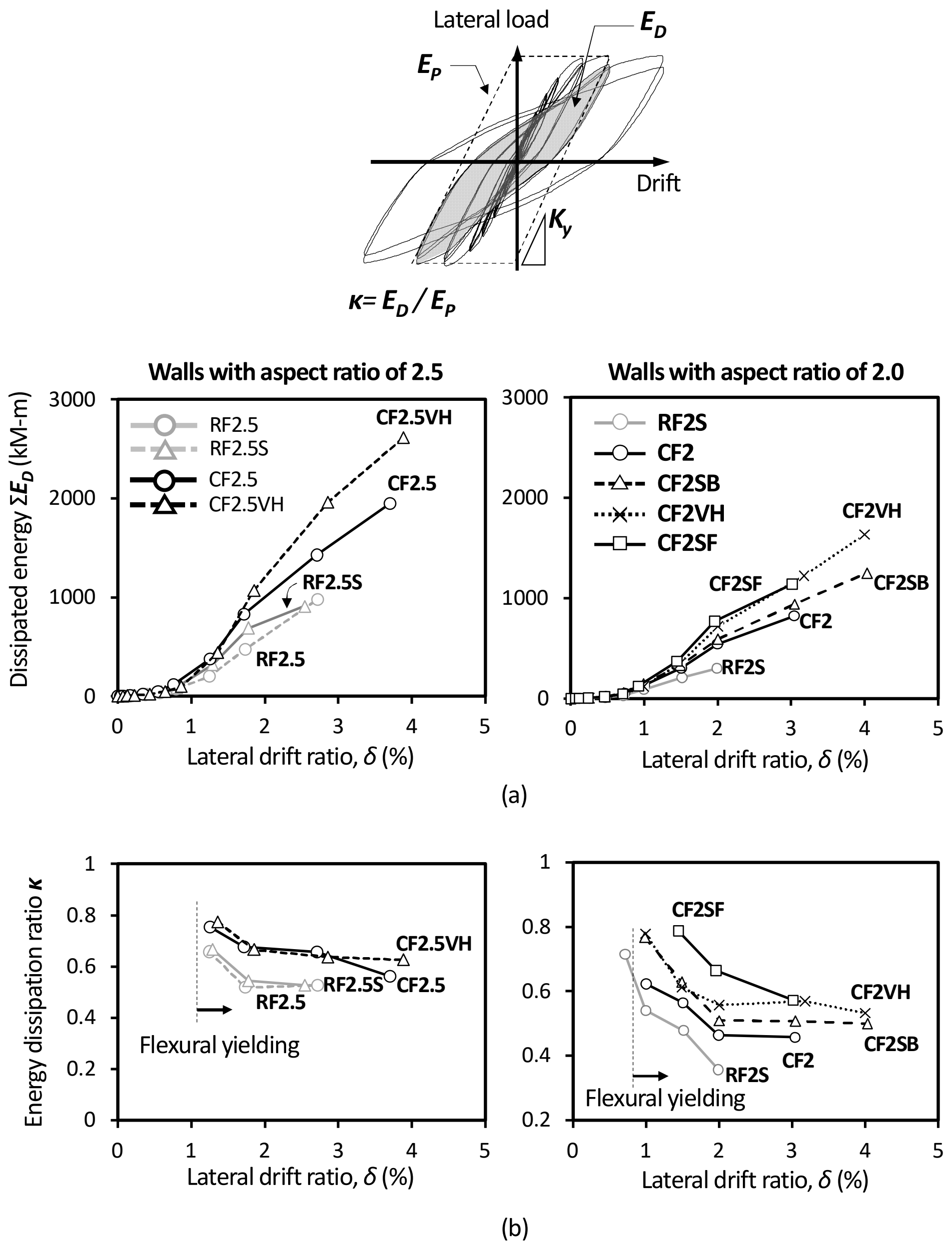

Fig. 3-22 Cumulative energy dissipation and energy dissipation ratio.

3.4.9 Vertical strain distribution

Fig. 3-23 shows the vertical strain distribution of reinforcing bars and steel U-sections measured at 150 mm above the wall base, in the positive loading direction. For all flexural mode specimens, before flexural yielding, the vertical strains linearly increased from the compression face (origin in the horizontal axis) to the tension face (end point in the horizontal axis). After flexural yielding, the tensile strains of boundary reinforcements significantly increased beyond the yield strain. In particular, the linear strain distribution was distorted, as plastic tensile strains increased in the reinforcements and local shear deformation became severe at the wall base (i.e., D-region with fan-shaped cracks). **Fig. 3-23**(a) shows the test results of the 2.5-aspect ratio specimens. In **RF2.5**, the maximum tensile strain was 0.020 mm/mm at the peak strength (at δ_o = 1.6 %). In **RF2.5S**, the maximum tensile strain 0.013 mm/mm (at δ_o = 1.1 %) was less than that of **RF2.5**, because the flexural plastic deformation was less due to shear-sliding deformation. In **CF2.5** and **CF2.5VH**, the maximum tensile strains of the steel plates were 0.045 mm/mm (at δ = 1.7 %) and 0.043 mm/mm (at δ_u = 3.8 %), respectively, which were much greater than those of the vertical boundary rebars in **RF2.5** and **RF2.5S**. This result indicates that the steel plates of the composite walls experienced much greater plastic strains as shear cracking and shear sliding were restrained. Furthermore, their values were much greater than the hardening strain of ε_h = 0.01 mm/mm measured from the tension tests (see **Fig. 3-5**).

Similar tendency was shown in the specimens with the lower aspect ratio of 2.0. However, due to the early malfunction of strain gauges, the strains exceeding 0.02 mm/mm were excluded, thus the maximum tensile strains were not properly measured. In **RF2S**, plastic strains were limited, due to early horizontal shear sliding. In **CF2SF**, the compressive strains of the faceplate (1300 mm from the origin) were greater than that of the boundary element. This is because the plane section assumption (i.e., linear strain distribution) did not work due to local buckling of the faceplate and vertical sliding between the web and boundary elements

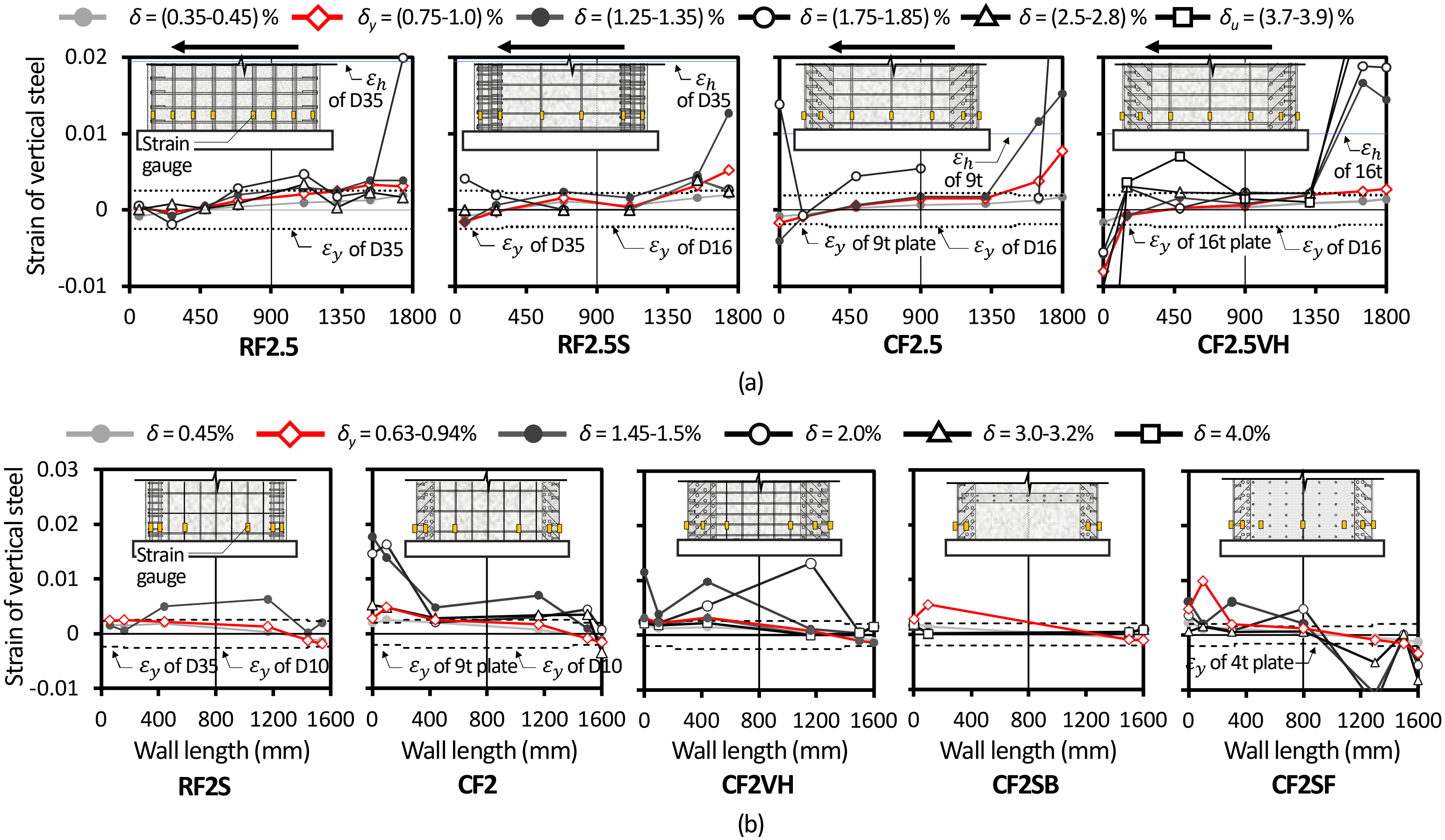

Fig. 3-23 Vertical strain distribution across the wall cross section measured in flexural yielding specimens.

3.4.10 Horizontal strain distribution

Fig. 3-24 and **Fig. 3-25** show the tensile strain distribution of horizontal reinforcements (including steel web faceplates in **CF2SF**) along the wall height, measured in the positive loading direction. Before flexural yielding (noted as red-colored lines), the horizontal strains were less than the yield strains. Then, the strains were maintained without notable increase. This results confirms that the specimens failed in flexure, rather than in shear. On the other hand, in **CF2SB** with steel plate beams (**Fig. 3-25**), the strain in the plastic hinge zone (within 1,600 mm from the wall base) significantly increased beyond the yield strain, though the tested strength (V_{test} = 1,193 kN) was less than the nominal shear strength (V_n = 1,426 kN). This is because plastic strains were developed at the ends of the plate beams subjected to combined flexural moment (frame action) and tension (truss action). In **CF2SF** with web faceplates (**Fig. 3-25**), the strains were very small, due to the large steel area of faceplates.

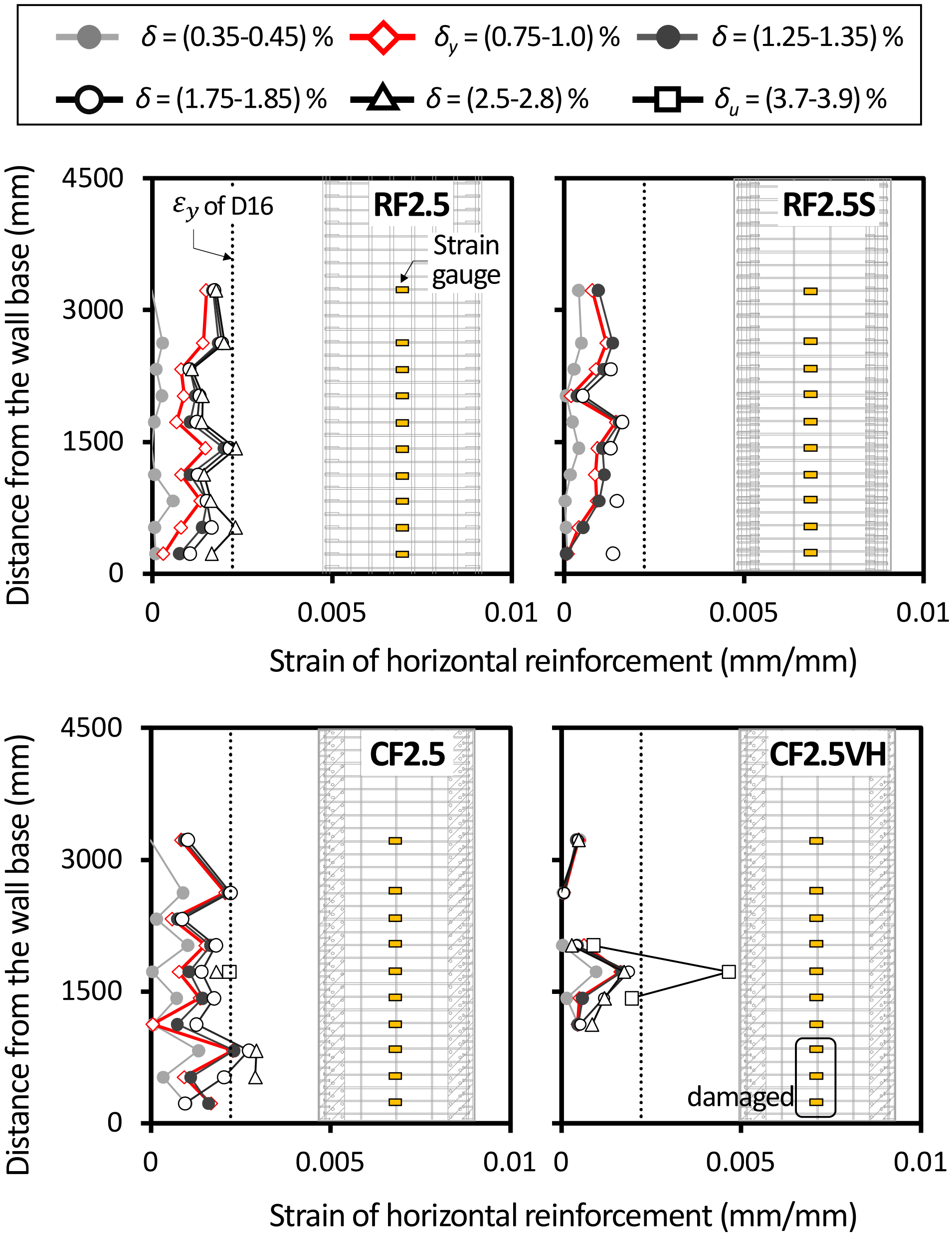

Fig. 3-24 Horizontal strain distribution measured in flexural yielding specimens with aspect ratio of 2.5.

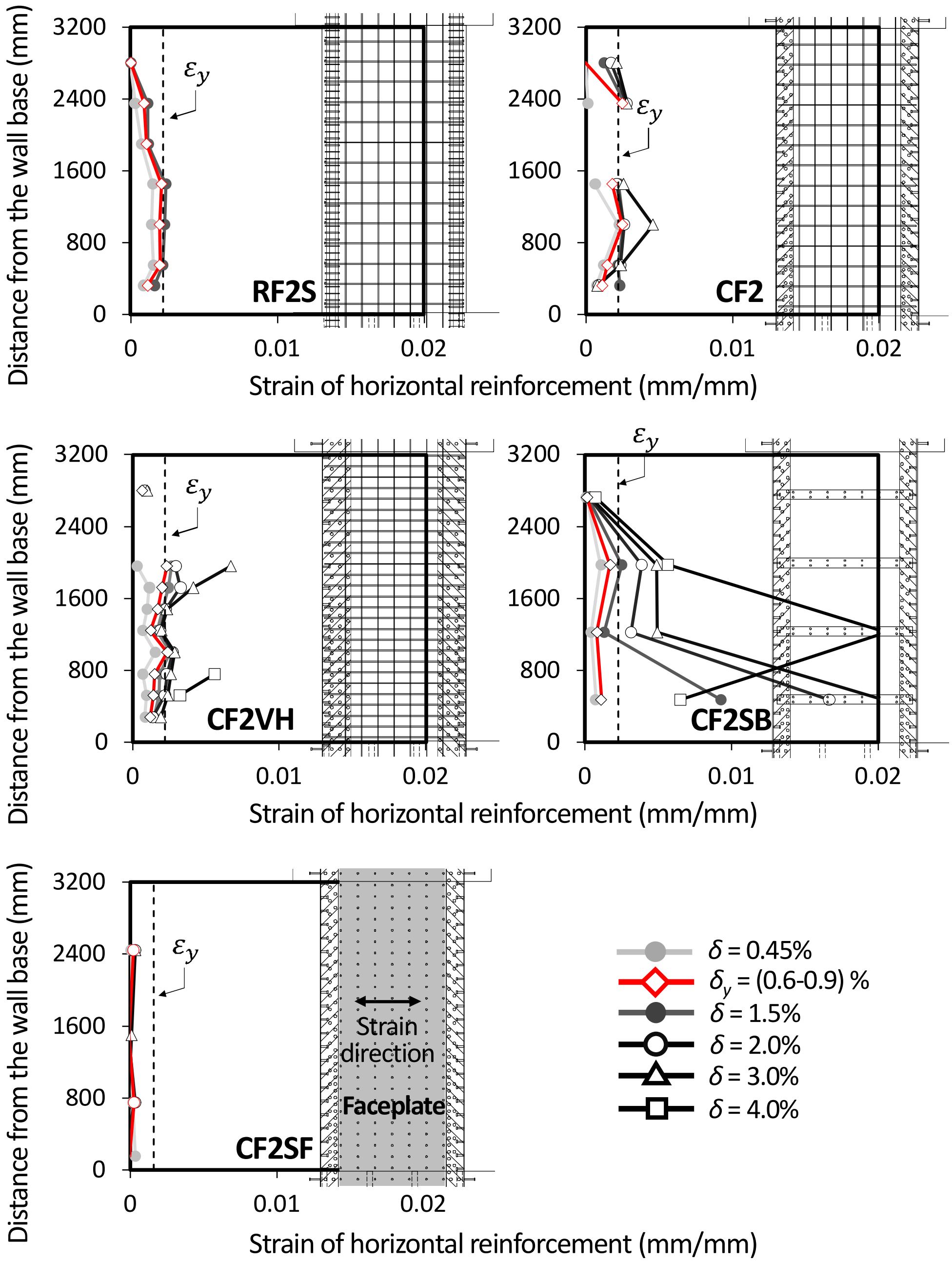

Fig. 3-25 Horizontal strain distribution measured in flexural yielding specimens with aspect ratio of 2.0.

3.4.11 Shear strain of steel plates

Fig. 3-26 shows the strains of the web plates of U-shaped steel elements measured in the specimens with aspect ratio of 2.5. The shear strain of the steel plates was measured from three-axial strain gauges arranged in two perpendicular directions and a 45^o angle between them. The shear strain was calculated using strain transformation, as follows:

$$\gamma_{xz} = 2\varepsilon_{45} - (\varepsilon_x + \varepsilon_z) \tag{3-6}$$

where, γ_{xz} = shear strain in *xz* axes, in which *x* and *z* axes indicate horizontal and vertical directions, respectively. In the 2.5 aspect ratio specimens, the strains were measured at 750 mm distance from the wall base (denoted as T1 and T2 in **Fig. 3-26**). **Fig. 3-26**(a) shows the strains ε_x and ε_z. Before tensile yielding of the web plates, the strain ε_x was inversely proportional to ε_z. Here, the strain ratio ε_x / ε_z ranged from –0.29 to –0.22, which is similar to Poisson's ratio of steel (≈ –0.3, Greaves et al. 2011). **Figs 3-26**(b) shows the shear strain γ_{xz}. In general, the shear strain at each location increased as the lateral drift ratio increased. However, in **CF2.5VH**, the direction of shear strains measured at T1 and T2 was not always the same as that of shear force on wall: the direction of T1-strains was opposite to that of shear force. To clarify this phenomenon, in the specimens with the lower aspect ratio of 2.0, more numbers of strain gauges were used to measure the shear strains of steel U-sections along the wall height.

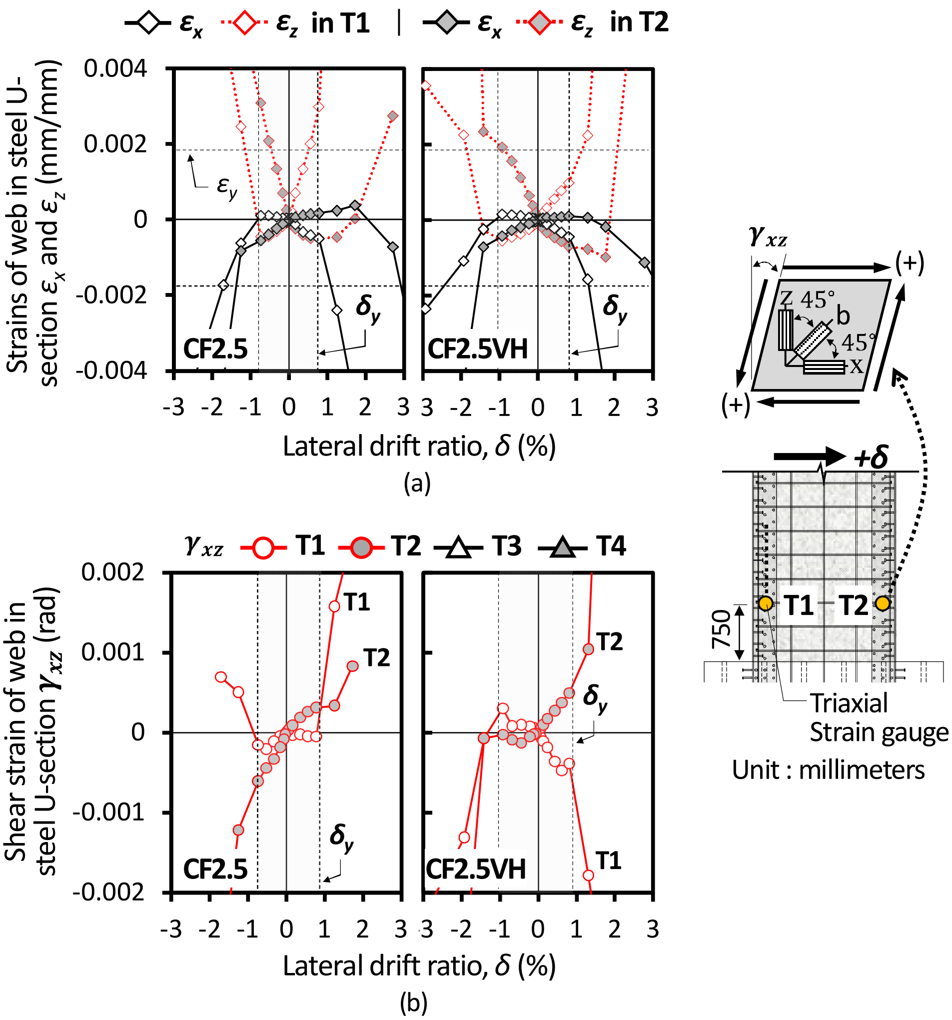

Fig. 3-26 Strains of steel U-sections in flexural yielding specimens with aspect ratio of 2.5.

Fig. 3-27 shows the shear strain distributions of steel plates (web plate of steel U-sections and steel faceplate) along the wall height, in the positive loading direction. In the steel U-sections (**Fig. 3-27**(a)), at flexural yielding, the strains were less than the shear yield strain (denoted as $\gamma_y = 0.6F_y/G_s$, G_s = elastic shear modulus of steel = 76.9 GPa) (AISC 360, 2016). Further, the strains varied with the wall height: the shear strain in the flexural tension side (denoted as "FT") was greater at the top of the walls, while the shear strain in the flexural compression side (denoted as "FC") was greater at the bottom. This is because, due to the diagonal tension cracking, the shear contribution of the steel U-sections was concentrated at the two ends of the diagonal struts (see points A and B in **Fig. 3-27**).

In the steel faceplate (**Fig. 3-27**(b)), at flexural yielding, the shear strains were relatively large in the mid height of the wall. At this time, the shear strains at the center of the faceplate section (denoted as "M") were greater than those at the two edges (denoted as "L" and "R"). After δ = 1.5 %, the shear strains in the plastic hinge zone increased beyond the shear yield strain.

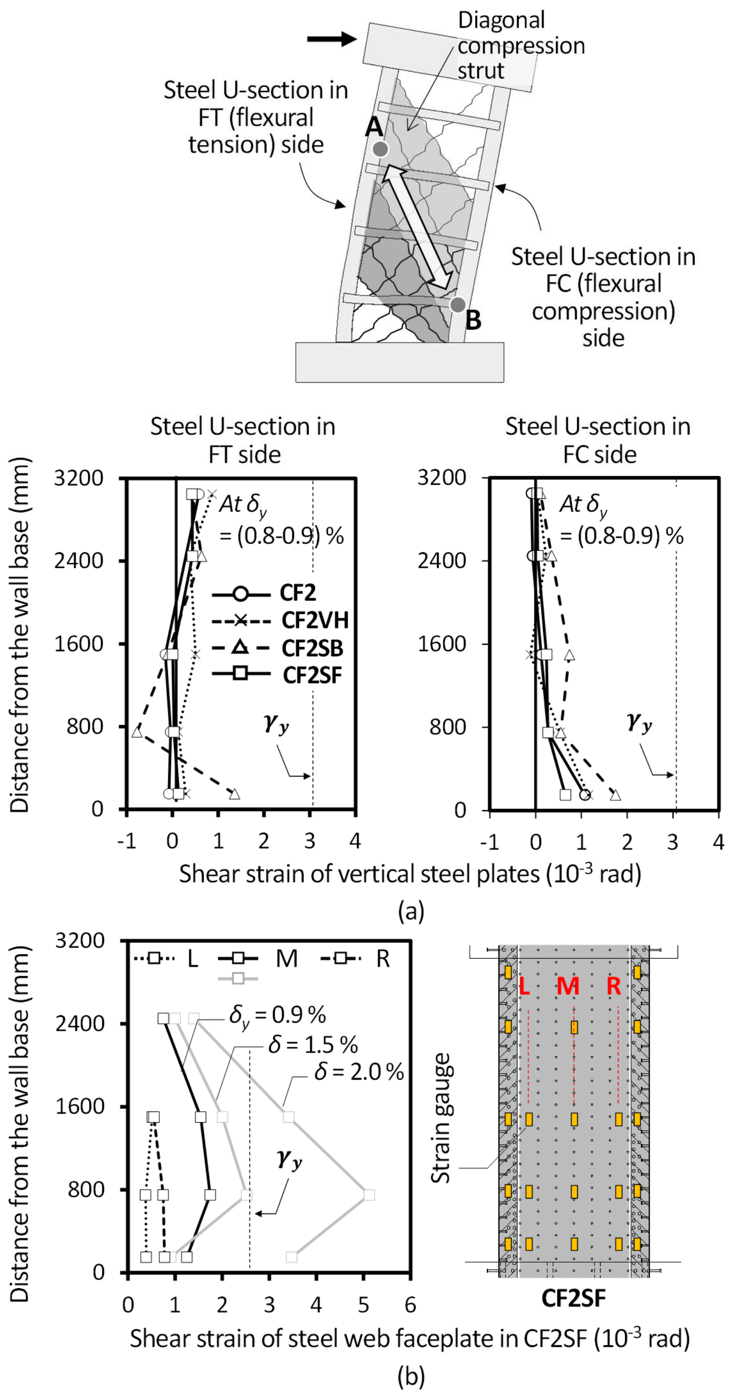

Fig. 3-27 Shear strains of steel U-sections in flexural yielding specimens with aspect ratio of 2.0.

3.5 Effect of Design Parameters

Two groups of wall specimens were tested: walls with aspect ratios of 2.5 and 2.0. For each group of specimens, the following design parameters were considered to investigate their effects on the flexural performance of the specimens: (1) The arrangement of vertical steel section (*uniform distribution or concentration at boundary element,* only tested in 2.5-aspect ratio specimens); (2) The type of boundary reinforcement (*reinforcing bar or steel U-section*); (3) The sectional area of steel U-section: web plate thickness (*of 9 or 16 mm*) and length (of *200 or 320 mm*); and (4) The type of web reinforcement (*horizontal reinforcing bar or steel plate beam or vertical steel faceplate,* only tested in 2.0-aspect ratio specimens). In the present study, the specimen properties of walls with aspect ratio of 2.5 were slightly different from those of walls with aspect ratio of 2.0 (e.g., section dimensions and concrete strength, refer to **Table 3-1** and **Table 3-2**). Thus, a direct comparison was performed within the walls with the same aspect ratio.

Table 3-6 shows the structural capacity ratio of the specimens, according to the relevant design parameters. In the table, the yield stiffness K_y, yield drift ratio δ_y, and lateral drift ductility μ were calculated from V–δ envelope curves of the specimens, as follows: K_y = the slope corresponding to $0.75V_{test}$; $\delta_y = V_{test} / (K_y l_s)$; and $\mu = \delta_u / \delta_y$.

3.5.1 Arrangement of vertical steel section

Fig. 3-28(a) compares the tested V–δ envelope curves of **RF2.5**, **RF2.5S**, and **CF2.5**. Note that the three specimens had the same area of vertical reinforcement (boundary and web steels). In the comparison of **RF2.5** and **RF2.5S**, the use of boundary reinforcement (ρ_{be} = 9.6 %, f_y = 499 MPa) increased V_{test} by 13%; K_y by 39%; and μ by 15%. However, μ increased due to shear sliding, thus the energy dissipation capacity $\sum E_D$ did not increase. The increase in overall lateral stiffness K_y was due to the increase in flexural stiffness K_f (55% increase), rather than in shear stiffness. In the comparison of **RF2.5** and **CF2.5**, by using steel U-sections, the deformation-related capacities δ_u, μ, and θ_p were more increased. However, the shear stiffness decreased as the large steel area was concentrated at wall boundaries.

3.5.2 Type of boundary reinforcement

In the comparison of **RF2.5S** and **CF2.5** (**Fig. 3-28**(a)) with the same boundary steel ratio, the use of boundary steel section of U-300×300×9×9 (ρ_{be} = 9.6%, F_y = 379 MPa) increased δ_u, μ and θ_p by 45%, 38% and 173%, respectively, as the boundary concrete was laterally confined and shear sliding was restrained. Further, V_{test} and K_y were similar, despite the lower yield strength of the steel U-sections (379 MPa of steel plate cf. 499 MPa of rebar) (i.e., mechanical steel ratio ($\rho_s F_y / f_c'$ = 0.18) of **CF2.5** was 26% less than that of **RF2.5S** ($\rho_s F_y / f_c'$ = 0.25)). Consequently, the energy dissipation capacity $\sum E_D$ was increased by 114%.

For a fair comparison, in **CF2** (**Fig. 3-28**(b)) with the lower aspect ratio of 2.0, the mechanical steel ratio was designed to be similar to that of **RF2S** ($\rho_s F_y / f_c'$ = 0.29 for **RF2S** and 0.30 for **CF2)**. The use of boundary steel section of U-200×200×9×9 (ρ_{be} = 13.1%, F_y = 404 MPa) increased V_{test} and K_y by 37% and 13%, respectively. This result indicates that the boundary steel U-sections provided better flexural compression (i.e., lateral confinement effect) and flexural tension capacities (i.e., strain hardening effect). Further, the deformation-related capacities δ_u, μ, and θ_p were increased by 53%, 26%, and 111%, respectively, presenting a similar trend to the the results shown in the specimens **RF2.5S** and **CF2.5** with the greater aspect ratio.

3.5.3 Sectional area of steel U-sections

In the comparison of **CF2.5** and **CF2.5VH** (**Fig. 3-28**(c)), the use of thicker plate (71% greater area) of U-300×300×16×16 section (ρ_{be} = 15.9%, F_y = 388 MPa) increased V_{test} by 52%, and K_y by 26%. However, for this reason, μ and θ_p of **CF2.5VH** were slightly less than those of **CF2.5**, as plastic hinge rotation was limited by the post-yield shear degradation in the plastic hinge zone. Nevertheless, the overall deformation capacity δ_u was equivalent to that of **CF2.5**, as the steel U-sections with greater area provided greater contribution to wall shear (shear deformation increased in the plastic hinge zone, see $\gamma_{L,max}$ in **Table 3-4**).

In **CF2** and **CF2VH** with the lower aspect ratio (**Fig. 3-28**(d)), the effect of steel U-section area was investigated by increasing the web plate length of a steel U-section (41% greater area). Unlike the comparison results shown in **CF2.5** and **CF2.5VH**, the use of greater area of U-200×320×9×9 section (ρ_{be} = 11.6 %, F_y = 404 MPa) not only increased V_{test} (by 34%) and K_y (by 8%), but also increased μ (by 6%) and θ_p (by 54%). Such discrepancy between the 2.5-aspect ratio specimens and 2.0-aspect ratio specimens was due to the relatively low deformation capacity of **CF2** (δ_u = 3.0% for **CF2** and δ_u ≈ 4.0% for **CF2VH**, **CF2.5**, and **CF2.5VH**); Early post-yield shear degradation (in plastic hinge zone) occurred in **CF2**, due to the greater shear demand (V_{test}/A_g = 3.78 MPa for **CF2**; and V_{test}/A_g = 2.62 MPa for **CF2.5**) and relatively low horizontal reinforcement ratio (ρ_h = 0.56% for **CF2**; ρ_h = 0.88% for **CF2.5**).

3.5.4 Type of web reinforcement

In the comparison of **CF2** and **CF2SB** (**Fig. 3-28**(e)), V_{test} and K_y of **CF2SB** were slightly less due to the absence of web reinforcing bars. However, the use of steel plate beams increased the inelastic deformation capacities δ_u, μ, and θ_p by 33%, 25%, and 35%, respectively, due to the less diagonal cracking and spalling of web concrete. Thus, the boundary steel sections were subjected to greater plastic strains, which increased the energy dissipation $\sum E_D$ and energy dissipation ratio κ by 52% and 15%, respectively. For the same reason, δ_u and μ were comparable to those of **CF2VH** with greater area of steel U-sections.

In the comparison of **CF2** and **CF2SF** (**Fig. 3-28**(f)), the use of steel web faceplates (ρ_v and ρ_h = 4.0 %) increased V_{test} by 36%. In particular, the faceplates significantly increased K_s by 124%. However, due to the relatively small effect on K_f (increased by 17%), the increase in overall lateral stiffness K_y was only 18%. Further, the increase in inelastic deformation capacities (δ_u, μ, and θ_p) were limited, due to the local buckling of faceplates, and subsequent crushing of web concrete. In the comparison of **CF2VH** and **CF2SF**, V_{test} and K_y were similar, even though the total vertical steel area of **CF2VH** was 26% less than that of **CF2SF**. Further, δ_u and $\sum E_D$ of **CF2SF** were 25% and 30% less than those of **CF2VH**, respectively.

Table 3-6 Comparison of structural capacities of flexural yielding specimens

Design parameters	Aspect ratio = 2.5				Aspect ratio = 2.0						
	#1	#1	#2	#3	#2	#2	#3	#4	#4	#4	#4
Relevant specimens	RF2.5 /RF2.5S	CF2.5 /RF2.5	CF2.5 /RF2.5S	CF2.5VH /CF2.5	CF2 /RF2S	CF2VH /RF2S	CF2VH /CF2	CF2SB /CF2	CF2SB /CF2VH	CF2SF /CF2	CF2SF /CF2VH
Peak strength V_{test}	1.13	1.10	0.97	1.52	1.37	1.84	1.34	0.99	0.74	1.36	1.01
Ultimate drift ratio δ_u	0.94	1.36	1.45	1.05	1.53	2.01	1.32	1.33	1.01	0.99	0.75
Drift ductility μ	1.15	1.59	1.38	0.87	1.26	1.33	1.06	1.25	1.18	0.86	0.81
Plastic hinge rotation θ_p	0.48	1.32	2.73	0.81	2.11	3.24	1.54	1.35	0.88	0.99	0.64
Lateral yield stiffness K_y	1.39	1.28	0.92	1.26	1.13	1.22	1.08	0.93	0.86	1.18	1.09
Flexural yield stiffness K_f	1.55	1.61	1.04	1.28	1.23	1.34	1.09	0.89	0.81	1.17	1.07
Shear yield stiffness K_s	1.00	0.83	0.83	1.04	0.94	1.03	1.10	0.81	0.74	2.24	2.04
Energy dissipation $\sum E_d$	0.93	1.99	2.14	1.34	2.73	5.42	1.98	1.52	0.77	1.38	0.70
Energy dissipation ratio κ	1.02	1.17	1.15	1.02	1.15	1.27	1.11	1.16	1.05	1.28	1.16

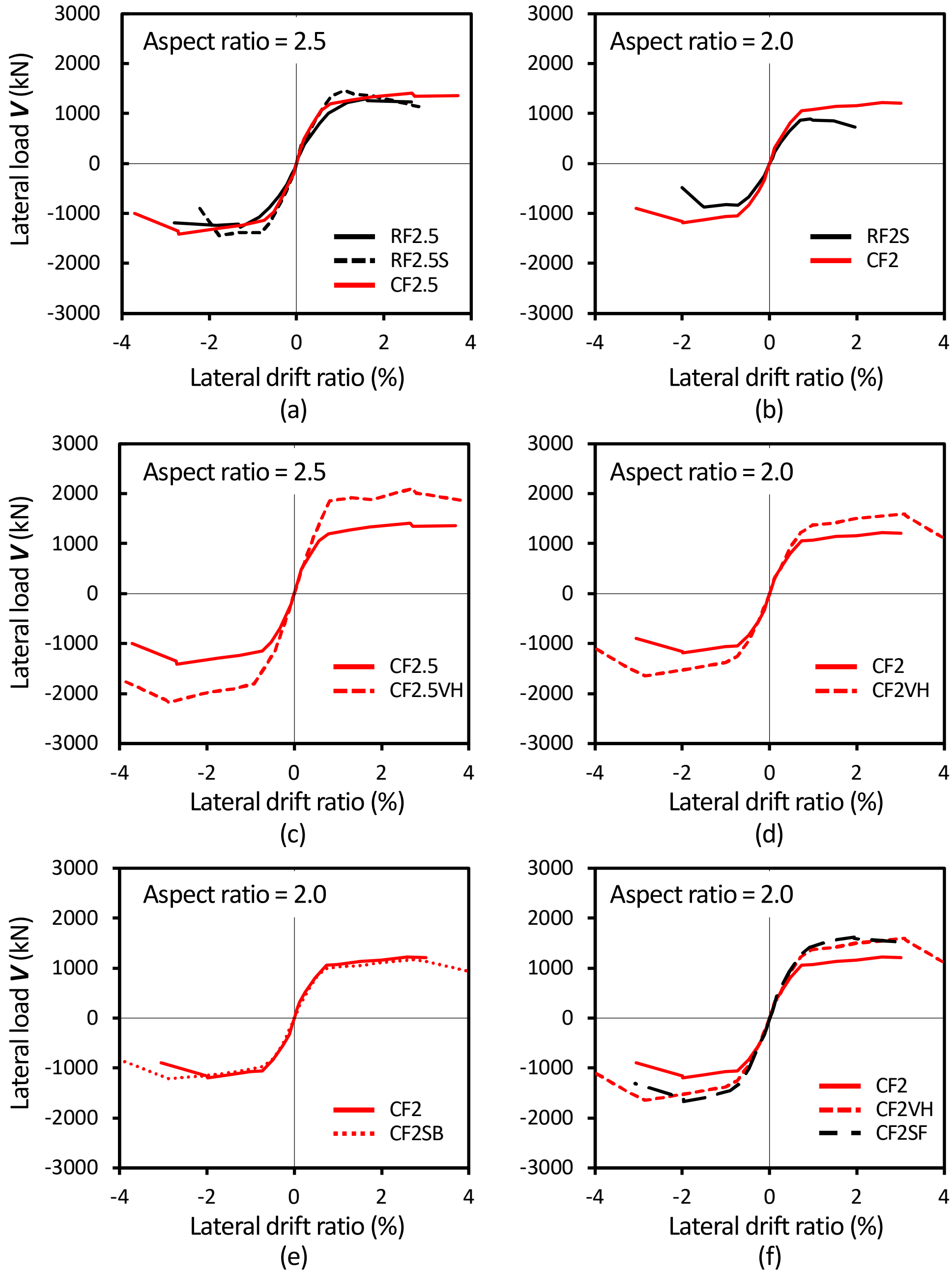

Fig. 3-28 Envelope curves of cyclic lateral load-drift ratio relationships measured in flexural yielding specimens.

3.6 Evaluation of Flexural Capacity

3.6.1 Flexural strength

Table 3-7 shows the nominal flexural strengths V_f (= M_n / l_s) calculated based on strain compatibility and crushing strain of 0.003 (ACI 318, 2019). In the RC specimens, the peak strengths V_{test} were close to or slightly greater than the nominal flexural strengths V_f, showing the flexural strength ratios V_{test} / V_f = 0.99 – 1.06. In the composite specimens, the flexural strength ratios increased to V_{test} / V_f = 1.07 – 1.31. This result indicates that, as shear sliding and flexural crushing were restrained, the boundary steel U-sections provided greater flexural compression (due to lateral confinement to boundary concrete) and flexural tension capacities (due to strain hardening). Note that the strain hardening stress of the steel sections and lateral confinement effect on boundary concrete were not considered in the calculation of V_f.

For simple estimation, the nominal flexural strength of composite sections can be predicted based on the plastic stress distribution across the cross section (AISC 360, 2016). The yield strength and effective compressive strength ($0.85f_c'$) are used for the plastic stress distribution of steel sections and concrete, respectively. **Fig. 3-29** compares the plastic stress-based flexural strength predictions V_f with the test results V_{test} of composite wall specimens that include four present specimens (denoted as **SUB-C**) and 91 existing rectangular SC wall specimens: 53 concrete-filled steel plate wall specimens (denoted as **CFSP**, Nie et al. 2013; Ji et al. 2013; Epackachi et al. 2015; Chen et al. 2015; Yan et al. 2018; Zhang et al. 2019; Ma et al. 2019; and Zhao et al. 2020), 21 concrete-encased steel plate wall specimens (denoted as **CESP**, Xiao et al. 2012; Hu et al. 2016; Wang et al. 2018; and Jiang et al. 2019), and 17 RC walls with steel boundary elements (denoted as **RC-SBE**, Dan et al. 2011; Qian et al. 2012; Ji et al. 2014; and Ren et al. 2018) (Note that V_f of the existing walls was predicted by the same procedure as that used for the present specimens). The detailed properties of the existing SC wall specimens were presented in **Appendix II**. In general, the nominal strengths based on plastic stress distribution underestimated the test strengths, except for several CFSP and CESP walls with web steel plates (in the middle of the cross section, strains of the web steel plates were less than the yield strain).

Table 3-7 Comparison with flexural strength prediction

Specimens		V_{test} [kN]	V_f [kN]	V_{test}/V_f
Aspect Ratio = 2.5	RF2.5	1,286	1,290	1.00
	RF2.5S	1,455	1,465	0.99
	CF2.5	1,412	1,209	1.17
	CF2.5VH	2,143	2,000	1.07
Aspect Ratio = 2.0	RF2	880	828	1.06
	CF2	1,210	1,012	1.20
	CF2VH	1,622	1,303	1.24
	CF2SB	1,193	914	1.31
	CF2SC	1,646	1,421	1.16

Note: flexural strength V_f was predicted based on strain compatibility

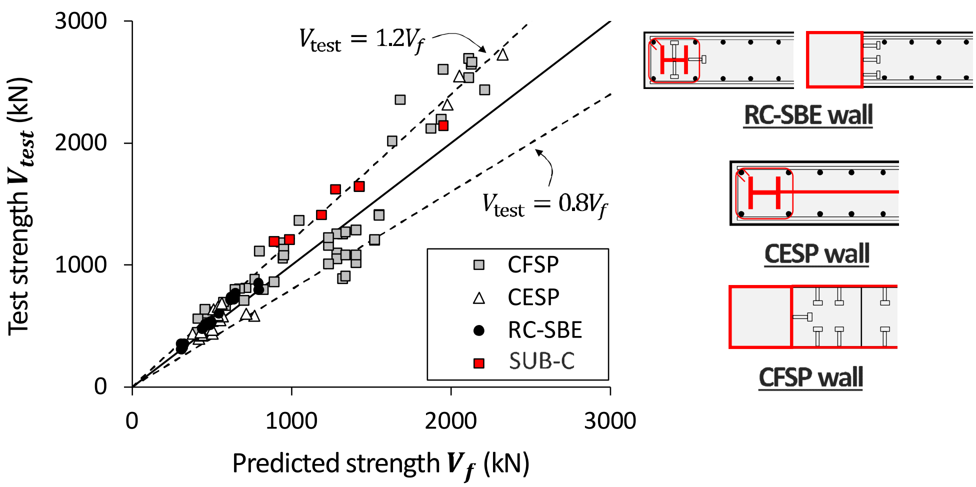

Fig. 3-29 Comparison of the tested flexural strengths with the predictions.

In the proposed walls, the use of steel U-sections is intended to maximize the flexural strength, for the same amount of steel. To verify this, for the composite wall specimens, the contribution of the vertical steel sections to flexural strength (i.e., flexural strength efficiency of steel sections) was evaluated: flexural tension force T at the peak strength (resisted by steel sections alone) was normalized upon the tensile strength of the overall steel area ($\sum A_s F_y$). Here, T was calculated considering the level of axial compression (axial force ratio $\leq$ 0.6), as follows (refer to **Fig. 3-30**):

$$T = \frac{M_p - N\left(\frac{l_e}{2}\right)}{l_e} \tag{3-7}$$

where, M_p = the tested flexural strength, and l_e = the effective moment-arm length which was assumed to be $0.8l_w$ (Eurocode 8, 2004). **Fig. 3-30** shows T / $\sum A_s F_y$, according to the mechanical steel ratio (= $\rho_s F_y / f_c'$). Generally, in RC-SBE and SUB-C walls, by using steel area concentrated in boundary elements, T / $\sum A_s F_y$ was greater than those of CFSP and CESP walls with web steel plates, despite the less $\rho_s F_y / f_c'$. Further, generally, the flexural strength efficiency T / $\sum A_s F_y$ of the present SUB-C specimens was greater than that of the RC-SBE walls, due to the greater flexural contribution of the steel U-sections. For the same reason, T / $\sum A_s F_y$ of **CF2SF** was greater than those of the existing CFSP and CESP walls, despite the use of web steel plates.

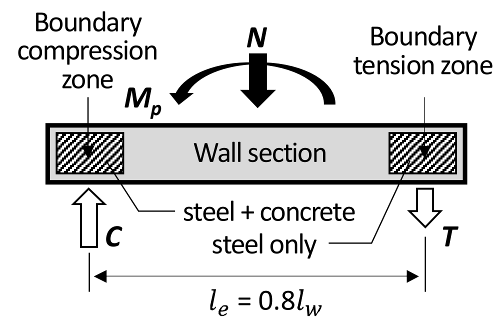

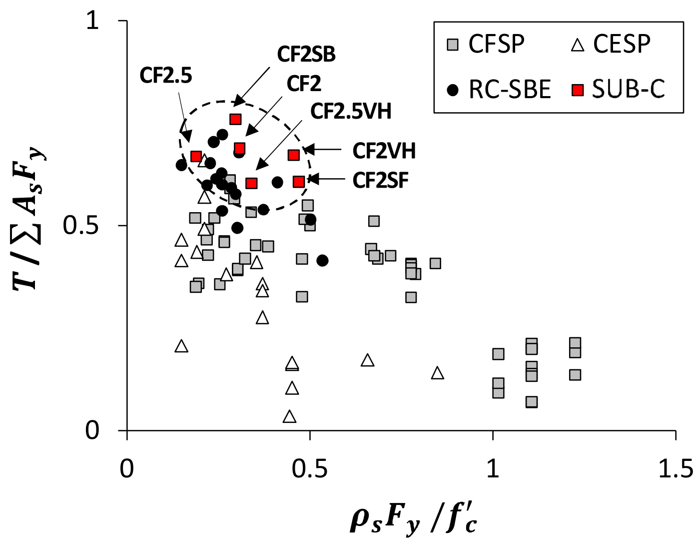

Fig. 3-30 Flexural strength efficiency of steel section in composite wall specimens.

3.6.2 Flexural stiffness

For elastic analysis of a flexural member, an estimation of effective flexural stiffness $(EI)_{eff}$ is required. Various studies have been conducted to estimate the effective flexural stiffness, where a reduction factor α_f for the moment of inertia of the gross section was suggested as follows:

$$(EI)_{eff} = \alpha_f E_c I_g \tag{3-8}$$

where, E_c = elastic modulus of concrete (= $4{,}700\sqrt{f_c'}$); and I_g = moment of inertia of the gross wall section.

ACI 318 defines α_f as 0.7 for uncracked sections and 0.35 for cracked sections, while ASCE 41 (2017) defines α_f as 0.8 for uncracked sections and 0.5 for cracked sections. In Adebar et al. (2007), the upper and lower-bound flexural stiffnesses were provided based only on the level of axial compression N. The upper and lower bounds of α_f are calculated as follows:

$$\alpha_f = 0.6 + \frac{N}{f_c' A_g} \leq 1 \qquad \text{(upper bound)} \tag{3-9}$$

$$\alpha_f = 0.2 + 2.5\frac{N}{f_c' A_g} \leq 0.7 \qquad \text{(lower bound)} \tag{3-10}$$

Paulay and Priestley (1992) proposed α_f as follows:

$$\alpha_f = \frac{100}{F_y} + \frac{N}{f_c' A_g} \tag{3-11}$$

Alternatively, Bachmann (2004) proposed α_f as follows:

$$\alpha_f = \frac{12}{\kappa_1}\frac{E_s}{E_c}\left[\rho_s \xi_1 \xi_2 + n_{ar} \xi_3 \frac{f_c'}{F_y}\right] \tag{3-12}$$

where, κ_1 = 2; ρ_s = area ratio of overall vertical reinforcement to the gross section (average steel ratio); ξ_1, ξ_2, and ξ_3 = 0.9, 0.55, and 0.4, respectively.

Priestley et al. (2007) assumed constant yield curvature for structural members with various reinforcement ratios, whereby the effective flexural stiffness is directly calculated from the nominal flexural strength.

$$\alpha_f = \frac{M_y}{\phi_y}\frac{1}{E_c I_g} \tag{3-13}$$

where, M_y = flexural yield moment at which tensile stress in the outer reinforcement reaches yield strain or the stress at extreme compression fiber reaches crushing strain (= 0.002); and ϕ_y = yield curvature = $2\varepsilon_y/l_w$.

Table 3-8 and **Fig. 3-31** compare the tested α_f with the predictions of the existing RC models. The tested α_f was calculated based on elastic theory, as follows:

$$\alpha_f = \frac{(EI)_{test}}{E_c I_g} = \frac{K_f l_s^3}{3E_c I_g} \tag{3-14}$$

The tested α_f varied 0.25–0.47 for RC specimens; and 0.39–0.68 for composite specimens, which were almost placed between the lower-bound and upper-bound of Adebar et al. (2007). In general, the models of ACI 318 (2018), Paulay and Priestley (1992) and Priestley et al. (2007) underestimated the test results. Bachmann (2004) provided relatively good accuracy for the specimens with aspect ratio of 2.0, while the stiffness of the specimens with aspect ratio of 2.5 was overestimated. Similar tendency was shown in the comparison with ASCE 41 (2017).

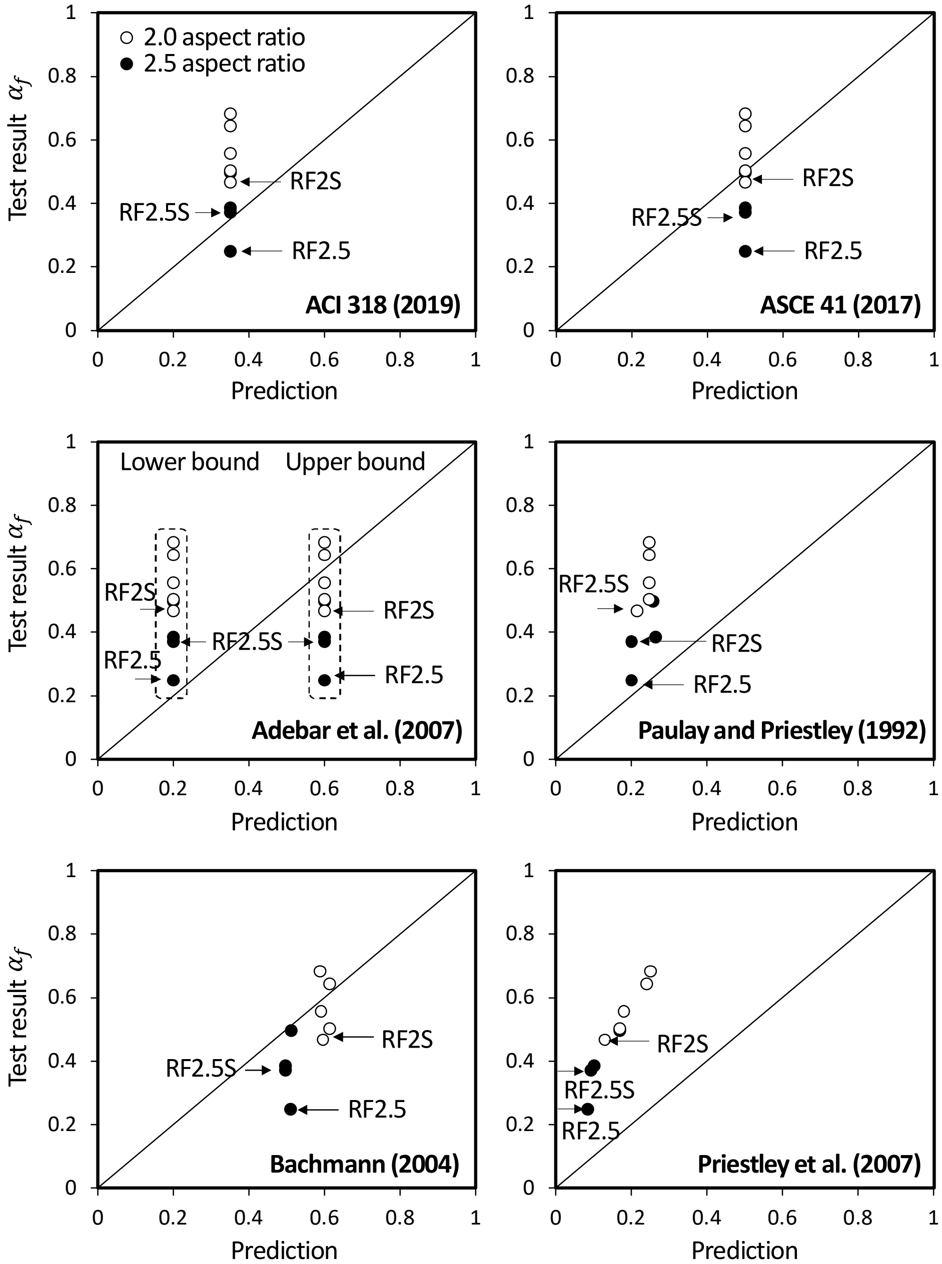

Fig. 3-31 Comparison of the tested flexural stiffness reduction factors with the predictions.

Table 3-8 Flexural stiffness reduction factor

Specimen		Test result	ACI 318	ASCE 41	Adebar et al.		Paulay et al.	Bach-mann	Priest-ley
					lower	upper			
Aspect ratio = 2.5	RF2.5	0.25	0.35	0.5	0.2	0.6	0.20	0.51	0.08
	RF2.5S	0.37	0.35	0.5	0.2	0.6	0.20	0.50	0.09
	CF2.5	0.39	0.35	0.5	0.2	0.6	0.26	0.50	0.10
	CF2.5VH	0.50	0.35	0.5	0.2	0.6	0.26	0.51	0.17
Aspect ratio = 2.0	RF2S	0.47	0.35	0.5	0.2	0.6	0.21	0.60	0.13
	CF2	0.56	0.35	0.5	0.2	0.6	0.25	0.59	0.18
	CF2SB	0.50	0.35	0.5	0.2	0.6	0.25	0.61	0.17
	CF2VH	0.64	0.35	0.5	0.2	0.6	0.25	0.61	0.24
	CF2SC	0.68	0.35	0.5	0.2	0.6	0.25	0.59	0.25

3.6.3 Displacement ductility and plastic rotation

Fig. 3-32(a) shows the displacement ductility μ and plastic drift ratio δ_{pl} (= ultimate drift ratio δ_u – yield drift ratio δ_y) of the present and existing composite wall specimens. In the composite specimens, the plastic drift ratio varied δ_{pl} = 2.2–3.3%, which was greater than that of the RC specimens (δ_{pl} = 1.4–1.8%). Note the ductility and plastic rotation of the existing specimens was recalculated according to the definition that used for the present test specimens (see **Appendix II**). In general, as the axial force ratio increased, both μ and δ_{pl} decreased. In the present test specimens without compression force, the displacement ductility was greater than that of the existing composite walls with similar axial loading condition: low compression force (axial force ratio = 0.02) or without compression force. **Fig. 3-32**(b) shows the displacement ductility and plastic rotation of the test specimens with low axial force ratio ($\leq$ 0.02), according to the overall mechanical steel ratio $\rho_s F_y / f_c'$. In the present test specimens, both μ and δ_{pl} were greater than those of the existing SC wall specimens, even in the cases for lower $\rho_s F_y / f_c'$. Generally, both μ and δ_{pl} of the present test specimens decreased with the increase of $\rho_s F_y / f_c'$. This is because, as the steel area in boundary elements increased, the maximum shear demand (i.e., flexural strength) increased, which caused more severe damage in the web of plastic hinge zone. Indeed, both μ and δ_{pl} of the present test specimens generally decreased with the increase of shear demand (V_{test} / A_g)

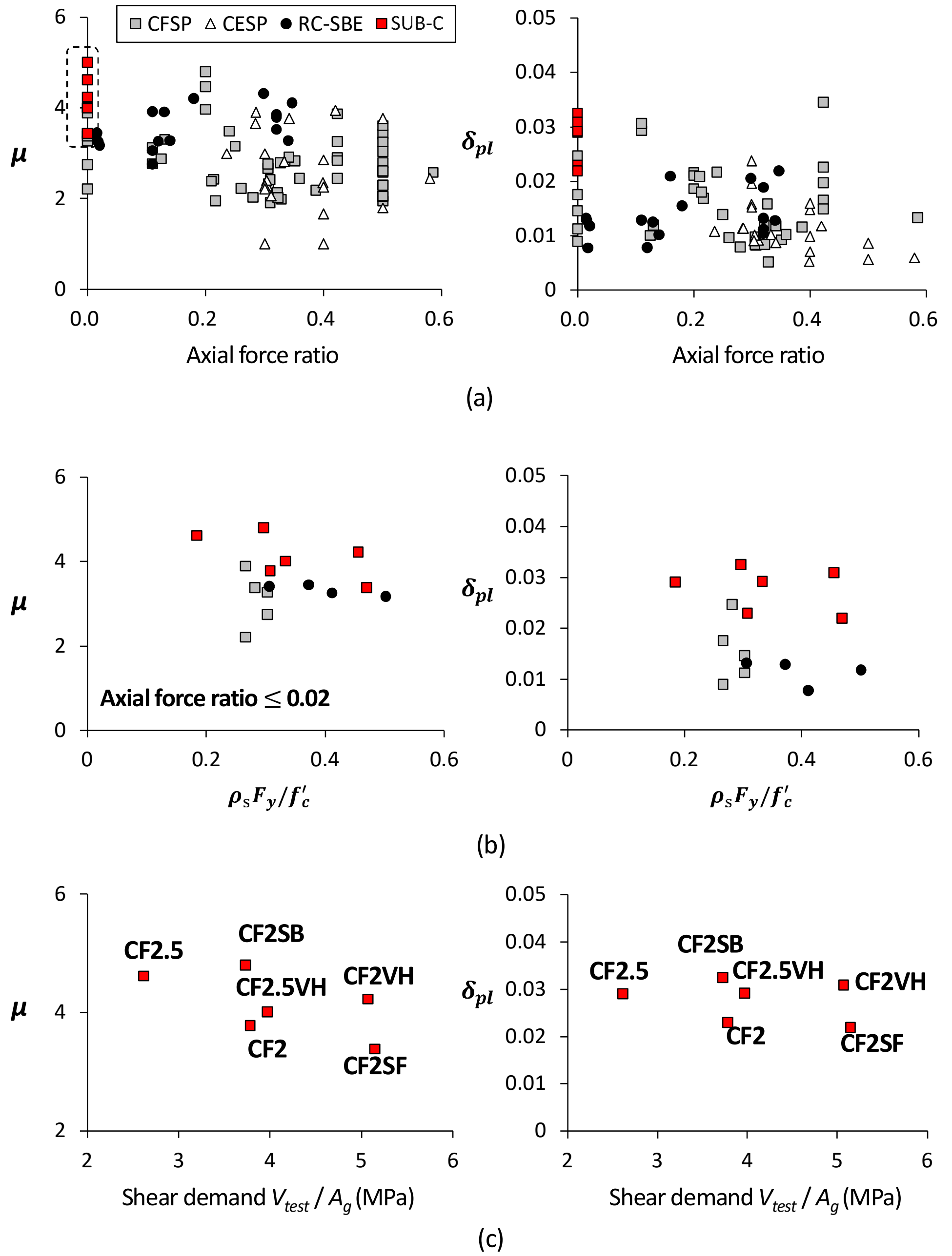

Fig. 3-32 Comparison of displacement ductility and plastic drift ratio of composite walls according to (a) the axial force ratio; (b) mechanical vertical steel ratio; and (c) the tested shear demand.

3.7 Summary

In this chapter, cyclic lateral load tests were performed for three RC walls and six composite (SUB-C) walls, to investigate the effect of boundary steel U-sections on the flexural performances of the walls. The design parameters included the arrangement of vertical steel section (uniform distribution vs concentration at wall boundaries), type of boundary reinforcement (rebar vs steel U-section), sectional area of steel U-sections, and the type of web reinforcement (rebar vs steel plate beam vs steel faceplate). Existing design methods were used to predict the flexural strength and stiffness of the specimens, and their prediction results were compared with the test results. The major findings are summarized as follows:

1) In RC specimens with heavily reinforced boundary elements (ρ_{be} = 9.6%), the inelastic deformation capacity was limited by shear sliding at the wall bottom, even though the shear demand (i.e., flexural strength) was significantly less than the nominal shear-friction strength. In the proposed composite walls with steel U-sections, such shear sliding was restrained. However, the composite walls failed due to crushing and spalling of the web concrete (i.e., post-yield shear failure) in the plastic hinge zone, without failure of the steel U-sections. The steel U-sections restrained diagonal cracking of the web concrete and crushing of the boundary concrete.

2) The flexural strength of the SUB-C wall was 37% greater than that of the counterpart RC wall. This is because the steel U-sections experienced large strain hardening stress by restraining shear sliding, diagonal cracking of the web concrete, and crushing and spalling of the boundary concrete. For the same reason, the deformation capacity and energy dissipation were increased by 38%-53% and 99%-173%, respectively. When steel U-sections with greater area were used, such advantages were more pronounced.

3) In the SUB-C wall with steel plate beams, the plate beams provided adequate

shear resistance without conventional shear reinforcing bars. Further, diagonal cracking and spalling of web concrete were better restrained, despite the absence of reinforcing bars. Thus, the deformation capacity and energy dissipation were 33% and 52% greater than those of the SUB-C wall without steel plate beams, respectively.

4) In the SUB-C wall with steel faceplates (web steel ratio = 4.0%), the flexural strength and lateral stiffness were increased by 36% and 18%, respectively, even though the web faceplates were not connected to boundary steel elements. However, local buckling was initiated at the free edges of the faceplates, followed by the crushing of web concrete, and eventually, strength degradation. For better ductility, vertical connections between the web plates and boundary steel sections are required in the plastic hinge zone.

5) The nominal flexural strengths based on strain compatibility and plastic stress distribution underestimated the test results of the SUB-C walls, neglecting the lateral confinement (to infill concrete), and strain hardening of the steel U-sections. The over-strength ratio was 7% – 31%.

6) In the comparison of the present test results and those of existing the composite walls, the normalized flexural strength and ductility of SUB-C walls were greater than those of the existing composite specimens, even with the low mechanical steel ratio (= $\rho_s F_y / f_c'$): the flexural strength efficiency of the SUB-C walls was better.

Chapter 4. Cyclic Lateral Test of Shear Specimens

4.1 Overview

It is generally acknowledged that, in concrete walls with large-sized boundary elements (e.g., barbell or flanged wall), their actual shear strength may be greater than the code-based shear strength based on the reinforced concrete web only (concrete plus web reinforcement). Nevertheless, many design codes do not consider the shear strength contribution of boundary elements, as the boundary elements are generally subjected to high level of axial stresses resulting from flexural moments on walls. However, in the proposed composite walls, by using steel U-sections, large steel area in the boundary elements can be structurally integrated with the web concrete, thus the steel U-section is expected to resist shear transferred from the wall web, even though the steel U-section is subjected to high flexural compression or flexural tension force. Further, as the boundary concrete is laterally confined by the steel U-section, shear resistance of the boundary concrete can be increased.

In this chapter, cyclic lateral loading tests were performed to investigate the effect of boundary steel U-sections on the shear strength of walls. Here, the shear strength indicates the strength developed by shear failure before flexural yielding. The tested shear strengths were compared with the predictions of existing design methods.

4.2 Test Plan

4.2.1 Design of shear failure mode

In this chapter, wall specimens were designed to show shear failure before flexural yielding: Nominal shear strength V_n is less than the shear demand resulting from nominal flexural strength M_n. Here, V_n was predicted according to the existing design methods of ACI 318 (2019), Eurocode 2 (2004), and fib MC (2010). M_n was predicted by section analysis, using strain compatibility method of ACI 318 (2019) (The same method that used for flexural yielding specimens, see Section 3.2.1 “Nominal flexural strength”).

4.2.2 Test parameters and specimens

Table 4-1, **Table 4-2,** and **Table 4-3** shows the major design properties of the specimens with aspect ratios of 2.5, 2.0, and 1.0, respectively. The dimensions of the specimens were length (l_w) × thickness (t_w) × height (h_w) = 1,800 mm × 300 mm × 4,500 mm for the specimens with aspect ratio of 2.5; 1,600 mm × 200 mm × 3,200 mm for the specimens with aspect ratios of 2.0; and 1,600 mm × 200 mm × 1,600 mm for the specimens with aspect ratios of 1.0. The naming rule for the specimens was the same as that used for flexural yielding-mode specimens (Section 3.3.1), except for some specimens with the following properties: At the end of the specimen name, **M** indicates the maximum shear reinforcement ratio; **VL** indicates the steel U-sections with lesser area; **TH** indicates the steel plate beams placed at smaller spacing.

Fig. 4-1 and **Fig. 4-2** show the details of the wall specimens with aspect ratio of 2.5. Specimens **RS2.5**, **CS2.5**, and **CS2.5VH** were designed to have identical nominal shear strength (ACI 318, 2019), to investigate the contribution of the steel U-sections to the shear strength. For this purpose, horizontal web reinforcement was the same: D16 bars with s_h = 300 mm (ρ_h = 0.44%, f_y = 445 MPa). In RC specimen **RS2.5** (**Fig. 4-1**(a)), the area of boundary rebars was increased using eleven D41 bars (A_r = 1,340 mm^2 each, l_{be} = 380 mm, ρ_{be} = 12.9%, f_y = 670 MPa). Such a large reinforcement ratio, which exceeds the maximum limit (8% for RC column) of ACI 318 (2019), was used to ensure shear failure before flexural yielding and to provide the same steel area as that of the steel U-section in the counterpart **CS1**. For vertical web reinforcement, six D16 bars were placed in two layers (ρ_v = 0.49%). In composite wall specimen **CS2.5** (**Fig. 4-1**(b)), the structural details were the same as those of **CF2.5** (flexural yielding specimen addressed in Chapter 3, **Fig. 3-2**(a)), except for the spacing of horizontal web bars, which was increased to s_h = 300 mm and the yield strength of steel U-sections, which was increased to F_y = 596 MPa. The total steel area in the boundary region (two U-300×300×16×16 plates and four D16 bars) was similar to that of **RS1** (twenty-two D41 bars) (**Table 4-1**). In **CS2.5VH** (**Fig**. **4-2**(a)), only the web length of steel U-sections (U-300×450×16×16, A_b = 18,688 mm^2 each, l_{be} = 450 mm, ρ_{be} = 14.1%, F_y = 596 MPa) was increased by 50%, maintaining the other details (i.e., the same details as those of **CS2.5**). Thus, the effect of the increased steel plate area on the shear strength was investigated. In existing design methods (ACI 318, 2019; Eurocode 2, 2004; and fib MC, 2010), the shear strength of a concrete wall is limited by the maximum shear strength corresponding to diagonal compression failure (i.e., web crushing failure). To investigate the effect of steel U-sections on the maximum shear strength of walls, in **CS2.5M** (**Fig. 4-2**(b)), the wall thickness was decreased to t_w = 200 mm, and the horizontal reinforcement ratio (D16 bars of s_h = 200 mm) was increased to the maximum ratio of ρ_h = 0.99% (ACI 318, 2019). For boundary reinforcement, U-200×450×16×16 steel sections (A_b = 17,088 mm^2 each, l_{be} = 450 mm, ρ_{be} = 19.4%, F_y = 596 MPa) were used.

Fig. 4-3 and **Fig. 4-4** show the details of the specimens with aspect ratio of 2.0. In RC wall **RS2** (**Fig. 4-3**(a)), six vertical D41 bars (A_r = 1,340 mm^2 each, f_y = 670 MPa) and two D38 bars (A_r = 1,140 mm^2 each, f_y = 602 MPa) were used at each boundary element (l_{be} = 320 mm, boundary reinforcement ratio ρ_{be} = 16.1%). For vertical web reinforcement, two layers of ten D10 bars (ρ_v = 0.39 %, A_r = 71 mm^2 each, f_y = 514 MPa) were uniformly placed along the web length. Here, the vertical web reinforcement ratio was close to the minimum ratio (= $0.0025 + 0.5(2.5 - h_w/l_w)(\rho_h - 0.0025)$ = 0.31 %) of ACI 318 (2019). For horizontal web reinforcement, D13 bars (A_{sh} = 127 mm^2 each, f_y = 445 MPa) with 180° end hooks were placed at a vertical spacing of s_h = 250 mm (ρ_h = 0.51 %). In composite wall **CS2** (**Fig. 4-3**(b)), a steel section of U-200×320×12×16 (A_b = 10,496 mm^2 each, l_{be} = 320 mm, ρ_{be} = 16.4%, F_y = 444 MPa for web plate and 448 MPa for flange plate) was used for boundary elements, while the other properties were the same as those of **RS2**, except for horizontal D13 bars with 90° end hooks. To investigate the effect of steel U-sections on the shear strength, the boundary reinforcement ratio ρ_{be} was the same as that of the vertical boundary rebars in **RS2**. In **CS2VL** (**Fig. 4-3**(c)), to investigate the effect of steel plate area on the shear strength, thinner steel U-sections (U-200×320×9×9, A_b = 7,398 mm^2 each, l_{be} = 320 mm,

ρ_{be} = 11.6%, F_y = 469 MPa) were used, while the other properties were the same as those of **CS2**. A steel-framed composite wall was considered for **CS2SB** (**Fig. 4-4**(a)): steel plate beams of PL-105×6 (width × thickness, length = 1400 mm) were used, and the plate beams were welded to boundary elements that were the same as those of **CS2**. The vertical spacing of steel plate beams was s_h = 1,000 mm (ρ_h = 0.63%). Vertical and horizontal web reinforcements were not used. In **CS2TH** (**Fig. 4-4**(b)), only the spacing of steel plate beams was decreased to s_h = 600 mm (ρ_h = 1.05%), to investigate the effect of the plate spacing on the shear strength. In both **CS2SB** and **CS2TH**, s_h was greater than the maximum spacing (l_w/5 = 320 mm) of shear reinforcement specified in ACI 318 (2019). For steel–concrete composite action, eight shear studs (diameter = 12 mm, length = 80 mm) were uniformly placed along the plate beam length. In **CS2SF** (**Fig. 4-4**(c)), two steel faceplates of PL-960×4 (ρ_v and ρ_h = $2t_p$ / t_w = 4.0 %, in which t_p = thickness of faceplate) were used for web reinforcement, without vertical and horizontal reinforcements. Boundary steel U-sections were the same as those of **CS2**. For composite action between the faceplates and web concrete, shear studs (diameter = 12 mm) were welded to the entire faceplates, according to AISC N690 (2018). However, for better constructability, lateral ties were not used for the faceplates. Furthermore, the boundary steel U-sections and web faceplates were unconnected on purpose. Instead, for shear connection, horizontal D19 bars with a vertical spacing of 250 mm (length = 500 mm) were used between boundary elements and web concrete. If such construction method is structurally verified, a commercial floor steel deck may be used for concrete-filled steel plate walls.

Fig. 4-5 shows the details of the specimens with aspect ratio of 1.0. In RC wall **RS1** (**Fig. 4-5**(a)), the specimen details were the same as those of **RS2**, only except for the wall height decreased to h_w = 1600 mm. Similarly in composite walls **CS1** (**Fig. 4-5**(b)), **CS1VL** (**Fig. 4-5**(c)), and **CS1SF** (**Fig. 4-5**(d)), their properties were the same as those of **CS2**, **CS2VL**, and **CS2SF**, respectively, except for the reduced wall height: h_w = 1600 mm.

Basically, the design concept and fabrication method for steel U-sections was the same to those for flexural yielding specimens. In the steel U-sections, a flange plate and two web plates were connected using full-penetration groove welds. To minimize inelastic local buckling of the plates, compact section (i.e., width-to-thickness ratio $\leq 2.26\sqrt{E_s/F_y}$, E_s = elastic modulus of steel, AISC 360 (2016)) and shear studs (diameter = 16 mm, length = 120 mm) were used for the entire length of the plates. In the lower part of walls (within 1600 mm above the wall base), to confine the boundary zone, lateral tie bars (diameter = 16 mm, length = 180 mm, denoted as solid circles in **Fig. 4-1** through **Fig. 4-4**) were welded along the edges of the web plates.

Table 4-1 Design parameters of shear failure-mode specimens (aspect ratio = 2.5)

Specimens	**RS2.5**	**CS2.5**	**CS2.5VH**	**CS2.5M**
Structural type	RC	SUB-C[a]	SUB-C[a]	SUB-C[a]
Wall height h_w, mm	4,500	4,500	4,500	4,500
Wall length l_w, mm	1,800	1,800	1,800	1,800
Wall thickness t_w, mm	300	300	300	200
Concrete strength f_c', MPa	64.3	64.3	64.3	64.3
Vertical boundary steel	D41	U-300×300×16×16[b]	U-300×450×16×16[b]	U-200×450×16×16[b]
Boundary length l_{be}, mm	380	300	450	450
Steel ratio ρ_{be}[c], %	12.9	15.9	14.1	19.4
Total area, mm^2	29,472	27,776	37,376	34,176
f_y (or F_y), MPa	670	596	596	596
f_u (or F_u), MPa	870	659	659	659
Vertical web steel	D16	D16	D16	D16
Horizontal spacing s_v, mm	270	412.5	412.5	412.5
Reinforcement ratio ρ_v[d], %	0.49	0.32	0.32	0.48
f_y, MPa	445	445	445	445
f_u, MPa	597	597	597	597
Vertical steel ratio ρ_s[e], %	5.6	5.5	7.3	9.9
Horizontal web steel	D16	D16	D16	D16
Vertical spacing s_h, mm	300	300	300	200
Reinforcement ratio ρ_h[f], %	0.44	0.44	0.44	0.99
f_y, MPa	445	445	445	445
f_u, MPa	597	597	597	597

[a]Steel–concrete composite wall with boundary elements of steel U-section.
[b]Steel U-section: U-flange length × web length × web thickness × plate thickness.
[c]Area ratio of vertical boundary steel reinforcement to boundary concrete section = $\sum A_r / (l_{be} \cdot t_w)$ for RC; $A_b / (l_{be} \cdot t_w)$ for SUB-C.
[d]Area ratio of vertical web steel reinforcement to web concrete section = $2A_r / (s_v \cdot t_w)$.
[e]Total area ratio of vertical steel sections to gross wall section = $\sum A_s / (l_w \cdot t_w)$.
[f]Area ratio of horizontal web steel reinforcement to web concrete section = $2A_{sh} / (s_h \cdot t_w)$.

Table 4-2 Design parameters of shear failure-mode specimens (aspect ratio = 2.0)

Specimens	RS2	CS2	CS2VL	CS2SB	CS2TH	CS2SF
Structural type	RC	SUB-C	SUB-C	SUB-C	SUB-C	SUB-C
Wall height h_w, mm	3,200	3,200	3,200	3,200	3,200	3,200
Wall length l_w, mm	1,600	1,600	1,600	1,600	1,600	1,600
Wall thickness t_w, mm	200	200	200	200	200	200
Concrete strength f_c', MPa	55.7	54.9	47.4	49.6	55.7	54.9
Vertical boundary steel	D41 & D38	U-200×320×12×16	U-200×320×9×9	U-200×320×12×16	U-200×320×12×16	U-200×320×12×16
Boundary length l_{be}, mm	320	320	320	320	320	320
Steel ratio ρ_{be}, %	16.1	16.4	11.6	16.4	16.4	16.4
f_y (or F_y), MPa	670 for D41 602 for D38	444 for 12t plate 448 for 16t plate	469	444 for 12t plate 448 for 16t plate	444 for 12t plate 448 for 16t plate	444 for 12t plate 448 for 16t plate
f_u (or F_u), MPa	870 for D41 746 for D38	556 for 12t plate 618 for 16t plate	642	556 for 12t plate 618 for 16t plate	556 for 12t plate 618 for 16t plate	556 for 12t plate 618 for 16t plate
Total area, mm^2	20,636	20,992	14,796	20,992	20,992	20,992
Vertical web steel	D10	D10.	D10	-	-	PL-960×4
Horizontal spacing s_v, mm	180	180	180	-	-	-
Reinforcement ratio ρ_v, %	0.39	0.39	0.39	-	-	4.0
f_y (or F_y), MPa	514	514	514	-	-	321
f_u (or F_u), MPa	600	600	600	-	-	473
Vertical steel ratio ρ_s, %	6.7	6.8	4.8	6.6	6.6	9.0
Horizontal web steel	D13	D13	D13	PL-105×6	PL-105×6	-
Vertical spacing s_h, mm	250	250	250	1000	600	-
Reinforcement ratio ρ_h, %	0.51	0.51	0.51	0.63	1.05	-
f_y (or F_y), MPa	445	445	445	456	456	-
f_u (or F_u), MPa	584	584	584	597	597	-

Table 4-3 Design parameters of shear failure-mode specimens (aspect ratio = 1.0)

Specimens	**RS1**	**CS1**	**CS1VL**	**CS1SF**
Structural type	RC	SUB-C[a]	SUB-C[a]	SUB-C[a]
Wall height h_w, mm	1,600	1,600	1,600	1,600
Wall length l_w, mm	1,600	1,600	1,600	1,600
Wall thickness t_w, mm	200	200	200	200
Concrete strength f_c', MPa	54.6	54.6	53.1	55.5
Vertical boundary steel	D41 & D38	U200x320x12x16	U200x320x9x9	U200x320x12x16
Boundary length l_{be}, mm	320	320	320	320
Steel ratio ρ_{be}[c], %	16.1	16.4	11.6	16.4
Total area, mm^2	20,636	20,992	14,796	20,992
f_y (or F_y), MPa	670 for D41 602 for D38	444 for 12t plate 448 for 16t plate	469	444 for 12t plate 448 for 16t plate
f_u (or F_u), MPa	870 for D41 746 for D38	556 for 12t plate 618 for 16t plate	642	556 for 12t plate 618 for 16t plate
Vertical web steel	D10	D10	D10	PL960x4[a]
Horizontal spacing s_v, mm	180	300	300	-
Reinforcement ratio ρ_v[d], %	0.39%	0.24%	0.24%	4.00%
f_y, MPa	514	514	514	321
f_u, MPa	600	600	600	473
Vertical steel ratio ρ_s[e], %	6.67	6.56	4.76	8.96
Horizontal web steel	D13	D10	D10	-
Vertical spacing s_h, mm	250	300	300	-
Reinforcement ratio ρ_h[f], %	0.51%	0.24%	0.24%	-
f_y, MPa	445	514	514	-
f_u, MPa	584	600	600	-

[a]Flat plate section: PL-width × thickness.

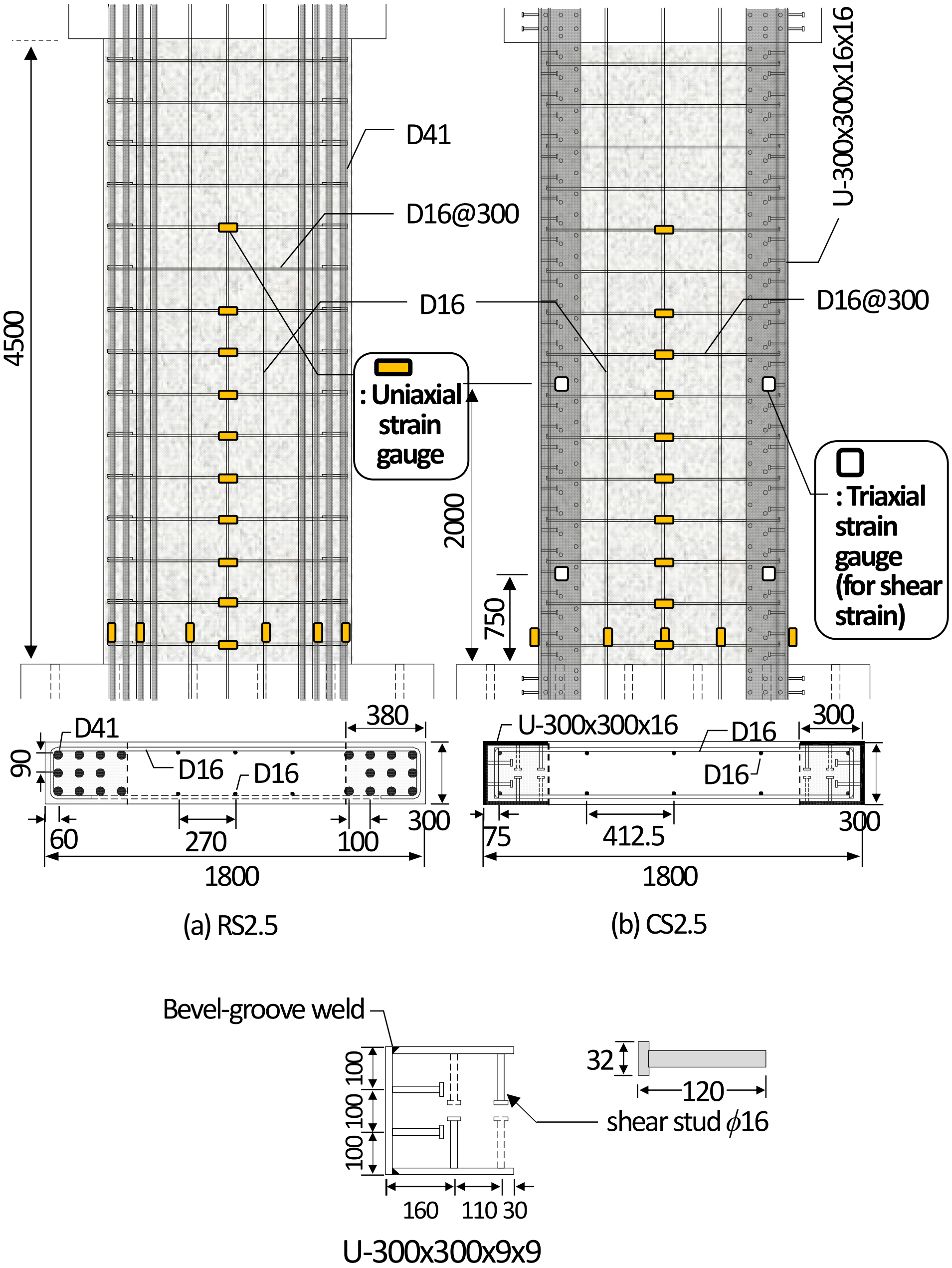

Fig. 4-1 Details of shear failure-mode specimens with aspect ratio of 2.5: (a) RS2.5; (b) CS2.5.

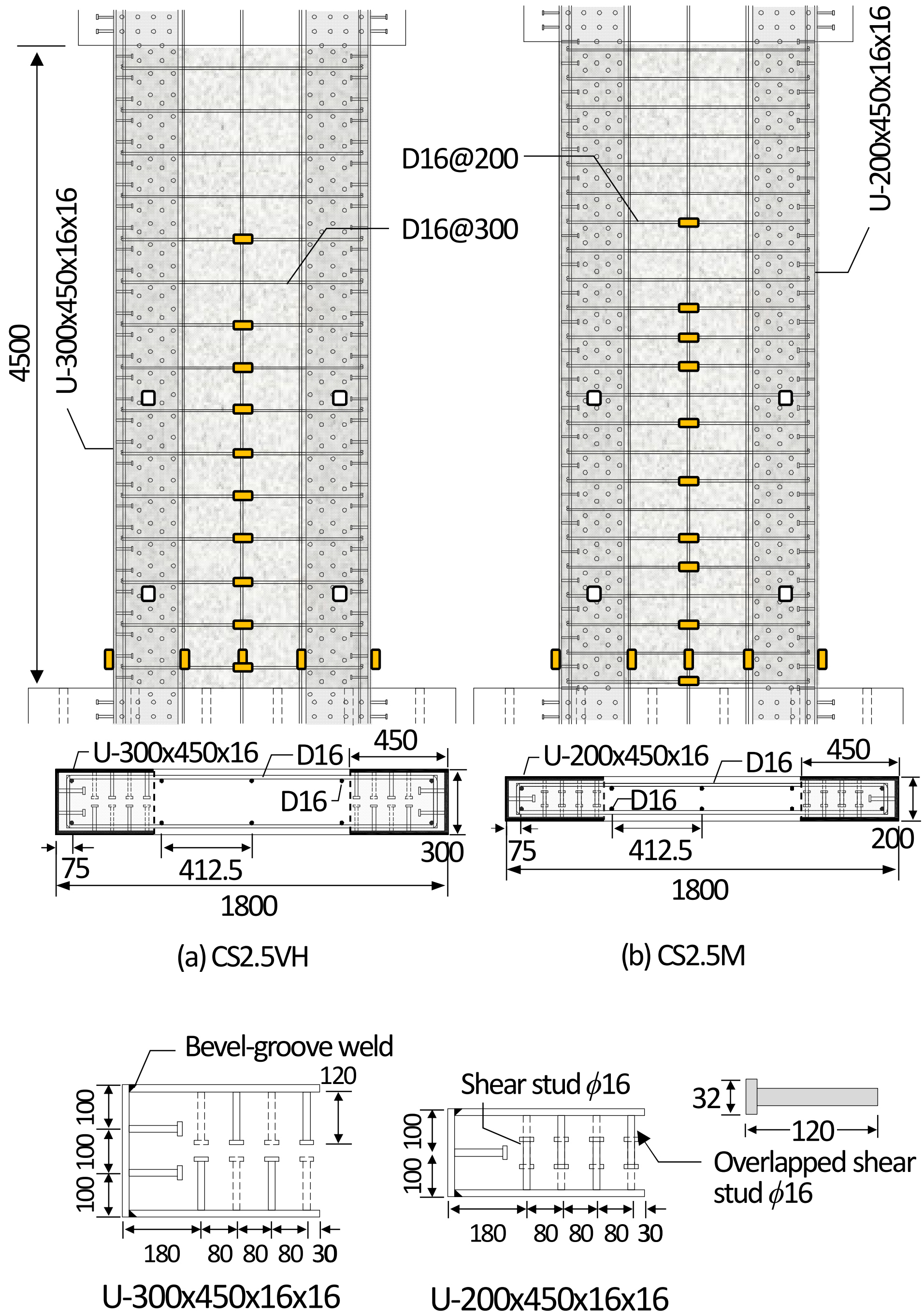

Fig. 4-2 Details of shear failure-mode specimens with aspect ratio of 2.5: (a) CS2.5VH; and (b) CS2.5M.

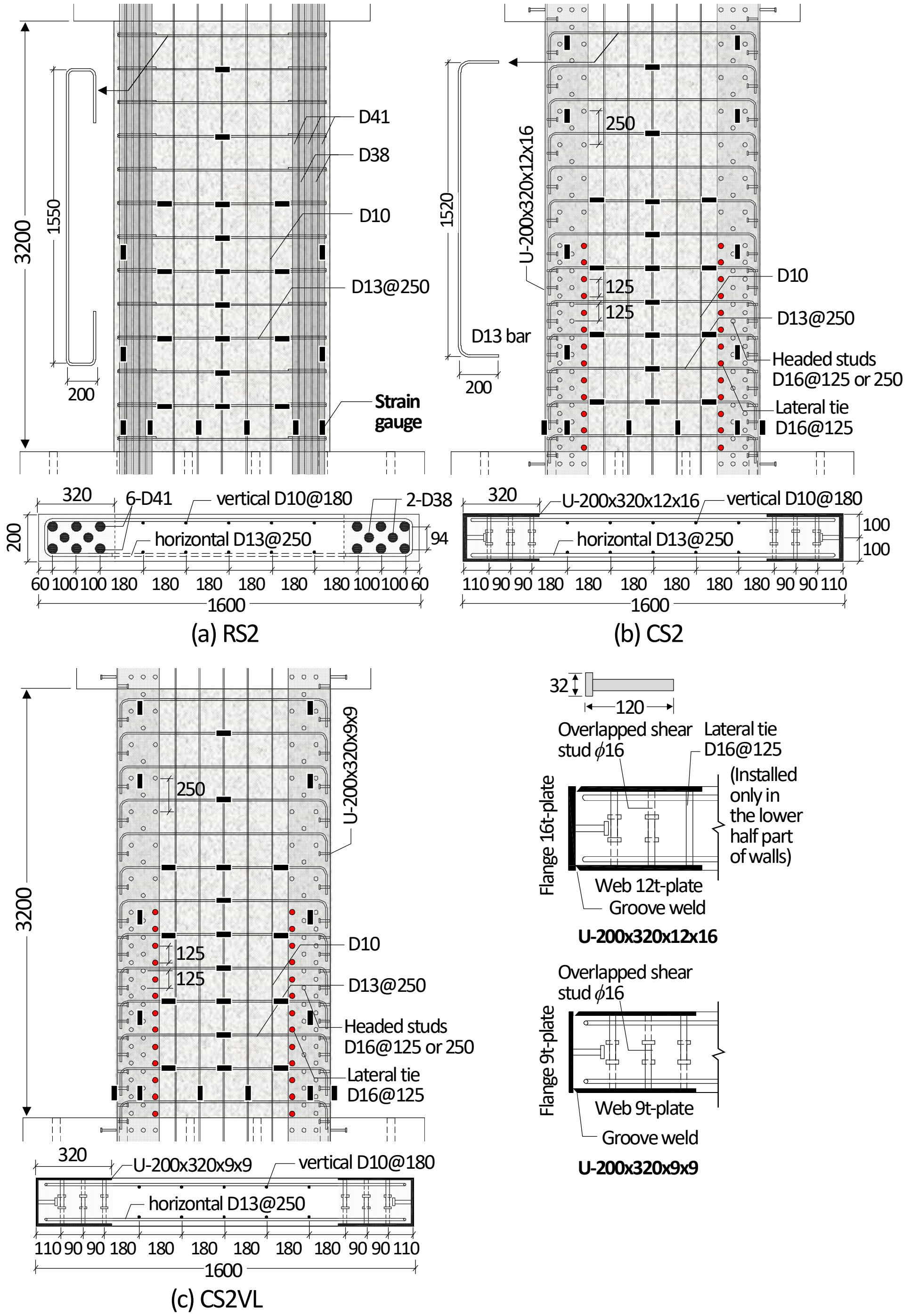

Fig. 4-3 Details of shear failure-mode specimens with aspect ratio of 2.0: (a) RS2; (b) CS2; and (c) CS2VL.

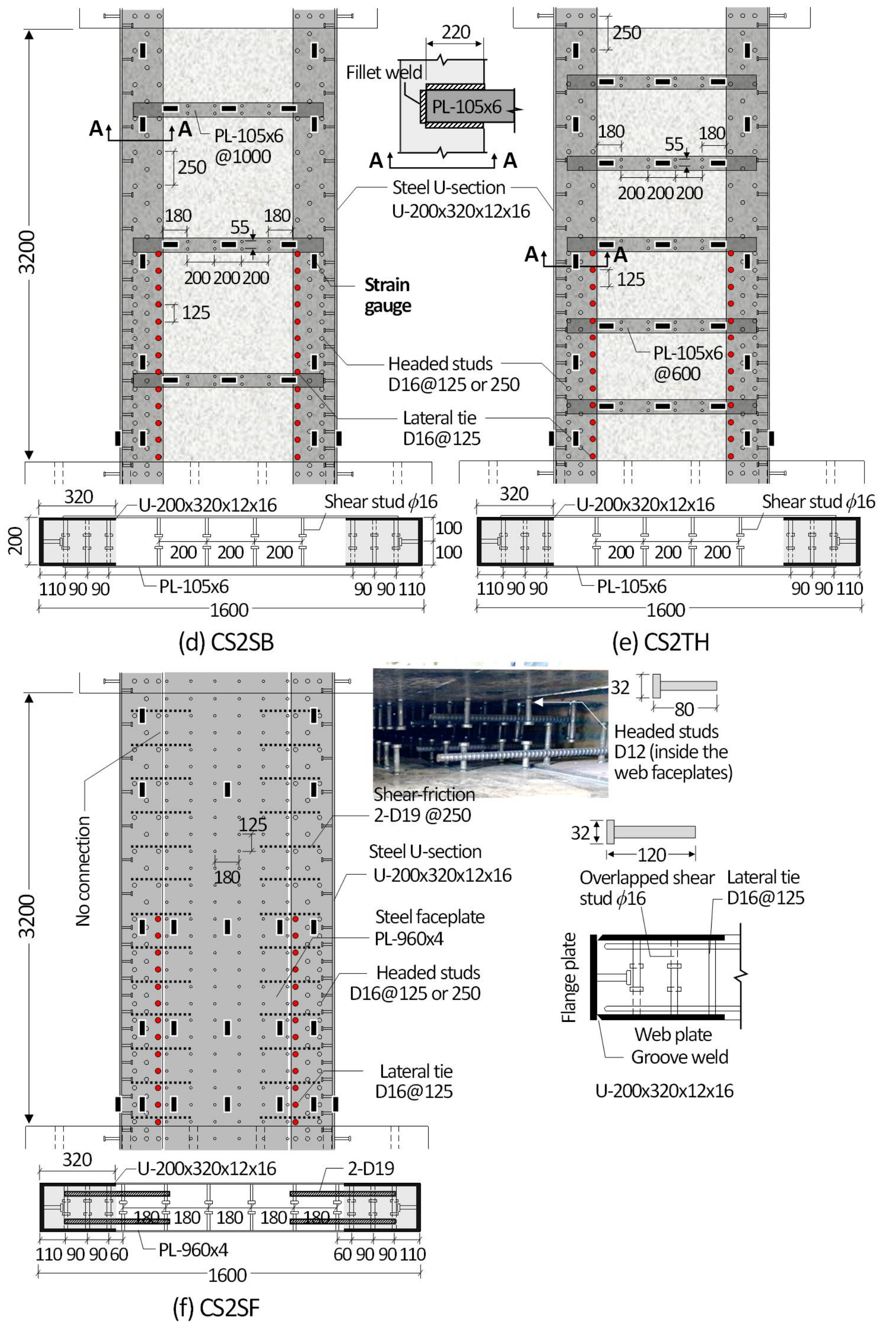

Fig. 4-4 Details of shear failure-mode specimens with aspect ratio of 2.0: (a) CS2SB; (b) CS2TH; (c) CS2SF.

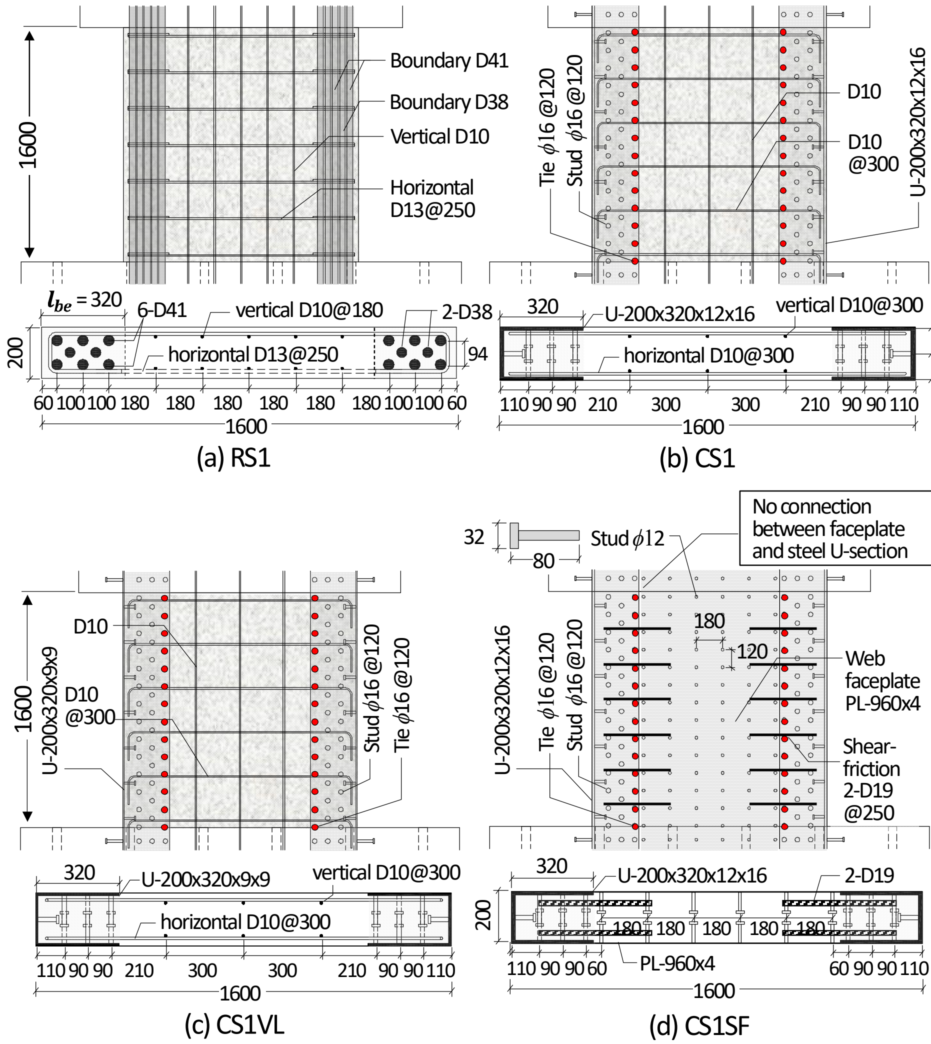

Fig. 4-5 Details of shear failure-mode specimens with aspect ratio of 1.0: (a) RS1; (b) CS1; (c) CS1VL; (d) CS1SF.

4.2.3 Material strengths

Table 4-1, **Table 4-2**, and **Table 4-3** show the strengths of the materials used for shear failure-mode specimens. The compressive strength of concrete measured from concrete cylinder tests was f_c' = 64.3 MPa for specimens with aspect ratio 2.5; 47.4–55.7 MPa for specimens with aspect ratio 2.0; and 53.1–55.5 MPa for specimens with aspect ratio 1.0. For steel plates and reinforcing bars, their strengths were obtained from tension, following KS B 0802 (2018). In **Table 4-1**, in the specimens with aspect ratio 2.5, the steel strengths were f_y = 445–670 MPa (f_u = 597–870 MPa) for reinforcing bars; and F_y = 596 MPa (F_u = 659 MPa) for steel plates. In the specimens with aspect ratios of 2.0 and 1.0, the steel strengths were f_y = 514–670 MPa (f_u = 600–870 MPa) for reinforcing bars; and F_y = 444–469 MPa (F_u = 556–642 MPa) for steel plates. The measured material strengths were used for design of test specimens.

4.2.4 Test setup for loading and measurement

For the specimens with aspect ratios of 2.5 and 2.0, the test setup for loading and measurement was the same as that used for the corresponding flexural yielding specimens, as shown in **Fig. 3-6**. Similar test setup was used for the specimens with aspect ratio of 1.0 (**Fig. 4-6**), except for the reduced distance from the wall base to the lateral loading point (i.e., shear span l_s = 1,850 mm), and the measurement length (= 500 mm for lower part; 1300 mm for upper part) for vertical LVDTs (R1 and R2). Further, lateral supports were neglected due to the relatively low aspect ratio. Lateral loading protocol followed the rules of ACI 374.2R (2013).

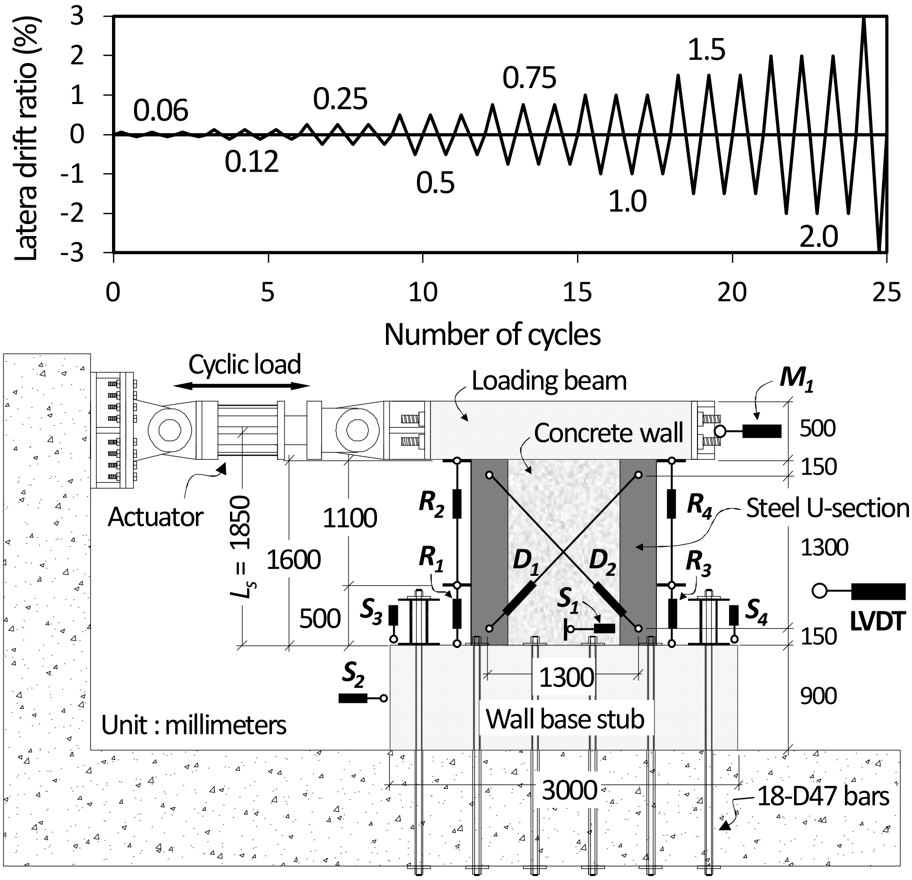

Fig. 4-6 Test setup for wall specimens with aspect ratio of 1.0.

4.3 Test Results

4.3.1 Lateral load-displacement relationship and failure mode

Fig. 4-7 and **Fig. 4-8** show the lateral load-drift ratio relationships and failure mode of the specimens with aspect ratio of 2.5, respectively. In the specimens, the peak strengths were less than the nominal flexural strengths V_f (= M_n / l_s = 2,950 – 3,643 kN, see **Table 4-6**), but were greater than the nominal shear strengths V_n. the post-peak strengths were degraded in a brittle manner. This result indicates that the test strength was determined by shear failure before flexural yielding. **Table 4-4** shows the test results including the peak strength V_{test}, drift ratio δ_o at the peak strength, and failure mode. In RC specimen **RS2.5** with boundary vertical rebars (**Fig. 4-7**(a)), the peak strengths of V_{test} = +2,164 and –2,067 kN occurred at δ_o = $\pm$1.35%, respectively. At the first load cycle of δ = $\pm$2.0 %, diagonal cracking significantly increased at the wall bottom, showing diagonal tension failure mode (denoted as DT). At the next loading cycle (δ_u = +1.87% and –1.94%), the load-carrying capacity decreased due to crushing of concrete in the web and boundary regions (**Fig. 4-8**(a)), showing web crushing failure mode (denoted as WC in **Fig. 4-7**(a)).

In composite specimen **CS2.5** having the same horizontal reinforcement ratio ρ_h as that of **RS2.5** (**Fig. 4-7**(b)), the initial stiffness was similar to that of **RS1**, but V_{test} (= +2,441 and –2,350 kN) and δ_o (= +1.82% and –1.87%) were 13% and 36% greater than those of **RS2.5**, respectively. After inelastic shear deformation, strength degradation occurred due to the crushing of web concrete (**Fig. 4-8**(b)). In **CS2.5VH** with the greater web length of steel U-sections (**Fig. 4-7**(c)), the peak strength was increased to V_{test} = $\pm$2,730 kN (at δ_o = +1.66% and –1.74%), but it was limited by the loading capacity of the actuator, without significant damage in the concrete. Thus, cyclic loading was repeated at $\pm$2,700 kN, until the strength was degraded due to the crushing of web concrete at δ_u = $\pm$2.28% (**Fig. 4-8**(c)). Thus, the actual strength of **CS2.5VH** may be greater than the test strength. Nevertheless, the tested V_{test} of **CS2.5VH** was 14% greater than that of **CS2.5**. In

CS2.5M (**Fig. 4-7**(d)), despite the smaller wall thickness, the load-carrying capacity was not significantly less than that of **CS2.5VH**: the peak strengths of V_{test} = +2,696 and –2,709 kN occurred at δ_o = +1.75% and –1.78%. After V_{test}, the load-carrying capacity decreased, due to crushing of the web concrete (δ_u = +1.76% and –1.80%) (**Fig. 4-8**(d)).

Table 4-4 Summary of tested lateral load-drift ratio relationships of shear failure-mode specimens

Specimens		Peak strength V_{test} [kN]			Drift ratio δ_o at V_{test} [%]			Failure mode
		+ve	–ve	Avg.	+ve	–ve	Avg.	
Aspect ratio = 2.5	RS2.5	2,164	-2,067	2,115	1.35	-1.35	1.35	DT → WC
	CS2.5	2,441	-2,350	2,395	1.82	-1.87	1.84	WC
	CS2.5VH	2,730	-2,730	2,730	1.66	-1.74	1.70	WC
	CS2.5M	2,696	-2,709	2,702	1.75	-1.78	1.77	WC
Aspect ratio = 2.0	RS2	1,470	-1,373	1,421	0.89	-0.67	0.78	DT → WC
	CS2	1,960	-1,876	1,918	1.39	-1.34	1.37	WC
	CS2VL	1,545	-1,609	1,577	1.41	-1.50	1.46	WC
	CS2SB	2,009	-2,094	2,052	1.36	-1.41	1.38	WC
	CS2TH	2,242	-2,277	2,259	2.15	-1.85	2.00	FY + WC
	CS2SF	2448	-2639	2,544	1.74	-1.56	1.65	PB + WC
Aspect ratio = 1.0	RS1	1,933	-1,974	1,953	0.70	-0.64	0.67	DT
	CS1	3,159	-2,869	3,014	1.44	-1.11	1.28	WC
	CS1VL	2,498	-2,251	2,375	1.24	-1.06	1.15	WC
	CS1SF	3,749	-3,573	3,661	2.12	-0.84	1.48	SY

Note: DT = diagonal tension failure; WC = web crushing failure; FY = flexural yielding; PB = buckling of faceplate; and SY = shear yielding.

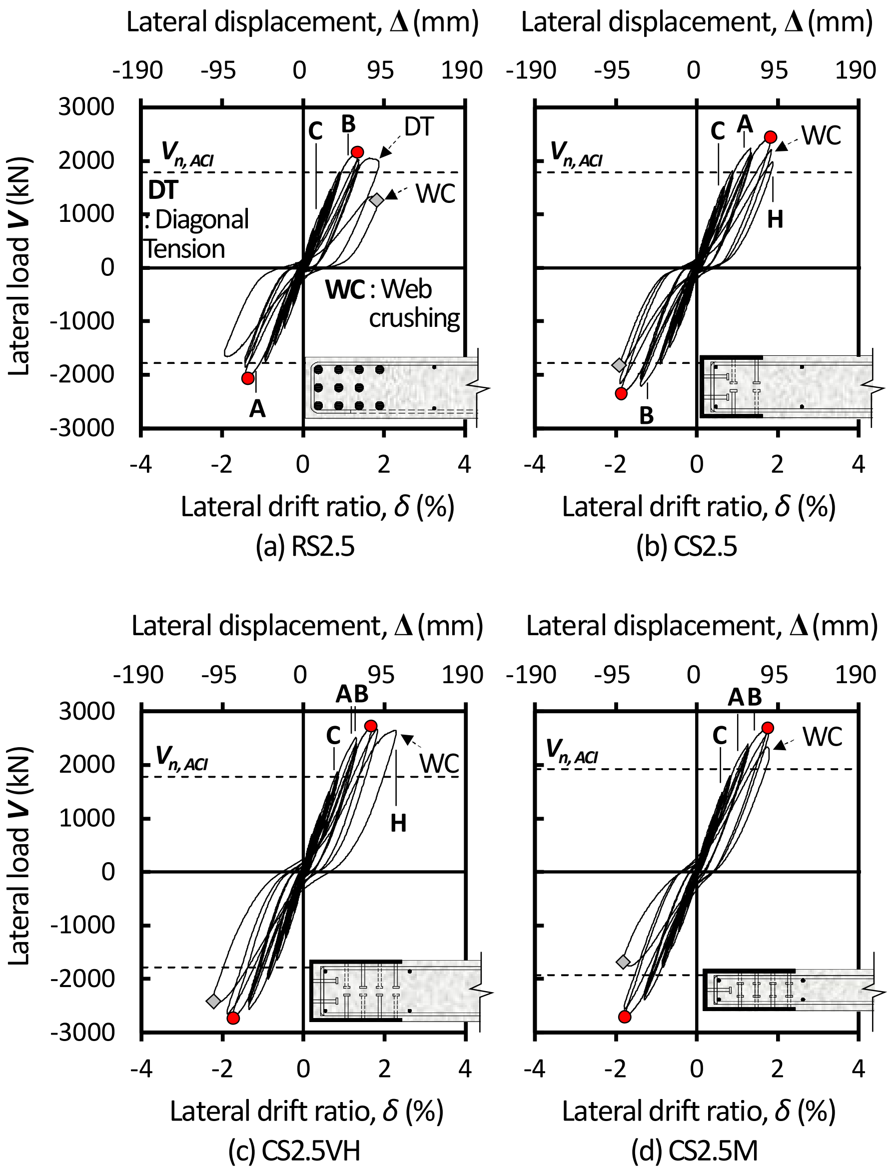

Fig. 4-7 Lateral load-drift ratio relationships of shear failure-mode specimens with aspect ratio of 2.5.

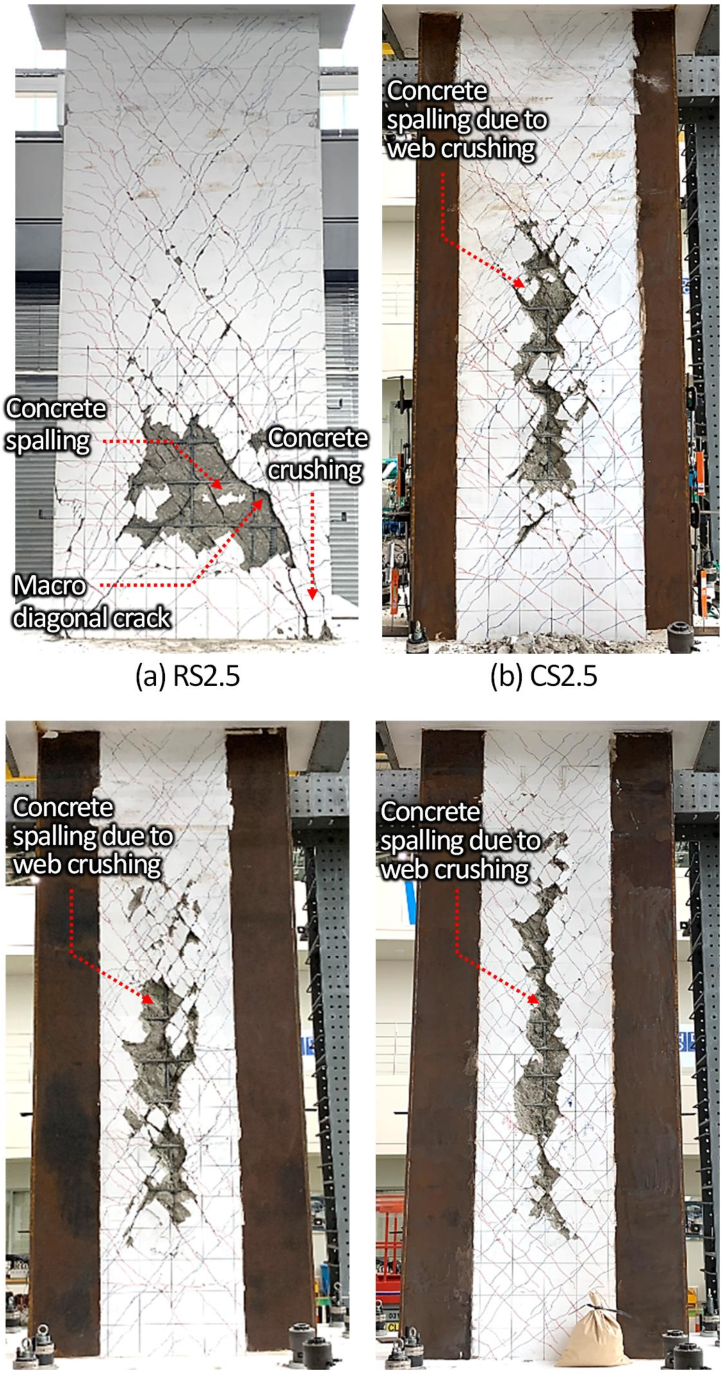

(a) RS2.5 (b) CS2.5 (c) CS2.5VH (d) CS2.5M

Fig. 4-8 Failure mode of shear failure-mode specimens with aspect ratio of 2.5.

Similar load-displacement behavior and failure pattern were also shown in the specimens with aspect ratio of 2.0. Their tested strengths (V_{test} = 1,421 – 2,544 kN) were greater than the nominal shear strengths $V_{n,ACI}$ (= 1,120 – 1,592 kN). **Fig. 4-9** and **Fig. 4-10** show the lateral load-drift ratio relationships and failure mode of the specimens with aspect ratio of 2.0, respectively. In RC specimen **RS2** (**Fig. 4-9**(a)), as the drift ratio increased, the number and width of diagonal cracks increased, and horizontal cracks occurred in the wall boundaries (**Fig. 4-10**(a)). During the first load cycle of δ = 1.0 %, a macro diagonal crack propagated toward the boundary concrete at the wall base, and shear sliding occurred along the macro crack (i.e., diagonal tension failure, **Fig. 6**(a)). At this drift level, the peak strength for the positive loading direction was developed: V_{test} = +1,470 kN at δ_o = +0.89%. Due to the immediate strength degradation, the peak strength for the negative loading direction was developed at the previous loading cycle: V_{test} = –1,373 kN at δ_o = –0.67%. At the next load cycle of δ = 1.5%, crushing and spalling of web concrete occurred at the wall bottom, followed by the crushing of boundary concrete.

In the composite specimens with boundary steel U-sections, until δ = 1.0%, similar cracking pattern appeared in the web concrete. However, diagonal tension failure was prevented, and the strength degradation occurred due to crushing of web concrete in the mid-height of the walls, without failure of boundary zone (**Fig. 4-10**(b)-(e)). In **CS2** (**Fig. 4-9**(b))**,** the peak strengths increased to V_{test} = (+1,960 and –1,876) kN, which were on average 35% greater than those of **RS2**. Further, the corresponding drift ratios δ_o = +1.39% and –1.34% increased. This result indicates that the steel U-sections increased the shear strength and deformation. In **CS2VL** with thinner steel U-sections (30% smaller area) (**Fig. 4-9**(c)), the average of V_{test} = +1,545 and –1,609 kN (at δ_o = +1.41% and –1.50%, respectively) was 18% less than that of **CS2**. In **CS2SB** with steel plate beams (**Fig. 4-9**(d)), the peak strengths of V_{test} = +2,009 and –2,094 kN (at δ_o = +1.36% and –1.41%) were slightly greater than those of **CS2**. This result indicates that the steel plate beams provided good shear resistance, even though their spacing exceeded the detailing requirement of existing design methods. Further, the number of diagonal cracks significantly decreased due to the relatively large spacing s_h of steel plate beams. Thus, the post-peak strength degradation was less brittle than that of **CS2** with conventional shear reinforcing bars. In **CS2TH** with the smaller spacing of steel plate beams (**Fig. 4-9**(e)), the peak strengths increased to V_{test} = +2,242 and –2,277 kN (at δ_o = +2.15% and –1.85%), showing flexural yielding (at $\delta \approx$ 1.0%, $V_{test} > V_f$) and greater post-yield inelastic deformation. Thus, due to early flexural yielding, the actual shear strength of **CS2** may be greater than the V_{test}. In **CS2SF** with steel web faceplates (**Fig. 4-9**(f)), notable damage was not observed until the peak strength (**Fig. 4-10**(f)). The peak strength was the greatest due to high strength contribution of the faceplates, showing V_{test} = +2,448 and –2,639 kN at δ_o = +1.74% and –1.56%. At the peak strength (δ = 2.0%), local buckling was initiated at the edge of the faceplate, followed by crushing of web concrete and vertical sliding between the web and boundary elements. Thus, the post-peak strength degradation was relatively significant. After δ = 3.0% (after significant strength degradation), the buckling deformation of the faceplates significantly increased, and separation between the faceplate and web concrete occurred. For this reason, boundary steel U-sections resisted shear force by the moment-resisting frame action, showing double-curvature flexural deformation (refer to **Fig. 3-14**).

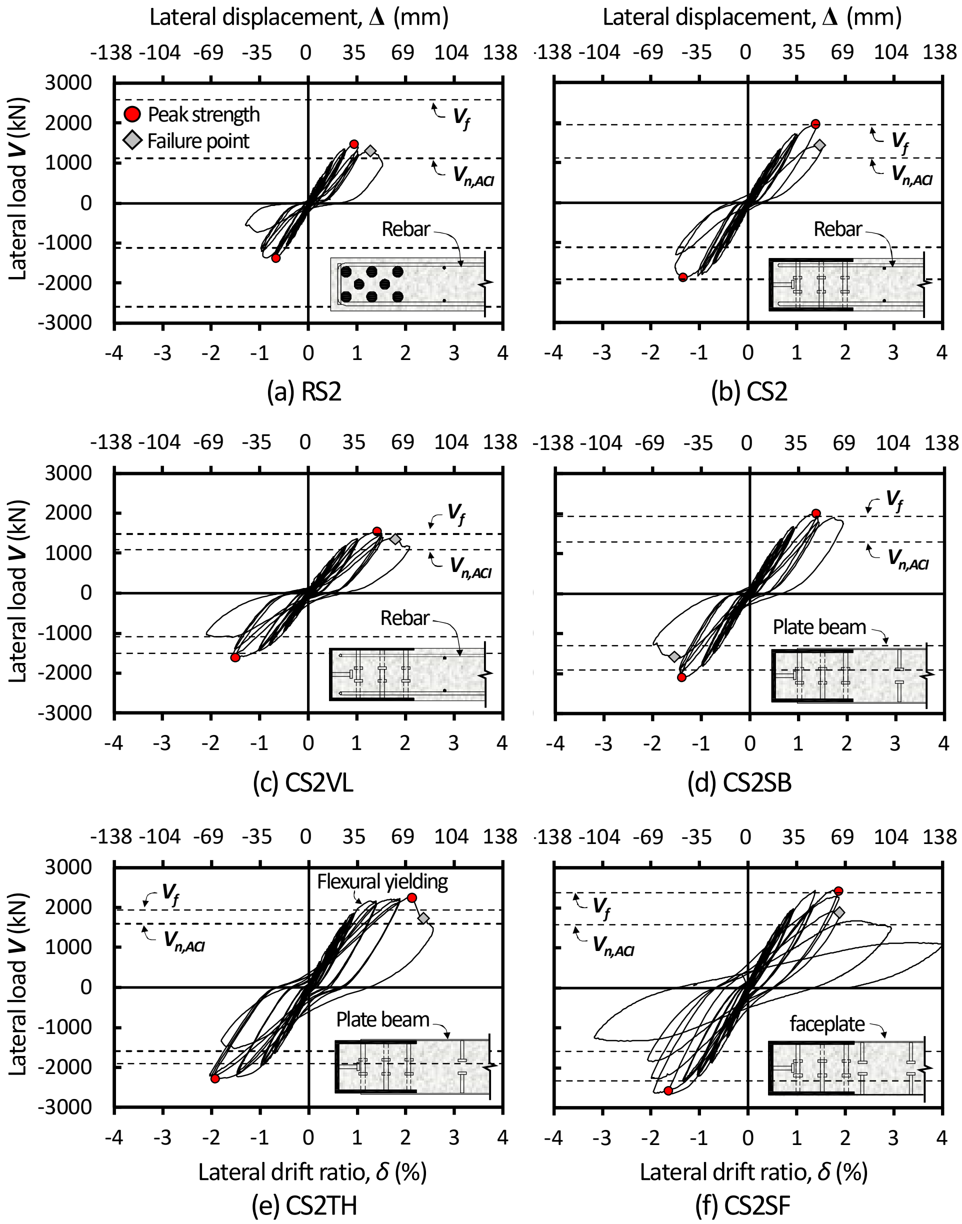

Fig. 4-9 Lateral load-drift ratio relationships of shear failure-mode specimens with aspect ratio of 2.0.

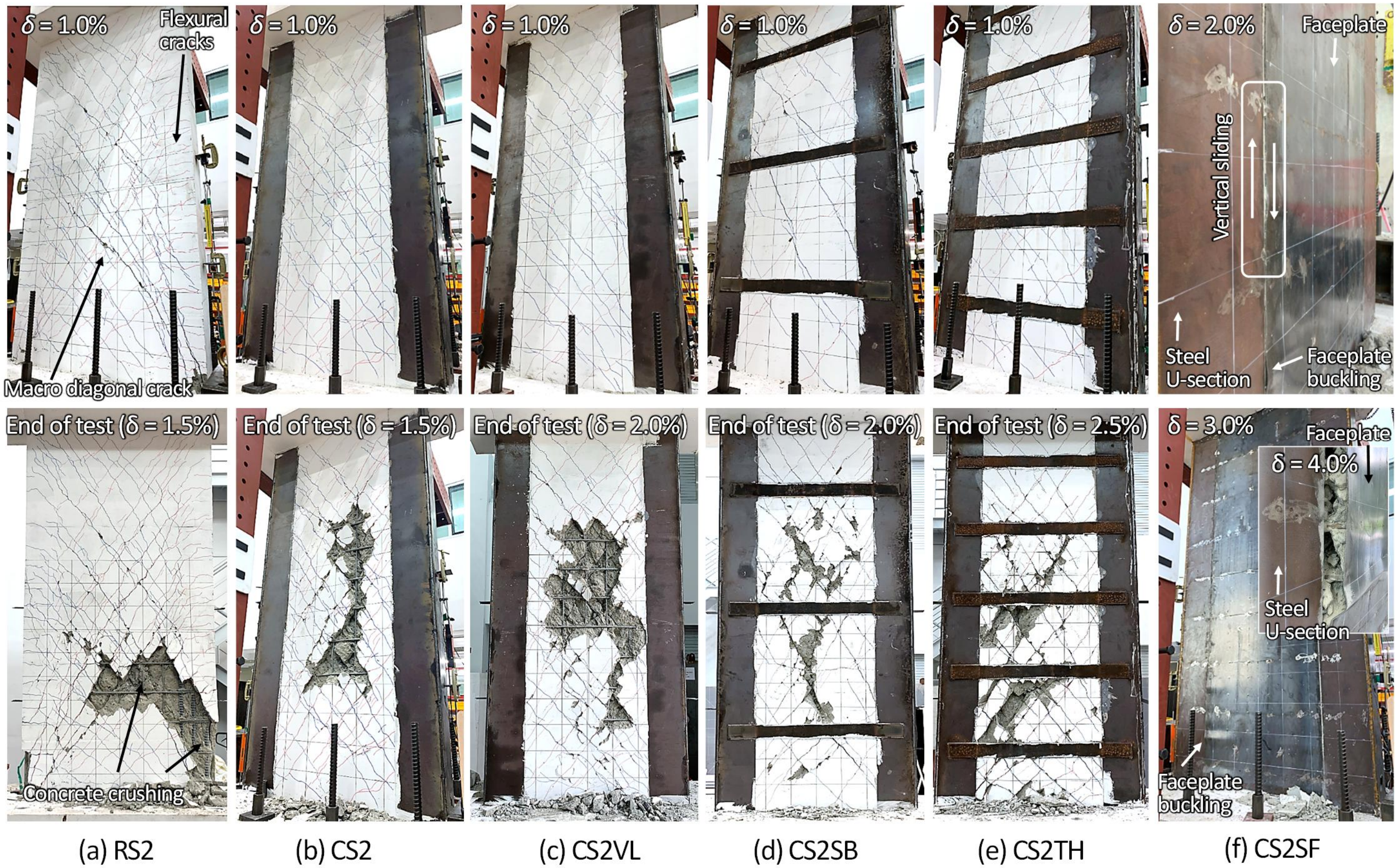

Fig. 4-10 Failure mode of shear failure-mode specimens with aspect ratio of 2.0.

Interestingly, the specimens with the lowest aspect ratio of 1.0 also showed the similar lateral loading behavior and failure mode. In RC wall **RS1** with vertical boundary rebars (**Fig. 4-11**(a)), the diagonal cracks occurred at 45 degrees, forming diagonal struts between the upper part of the flexural tension zone and the lower part of the flexural compression zone (denoted as macro diagonal crack in **Fig. 4-12**(a)). At $\delta \approx 1.0\%$, excessive sliding occurred at the macro diagonal crack, and ultimately, the web concrete was fully divided by the diagonal crack (i.e., diagonal tension failure). The peak strengths of V_{test} = +1,933 and –1,974 kN occurred at δ_o = +0.70% and –0.64%, respectively. After V_{test}, the post-peak strength was degraded significantly.

In **CS1** with boundary steel U-sections (**Fig. 4-11**(b)), the overall behavior was similar to that of **RS1**. However, despite the lesser web reinforcement, the peak strength and deformation much increased to V_{test} = +3,159 and –2,869 kN and δ_o = +1.44% and –1.11%, which were 63% and 91% greater than those of **RS1**, respectively. This result indicates that the steel U-sections provided the shear resistance, and their shear contribution was significant. Thus, the V_{test} was about three times the nominal shear strength $V_{n,ACI}$ (= 980 kN) estimated neglecting the contribution of steel U-sections. In **CS1VL** with the smaller area of steel U-sections (**Fig. 4-11**(c)), the peak strengths decreased to V_{test} = +2,498 and –2,251 kN (at δ_o = +1.24% and –1.06%), which were on average 21% less than those of **CS1**. Nevertheless, the V_{test} was 22% greater than that of **RS1** with the greater boundary reinforcement ratio. In **CS1** and **CS1VL** (**Figs. 4-12**(c) and (d)), only diagonal cracks were shown in the web concrete. When compared to **RS1**, the number of diagonal cracks was less, while their spacing and width were greater (until $\delta \approx 0.7\%$), due to the less vertical and horizontal web reinforcement ratios (ρ_v and ρ_h, **Table 4-1**). Unlike counterpart **RS1**, diagonal tension failure did not occur, despite the very small web reinforcement ratio. Ultimately, crushing of web concrete occurred at $\delta \approx 1.5\%$, without damage of steel U-sections. In **CS1SF** with steel faceplates (**Fig. 4-11**(d)), no notable damage was observed in both the faceplates and steel U-sections (**Fig. 4-12**(d)). The peak strength V_{test} = –3,573 kN (at δ_o = –0.84%) in the negative loading direction was limited by the loading capacity of the actuator (= +4,000 and –3,500 kN for positive and negative loading directions). Nevertheless, the V_{test} was greater than that of **CS1** and **CS1VL** without faceplates. In the positive loading direction, after V = +3,500 kN (at δ = +1.14%), cyclic loading was replaced by a monotonic loading, and it was maintained until wall failure. During the monotonic loading, shear yielding occurred at V_y = +3,611 kN (δ_y = +1.51%), and the post-yield strength gradually increased until the peak strength V_{test} = +3,749 kN (at δ_o = +2.12%).

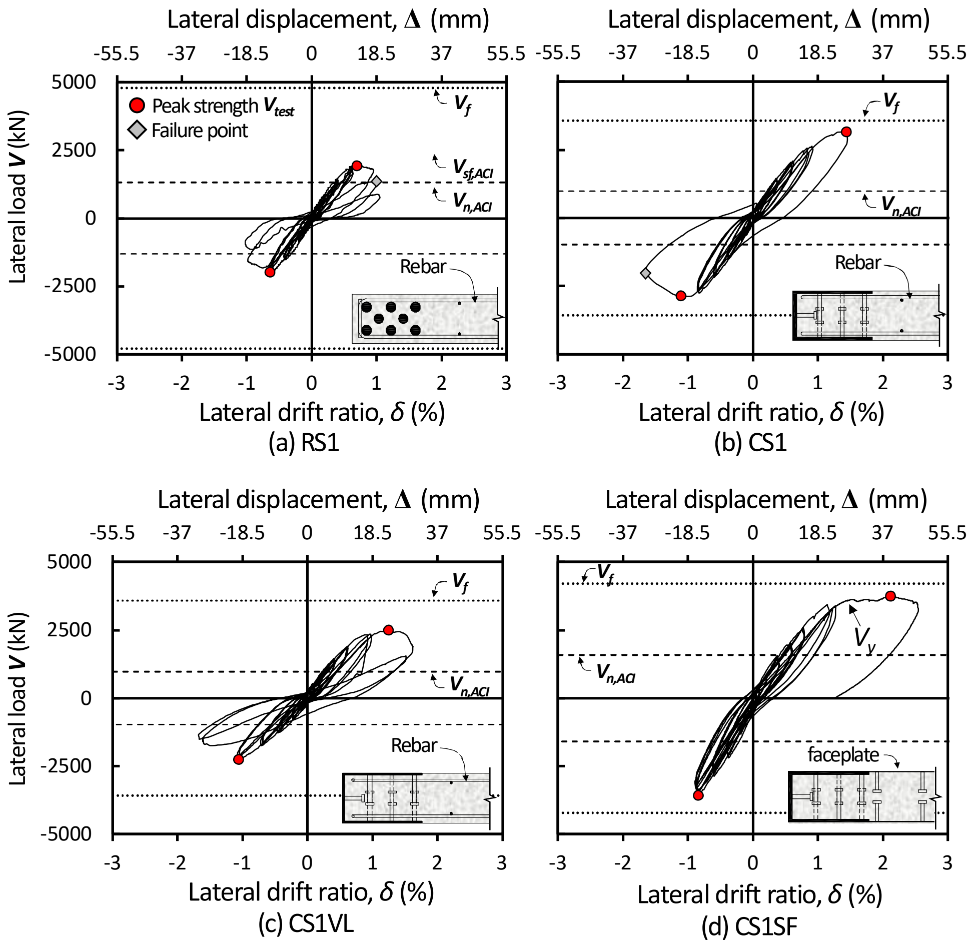

Fig. 4-11 Lateral load-drift ratio relationships of shear failure-mode specimens with aspect ratio of 1.0.

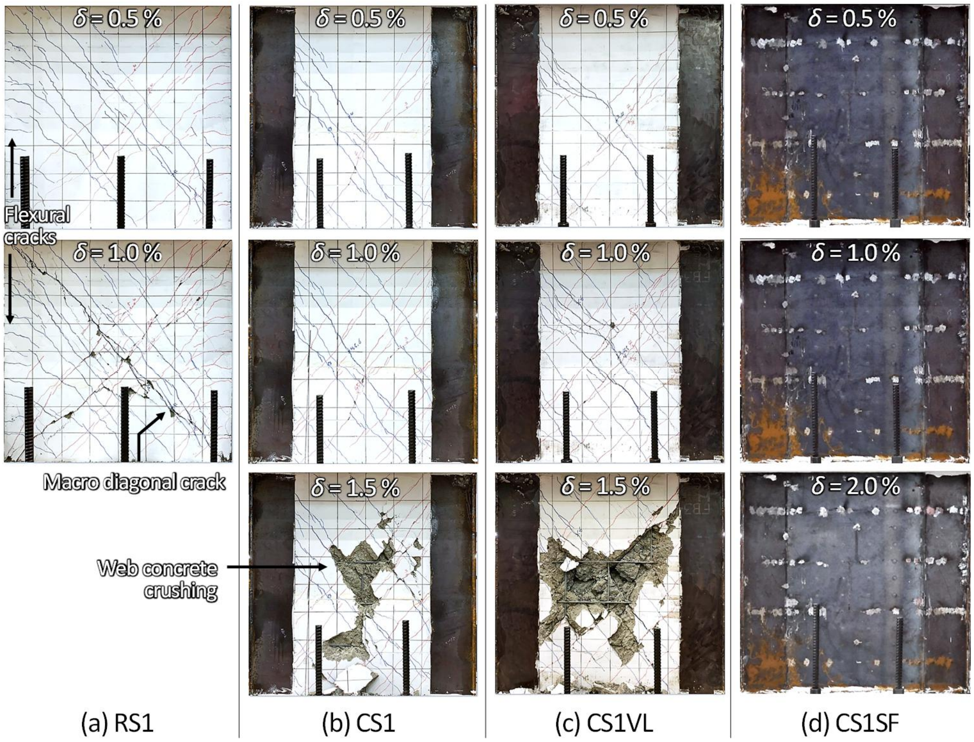

Fig. 4-12 Failure mode of shear failure-mode specimens with aspect ratio of 1.0.

4.3.2 Cracking and maximum crack width

The diagonal cracks began to occur after δ = 0.21%–0.25% for 2.5-aspect ratio specimens (corresponding to 30%–34% of the peak strength V_{test} for **RS2.5**; 0.21–0.27V_{test} for composite specimens); δ = 0.12% for 2.0-aspect ratio specimens (corresponding to 0.25V_{test} for **RS2**; 0.15–0.20V_{test} for composite specimens); and δ = 0.06%–0.09% for 1.0-aspect ratio specimens (0.25V_{test} for **RS1**; 0.14–0.20V_{test} for composite specimens). For all specimens, as the lateral drift ratio increased, the number and width of diagonal cracks increased. Only in RC specimens, horizontal flexural cracks occurred at the wall boundaries. In composite specimens, only diagonal cracks were seen in the web concrete, due to the boundary steel U-sections (see **Figs. 4-8**, **4-10**, and **4-12**).

Fig. 4-13 shows the maximum widths of diagonal shear cracks, measured according to the lateral drift ratio. In the case of specimens with aspect ratios of 2.0 and 2.5, the crack width was measured in the mid-height of the walls. In general, the maximum crack widths of the composite specimens were less than those of RC specimens with conventional boundary rebars, as the steel U-sections restrained the development of macro diagonal cracks and crushing of concrete in the boundary zone. In particular, as the drift ratio increased, the rate of increase in crack width gradually decreased, particularly at the boundary zone. This result indicates that the steel U-sections restrained shear sliding between the diagonal cracks and crack penetration into the boundary zone. For this reason, crushing and spalling of concrete were limited to the center of the web.

In **CS2SB** showing restrained shear cracking (**Fig. 4-13**(b)), at early loading, the maximum crack widths were relatively large, as crack opening was localized at a smaller number of diagonal cracks. In **CS1** and **CS1VL**, the crack widths were greater than the counterpart **RS1**, due to the lower horizontal reinforcement ratio (i.e., greater spacing of horizontal rebars) (**Fig. 4-13**(c)).

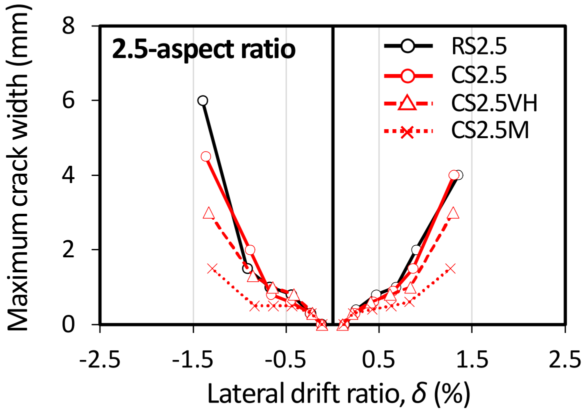

(a)

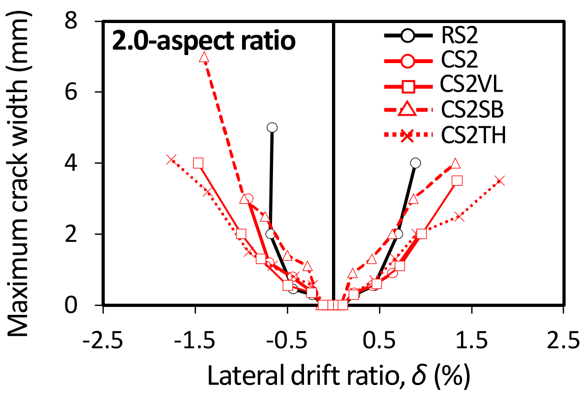

(b)

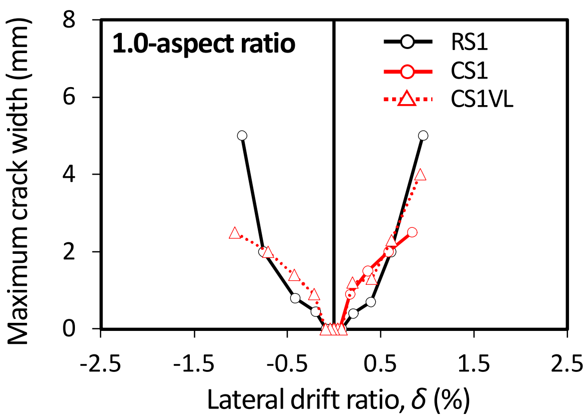

(c)

Fig. 4-13 Maximum diagonal crack widths measured in shear failure-mode specimens.

4.3.3 Displacement contributions

For the shear failure-mode specimens, the contributions of flexural (Δ_f), shear (Δ_s), and sliding deformations (Δ_{sl}) to the overall lateral displacement Δ were calculated according to the same method that used for flexural yielding-mode specimens (see Section 3.4.5). In the specimens with the smallest aspect ratio of 1.0, the flexural contribution Δ_f indicates the displacement contribution of overall flexural deformation over the entire height of the walls. For all specimens, overall, the sum of Δ_f (= $\Delta_{f,L}$ + $\Delta_{f,U}$), Δ_s, and Δ_{sl} agreed with the measured Δ, except for specimens **CS2SF** and **CS1SF** with steel faceplates. In **CS2SF** and **CS1SF**, the sum of the contributions was 15%–20% less than Δ due to the high shear demand, because slip occurred at concrete cracks in the base stub. The contribution ratios of each displacement component were similar, regardless of the type of boundary reinforcement (steel U-section vs. rebars)

In the 2.5-aspect ratio specimens (**Fig. 4-14**(a)), The flexural contribution $\Delta_{f,L}$ in the lower part of walls (within 1,600 mm above the wall base) was almost 50% of Δ, on average. In **RS2.5**, the ratio decreased at δ = 1.9%, while in **CS2.5**, **CS2.5VH**, and **CS2.5M**, the ratio was not changed, as shear failure occurred before flexural yielding. The shear deformation contribution ratios were Δ_s / Δ = 25%–36%. In **RS2.5**, Δ_s / Δ significantly increased at the ultimate drift ratio because the shear stiffness was degraded due to the propagation of diagonal tension cracking. In composite specimens, the increase of Δ_s / Δ was less, which indicates that the boundary steel U-sections restrained full penetration of diagonal tension cracking.

In the 2.0-aspect ratio specimens except **CS2SF** (with steel faceplates) (**Fig. 4-14**(b)), the shear deformation contribution ratio slightly increased to 39%–47%, due to the lower aspect ratio. The flexural contribution ratio ratios were 51%–58%. **CW2SF** showed the smallest Δ_s / Δ, due to the high shear stiffness of the web faceplates. In **CS2TH** with closely spaced steel plate beams (ρ_h = 1.05%), Δ_s / Δ was less than those of **RS2**, **CS2**, and **CS2VL** (ρ_h = 0.51%–0.63%). In all 2.0-

aspect ratio specimens, Δ_s / Δ significantly increased after failure of the specimens (at δ = 1.4%–3.1%), which confirms that the specimens failed due to shear.

In **RS1**, **CS1**, and **CS1VL** with the smallest aspect ratio (**Fig. 4-14**(c)), the contribution ratios of each displacement component were similar, regardless of the type of boundary reinforcement (steel U-section vs. rebars). Here, the shear component (Δ_s / Δ = 50%–57%) showed the greatest contribution ratio, followed by the flexural component (Δ_f / Δ = 39%–42%). In particular, as Δ increased, Δ_s / Δ slightly increased. The increase of Δ_s / Δ was pronounced at the peak strength V_{test} where shear failure was initiated. In **CS1SF** with steel faceplates, the shear component Δ_s (Δ_s / Δ = 34 % on average) was less than those of **CS1** and **CS1VL**, due to high shear stiffness of the faceplates. However, at V_{test}, Δ_s (or Δ_s / Δ) significantly increased due to shear yielding.

For all specimens, regardless of the aspect ratio, the sliding contribution was not significant, showing 3%–9% of Δ.

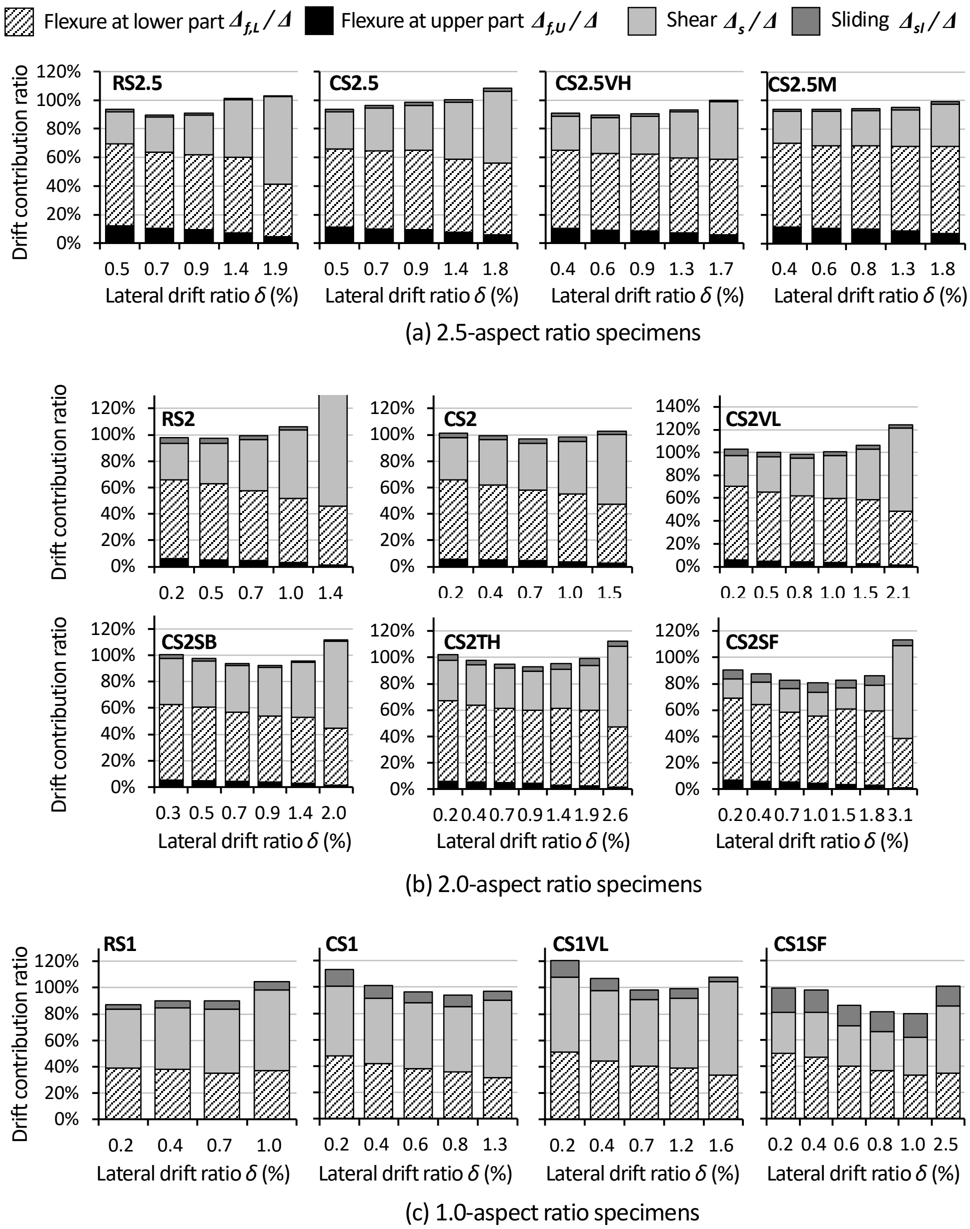

Fig. 4-14 Lateral displacement contributions measured in shear failure-mode specimens.

4.3.4 Horizontal strain distribution

Tensile strains of horizontal reinforcement were measured along the wall height. **Fig. 4-15** shows the horizontal strain distribution of the specimens with aspect ratio of 2.5, measured in the positive loading direction. Except **CS2.5** and **CS2.5VH**, the strain distribution was not uniform as large inelastic strains were developed near the shear cracks. In **RS2.5** (**Fig. 4-15**(a)), the strains reached to the yield strain at δ = 0.38%, corresponding to $0.44V_{test}$. At the peak strength, the strains significantly increased due to diagonal tension failure. In **CS2.5**, **CS2.5VH**, and **CS2.5M**, tensile yielding of the horizontal bars occurred later than in **RS2.5** (at δ = 0.55% for **CS2.5**; 0.75% for **CS2.5VH**; and 0.60% for **CS2.5M**), and the shear forces at the rebar yielding increased to $0.56V_{test}$, $0.63V_{test}$, and $0.53V_{test}$, respectively. In particular, at the peak strength (at δ_o), **CS2.5** and **CS2.5VH** showed the smaller strains than in the previous load cycles. This result indicates that, as the lateral drift ratio increased, the contribution of horizontal reinforcing bars to the shear strength decreased, while the contribution of U-shaped steel elements increased. However, in **CS2.5M** with smaller wall thickness, the strains significantly increased due to the greater shear demand applied to the gross section: V_{test} / A_g = 4 MPa for **RS1**; 4.5 MPa for **CS1**; 5.1 MPa for **CS2**; and 7.5 MPa for **CS3**.

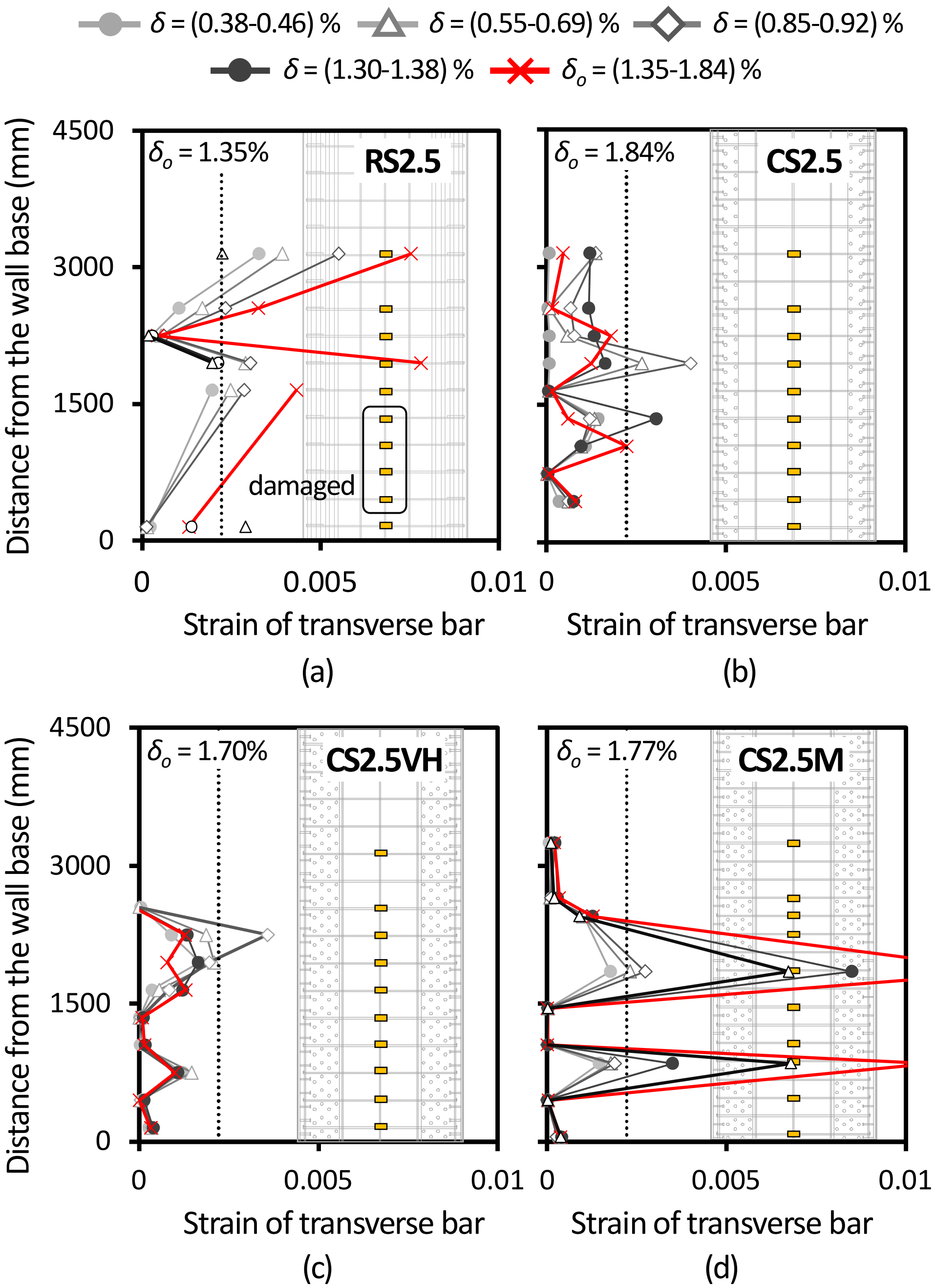

Fig. 4-15 Horizontal strain distribution measured in shear failure-mode specimens with aspect ratio of 2.5.

Fig. 4-16 shows the horizontal strain distribution of the specimens with aspect ratio of 2.0, measured in the positive loading direction. The strains were measured at the center and end of the horizontal reinforcements (refer to the locations of strain gauges in **Fig. 4-3** and **Fig. 4-4**). In general, until yielding of the horizontal reinforcements, the tensile strains were uniformly distributed along the wall height. In **RS2** (**Fig. 4-16**(a)), the tensile strains at the center and end of horizontal rebars exceeded the yield strain at $0.65V_{test}$, and the post-yield strains were maintained without increase. Similarly in **CS2** and **CS2VL** (**Figs. 4-16**(b) and (c)), tensile yielding of horizontal rebars occurred at $0.47V_{test}$ and $0.51V_{test}$, respectively. However, as the shear deformation increased, relatively large inelastic strains occurred at both the center and end of horizontal rebars, due to the greater shear demand V_{test}. In **CS2SB** and **CS2TH** (**Figs. 4-16**(d) and (e)), tensile yielding at the ends of steel plate beams (at $0.49V_{test}$ for **CS2SB**, $0.65V_{test}$ for **CS2TH**) occurred earlier than at the center (at $0.82V_{test}$ for both), and subsequent inelastic strains were concentrated at the ends of steel plate beams. This is because plastic strains were developed at the ends of the plate beams subjected to combined flexural moment (frame action) and tension (truss action) (see **Fig. 4-17**(a)). Thus, as shown in **Fig. 4-17**(b), the tensile strains measured at the end of steel plate beams showed gradual increase under cyclic loading.

Fig. 4-18 shows the horizontal strains of steel web faceplates in **CS2SF**. The horizontal strains at both the center and edge of the faceplate were significantly less than the yield strain.

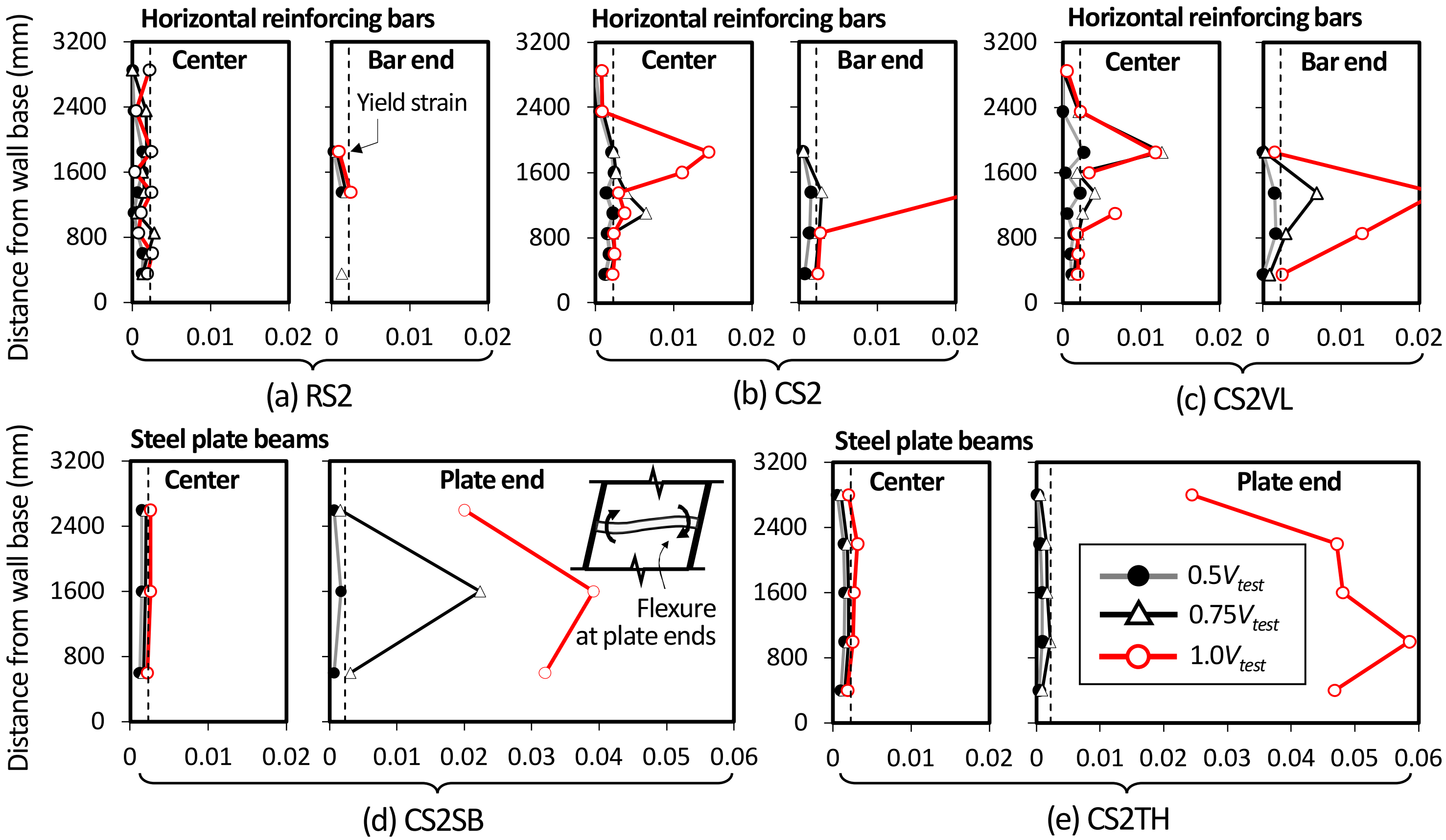

Fig. 4-16 Horizontal strain distribution measured in shear failure-mode specimens with aspect ratio of 2.0.

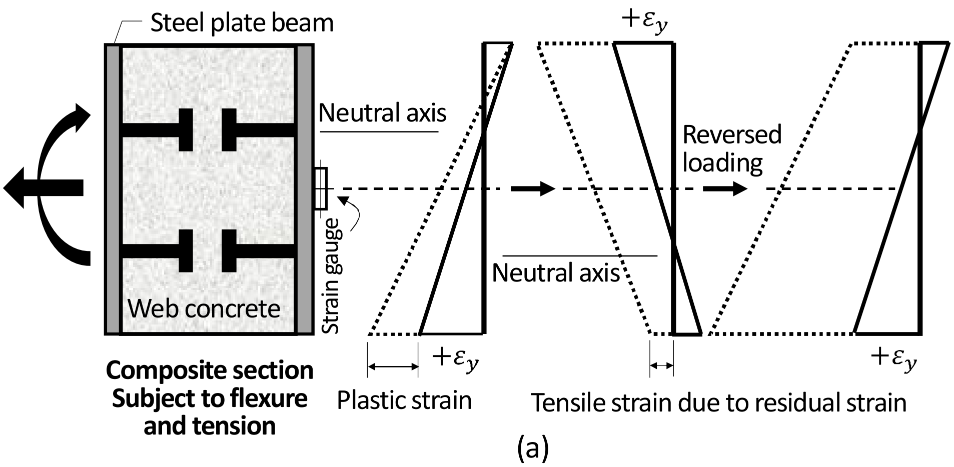

Fig. 4-17 Strains at the ends of steel plate beams.

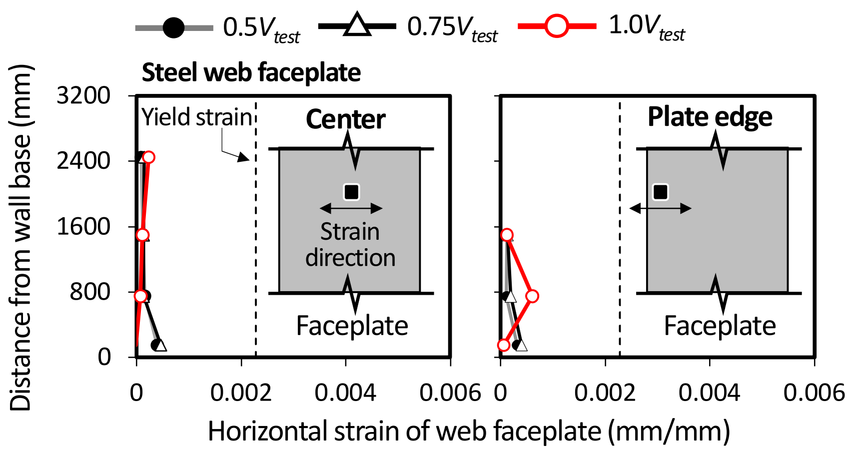

Fig. 4-18 horizontal tensile strain of faceplates measured in CS2SF.

In the specimens with aspect ratio of 1.0, tensile strains of horizontal reinforcing bars (in **RS1**, **CS1**, and **CS1VL**) were measured along the diagonal strut. **Fig. 4-19** shows the horizontal strain distribution of the specimens with aspect ratio of 1.0, measured in the positive loading direction. In **RS1** (**Fig. 4-19**(a)), the tensile strain exceeded the yield strain, when the lateral load reached $0.68V_{test}$. Similarly in **CS1** and **CS1VL** (**Figs. 4-19**(b) and (c)), tensile yielding of horizontal rebars occurred, but the corresponding lateral load was only 41% and 38% of V_{test} for **CS1** and **CS1VL**, respectively, due to the lower horizontal reinforcement ratio. The post-yield inelastic strains occurred in the horizontal rebars throughout the wall height.

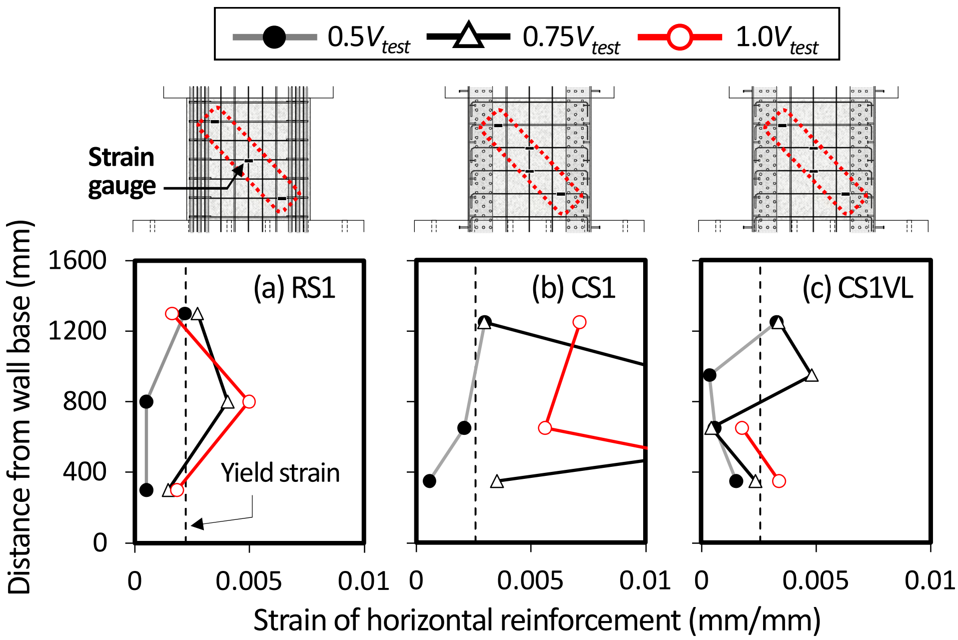

Fig. 4-19 Horizontal strain distribution measured in shear failure-mode specimens with aspect ratio of 1.0.

4.3.5 Vertical strain distribution

For all specimens, strains of vertical reinforcement (rebars and steel U-sections) were measured at 150 mm-distance from the wall base. **Fig. 4-20** shows the vertical strain distribution, measured at the peak strength $+V_{test}$ in the positive loading direction. In RC specimens **RS2.5**, **RS2.0**, and **RS1.0**, the vertical strains were linearly distributed from the compression face (origin in the horizontal axis) to tension face (end point in the horizontal axis). As the wall aspect ratio decreased, the vertical strains decreased due to the less flexural moment applied at the wall bottom. Only in **RS2.5** (**Fig. 4-20**(a)), compressive yielding of boundary rebars occurred due to crushing of the boundary concrete.

The linear strain distribution was also seen in the composite specimens with boundary steel U-sections. Generally, the strains were greater than those of the RC specimens, due to the increased shear strength (i.e., shear demand). The compressive and tensile strains of flange plates in steel U-sections (at the tips on the horizontal axis) were greater than the yield strain, while the strains measured at the center of the web plates in steel U-sections were close to, or less than, the yield strain, except for **CS2TH**. This result indicates that in the specimens, shear failure occurred before full flexural yielding. In **CS2TH** showing post-yield ductile behavior (**Fig. 4-20**(b)), the tensile strains of both the flange and web plates were greater than the yield strain. In **CS2SF** with steel faceplates (**Fig. 4-20**(b)), the vertical strains were not linearly distributed due to local buckling of the faceplate and vertical sliding between the web and boundary elements. For this reason, the compressive strains occurred in half the cross section.

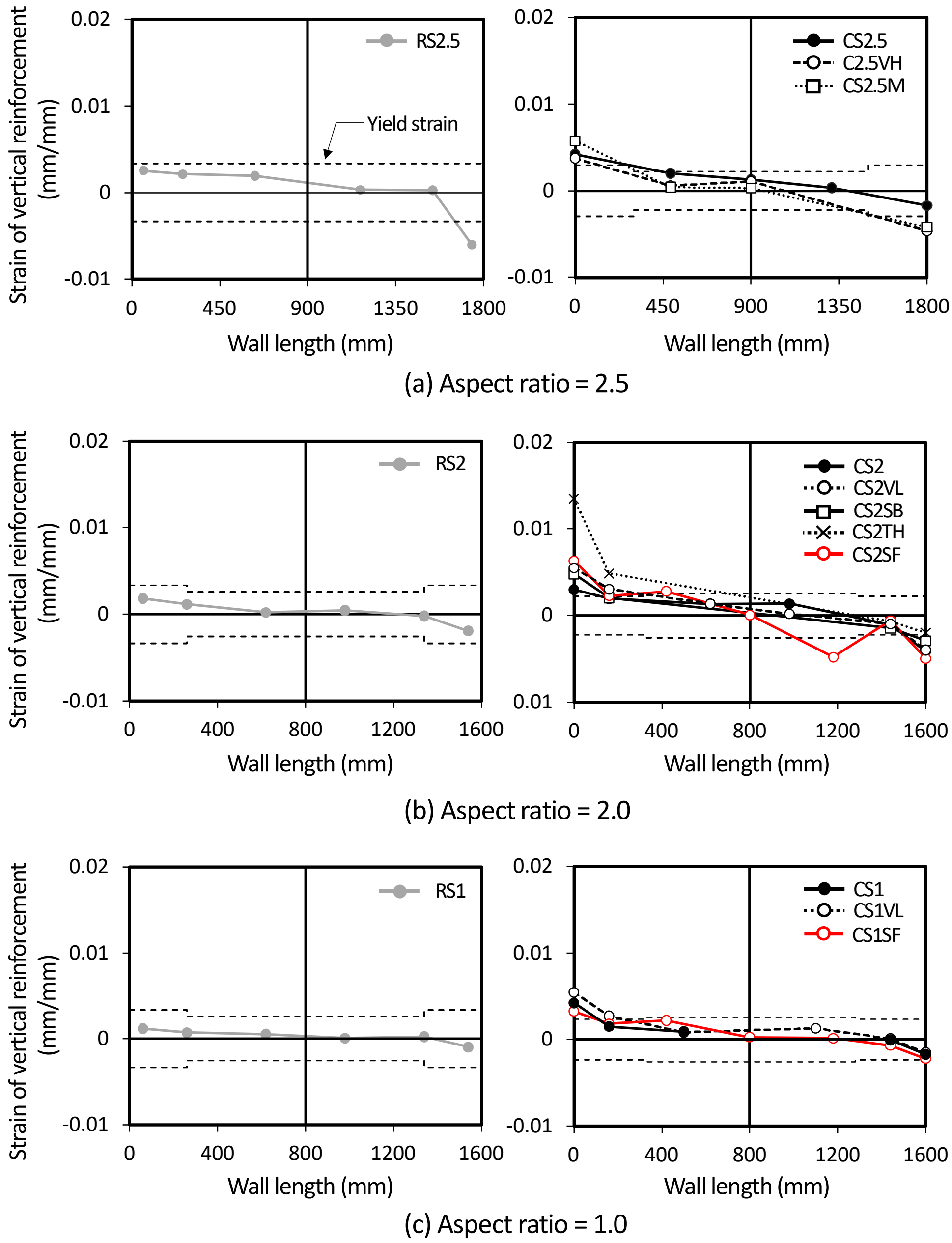

Fig. 4-20 Vertical strain distribution across the cross section measured in shear failure-mode specimens.

4.3.6 Strains of steel plates

In the 2.5-aspect ratio specimens, strains of boundary steel U-sections were measured at 750 mm distance from the wall base (denoted as T1 and T2 in **Fig. 4-21**), and 2,000 mm distance from the wall base (denoted as T3 and T4). **Fig. 4-21**(a) shows the horizontal (ε_x) and vertical strains (ε_z) of the steel U-sections in the 2.5-aspect ratio specimens. Both the horizontal and vertical strains were less than the yield strain, and the strain ratio ε_x / ε_z was similar to Poisson's ratio of steel (≈ –0.3, Greaves et al. 2011). **Fig. 4-21**(b) shows the shear strain γ_{xz}. The shear strains were less than the shear yield strain (= $0.6F_y/G_s$, AISC 360, 2016). As similar to the strain results shown in flexural yielding-mode specimens, the direction of shear strains was not coincide with that of shear force on walls, as the shear transferred from diagonal struts increased the plate stress at the ends of the diagonal strut. Assuming elastic state of steel plates, the principal stresses σ_1 and σ_2 of boundary steel U-sections were calculated based on the measured steel strains, as follows:

$$\sigma_{1,2} = \frac{\sigma_x + \sigma_z}{2} \pm \sqrt{\left(\frac{\sigma_x - \sigma_z}{2}\right)^2 + \tau_{xz}^2} \tag{4-1}$$

where, σ_x and σ_z = normal stresses of steel U-sections in the x- and z-directions, respectively; and τ_{xz} = shear strains of steel U-sections. Here, the steel stresses were calculated based on elastic plane stress condition. To investigate whether plastic strains occur in the steel plates, Von-Mises yield curves were calculated as follows:

$$F_y{}^2 = \sigma_1{}^2 - \sigma_1\sigma_2 + \sigma_2{}^2 \tag{4-2}$$

Fig. 4-21(c) compares Von-Mises yield curves with the tested principal stresses of the steel plates measured in **CS2.5** and **CS2.5VH**. In the specimens, the tested principal stresses σ_1 and σ_2 were less than or slightly greater than the Von-

Mises yield curves. This result indicates that, as assumed, the steel U-sections were almost elastic until shear failure. The same results were also seen in **CS2.5M** and the specimens with lower aspect ratios of 2.0 and 1.0.

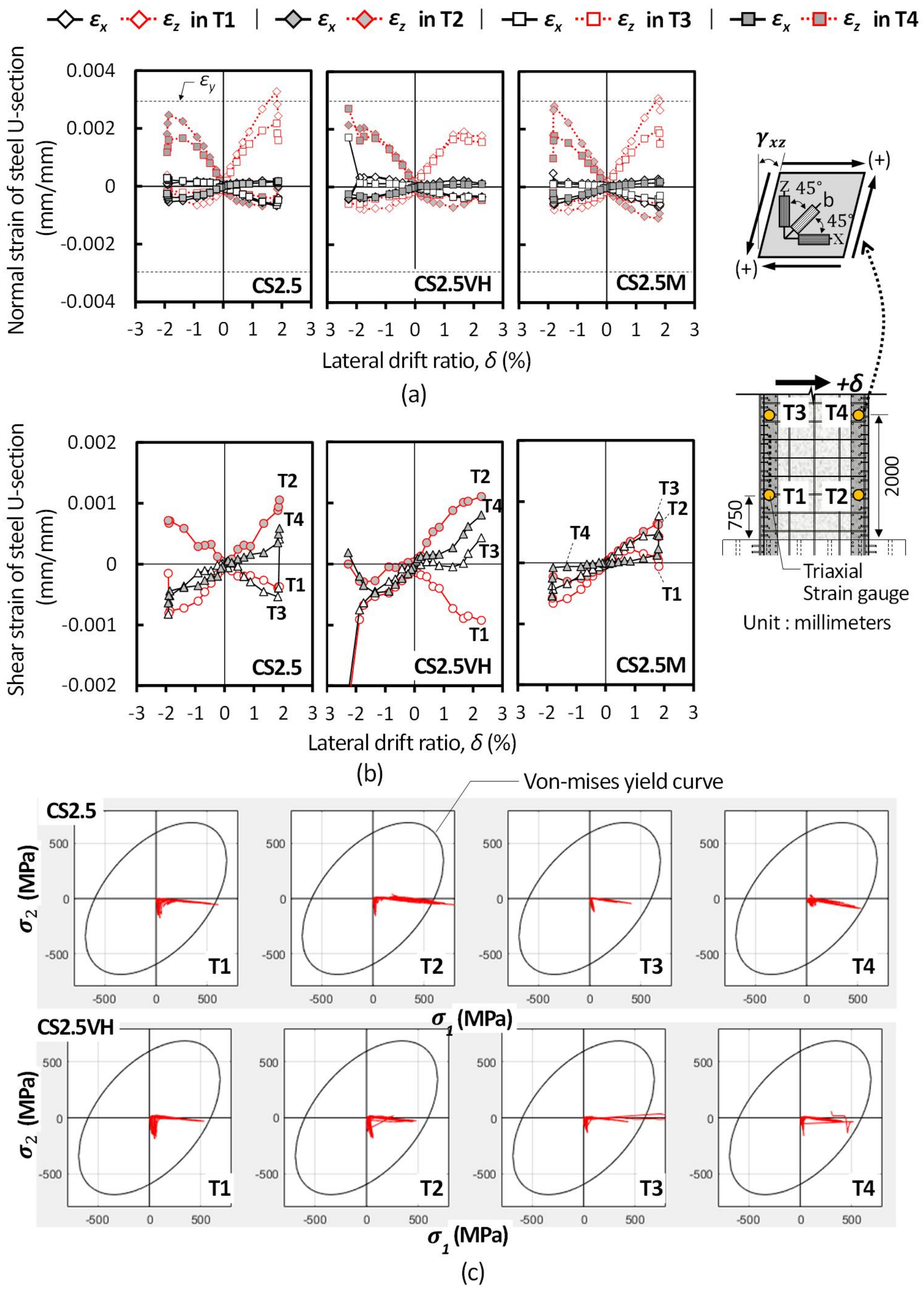

Fig. 4-21 Strains of steel U-sections measured in shear failure-mode specimens with aspect ratio of 2.5: (a) normal strains; (b) shear strains; (c) principal stresses.

Fig. 4-22 shows the shear strain distributions of steel plates (web plate of steel U-sections and steel web faceplate) along the wall height, for the specimens with aspect ratio of 2.0. In **CS2** and **CS2VL** (**Figs. 4-22**(a) and (b)), as the lateral load increased, the shear strains of steel U-sections increased, particularly at the ends of the diagonal strut (refer to **Fig. 3-27**). This result indicates that the steel U-sections provided shear resistance and their shear contribution was concentrated at the ends of the diagonal strut. Similar strain pattern was also seen in **CS2SB** and **CS2TH**. However, in **CS2SB** (**Fig. 4-22**(c)), the shear strains were relatively large, particularly at the locations between the steel plate beams. This result indicates that, due to the absence of horizontal reinforcing bars, the shear contribution of steel U-sections increased between the steel plate beams. On the other hand, in **CS2TH** with the smaller spacing of steel plate beams (**Fig. 4-22**(d)), shear strains of steel U-sections decreased, due to the increased shear contribution of steel plate beams. Similarly in **CS2SF** (**Fig. 4-22**(e)), the shear strains of steel U-sections were relatively small due to the high contribution of steel faceplates. However, as the lateral load increased, the shear strains of the faceplate rapidly increased. Ultimately, at the peak strength V_{test}, the shear strains measured at the center of the faceplate section reached the shear yield strain. For all 2.0-aspect ratio specimens, the shear strains of steel U-sections did not reach the shear yield strain.

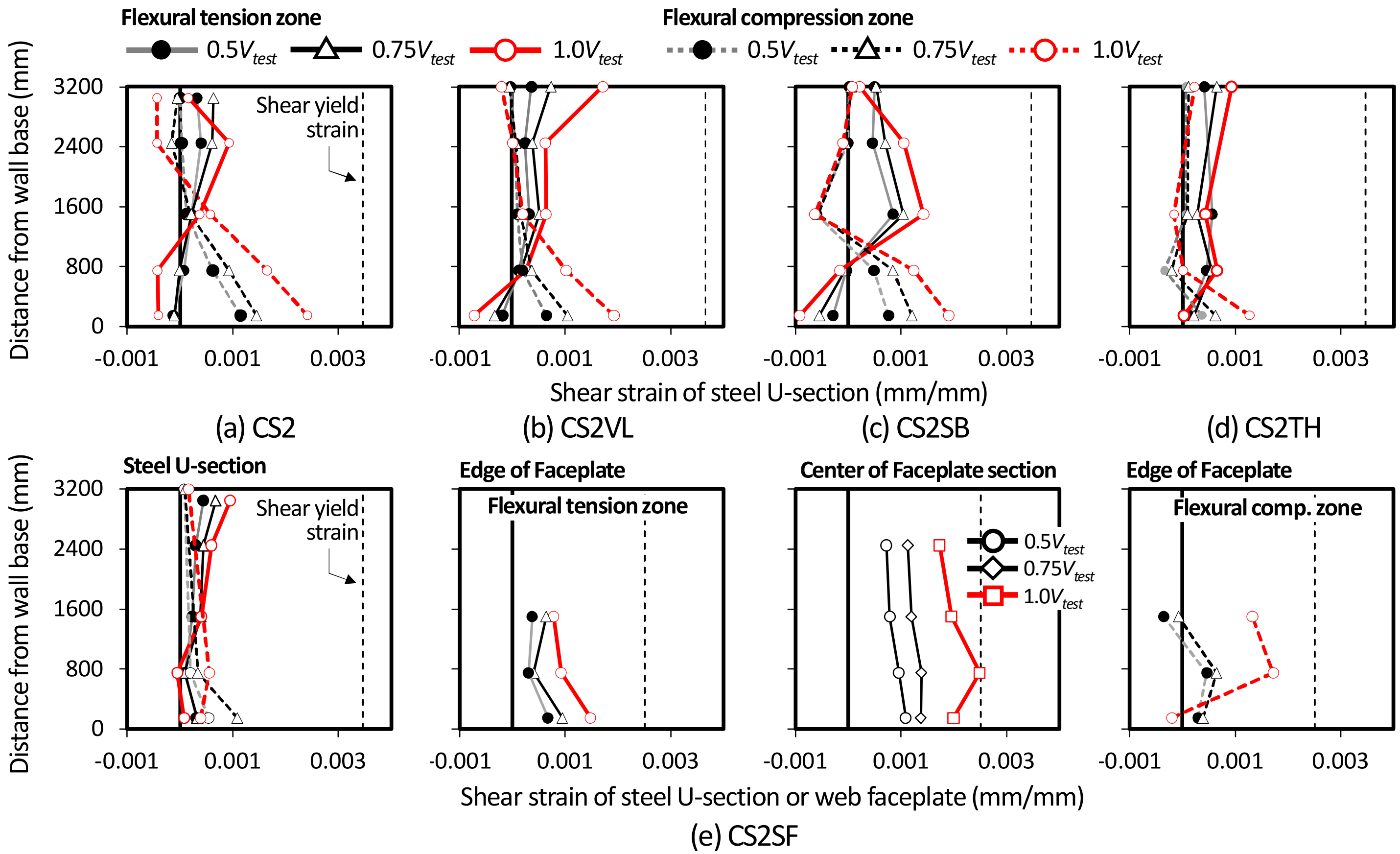

Fig. 4-22 Shear strains of steel plates measured in shear failure-mode specimens with aspect ratio of 2.0.

Similar results were also seen in the specimens with aspect ratio of 1.0. In **CS1** and **CS1VL** (**Figs. 4-23**(a) and (b)), the increase of shear strain was pronounced at the upper part of the flexural tension zone and the lower part of the flexural compression zone (i.e., at the two ends of the diagonal strut). On the other hand, in **CS1SF** with steel faceplates (**Fig. 4-23**(c)), the shear strains were relatively uniform along the wall height. **Fig. 4-23**(d) shows the shear strains of the steel faceplate measured in **CS1VL**. Until shear yielding (at V_y) of the wall, the shear strains measured at the center (denoted as M) of the faceplate were greater than those at the edges (denoted as L and R). After V_y, the shear strains at the flexural tension zone (L and M) significantly increased beyond the shear yield strain.

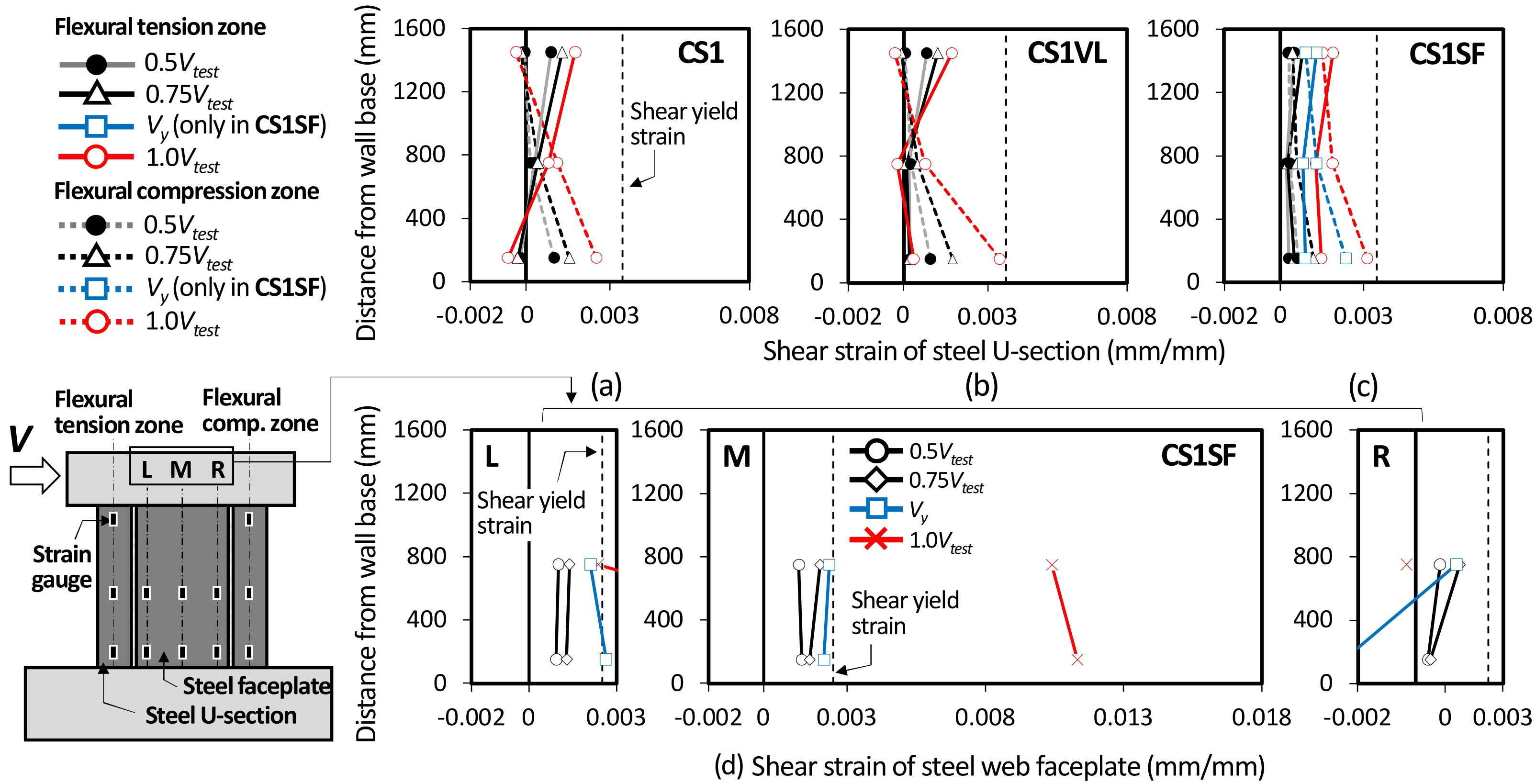

Fig. 4-23 Shear strains of steel plates measured in shear failure-mode specimens with aspect ratio of 1.0.

4.3.7 Shear strength contributions

For shear failure-mode specimens, the shear strength contributions of the horizontal reinforcements (reinforcing bars and steel plate beams), V_s, boundary steel U-sections V_b, and steel web faceplates V_w were estimated based on the steel strains. In the 2.5-aspect ratio specimens, the steel strains measured in the lower part of walls were used, while in the specimens with lower aspect ratios of 2.0 and 1.0, the steel strains measured at the mid height were used. V_s, V_b, and V_w were calculated as follows:

$$V_s = \rho_h f_{sh} t_w l_e \cot \theta_c \tag{4-3}$$

$$V_b = (\tau_{b,t} + \tau_{b,c}) A_{b,w} \tag{4-4}$$

$$V_w = \tau_w A_w \tag{4-5}$$

where, f_{sh} = average tensile stress of horizontal reinforcements, calculated assuming elastic-perfectly plastic behavior (= $E_s\varepsilon_{sh} \leq f_y$, ε_{sh} = tensile strain measured at the center of horizontal reinforcing bars or steel plate beams); l_e = effective shear depth (= $0.8l_w$, Eurocode 8, 2004); θ_c = average inclination angle of diagonal cracks at the measuring location (33.5° – 38.9° for 2.5-aspect ratio specimens; 31.5° – 36° for 2.0-aspect ratio specimens; and 45° for 1.0-aspect ratio specimens); $\tau_{b,t}$ and $\tau_{b,c}$ = average shear stresses of web plates of the two steel U-sections located at the ends of diagonal cracks (see points A and B in **Fig. 4-24** and **Fig. 4-25**); $A_{b,w}$ = total sectional area of two web plates in a steel U-section; τ_w = average shear stress of steel web faceplate; and A_w = total sectional area of two steel faceplates in the web. In the present study, V_b and V_w were calculated until plastic strains occurred in the steel sections (δ = 1.5%). Thus, $\tau_{b,t}$ (or $\tau_{b,c}$) of steel U-sections was regarded as 80% of the shear stress τ_{cen} (= $G_s\gamma_{xz} \leq 0.6F_y$, see) measured at the center of the web plate section, considering the elastic shear flow in a thin U-section plate (**Fig. 4-24**). Similarly in faceplates with rectangular section, τ_w was estimated as 66% of τ_{cen} calculated using the strain measured at the center of the faceplate section. The concrete contribution V_c of the flexural compression zone (see **Fig. 4-25**, Choi et al. 2016) was calculated by extracting V_s, V_b, and V_w from the lateral load V. In the mid height of **CS2SB**, due to the relatively large spacing s_h of steel plate beams, only two plate beams located at mid height were intersected with diagonal cracks (see **Fig. 4-10**(d)). Thus, for **CS1**, $l_e\cot\theta_c$ in Eq. (4-3) (i.e., height of cracked shear panel, see **Fig. 4-25**) was replaced by s_h ($< l_e\cot\theta_c$), to avoid the overestimation of V_s. **Table 4-3** shows the calculated shear strength contributions of the test specimens.

Fig. 4-24 compares V_s, V_b, and V_c with the overall lateral load V for the specimens with aspect ratio of 2.5. In RC specimen **RS2.5** (**Fig. 4-24**(a)), V_s began to increase after initial diagonal cracking (at δ = 0.25 %). After δ = 0.9%, V_s no longer increased as yielding of the horizontal reinforcing bars was propagated along the wall height. At the peak strength V_{test} (= 2,115 kN), V_s was estimated to be 48% of V_{test} (V_c / V_{test} = 0.52). The main cause of strength degradation was the decrease in V_c.

In composite specimens **CS2.5** and **CS2.5VH** (**Figs. 4-24**(b) and (c)), as the lateral drift ratio increased, V_b gradually increased. On the other hand, as V_b increased, the contribution of V_s was less than that of **RS2.5**, despite yielding of the horizontal rebars. For this reason, the overall lateral stiffness of **CS2.5** (69.1 kN/mm) was similar to that of **RS2.5** (68.1 kN/mm). In **CS2.5** (**Fig. 4-24**(b)), at V_{test} (= 2,395 kN), the ratios of V_b / V_{test} and V_s / V_{test} were 0.31 and 0.35, respectively. In **CS2.5VH** with greater area of steel U-sections (**Fig. 4-24**(c)), at V_{test} (= 2,730 kN), V_b / V_{test} increased to 0.39, while V_s / V_{test} decreased to 0.27. This is because, due to the larger cross section of steel plates, the shear contribution of the steel U-sections increased, while the shear contribution of the horizontal reinforcing bars decreased.

In **CS2.5M** (**Fig. 4-24**(d)), at V_{test} (= 2,702 kN), V_b / V_{test} (= 0.30) was less than that of **CS2.5VH**. On the other hand, V_s / V_{test} increased to 0.47, due to the greater horizontal reinforcement ratio. The concrete contribution V_c / V_{test} (= 0.23) was less than those of **CS2.5VH** and **CS2.5M** (V_c / V_{test} = 0.33), due to the smaller wall thickness.

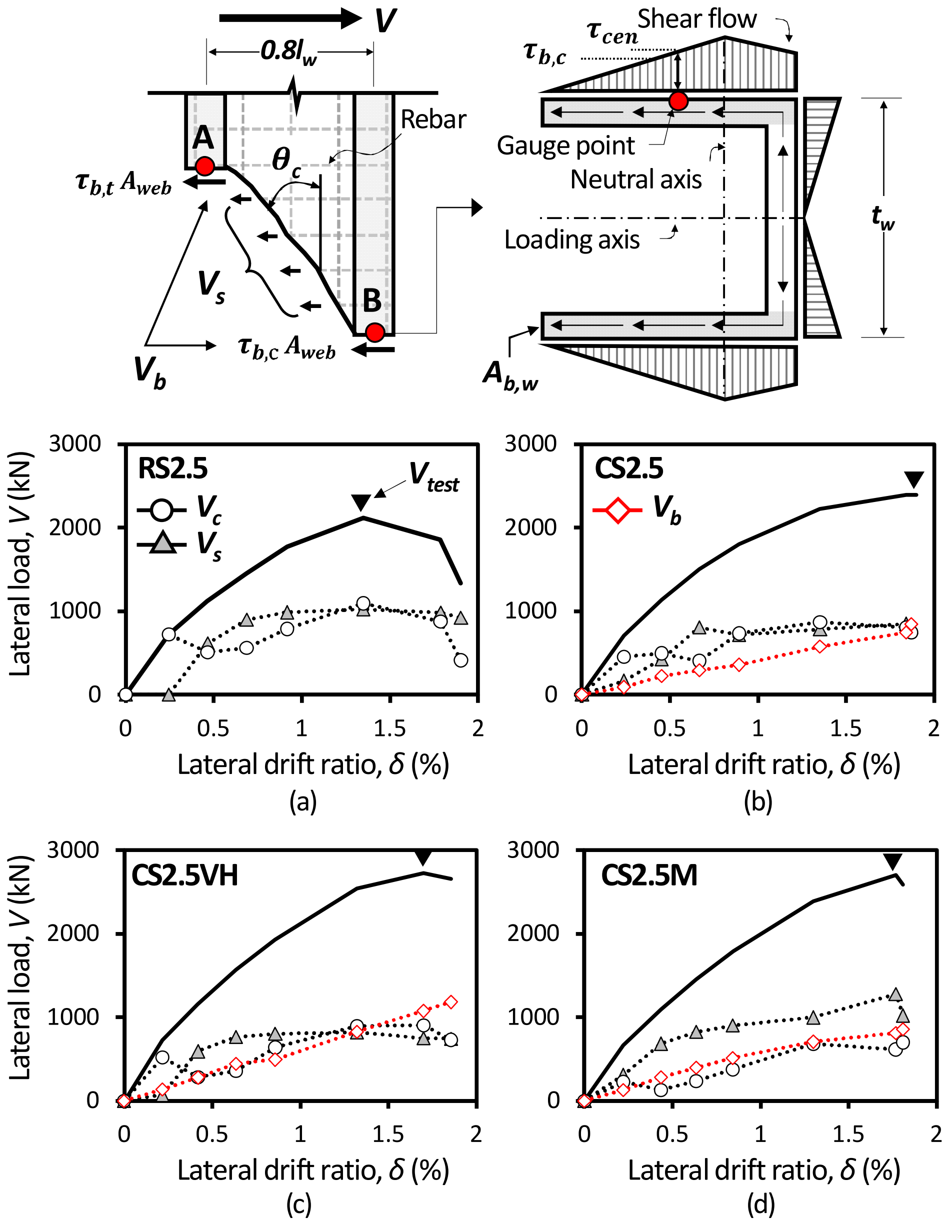

Fig. 4-24 Contributions to shear strength measured in shear failure-mode specimens with aspect ratio of 2.5.

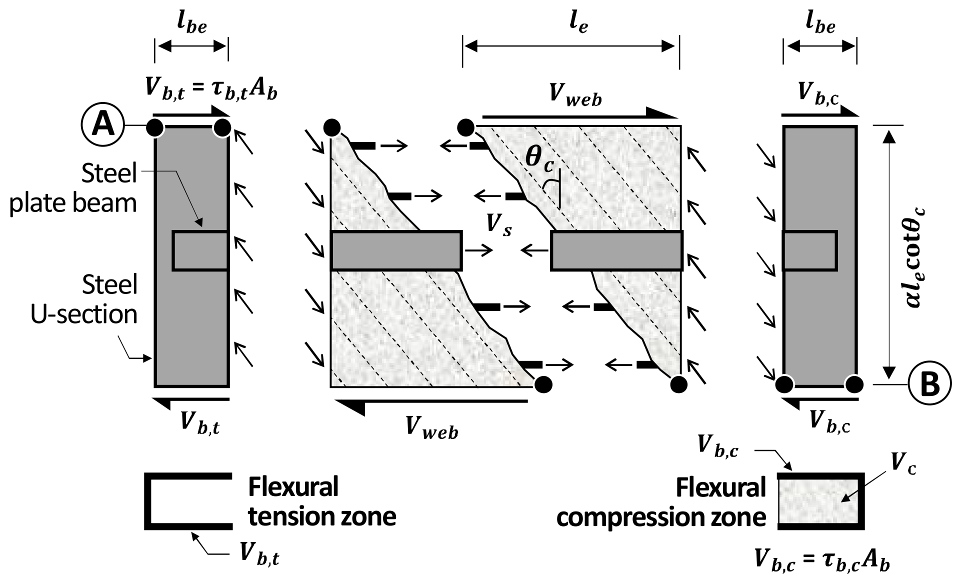

Fig. 4-25 Shear strength contributions of concrete and steel reinforcements.

Similar results were shown in the specimens with aspect ratio of 2.0 (**Fig. 4-26**). In RC specimen **RS2** (**Fig. 4-26**(a)), V_s gradually increased until the tensile yielding of horizontal rebars (almost at δ = 0.5%), and, at the rebar yielding, V_s / V reached its maximum (= 80%). Then, V_s was maintained without increase, though V continued to increase. Thus, at V_{test}, V_s / V_{test} (V_s = 869 kN) decreased to 61% ($V_c = 0.39V_{test}$ = 549 kN). Similar trend was also seen in V_s of the composite specimens.

However, in **CS2** and **CS2VL** (**Figs. 4-26**(b) and (c)), V_s was less than that of **RS2**, as the contribution V_b of steel U-sections gradually increased until V_{test}. At V_{test}, V_b of **CS2** (= 779 kN, V_b / V_{test} = 41%) was 13% greater that of **CS2VL** (= 689 kN, V_b / V_{test} = 44%), while V_s was similar (V_s = 629 kN, V_s / V_{test} = 33% for **CS2**; V_s = 587 kN, V_s / V_{test} = 37% for **CS2VL**). This result confirms that the shear strength of **CS2** increased due to the greater area of steel U-sections. Based on the V_s and V_b, the concrete contribution V_c (= 510 kN for **CS2**, 300 kN for **CS2VL**) was estimated as $0.27V_{test}$ for **CS2**; and $0.19V_{test}$ **CS2VL**

In **CS2SB** with steel plate beams (**Fig. 4-26**(d)), At V_{test}, the shear strength contribution of steel U-sections was slightly greater than that of **CS2** with conventional shear rebars, showing V_b = 823 kN (V_b / V_{test} = 40%). However, V_s (= 575 kN, V_s / V_{test} = 28%) decreased due to the large spacing of plate beams. The concrete contribution was V_c = 654 kN (V_c / V_{test} = 32%). On the other hand, in **CS2TH** with the smaller s_h (**Fig. 4-26**(e)), V_b decreased, while V_s and V_c increased. Thus, at flexural yielding ($V_y = 0.96V_{test}$), V_b (= 668 kN), V_s (= 1,149 kN), and V_c (= 382 kN) were estimated as 30%, 52%, and 17% of V_y, respectively. This result indicates that, as the spacing of plate beams increased, the shear contribution of steel U-sections increased due to the diagonal strut action. On the other hand, in the case of smaller spacing of plate beams, the shear contribution of steel U-sections was similar to that of **CS2** and **CS2VL** with conventional shear reinforcement.

In **CS2SF** (**Fig. 4-26**(f)), V_b further decreased, even though the contribution V_w of steel faceplates was less than V_s of steel plate beams in **CS2TH**. This is because as the faceplates confined the web concrete, V_c significantly increased. Thus, at V_{test}, V_b (= 634 kN), V_w (= 703 kN), and V_c (= 1,202 kN) were estimated as 25%, 28%, and 47% of V_{test}, respectively.

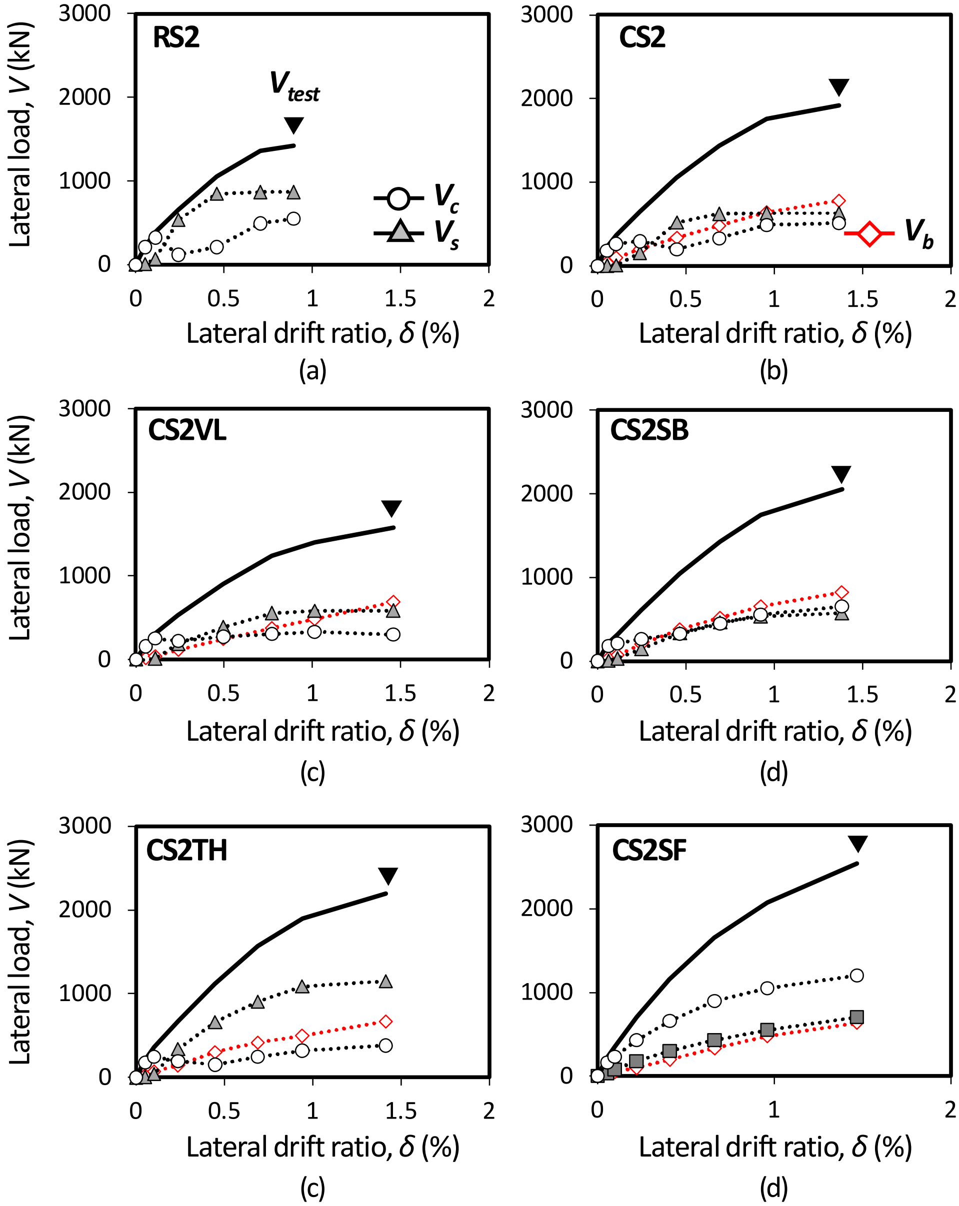

Fig. 4-26 Contributions to shear strength measured in shear failure-mode specimens with aspect ratio of 2.0.

In squat walls with aspect ratios less than 1.0, many existing studies revealed that the shear strength provided by vertical reinforcement (including boundary and web reinforcements) is significant (Wood 1990, Hwang et al. 2001, Gulec and Whittaker 2011, and ASCE 43, 2019). Thus, in the present test specimens with aspect ratio of 1.0, the shear strength contribution V_v of vertical web reinforcement was additionally considered, using truss analogy as shown in **Fig. 4-27**.

$$V_v = 2\rho_v f_{sv} l_{web} t_w \cot\theta_v \tag{4-6}$$

where, f_{sv} = average stress of vertical web reinforcement, calculated assuming elastic-perfectly plastic behavior; l_{web} = depth of web concrete (= $l_w - 2l_{be}$); and $\cot\theta_v = 0.5l_e / l_s$.

In RC specimen **RS1** (**Fig. 4-27**(a)), after diagonal cracking (at $\delta \approx 0.1\%$), V_s and V_v from web reinforcements began to increase until tensile yielding of horizontal rebars (at $\delta \approx 0.4\%$). At the horizontal rebar yielding, V_s / V (= 0.34) and V_v / V (= 0.10) reached their maximum, respectively. However, V_v / V was relatively small, despite the low aspect ratio. Thereafter, V_s and V_v values were maintained or slightly decreased, while V_c / V increased until the peak strength V_{test}. At V_{test}, the contribution ratios of V_c (= 1,308 kN), V_s (= 550 kN), and V_v (= 116 kN) were 66%, 28%, and 6% of V_{test}, respectively; V_c contributed to the shear strength the most.

In composite specimens **CS1** and **CS1VL** (**Fig. 4-27**(b) and (c)), V_c, V_s, and V_v showed the similar trends, but their contribution ratios were less than those of **RS1**, due to the boundary steel U-sections: as the drift ratio increased, V_b gradually increased. Further, at V_{test}, V_b showed the greatest contribution ratio (V_b / V_{test} = 45% for **CS1**; V_b / V_{test} = 40% for **CS1VL**), followed by V_c, V_s, and V_v (= 42%, 11%, and 3% of V_{test} for **CS1**; 48%, 8%, and 4% of V_{test} for **CS1VL**, respectively). In **CS1**, the contribution ratio of V_b (= 1,345 kN) was slightly greater than that of **CS1VL** (V_b = 1,005 kN) with the smaller steel U-sections.

In **CS1SF** with steel faceplates (**Fig. 4-27**(d)), the contribution of steel U-sections (V_b) and faceplates (V_w) gradually increased under lateral loading, and their contribution ratios were almost constant until V_{test}. In particular, V_c (= 1,860 kN) was greater than those of **CS1** (V_c = 1,263 kN) and **CS1VL** (V_c = 1,201 kN), as the web concrete was laterally confined by steel faceplates. At V_{test}, the contribution ratios of V_d, V_w, and V_b were 53, 24, and 23% of V_{test}, respectively.

In the walls with aspect ratio of 1.0, the contribution V_s of horizontal reinforcement significantly reduced, while the contribution V_c of concrete increased. This is because the majority of shear was directly transferred by diagonal struts, rather than horizontal reinforcement by truss action. The contribution ratios V_b / V_{test} of steel U-sections were close to, or slightly greater, than those of the walls with greater aspect ratios.

Note that the shear strength contributions of each structural components were calculated based on the free-body diagram defined with respect to the inclined crack plane (see **Fig. 4-24** and **Fig. 4-25**). This was intended to assess the contribution of shear reinforcement crossing the diagonal cracks. For this reason, the concrete contribution was inevitably limited to the flexural compression zone, because the shear contribution in the diagonal cracked plane is negligible.

When the free-body diagram is defined with respect to the wall cross section, the contributions of each structural components may be significantly different from those by the free-body diagram previously defined. This is because the contribution of steel U-sections is highly variable depending on the wall height (see **Fig. 4-22** and **Fig. 4-23**). Further, the contribution of horizontal reinforcement cannot be evaluated at all. The shear strength model discussed in Chapter 6 evaluates the shear strength contributions with respect to the cross section of walls, to identify the shear strength contribution of steel U-section on the web crushing strength.

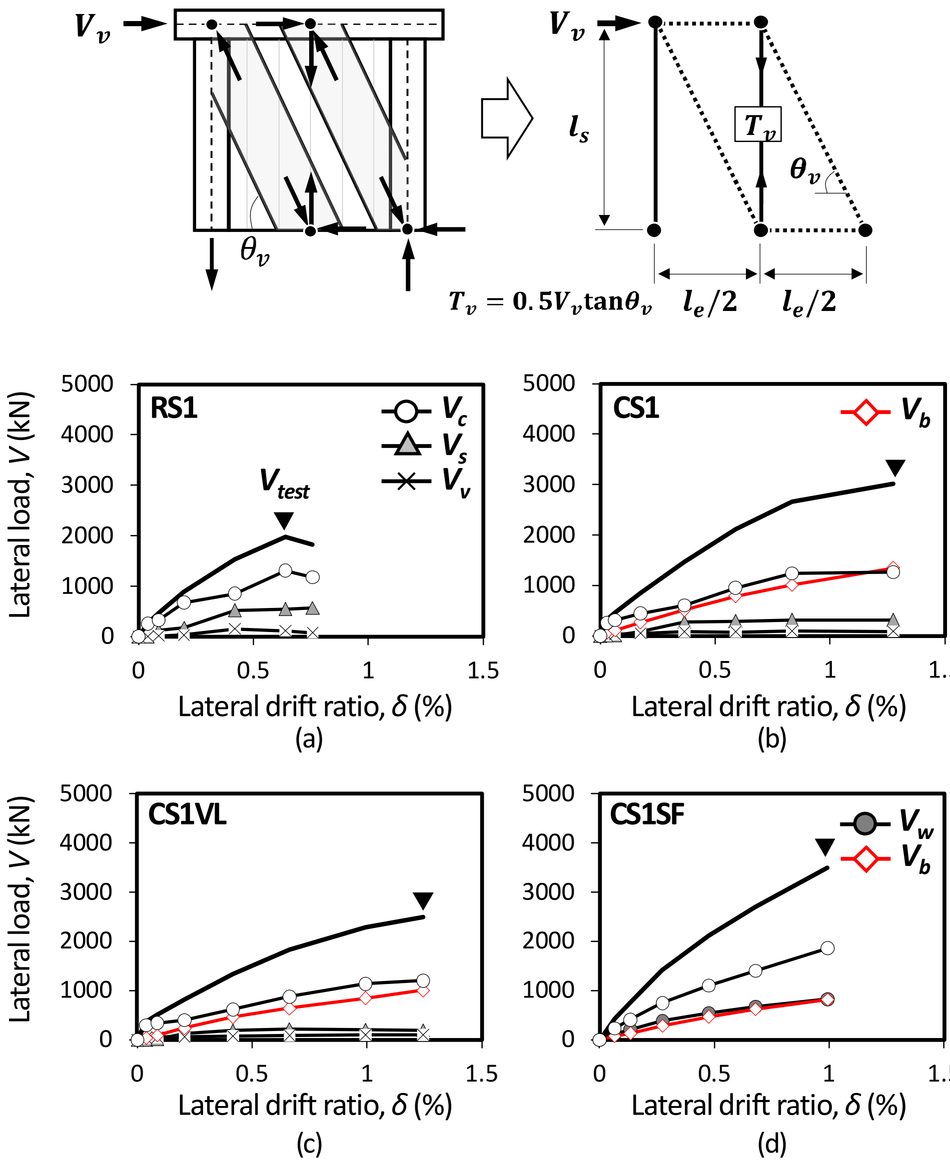

Fig. 4-27 Contributions to shear strength measured in shear failure-mode specimens with aspect ratio of 1.0.

4.4 Effect of Design Parameters

For verification of shear performance, the following design parameters were considered to investigate their effects on the shear strength of the specimens: (1) The type of boundary reinforcement (*reinforcing bar or steel U-section*); (2) The sectional area of steel U-section: web plate length (*300 mm or 450 mm*) or web plate thickness (*9 mm or (12–16) mm*); (3) The type of web reinforcement (*horizontal reinforcing bar or steel plate beam or vertical steel faceplate,* only tested in specimens with aspect ratios of 2.0 and 1.0); and (4) The spacing of web reinforcement (*300 mm or 200 mm for rebars*; *1000 mm or 600 mm for steel plate beams*). The effect of the test parameters was evaluated for the walls with aspect ratios of 2.5, 2,0, and 1.0.

4.4.1 Type of boundary reinforcement

Fig. 4-28 compares the envelope curves of the tested V–δ relationships, according to the design parameter (1). In the comparison of **RS2.5** and **CS2.5** (with the same nominal shear strength) (**Fig. 4-28**(a)), the use of boundary steel section of U-300×300×16×16 (ρ_{be} = 15.9%, F_y = 596 MPa) increased the shear strength V_{test} by 13%. When the aspect ratio decreased, the effect of steel U-sections was more pronounced: In the comparison of **RS2** and **CS2** (**Fig. 4-28**(b)), the use of boundary steel section of U-200×320×12×16 (ρ_{be} = 16.4%, F_y = 444 MPa for web plate and 448 MPa for flange plate) increased the peak strength V_{test} by 35%, even though the average yield strength of the steel U-sections (444–448 MPa) was 26%–33% less than that of boundary reinforcing bars (670 MPa for D41, 602 MPa for D38); and in the comparison of **RS1** and **CS1** with the lower aspect ratio (**Fig. 4-28**(c)), by using the same steel section, the shear strength was increased by 54%. These results indicate that, as the aspect ratio decreased, the shear strength contribution of boundary steel U-sections increased.

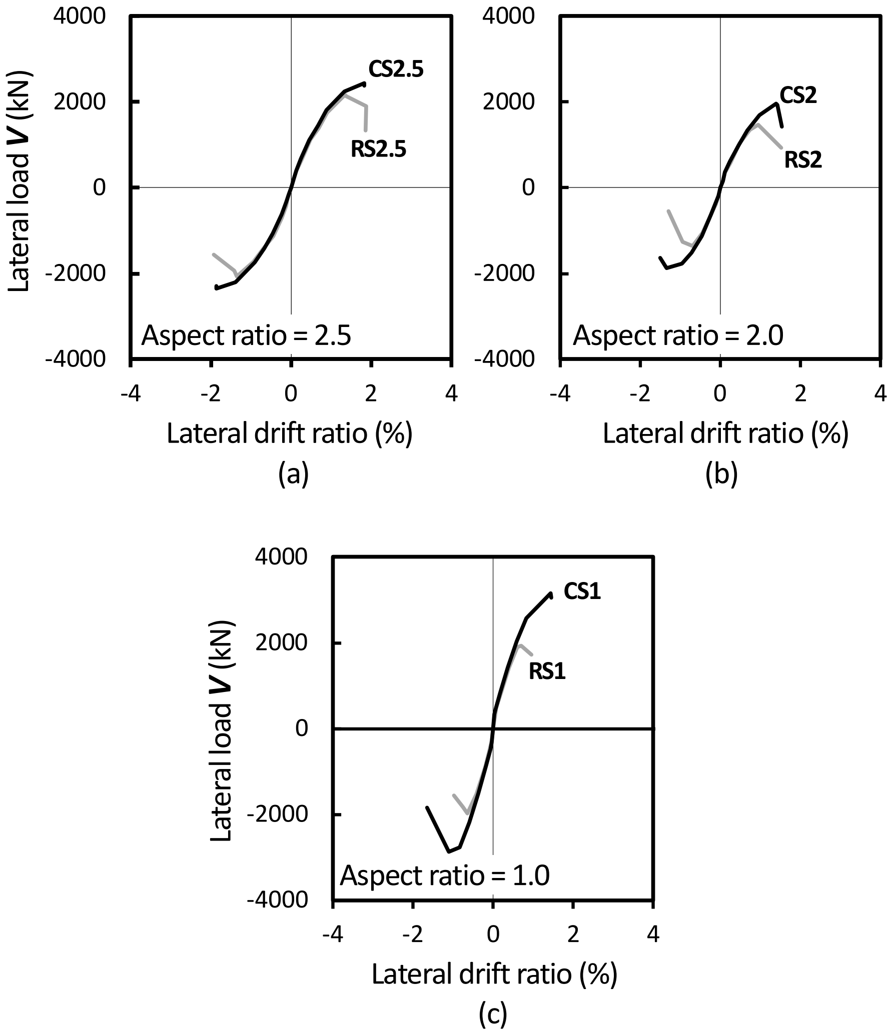

Fig. 4-28 Comparison of envelope curves according to the type of boundary reinforcement.

4.4.2 Sectional area of steel U-sections

Fig. 4-29 compares the envelope curves of the tested V–δ relationships, according to the design parameter (2). In the comparison of **CS2.5** and **CS2.5VH** (with identical horizontal web reinforcement, ρ_h = 0.44%) (**Fig. 4-29**(a)), the use of greater web length of U-300×450×16×16 (ρ_{be} = 14.1 %, F_y = 596 MPa) (34% greater area) increased V_{test} by 14%. Note that the increase in shear strength may be underestimated because the tested strength of **CS2** was limited by the loading capacity of the actuator. When compared to **RS2.5**, V_{test} was 29 % greater. When the aspect ratio decreased, the effect of boundary steel section area was more pronounced: In the comparison of **CS2** and **CS2VL** (ρ_h = 0.51%) (**Fig. 4-29**(b)), the use of thicker steel U-sections (42% greater area) increased V_{test} by 22%. Further, V_{test} of **CS2VL** was 11% greater than that of **RS2**, despite 30% smaller area and 28% less yield strength of boundary reinforcements (**Fig. 4-29**(c)). In the comparison of **CS1** and **CS1VL** with the lower aspect ratio (ρ_h = 0.24%) (**Fig. 4-29**(c)), by using the steel sections with greater area, the shear strength was increased by 27%. Further, V_{test} of **CS1VL** was 22% greater than that of **RS1** (ρ_h = 0.51%), despite the smaller area of boundary reinforcement and less horizontal reinforcement ratio.

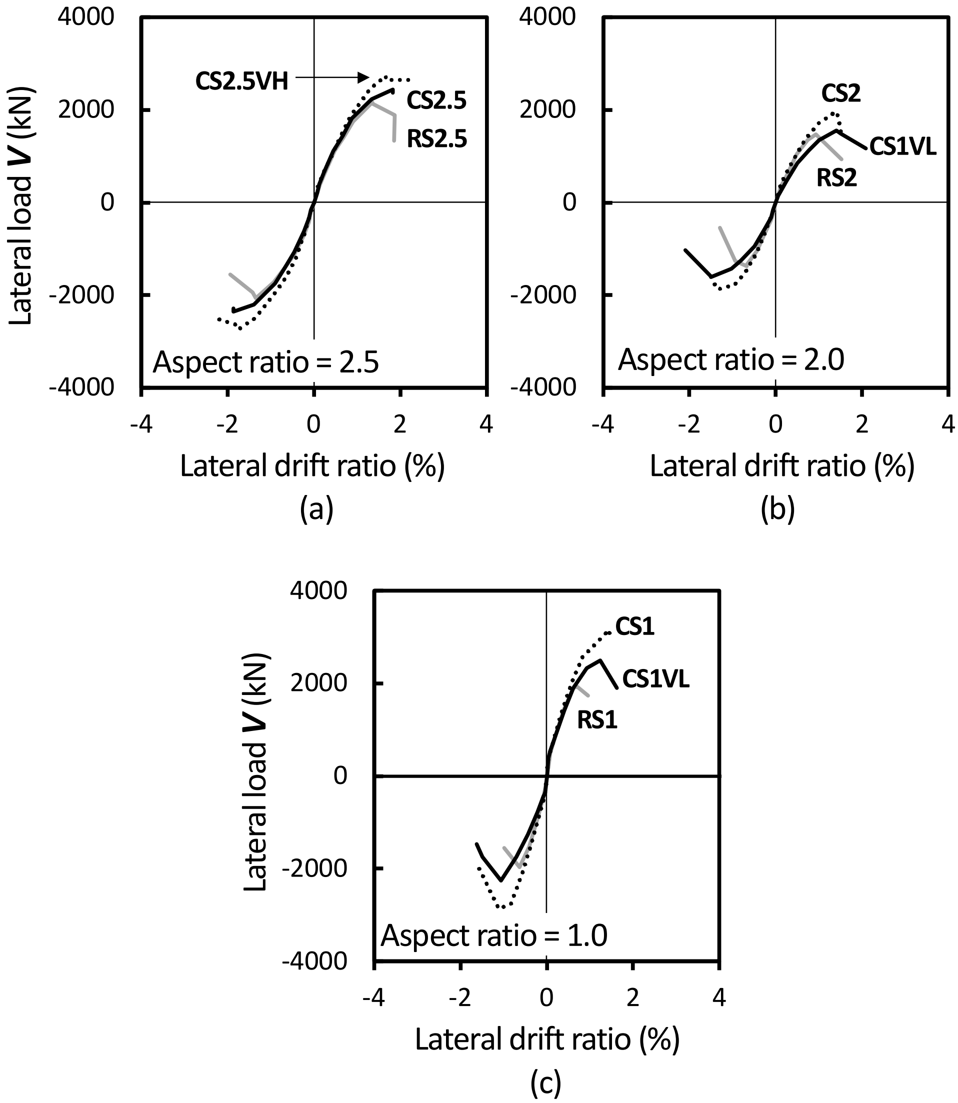

Fig. 4-29 Comparison of envelope curves according to the sectional area of boundary steel U-sections.

4.4.3 Type of web reinforcement

Fig. 4-30 compares the envelope curves of the tested V–δ relationships, according to the design parameter (3). In the comparison of **CS2** and **CS2SB** (with identical steel U-sections) (**Fig. 4-30**(a)), V_{test} of **CS2SB** with steel plate beams was similar to that of **CS2** with horizontal reinforcing bars, despite the greater spacing of plate beams. This result indicates that the steel plate provided adequate shear resistance. Furthermore, the use of steel plate beams (ρ_h = 0.63%) alleviated brittle shear failure mode, due to the less diagonal cracking and spalling of web concrete. In the comparison of **CS2** and **CS2SF** (with identical steel U-sections) (**Fig. 4-30**(a)), the use of steel web faceplates (ρ_h = 4.0%) increased V_{test} by 33%, though the faceplates and steel U-sections were not connected. When the aspect ratio decreased to 1.0, the increase in shear strength was 21% (see the comparison between **CS1** and **CS2SF**, **Fig. 4-30**(b)). These results indicate that the use of steel web faceplates was effective in increasing the shear strength.

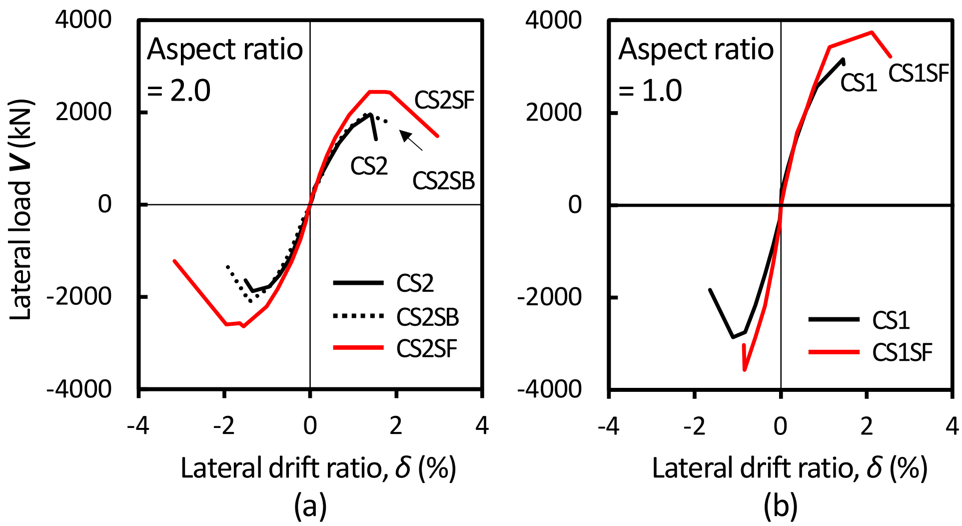

Fig. 4-30 Comparison of envelope curves according to the type of web reinforcement.

4.4.4 Spacing of web reinforcement

Fig. 4-31 compares the envelope curves of the tested *V*–*δ* relationships, according to the design parameter (4). In **CS2.5M**, by using smaller spacing of horizontal rebars, the horizontal reinforcement ratio was increased to ρ_h = 0.99%, which is the maximum ratio of ACI 318 (2019). As a result, V_{test} of **CS2.5M** was close to that of **CS2.5VH** (with similar area of steel U-sections), despite 33% smaller wall thickness (t_w = 300 mm for **CS2.5VH**; 200 mm for **CS2.5M**) (**Fig. 4-31**(a)). Note that the tested strength of **CS2.5VH** was limited by the loading capcity of the actuator. Thus, V_{test} of **CS2.5VH** may be greater than that of **CS2.5M**.

Similarly in **CS2TH** with smaller spacing of steel plate beams (ρ_h = 1.05%), V_{test} of **CS2TH** was limited by flexural yielding before shear failure. Nevertheless, V_{test} of **CS2TH** was 10% greater than that of **CS2SB** (ρ_h = 0.63%) (**Fig. 4-31**(b)). Due to the flexural yielding, **CS2TH** showed greater inelastic deformation.

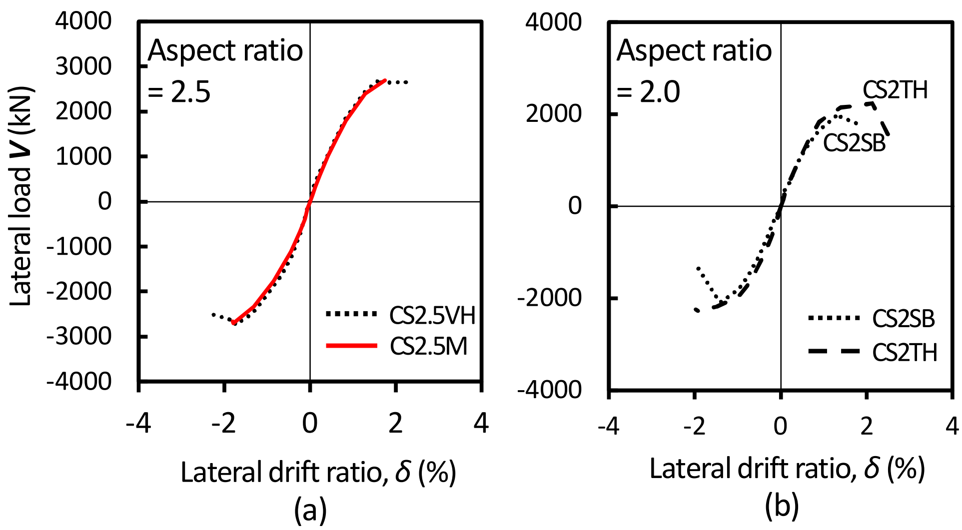

Fig. 4-31 Comparison of envelope curves according to the horizontal reinforcement ratio.

4.4.5 Effect of wall aspect ratio

In the tests, the aspect ratio of walls highly influenced the shear strength of walls: as the aspect ratio decreased, the shear strength of wall increased. This can be explained as follows:

1) The wall shear was resisted primarily by the diagonal struts, some of which was directly transferred to the flexural compression zone confined by the steel U-sections (the remaining wall shear was resisted by the truss action of horizontal shear reinforcement). Such shear transfer mechanism was pronounced in the specimens with the lower aspect ratio.

2) The shear contribution of the steel U-sections increased due to their shorter lengths (lateral stiffness of the steel U-section is inversely proportional to the plate length).

3) Due to the decreased flexural moment, the flexural strains and relevant deformation decreased, which alleviated the shear strength degradation.

4.5 Strength Predictions of Existing Design Methods

4.5.1 Diagonal tension strength

In the present study, to investigate the contribution of steel U-sections to the shear strength, the nominal shear strengths (i.e., diagonal tension strength) $V_{n,ACI}$, $V_{n,Euro}$, $V_{n,fib}$ of the test specimens were predicted according to existing RC design methods: ACI 318 (2019), Eurocode 2 (2004), and fib MC (2010). In ACI 318, the shear strength of a wall is provided by concrete and shear reinforcement, assuming a 45° truss mechanism. Eurocode 2 considers shear reinforcement only, assuming variable angle θ_c of diagonal compression field (22 $\leq \theta_c \leq$ 45)°. In the present study, 22° was used to maximize the nominal shear strength. In fib MC, the shear strength equation is the same as that of Eurocode 2, but the minimum of θ_c is 30° (see Section 2.1). The contribution of steel U-sections was not considered in the calculation of nominal shear strength. The contributions of steel plate beams and steel faceplates were calculated assuming uniformly distributed horizontal reinforcement with the same steel area.

Table 4-5 and **Fig. 4-32** compare the nominal shear strengths $V_{n,ACI}$, $V_{n,Euro}$, and $V_{n,fib}$ with the tested strengths V_{test}. The figure also shows the shear strength ratios (V_{test} / V_n) according to the aspect ratio of walls. For all specimens, the tested strengths V_{test} were greater than the predictions, particularly in the composite specimens with boundary steel U-sections. Further, in the composite specimens, the over-strength ratios increased as the aspect ratio decreased. These results indicate that the steel U-sections provided the shear resistance, and their shear contributions increased with an decrease of the aspect ratio.

In shear-failure mode RC specimens, the shear strength ratios were V_{test} / $V_{n,ACI}$ = 1.19 – 1.49 for ACI 318, V_{test} / $V_{n,Euro}$ = 0.97 – 1.34 for Eurocode 2; and 1.4 – 1.93 for fib MC. In the case of the composite specimens, the shear strength ratios increased to V_{test} / $V_{n,ACI}$ = 1.34 – 3.08 for ACI 318, V_{test} / $V_{n,Euro}$ = 0.93 – 3.83 for Eurocode 2; and 1.05 – 5.53 for fib MC. Generally, as the aspect ratio decreased, the over-strength ratio increased significantly (**Fig. 4-32**). In the specimens except for **CS2.5M**, **CS2TH**, **CS2SF**, and **CS1SF**, the nominal shear strengths were determined by diagonal tension failure, because the horizontal reinforcement ratio ρ_h (= 0.24% – 0.63%) was less than the maximum reinforcement ratio $\rho_{h,max}$ (= 0.59% – 1.15% for ACI 318; 0.68% – 1.12% for Eurocode 2; and 1.17% – 1.94% for fib MC) corresponding to web crushing failure. However, the actual failure mode of the test specimens was crushing of web concrete, without diagonal tension failure. This is because the steel U-sections restrained diagonal cracking and resisted shear transferred from the diagonal strut until web crushing. Among the design codes, the prediction of Eurocode 2 was relatively close to the test result. However, this agreement was attributed to the use of the minimum strut angle of 22° (the actual crack angle (> 30°) was greater than 22°), not to the actual shear contribution of horizontal reinforcement (i.e., the contribution of horizontal reinforcement was overestimated). In Eurocode 8, which provides the provisions for seismic design, the strut angle is defined 45°, which further underestimates the shear strength of the proposed composite wall specimens.

4.5.2 Web crushing strength

Table 4-5 and **Fig. 4-33** compare the tested strengths V_{test} with the maximum shear strength $V_{n,max}$ (i.e., web crushing strength) predicted by the existing RC design methods (see Section 2.1). In **CS2.5** and **CS2.5VH** with aspect ratio of 2.5, the tested strengths V_{test} were less than the maximum shear strengths $V_{n,max}$ of ACI 318, though web crushing failure occurred. This is because the actual web crushing strength was degraded due to yielding of shear reinforcement: the shear strength of the specimens was determined by the diagonal tension cracking, though the ultimate failure mode was web crushing. Nevertheless, when the aspect ratio decreased to 2.0 and 1.0, the test strengths were greater than $V_{n,max}$ of ACI 318, even though the horizontal reinforcement ratio ρ_h was less than the maximum ratio $\rho_{h,max}$. This result indicates that ACI 318 significantly underestimated the web crushing strength of the composite specimens. Generally, except for the specimens with aspect ratio of 1.0, V_{test} was less than $V_{n,max}$ of Eurocode 2 and Fib MC.

Table 4-5 Comparison with strength predictions of existing RC design methods

Specimens	Aspect Ratio	Flexural strength prediction	Shear strength prediction											
			ACI 318				fib MC				Eurocode 2			
		V_f [kN]	V_n [kN]	V_{test} $/V_n$	$V_{n,max}$ [kN]	V_{testr} $/V_{n,max}$	V_n [kN]	V_{test} $/V_n$	$V_{n,max}$ [kN]	V_{testr} $/V_{n,max}$	V_n [kN]	V_{test} $/V_n$	$V_{n,max}$ [kN]	V_{testr} $/V_{n,max}$
RS2.5	2.5	3063	1,782	1.19	2,887	0.73	1,487	1.42	5,397	0.39	2,147	0.99	4,354	0.49
CS2.5	2.5	2950	1,782	1.34	2,887	0.83	1,487	1.61	5,397	0.44	2,147	1.12	4,354	0.55
CS2.5VH	2.5	3643	1,782	1.53	2,887	0.95	1,487	1.84	5,397	0.51	2,147	1.27	4,354	0.63
CS2.5M	2.5	3222	1,924	1.40	1,924	1.40	2,231	1.21	3,598	0.75	2,902	0.93	2,902	0.93
RS2	2	2568	1,120	1.27	1,592	0.89	1,012	1.40	2,907	0.49	1,461	0.97	2,338	0.61
CS2	2	1961	1,117	1.72	1,581	1.21	1,012	1.89	2,879	0.67	1,461	1.31	2,314	0.83
CS2VL	2	1468	1,089	1.45	1,469	1.07	1,012	1.56	2,610	0.60	1,461	1.08	2,075	0.76
CS2SB	2	1898	1,295	1.58	1,502	1.37	1,290	1.59	2,690	0.76	1,862	1.10	2,148	0.96
CS2TH	2	1902	1,592	1.42	1,592	1.42	2,150	1.05	2,907	0.78	2,338	0.97	2,338	0.97
CS2SF	2	2257	1,581	1.61	1,581	1.61	2,879	0.88	2,879	0.88	2,314	1.10	2,314	1.10
RS1	1	4785	1,313	1.49	1,576	1.24	1,012	1.93	2,868	0.68	1,461	1.34	2,305	0.85
CS1R	1	3585	980	3.08	1,576	1.91	545	5.53	2,868	1.05	787	3.83	2,305	1.31
CS1VL	1	2704	972	2.44	1,555	1.53	545	4.35	2,815	0.84	787	3.02	2,259	1.05
CS1SF	1	4212	1,589	2.30	1,589	2.30	2,900	1.26	2,900	1.26	2,332	1.57	2,332	1.57
Mean for SUB-C				1.77		1.42		2.07		0.78		1.57		0.97

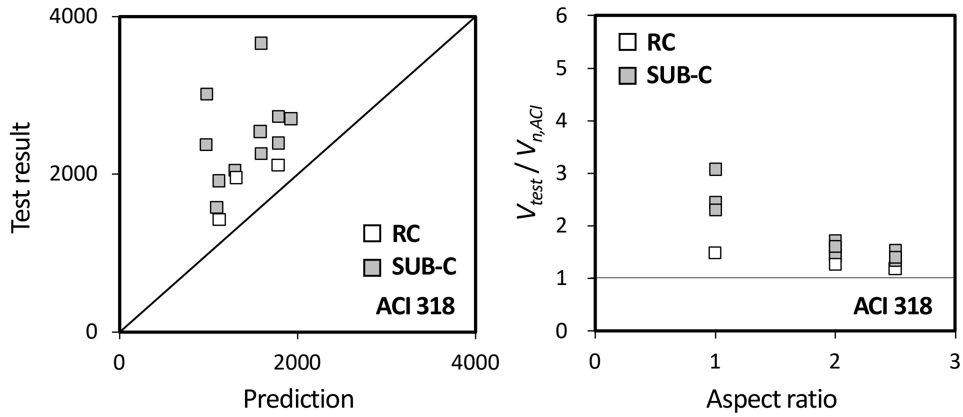

(a)

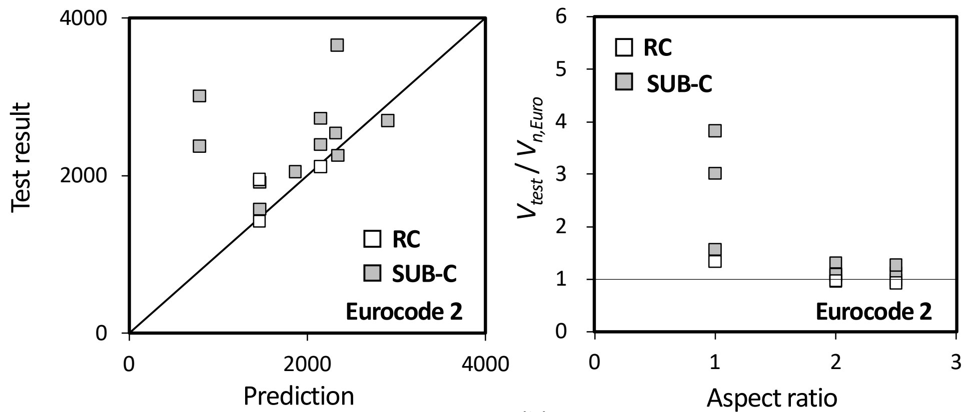

(b)

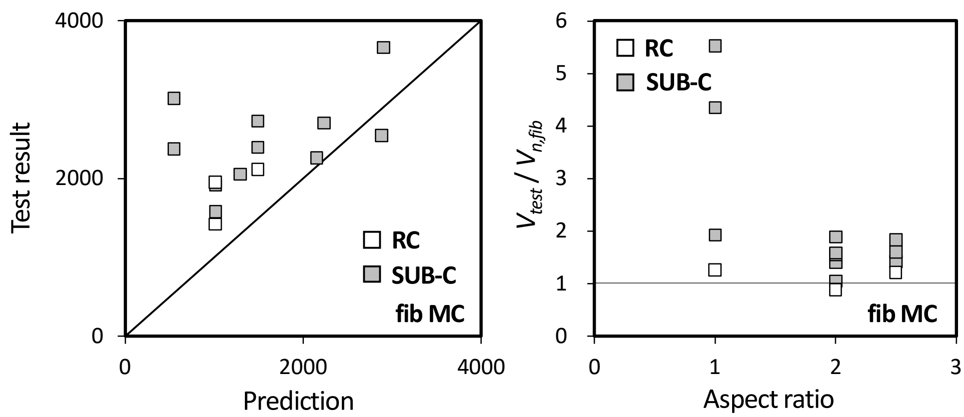

(c)

Fig. 4-32 Comparison with nominal shear strengths predicted by: (a) ACI 318 (2019); (b) Eurocode 2 (2004); and fib MC (2010).

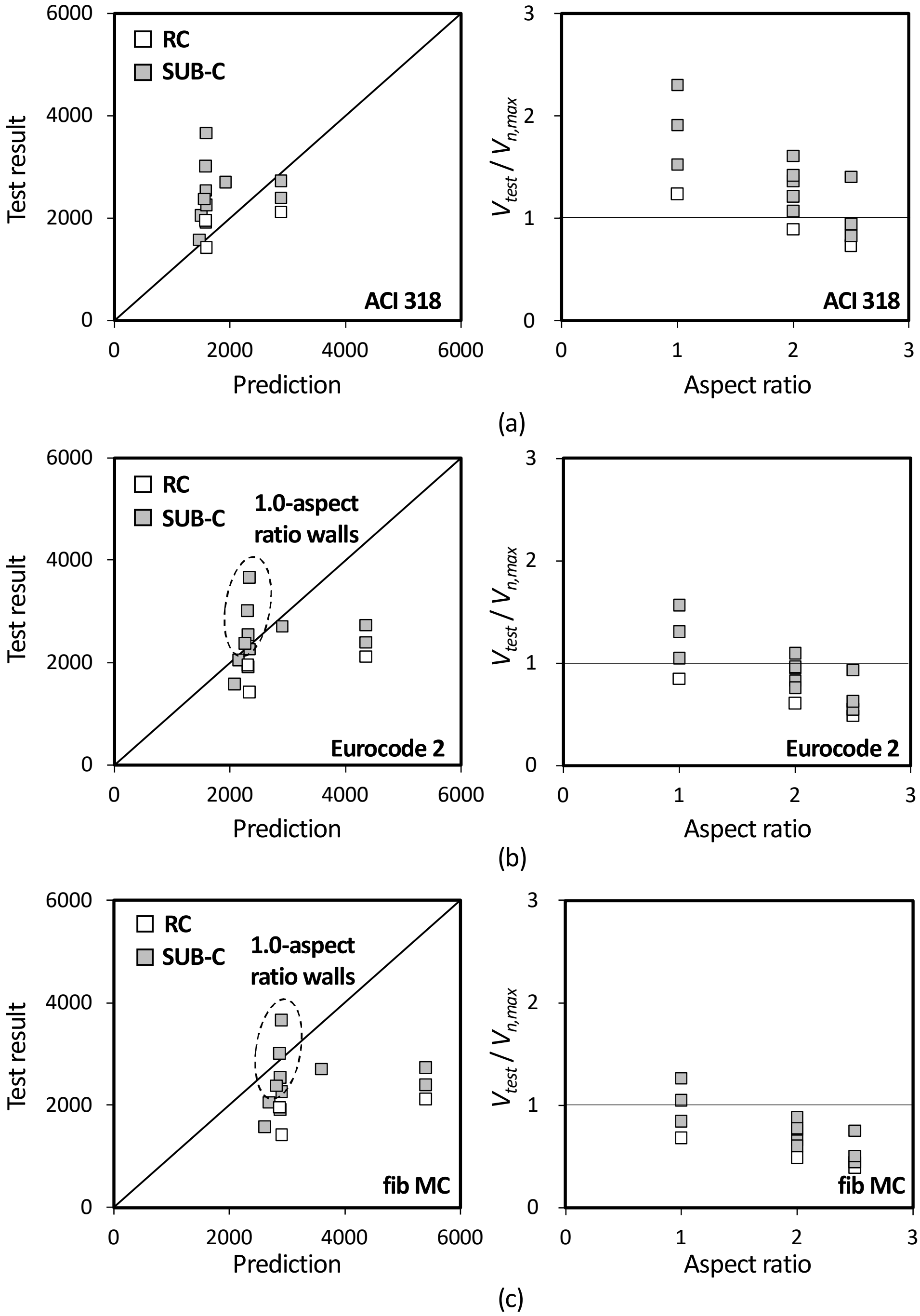

Fig. 4-33 Comparison with maximum shear strengths predicted by: (a) ACI 318 (2019); (b) Eurocode 2 (2004); and fib MC (2010).

4.5.3 Comparison with composite design methods

Table 4-6 shows the nominal shear strengths $V_{n,JGJ}$ and $V_{n,AISC}$ calculated according to the seismic provisions of JGJ 138 (2016) and AISC N690 (2018). JGJ 138 includes the contributions of boundary steel plates (V_b) and reinforced concrete web ($V_c + V_s$). On the other hand, AISC N690 provides the shear strength provided by steel faceplates and cracked web concrete. Thus, the nominal shear strengths of the specimens without steel faceplates were calculated according to JGJ 138, and AISC N690 was only used to predict the shear strength of the composite specimens with steel faceplates. In the calculation of $V_{n,AISC}$, the contribution of boundary steel U-sections was neglected. The detailed calculations of $V_{n,JGJ}$ and $V_{n,AISC}$ were summarized in Section 2.3.

Fig. 4-34 compares the test results with the predictions of JGJ 138 and AISC N690. In the figure, only the test results of the composite specimens were presented. In general, JGJ 138 safely predicted the shear strengths of the proposed composite walls, showing reasonable accuracy of V_{test} / $V_{n,JGJ}$ = 1.01 – 1.63 (**Fig. 4-34**(a)). However, a slight conservatism was observed in the specimens with the smallest aspect ratio of 1.0. The prediction of AISC N690 agreed with the tested strengths of **CS2SF** and **CS1SF** with steel faceplates, even though the shear contribution of boundary steel U-sections was neglected (**Fig. 4-34**(b)). The web crushing strength $V_{n,max}$ of composite walls was also predicted by AISC N690. Generally, the tested strengths were less than $V_{n,max}$, particularly when the aspect ratio was 2.5 (**Fig. 4-34**(c)).

Fig. 4-35 compares the tested shear strength contribution (V_c, V_s, and V_b) of each structural component with the prediction ($V_{c,JGJ}$, $V_{s,JGJ}$, and $V_{b,JGJ}$) of JGJ 138. The prediction underestimated the contributions of concrete (V_c) and boundary steel sections (V_b), particularly when the aspect ratio was small. The predicted contribution of horizontal shear reinforcement relatively agreed with the test result.

Table 4-6 Comparison with strength predictions of existing composite design methods

Specimens	Aspect Ratio	JGJ 138				AISC N690	
		V_n [kN]	V_{test}/V_n	$V_{n,max}$ [kN]	$V_{testr}/V_{n,max}$	V_n [kN]	V_{test}/V_n
RS2.5	2.5	-	-	-	-	-	-
CS2.5	2.5	2,373	1.01	4,322	0.55	-	-
CS2.5VH	2.5	2,595	1.05	4,455	0.61	-	-
CS2.5M	2.5	2,635	1.03	3,256	0.83	-	-
RS2	2	-	-	-	-	-	-
CS2	2	1,533	1.25	2,368	0.81	-	-
CS2VL	2	1,294	1.22	1,944	0.81	-	-
CS2SB	2	1,639	1.25	2,201	0.93	-	-
CS2TH	2	2,122	1.06	2,393	0.94	-	-
CS2SF	2	-	-	-	-	2,460	1.03
RS1	1	-	-	-	-	-	
CS1R	1	1,849	1.63	2,657	1.13	-	
CS1VL	1	1,557	1.53	2,335	1.02	-	
CS1SF	1	-	-	-	-	2,461	1.49
MEAN for SUB-C			1.23		0.85		1.26

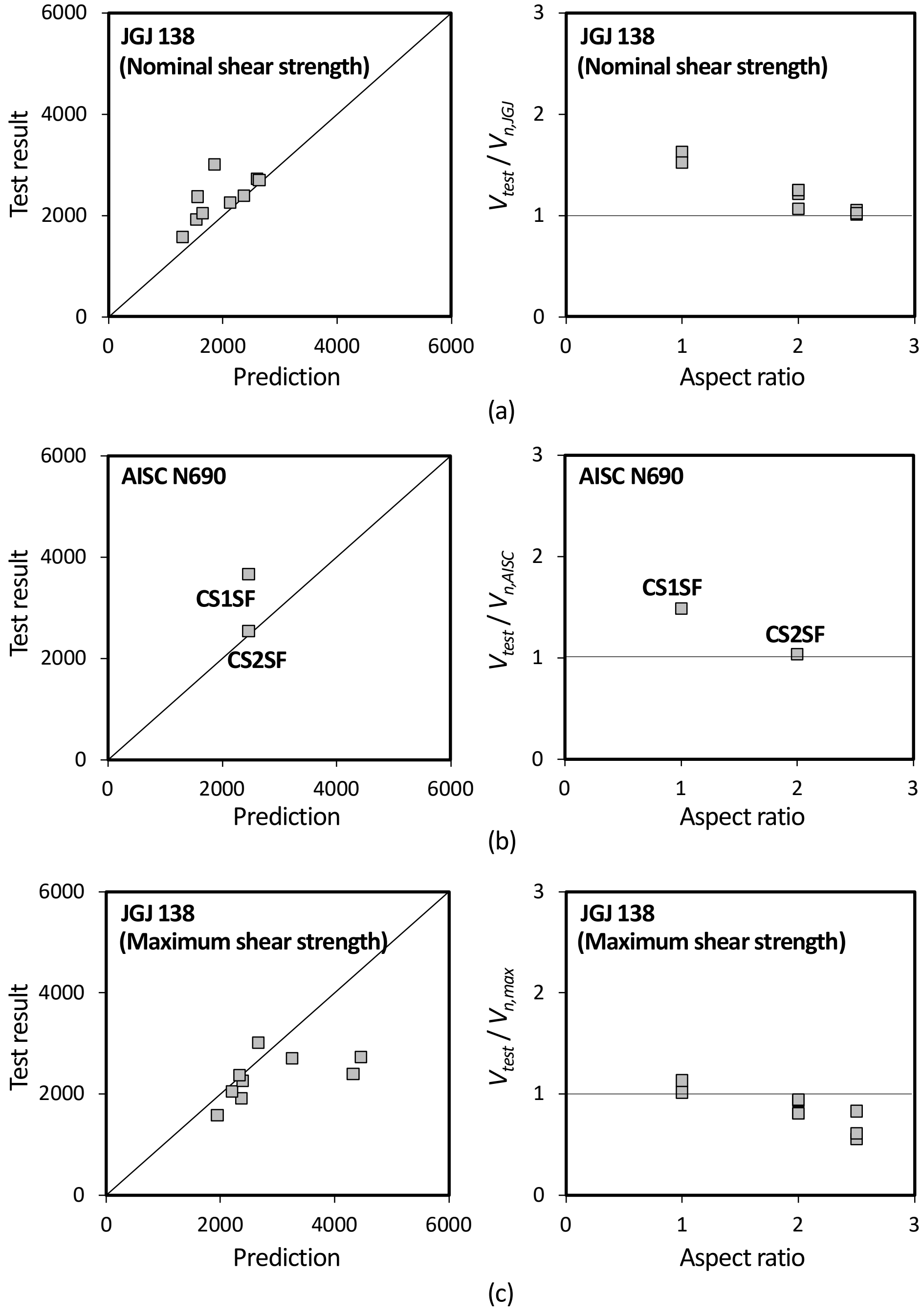

Fig. 4-34 Comparison with nominal shear strengths predicted by: (a) JGJ 138 (2016) (b) AISC N690 (2018); and (c) maximum shear strength predicted by JGJ 138 (2016).

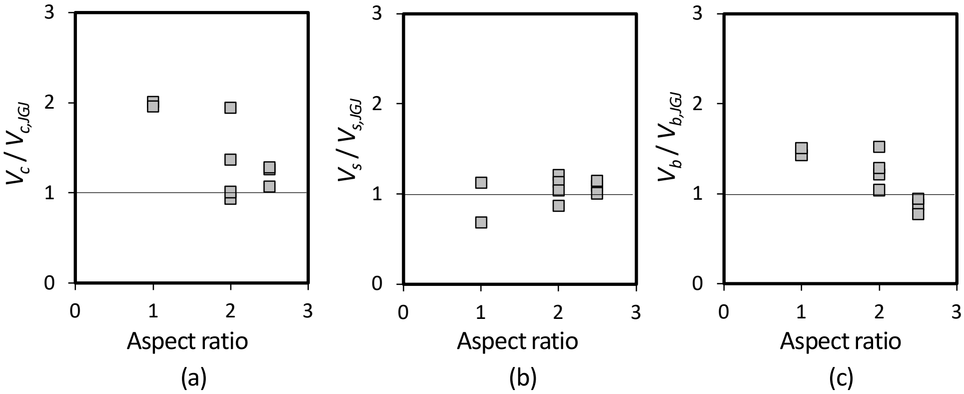

Fig. 4-35 Comparison with shear strength contributions of JGJ 138 (2016).

4.6 Summary

In this chapter, cyclic lateral load tests were performed for three RC walls and eleven composite (SUB-C) walls, to investigate the effect of boundary steel U-sections on the shear performances of the walls. The major design parameters were the type of boundary reinforcement (rebar vs steel U-section), sectional area of steel U-sections, type and spacing of horizontal web reinforcement. Existing design methods were used to predict the shear strengths of the specimens, and their prediction results were compared with the test results. The major findings drawn from the tests are summarized as follows:

1) The RC walls with boundary vertical rebars showed typical shear failure mode: diagonal tension failure (full penetration of diagonal cracking and tensile yielding of shear reinforcement), and subsequent web concrete spalling. On the other hand, SUB-C walls showed web crushing, without diagonal tension failure. This is because the steel U-sections restrained diagonal cracking and protected the boundary zone (full crack penetration was prevented).

2) The shear strength of the SUB-C walls was 13%–54% greater than that of the counterpart RC walls, due to the contribution of boundary steel U-sections (23%–45% of the shear strength for the inclined crack plane): The steel U-sections resisted shear transferred from the diagonal strut. As the steel plate area increased, the contribution of steel U-sections increased.

3) In the SUB-C wall with steel plate beams, the plate beams acted as shear reinforcement, providing adequate shear resistance. Further, the shear failure mode was less brittle, as the diagonal cracking and spalling of web concrete were better restrained by the plate beams. As the vertical spacing of steel plate beams decreased, the shear strength of SUB-C walls increased, due to the increased contribution of steel plate beams.

4) In the SUB-C walls with steel web faceplates (steel ratio = 4.0%), shear yielding of the faceplates occurred, though the faceplates and boundary steel U-sections were not connected. Further, as the faceplates and steel U-sections confined the concrete subjected to flexural compression, the shear strength contribution of concrete increased. Thus, the shear strength was 13%–54% greater than that of the SUB-C walls without faceplates. The shear strength of SUB-C walls with faceplates can be predicted according to AISC N690 (2018).

5) Existing RC design methods underestimated the shear strengths of SUB-C walls, neglecting the contribution of steel U-sections. On the other hand, JGJ 318 (2016) provided better accuracy, by including the contribution of steel boundary elements. For design of composite walls, the steel plate beams and steel faceplates can be regarded as horizontal reinforcement.

Chapter 5. Nonlinear Finite Element Analysis

5.1 Overview

In the previous chapters 3 and 4, the proposed composite walls (SUB-C walls) with steel U-section boundary elements were tested under cyclic loading, to investigate the effect of the steel U-sections on the lateral load resistance and deformation capacity of the walls. For design parameters, aspect ratio of walls (1.0, 2.0, or 2.5), horizontal shear reinforcement ratio (0.24%–1.0%), area of vertical steel U-sections (i.e., boundary reinforcement ratio = 11.6%–19.0%), and type of web reinforcement (conventional rebars or steel plate beams or steel web plates) were considered.

Among the tested seventeen composite walls, sixteen specimens showed shear failure owing to web crushing, and only one specimen failed due to unexpected weld fracture of boundary steel U-sections. Here, seven composite specimens with lower shear demand (i.e., lower flexural strength) showed web crushing in the plastic hinge zone after significant flexural yielding, while the remaining nine composite specimens with higher shear demand (i.e., greater flexural strength) showed web crushing before flexural yielding in the mid-height of the walls. On the other hand, diagonal tension shear failure, which is the general shear failure mode of traditional RC walls, was not observed in any of the composite specimens, even though the shear reinforcement ratio in most of the composite walls was designed to be less than the maximum reinforcement ratio (corresponding to web crushing failure) of ACI 318. This result indicates that, by using boundary steel U-sections, web crushing could be a critical failure criterion to determine the deformation and load-carrying capacities of the proposed composite walls.

Nonlinear finite element analysis was performed for SUB-C walls using ATENA program (Cervenka Consulting, 2016), which is a commercial program specially designed for concrete structures. The main objectives of performing FE analysis are 1) to identify the web crushing mechanism developed by horizontal elongation (horizontal tensile deformation in the web concrete), 2) to investigate the contribution of boundary steel U-sections to the shear strength, and 3) to assess the degree of horizontal elongation before elastic web crushing. Regarding 3), a parametric analysis was performed to expand the test data and to incorporate the effect of various design parameters into the trend of horizontal elongation. The analysis on SUB-C walls using steel web plates (i.e., faceplates) was excluded from the scope of this chapter, to focus on the web crushing mechanism developed by horizontal elongation (their failure mode depends on the composite mechanism without horizontal elongation).

Three-dimensional FE models were developed based on the geometric and material properties of the tested wall specimens. The same model was also used for parametric analysis. Although the tested wall behaviors were based on cyclic loading, the static analysis of the FE models was performed under a monotonically increasing lateral load at the top of the cantilever walls. The analysis results were used to develop the shear strength model of the proposed composite walls.

5.2 Finite Element Modeling

One advantage using ATENA for nonlinear FE analysis is that it provides a material library and good default values for design of reinforced concrete structures. For three-dimensional solid concrete, a fracture-plastic model (named "CC3DNonLinCementitious2" in program), which combines constitutive models for tensile (fracturing) and compressive (plastic) behavior, was used to simulate various mechanical features of damaged concrete, including concrete cracking, crushing under high confinement, and crack closure due to crushing in other material directions. The fracture model is based on the classical orthotropic smeared crack formulation and crack band model, which employs Rankine failure criterion, exponential softening, and rotated or fixed crack model. In the present study, the fixed crack model was used, assuming that the crack direction determined at the moment of the crack initiation is fixed and represents the orthotropic material. The shear strength of a cracked concrete is calculated using the Modified Compression Field Theory (MCFT, Vecchio and Collins 1986). The plasticity model for concrete crushing is based on the failure surface of Menétrey-Willam (1995), where uniaxial compressive hardening/softening behavior of Van Mier (1986) is assumed until failure. The compressive strength reduction in the crack direction is based on MCFT. The lower bound for the concrete strength was defined as 20% of the original compressive strength, to allow all possible strength degradation under significant tensile cracking. The values of basic input variables, such as compressive strength and elastic modulus, were determined from test data, and the other relevant variables followed the recommendations of ATENA and Eurocode 2 (2004).

For 1D steel reinforcement, a multi linear stress-strain model (named "CCReinforcement") was used to simulate strain hardening after yielding. The reference points to determine the overall behavior were based on test data. For 3D steel U-section plates, The Von-Mises plasticity model (named "Steel VonMises 3D") was implemented, with the tested values of yield strength and hardening modulus. The associated flow rule is based on the work of Chen (2013). The effect of local buckling was neglected because the damage of the steel plates was marginal in the tests. Both loading beams and base stubs were assigned elastic solid materials, without reinforcement.

8-node hexahedra elements were used for all 3D volumetric elements, except for 1D discrete reinforcing bars modeled using 2-node truss elements. In the interface between boundary steel U-sections and infilled concrete, all boundary nodes were connected without interface elements, assuming full composite action (no shear connectors were modeled). When steel plate beams were used for shear reinforcement, the connections between the plate beams and boundary steel U-sections were modeled using fixed contact elements. Each volumetric elements were meshed separately with the reinforcing bars embedded in the concrete elements. The mesh density of FE models significantly affects the accuracy of the analysis results. The mesh size was designed to be 80 mm at maximum, along the lengths of the walls (1600–1800 mm depth; 200–300 mm thickness; and 1600–4500 mm height), aiming for an element aspect ratio close to 1.0. The meshed models and brief summaries on FE modeling were shown in **Fig. 5-1**.

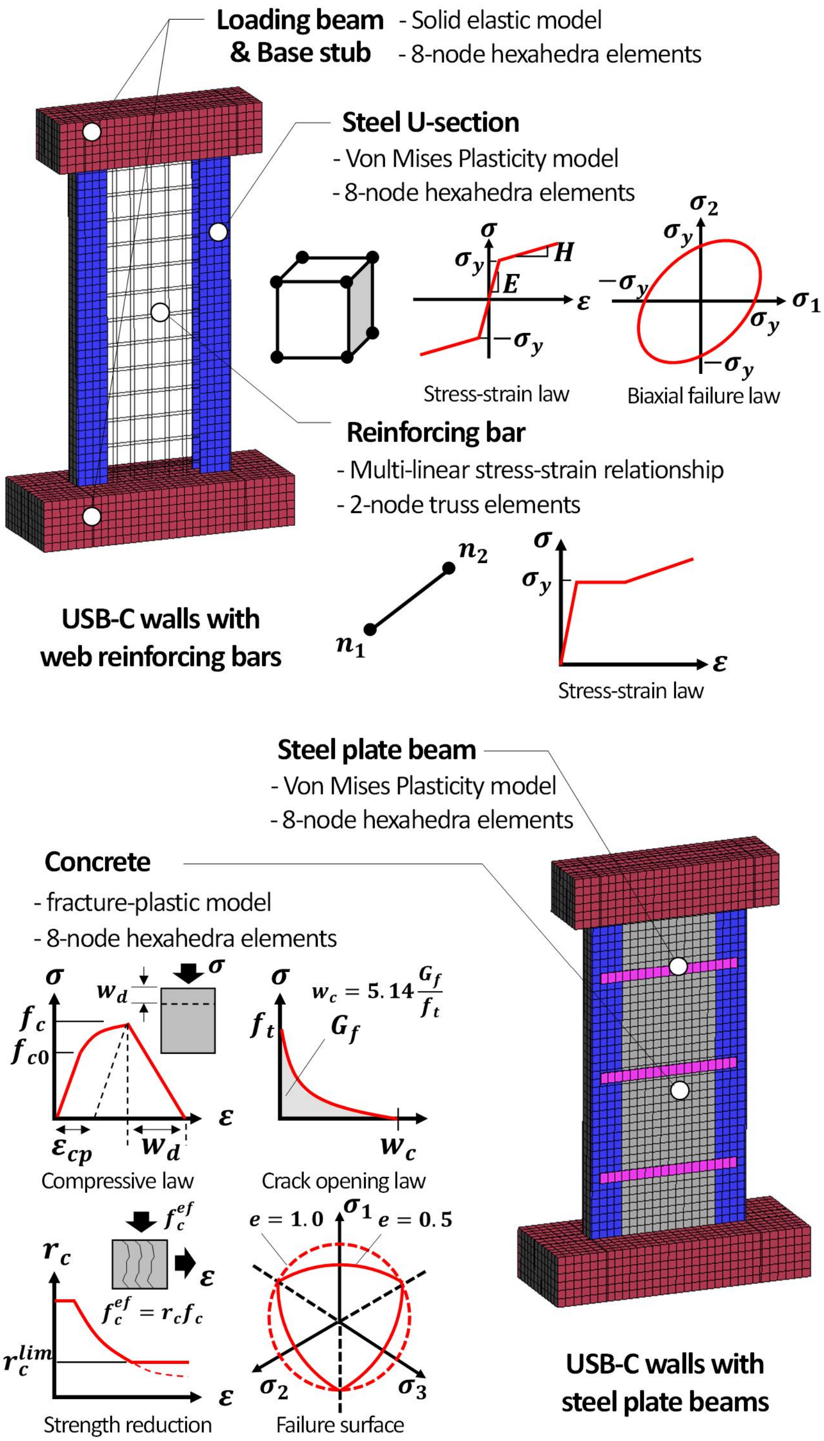

Fig. 5-1 Finite element modeling using ATE

5.3 Comparison with Test Results

5.3.1 Strength and load-displacement behavior

Fig. 5-2 compares the tested strengths with the predictions based on FE analysis, for both the specimens that showed flexural yielding (denoted as dark-colored) and premature shear failure (denoted as white-colored). Although the analysis was conducted under monotonic loading, the proposed FE analysis procedure reasonably predicts the flexural and shear strengths of the walls subjected to cyclic loading. The test result-to-prediction ratio is 1.08 on average. This result indicates that the strength contributions of each structural components can also be determined satisfactorily with the adopted nonlinear FE analysis method. However, it should be noted that the local responses may be significantly different from those under cyclic loading, particularly in the plastic hinge zone with large inelastic deformation demand: cyclically loaded walls may sustain more complex stress distribution in the web concrete, primarily due to the cumulative damage on the concrete cracked in both loading directions. Thus, the present FE analysis was not intended to figure out all specific inelastic responses, but focused on the approximate trend on the load-transfer and failure mechanisms shown in the almost elastic range. That is, only the results on SUB-C walls that failed in premature web crushing (before flexural yielding) were discussed.

Fig. 5-3 shows the lateral load-drift ratio relationship predicted for an example wall of **CS2.5** that failed in premature web crushing. The prediction of FE analysis agrees quite well with the tested peak strength. However, the predicted post-peak strength degradation behavior is less brittle than the actual behavior under cyclic loading. Such trend is also seen in the results of other shear failure-mode walls. Thus, for further analysis on inelastic behavior, more refined analysis procedures that reflect the effect of cyclic loading should be considered.

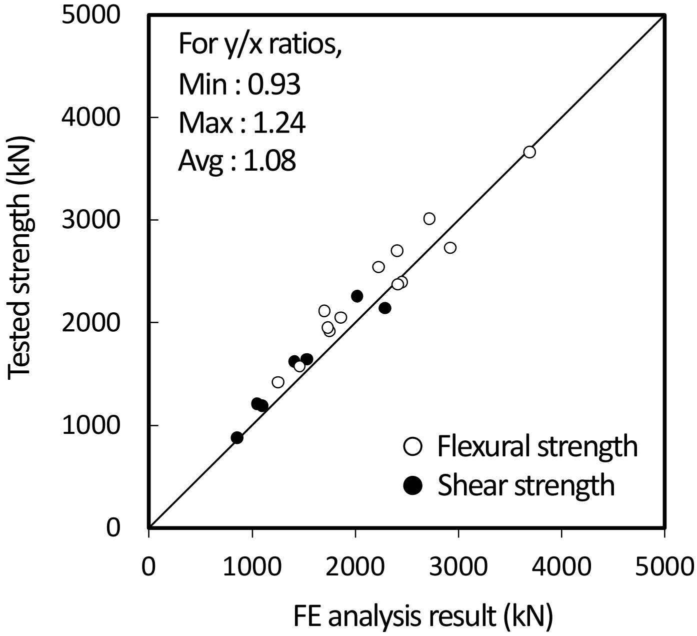

Fig. 5-2 Comparison of tested strengths with FE analysis results.

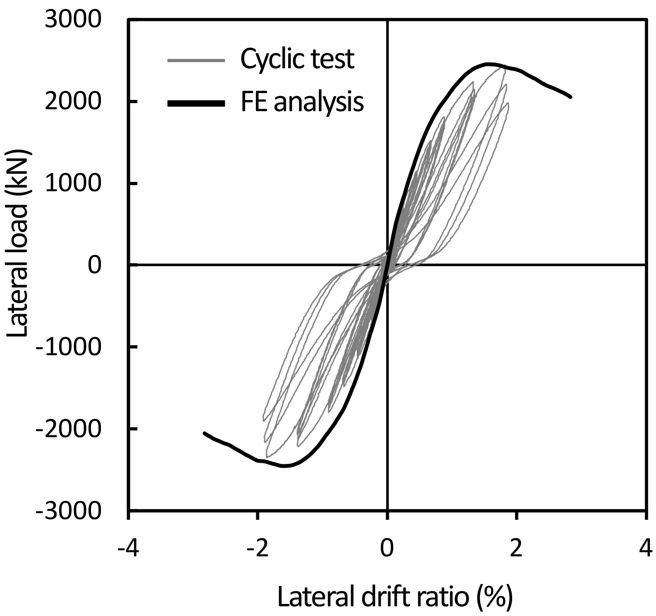

Fig. 5-3 Comparison of FE analysis result with tested cyclic lateral load-drift ratio relationship of Specimen CS2.5

5.3.2 Damage pattern of concrete

Figs. 5-4 through **Fig. 5-10** show the analysis results on the damage pattern of concrete in seven shear failure-mode walls **RS2.5**, **CS2.5**, **RS2**, **CS2**, **CS2SB**, **RS1**, and **CS1**, respectively. In the figures, the distributions of principal compressive stress, horizontal tensile strain, and compressive strength reduction for the concrete are captured at the moment of shear failure. In RC specimen **RS2.5** (**Fig. 5-4**), diagonal compressive stress fields are formed in the web region between the loading point and the base (flexural) compression zone (**Fig. 5-4**(b)). Here, the compression zone near the wall base is stressed the most, and the level of the stresses gradually decreases as they spread up the height of the wall. On the other hand, below the diagonal compression fields, horizontal tensile strains are concentrated along the diagonal cracks, due to the truss action provided by shear reinforcement (**Fig. 5-4**(c)). In particular, the strains highly increase across the cross section of the lower panel zone where significant diagonal cracking occurs. As the Modified Compression Field Theory (MCFT) is implemented, the tensile strain distribution matches the distribution of the compressive strength reduction (the effect of longitudinal strains on the strength degradation is negligible because the wall failed before flexural yielding) (**Fig. 5-4**(d)). The strength reduction propagates to the small region of the boundary compression zone subjected to high levels of stresses. Thus, the boundary concrete at the wall base becomes susceptible to crushing. Such prediction result agrees with the tested failure mode as shown in **Fig. 5-4**(a): crushing of the boundary concrete occurred, followed by extensive shear sliding along the diagonal cracks at the bottom panel zone (i.e., diagonal tension failure, see **Fig. 4-7**(a)). In the figure, spalling and crushing of the web concrete occurred after diagonal tension failure.

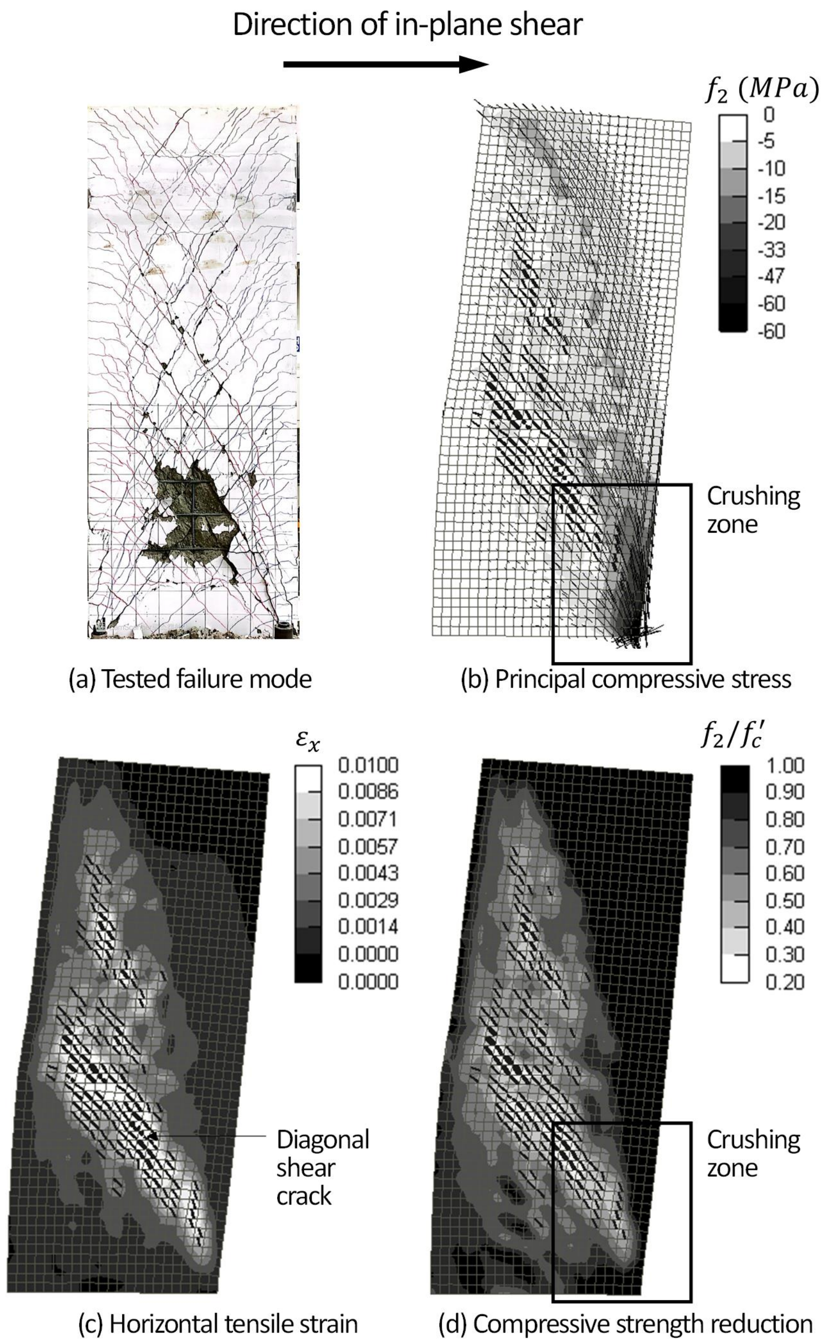

Fig. 5-4 Damage pattern of concrete in RS2.5 at shear failure: (a) test result and analysis results of (b) principal compressive stress, (c) horizontal tensile strain, and (d) compressive strength reduction.

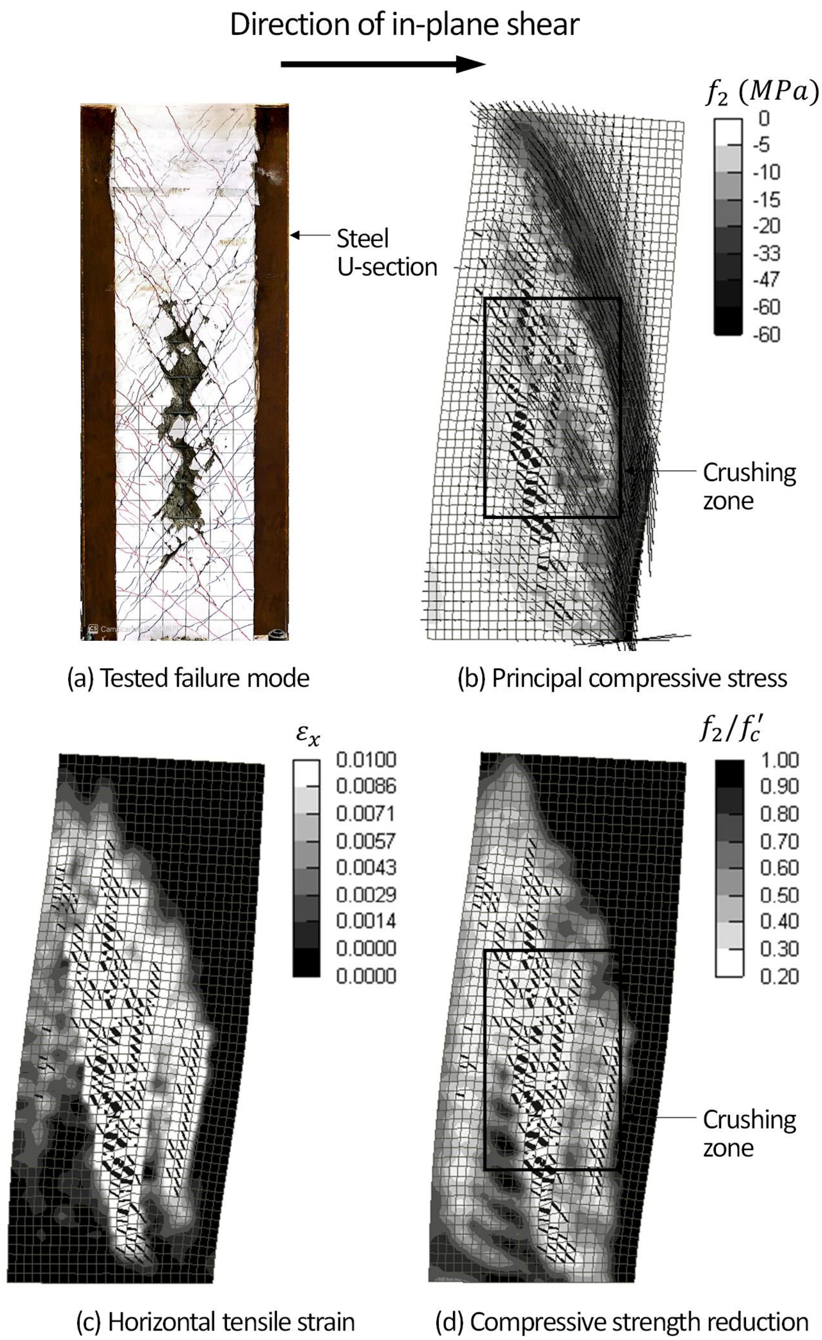

Fig. 5-5 Damage pattern of concrete in CS2.5 at shear failure: (a) test result and analysis results of (b) principal compressive stress, (c) horizontal tensile strain, and (d) compressive strength reduction.

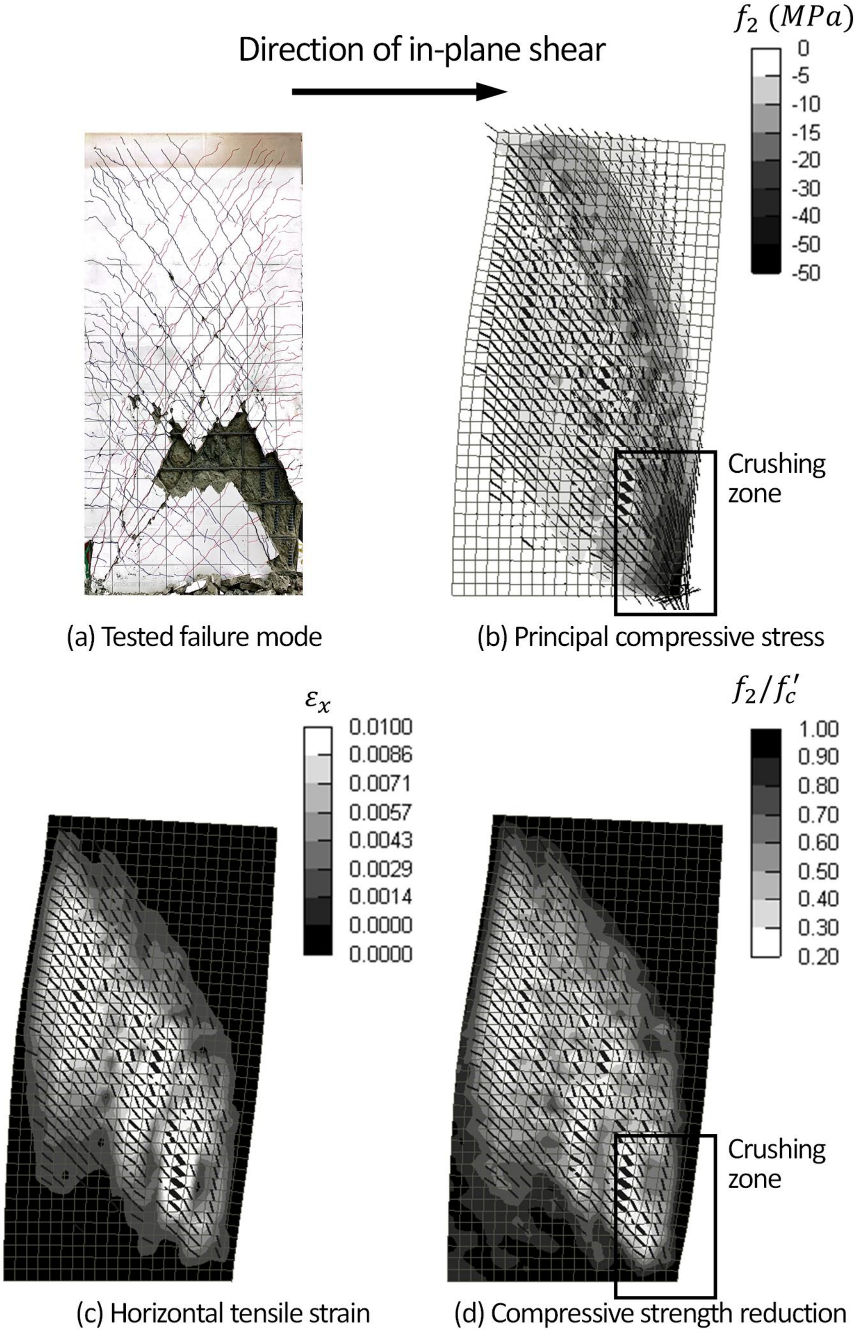

Fig. 5-6 Damage pattern of concrete in RS2 at shear failure: (a) test result and analysis results of (b) principal compressive stress, (c) horizontal tensile strain, and (d) compressive strength reduction.

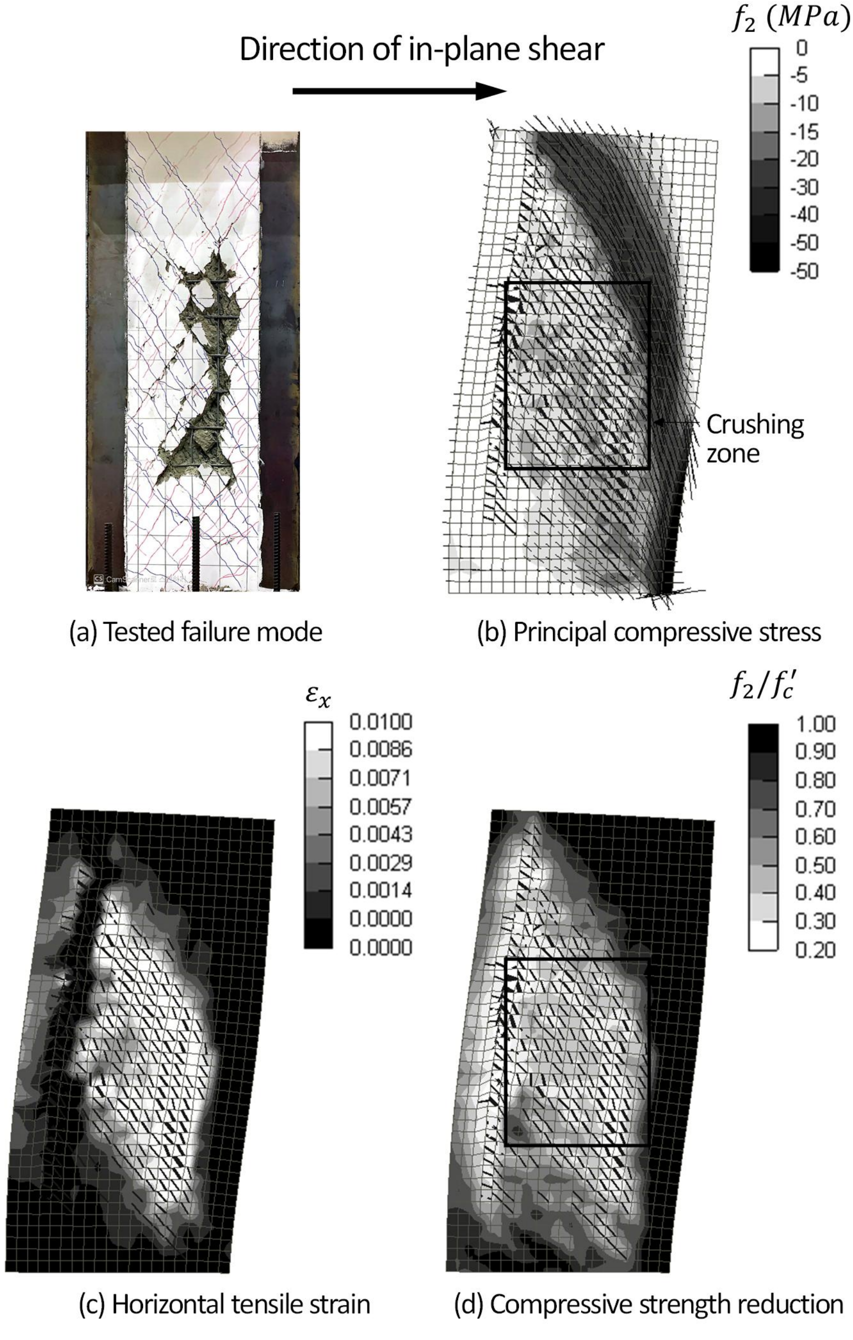

Fig. 5-7 Damage pattern of concrete in CS2 at shear failure: (a) test result and analysis results of (b) principal compressive stress, (c) horizontal tensile strain, and (d) compressive strength reduction.

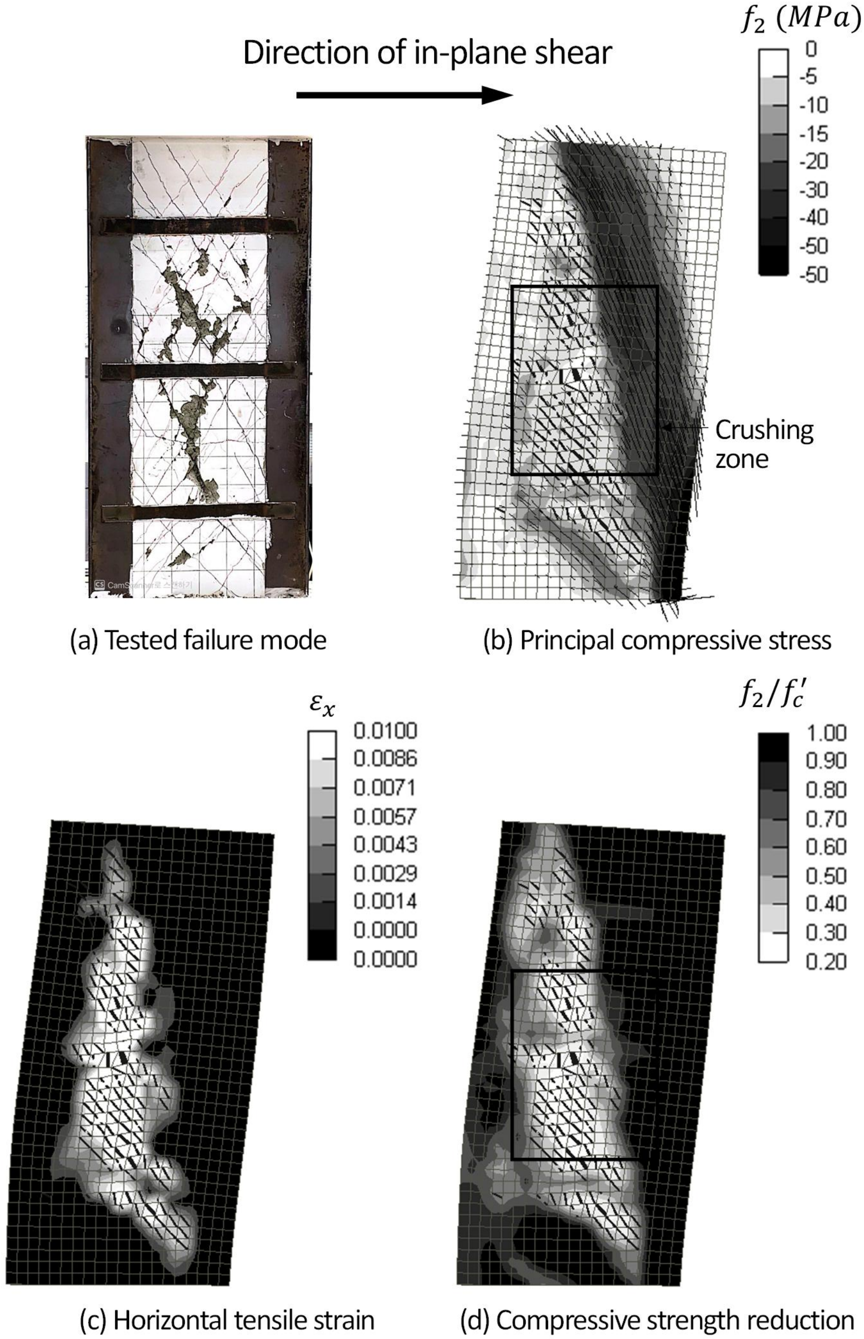

Fig. 5-8 Damage pattern of concrete in CS2SB at shear failure: (a) test result and analysis results of (b) principal compressive stress, (c) horizontal tensile strain, and (d) compressive strength reduction

In composite specimen **CS2.5** (**Fig. 5-5**), diagonal compressive stress fields are formed primarily at the upper panel zone, with higher levels of stresses (**Fig. 5-5**(b)); The stress demand increases as the predicted shear strength is increased by 44%. The diagonal compression is transmitted to the vertical compression boundary element (steel U-section plus infill concrete) in the lower panel zone. The diagonal compression fields with lower levels of stresses is also formed in the lower panel zone. In **Fig. 5-5**(c), horizontal tension zone appear in most of the web region where significant diagonal cracking occurs. Overall, the horizontal tensile strains are greater than those in the counterpart **RS2.5**, which indicates that the cracked web concrete experiences larger horizontal deformation until failure. The tension zone is more pronounced in the mid-height of the wall. On the other hand, in the lower panel zone, the increase of the strains is limited to the small area of the web region. Such phenomenon is due to the presence of boundary steel U-sections with high stiffness: the steel U-section in compression resists a part of shear transferred from the diagonal compression, relatively decreasing the contributions of shear reinforcement and web concrete. Further, cracks do not penetrated into the boundary zone confined by the steel U-sections, thus no strength degradation occurs in the boundary zone (**Fig. 5-5**(d)). Despite the high stresses around the boundary zone, the stress demands do not reach the strength of the boundary concrete; crushing of the boundary concrete and subsequent diagonal tension failure do not occur. This result is also seen in the diagonal compression fields in the upper panel zone where cracking and strength degradation are restrained. On the other hand, in the web of the mid-height where large horizontal tension zone is developed, the stress demands (= 10–20 MPa) are almost equal to the reduced strength (0.2–0.3f_c', in which f_c' = 64.3 MPa), thus crushing tends to occur. The strength reduction shown in the tensile boundary elements is attributed to the flexural tension, not to the associated shear damage. The predicted cracking and damage patterns of the concrete agree with the test results shown in **Fig. 5-5**(a).

In the walls with lower aspect ratio of 2.0 (**RS2** and **CS2** in **Fig. 5-6** and **Fig.**

5-7, respectively), there are also similar tendency and good agreement with the test results.

In **CS2SB** (aspect ratio = 2.0) with steel plate beams (**Fig. 5-8**), diagonal cracking in the tension zone is relatively marginal (i.e., decreased number of cracks), despite the relatively large spacing of the plate beams. Further, thicker diagonal compression fields are formed over the wall height (**Fig. 5-8**(b)). Due to the alleviated cracking, the areas of horizontal tension zone and strength degradation zone are also reduced (**Fig. 5-8**(c) and (d)). Thus, the predicted peak strength is 6.3% greater than that of the counterpart SUB-C wall. Such distinct damage pattern and strength increase agree with the test results.

When the aspect ratio decreases to 1.0 (**RS1** and **CS1** in **Fig. 5-9** and **Fig. 5-10**, respectively), horizontal tensile strains and strength reduction of concrete are less than those of the walls with the greater aspect ratios. This is because, due to the low aspect ratio, the shear force on walls is directly transferred to the wall base by diagonal struts, rather than by the truss action of shear reinforcement. In **CS1**, however, higher compressive stresses are applied at slightly upper location from the diagonal, and the compressive forces are transferred to the boundary zone slightly above the wall base (**Fig. 5-10**(b)).

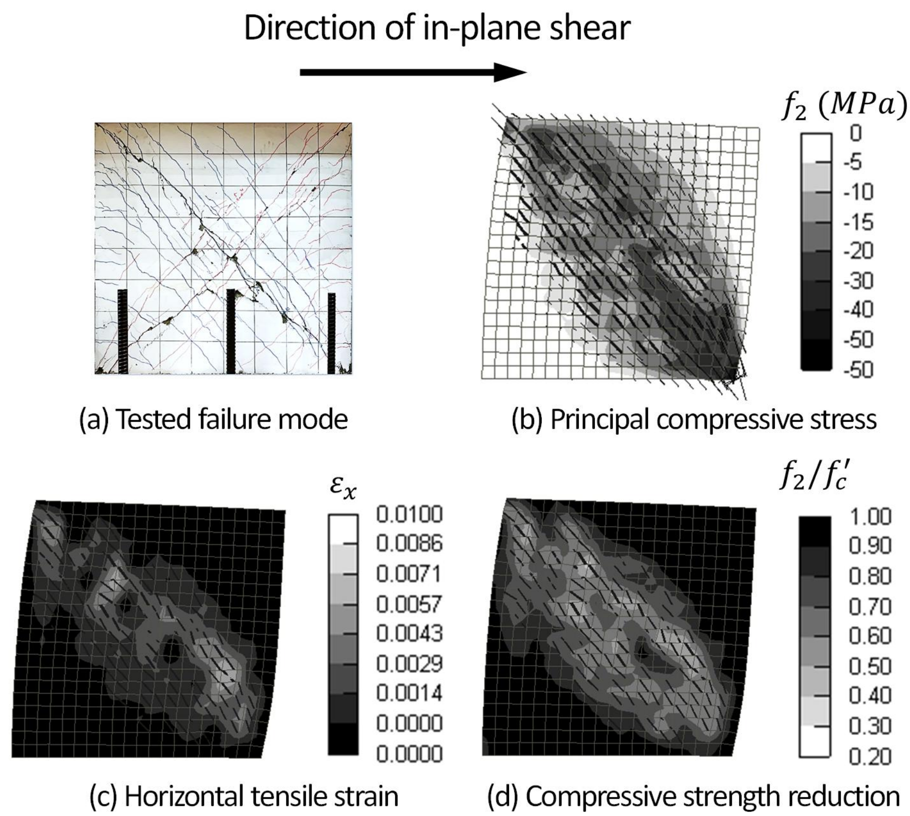

Fig. 5-9 Damage pattern of concrete in RS1 at shear failure: (a) test result and analysis results of (b) principal compressive stress, (c) horizontal tensile strain, and (d) compressive strength reduction.

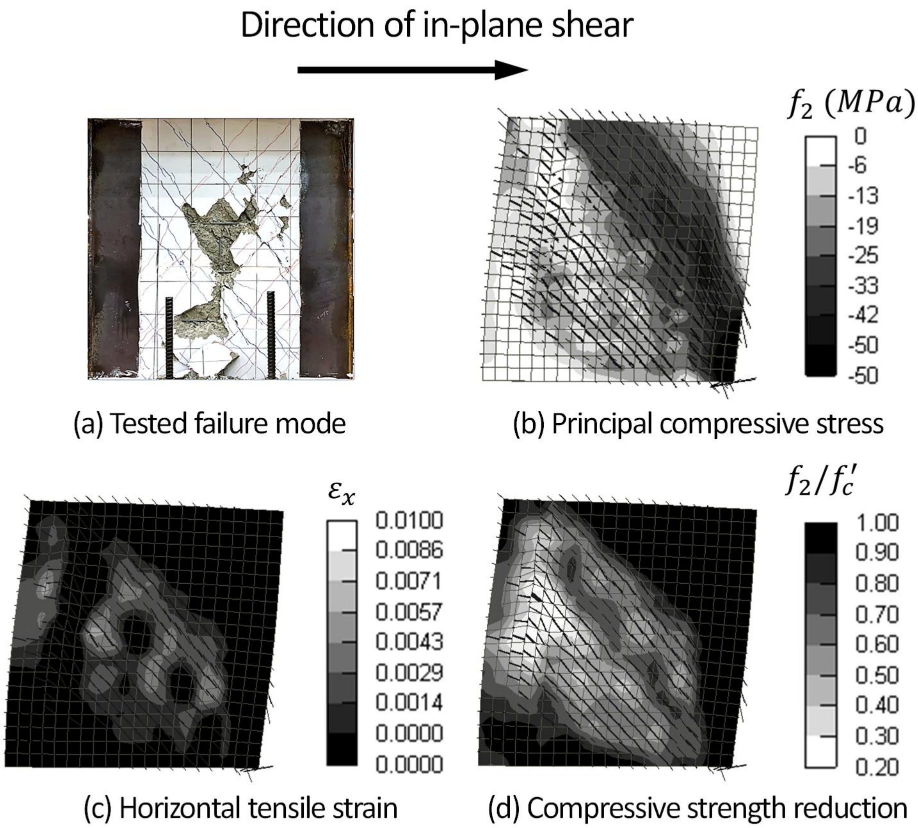

Fig. 5-10 Damage pattern of concrete in CS1 at shear failure: (a) test result and analysis results of (b) principal compressive stress, (c) horizontal tensile strain, and (d) compressive strength reduction.

To clarify the failure mode, **Fig. 5-11** and **Fig. 5-12** show the damage patterns of concrete corresponding to post-peak strength degradation. In **RS2.5** (**Fig. 5-11**(a)), as the strength is degraded after the peak strength, the boundary concrete at the wall base is significantly damaged, and shows large local deformation in the shear direction. At the same time, the macro diagonal crack is formed in the lower panel zone, and extensive shear sliding occurs along the macro crack, showing diagonal tension failure mechanism.

On the other hand, in **CS2.5** (**Fig. 5-11**(b)), due to the boundary steel U-sections, such shear sliding is not observed in the lower panel zone, while diagonal compression fields in the mid-height gradually disappear due to the damage of web concrete (i.e., compressive struts do not work properly). Thus, for load redistribution, the diagonal compression fields in the upper panel zone have slightly shifted toward the uncracked zone. Such phenomenon is also seen in the walls with the lower aspect ratios, even with steel plate beams (**Fig. 5-12**).

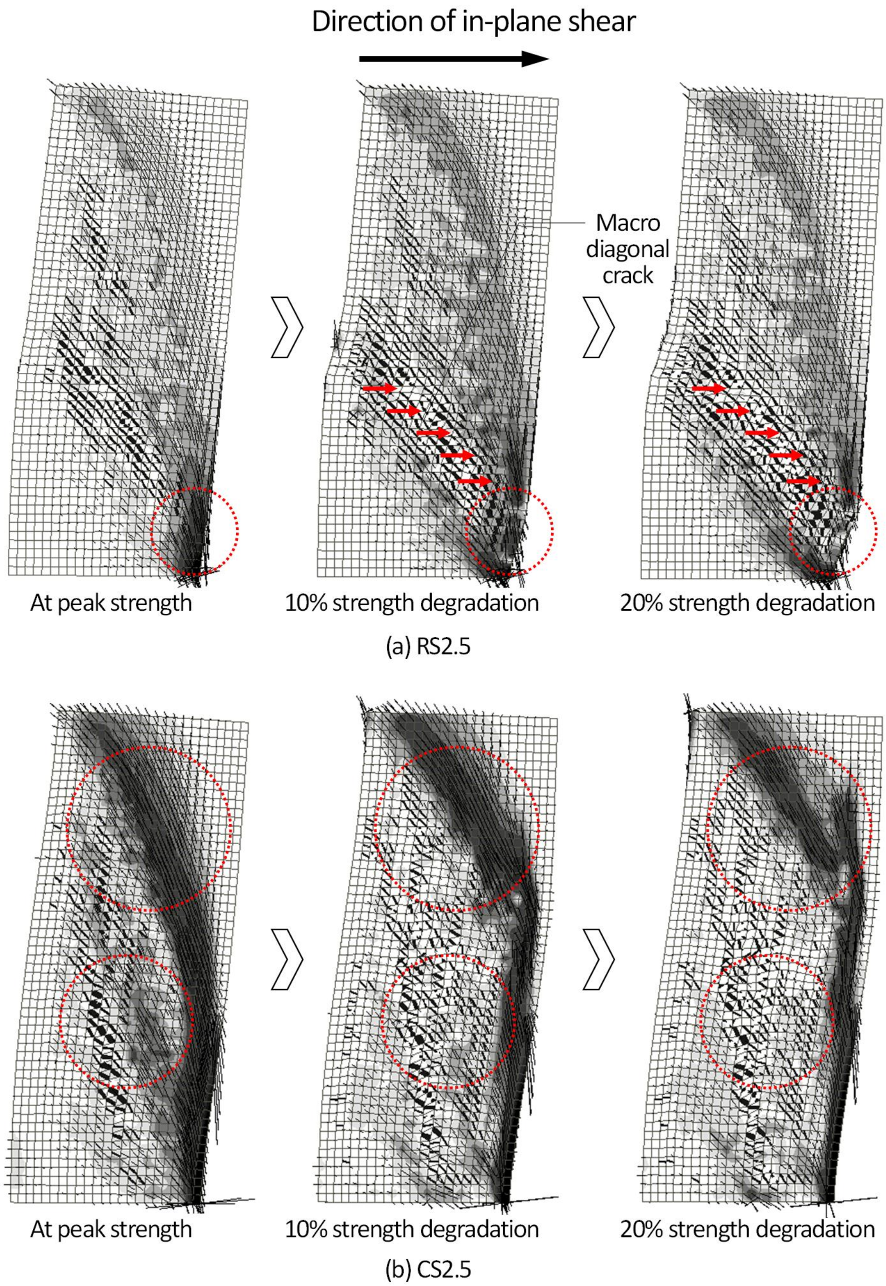

Fig. 5-11 Damage pattern of concrete in 2.5-aspect ratio walls according to the strength degradation: (a) RS2.5; and (b) CS2.5.

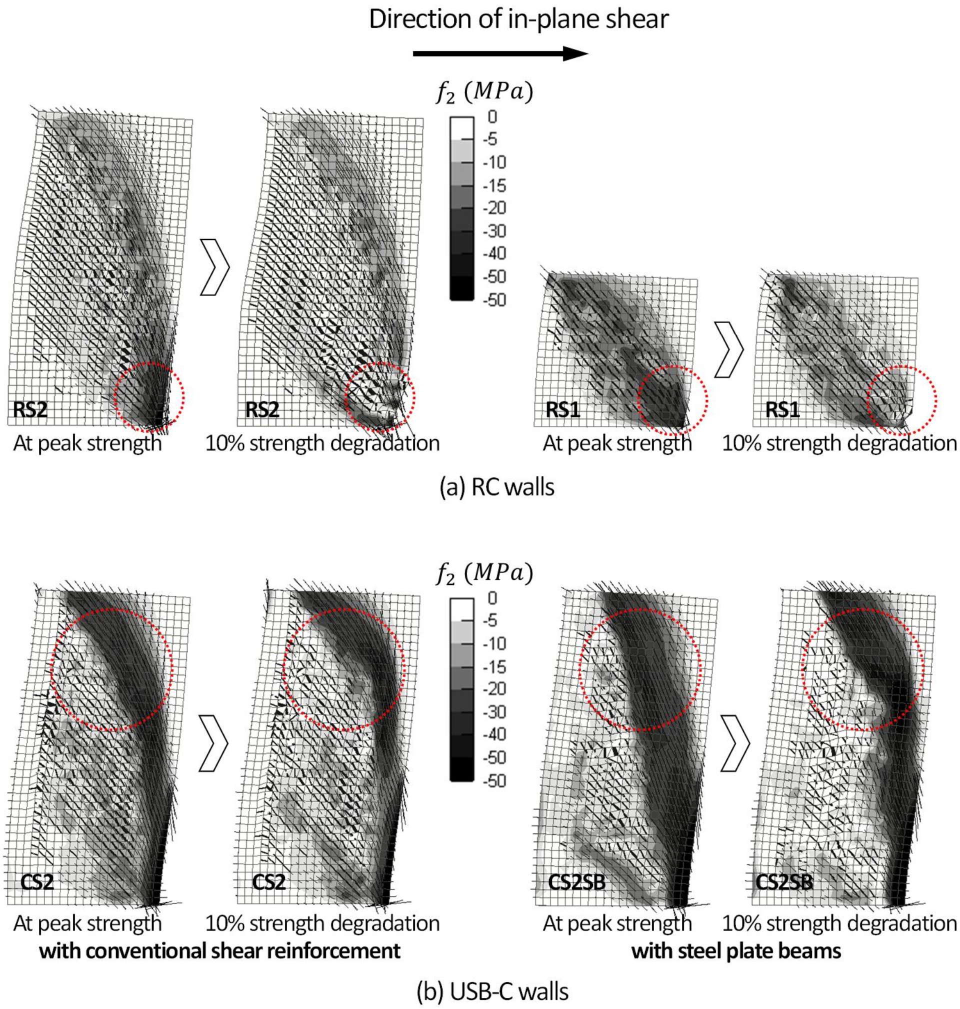

Fig. 5-12 Damage pattern of concrete in 2.0- and 1.0-aspect ratio walls according to the strength degradation: (a) RC walls; and (b) SUB-C walls.

5.4 Shear Strength Contribution

It is revealed that the boundary steel U-sections restrain cracking and crushing of the boundary concrete and provide alternate load-path to transfer the shear force. **Fig. 5-13** and **Fig. 5-14** show the shear stress distribution of concrete and steel U-sections, respectively. In RC specimens **RS2.5**, **RS2**, and **RS1**, generally, the shear stresses of concrete are quite well distributed in the web region. The peak shear stress appears in the boundary compression zone at the wall base. On the other hand, in SUB-C specimens **CS2.5**, **CS2**, and **CS1**, relatively high shear stresses are applied to the diagonal compression fields in the upper panel zone, which are close to or even greater than those in the boundary compression zone. The concrete stresses in the boundary compression zone are not significantly different from those in the RC specimens, as the steel U-sections resist shear transferred from the diagonal compression fields. Thus, as shown in **Fig. 5-14**, the shear stresses of the steel U-sections are concentrated at the ends of the diagonal compression fields, regardless of the aspect ratio.

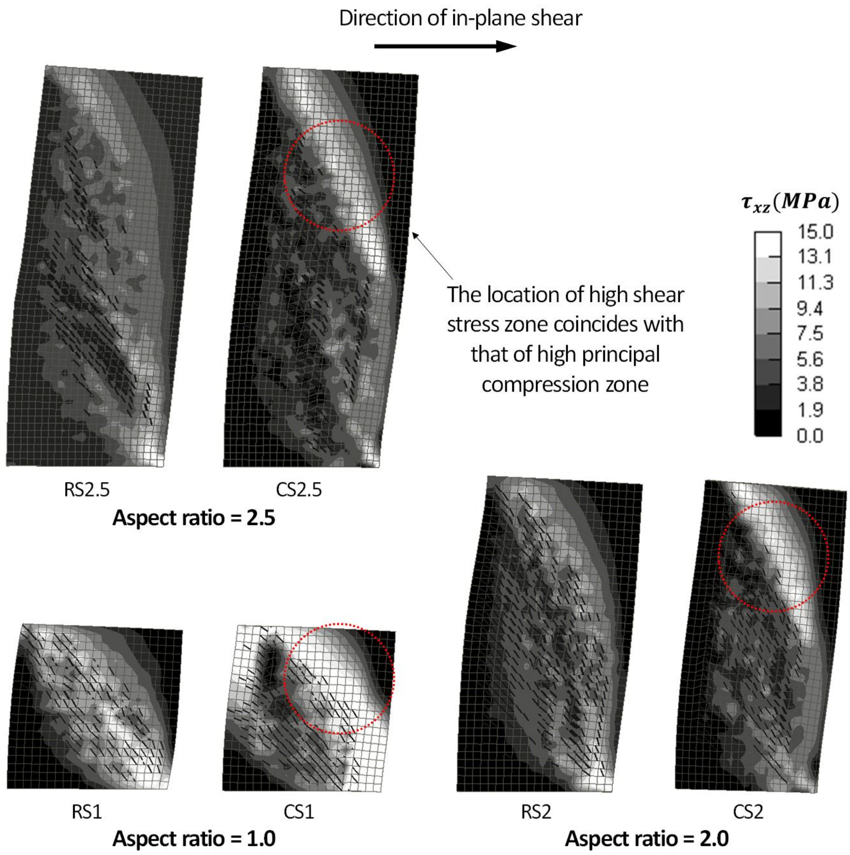

Fig. 5-13 Shear stress distribution of concrete.

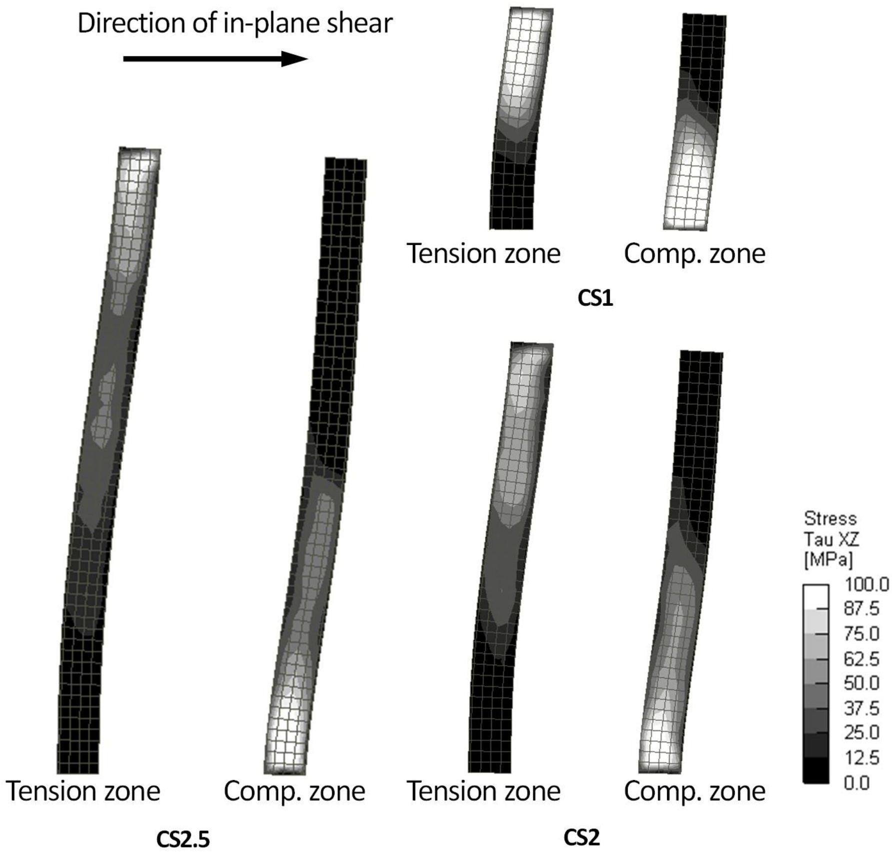

Fig. 5-14 Shear stress distribution of steel U-section.

To investigate the contribution of boundary steel U-sections to the shear strength, the resultant shear force transferred by the steel U-sections was calculated at every cross section along the wall height (Note that in Chapter 4, the shear strength contribution of steel U-sections was calculated with respect to the inclined crack plane). The shear strength contribution of the remaining RC walls (including boundary infilled concrete) was calculated by extracting the contribution of steel U-sections from the overall shear force on walls. In the case of walls with steel plate beams or steel web plates, the RC contribution was replaced by the sum of contributions of concrete and those steel plates. **Fig. 5-15**(a) shows the vertical distributions of the resultant shear forces, predicted from the FE analysis of the example walls **CS2.5** and **CS1**. In the figure, the shear contributions of the tensile and compressive steel U-sections are presented at the left and right sides, respectively, and the contribution of the RC section is presented in the center. Generally, the RC contribution is uniform along the wall height, while the contributions of boundary steel U-sections are concentrated at the ends of diagonal struts. This confirms that a part of shear is transferred from the tension boundary elements to compression boundary elements by the diagonal struts (see **Fig. 5-15**(b)).

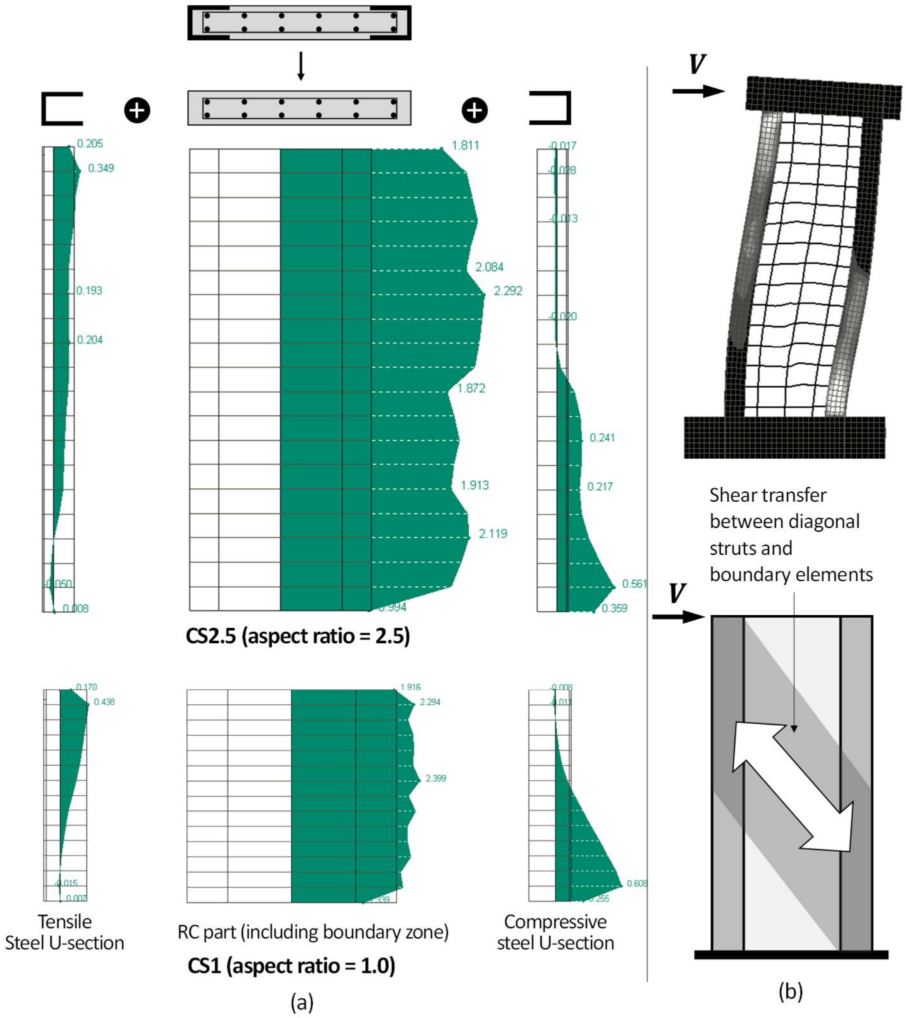

Fig. 5-15 Shear strength contributions of steel U-sections and remaining RC walls.

Fig. 5-16 shows the shear strength contributions (V_b) and contribution ratios (V_b / V) of steel U-sections calculated in the shear failure-mode walls. Here, V_b was calculated as the sum of contributions of the tensile steel U-section ($V_{b,t}$) and compressive steel U-section ($V_{b,c}$). The figure also includes the contribution V_{RC} of RC components: the sum of the contributions of concrete and shear reinforcement (including steel plate beams). In general, the calculated V_b shows the maximum at the bottom of the walls, while the minimum at the top. However, the variation of V_b (or V_b / V) is insignificant, because the contributions of tensile and compressive steel U-sections show the opposite trends along the wall height (see **Fig. 5-15**(a)). For all specimens, the average of V_b for the entire height ranges only 10%–23% of the overall shear strength V. This result indicates that the contribution V_{RC} of RC components is much greater than that of the boundary steel U-sections, regardless of the variation of the major design parameters: vertical boundary reinforcement ratio (= area ratio of steel U-section to boundary zone = 11.6% – 19.4%), horizontal shear reinforcement ratio (= 0.24% – 1.05%), and type of shear reinforcement (conventional rebars or steel plate beams). The detailed discussions for each specimens are as follows.

In the walls with aspect ratio of 2.5 (**Fig. 5-16**(a)), the variation of V_b is relatively large, showing $0.07V – 0.36V$. In control specimen **CS2.5**, the averages of V_b and V_b / V are 300 kN and 0.12, respectively. When the area of steel U-sections is increased by 35%, the average of V_b (= 523 kN for **CS2.5VH**) is increased by 74%. However, compared to the overall shear strength, the increase of V_b is marginal (V_b / V increases from 0.12 to 0.18), due to the basically large contribution of RC components. In **CS2.5M**, by decreasing the wall thickness, the steel U-sections with the highest reinforcement ratio (= 19.4%) are used for boundary elements. Thus, V_b / V shows the greatest contribution ratio, almost reaching 0.36 at the wall bottom. However, as the distance from the wall base increases, the V_b / V values significantly decrease. Thus, at the mid-height, the V_b / V values are comparable to those of other 2.5-aspect ratio walls. The average of the V_b / V for the entire height is calculated as 0.23. This result indicates that the effect of the steel plate area on the shear contribution ratio (V_b / V) is insignificant, particularly in the mid-height of the walls. Such phenomenon is more pronounced in the walls with the lower aspect ratios: the difference of V_b / V is 0.04 in the comparison of **CS2** and **CS2VL** (**Fig. 5-16**(b)); and 0.03 in the comparison of **CS1** and **CS1VL** (**Fig. 5-16**(c)). From the results of **CS2SB** and **CS2TH** (**Fig. 5-16**(b)), it is revealed that the use of steel plate beams and their spacing have little effect on the contribution of steel U-sections. Interestingly, as the area of steel U-sections increases, the RC contribution V_{RC} tends to increase. It can be presumed that, as concrete cracking is better restrained by the greater plate area, the contribution of the web concrete slightly increases, which increases V_{RC}.

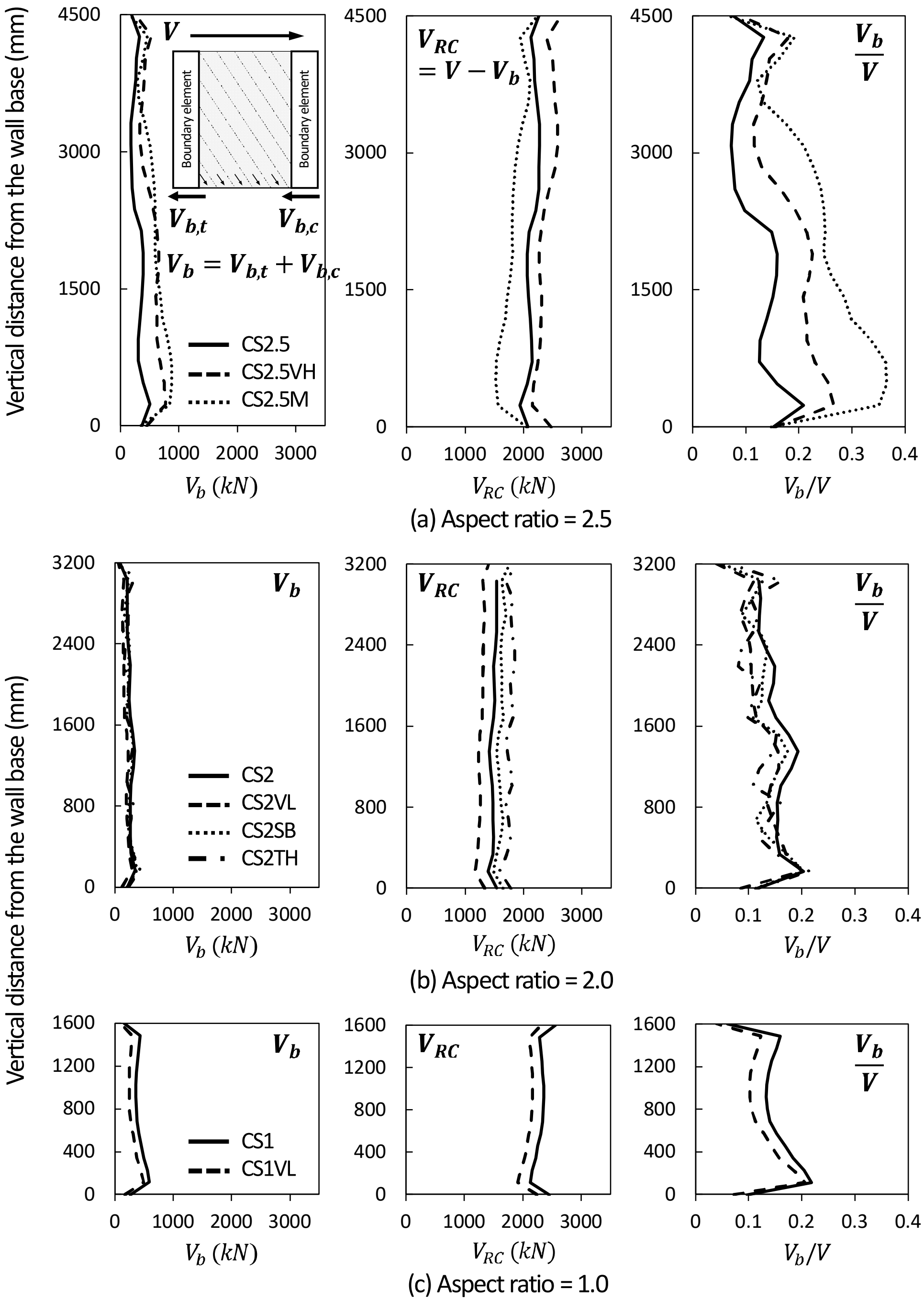

Fig. 5-16 Shear strength contributions of boundary steel U-sections and the remaining RC walls according to the wall height.

5.5 Horizontal Elongation Model

The FE analysis results clearly show that the main cause of web crushing is the strength degradation of diagonal concrete struts resulting from large horizontal tension deformation in the mid-height of walls; According to MCFT, as the horizontal tension deformation increases, the shear deformation (or principal tensile strain) increases (refer to deformation shapes in **Fig. 5-4** through **Fig. 5-10**). In the present study, such mechanism is named "Horizontal elongation". In the lower panel zone of the slender walls (aspect ratio > 2), the horizontal elongation is relatively restrained due to the shear contribution of the compressive steel U-section. For this reason, the web crushing is concentrated at the mid-height of the walls. In the squat walls (aspect ratio = 1), the horizontal elongation is also restrained due to the increased diagonal strut action (i.e., decreased truss action)

Thus, for prediction of web crushing strength, it is necessary to estimate the horizontal elongation corresponding to web crushing failure. In the present study, by using the proposed FE models, a parametric analysis was performed on the major design parameters which are assumed to affect the horizontal elongation: shear span ratio (l_s/l_w= 1.16 – 2.64), mechanical shear reinforcement ratio ($\rho_h f_{yh}/f_c'$ = 0.028 – 0.082, in which shear reinforcement ratio = 0.24%–1.05%), and mechanical steel ratio ($\rho_s F_y/f_c'$ = 0.42 – 0.90, in which overall vertical steel ratio ρ_s = 4.8%–10.0%). The variation of the parameters reflected the feasibility in practice, and also included the tested properties. Note that the high ratio of steel U-sections was to prevent flexural yielding before web crushing. For the same purpose, the aspect ratio of walls was limited to 2.5. Otherwise, a very large-sized steel U-section is required, which is impractical for design. For web reinforcement, typical reinforcing bars were used, without steel plate beams. The detailed properties for the parametric analysis were summarized in **Table 5-1**.

The horizontal elongation e_h is defined as the average tensile deformation within the web region (denoted as $\Delta_{h,c} - \Delta_{h,t}$ in **Fig. 5-17**), and the maximum of e_h is obtained at web crushing failure. In the present study, the horizontal elongation was calculated as the average tensile strain ε_h of horizontal shear reinforcement within the mid-height panel zone, assuming strain compatibility (**Fig. 5-17**). The height of the panel zone was defined as the wall length l_w, except for 1.0-aspect ratio walls where the panel zone height was defined as $0.8l_w$. The horizontal elongation ratio is defined as follows:

$$\alpha_h = \frac{e_h}{(0.8l_w)\varepsilon_{yh}} = \frac{\varepsilon_h}{\varepsilon_{yh}} \tag{5-1}$$

where, $0.8l_w$ = effective depth of the web region; and ε_{yh} = yield strain of shear reinforcement. **Fig. 5-17** shows the maximum horizontal elongation ratio $\alpha_{h,max}$, according to the mechanical (vertical) steel ratio $\rho_s F_y/f_c'$ (ρ_s = area ratio of overall vertical steel sections to gross wall section, which is close to boundary steel ratio to gross wall section). In **Fig. 5-17**(a), the data points are classified as the mechanical shear reinforcement ratio. In **Fig. 5-17**(b), the data points are classified as the aspect ratio of walls. In these two figures, the calculated $\alpha_{h,max}$ range 0.60 – 4.51, which indicates that $\alpha_{h,max}$ is highly dependent on the design parameters. However, there are no clear trends according to $\rho_s F_y/f_c'$; the horizontal elongation is independent of the boundary steel area. This result is probably due to the following two opposing effects: 1) in view of relative stiffness, the increase of the boundary steel area is expected to decrease the shear strength contribution of shear reinforcement and subsequent horizontal elongation. However, 2) the increase of boundary steel area alleviates the damage of concrete by restraining shear cracking, which increases the shear demand on the web region and subsequent horizontal elongation.

Table 5-1 Design parameters of test specimens for parametric analysis

Specimen	l_s/l_w	ρ_{be}	$\frac{\rho_s F_y}{f_c'}$	t_w [mm]	f_c' [MPa]	ρ_h	$\frac{\rho_h f_{yh}}{f_c'}$	V_{pre} [kN]
E1	2.64	5.1%	0.48	300	64.3	0.40%	0.028	2,424
E2	2.64	5.1%	0.48	300	64.3	0.60%	0.042	2,656
E3	2.64	5.1%	0.48	300	64.3	0.80%	0.056	2,916
E4	2.64	5.1%	0.48	300	64.3	1.02%	0.070	3,089
E5	2.64	7.9%	0.73	300	64.3	0.40%	0.028	2,831
E6	2.64	7.9%	0.73	300	64.3	0.60%	0.042	3,116
E7	2.64	7.9%	0.73	300	64.3	0.80%	0.056	3,475
E8	2.64	7.9%	0.73	300	64.3	1.02%	0.070	3,814
E9	2.16	6.6%	0.53	200	54.9	0.40%	0.032	1,651
E10	2.16	6.6%	0.53	200	54.9	0.60%	0.049	1,787
E11	2.16	6.6%	0.53	200	54.9	0.79%	0.064	1,864
E12	2.16	6.6%	0.53	200	54.9	1.01%	0.082	1,926
E13	2.16	10.0%	0.81	200	54.9	0.40%	0.032	2,086
E14	2.16	10.0%	0.81	200	54.9	0.60%	0.049	2,122
E15	2.16	10.0%	0.81	200	54.9	0.79%	0.064	2,195
E16	2.16	10.0%	0.81	200	54.9	1.01%	0.082	2,302
E17	1.66	6.6%	0.52	200	55.7	0.40%	0.032	2,048
E18	1.66	6.6%	0.52	200	55.7	0.60%	0.048	2,116
E19	1.66	6.6%	0.52	200	55.7	0.79%	0.063	2,249
E20	1.66	6.6%	0.52	200	55.7	1.01%	0.081	2,460
E21	1.66	10.0%	0.80	200	55.7	0.40%	0.032	2,518
E22	1.66	10.0%	0.80	200	55.7	0.60%	0.048	2,620
E23	1.66	10.0%	0.80	200	55.7	0.79%	0.063	2,768
E24	1.66	10.0%	0.80	200	55.7	1.01%	0.081	2,904
E25	1.16	6.6%	0.52	200	55.7	0.40%	0.032	2,775
E26	1.16	6.6%	0.52	200	55.7	0.60%	0.048	2,784
E27	1.16	6.6%	0.52	200	55.7	0.79%	0.063	2,845
E28	1.16	6.6%	0.52	200	55.7	1.01%	0.081	2,951

Note: Steel U-section used for parametric analysis: U-300×300×16×16 for E1 to E4; U-300×300×25×25 for E5 to E8; U-200×320×12×16 for E9 to E12; U-200×320×20×20 for E13 to E16; U-200×320×12×16 for E17 to E20; U-200×320×20×20 for E21 to E24; and U-200×320×12×16 for E25 to E28.

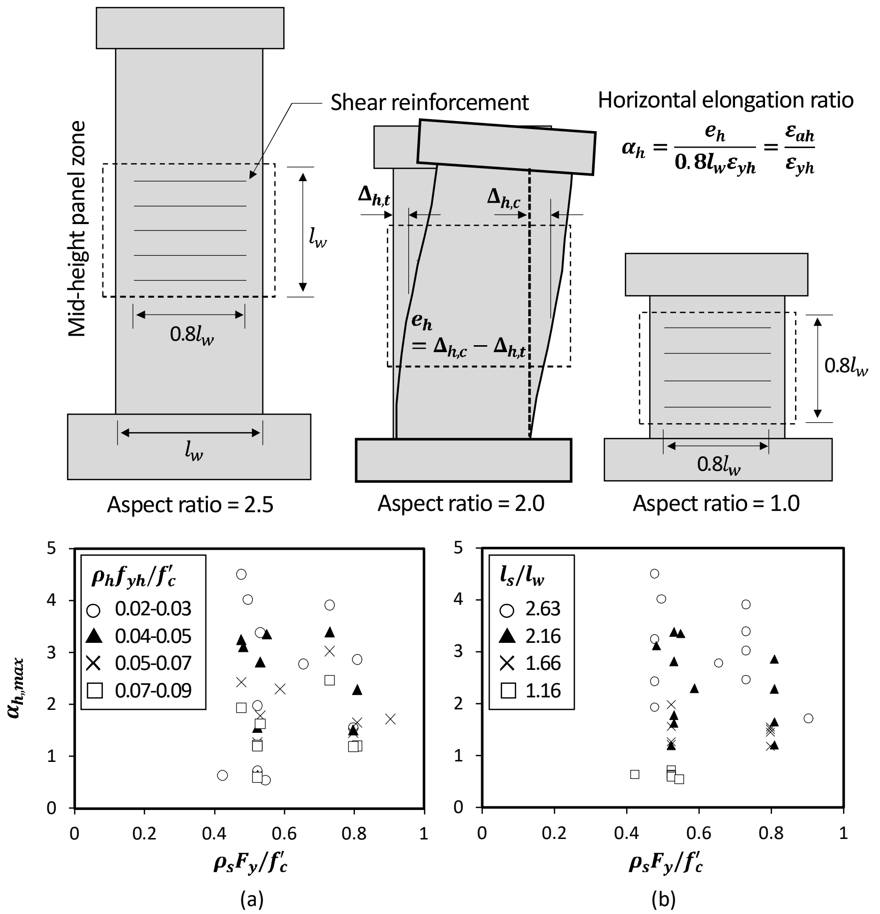

Fig. 5-17 Maximum horizontal elongation ratio according to mechanical steel ratio.

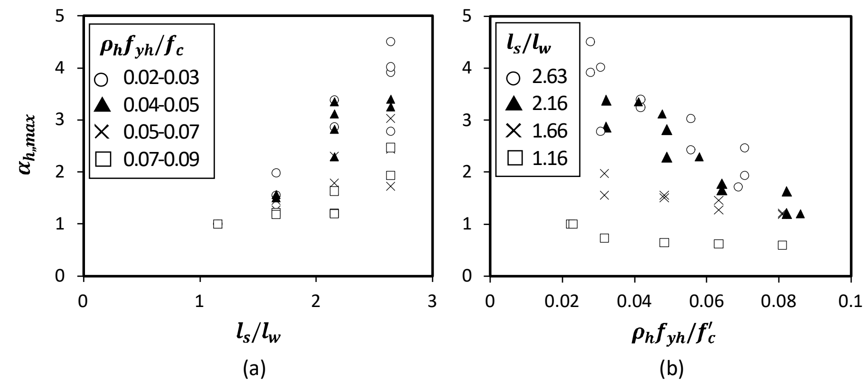

Fig. 5-18 Maximum horizontal elongation ratio according to (a) shear span ratio; and (b) mechanical shear reinforcement ratio.

Fig. 5-18(a) and (b) show the maximum horizontal elongation ratio $\alpha_{h,max}$, according to the shear span ratio l_s/l_w and mechanical shear reinforcement ratio $\rho_h f_{yh}/f_c'$, respectively. In general, the calculated $\alpha_{h,max}$ increases in proportion to the shear span ratio. This result is consistent with the theoretical knowledge that the truss action of shear reinforcement increases as the shear span ratio increases (i.e., beam action). On the other hand, as expected, the maximum horizontal elongation decreases as the mechanical shear reinforcement ratio increases, particularly in the walls with large shear span ratio. Based on these results, the simplified relationship for $\alpha_{h,max}$ is suggested by regression analysis, as follows:

$$\frac{1}{\alpha_{h,max}} = -0.42 + \frac{1.2}{(l_s/l_w)} + 5.5\left(\frac{\rho_h f_{yh}}{f_c'}\right) \geq 0.2 \qquad (5\text{-}2)$$

Fig. 5-19 compares the calculated $\alpha_{h,max}$ with the values from the FE analysis. Eq. (19) provides a reasonable estimate of horizontal elongation. Note that this equation is provided to develop the shear (web crushing) strength model of SUB-C walls. In **Fig. 5-20**, although some predictions of $1/\alpha_{h,max}$ are slightly less than those of FE analysis, this will produce a conservative estimate of web crushing strength (lower $1/\alpha_{h,max}$ indicates greater horizontal elongation).

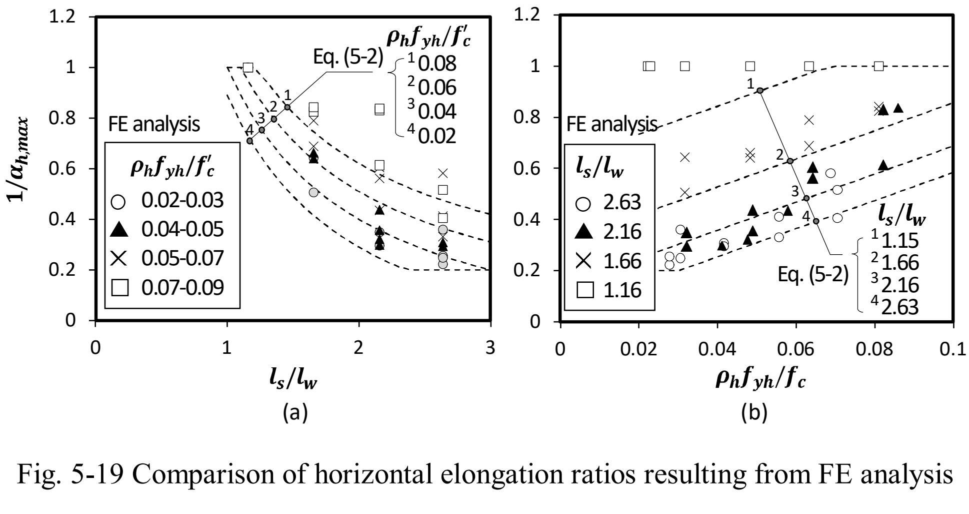

Fig. 5-19 Comparison of horizontal elongation ratios resulting from FE analysis and proposed simplified model of Eq. (5-2) (Ver.1).

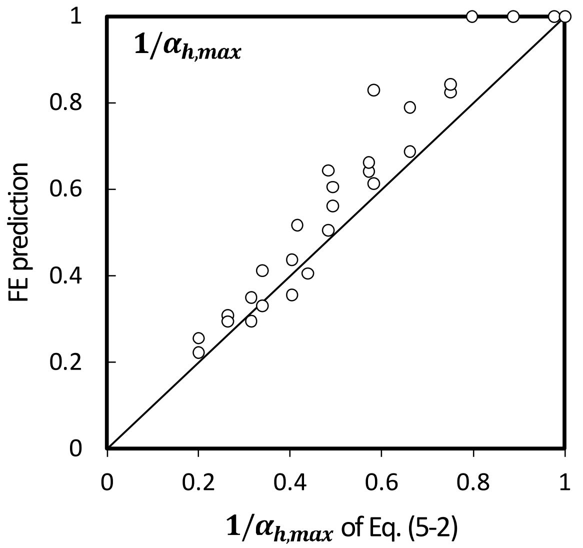

Fig. 5-20 Comparison of horizontal elongation ratios resulting from FE analysis and proposed simplified model of Eq. (5-2) (Ver.2).

5.6 Summary

In this chapter, nonlinear FE analysis was performed to investigate the elastic shear behavior of SUB-C walls. The major findings drawn are as follows:

1) The FE analysis confirms that the web crushing before flexural yielding is primarily due to the large horizontal tensile deformation (i.e., horizontal elongation) in the mid-height panel zone. In the lower panel zone, the horizontal elongation decreased due to the steel U-section with high stiffness.

2) The FE analysis confirms that diagonal tension failure is prevented as the steel U-sections protect the boundary zone. Thus, the shear strength is increased until web crushing occurs. Here, the increase in shear strength is attributed to the shear strength contribution of the steel U-sections and the increased contribution of concrete.

3) For various design parameters (mechanical shear reinforcement ratio, mechanical vertical steel ratio, and aspect ratio), the contribution of boundary steel U-sections (calculated for the wall cross section) to the web crushing strength ranges 10%–23%. That is, the shear contribution ratio of the steel U-section is much less than that of the RC wall, and its variation is not significant.

4) From the parametric analysis, the maximum horizontal elongation at web crushing is equivalent to 0.6–4.5 times the yield strain of horizontal reinforcement. The maximum horizontal elongation increases in proportion to the wall aspect ratio and inversely proportional to mechanical shear reinforcement ratio. However, it is almost independent of the boundary steel area. From the regression analysis, an empirical equation to predict the maximum horizontal elongation was proposed. In general, the calculated horizontal elongation agrees with the prediction of FE analysis.

Chapter 6. Development of Shear Strength Model

6.1 Overview

In the present study, the shear strength model for SUB-C walls was developed modifying the traditional truss analogy, since shear failure was basically determined from crushing of web concrete, rather than from damage of the composite boundary zone. For failure criteria, two distinct compression failure modes were considered: 1) elastic web crushing failure; and 2) inelastic web crushing failure. The possibility of diagonal tension failure and shear sliding failure was neglected due to the presence of boundary steel U-sections. For both mechanisms, the compressive strength of diagonal struts was defined as a function of shear deformation, based on the existing model of Oesterle et al. (1984). For the elastic web crushing mechanism, the model improvement was achieved by considering the effect of the horizontal elongation on the shear deformation. For the inelastic web crushing mechanism, the relationship between overall wall deformation (i.e., lateral drift ratio) and local shear deformation in the plastic hinge zone was developed based on the longitudinal elongation mechanism (Eom and Park 2010), so that the web crushing strength was defined as a function of deformation demand. In particular, in the large elastic deformation, the boundary steel U-sections provided shear resistance by frame action. Thus, the shear strength contribution of the steel U-sections was included in the inelastic web crushing strength, considering the axial–flexural capacity the steel U-section. For verification, the shear strengths predicted by the proposed model were compared with the test results.

6.2 Background

6.2.1 Web crushing capacity

A reinforced concrete panel subjected to pure shear shows parallel shear cracking in the diagonal direction, forming diagonal concrete struts between shear cracks. For wall elements, due to the presence of axial stresses, the diagonal crack angle tends to be greater than 45 degrees from the horizontal. The shear force is then transferred through the truss action of the diagonal struts and transverse ties (shear reinforcement). Web crushing, or diagonal compression failure, occurs when the shear demand reaches the compressive strength of the strut. However, when light reinforcement is used, diagonal tension failure precedes web crushing, due to early yielding of shear reinforcement and subsequent sliding between shear cracks (i.e., shear yielding). For heavily reinforced walls, web crushing may occur before flexural yielding, without tensile yielding of shear reinforcement. Such failure mechanism is referred to as an "elastic web crushing failure". RC walls that fail in such kind of mechanism have very limited deformation capacity. Thus, current design methods restrict elastic web crushing failures by providing requirements on the configuration of shear reinforcement and thus limit the nominal shear strength of walls by diagonal tension failure. The design provision of ACI 318 (2019) provides the maximum shear strength corresponding to elastic web crushing failure, based on the following assumptions:

1) Web crushing strength is independent of deformation demand.

2) Web crushing strength is proportional to concrete tensile strength $\sqrt{f_c'}$.

3) Web crushing strength depends on average shear stresses.

On the other hand, work in the 1970s through early 1990s emphasizes the possibility of web crushing failure under inelastic deformation, based on the test results on thin-webbed walls with flanged and barbell cross sections. Further, contrary to the assumption of average stresses on a shear section, plastic flexural strains force the diagonal struts within the plastic hinge zone to realign so that they all converge near the base of the boundary compression zone. Such fanning crack pattern results in the formation of a relatively small region subjected to higher compressive stresses, where web crushing tends to occur (refer to **Fig. 6-1**). For these reasons, researchers define the strength of the critical diagonal strut within the plastic hinge zone as a function of effective compressive strength (kf_c') of concrete. Due to its dependence on inelastic deformation, the effective concrete strut strength is generally defined as a function of deformation demand (Oesterle et al. 1984; Paulay and Priestley 1992; Hines and Seible 2004; and Eom and Park 2013). This web crushing failure mechanism is referred to as an "Inelastic web crushing failure", which is distinguished from elastic web crushing mechanism. The strength corresponding to inelastic web crushing failure is generally lower than that for elastic web crushing failure, because the inelastic web crushing basically entails greater shear deformation due to post-yield ductile behavior.

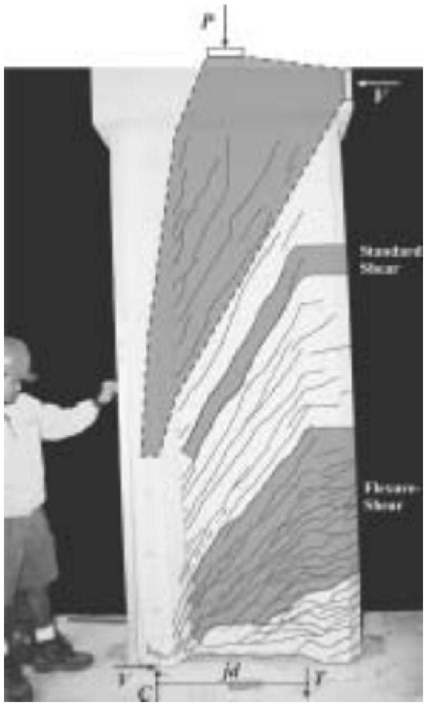

Fig. 6-1 Web crushing load paths (Hines and Seible 2004).

For composite walls with steel boundary elements (without steel plates in the web region), there have been few studies on the web crushing behavior, because the research trends for composite walls have more focused on ductile flexural behavior, by preventing premature shear failure. Nevertheless, in the past experimental tests, a few composite wall specimens showed web crushing in the plastic hinge zone after ductile behavior (e.g., Specimen SWT4 in Zhang et al. 2021). Further, the experimental studies on the proposed composite walls with steel U-section boundary elements reported that the inelastic deformation capacity of the walls was limited by the post-yield web crushing failure in the plastic hinge zone (Kim and Park, 2022). Here, the shear cracking patterns in the wall web, consisting of parallel cracking in elastic zone and fan-shape cracking in plastic hinge zone, were similar to those of conventional RC walls. This result implies that, despite the use of steel boundary elements, web crushing may occur in the elastic and plastic hinge zones because the majority of shear is transferred through the concrete in the wall web. In other words, web crushing can be an important limit to determine the lateral load-carrying capacity and deformation capacity of composite walls. Intuitively, the shear design only based on the contribution of reinforced concrete webs may be a conservative solution. Nevertheless, the lack of studies on the web crushing behavior hinders the possible efficient design of composite walls limited by web crushing failure. In view of this, the present study includes closer observation of the existing test results on the proposed composite walls and development of analytical models to predict the shear strengths corresponding to elastic and inelastic web crushing failures.

6.2.2 Observed web crushing behavior

Fig. 6-2(a–c) shows the shear cracking patterns and failure mode of the tested SUB-C walls that failed in web crushing before flexural yielding (shear failure-mode specimens). In the figure, for comparison, the results of the counterpart RC wall specimens were also presented. In the RC specimens, the diagonal shear cracking was prevalent in the wall web, while horizontal flexural cracking appeared along the wall boundaries. The shear cracks were aligned almost parallel along the wall height. However, at the wall bottom, the cracks showed a pattern of converging into the boundary compression zone subjected to higher stresses. Thus, diagonal tension failure occurred immediately after the crushing of boundary concrete, followed by spalling and crushing of the web concrete. Note that this cracking pattern differs from the typical fanning crack pattern shown in the ductile walls subjected to large flexural tensile strain.

In the SUB-C walls, on the other hand, parallel shear cracking was more uniform along the wall height, as the boundary steel U-sections restrained cracking in the boundary zone. Further, web crushing occurred primarily at the mid-height of the walls, where horizontal elongation was concentrated. The horizontal elongation mechanism can be understood by the simplified truss model as shown in **Fig. 6-2**(d): As the boundary steel U-sections resist shear transferred from diagonal struts, diagonal tension failure is prevented even after significant yielding of horizontal reinforcement, but large post-yield tensile deformation is developed at the mid-height of walls. Such horizontal elongation may decrease the effective compressive strength of diagonal struts by increasing diagonal tensile cracking. Thus, the possibility of web crushing highly increases in the mid-height of the walls subjected to large horizontal elongation. Note that the web crushing mechanism shown in the shear failure-mode composite specimens entails early yielding of shear reinforcement, which does not belong to the typical elastic web crushing mechanism of RC walls.

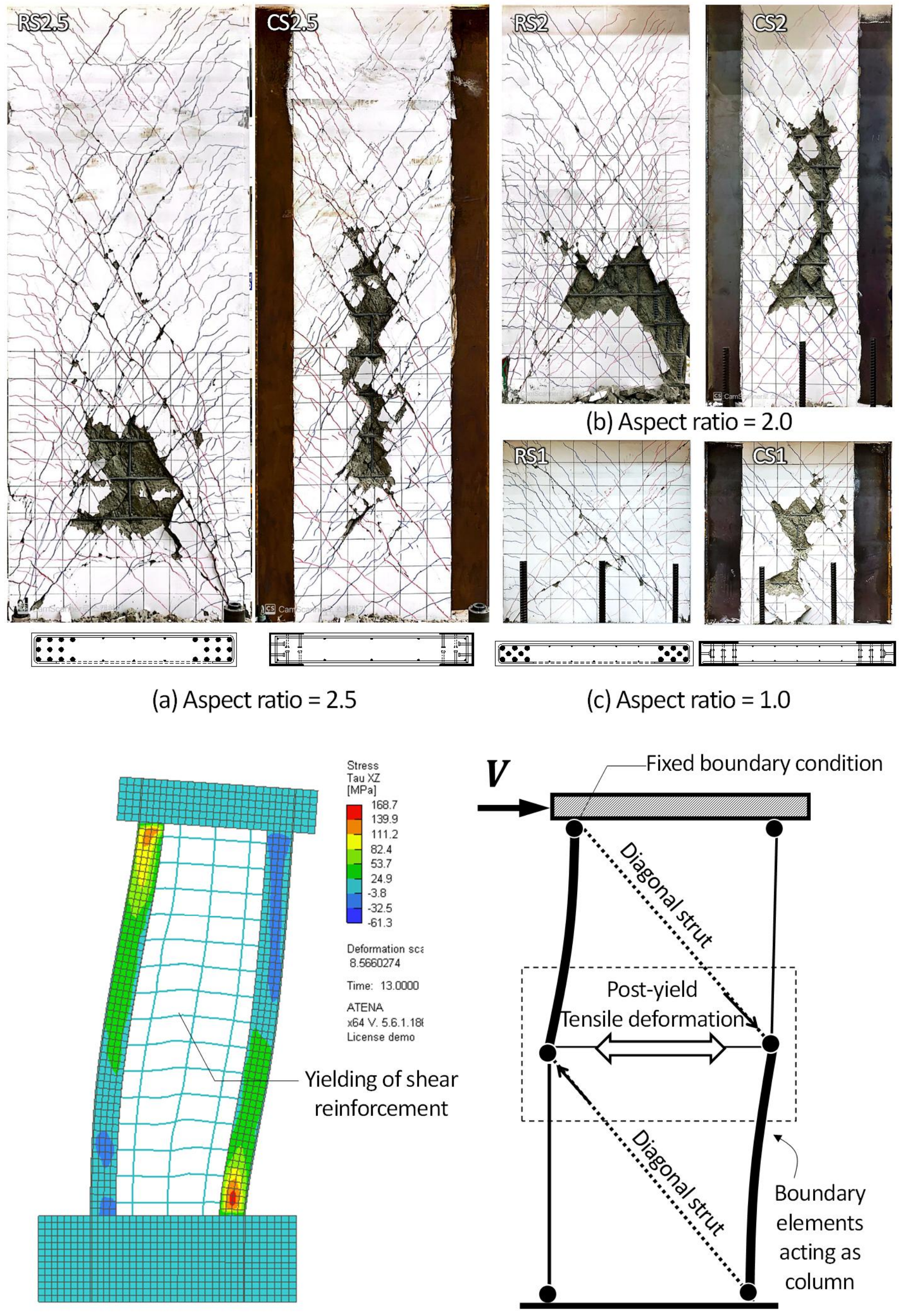

Fig. 6-2 Elastic web crushing mode and horizontal elongation mechanism.

Nevertheless, such web crushing mechanism is still named “elastic web crushing mechanism”, in the aspect that the web crushing occurs before flexural yielding of walls and that the wall deformation at the web crushing is not significant (almost in elastic range). Similar web crushing pattern was also seen in the SUB-C walls with steel plate beams, except that the number of shear cracks significantly decreased due to the relatively large spacing of the steel plate beams. For the SUB-C walls with steel web plates, due to the high stiffness and strength of the web plates, the web crushing failure mode was not affected by the horizontal elongation mechanism.

In the SUB-C walls that experienced flexural yielding (with conventional shear rebars, **Fig. 6-3**), before flexural yielding, the shear cracking pattern was almost the same as shown in the shear failure-mode specimens. However, after flexural yielding, more cracks appeared in the plastic hinge zone, while no longer cracking occurred in the above the plastic hinge zone (i.e., elastic zone). The inelastic struts with fanning crack patterns were formed in the plastic hinge zone, showing fairly flat cracks near the wall bottom and much steeper cracks at the top. However, the fan-shaped cracking is less severe than in the ordinary RC walls, because the boundary steel U-sections provide an alternate load-path for shear transfer. As the inelastic deformation in the plastic hinge zone increased, the strength of the inelastic struts was significantly degraded with crushing and spalling of the web concrete. Such inelastic web crushing mechanism was pronounced due to cyclic loading and low compressive force: longitudinal elongation occurs due to cumulative plastic deformation of flexural reinforcement, which in turn causes extensive crack opening, crack misalignment, stress concentration and crushing of the inelastic struts. Despite the longitudinal elongation, the inelastic web crushing occurred only in the web region, as the boundary steel U-sections effectively confined the boundary zone.

On the other hand, in the SUB-C walls with steel plate beams, overall cracking was restrained due to the absence of web reinforcement (a crack occurs due to bond stresses developed by tensile rebars), forming thicker struts for the entire web region. For this reason, the fanning crack pattern was not clearly seen in the plastic hinge zone. Nevertheless, the inelastic web crushing failure mode was similar to that of the SUB-C walls without steel plate beams.

As the inelastic struts degraded, the boundary steel U-sections within the plastic hinge zone resisted shear by frame action (i.e., short column effect), showing double-curvature flexural deformation (see **Fig. 3-11**). This result indicates that the steel U-sections contributed to the inelastic shear capacity of the plastic hinge zone. Thus, for better prediction of the inelastic web crushing strength, the shear contribution of the steel U-sections should be considered.


(a) Aspect ratio = 2.5 and conventional shear reinforcement
(b) Aspect ratio = 2.0 and conventional shear reinforcement
(c) Aspect ratio = 2.0 and steel plate beams

Fig. 6-3 Inelastic web crushing mode of tested SUB-C walls.

6.3 Modified Truss Analogy

The truss model not only provides practical simplicity but also physical rigor, particularly for explaining the shear transfer mechanism of RC web walls with boundary elements: boundary (flexure) compression chord, boundary (flexure) tension chord, horizontal ties, and diagonal strut. As illustrated in **Fig. 6-4**, the shear strength model for SUB-C walls was developed based on the traditional truss analogy, and shear resistance of boundary steel U-sections was incorporated into the truss model by considering the compression and tension chords as beam-column elements. That is, the shear strength of SUB-C walls is provided by the steel U-sections, in addition to the contributions of reinforced concrete. Since the present study is primarily concerned with web crushing, a failure criterion was determined from the compressive strength of diagonal concrete struts.

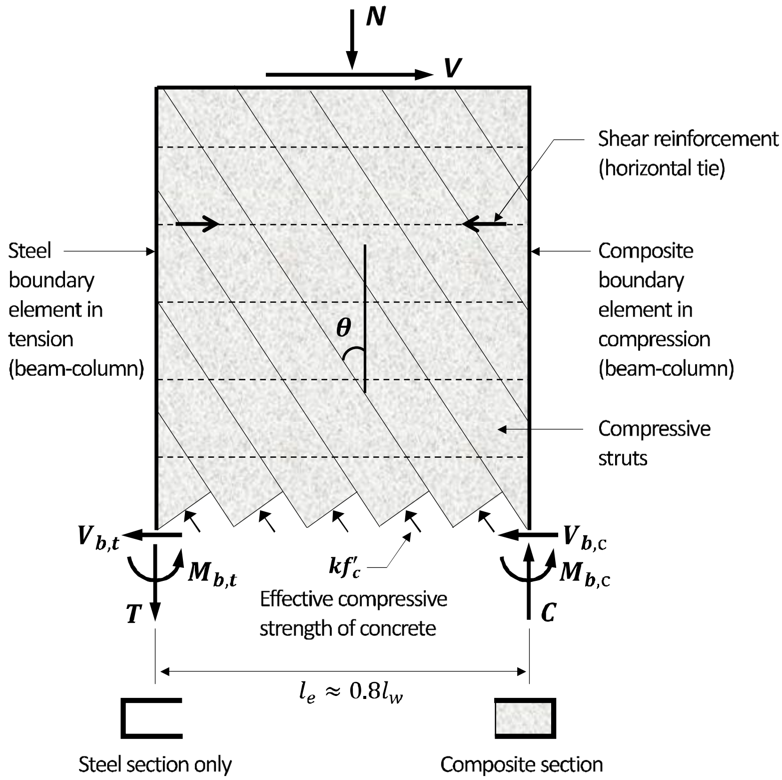

Fig. 6-4 Modified truss model with boundary beam elements

From equilibrium, the shear strength V_n of SUB-C walls is calculated as follows:

$$V_n = V_{wc} + V_b \tag{6-1}$$

Where,

$$\frac{V_{wc}}{t_w l_e} = v_{wc} = k f_c' \cos\theta \sin\theta \tag{6-2}$$

$$V_b = V_{b,t} + V_{b,c} \tag{6-3}$$

where, V_{wc} = shear strength contributed by diagonal concrete struts; V_b = shear strength contributed by boundary steel U-sections; l_e = effective shear depth, which is approximately defined as $0.8l_e$; k = effective average strength factor for concrete; θ = inclination angle of diagonal struts with respect to vertical axis of walls; and $V_{b,t}$ and $V_{b,c}$ = shear strength contributions of the steel U-sections in flexural tension and compression zones, respectively.

6.4 Elastic Web Crushing Strength

6.4.1 Model assumptions

In the FE analysis, it is revealed that the shear stresses on concrete are concentrated along the macro diagonal strut formed in the upper panel zone of walls (**Fig. 5-5**). Nevertheless, in the present study, the web crushing strength is defined in terms of average shear stresses, to be consistent with current design approaches (Eurocode 2, 2004; fib MC, 2010). For the shear strength model controlled by elastic web crushing, the following assumptions are used:

1) Parallel shear cracking appears in the entire web region; θ is constant.

2) Web crushing occurs in the mid-height panel zone where horizontal elongation is maximized.

3) Shear strength contribution V_b of steel U-sections is neglected; $V_n = V_{wc}$.

4) The elastic web crushing strength is independent of deformation demand.

5) The steel U-sections are strong enough to remain elastic at web crushing.

From the experimental tests and FE analysis, the first two assumptions are quite obvious. The third assumption reflects the facts that the shear strength contribution of steel U-sections (< 25% of overall shear strength V) is much less than that of RC components, and the variation of the shear contribution ratio V_b / V depending on the design parameters is insignificant. Further, in order to estimate V_b, refined calculations of force demands on the steel U-sections are required, and, generally, iterative procedures dealing with nonlinearities resulting from early yielding of shear reinforcement are required, which is undesirable for practical design. More importantly, Regarding the fourth assumption, it is assumed that, when large deformation demand is required due to flexural yielding, the elastic web crushing mechanism is restrained, and is transformed to the inelastic web crushing mechanism. This is because, after flexural yielding, shear degradation is attracted primarily in the plastic hinge zone. In the tests, by using the large-sized steel U-sections, the damage of the boundary zone was fairly restrained, thus preventing diagonal tension failure. However, if a weaker steel U-section is used, local yielding or fracture of the steel plates may occur, which leads to crushing of the boundary concrete and subsequent premature shear failure, such as diagonal tension failure. In particular, the wall strength may be limited by flexural yielding. Thus, the elastic web crushing strength is only valid when the damage of steel U-sections is insignificant, which is accounted in the last assumption.

6.4.2 Shear degradation of concrete

Oesterle et al. (1984) proposed the effective average strength factor k as a function of shear distortion γ_m (see Eq. 2-34). However, their suggestion for k was based on the test results of thin-webbed RC walls with flanged or barbell cross sections (Kuyt 1972; Collins 1978; Oesterle et al. 1979; and Oesterle et al. 1984). Thus, based on the present test results, the relationship for k was modified as:

$$k = \frac{2}{1 + \frac{1.5\gamma_m}{\varepsilon_o}} \le 0.35 \qquad (6\text{-}4)$$

where, γ_m = maximum average shear distortion measured within the mid-height panel zone; and ε_o = axial strain at peak compressive stress f_c' of concrete, which is defined approximately according to Foster and Gilbert (1996) (= 0.002 + 0.001(f_c' – 20)/80).

Table 6-1 shows the measured k, γ_m, and ε_o values for the wall specimens including the present composite wall specimens. For the proposed walls that failed in elastic web crushing (shear failure-mode specimens), neglecting the contribution of steel U-sections, k values were calculated by Eq. (6-2), using the tested peak wall strengths ($V_n = V_{wc} = V_{test}$) and $\cos\theta \sin\theta \approx 0.45$. Thus, the actual contribution of steel U-sections was incorporated in the calculation of k.

Fig. 6-5 shows the relationship between the k values and normalized shear distortions (= γ_m/ε_o) for the wall specimens. For the shear failure-mode SUB-C specimens, the test data correlated well with the proposed prediction of Eq. (6-4), but was slightly less than the original prediction of Eq. (2-34). This is probably because in RC walls with large boundary elements (flange walls and barbell columns) relative to the thin web, a shear force was more attracted in the boundary elements, and this was reflected in the calculation of k; the k values were calculated based on the large shear strength and small web area, which resulted in larger k. On the other hand, in the proposed walls with rectangular cross section, the shear stiffness of the web region is much greater than that of steel U-sections. Thus, the contribution of steel U-sections to the shear strength was relatively limited, which resulted in smaller k. The shear distortion levels (γ_m/ε_o = 3.3 – 6.5) for the SUB-C specimens are greater than those for the existing RC squat walls (aspect ratio $\leq$ 1.0) that failed in elastic web crushing. However, the γ_m/ε_o values do not reach those for the existing RC slender walls (aspect ratio $\geq$ 2.0) that failed in inelastic web crushing. The result indicates that the horizontal elongation increased the shear distortion, but its effect on shear distortion was not enough to cause inelastic web crushing. Further, in the shear distortion range of the proposed walls, no test data for the RC walls is plotted, indicating that the elastic web crushing mechanism with horizontal elongation is unique for SUB-C walls. Due to the lack of test data, the maximum of k for Eq. (6-4) is limited to 0.35. The results on the SUB-C walls that failed in inelastic web crushing (flexural yielding specimens) are discussed in Section 6.5.

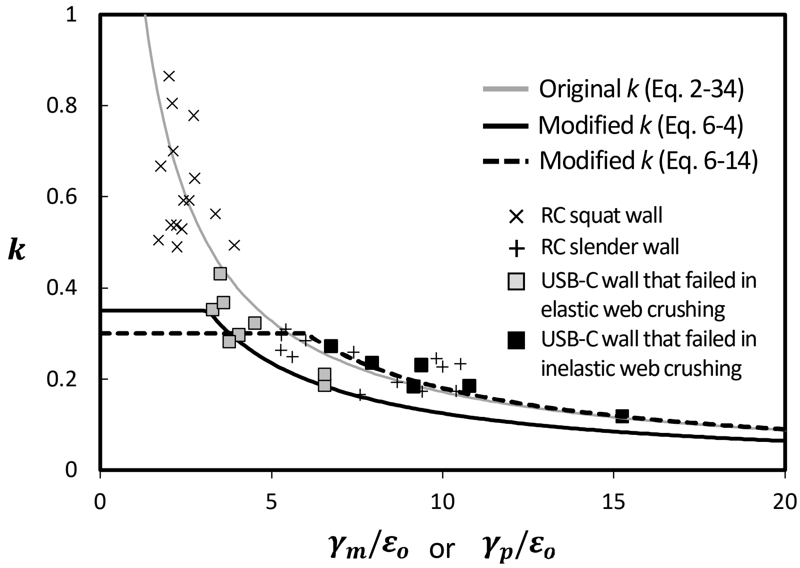

Fig. 6-5 Effective strength factor versus normalized shear distortion relationship.

Table 6-1 Tested effective average strength factor and maximum shear distortion

Oesterle et al. (1984)				Present study			
Specimen	k	γ_m [rad]	ε_o [mm/mm]	Specimen	k	γ_m [rad]	ε_o [mm/mm]
B2	0.16	0.028	0.003	CF2.5VH	0.12	0.039	0.0026
B5	0.22	0.026	0.0026	CS2.5	0.19	0.017	0.0026
B5R	0.23	0.027	0.0026	CS2.5VH	0.21	0.017	0.0026
B6	0.49	0.009	0.0022	CS2.5M	0.32	0.012	0.0026
B7	0.26	0.014	0.0022	CF2	0.18	0.022	0.0024
B8	0.3	0.014	0.0027	CF2SB	0.19	0.025	0.0023
B9	0.29	0.014	0.0027	CF2VH	0.24	0.018	0.0023
B9R	0.16	0.02	0.0026	CF2SC	0.23	0.022	0.0024
B11	0.17	0.027	0.0026	CS2TH	0.27	0.017	0.0024
B11R	0.23	0.025	0.0025	CS2	0.30	0.010	0.0024
B12	0.25	0.019	0.0026	CS2VL	0.28	0.009	0.0023
F1	0.28	0.016	0.0027	CS2SB	0.35	0.008	0.0024
F2	0.25	0.015	0.0027	CS1R	0.43	0.009	0.0024
F3	0.19	0.021	0.0024	CS1VL	0.37	0.009	0.0024

6.4.3 Strain compatibility

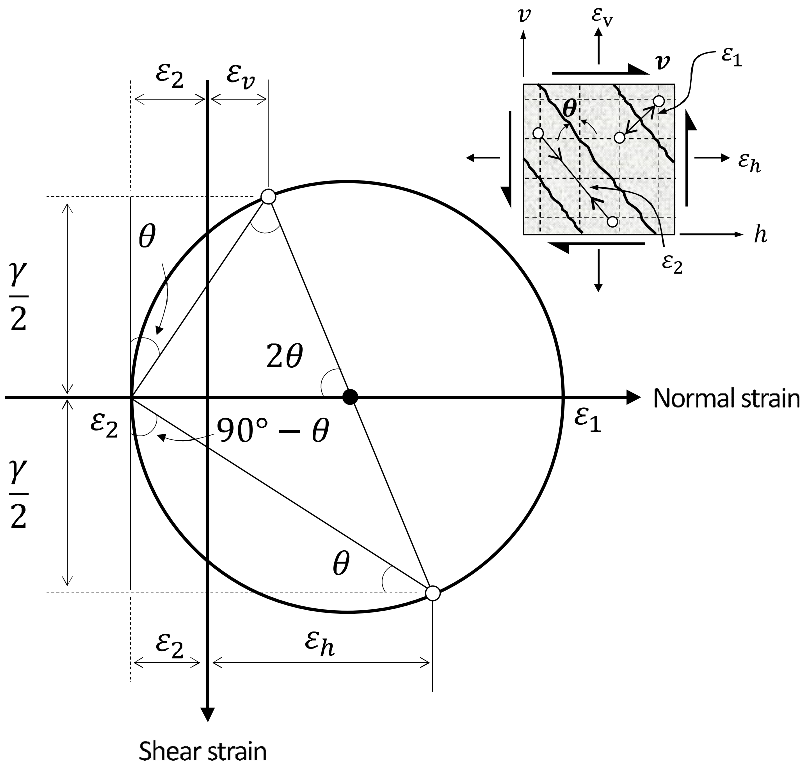

Fig. 6-6 Mohr circle for strain in wall web.

From the Mohr circle for strain, the shear distortion in a wall panel is defined as follows (**Fig. 6-6**):

$$\gamma = 2(\varepsilon_h + \varepsilon_2)\tan\theta \tag{6-5}$$

Where,

$$\tan\theta = \sqrt{\frac{\varepsilon_v + \varepsilon_2}{\varepsilon_h + \varepsilon_2}} \tag{6-6}$$

where, ε_h and ε_v = average strains in the horizontal and vertical axes of walls, respectively (> 0 for tension); and ε_2 = principal compressive strain (> 0 for compression). Since flexural yielding is restrained at elastic web crushing, the average vertical strain is assumed to be ε_v = 0.00125, which corresponds to half the yield strain for a steel material with F_y = 500 MPa (fib MC 2010). When web crushing occurs, $\varepsilon_2 = \varepsilon_o$, which is approximately 0.0025 for normal-strength concrete. Further, the average horizontal strain is equivalent to the maximum horizontal elongation measured in shear reinforcement within the mid-height panel zone. Thus, $\varepsilon_h = \varepsilon_{h,max}$, which is calculated as follows:

$$\varepsilon_{h,max} = \alpha_{h,max}\varepsilon_{yh} \tag{6-7}$$

where, the maximum horizontal elongation ratio $\alpha_{h,max}$ is calculated according to Eq. (5-2). Note that Eq. (5-2) was derived based on FE analysis, not on the test results. In the tests, only a single gauge per shear reinforcing bar was used, so that the average horizontal strain along the entire bar length could not be properly measured.

Therefore, from Eq. (6-7), $\varepsilon_v \approx 0.00125$, and $\varepsilon_o \approx 0.0025$, Eq. (6-5) and (6-6) can be defined as a function of $\varepsilon_{h,max}$, respectively.

$$\gamma_m = 2(\varepsilon_{h,max} + 0.0025)\sqrt{\frac{0.00125 + 0.0025}{\varepsilon_{h,max} + 0.0025}} \tag{6-8}$$

$$\tan\theta = \sqrt{\frac{0.00125 + 0.0025}{\varepsilon_{h,max} + 0.0025}} \tag{6-9}$$

The shear distortion γ in Eq. (6-5) was replaced by γ_m in Eq. (6-8) as it indicates the maximum shear distortion corresponding to elastic web crushing. **Fig. 6-7** shows the θ values calculated from Eq. (6-9), which is denoted as shaded area. The calculated θ values agree with the tested θ values measured in the mid-height of the wall specimens.

In the FE analysis, the maximum horizontal elongation ratio $\alpha_{h,max}$ ranged

1.0 – 5.0. For reinforcing bars with f_y = 400 MPa, ε_{yh} is approximately 0.002. Thus, $\varepsilon_{h,max}$ varies between 0.002 and 0.01. Within the available range of $\varepsilon_{h,max}$, Eq. (6-8) is simplified as follows:

In the FE analysis, the maximum horizontal elongation ratio $\alpha_{h,max}$ ranged 1.0 – 5.0. For reinforcing bars with f_y = 400 MPa, ε_{yh} is approximately 0.002. Thus, $\varepsilon_{h,max}$ varies between 0.002 and 0.01. Within the available range of $\varepsilon_{h,max}$, Eq. (6-8) is simplified as follows:

$$\gamma_m = 0.0066 + 0.74\varepsilon_{h,max} \tag{6-10}$$

Fig. 6-8 shows that Eq. (6-10) reasonably simplifies Eq. (6-8). Further, in **Fig. 6-9**, the γ_m values calculated from Eq. (6-7) and (6-10) generally agrees with the test results.

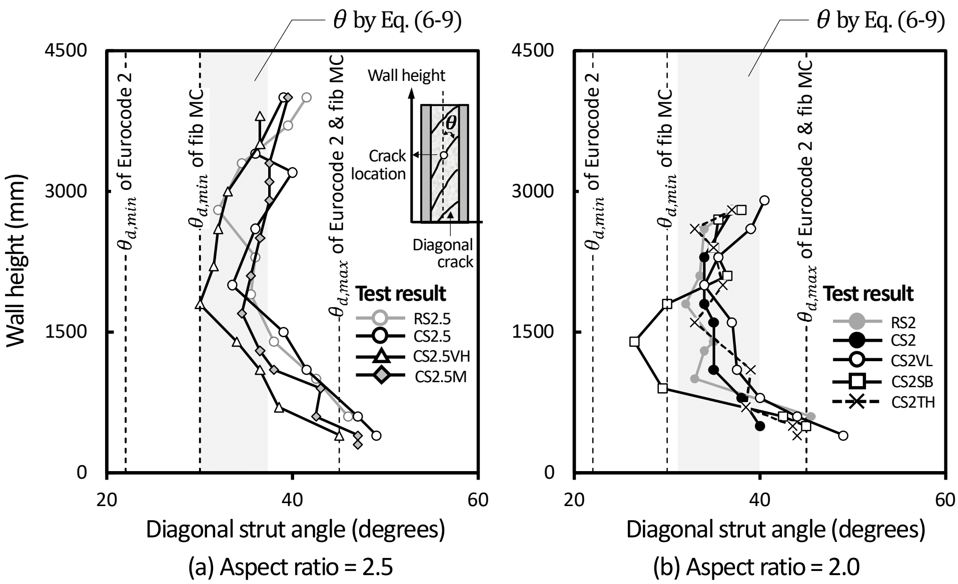

Fig. 6-7 Comparison of calculated strut angles and tested crack angle

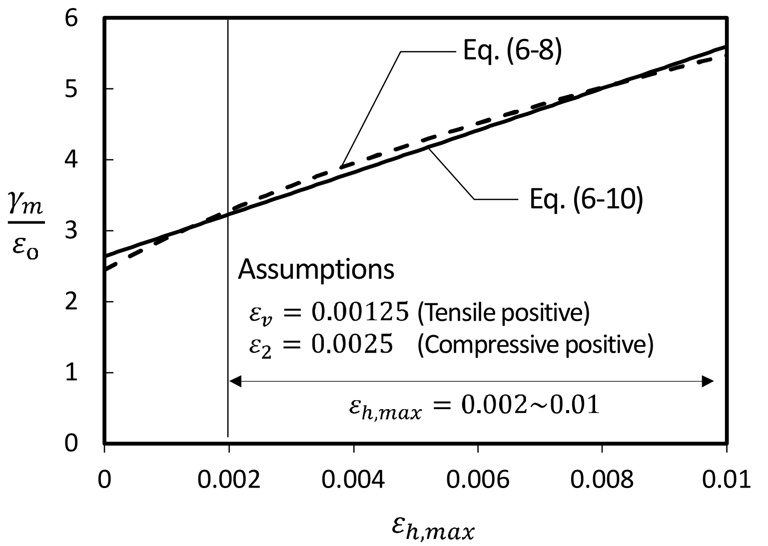

Fig. 6-8 Shear distortion- horizontal strain relationship calculated by Eq. (6-8) and Eq. (6-10).

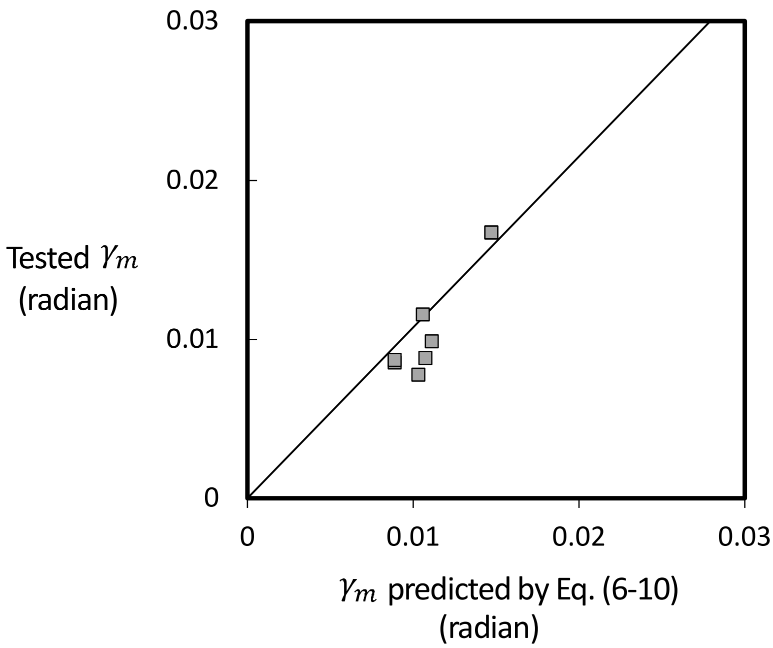

Fig. 6-9 Comparison of shear distortion calculated by Eq. (6-10) and test results.

6.4.4 Strength equation and verification

From Eq. (6-4), (6-7), (6-10), $\varepsilon_o \approx 0.0025$, and $\varepsilon_{yh} \approx 0.002$, the relationship for k is redefined as a function of the maximum horizontal elongation ratio $\alpha_{h,max}$, as follows:

$$k = \frac{2}{5 + 0.9\alpha_{h,max}} \leq 0.35 \tag{6-11}$$

Generally, it is known that the diagonal strut angle ranges from 30 to 45 degrees (fib MC, 2010), which agrees with the test results and the predictions of Eq. (6-6), as shown in **Fig. 6-7**. For the strut angles, $\cos\theta \sin\theta$ varies only between 0.43 and 0.50. Therefore, using Eq. (6-11) and assuming $\cos\theta \sin\theta \approx 0.45$, Eq. (6-2) is simplified as follows:

$$V_n = V_{wc} = \frac{0.9f_c'}{5 + 0.9\alpha_{h,max}} t_w l_e \leq 0.15 f_c' t_w l_e \tag{6-12}$$

Fig. 6-10 shows the comparison of the calculated and tested strengths (V_n versus V_{test}) for the present test specimens that failed in elastic web crushing. The figure also compares V_n with the predictions of FE analysis (V_{FE}). Table. 6-2 summarizes the values of V_n, V_{test}, and V_{FE}. In general, Eq. (6-12) reasonably predicts the elastic web crushing strength of the test specimens: The test-to-prediction ratio is V_{test}/V_n = 1.12 on average, which is less than that of JGJ 138 (2016) (V_{test}/V_n = 1.23, **Table 4-6**). However, a notable overestimation is observed in the walls with aspect ratio of 1.0 (denoted as a circle in **Fig. 6-10**). This is because, particularly in the 1.0-aspect ratio walls, the proposed Eq. (5-2) overestimates the horizontal elongation, which decreases k (see **Fig. 5-19** and **Fig. 5-20**).

To further investigate the applicability of the proposed model, the elastic web crushing strengths V_n of the example walls for the parametric FE analysis (see **Table 5-1**) were also calculated according to Eq. (6-12). **Fig. 6-11** shows the comparison of V_n and V_{FE} for the example walls. In the figure, the data points are categorized as the mechanical vertical steel ratio $\rho_s F_y/f_c'$. Overall, the proposed model safely predicted the elastic web crushing strength. Further, the prediction conservatism was more pronounced in the walls with greater boundary steel area ($\rho_s F_y/f_c' \geq 0.7$). This result indicates that the conservatism was attributed to the shear strength contribution of steel U-sections. The strength overestimation was observed only in the 2.5-aspect ratio walls with smaller boundary steel area ($\rho_s F_y/f_c' \leq 0.5$), due to early flexural yielding.

Note that the maximum horizontal elongation ratio $\alpha_{h,max}$ in Eq. (6-12) is only the function of the shear span ratio and mechanical shear reinforcement ratio. Therefore, the effect of boundary steel U-sections was not implemented in the proposed shear strength model. Instead, only the design requirement, that the steel U-sections should be strong enough to be elastic, supports the validity of the elastic web crushing strength model. Thus, Chapter 7 proposed the alternative design method to improve the strength prediction and to verify the structural safety of the steel U-sections.

Table 6-2 Elastic web crushing strength of test specimens

Specimen	Test result	Prediction		Test-to-Prediction ratio	
	V_{test} [kN]	V_{FE} [kN]	V_n of Eq. (6-12) [kN]	V_{test} / V_{FE}	V_{test} / V_n
CS2.5	2,395	2,452	2,648	0.98	0.90
CS2.5VH	2,730	2,921	2,648	0.93	1.03
CS2.5M	2,702	2,405	2,321	1.12	1.16
CS2	1,918	1,750	1,693	1.10	1.13
CS2VL	1,577	1,460	1,504	1.08	1.05
CS2SB	2,052	1,861	1,638	1.10	1.25
CS1R	3,014	2,717	2,239	1.11	1.35
CS1VL	2,375	2,412	2,179	0.98	1.09
Mean				1.05	1.12

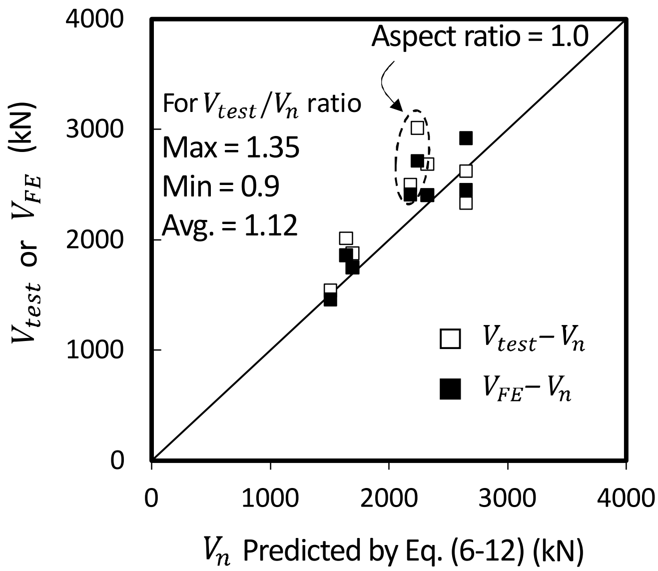

Fig. 6-10 Comparison of elastic web crushing strength for test specimens.

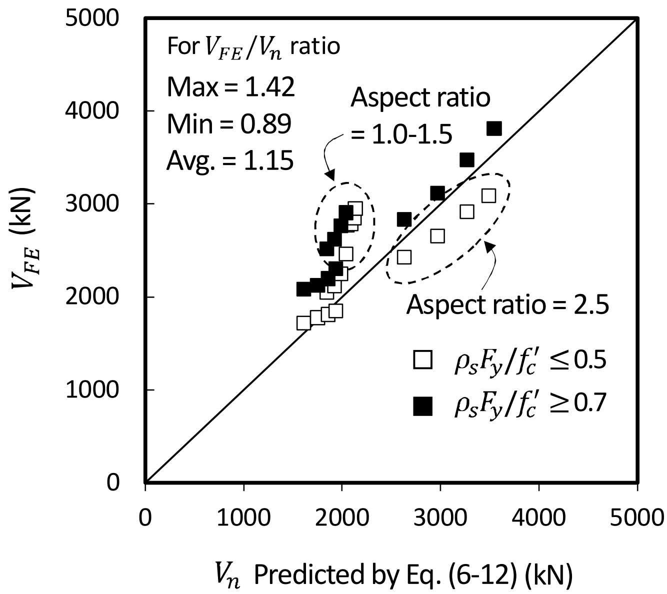

Fig. 6-11 Comparison of elastic web crushing strength for example SUB-C walls.

6.5 Inelastic Web Crushing Strength

6.5.1 Model assumptions

After flexural yielding of walls, shear failure of SUB-C walls is controlled by inelastic web crushing: the cumulative longitudinal elongation e_v occurs in the plastic hinge zone, developing fanning crack pattern and, eventually, shear degradation (**Fig. 6-12**). Further, due to the large post-yield inelastic deformation, more complex stress distribution and higher peak stresses appear in the web region. Nevertheless, the present study still adopts the concept of average shear stresses in formulating the inelastic web crushing strength model; the inelastic web crushing strength is calculated based on Eq. (6-2), which is consistent with the shear strength model controlled by elastic web crushing. The major assumptions for the inelastic web crushing model are summarized as follows:

1) Inelastic web crushing occurs after flexural yielding; yielding of the steel U-section in flexural tension.

2) Plastic hinge zone is square region, which is $l_p = l_e$ (= $0.8l_w$) and $\theta = 45$ degrees.

3) At inelastic web crushing, the web in the plastic hinge zone is completely deteriorated, developing frame action of boundary steel U-sections.

4) The inelastic web crushing strength varies with deformation demand, solely by the contribution V_{wc} of concrete; V_b is constant.

5) Symmetric wall cross section.

The first assumption is the most important for the formulation of the inelastic web crushing strength. This is because, by using the assumption, the inelastic web crushing strength and its degradation can be determined according to the longitudinal elongation and subsequent shear distortion in the plastic hinge zone. The second assumption follows the recommendation of Lee and Watanabe (2003),

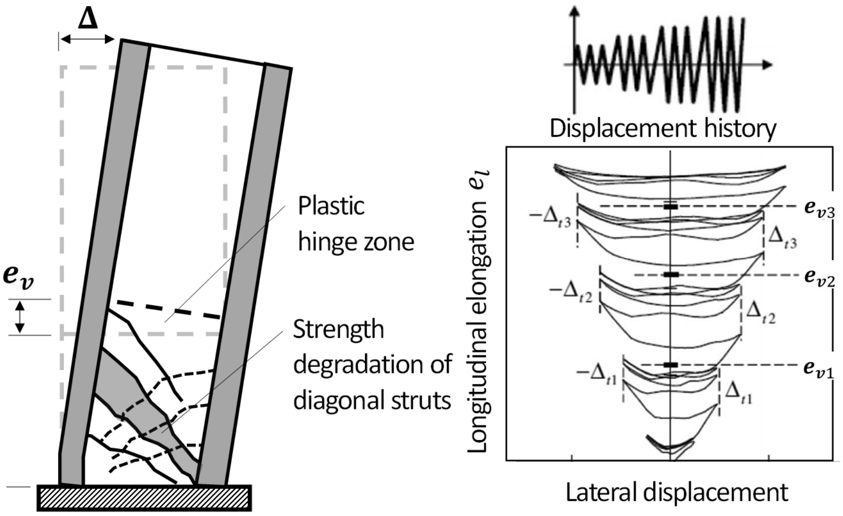

Fig. 6-12. Longitudinal Elongation Mechanism (Eom and Park, 2010).

which is originally developed for RC walls. The same plastic hinge zone length is also assumed for the proposed composite walls (to accurately estimate the actual plastic hinge zone length, further studies are required).

In the large inelastic deformation of SUB-C walls, the web concrete in the plastic hinge zone is significantly damaged, losing its strength and stiffness; the structural integrity between the web and boundary elements becomes very poor. Thus, the shear force is redistributed to the steel U-sections in proportion to the degraded strength of the diagonal strut. Here, the boundary elements within the plastic hinge zone are prone to act as a beam element fixed at the top and bottom of the plastic hinge zone, without intermediate loading on the element. That is, the steel U-sections resist shear by moment-resisting frame action, which is accounted in the third assumption.

It is generally acknowledged that the inelastic web crushing strength occurs in the walls subjected to large post-yield deformation, ultimately limiting the deformation capacity. Thus, as shown in the last assumption, the inelastic web crushing strength should be related to the deformation demand. Once it is realized, full nonlinear behavior of the proposed walls can be simulated, which improves the applicability to the performance-based seismic design (PBD). Further, it is assumed that the web crushing strength is degraded solely by the concrete, while the contribution of the steel U-sections remain constant. That is, the possibility of the steel strength reduction due to local damage or instability (e.g., local buckling) is neglected.

6.5.2 Strength degradation of concrete

Fig. 6-5 shows the effective average strength factor k measured in the wall specimens that failed in inelastic web crushing (i.e., post-yield shear failure). The k values were calculated from Eq. (6-1), (6-2), and (6-3), excluding the contribution V_b of boundary steel U-sections from the tested peak wall strength V_{test}.

$$\frac{V_{test} - V_b}{f_c' t_w l_e \cos\theta \sin\theta} = k \tag{6-13}$$

The detailed calculation of V_b is discussed in Section 6.5.7. Due to the large post-yield deformation, the maximum shear distortions γ_m are greater than those of the SUB-C specimens that failed in elastic web crushing, and are equivalent to those of the existing RC slender walls. Note that, for the existing RC walls, the k values are calculated only based on Eq. (6-2) and peak wall strengths, which indicates that the actual shear contribution of the large-sized RC boundary elements (e.g., flange or barbell) may overestimate k. Nevertheless, in the SUB-C walls, the measured k values are equivalent to those of the RC slender walls that failed in inelastic web crushing. This result indicates that, in the SUB-C walls, the shear degradation is better restrained in the same deformation levels, due to the confinement effect of the steel U-sections. Thus, for the inelastic web crushing strength, the effective average strength factor k is slightly modified from the original prediction of Eq. (2-34), as follows:

$$k = \frac{1.8}{\gamma_p / \varepsilon_o} \leq 0.3 \tag{6-14}$$

where, γ_p = average shear distortion in the plastic hinge zone.

The maximum limit for k in Eq. (6-14) is defined as 0.3, based on the test results.

6.5.3 Truss-beam model (Modified truss analogy)

According to Eom and Park (2013), the shear degradation of concrete in the plastic hinge zone is predicted based on the longitudinal elongation mechanism: cumulative plastic strains of boundary reinforcement increases the longitudinal elongation over the plastic hinge zone, which degrades the effective compressive strength of the web concrete (**Fig. 6-12**). To predict the longitudinal elongation behavior, the plastic hinge zone is idealized as the truss model, which consists of a diagonal strut truss element of $\mathbf{D_C}$, a horizontal tie truss element of $\mathbf{H_T}$ and vertical boundary truss elements of $\mathbf{L_T}$ and $\mathbf{L_C}$ at flexural tension and compression zone, respectively. For the proposed walls, the composite boundary elements resist shear by frame action (acting as short columns). Thus, the boundary elements ($\mathbf{L_T}$ and $\mathbf{L_C}$) in the plastic hinge zone are modeled as beam elements, to develop additional shear (see $V_{b,t}$ and $V_{b,c}$ in **Fig. 6-13**) and flexural reactions (see $M_{b,t}$ and $M_{b,c}$) at the supports of both in flexural tension and compression zones. Thus, for the proposed composite walls, the plastic hinge model was named as "Truss-beam model". Further, since here, the term "longitudinal elongation" is replaced by "vertical elongation", to limit its meaning to wall members and to maintain the consistency with the term "horizontal elongation" used for elastic web crushing strength. Due to the relatively large boundary reinforcement ratio, the modeling of vertical web reinforcement was neglected.

Note that most of the following equations for the plastic hinge model are originated from the studies of Eom and Park (2010 and 2013).

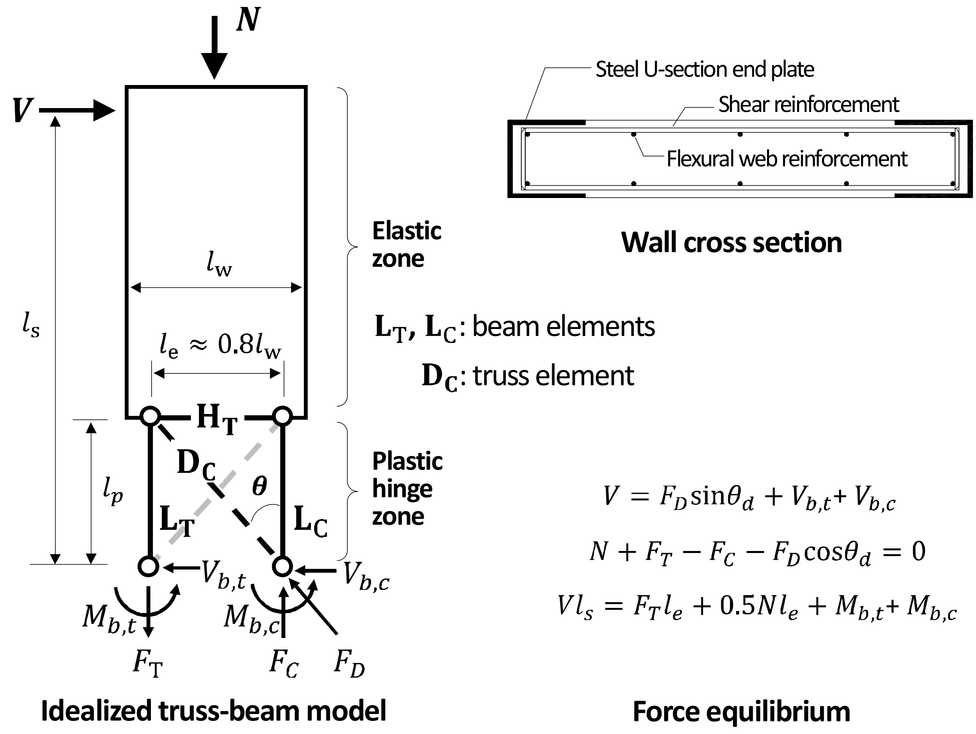

Fig. 6-13 Truss-beam model and force equilibrium for plastic hinge zone.

From the truss-beam model shown in **Fig. 6-13**, the force equilibrium provides the following three equations:

$$V = F_D \sin\theta + V_b \quad \text{(for the horizontal force)} \tag{6-15}$$

$$N + F_T - F_C - F_D \cos\theta = 0 \quad \text{(for the vertical force)} \tag{6-16}$$

$$Vl_s = F_T l_e + 0.5Nl_e + M_b \quad \text{(for the flexural moment)} \tag{6-17}$$

where, F_T, F_C, and F_D = internal axial forces of $\mathbf{L_T}$, $\mathbf{L_C}$, and $\mathbf{D_C}$, respectively; V_b = the sum of internal shear forces of $\mathbf{L_T}$ and $\mathbf{L_C}$ (= $V_{b,t}$ + $V_{b,c}$); M_b = the sum of flexural reactions of $\mathbf{L_T}$ and $\mathbf{L_C}$ (= $M_{b,t}$ + $M_{b,c}$); and V and N = lateral shear force and axial compression force imposed on walls, respectively.

In Eq. (6-16), F_D is eliminated by using Eq. (6-15) and (6-17), and rearranging with respect to F_C gives

$$F_C = N\left(1 - \frac{l_e \cot\theta}{2l_s}\right) + F_T\left(1 - \frac{l_e \cot\theta}{l_s}\right) - \left(\frac{M_b}{l_s} - V_b\right)\cot\theta \tag{6-18}$$

The term $(M_b/l_s - V_b)$ in Eq. (6-17), which indicates the internal shear forces, is significantly less than the other axial force terms of N and F_T (about less than 5%). Further, the plastic hinge zone is assumed as a square panel, which is $\cot\theta$ = 1.0 (θ = 45 degrees). For such conditions, using $l_e = 0.8l_w$ and introducing a symbol of $a = l_s/l_w$ (shear span ratio), Eq. (6-18) is simplified as follows:

$$F_C = N\left(1 - \frac{2}{5a}\right) + F_T\left(1 - \frac{4}{5a}\right) \tag{6-19}$$

When substantial elongation occurs under reversed cyclic loading, the compressive force F_C is resisted fully by boundary steel U-sections: due to the residual plastic strains, the boundary steel U-sections resist compressive force even in tensile strains (refer to **Fig. 6-14**). Thus, the compressive stress σ_{vc} (> 0 for compression) of the steel U-sections can be calculated by dividing both the terms in Eq. (6-19) by the area A_b of the steel U-section element $\mathbf{L_C}$ in compression. For symmetric wall cross section, σ_{vc} is calculated as follows:

$$\begin{aligned}\sigma_{vc} = \frac{F_C}{A_b} &= \frac{N}{A_b}\left(1 - \frac{2}{5a}\right) + \frac{F_T}{A_b}\left(1 - \frac{4}{5a}\right) \\ &\approx \frac{N}{A_b}\left(1 - \frac{2}{5a}\right) + F_y\left(1 - \frac{4}{5a}\right)\end{aligned} \tag{6-20}$$

Eq. (6-20) can be rewritten by dividing the both terms by the yield strength F_y of the steel U-section, which is defined as the index α_v to represent the stress levels of the steel U-section in compression.

$$\alpha_v = \frac{\sigma_{vc}}{F_y} = \frac{N}{A_b F_y}\left(1 - \frac{2}{5a}\right) + \left(1 - \frac{4}{5a}\right) \tag{6-21}$$

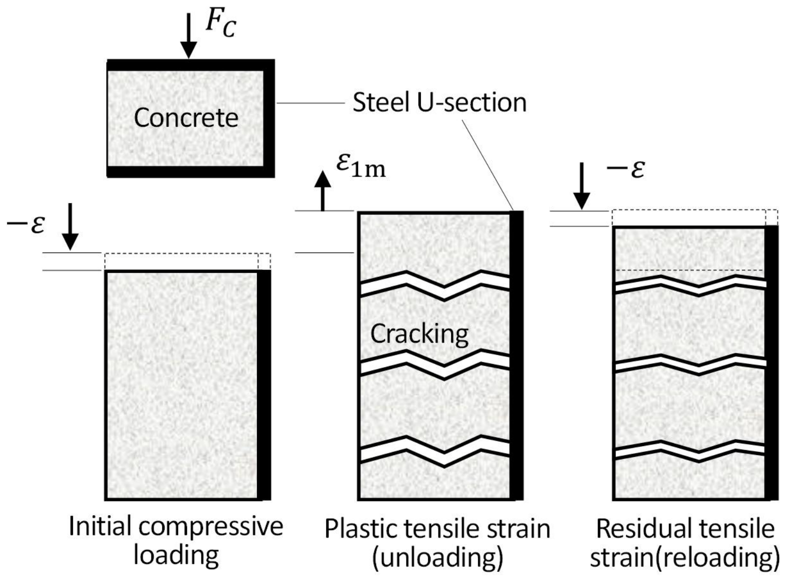

Effect of residual tensile strain

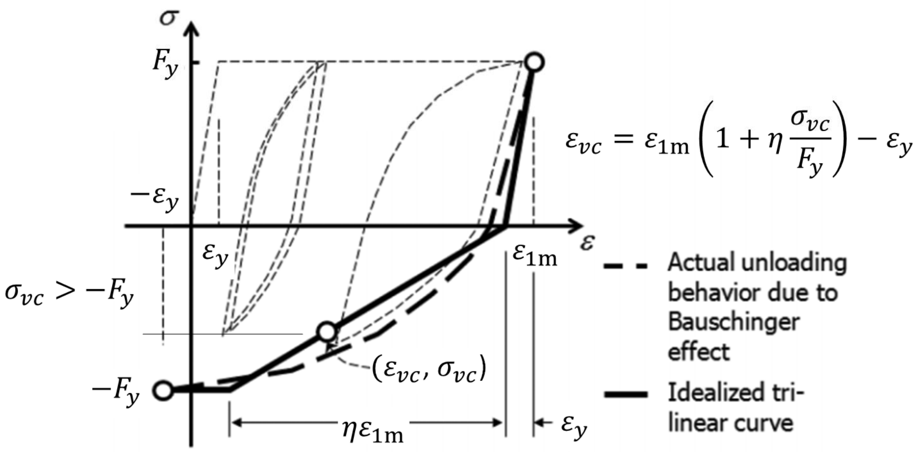

Constitutive relationship of boundary steel

Fig. 6-14 Cyclic loading behavior of boundary steel reinforcements in plastic hinge zone (Eom and Park, 2013).

6.5.4 Displacement compatibility

Fig. 6-15 shows the displacements of the walls and the strains of the elements in the truss-beam model of the plastic hinge zone. The lateral displacement of a cantilever wall is defined as follows:

$$\Delta = \Delta_p + \Delta_\theta + \Delta_e \tag{6-22}$$

where, Δ_p = lateral displacement at the top of the plastic hinge zone; Δ_θ = lateral displacement of the elastic zone (the remaining region above the plastic hinge zone) due to rigid body rotation; and Δ_e = lateral displacement of the elastic zone due to flexural and shear deformations.

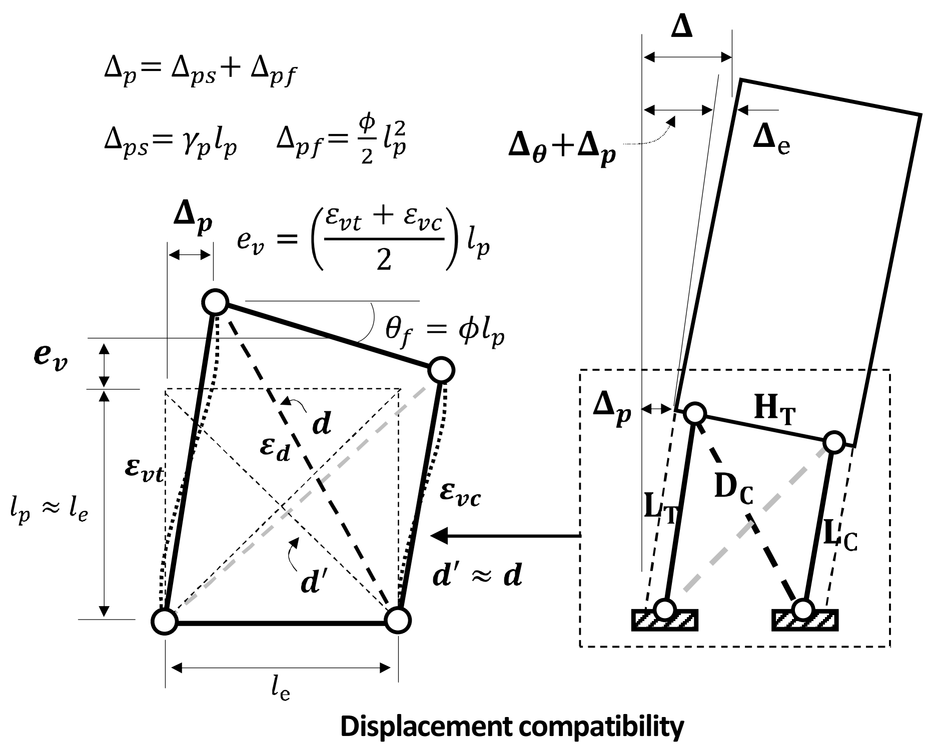

Fig. 6-15 Displacement compatibility in plastic hinge model.

In the tests, although the post-yield deformation was concentrated in the plastic hinge zone, flexural and shear cracking also occurred in the elastic zone (see **Fig. 6-3**), due to the high shear demand (i.e., flexural strength) resulting from the large steel U-sections. **Fig. 6-16** shows the ratio of Δ_e to the overall deformation Δ measured in the tests, where Δ_e was 15% of Δ on average. The displacement contribution of the elastic zone was almost uniform according to the shear span ratio, because the contribution of shear deformation was relatively increased at low shear span ratios, whereas the contribution of flexural deformation was relatively increased at high shear span ratios.

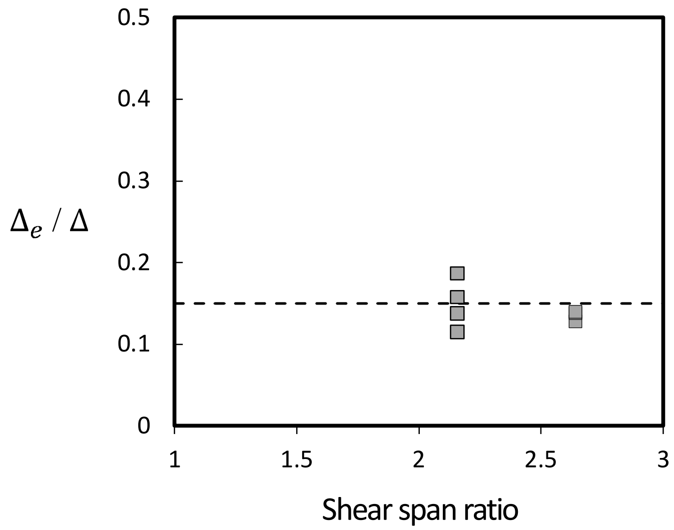

Fig. 6-16 Displacement contribution of elastic zone.

In the plastic hinge zone, the steel U-sections resist both shear forces and flexural moments, developing shear strains and flexural curvatures. However, the contributions of these deformations to the plastic hinge deformation Δ_p are very limited, because Δ_p is more affected by vertical elongation resulting from plastic axial strains of the boundary elements (**L_T** an **L_C**). Thus, for simplicity, Δ_p is determined from the axial strains of the elements in the plastic hinge model, neglecting the shear and flexural deformations of the boundary elements. In this condition, the following displacement compatibility should be satisfied within the plastic hinge model (**Fig. 6-15).**

$$-\left(\Delta_p - \frac{\varepsilon_h l_e}{2}\right)\sin\theta + \varepsilon_{vt} l_p \cos\theta = -\varepsilon_d \frac{l_p}{\cos\theta} \tag{6-23}$$

where, ε_h (> 0 for tension), ε_{vt} (> 0 for tension), and ε_d (> 0 for compression) = strains of $\mathbf{H_T}$, $\mathbf{L_T}$, and $\mathbf{D_C}$, respectively; and l_p = length of plastic hinge zone, which is assumed as $l_e = 0.8 l_w$. For better estimate of l_p, more refined calculations can be used considering various design parameters, including load condition, material strength, and shear span ratio.

The average flexural curvature in the plastic hinge zone is defined as follows:

$$\phi = \frac{\varepsilon_{vt} - \varepsilon_{vc}}{l_e} \tag{6-24}$$

where, ε_{vc} (< 0 for compression) = strain of $\mathbf{L_C}$. From Eq. (6-24) and $\theta_d \approx$ 45 degrees, Eq. (6-23) can be rearranged with respect to Δ_p, as follows:

$$\Delta_p = \left(\phi + \frac{\varepsilon_{vc}}{l_e}\right) l_p^2 + \varepsilon_d \left(\frac{l_p^2 + l_e^2}{l_e}\right) + \frac{\varepsilon_h l_e}{2} \tag{6-25}$$

The lateral displacement Δ_θ due to the rigid body rotation of the elastic zone is derived from the flexural deformation in the plastic hinge zone.

$$\Delta_\theta = \theta_f (l_s - l_p) = \phi l_p (l_s - l_p) \tag{6-26}$$

where, θ_f = flexural rotation at the top of the plastic hinge zone; and ϕ = average flexural curvature in the plastic hinge zone.

On the other hand, the lateral displacement Δ_p of the plastic hinge zone, which consists of flexural Δ_{pf} and shear deformations Δ_{ps}, can be defined based on the fundamental structural analysis, as follows:

$$\Delta_p = \Delta_{pf} + \Delta_{ps} = \frac{\phi l_p^2}{2} + \gamma_p l_p \tag{6-27}$$

where, γ_p = average shear strain in the plastic hinge zone.

From Eq. (6-25), and (6-27), the shear strain γ_p is defined as follows:

$$\gamma_p = \frac{1}{2}\phi l_p + \left[\varepsilon_{vc}\frac{l_p}{l_e} + \varepsilon_d\left(\frac{l_e}{l_p} + \frac{l_p}{l_e}\right) + \frac{\varepsilon_h}{2}\frac{l_e}{l_p}\right] \tag{6-28}$$

The vertical elongation e_v of the plastic hinge zone is determined by averaging the axial strains of the boundary elements $\mathbf{L_T}$ and $\mathbf{L_C}$, as follows:

$$e_v = \left(\frac{\varepsilon_{vt} + \varepsilon_{vc}}{2}\right) l_p \tag{6-29}$$

From Eq. (6-24) and (6-29), the strain of the compressive boundary element $\mathbf{L_C}$ is calculated as follows:

$$\varepsilon_{vc} = \frac{e_v}{l_p} - \phi\frac{l_e}{2} \tag{6-30}$$

By substituting Eq. (6-30) into Eq. (6-28), and using $l_e \approx l_p$, the average shear strain γ_p is redefined as follows:

$$\gamma_p = \frac{e_v}{l_e} + \left[2\varepsilon_d + \frac{\varepsilon_h}{2}\right] \tag{6-31}$$

In Eq. (6-31), the shear strain of the plastic hinge zone is determined from the vertical elongation e_v, compressive strain ε_d (> 0 for compression) of the diagonal strut $\mathbf{D_C}$; and tensile strain ε_h (> 0 for tension) of the horizontal tie $\mathbf{H_T}$. When flexural yielding occurs, the vertical elongation significantly increases, while the diagonal strut strain (see the length of the diagonal **D$_C$** before deformation (d') and after deformation (d)) and horizontal tie strain remain almost constant. Thus, assuming substantial vertical elongation at inelastic web crushing, Eq. (6-31) is further simplified as follows:

$$\gamma_p = \frac{e_v}{l_e} \tag{6-32}$$

Thus, the shear strain of the plastic hinge zone is approximately equivalent to the vertical elongation.

6.5.5 Strength contribution of concrete

From Eq. (6-32) and $\varepsilon_o \approx 0.0025$, the effective average strength factor k in Eq. (6-14) is redefined as follows:

$$k = \frac{1.8}{400(e_v/l_e)} \leq 0.3 \tag{6-33}$$

The vertical elongation e_v can be estimated from the iterative procedures according to Eom and Park (2010), by using Eq. (6-22), (6-25), (6-26), (6-29) and the constitutive relationship of the steel subjected to cyclic loading ($\varepsilon_{vc} = \varepsilon_{1m}\left(1+\eta\sigma_{vc}/F_y\right) - \varepsilon_y$ in **Fig. 6-14**, in which ε_{1m} = maximum tensile strain of the boundary element **L**$_C$ developed in the previous load cycle). The derivation of e_v is available in Eom and Park (2010). For a symmetric wall cross section and the condition of $\sigma_{vc} \leq F_y$ ($\alpha_v \leq 1$), the vertical elongation e_v in the plastic hinge zone is simply calculated as follows:

$$e_v = \frac{(\Delta - \Delta_e)\frac{l_e}{l_s}\left(1-\eta\frac{\sigma_{vc}}{2F_y}\right) - \left(1-\frac{l_p}{2l_s}\right)\varepsilon_y l_p}{1-\left(1-\eta\frac{\sigma_{vc}}{F_y}\right)\left(1-\frac{l_p}{l_s}\right)} \tag{6-34}$$

where, η = coefficient to take into account the Bauschinger effect for a steel plate subjected to reversed cyclic loading; and ε_y = yield strain of boundary steel U-sections. In Eom and Park (2010), η is defined as 0.6 for a reinforcing bar, which is also assumed for the steel U-section. Further, the lateral displacement Δ_e of the elastic zone is defined as a function of the elastic flexural deformation (= $\phi_y(l_s - l_p)^2$ / 3, in which ϕ_y = yield curvature of the wall cross section = $2.0\varepsilon_y/l_w$). In the present study, when the shear span ratio is greater than 2.0, the contribution ratio of Δ_e to the overall lateral displacement Δ is assumed as 15% ($\Delta - \Delta_e = \Delta - 0.15\Delta = 0.85\Delta$), based on the test results (**Fig. 6-16**). Thus, 0.85Δ indicates the lateral displacement contributed by plastic hinge zone. When the shear span ratio is less than 2.0, the elastic zone area and its displacement contribution decrease, and those become zero when the shear span ratio is 1.0 (note that the plastic hinge zone is assumed to be square region). Thus, for 1.0 $\leq a < 2.0$, Δ_e is calculated by linear interpolation between zero and 0.15Δ. From Eq. (6-21), $l_e = 0.8l_w$, $l_p = l_e$, and $\eta = 0.6$, Eq. (6-34) is simplified as follows:

$$e_v = \frac{0.8\psi\Delta(1-0.3\alpha_v) - 0.8(a-0.4)\varepsilon_y l_w}{0.8 - 0.48\alpha_v + 0.6a\alpha_v} \geq 0 \qquad (6\text{-}35)$$

where, ψ = contribution ratio of the plastic hinge deformation to the overall lateral displacement = 0.85 for $a \geq 2.0$; and $1.15 - 0.15a$ for $1.0 \leq a < 2.0$. Inserting Eq. (6-33) into Eq. (6-2), and using θ = 45 degrees, the concrete contribution V_{wc} for the inelastic web crushing strength is defined as follows:

$$V_{wc} = \frac{0.9 f_c' t_w l_e}{400(e_v/l_e)} \leq 0.15 f_c' t_w l_e \qquad (6\text{-}36)$$

The vertical elongation e_v in Eq. (6-36) is the function of the lateral displacement Δ. Therefore, V_{wc} can be calculated for a given lateral displacement Δ of walls. Because e_v increases in proportion to Δ, the concrete contribution V_{wc} for the inelastic web crushing strength decreases as Δ increases.

Note that Eq. (6-34) is only valid when the compressive stress σ_{vc} of the steel U-section $\mathbf{L_C}$ is less than or equal to its yield strength (i.e., $\sigma_{vc} \leq F_{yb}$ or $\alpha_v \leq 1$). For the walls subjected to high axial compression, σ_{vc} by Eq. (6-20) may be greater than F_y ($\alpha_v > 1$). In this case, the vertical elongation is not increased by cyclic loading: as the load is reversed, the tensile strain of the steel U-section is fully recovered without residual strains. Thus, the vertical elongation e_v by Eq. (6-34) is redefined as follows (Eom and Park, 2013):

$$e_v = (\Delta - \Delta_e)\frac{l_e}{2l_s} \approx 0.425 l_e \delta \tag{6-37}$$

where, δ = overall drift ratio of walls (= Δ/l_s).

By substituting Eq. (6-37) into Eq. (6-33), the effective average strength factor k is redefined as follows:

$$k = \frac{1.8}{170\delta} \le 0.3 \tag{6-38}$$

From Eq. (6-2), (6-38), and θ_d = 45 degrees, the concrete contribution V_{wc} for the inelastic web crushing strength (for α_v > 1) is defined as follows:

$$V_{wc} = \frac{0.9 f_c' t_w l_e}{170\delta} \le 0.15 f_c' t_w l_e \qquad \text{for } \alpha_v > 1 \tag{6-39}$$

6.5.6 Simplified expression for concrete contribution

Although Eq. (6-35) and (6-36) are enough to calculate the concrete contribution V_{wc} for the inelastic web crushing strength (for $\alpha_v \leq 1$), the simpler equation is provided for use in practice.

In the walls subjected to large inelastic deformation, the term $\varepsilon_y l_w$ in Eq. (6-35) is significantly less than the lateral displacement Δ. For examples, when the shear span ratio, the wall length l_w, and the yield strain ε_y are defined as 2.0, 1,600 mm, and 0.002 respectively, the lateral displacement becomes 64 mm at the target drift ratio of 2.0 %, which is significantly greater than the term $\varepsilon_y l_w$ of 3.2 mm. Thus, Eq. (6-35) can be simplified as follows:

$$e_v = \frac{0.8\psi\Delta(1 - 0.3\alpha_v)}{0.8 - 0.48\alpha_v + 0.6a\alpha_v} \geq 0 \tag{6-40}$$

By inserting Eq. (6-40) into Eq. (6-32), the average shear strain γ_p in the plastic hinge zone is redefined as follows:

$$\gamma_p = \left[\frac{0.8\psi a(1 - 0.3\alpha_v)}{0.8 - 0.48\alpha_v + 0.6a\alpha_v}\right]\delta = k_\alpha \delta \tag{6-41}$$

where, k_α represents the relationship between the average shear strain γ_p in the plastic hinge zone and the overall drift ratio δ.

On the other hand, the stress index α_v for the compressive steel U-section in Eq. (6-21) is redefined using the axial force ratio ($n_a = N/f_c' A_g$) and mechanical vertical steel ratio ($\rho_s F_y/f_c'$, in which $\rho_s \approx 2A_b/A_g$), as follows:

$$\alpha_v = \frac{2n_a}{\rho_s F_y/f_c'}\left(1 - \frac{2}{5a}\right) + \left(1 - \frac{4}{5a}\right) \tag{6-42}$$

For the practical range of n_a (= 0–0.3), $\rho_s F_y/f_c'$ (= 0.2–1.0), and a (= 1.5–

3.0), k_α in Eq. (6-41) can be simplified as follows:

$$k_a \approx (1.3 + 0.12a - 0.8\alpha_v)\psi \geq 0 \tag{6-43}$$

Fig. 6-17 shows the comparison of k_a values calculated according to Eq. (6-41) and (6-43). For the walls with shear span ratios greater than 1.5, Eq. (6-43) reasonably simplifies k_α in Eq. (6-41). However, when the shear span ratio decreases to 1.0, k_α is overestimated because the regression analysis is performed for the shear span ratios greater than 1.5 for the following reasons: 1) The overall accuracy of the regression analysis significantly decreased when the aspect ratios less than 1.5 were considered, which indicates that k_a shows an distinct trend in the low-rise walls. Further, 2) in the squat walls, strength design is often controlled by shear (elastic web crushing for SUB-C walls), rather than flexure, due to their small aspect ratio; the possibility of inelastic web crushing is significantly reduced. Even if it happens, 3) the overestimation of k_α increases the shear deformation ($k_a\delta = \gamma_p$), which will produce a conservative estimate of shear strength. When the shear span ratio is greater than 3.0, k_a is assumed to be the same as the value corresponding to *a* = 3.0.

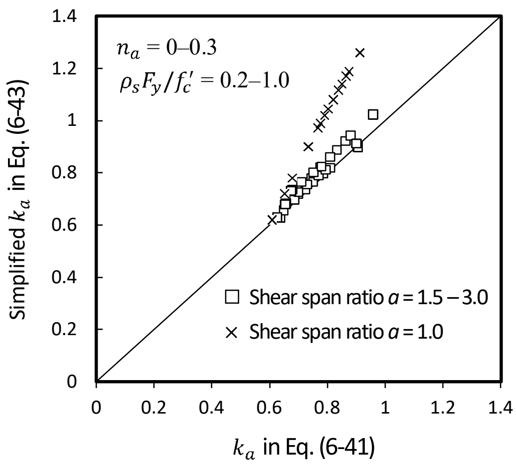

Fig. 6-17 Comparison of the shear deformation contribution parameters calculated by Eq. (6-41) and Eq. (6-43).

From Eq. (6-14), (6-41), (6-43), $\varepsilon_o \approx$ 0.0025, and γ_m = γ_p, the effective average strength factor k is redefined as follows:

$$k = \frac{1.8}{400\psi(1.3 + 0.12a - 0.8\alpha_v)\delta} \leq 0.3 \qquad (6\text{-}44)$$

Inserting Eq. (6-44) into Eq. (6-2), and using θ = 45 degrees, the concrete contribution V_{wc} for the inelastic web crushing strength (for α_v ≤ 1) is redefined as follows:

$$V_{wc} = \frac{0.9 f_c' t_w l_e}{\psi(520 + 48a - 320\alpha_v)\delta} \leq 0.15 f_c' t_w l_e \qquad \text{for } \alpha_v \leq 1 \qquad (6\text{-}45)$$

In Eq. (6-39) and (6-45), the concrete contribution V_{wc} for the inelastic web crushing strength is directly calculated from the overall drift ratio δ of the walls. Thus, compared to Eq. (6-36) which is the function of the vertical elongation, it is more convenient to assess the web crushing capacity depending on the deformation demand. Further, because of the closed-form expression, the post-yield deformation capacity can be calculated from the maximum shear demand (i.e., flexural strength) of walls. The relevant discussion is presented in Chapter 7.

6.5.7 Strength contribution of steel U-section

Fig. 6-18 shows the force demands in the proposed plastic hinge model. After flexural yielding, the boundary element in tension $\mathbf{L_T}$ is subjected to tensile yield stress F_y, while the stress of the compressive boundary element $\mathbf{L_C}$ reaches σ_{vc} ($< F_y$) as defined in Eq. (6-21). The stresses are uniform along the element lengths of $\mathbf{L_T}$ and $\mathbf{L_C}$, respectively: $\sigma_A = \sigma_B = F_y$ in $\mathbf{L_T}$; and $\sigma_C = \sigma_D = \sigma_{vc}$ in $\mathbf{L_C}$. On the other hand, as the inelastic deformation of the plastic hinge zone increases, the strength and stiffness of the diagonal strut element $\mathbf{D_C}$ are significantly degraded, and the boundary elements begin to resist shear by moment-resisting frame action. In such condition, it can be assumed that the internal shear force (see $V_{b,c}$ and $V_{b,t}$ in **Fig. 6-18**) in $\mathbf{L_T}$ and $\mathbf{L_C}$ is uniform along the element length l_p. Thus, the shear strength contributions $V_{b,t}$ and $V_{b,c}$ of the boundary elements $\mathbf{L_T}$ and $\mathbf{L_C}$, respectively, are calculated from their flexural demands (fixed end moments), as follows:

$$V_{b,t} = \frac{M_A + M_B}{l_p} \tag{6-46a}$$

$$V_{b,c} = \frac{M_C + M_D}{l_p} \tag{6-46b}$$

where, M_A, M_B, M_C, and M_D = flexural demands at the locations of A, B, C, and D in the plastic hinge zone, respectively (**Fig. 6-18**). In Eq. (6-46), the shear contributions of the boundary elements increase proportionally to their flexural demand. However, the flexural demand should be limited by the axial-flexural capacity of the boundary elements. Note that both the boundary elements in the plastic hinge zone are subjected to tensile strains due to cyclic loading. Thus, the axial-flexural capacity of the boundary elements is calculated from the steel U-sections, neglecting the contribution of infilled concrete.

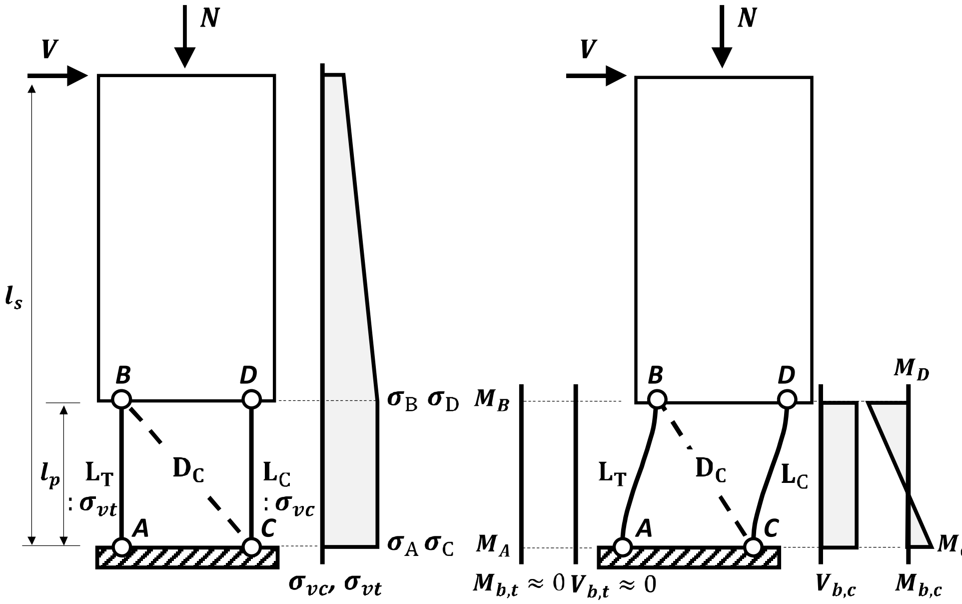

Fig. 6-18 Force demands of boundary elements in plastic hinge zone.

Fig. 6-19 shows the axial-flexural capacity curve of the steel U-section and the flexural demands M_A, M_B, M_C, and M_D in the plastic hinge zone. At the points A and B in $\mathbf{L_T}$, tensile yield stresses are fully developed after flexural yielding of walls, and the yield stresses are maintained without decrease because the shear demand V on walls is also maintained until inelastic web crushing. Therefore, the axial-flexural capacity of $\mathbf{L_T}$ is negligible ($M_A = M_B \approx 0$) and the shear contribution $V_{b,t}$ in Eq. (6-46a) can be assumed to be zero. Similarly, at the points C and D in $\mathbf{L_C}$, the compressive stress of σ_{vc} ($< F_{yb}$) is developed, and the resulting axial-flexural capacities are calculated from the idealized axial-flexural capacity curve, for convenience in calculation (**Fig. 6-19**), as follows:

$$M_C = M_D = (1 - \alpha_v) M_{bp} \tag{6-47}$$

where, M_{bp} = plastic moment capacity of steel U-sections subjected to pure bending.

From Eq. (6-3), (6-46), and (6-47), the contribution V_b of the boundary elements (steel U-sections) to the inelastic web crushing strength is calculated as follows:

$$V_b = \frac{2(1-\alpha_v)M_{bp}}{l_p} \approx \frac{2(1-\alpha_v)M_{bp}}{l_e} \tag{6-48}$$

Note that the shear strength contribution V_b of the steel U-sections is defined as a constant value, which indicates that V_b is independent of the deformation demand. Further, Eq. (6-48) is only valid when $\alpha_v \leq 1$. Otherwise, it becomes zero. This practice is fairly reasonable because, when high axial force is applied to walls, the steel U-section is subjected to high levels of stresses, and they prone to buckle or fully yield, limiting vertical elongation.

Eq. (6-48) is developed assuming the completely deteriorated web. However, until web crushing, the structural integrity between the web and boundary elements is not fully degraded due to the bond stress between the steel and concrete, aggregate interlocking, and the shear-friction mechanism of the shear reinforcement between the web and boundary elements, which provides resistance to the complete frame action of the boundary elements. Thus, for better estimate of V_b, these effects should be added to the right term in Eq. (6-46). That is, Eq. (6-47) may provide a conservative solution until web crushing but is reasonable for assessing the contribution of the steel U-sections at the moment of web crushing.

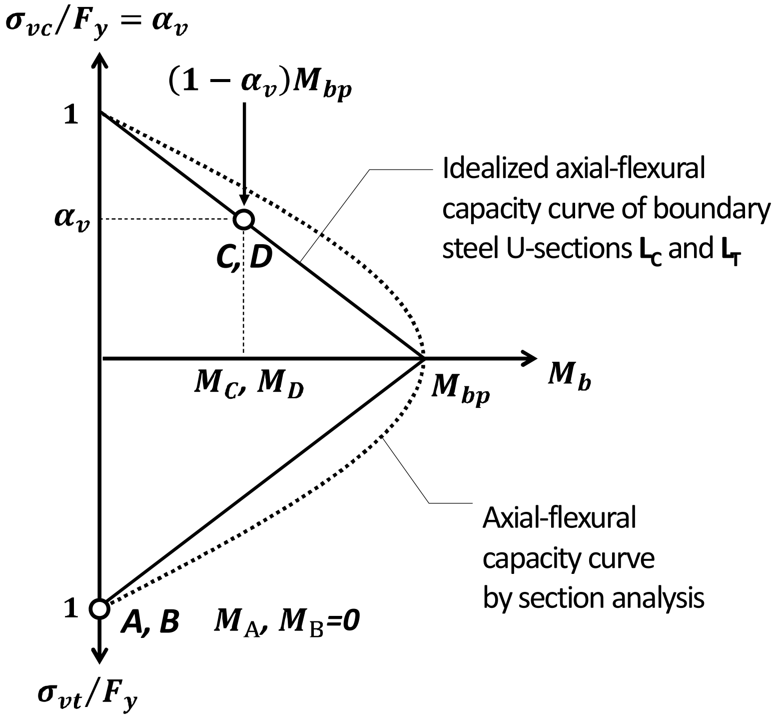

Fig. 6-19 Axial-flexural capacity curve of steel U-section.

6.5.8 Strength equation

Finally, from Eq. (6-1), (6-36), and (6-48), the inelastic web crushing strength is calculated as follows:

$$V_n = \frac{0.9f_c' t_w l_e}{400(e_v/l_e)} + \frac{2(1-\alpha_v)M_{bp}}{l_e} \leq 0.15 f_c' t_w l_e + \frac{2(1-\alpha_v)M_{bp}}{l_e} \tag{6-49}$$

For direct calculation from the deformation demand, Eq. (6-39) and (6-45) can be used instead of Eq. (6-36). Thus, the simplified inelastic web crushing strength is defined as follows:

$$V_n = \frac{0.9f_c' t_w l_e}{\psi(520 + 48a - 320\alpha_v)\delta} + \frac{2(1-\alpha_v)M_{bp}}{l_e} \leq 0.15 f_c' t_w l_e + \frac{2(1-\alpha_v)M_{bp}}{l_e} \quad \text{for } \alpha_v \leq 1$$

$$V_n = \frac{0.9f_c' t_w l_e}{170\delta} \leq 0.15 f_c' t_w l_e \quad \text{for } \alpha_v > 1 \tag{6-50}$$

6.6 Comparison with Test Results

For verification of the proposed model, the elastic and inelastic web crushing strengths were calculated for all test specimens, including the walls with steel web plates. The calculated strengths were compared with the tested cyclic load-displacement relationships. **Fig. 6-20** and **Fig. 6-21** show the comparison for the specimens that failed in web crushing after flexural yielding. The figures also show the tested failure modes of the walls. Further, the shear demands for each walls (denoted as dark solid lines) are presented by connecting the tested peak strengths at each displacement levels. The tested peak strengths of the walls are less than the elastic web crushing strengths (denoted as horizontal dotted lines) calculated according to Eq. (6-12). Except for **CF2.5**, the shear demand reaches both the inelastic web crushing strengths of Eq. (6-49) (denoted as thick dotted lines) and (6-50) (denoted as thick solid lines). These results agree with the tested failure mode. Particularly in **CS2TH** (**Fig. 6-21**(c)), the shear demand reaches both the elastic and inelastic web crushing strengths. For this reason, both the web crushing mechanisms appear in the actual failure mode. On the other hand, in **CF2.5** (**Fig. 6-20**(a)), the maximum shear demand does not reach the predicted inelastic web crushing strength even at large wall deformation, because the strength and deformation capacity were limited by the weld-fracture of the steel U-sections (refer to Section 3.4.1). For all specimens, the predictions from Eq. (6-49) were similar to those from Eq. (6-50), which indicates that the simplified inelastic web crushing strength model reasonably simulates the original model.

The post-yield deformation capacity of the walls is estimated from the intersection point between the shear demand and the shear degradation curve. Here, the shear degradation curve indicates the inelastic web crushing strength varying with the lateral drift ratio. In view of this, the proposed methods of Eq. (6-49) and (6-50) reasonably predict the post-yield deformation capacity of the walls. In **CF2SF** with steel web faceplates (**Fig. 6-21**(b)), the prediction underestimates the deformation capacity, because the proposed model does not consider the contribution of the web plates to the shear strength. Nevertheless, this result indicates that, for safe prediction, the proposed method can also be used for the walls with steel web faceplates.

Figs. 6-22, **6-23**, and **6-24** show the results for the specimens that failed in web crushing before flexural yielding. In fact, some of the results are also discussed in Section 6.4.4. In the walls with aspect ratios of 2.5 and 2.0 (**Fig. 6-22** and **Fig. 6-23**), generally, the shear demand reaches the proposed elastic web crushing strength, and significant strength degradation then occurs. On the other hand, the maximum shear demand is less than the proposed inelastic web crushing strength. This result agrees with the tested failure mode: web crushing only in the mid-height panel zone without significant damage in the plastic hinge zone. Only in **CS2SF** (**Fig. 6-23**(c)) with steel web plates, the maximum shear demand exceeds the inelastic web crushing strength, showing web crushing and plate buckling in the plastic hinge zone. This result indicates that, because of the web faceplates, the wall strength is limited by inelastic web crushing in the plastic hinge zone, rather than by elastic web crushing resulting from the horizontal elongation. Further, because the faceplates are not weld-connected to the boundary steel U-sections, large out-of-plane deformation of the faceplates occurs, which degrades their strength and stiffness significantly. Thus, although the proposed model does not consider the contribution of the faceplates, the tested load-carrying capacity is degraded along the proposed shear degradation curve (inelastic web crushing strength).

On the other hand, in **CS1** (**Fig. 6-24**(a)) and **CS1SF** (**Fig. 6-24**(c)) with the smaller aspect ratio of 1.0, the shear strengths calculated by the proposed model are less than the tested strengths. This is partly because the horizontal elongation estimated by Eq. (5-2) is overestimated in the squat walls, which underestimates the elastic web crushing strength.

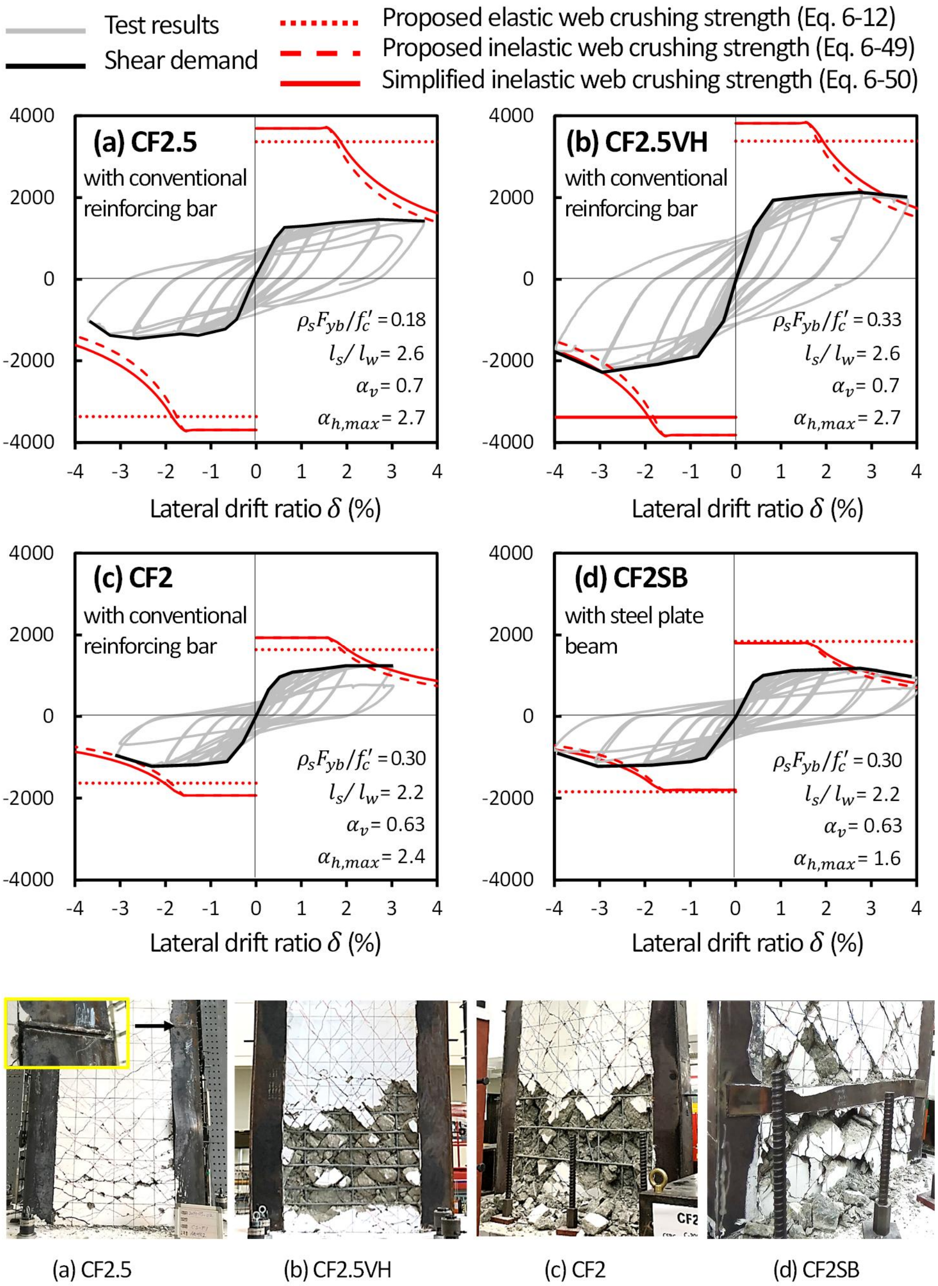

Fig. 6-20 Shear strength prediction for test specimens that showed inelastic web crushing (Part 1).

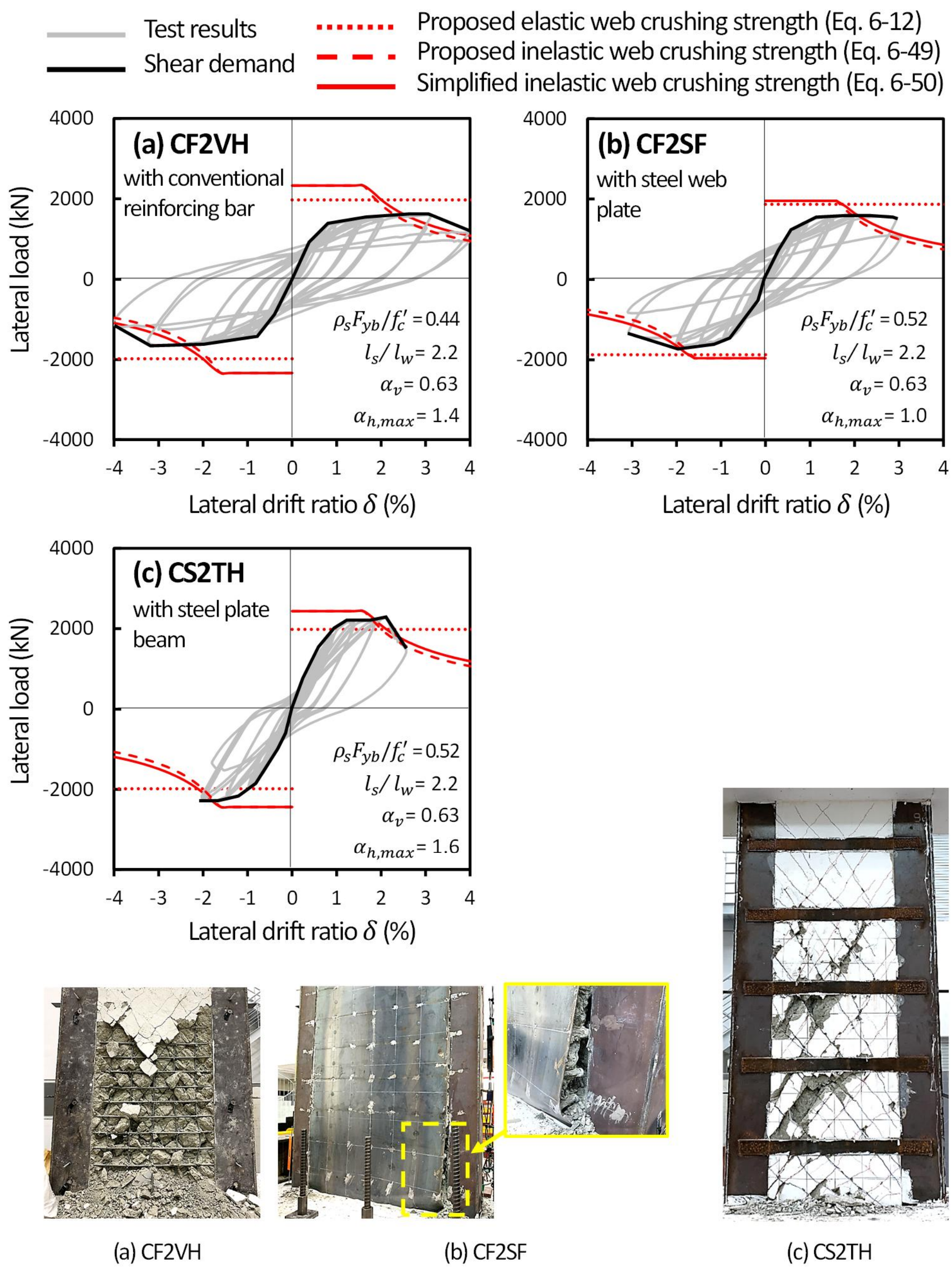

Fig. 6-21 Shear strength prediction for test specimens that showed inelastic web crushing (Part 2).

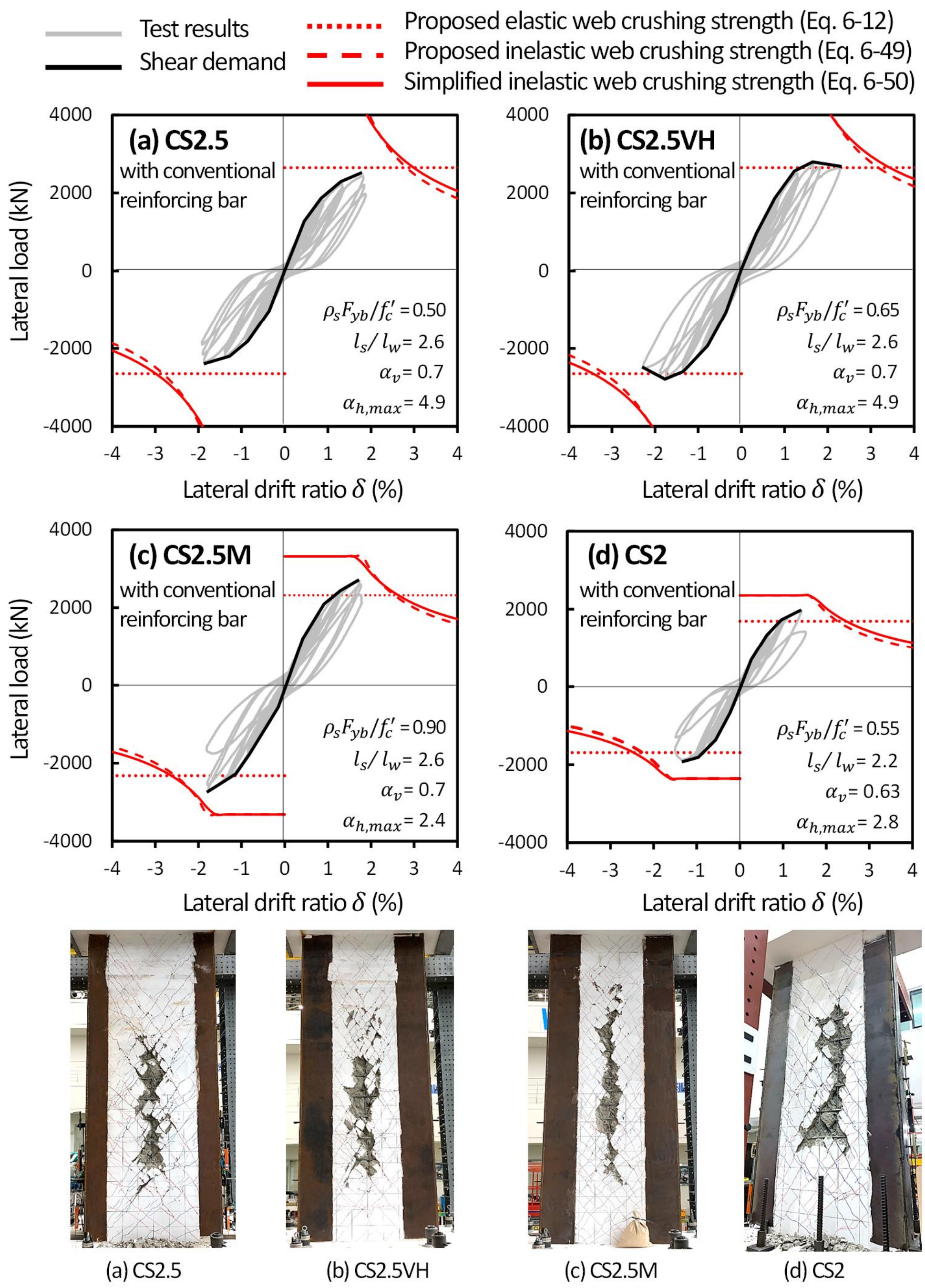

Fig. 6-22 Shear strength prediction for test specimens that showed elastic web crushing (Part 1).

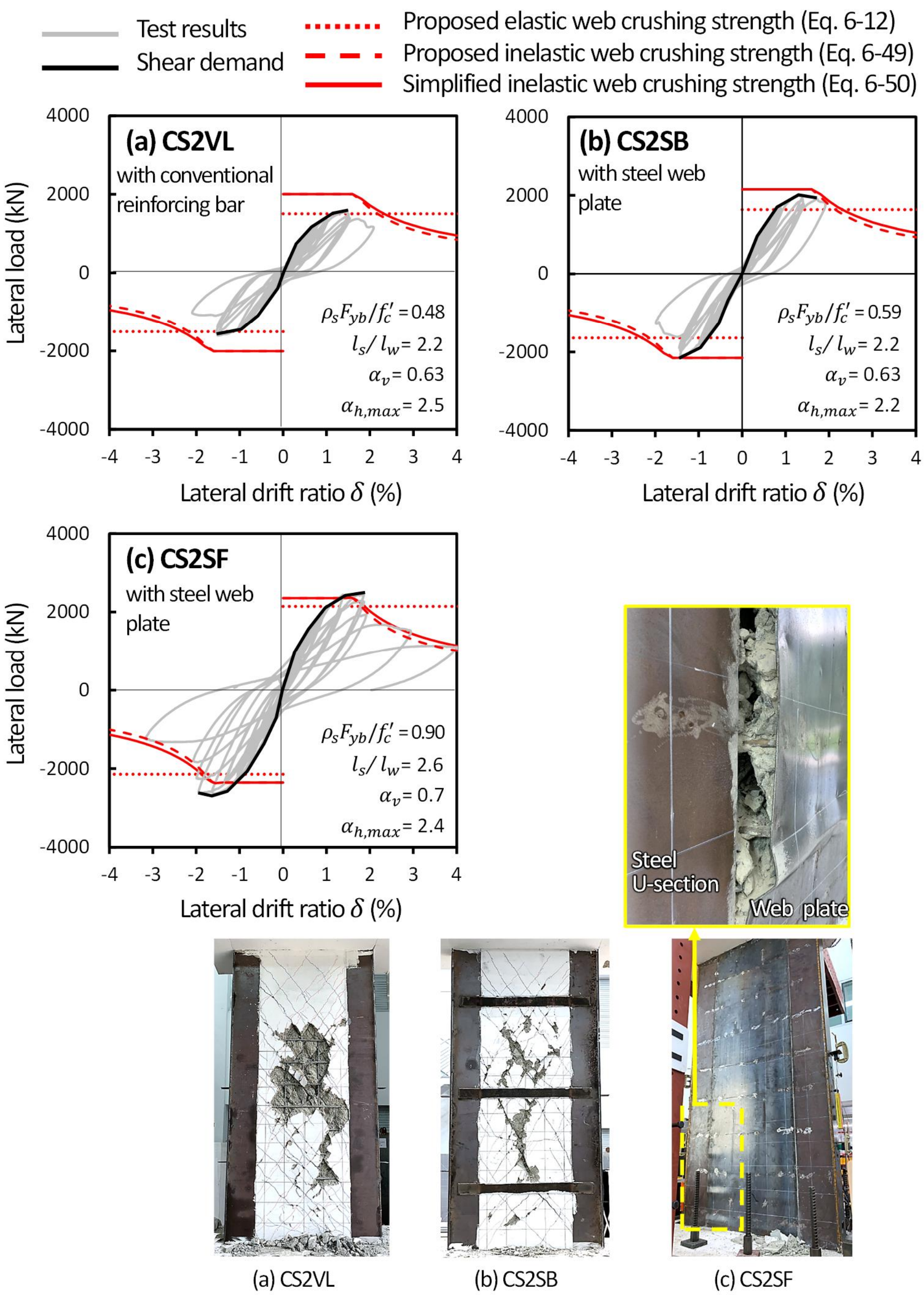

Fig. 6-23 Shear strength prediction for test specimens that showed elastic web crushing (Part 2).

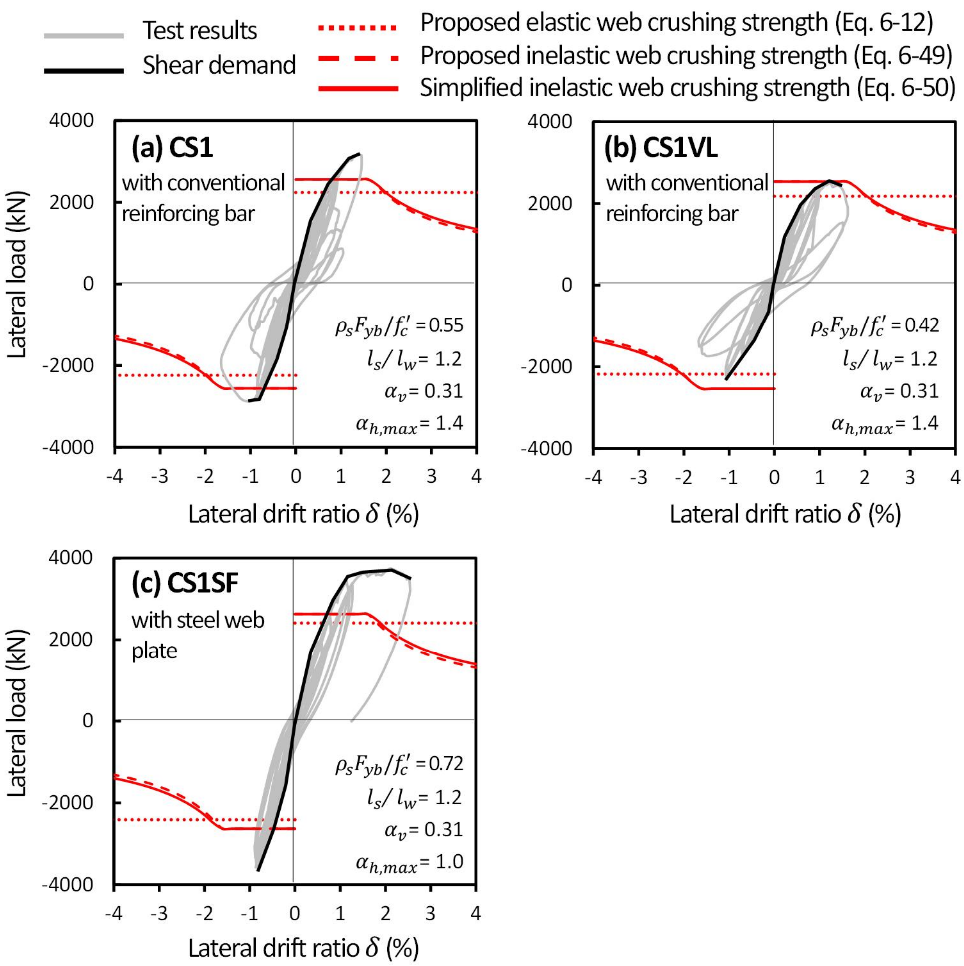

(a) CS1 (b) CS1VL (c) CS1SF

Fig. 6-24 Shear strength prediction for test specimens that showed elastic web crushing (Part 3).

6.7 Effect of Axial Force

In the present study, both the experimental tests and FE analysis did not verify the effect of axial force on the shear strength of SUB-C walls, even though it is generally believed that the axial force increases the shear strength of walls by restraining shear cracking and eventually reducing the shear deformation. The existing study of Oesterle et al. (1984) supported this belief, based on their tests on RC walls with highly confined large-sized boundary elements: increased web crushing strength with increased axial load. Based on the test results, they defined the web crushing strength as a function of shear deformation, where the shear deformation is defined according to the axial force. However, due to the lack of test data, the increase of shear strength depending on the axial force was limited to the axial force ratio of $N/A_g f_c'$ = 0.09 (n_a = 0.09).

In the proposed shear strength model, the shear strengths for both the elastic and inelastic web crushing mechanisms were also defined based on the shear deformation. However, only the inelastic web crushing strength considered the effect of axial force on the shear deformation: the axial force increases the compressive stress of vertical flexural reinforcement (i.e., boundary steel U-section), which decreases the vertical elongation and subsequent shear deformation. On the other hand, for the elastic web crushing strength, it was assumed that the horizontal elongation (due to yielding of horizontal shear reinforcement) primarily affects the shear deformation. For this reason, the horizontal elongation was defined only based on the mechanical shear reinforcement ratio and aspect ratio of walls, neglecting the effect of axial force. However, there had been the possibility to consider the effect of axial force on the shear deformation, because the shear deformation was defined based on the strain compatibility in the shear panel: the shear deformation depends on the levels of average vertical strain, horizontal strain, and principal compressive strain. Among them, the present study assumed that the horizontal strain is only variable (to consider the effect of horizontal elongation), and the rest were regarded as constants for practical simplicity (ε_v = 0.00125, ε_2 = 0.0025, see Eq. (6-5) through (6-10)). Thus, in order to consider the effect of axial force, the vertical strain should be defined as a function of axial force, and included in the calculation of shear deformation. The vertical strain $\Delta\varepsilon_v$ contributed by axial force is calculated at the mid-depth of the effective shear depth, as follows (fib MC 2010):

$$\Delta\varepsilon_v = \frac{N}{4E_sA_b} = 0.5\varepsilon_y\frac{n_a}{\rho_m} \tag{6-51}$$

where, ρ_m = mechanical vertical steel ratio = $\rho_s F_y/f_c'$.

The net vertical strain is calculated by subtracting $\Delta\varepsilon_v$ from the initial average vertical strain of 0.00125, as follows:

$$\varepsilon_v = 0.00125 - \Delta\varepsilon_v = 0.00125 - 0.5\varepsilon_y\frac{n_a}{\rho_m} \tag{6-52}$$

According to Fib MC (2010), when ε_v is negative, it must be taken as zero. In view of this, Eq. (6-52) reveals that the average vertical strain ε_v is decreased from 0.00125 to zero, with the increase of axial force. **Fig. 6-25** shows the effect of axial force on the prediction of the elastic web crushing strength, in which shear deformation γ and effective average strength factor k are calculated according to Eq. (6-5) and (6-4), respectively. As expected, the increase of axial force decreases γ, thus increasing k. The increase of k was 20% at maximum. This result indicates that, for the proposed model, the shear strength increase due to the effect of axial force can be considered up to 20%. However, such increase is insignificant, considering the uncertainty from the materials, construction, and loading condition. For this reason, the present study safely considered the elastic web crushing strength model, by neglecting the effect of axial force.

On the other hand, the effect of axial force was considered in the proposed inelastic web crushing strength. **Fig. 6-26** shows the effect of axial force on the prediction of the inelastic web crushing strength for an example wall with shear span ratio of a = 2.0 and mechanical vertical steel ratio of ρ_m = 0.5. Until the axial force ratio of n_a = 0.13, the compressive stress of the boundary steel U-section calculated by Eq. (6-21) does not reach the yield stress (α_v < 1), and k values are calculated by Eq. (6-44), considering the effect of cyclic loading on the vertical elongation. Consequently, the k values increase in proportion to the axial fore ratio n_a. However, when $n_a \geq 0.13$, the increase of k values is more pronounced, because compressive yielding of the steel U-sections is expected under the increased axial force ($\alpha_v \geq 1$), limiting vertical elongation due to cyclic loading. Note that the k values are calculated by Eq. (6-39), following the condition of $\alpha_v \geq 1$. This result indicates the proposed inelastic web crushing strength is highly affected by the axial force ratio. Thus, for the design of SUB-C walls, the effect of axial force should be carefully considered in evaluating their strength and deformation capacity. In addition, the proposed shear strength model should be verified and improved by further studies on SUB-C walls subjected to combined lateral loading and axial force.

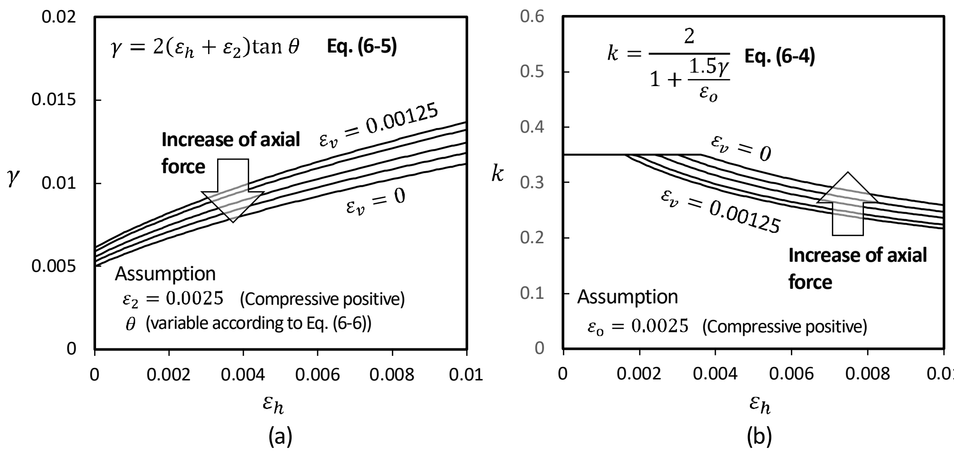

Fig. 6-25 Effect of axial force on elastic web crushing strength: (a) shear deformation and (b) effective strength factor for concrete.

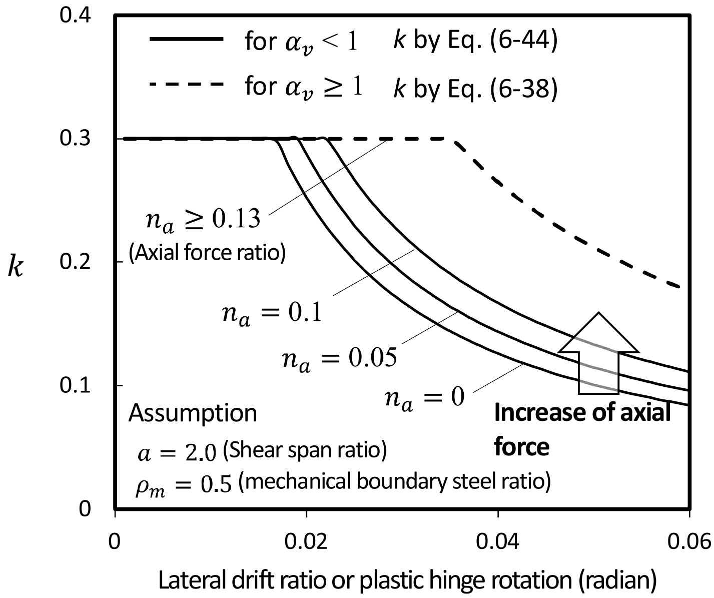

Fig. 6-26 Effect of axial force on inelastic web crushing strength.

6.8 Summary

In this chapter, the shear strength model of SUB-C walls was developed based on the two failure mechanisms: elastic and inelastic web crushing failures. Both failure mechanisms were implemented in the truss-beam model modified from the traditional truss analogy. The shear resistance of the boundary steel U-sections was incorporated into the truss model by replacing the vertical compression and tension truss elements with beam-column elements. The shear strength degradation of the web concrete was determined from the effective average strength of the diagonal concrete struts.

For the elastic web crushing strength, the effective strength of the diagonal struts was defined based on the horizontal elongation mechanism; as the horizontal elongation increases, the elastic web crushing strength decreases, Based on the FE analysis results, the contribution of the steel U-sections was neglected, for simplicity in design. Nevertheless, the proposed model reasonably predicts the elastic web crushing strength of the test specimens, except for a slight conservatism shown in the walls with aspect ratio of 1.0. The prediction error is 12% on average, which is less than that of JGJ 138 method (23%). The proposed elastic web crushing strength is valid only if the steel U-sections remain elastic at web crushing (without flexural yielding).

The inelastic web crushing strength was defined as the sum of the contributions of the concrete and boundary steel U-sections in the plastic hinge zone. The concrete contribution was defined as a function of the deformation demand, based on the vertical elongation mechanism. The contribution of the steel U-section was determined from its axial-flexural capacity, assuming full frame action of the steel U-section. The proposed inelastic web crushing model reasonably predicted the test results, in terms of the shear strength, failure mode, and deformation capacity.

Chapter 7. Design Strengths and Recommendations

This chapter provides the design strengths and recommendations for SUB-C walls subjected to cyclic lateral loading. This chapter consists of three sections: 1) Section 7.1 introduces the equivalent elastic analysis (EEA) method to obtain more accurate and economic design of the elastic shear strength of SUB-C walls; 2) Section 7.2 introduces the design flexural/shear strengths and deformation capacity, to predict the lateral load-displacement relationship of SUB-C walls; and 3) Section 7.3 provides the materials and detailing recommendations for design of SUB-C walls.

7.1 Equivalent Elastic Analysis

7.1.1 Background

For SUB-C walls, the shear strength model controlled by elastic web crushing (discussed in Chapter 6) was developed based on the horizontal elongation mechanism; The effective strength of the diagonal struts was defined as a function of the horizontal elongation. For the slender walls (aspect ratio > 2.0), the proposed elastic web crushing model provided reasonable accuracy, but the prediction for the squat walls (aspect ratio = 1.0) showed relatively large conservatism, due to the overestimation of horizontal elongation. This is because the horizontal elongation mechanism was not fully understood, and the prediction model for horizontal elongation was empirically developed based on a few FE analysis data and limited design parameters (see Section 5.5). Thus, the proposed model neglected the contribution of boundary steel U-sections, for safety in design.

As an alternative, the equivalent elastic analysis (EEA) method to predict the shear strength (elastic web crushing strength) of SUB-C walls was developed. The EEA is more convenient and cost-effective than the traditional nonlinear FE analysis, and ensures reasonable accuracy by replacing the potential inelastic properties by the equivalent elastic properties. The EEA can be performed by using commercial structural analysis programs. The major objectives of performing EEA are summarized as follows:

1) The contribution of composite boundary elements (steel U-sections plus infilled concrete) to the shear strength can be considered, which improves economy in design.

2) The structural safety of the steel U-sections can be evaluated by comparing their force demand and capacity.

3) The proposed shear strength prediction of Eq. (6-12) can be improved, especially for the low-rise SUB-C walls with aspect ratios less than 1.5.

In the proposed EAA, the inelastic response and behavior of SUB-C walls is assessed using a strip model. The horizontal elongation e_h in the mid-height panel zone is simulated by adopting the equivalent elastic stiffness of the horizontal ties. Thus, the nonlinear ($V-\Delta$) behavior from early yielding of shear reinforcement is idealized as an equivalent elastic behavior (**Fig. 7-1**). Further, from the FE analysis, it is revealed that the steel U-section near the wall base is vulnerable to local flexural yielding, because of the combined axial forces and flexural moments. Accordingly, the proposed EEA provides a technique to deal with this nonlinearity.

From the analysis on the strip model, the force demands for all major structural elements are obtained, and by comparing the force demands with the expected capacities, the structural safety of the elements can be evaluated, improving the accuracy of the shear strength prediction.

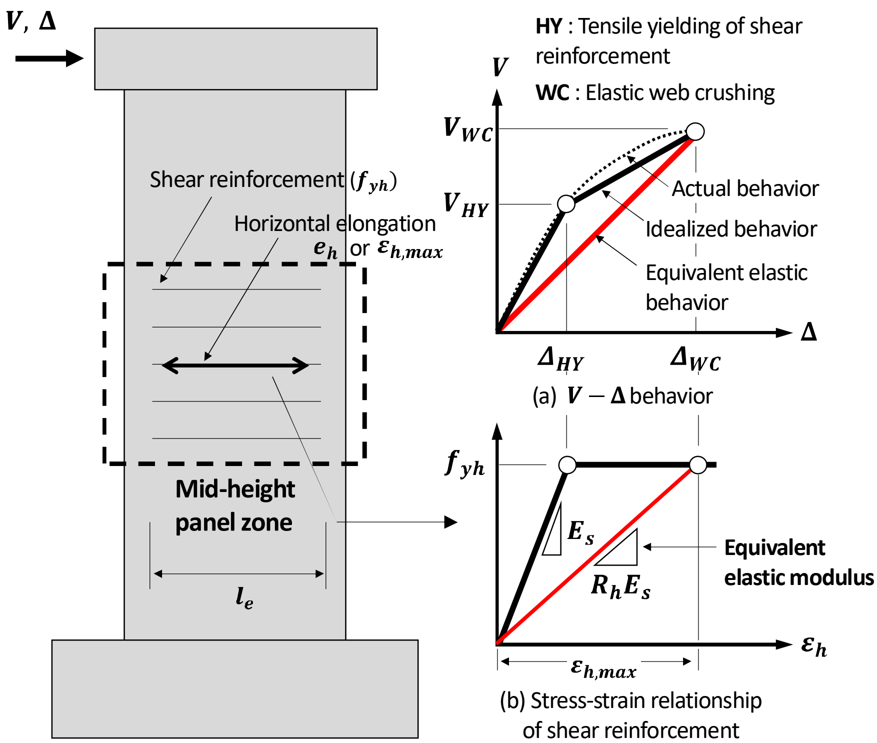

Fig. 7-1 Concept of equivalent elastic analysis for SUB-C walls

7.1.2 Strip model

Originally, the strip model approach has been developed to predict the post-buckling behavior of steel plate shear walls (Thorburn et al. 1983): After buckling of the steel plate, diagonal tension fields appear in the plate, and the tension field behavior is modeled as a series of tension-only strips oriented at the uniform inclination angle. Similarly, such idea can be applied to the modeling of the concrete cracked in diagonal tension: After diagonal tension cracking, diagonal compression fields appear in the cracked concrete, which is modeled using multiple diagonal strips.

Fig. 7-2 shows the geometric arrangement of the proposed strip model. The strip model consists of diagonal concrete strips, horizontal ties of shear reinforcement, vertical compression and tension chords of boundary elements that are capable of bending. In particular, the strips are modeled using beam-column elements. This practice allows the strips to resist flexural moment and shear as well as axial compression, which reduces the flexural demands in the boundary elements. In actual walls, such effect is attributed to the good structural integrity between the wall web and boundary elements. However, as a reaction to this, the stress demands in the strips increases particularly at the ends of the strips where boundary steel U-sections are located. Nevertheless, the flexural resistance of the strip ends can be justified from the confinement effect of boundary steel U-sections: As the steel U-sections confine the boundary zone, higher strength and stiffness of the boundary concrete are expected (see **Fig. 7-3**: relatively restrained cracking near the boundary elements). Further, as the strip is basically under compression, tensile cracking due to its flexural action is restrained, which ensures flexural resistance of the strips.

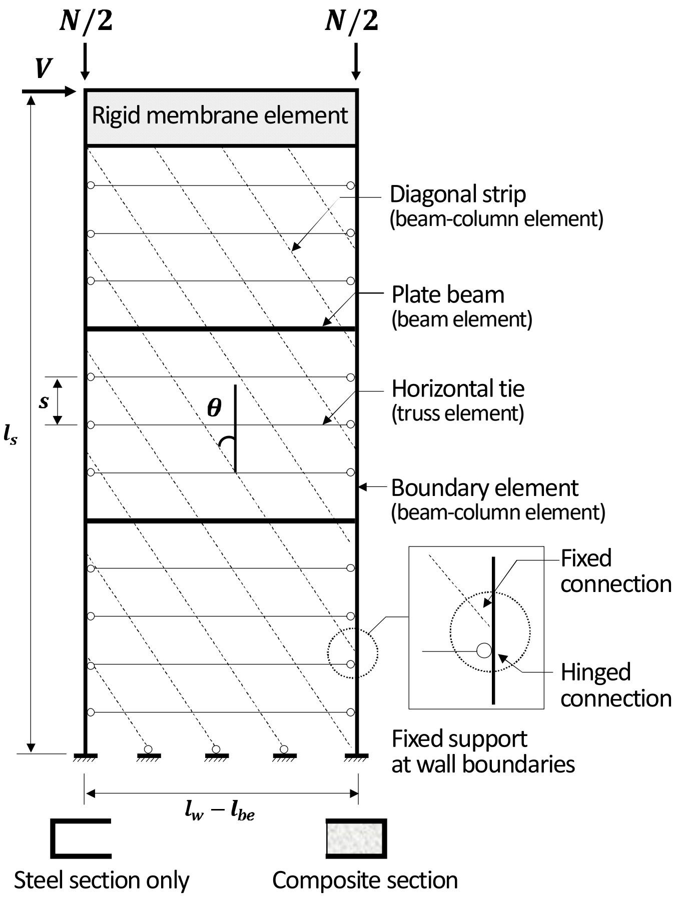

Fig. 7-2 Proposed strip model for elastic analysis of SUB-C wall subjected to lateral loading.

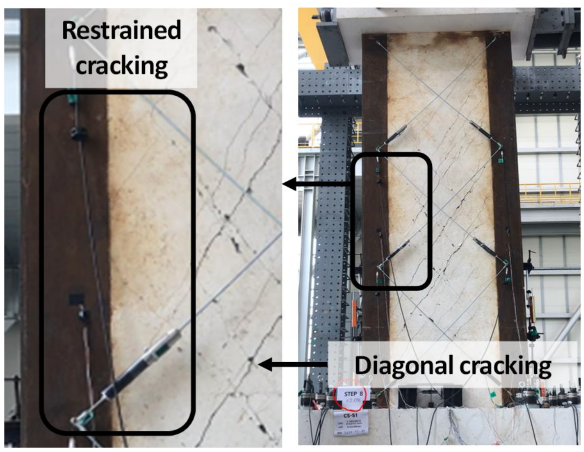

Fig. 7-3 Restrained concrete cracking near the boundary steel U-section.

7.1.3 Diagonal strip

1) Inclination angle

The strength and stiffness of the strip model is highly dependent on the inclination angle of diagonal strips, because the behavior of the strips is analogous to that of the struts in the proposed truss-beam model (Chapter 6). Accordingly, from Eq. (6-6), the diagonal strip angle is calculated in the same way as the strut angle (θ), as follows:

$$\tan\theta = \sqrt{\frac{\varepsilon_v + \varepsilon_2}{\varepsilon_h + \varepsilon_2}} \approx \sqrt{\frac{0.00125 + 0.0025}{\alpha_{h,max}\varepsilon_{yh} + 0.0025}} \tag{7-1}$$

where, $\alpha_{h,max}$ = maximum horizontal elongation ratio in the mid-height panel zone, which is calculated from Eq. (5-2); and ε_{yh} = yield strain of shear reinforcement. For practical simplicity, Eq. (7-1) is simplified as follows:

$$\tan\theta \approx 1 - 50\alpha_{h,max}\varepsilon_{yh} \tag{7-2}$$

Fig. 7-4(a) shows that Eq. (7-2) reasonably simplifies Eq. (7-1) within the available range of $\alpha_{h,max}$ = 1.0 – 5.0 (for ε_{yh} = 0.002). The limits for θ is defined according to fib MC (2010), as follows:

$$30^{\circ} \le \theta \le 45^{\circ} \tag{7-3}$$

2) Width and thickness

In the present study, the strip is assumed to resist flexural moment as well as axial compression. Thus, sufficient stiffness of the strips should be provided. For reasonable estimate of the strip stiffness, the width of the strips is assumed to be equal to the spacing of shear cracks. According to Bentz et al. (2006), the crack spacing is highly influenced by the spacing of shear reinforcement. Therefore, the strip width w_s is calculated as follows:

$$w_s = \frac{1}{\left(\frac{\cos\theta}{s_h} + \frac{\sin\theta}{s_v}\right)} \leq w_{s,max} \tag{7-4}$$

where, s_h = vertical spacing of horizon web reinforcement; and s_v = horizontal spacing of vertical web reinforcement. For walls with no vertical web reinforcement, Eq. (7-4) is replaced by $w_s = s_h/\cos\theta$. To avoid overestimation of the strip stiffness, the upper bound for w_s is defined as follows:

$$w_{s,max} = \min(1.2s_h, 0.2l_w, 3t_w, 450\ \ mm) \tag{7-5}$$

In Eq. (7-5), the last three criteria are determined from the maximum spacing of shear reinforcement specified in ACI 318 (2019).

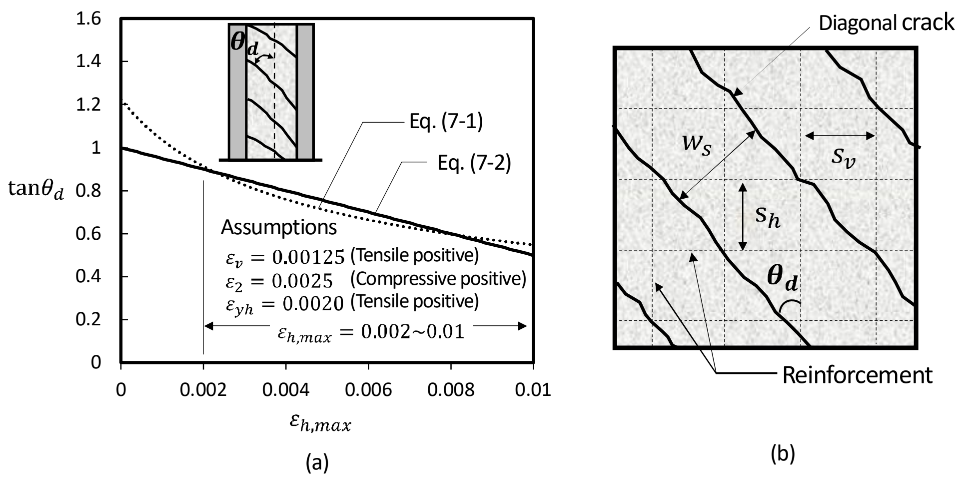

Fig. 7-4 Prediction of (a) inclination angle and (b) spacing of diagonal cracks.

3) Stiffness

According to Ozaki et al. (2004), the reduced stiffness of the concrete in the direction parallel to the crack plane is estimated as 70% of the elastic stiffness (= $0.7E_c$).

4) Force demand

The strip is subjected to the combined flexural moment and axial force, in which the flexural demand is developed from the resistance to rotation of the boundary elements. The flexural moment linearly decreases from the ends of the strip, and become zero at the center of the strip. On the other hand, the axial force is uniform along the strip length. Thus, the maximum demand for axial-flexure force is evaluated at the end of the strip (denoted as A in **Fig. 7-5**(a)). **Fig. 7-6** shows possible stress conditions at the crack plane of actual walls: shear stresses due to aggregate interlock and shear friction (**Fig. 7-6**(a)), and tensile stress of shear reinforcement at cracks (**Fig. 7-6**(b)). The resultant flexural moment due to these stresses are expected to reduce the flexural demand in the middle of the strips. For this reason, in the web region, only the axial force demand is considered, neglecting the flexural demand.

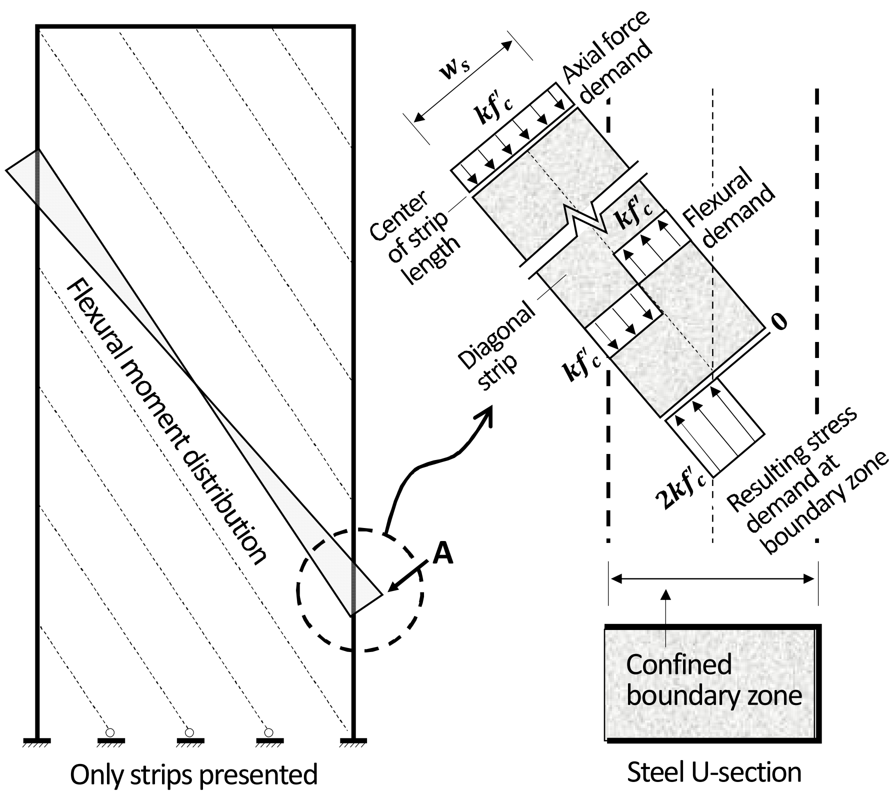

Fig. 7-5 flexural resistance of diagonal strips

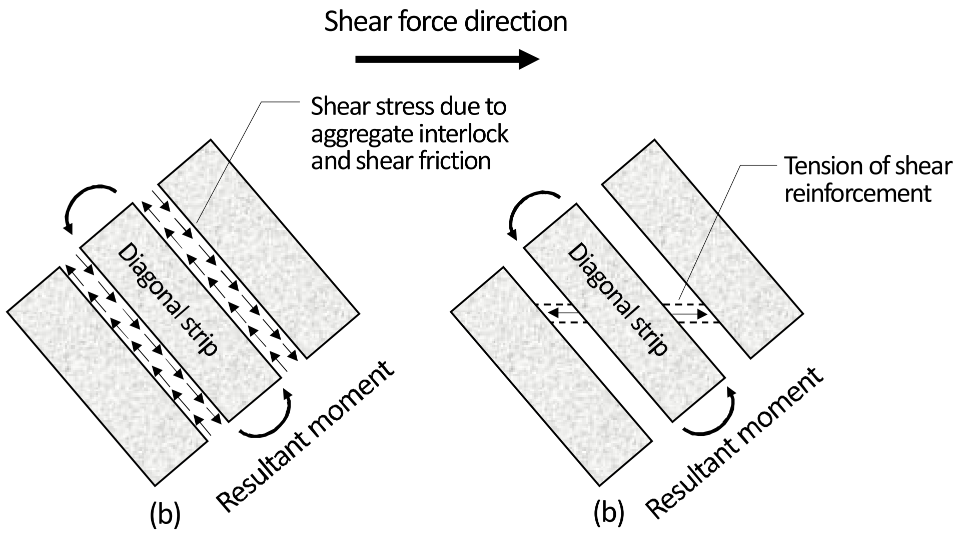

Fig. 7-6 Restraint moment due to stresses at the crack plane

In the proposed strip model, the axial force demand σ_{ds} is calculated by averaging the compressive stresses of the strips in the mid-height square panel zone where elastic web crushing occurs (**Fig. 7-7**(a)). On the other hand, the flexural demand in the flexural tension and compression zones are calculated by averaging all flexural moments at the ends of the strips at each zones (see $M_{ds,T}$ and $M_{ds,C}$ in **Fig. 7-7**(b)), considering force redistribution between strips (It is revealed that the excess in flexural moment of a few strips can be stabilized by moment redistribution to the other strips).

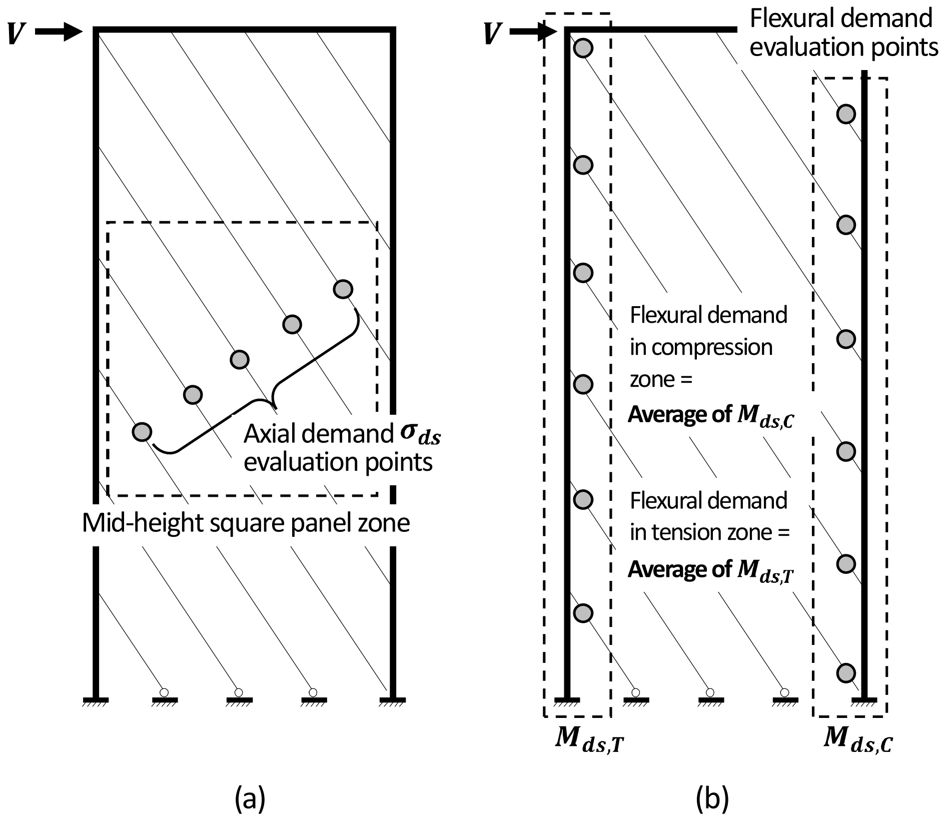

Fig. 7-7 Calculation of axial force and flexural demands in diagonal strips.

5) Force capacity

Since this study is concerned with web crushing, the failure of the strips is controlled by compression failure. The effective strength of the strips in compression is calculated from the effective average strength factor k, to be consistent with the proposed inelastic web crushing model (Eq. 6-11) in Chapter 6). Thus, the compression force capacity σ_{cs} of the strips is calculated as follows:

$$\sigma_{cs} = kf_c' = \frac{2f_c'}{5 + 0.9\alpha_{h,max}} \leq 0.35f_c' \tag{7-6}$$

In the boundary zone where flexural moment is developed, it is assumed that the concrete strength is not degraded at all, considering the confinement effect of steel U-sections. The plastic flexural moment capacity M_{cs} of the strip is calculated considering the axial force demand, as follows:

$$M_{cs} = \frac{1}{4}kf_c' t_w w_s^2 \tag{7-7}$$

Eq. (7-7) represents the flexural strength of the strip at which the net tensile stress due to the axial and flexural demands would be zero (see Fig. 7-5).

7.1.4 Horizontal tie

1) Tie spacing

The horizontal tie action is developed by shear reinforcement aligned transverse to the vertical axis of walls. Thus, it is recommended that the spacing of horizontal ties be identical to that of shear reinforcement. However, it is revealed that, for the same area of horizontal ties, a slight difference in tie spacing has little effect on the overall strength of the strip model. Thus, an error up to 10% is allowable. In the present study, the use of inclined shear reinforcement is not considered.

2) Sectional area

The sectional area of a horizontal tie is calculated as the total area of the shear reinforcement within the spacing of s_h.

3) Stiffness reduction factor (equivalent elastic stiffness)

The proposed EEA allows the nonlinearity from yielding of shear reinforcement. For this purpose, the post-yield behavior of horizontal ties and its effect on the overall strength of walls are considered by adopting the equivalent (reduced) elastic stiffness of the horizontal ties. The equivalent elastic stiffness E_{es} of horizontal ties is calculated based on the horizontal elongation at elastic web crushing, and assuming elastic-perfectly plastic behavior of shear reinforcement (**Fig. 7-1**).

$$E_{es} = \frac{f_{yh}}{\varepsilon_{h,max}} = \frac{f_{yh}}{\alpha_{h,max}\varepsilon_{yh}} = \frac{E_s}{\alpha_{h,max}} = R_h E_s \tag{7-8}$$

In Eq. (7-8), the equivalent elastic stiffness is calculated from the inverse of the maximum horizontal elongation ratio. From Eq. (7-8) and Eq. (5-2), the reduced stiffness factor R_h for horizontal ties is calculated as follows:

$$0.2 \le R_h = \frac{1}{\alpha_{h,max}} = -0.42 + \frac{1.2}{(l_s/l_w)} + 5.5\left(\frac{\rho_h f_{yh}}{f_c'}\right) \le 1.0 \quad (7\text{-}9)$$

4) Force demand

It is revealed that the horizontal elongation is the greatest at the mid-height panel zone, leading to elastic web crushing. Thus, the tensile force demand σ_{dt} in the horizontal ties is calculated by averaging the tensile stresses of shear reinforcement within the mid-height panel zone.

5) Force capacity

The proposed elastic web crushing strength basically assumes tensile yielding of shear reinforcement. Since the post-yield behavior of horizontal ties is assumed as elastic-perfectly plastic, the tensile capacity σ_{ct} of the horizontal tie is calculated as its yield strength.

$$\sigma_{ct} = f_{yh} \quad (7\text{-}10)$$

7.1.5 Boundary elements

1) Boundary element in tension

Neglecting the tensile strength of concrete, the boundary element in flexural tension consists only of steel U-sections. The material and sectional properties, including elastic stiffness, sectional area, and moments of inertia (in the direction of bending) are calculated using the actual properties of steel U-section consisting of flange and web plates. Since the steel U-sections are singly symmetric, for practical simplicity, the element axis is defined as the geometric center of the steel U-sections. No reduction of stiffness is assumed.

2) Boundary element in compression

In the boundary compression zone, the axial-flexural force (including shear) is resisted by the infill concrete as well as steel U-sections, assuming full composite action of the steel U-section and infill concrete. The element axis is defined as the geometric center of the composite section. At elastic web crushing, the boundary concrete in compression is undamaged, and global flexural buckling of the boundary element is restrained due to the strong lateral restraint and good structural integrity provided by the web concrete. Further, both the flange and web plates are designed as compact section, to prevent inelastic local buckling of the steel plates. Therefore, the effective axial stiffness and flexural stiffness of the composite section are calculated equal to those of concrete-filled steel columns with compact steel sections, as follows:

$$(EA)_{eff} = C_3 E_c A_{bc} + E_s A_b \tag{7-11}$$

$$(EI)_{eff} = C_3 E_c I_{bc} + E_s I_b \tag{7-12}$$

Where, A_{bc} and A_b = sectional areas of infilled concrete and steel U-sections in the boundary zone, respectively; I_{bc} and I_b = moments of inertia of infilled concrete and steel U-sections with respect to the center of the boundary elements, respectively; and $C_3 = 0.45 + 3\rho_{be} \leq 0.9$ (AISC 360, 2016), in which ρ_{be} = area ratio of a steel U-section to the boundary zone.

3) Force demand

The force demands, including axial force F_{db}, shear force V_{db}, and flexural moment M_{db}, are calculated for the entire length of the boundary elements in compression and tension zones.

4) Force capacity

The axial force capacity F_{cb} of the boundary element in tension is calculated based on the yield strength of steel U-sections only. On the other hand, F_{cb} of the boundary elements in compression is determined considering both the contributions of the steel U-section and infilled concrete. In the present study, F_{cb} of the boundary element in compression is calculated assuming concrete-filled steel columns of AISC 360 (2016).

$$F_{cb} = F_y A_b \qquad \text{for tension zone} \qquad (7\text{-}13a)$$

$$F_{cb} = 0.85 f_c' A_{bc} + F_y A_b \qquad \text{for compression zone} \qquad (7\text{-}13b)$$

Note that Eq. (7-13b) is valid only if compact steel section is used.

The plastic moment capacity M_{cb}, including the effect of axial force demand F_{db}, is calculated from section analysis, using either the plastic stress distribution method or the strain compatibility method (AISC 360, 2016). For the boundary element in tension, only steel U-section is considered. However, for the boundary element in compression, the composite section of the steel U-section and infilled concrete is considered. For the plastic stress distribution method, an uniform stress of $0.85 f_c'$ and yield stress are used for the concrete in compression and the steel U-section, respectively, neglecting tensile stress of concrete. For the strain compatibility method, the stress-strain relationship for the steel plates is idealized as elastic-perfectly plastic, neglecting buckling for compression and strain hardening for tension. The extreme compression fiber strain is assumed as 0.003 (ACI 318, 2019).

The shear force capacity V_{cb} for both the boundary elements in compression and tension zone is calculated based on the shear strength of the steel section alone, according to AISC 360 (2016). In the present study, the shear strength of the steel U-section is calculated based on the contribution of the web plates alone, for safe prediction.

$$V_{cb} = 0.6F_y A_{b,w} \tag{7-14}$$

where, $A_{b,w}$ = total area of the web plates in a steel U-section.

7.1.6 Boundary conditions

Fig. 7-2 shows the boundary conditions for each elements in the proposed strip model. For the diagonal strips, the fixed end condition is used for both ends of the strips, to develop restraint moments to the rotation of the boundary elements. This prevents the overestimation of flexural demands in the boundary elements. However, when one end of the strips is connected to the web region at the wall base, the corresponding boundary condition is defined as a hinge, because the concrete is not protected by the steel U-sections. For the horizontal ties, both ends of the ties are modeled using hinged connection. When steel plate beams are used for shear reinforcement, their end condition depends on the actual details of the connections between the plate beams and boundary elements. In the present study, fixed end conditions are used for the plate beams, considering the details of the test specimens: steel plate beams and boundary steel U-sections are connected by welding. For the boundary elements in compression and tension zones, their both ends are modeled using fixed connection.

7.1.7 Analysis procedure

In **Fig. 7-8**, overall procedures of the proposed EEA are shown as the flowchart. In the figure, general statements are denoted as rectangular boxes, and conditional statements are denoted as trapezoidal boxes. The step-by-step procedures are explained for a cantilever SUB-C wall, as follows:

1) Define the strip model from geometric and material properties of a given SUB-C wall, following the guidelines described in Section 7.1.2 to 7.1.6.

2) As an initial condition, calculate the stiffness reduction factor R_h of horizontal ties and the effective average strength factor k of concrete, and the elastic web crushing strength V_n by Eq. (7-9), (6-11), and (6-12), respectively.

3) Perform elastic analysis using a lateral loading condition of $V = V_n$.

4) Verify the stress states in horizontal ties by comparing their demand and capacity. Note that the proposed elastic web crushing strength model basically assumes yielding of shear reinforcement. Thus, the demand σ_{dt} should be equal or close to the capacity σ_{ct}. Otherwise, redefine the stiffness reduction factor R_h according to the demand-to-capacity ratio: If $\sigma_{dt} > \sigma_{ct}$, decrease R_h or If $\sigma_{dt} < \sigma_{ct}$, increase R_h. Then, update the tie stiffness E_{es} by the calculated R_h (Eq. 7-8). Further, update the axial σ_{cs} and flexural capacity M_{cs} of diagonal strips (= $1/\alpha_{h,max}$) by Eq. (7-6) and (7-7). Back to step 3).

5) Verify the safety of boundary elements against shear and axial forces. If the demands for shear V_{db} and axial forces F_{db} are greater than their capacities V_{cb} and F_{cb}, redesign the targeted SUB-C walls or boundary elements, and back to step 1). Since the proposed EEA is primarily concerned with identifying the elastic web crushing strength, its solution should be greater than the flexural demand V_f (or strength) of the walls.

Thus, the condition of $F_{db} > F_{cb}$ violates this fundamental assumption. Further, the condition of $V_{db} > V_{cb}$ probably results from the extremely thin web plates in steel U-sections, which is not desirable for safe design. The relevant discussion is provided in Section 7.3.

6) Verify the safety of boundary elements against flexural moments, by comparing the flexural demand M_{db} and capacity M_{cb} of the boundary elements. Basically, flexural yielding of the boundary elements at any location is not allowed. However, local flexural yielding of the boundary element is allowed only at the wall critical zone where the flexural demand is the greatest (i.e., boundary compression zone at the wall base). The nonlinearity from the yielding can be treated by replacing the fixed boundary condition at the yielding location (i.e., at wall base) by a hinged condition, and applying the external flexural moment equivalent to M_{cb} to the yielding location (refer to **Fig. 7-9**). If $M_{db} > M_{cb}$ at other locations, redesign the strip model or boundary elements. Then, back to step 1).

7) Verify the safety in flexure at the ends of the diagonal strips: The flexural demands $M_{ds,T}$ and $M_{ds,C}$ of the strips at the flexural tension and compression zone should be less than the flexural capacity M_{cs}. Otherwise, decrease V_n and back to step 3).

8) Finally, verify the web crushing condition by comparing the axial force demand σ_{ds} and capacity σ_{cs} of the diagonal strips. If σ_{ds} is close to σ_{cs}, then V currently selected is the elastic web crushing strength of the wall. If $\sigma_{ds} > \sigma_{cs}$, decrease V_n or If $\sigma_{ds} < \sigma_{cs}$, increase V_n. Then, back to step 3).

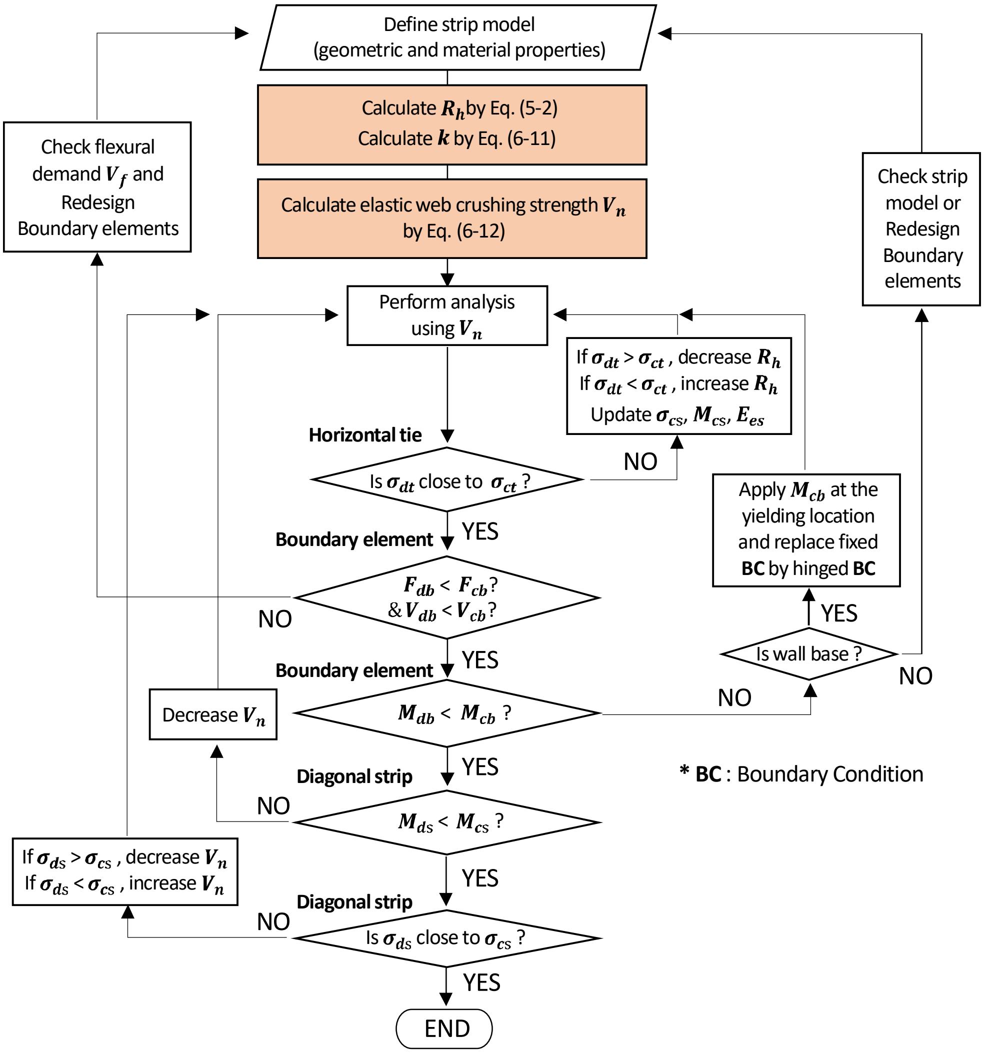

Fig. 7-8 Flowchart for equivalent elastic analysis.

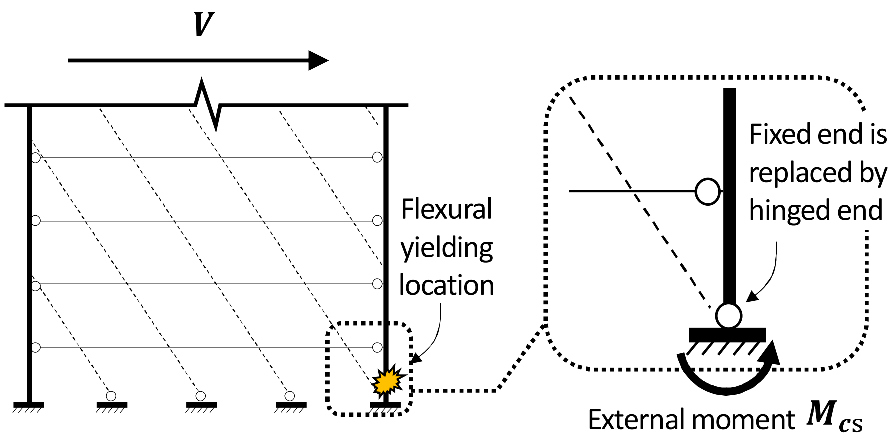

Fig. 7-9 Equivalent hinge and external moment for boundary element.

7.1.8 Application to test specimens

For verification, the elastic web crushing strength of the test specimens was calculated according to the proposed EEA, using MIDAS program (reference). For the wall with a symmetric cross section, 2-dimensional modeling is recommended. **Fig. 7-10** shows the modeling examples of the test specimens.

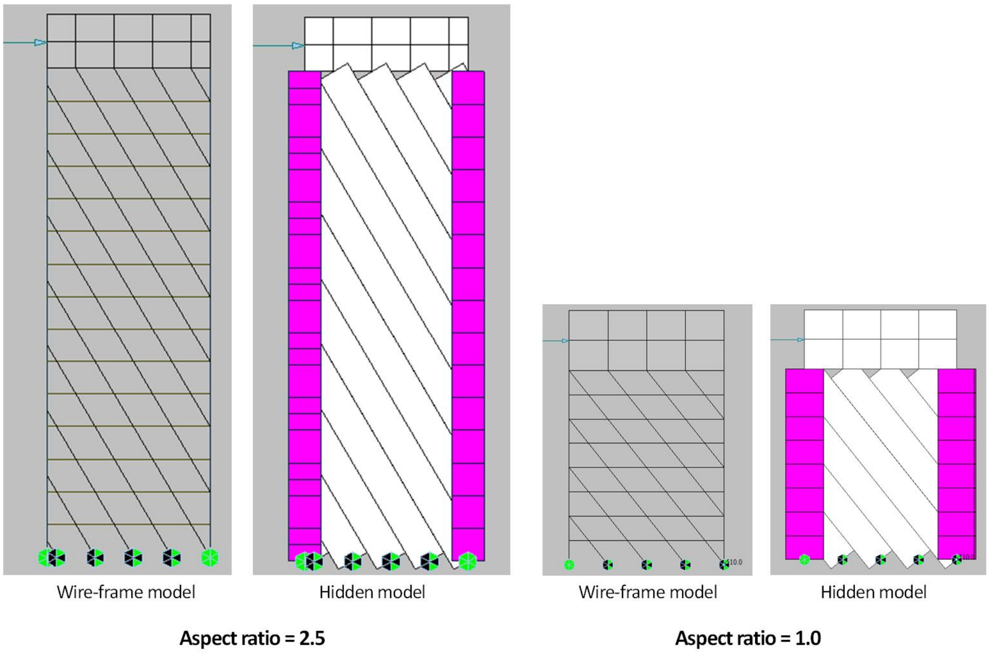

Fig. 7-10 Strip models for test specimens

The major considerations for use in MIDAS include:

1) Use the element type "**General beam/Tapered beam**" for diagonal strips, boundary elements, and steel plate beams; and the element type "**Truss**" for horizontal ties (**Fig. 7-1**1).

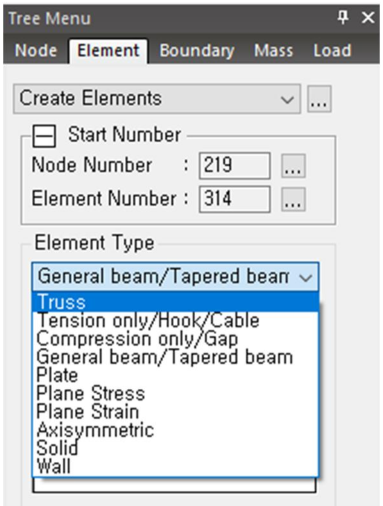

Element type
"**Truss**" → horizontal tie
"**General beam/Tapered beam**"
→ diagonal strip
→ boundary element
→ steel plate beam (for shear reinforcement)

Fig. 7-11 Element types

2) The boundary element in tension, a steel U-section, can be modeled using "**Channel section**" in the built-in library (by command **Properties** | **Section Properties** | **Section Data** in the Main Menu). To locate its center to the element axis, press **Change offset** button, and change the center location from the centroid to the center of section (**Fig. 7-12**(a)).

3) The boundary element in compression can be modeled using "**SRC-Box section**" in the menu of **SRC** in **Section Data**, due to the absence of the composite steel U-section. To simulate the sectional properties of U-section, set the thickness of one of the two flange plates as close to zero (0.1 mm for the present study). To provide the effective flexural stiffness $(EI)_{eff}$ to the composite section, the value of C_3 in Eq. (7-12) is used for **Combined Ratio of Conc.** in **Section Data** (**Fig. 7-12**(b)).

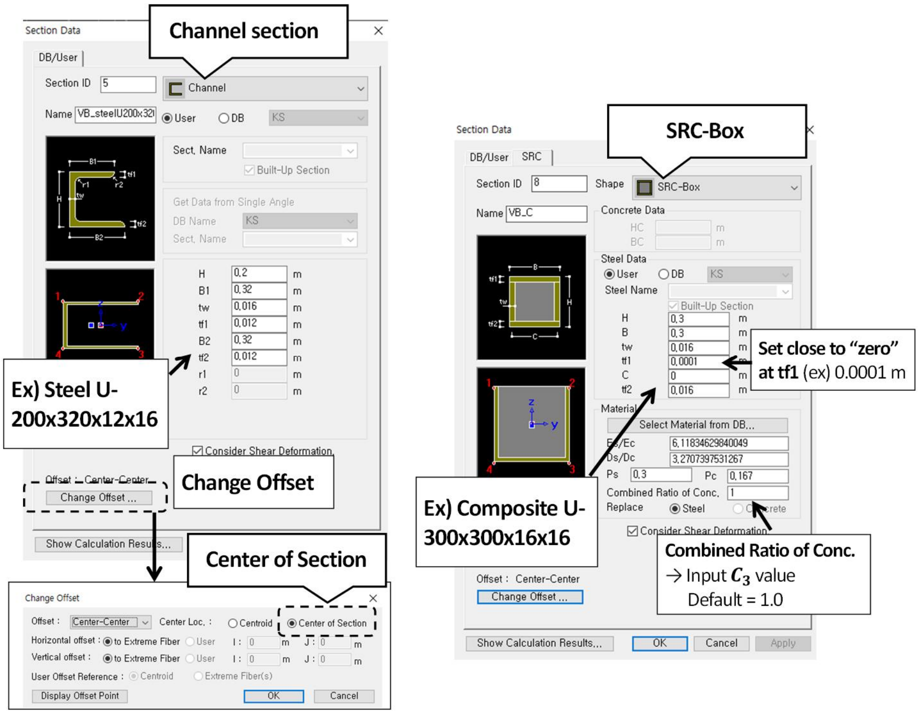

Fig. 7-12 Sectional properties of (a) steel U-section in tension and (b) concrete-filled steel U-section in compression.

4) The reduced stiffness for each elements can be realized in the menu of "**Section Stiffness Scale Factor**" (by command **Properties** | **Scale Factor** in the Main Menu). In the present study, the reduced stiffness is considered for the horizontal tie and diagonal strip elements. As an initial condition, enter the value of R_h in Eq. (7-9) into **Area** for the tie element. Enter 0.7 for **Area** and **moment of inertia** (denoted as $\boldsymbol{I_{yy}}$) for the strip element, considering $0.7E_c$ (refer to **Fig. 7-13**)

5) At the wall critical zone, the nonlinearity from local flexural yielding of boundary elements can be treated by applying an external moment M_{cb} at the node where $M_{db} > M_{cb}$ (by command **Load** | **Nodal Loads** in the Main Menu). In addition, the fixed end condition at the yielding location is replaced by the hinged (i.e., pin) condition (**Fig. 7-14**).

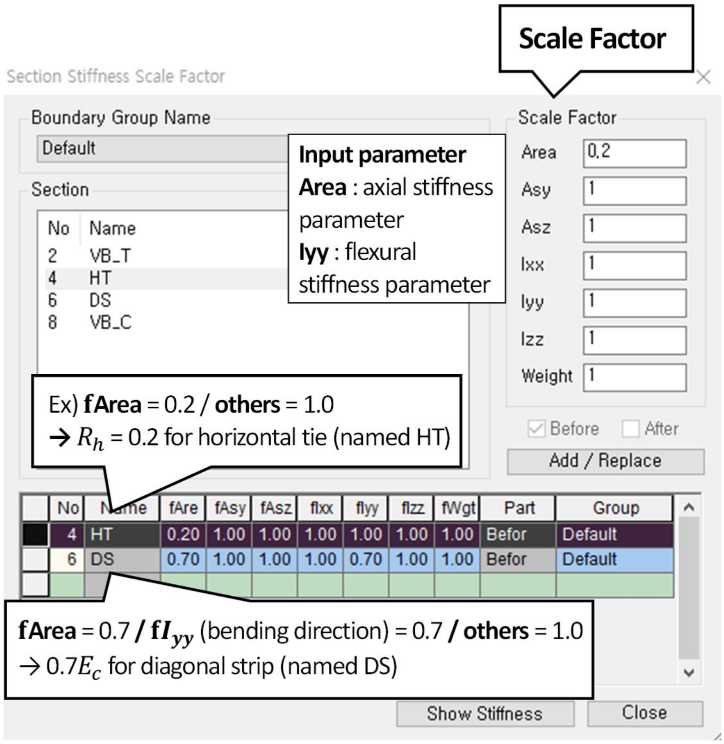

Fig. 7-13 Reduced stiffness factors for structural elements.

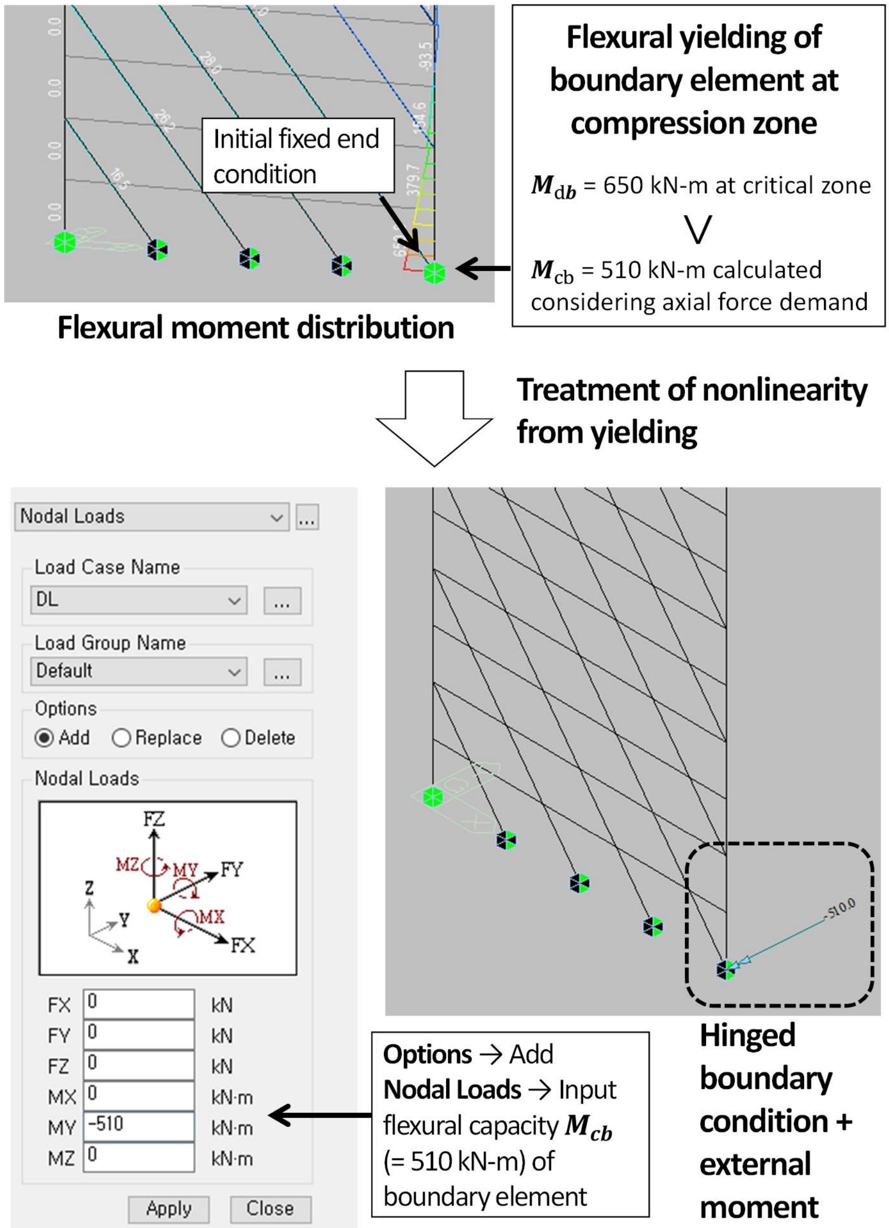

Fig. 7-14 Treatment of flexural yielding of boundary element

The major modeling parameters and the results of the proposed EEA for the test specimens are summarized in **Table 7-1**. **Fig. 7-15**(a) compares the tested strengths V_{test} with the elastic web crushing strength V_n of Eq. (6-12), while **Fig. 7-15**(b) compares the tested strengths V_{test} with V_n determined from the proposed EEA. The better agreement between V_{test} and V_n from the EEA indicates that the proposed strip model more accurately predicts the elastic web crushing strength of the SUB-C walls: Overall, the prediction error of the proposed EEA is only 4%, which is significantly less than that of the elastic web crushing model of Eq. (6-12) (12% on average). In particular, the improvement of prediction accuracy is pronounced in the walls with aspect ratio of 1.0.

The reason can be explained from **Fig. 7-16**(a) that compares the stiffness reduction factor R_h (i.e., horizontal elongation) calculated by Eq. (7-9) with the R_h obtained from the EEA. For the walls with aspect ratios of 2.5 and 2.0, generally, R_h calculated by Eq. (7-9) agree with R_h determined from the proposed EEA. On the other hand, in the walls with the lower aspect ratio of 1.0, Eq. (7-9) underestimates R_h of the proposed EEA. That is, the horizontal elongation is overestimated, which leads to the conservatism in shear strength prediction. **Fig. 7-16**(b) shows the effective average strength factor k calculated by Eq. (6-11) with k determined from the EEA. The good agreement between these two k values is clearly explained from the web crushing condition of the proposed EEA (see Step 8 in Section 7.1.7). Nevertheless, referring to **Fig. 7-16**(b), this result confirms that the proposed average strength factor k of Eq. (6-11) reasonably predicts the shear degradation behavior of the concrete in SUB-C walls.

Table 7-1 Modeling parameters and results of EEA

	Aspect ratio = 2.5			Aspect ratio = 2.0			Aspect ratio = 1.0	
Specimen	CS2.5	CS2.5VH	CS2.5M	CS2	CS2VL	CS2SB	CS1	CS1VL
Major modeling parameter								
l_s (mm)	4750	4750	4750	3450	3450	3450	1850	1850
h_w (mm)	4500	4500	4500	3200	3200	3200	1600	1600
l_w (mm)	1800	1800	1800	1600	1600	1600	1600	1600
t_w (mm)	300	300	200	200	200	200	200	200
f_c' (MPa)	64.3	64.3	64.3	54.9	47.4	49.6	54.6	53.1
ρ_h (%)	0.44	0.44	0.99	0.51	0.51	0.63	0.24	0.24
f_{yh} (MPa)	445	445	445	445	445	456	514	514
s_h (mm)	300	300	200	250	250	1000	300	300
ρ_{be} (%)	15.4	13.8	19	16.4	11.6	16.4	16.4	11.6
C_3 [a]	0.9	0.9	0.9	0.9	0.8	0.9	0.9	0.8
Preliminary calculation								
R_h	0.20	0.20	0.41	0.36	0.40	0.46	0.74	0.75
θ_d by Eq. (7-2) (deg)	30.0	30.0	41.8	39.8	41.4	42.9	45.0	45.0
w_s by Eq. (7-4) (mm)	346	346	240	300	300	320	320	320
Application to modeling								
θ_d (deg)	30	31	36	34	34	34	39	39
w_s (mm)	304	309	244	305	305	388	250	250

Table 7–1 Modeling parameters and results of EEA (Continuted)

	Aspect ratio = 2.5			Aspect ratio = 2.0			Aspect ratio = 1.0	
Specimen	CS2.5	CS2.5VH	CS2.5M	CS2	CS2VL	CS2SB	CS1	CS1VL
Application to modeling								
d_h[b] (mm)	22.5	22.5	23.0	18.9	18.9	23.7	11.1	11.1
Analysis result								
Boundary element								
M_{cb} (kN-m)	742	1475	1280	503	364	492	510	401
M_{db} (kN-m)	742	1475	1280	503	364	492	510	401
Diagonal strips								
M_{cs} (kN-m)	103.8	106.9	47.9	71.3	62.8	112.3	57.8	56.2
M_{db} (kN-m)	89.9	92.2	45.6	42.3	41.9	38.9	20.5	18.3
k (calculated from R_h)	0.23	0.23	0.25	0.28	0.29	0.30	0.34	0.34
σ_{cs} (MPa)	15.0	15.0	16.1	15.4	13.5	14.9	18.5	18.0
σ_{ds} (MPa)	14.5	15.4	16.0	15.4	13.6	15.8	18.3	18.1
R_h	0.25	0.25	0.3	0.42	0.45	0.55	1	1
V_{test} (kN)	2,395	2,730	2,702	1,918	1,577	2,052	3,014	2,375
V_n of EEA (kN)	2,400	2,900	2,550	1,770	1,550	1,850	2,800	2,330
V_n by Eq. (6-12) (kN)	2,648	2,648	2,321	1,693	1,504	1,638	2,239	2,179

[a]Effective stiffness factor for concrete in boundary elements = $0.45 + 3\rho_{be} \leq 0.9$ (AISC 360, 2016).
[b]Effective diameter of horizontal tie.

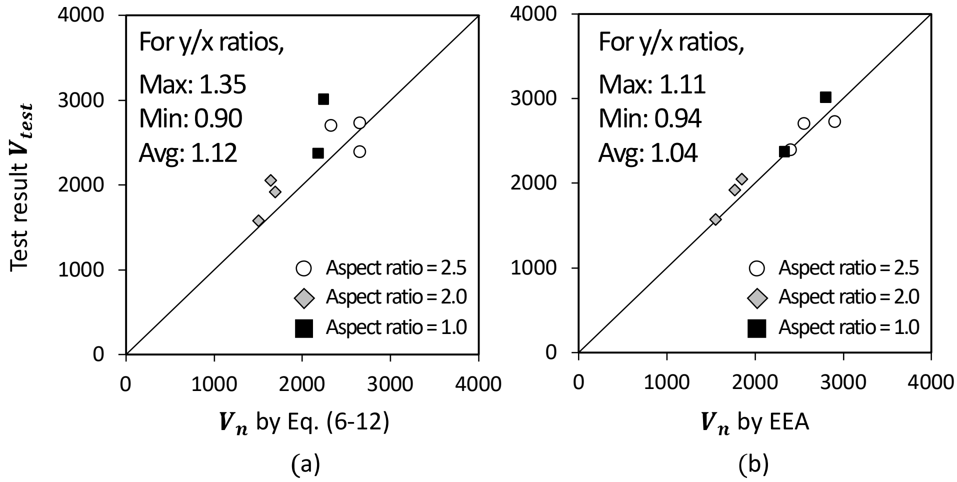

Fig. 7-15 Comparison of tested shear strengths and the predictions of (a) the proposed shear strength model (Eq. (6-12)); (b) proposed EEA method.

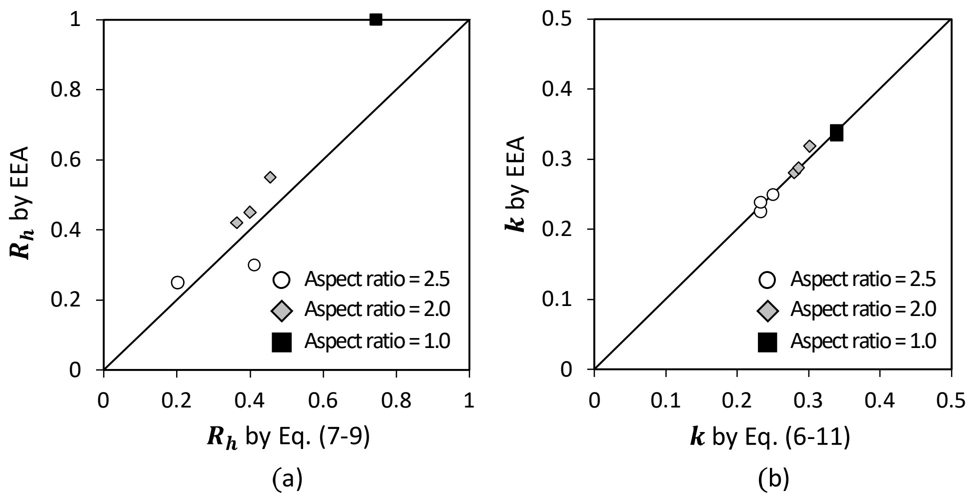

Fig. 7-16 Comparison of the proposed shear strength model and EEA method: (a) stiffness reduction factor for horizontal tie; (b) effective strength factor for concrete.

7.2 Design Strengths and Deformation Capacity

7.2.1 Deformation-based design approach

Fig. 7-17(a) shows possible failure modes of RC (or SUB-C) walls subjected to cyclic lateral loading (ASCE 41, 2017). When shear demand V_u (= V_f resulting from flexural strength) is greater than the maximum shear strength $V_{n,max}$ (Case 1), brittle shear failure without flexural yielding occurs. In the case of V_u < $V_{n,max}$ (Case 2), shear failure occurs after flexural yielding (post-yield shear failure; inelastic shear failure), and deformation capacity is defined at the intersection of the shear demand V_u and post-yield shear strength V_n. On the other hand, when V_u is extremely small (Case 3), the deformation capacity is limited by flexural failure, such as flexural-compression failure or flexural-tension failure. Thus, for ductile design of walls, the flexural strength should be less than the maximum shear strength, and the design parameters affecting the shear degradation behavior should be carefully considered. For ordinary RC walls, the shear strength degradation behavior is determined from diagonal tension failure mechanism (e.g., compression zone failure mechanism, Choi et al. 2016) and web crushing mechanism (e.g., longitudinal elongation mechanism, Eom et al. 2013). Extensive studies have been conducted to predict the shear strength degradation behavior, and provide shear strength-deformation relationship based on various design parameters including the shear span ratio, axial force ratio, concrete strength, rebar yield strength, vertical and horizontal reinforcement ratios, and the shape of sections (Duffey 1994; hidalgo 1996; Carrillo 2012; Sánchez 2010; Eom et al. 2013; Choi et al. 2016; and Epackachi et al. 2019).

On the other hand, in the proposed SUB-C walls, the shear strength is determined by web crushing failure only, but two types of web crushing mechanisms are defined: elastic and inelastic web crushing mechanisms. In the case of elastic web crushing, shear failure occurs before flexural yielding, thus deformation capacity is very limited (belongs to Case 1 in **Fig. 7-17**(a)). On the other hand, inelastic web crushing occurs after flexural yielding, showing ductile behavior until web crushing (belongs to Case 2). Further, the failure location is clearly different between the two web crushing mechanisms: The elastic web crushing occurs primarily in the mid-height of the walls where the horizontal elongation is concentrated. On the other hand, inelastic web crushing occurs in the plastic hinge zone where the vertical (longitudinal) elongation is concentrated. In the proposed shear strength model (Chapter 6), it is assumed that the elastic web crushing strength is independent of deformation demand, but depends on mechanical horizontal shear reinforcement ratio and aspect ratio of walls. On the other hand, the inelastic web crushing strength is highly dependent on the deformation demand, because, basically, the vertical elongation increases with the increase of deformation demand. Here, the vertical elongation is determined based on mechanical vertical boundary steel ratio, axial force ratio, and aspect ratio of walls. Further, due to the contribution of steel U-sections (= V_b), the maximum allowable strength (= $0.15f_c' t_w l_e$ + V_b) is greater than that of the elastic web crushing mechanism (= $0.15f_c' t_w l_e$).

Fig. 7-17(b) conceptually shows the deformation-based design of SUB-C walls. The maximum shear strength $V_{n,max}$ is determined from the elastic web crushing strength, and the shear strength degradation behavior is determined from the inelastic web crushing strength. Thus, the overall shear capacity curve is obtained from the envelops of the two web crushing strengths. On the other hand, the shear demand V_u is determined from the flexural strength of the walls. If V_u is greater than $V_{n,max}$, the elastic web crushing failure occurs without flexural yielding. In the case of V_u < $V_{n,max}$, the inelastic web crushing failure occurs after flexural yielding, and deformation capacity is defined at the intersection point of the shear demand V_u and the degraded inelastic web crushing strength. Thus, for reliable design of SUB-C walls, accurate predictions of flexural strength, shear strength, and post-yield shear strength are required.

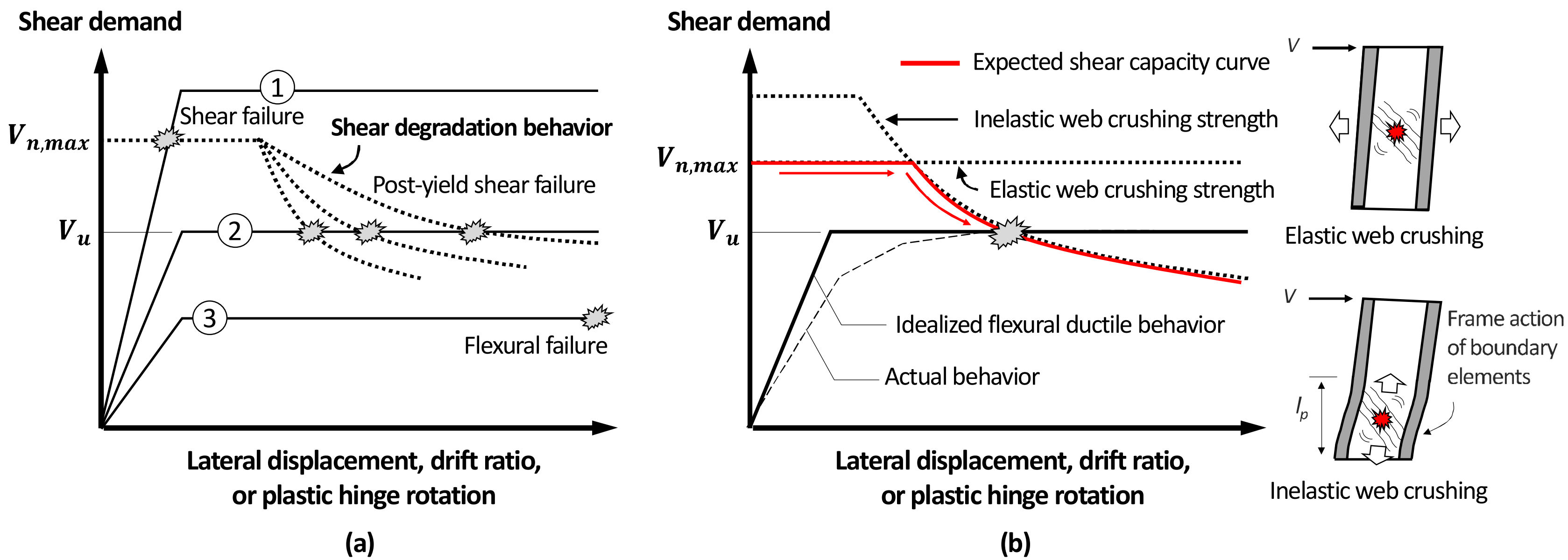

Fig. 7-17 Possible failure modes and deformation-based design of walls.

7.2.2 Flexural strength

The flexural strength M_n of SUB-C walls is determined from section analysis, using the strain compatibility method or plastic stress distribution method. In order to determine the maximum shear demand on walls, the flexural strength can be increased by multiplying over-strength factor of Ω = 1.1, considering the strain hardening and confinement (to infilled concrete) of steel U-sections. When M_n is calculated considering both the confinement and strain hardening, Ω is equal to 1.0.

1) Strain compatibility method

The flexural strength is calculated according to Section 3.2.1 (ACI 318 Method). The effective depth of the compression zone is defined as $\beta_1 c$, in which c = distance from the extreme compression fiber to the neutral axis; and β_1 is calculated as follows:

$$\beta_1 = 0.85 \qquad \text{for } f_c' \le 28 \text{ MPa} \qquad \text{(7-15a)}$$

$$\beta_1 = \max[0.65, 0.85 - 0.007(f_c' - 28)] \qquad \text{for } f_c' > 28 \text{ MPa} \qquad \text{(7-15b)}$$

2) Plastic stress distribution method

The uniform compressive stress of $0.85 f_c'$ and yield stress are assumed for the plastic stresses of concrete and steel sections, respectively.

3) Advanced flexural strength

More refined stress-strain relationships for the confined infill concrete and steel U-sections can be used. **Fig. 7-18** shows the available stress-strain models for the confined concrete (Tomii and Sakino 1979; Susantha et al. 2002; and Lai and Varma 2016), developed for use in concrete-filled rectangular steel tube section. For the steel U-section in compression (**Fig. 7-19**), the reduced strength due to buckling is calculated based on the slenderness ratio (width-to-thickness ratio, *b*/*t* ratio) of the steel plates. For the steel U-sections in tension (**Fig. 7-19**), the post-yield strain hardening behavior can be considered using a multilinear model.

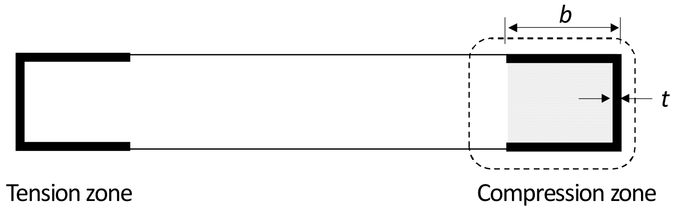

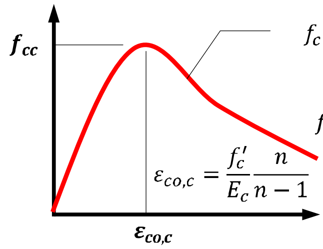

$$f_c = f_{cc}\left(\frac{\varepsilon_c}{\varepsilon_{co,c}}\right)\left(\frac{n}{n-1+\left(\varepsilon_c/\varepsilon_{co,c}\right)^n}\right)$$

$$f_{cc} = f'_c\left[0.8 + 0.18\left(\frac{b/t}{100} + \frac{F_y/f'_c}{30}\right)\right]$$

$$n = 0.058f'_c + 1$$

Lai and Varma (2016)

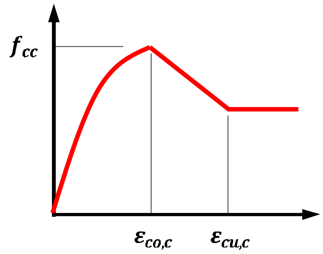

$$f_{cc} = f'_c + 4f_{c2} \qquad f_{c2} = -6.5\lambda_e\frac{(f'_c)^{1.46}}{F_y} + 0.12(f'_c)^{1.03}$$

$$\varepsilon_{co,c} = \varepsilon_{co}\left[1 + 5\left(\frac{f_{cc}}{f'_c} - 1\right)\right] \qquad \lambda_e = \frac{b}{t}\sqrt{\frac{F_y}{E_s}\frac{12(1-\upsilon^2)}{\pi^2 k}}$$

$$f_c = f_{cc}\left(\frac{\varepsilon_c}{\varepsilon_{co,c}}\right)\left(\frac{n}{n-1+\left(\varepsilon_c/\varepsilon_{co,c}\right)^n}\right) \qquad n = \frac{E_c}{E_c - \left(f_{cc}/\varepsilon_{co,c}\right)}$$

$$r = \lambda_e\frac{f_{ck}}{F_y} \qquad \varepsilon_{cu,c} = \begin{cases} 0.04 & \mathrm{r} \le 0.042 \\ 14.5(r)^2\text{-}2.4r + 0.116 & 0.042 \le \mathrm{r} \le 0.073 \\ 0.018 & \mathrm{r} \ge 0.073 \end{cases}$$

Susantha et al. (2001)

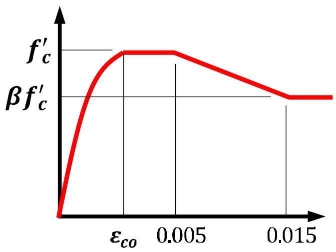

$$f_c = f_{cc}\left(\frac{\varepsilon_c}{\varepsilon_{co,c}}\right)\left(\frac{n}{n-1+\left(\varepsilon_c/\varepsilon_{co,c}\right)^n}\right)$$

$$n = \frac{E_c}{E_c - \left(f_{cc}/\varepsilon_{co,c}\right)}$$

$$\beta = \begin{cases} 1 & b/t \le 24 \\ 1.6 - 0.025b/t & 24 \le b/t \le 44 \\ 0.5 & b/t \ge 44 \end{cases}$$

Tomii and Sakino (1979)

Fig. 7-18 Stress-strain relationships of concrete confined by rectangular steel tubes.

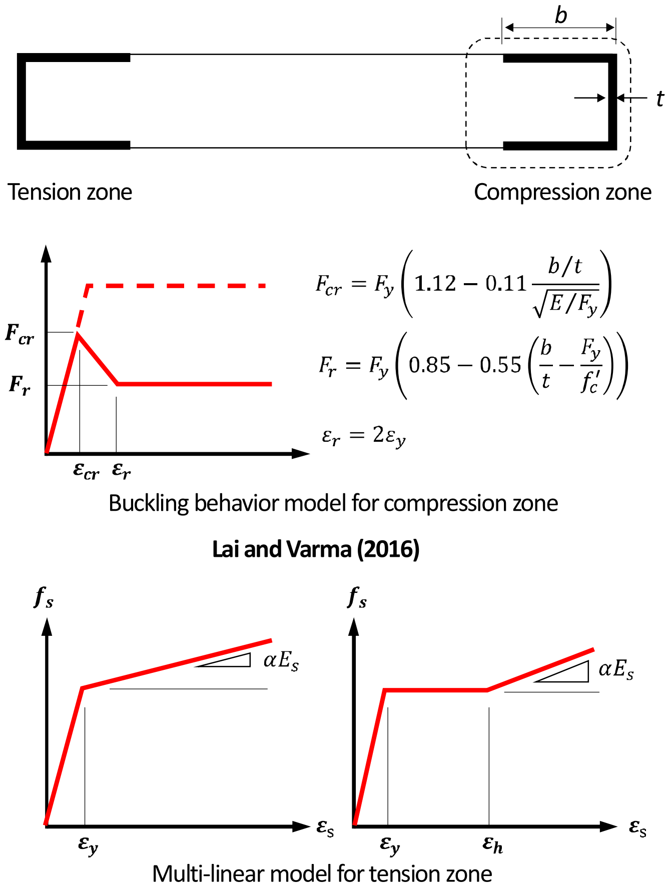

Fig. 7-19 Stress-strain relationships of steel U-sections in compression and tension zones.

However, for seismic design, it is recommended that the design of steel U-sections be compact section, to minimize their local buckling.

7.2.3 Shear strength

The shear strength (before flexural yielding) of SUB-C walls is determined by elastic web crushing, and the web crushing strength highly depends on the degree of horizontal elongation in the mid-height panel zone. Although the proposed elastic web crushing model provides a reasonable prediction accuracy for the tested specimens (see Sec 6.4.4), the shear strength for design should be conservatively defined considering both mechanical validity and practical simplicity.

Therefore, the design shear strength controlled by elastic web crushing was defined by simplifying the proposed elastic web crushing model with reasonable safety margin. Note that the proposed shear strength was defined using two design parameters: shear span ratio a (= h_s/l_w = M/Vl_w, in which M and V = force demands for in-plane flexure and shear, respectively), and mechanical shear reinforcement ratio ω_h (= $\rho_h f_{yh}/f_c'$), which are the variables to determine the maximum horizontal elongation (see Eq. (5-2)). The practical range of ω_h was 0.02 – 0.10, considering the available range of the relevant design parameters (ρ_h = 0.2%–1.0%, f_{yh} ≈ 400 MPa, and f_c' = 30 – 70 MPa). To clarify the effect of ω_h and a on the shear strength, **Fig. 7-20** shows the effective average strength factor k for concrete calculated according to Eq. (6-11).

For a = 1.0, the calculated k (denoted as original k in **Fig. 7-20**) is almost uniform, which is close to the maximum limit of k (= 0.35). Reminding that the proposed model provides a conservatism of the prediction on squat walls, the design k value for a < 1.0 is defined as its maximum limit, regardless of the mechanical shear reinforcement ratio.

$$k = 0.35 \qquad \text{for } a < 1.0 \qquad (7\text{-}16)$$

For a ≥ 1.0, as the mechanical shear reinforcement ratio ω_h increases, k increases noticeably. Further, as the shear span ratio a increases, k decreases.

Thus, the design k value for 1.0 $\leq$ a < 1.5 is conservatively determined as the k value corresponding to a = 1.5. Further, for simplicity in calculation, the design k is linearized as follows:

$$k = 0.28 + 0.55\omega_h \qquad \text{for } 1.0 \leq a < 1.5 \qquad (7\text{-}17)$$

For a $\geq$ 1.5, the dependence of k on ω_h much increases, particularly for low ω_h. Thus, the relationship for k is simplified as a bilinear curve.

For $1.5 \leq a < 2.0$, the design k is conservatively determined as the k value corresponding to a = 2.0, as follows:

$$k = 0.22 + 1.25\omega_h \qquad \text{for } \omega_h < 0.06 \qquad (7\text{-}18a)$$

$$k = 0.25 + 0.75\omega_h \qquad \text{for } \omega_h \geq 0.06 \qquad (7\text{-}18b)$$

For $2.0 \leq a < 2.5$, the design k is conservatively determined as the k value corresponding to a = 2.5, as follows:

$$k = 0.16 + 2\omega_h \qquad \text{for } \omega_h < 0.05 \qquad (7\text{-}19a)$$

$$k = 0.21 + \omega_h \qquad \text{for } \omega_h \geq 0.05 \qquad (7\text{-}19b)$$

For $2.5 \leq a < 3.0$, the design k is conservatively determined as the k value corresponding to a = 3.0, as follows:

$$k = 0.08 + 3\omega_h \qquad \text{for } \omega_h < 0.05 \qquad (7\text{-}20a)$$

$$k = 0.16 + 1.4\omega_h \qquad \text{for } \omega_h \geq 0.05 \qquad (7\text{-}20b)$$

Fig. 7-20(a) shows that the proposed design method reasonably approximates the k values from Eq. (6-11), within the practical range of ω_h = 0.02 – 0.10. Note that the k values in Eq. (7-17), (7-18), (7-19), and (7-20) are less than 0.35, according to Eq. (6-11). **Fig. 7-20**(b) shows the design k values according to the shear span ratio, where the mechanical shear reinforcement ratio is assumed as 0.05. The figure confirms that the proposed design method safely simplifies the k values. The design shear strength of SUB-C walls can be calculated by substituting the design k value into Eq. (6-2).

For comparison, **Fig. 7-20**(a) also shows the k values corresponding to the maximum shear strengths (i.e., web crushing strengths) of ACI 318 (2019), Eurocode 2 (2004), and fib MC (2010). Here, the k values, which are the function of concrete strength f_c', were obtained by equating Eq. (6-2) with Eq. (2-4), (2-8), and (2-15), respectively. In the figure, only the k values for f_c' = 30 MPa and 70 MPa are shown, which are the limiting values for the tested concrete strengths. Generally, the k values for the proposed design shear strength are greater than those of ACI 318, even when the mechanical shear reinforcement ratio ω_h is very small. This result confirms that ACI 318 significantly underestimates the shear strength of SUB-C walls. On the other hand, Eurocode 2 and fib MC overestimate k, for all possible values of ω_h and a. Note that the proposed shear strength model was not verified for slender walls with shear span ratios greater than 3.0. For this reason, when the shear span ratio is greater than 3.0, it is recommended that the shear strength design of SUB-C walls conservatively follow the RC design method of ACI 318 (Eq. (2-1)).

If advanced or economic design is necessary, the shear strength controlled by elastic web crushing can be calculated according to the equivalent elastic analysis method described in Section 7.1.

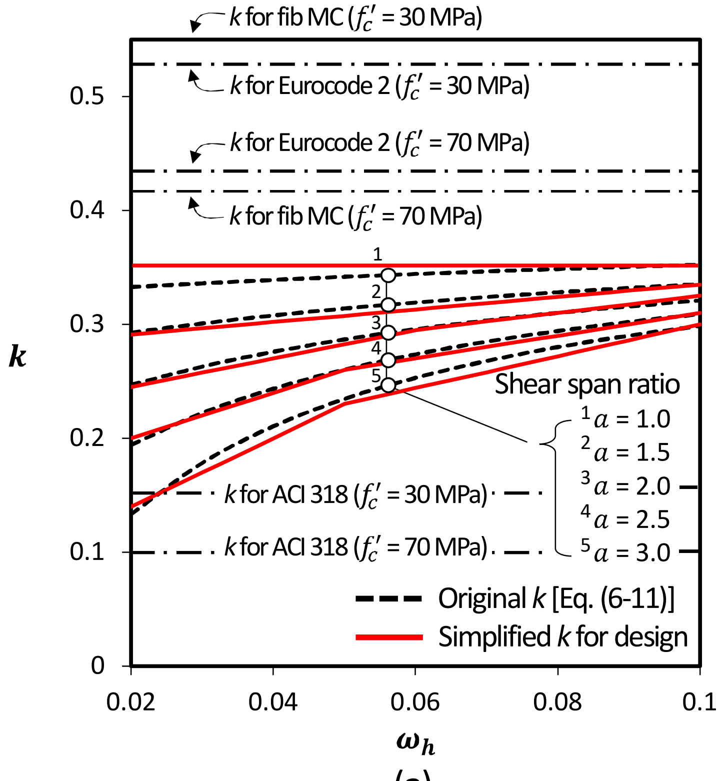

(a)

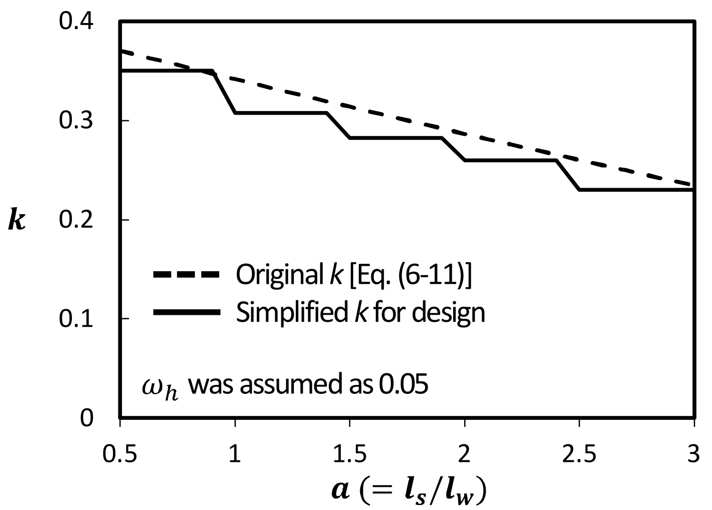

(b)

Fig. 7-20 Effective average strength factor for design.

7.2.4 Deformation capacity

Fig. 7-21 shows the shear force-deformation relationship of SUB-C walls. The shear demand V_f is calculated from the flexural strength M_n, as follows:

$$V_f = \frac{M_n}{l_s} \tag{7-21}$$

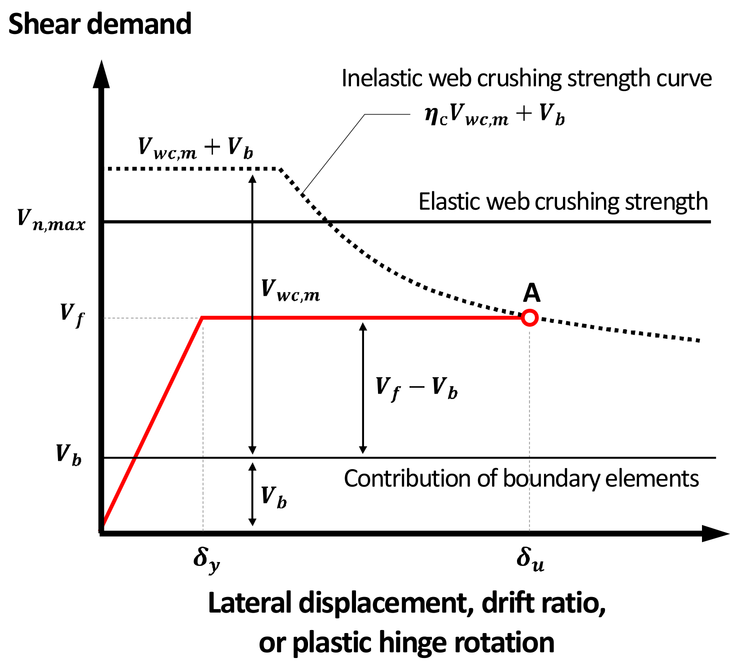

Fig. 7-21 Design shear force-deformation relationship of SUB-C walls.

In the proposed shear strength model, the deformation capacity is primarily concerned with inelastic web crushing mechanism. Thus, for prediction of deformation capacity, the inelastic web crushing strength V_n is redefined as follows:

$$V_n = V_{wc} + V_b = \eta_c V_{wc,m} + V_b \tag{7-22}$$

where, η_c = shear degradation factor for concrete; and $V_{wc,m}$ = maximum contribution of concrete to the inelastic web crushing strength, which is defined as follows:

$$\eta_c = \frac{V_{wc}}{V_{wc,m}} \tag{7-23}$$

$$V_{wc,m} = 0.15 f_c' t_w l_e \tag{7-24}$$

From Eq. (6-39), (6-45), (7-23), and (7-24), the shear degradation factor η_c is calculated as follows:

$$\begin{aligned} \eta_c &= \frac{6}{\psi(520 + 48a - 320\alpha_v)\delta} = \frac{D}{\delta} \qquad \text{for } \alpha_v \leq 1 \\ \eta_c &= \frac{6}{170\delta} = \frac{D}{\delta} \qquad \text{for } \alpha_v > 1 \end{aligned} \tag{7-25}$$

where, D = coefficient to represent the effect of the design parameters on the shear degradation of concrete. That is:

$$\begin{aligned} D &= \frac{6}{\psi(520 + 48a - 320\alpha_v)} \qquad \text{for } \alpha_v \leq 1 \\ D &= \frac{6}{170} \qquad \text{for } \alpha_v > 1 \end{aligned} \tag{7-26}$$

The deformation capacity (point A in **Fig. 7-21**) is defined at the intersection point between the V_n and V_f. Thus, equating Eq. (7-21) with Eq. (7-22), the shear degradation factor η_c is calculated as follows:

$$\eta_c = \frac{V_f - V_b}{V_{wc,m}} \tag{7-27}$$

From Eq. (7-25) and (7-27), the deformation capacity δ_u is defined as follows:

$$\delta_u = \frac{D}{\left(\frac{V_f - V_b}{V_{wc,m}}\right)} = \frac{D}{C_v} \tag{7-28}$$

where, C_v (= $\left(V_f - V_b\right)/V_{wc,m} \leq$ 1.0) = coefficient to represent the level of shear degradation of concrete (refer to **Fig. 7-21**). Note that, when a > 3, D in Eq. (7-26) and (7-28) is maintained as the value corresponding to a = 3 (refer to Section 6.5.6). Thus, δ_u in Eq. (7-28) is also maintained without change.

The yield drift ratio δ_y at flexural yielding is theoretically determined neglecting the shear deformation, as follows:

$$\delta_y = \frac{\Delta_y}{l_s} = \frac{\phi_y (l_s)^2}{3 l_s} = \frac{\phi_y l_s}{3} \tag{7-29}$$

where, ϕ_y = yield curvature of the wall cross section = $2\varepsilon_y/l_w$ (Priestley 2000).

For walls where flexure dominates inelastic response (i.e., with large shear span ratio), it is more useful to define the deformation level and its acceptable criteria in terms of plastic hinge rotation, rather than the total drift at the top of the walls (ASCE 41, 2017). Thus, in the present study, the inelastic web crushing strength is also defined in terms of the deformation demand Δ_p in the plastic hinge zone, where the plastic hinge deformation is calculated as the sum of the flexural rotation and shear distortion (Δ_p = Δ_{pf} + Δ_{ps}).

The plastic hinge deformation is normalized with respect to the plastic hinge length, as follows:

$$\delta_p = \frac{\Delta_p}{l_p} = \frac{\Delta_{pf} + \Delta_{ps}}{l_p} \tag{7-30}$$

where, the lateral displacement Δ_{pf} by the flexural rotation θ_f is calculated as follows:

$$\Delta_{pf} = \frac{1}{2}\theta_f l_p = \frac{\phi l_p^2}{2} \tag{7-31}$$

Inserting Eq. (6-25) and (6-26) into Eq. (6-22), the average flexural curvature ϕ in the plastic hinge zone is calculated as follows:

$$\phi = \frac{\Delta - \Delta_e}{l_p(l_s - 0.5l_p)} - \frac{e_v}{l_e(l_s - 0.5l_p)} + \left[2\varepsilon_d + \frac{\varepsilon_h}{2}\right]\frac{1}{(l_s - 0.5l_p)} \tag{7-32}$$

From Eq. (7-32), (6-31), and $l_p = l_e$, the plastic hinge displacement Δ_{pf} by flexural deformation is redefined as follows:

$$\Delta_{pf} = \frac{(\Delta - \Delta_e - \gamma_p l_p)}{2(l_s - 0.5l_e)} l_p \tag{7-33}$$

Finally, inserting Eq. (7-33) into Eq. (7-30), and using Eq. (6-41), $\Delta - \Delta_e \approx \psi\Delta$, and $\Delta_{ps} = \gamma_p l_p$, the normalized plastic hinge deformation δ_p is defined in terms of the total drift ratio, as follows:

$$\delta_p = \left[\frac{\psi a - k_\alpha}{2(a - 0.5)} + k_\alpha\right]\delta = k_p\delta \tag{7-34}$$

where, k_α can be calculated from both Eq. (6-41) and (6-43); and k_p indicates the relationship between the plastic hinge deformation and total drift ratio.

Fig. 7-22 shows k_p values calculated by Eq. (7-34), where k_α is calculated assuming $\rho_m = \rho_s F_y/f_c' = 0.3$ (ρ_m of flexural specimens = 0.18 – 0.44). k_p is calculated using two k_α values: Eq. (6-41) (original k_α, denoted as red-colored) and (6-43) (simplified k_α, denoted as dark-colored). The difference between the two resulting k_p is pronounced only when no axial force is applied ($n_a = 0$) and the shear span ratio is greater than 3.0. This is because the simplified k_α was derived within the range of 1.5 $\leq a \leq$ 3.0 (see Section 6.5.6). Further, for a > 3, the simplified k_α of Eq. (6-43) results in overestimation of k_p, which indicates that the plastic hinge deformation can be overestimated. Thus, it is recommended that k_p for a > 3 be calculated to the same as the k_p corresponding to a = 3, to avoid the overestimation of plastic hinge deformation. Alternatively, k_p can be calculated using the original k_α of Eq. (6-41).

In the figure, k_p is generally greater than 1.0, which indicates that the normalized plastic hinge deformation is greater than the total drift ratio. This contests the common knowledge that the total drift ratio is intuitively greater than the normalized plastic hinge deformation due to the additional deformation in the elastic zone (**Fig. 7-23**(a)). **Fig. 7-23**(b) explains the reason: due to the vertical elongation, the shear deformation contribution (Δ_{ps}) in the plastic hinge zone is significantly greater than the flexural deformation contribution (Δ_{pf}), and the displacement due to the rigid body rotation of the elastic zone (Δ_θ) is limited due to the relatively small contribution of the flexural deformation (i.e., rotation) in the plastic hinge zone (refer to Eq. (6-26)).

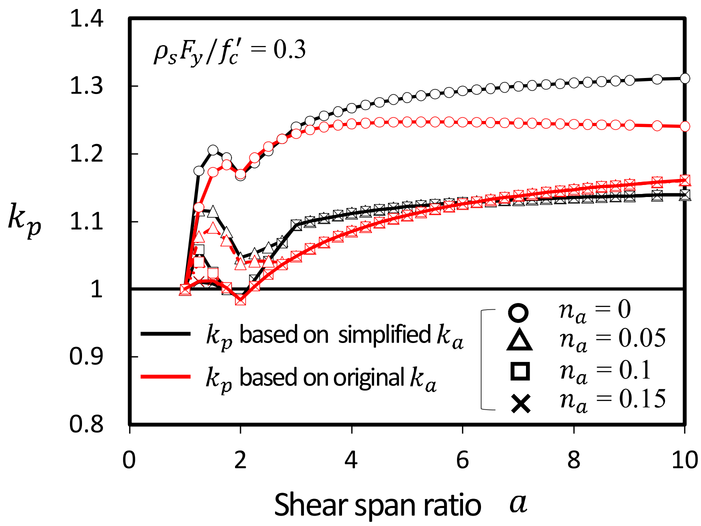

Fig. 7-22 Ratio of normalized plastic hinge deformation to total drift ratio.

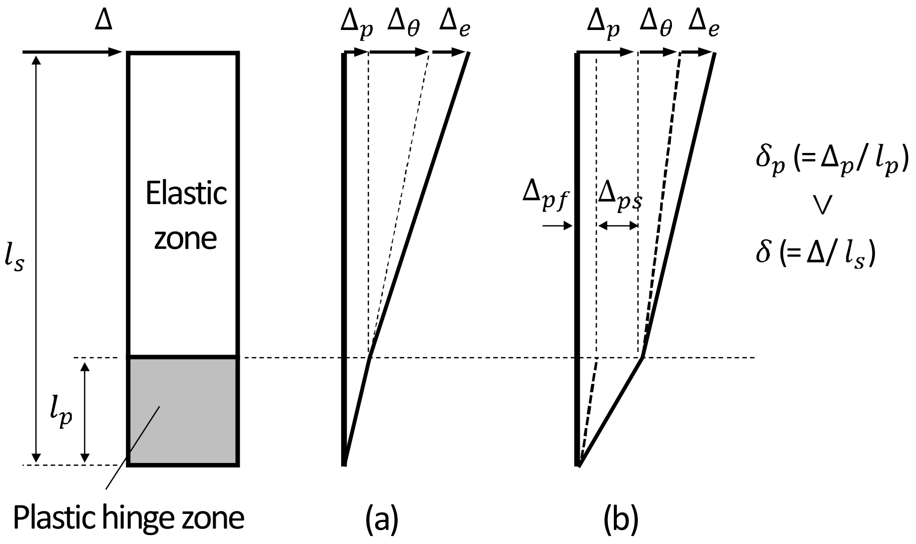

Fig. 7-23 Deformation contributions in flexural walls.

Using Eq. (7-28) and (7-34), the plastic hinge deformation capacity δ_{pu} is calculated as follows:

$$\delta_{pu} = k_p \delta_u \tag{7-35}$$

Table 7-2 and **7-3** summarize the design strengths and deformation capacity to define the lateral load-displacement relationship of SUB-C walls.

Table 7-2 Design flexural and shear strengths

Design strengths		Conditions		Methods or Equations	
Flexural strength V_f		$\Omega = 1.0$		Strain compatibility: Sec. 7.2.2.1) Plastic stress distribution: Sec. 7.2.2.2)	
		$\Omega = 1.0 - 1.1$		Advanced: Sec. 7.2.2.3)	
Shear strength V_n	Elastic web crushing strength $V_n = V_{wc} = 0.45kf_c'l_e t_w$	Shear span ratio	Mechanical shear reinforcement ratio	k values	
		$a < 1$	-	0.35	Equivalent Elastic Analysis: Sec. 7.1
		$1 \leq a < 1.5$	-	$0.28+0.55\omega_h \leq 0.35$	
		$1.5 \leq a < 2$	$\omega_h < 0.06$	$0.22+1.25\omega_h \leq 0.35$	
			$\omega_h \geq 0.06$	$0.25+0.75\omega_h \leq 0.35$	
		$2 \leq a < 2.5$	$\omega_h < 0.05$	$0.16+2.0\omega_h \leq 0.35$	
			$\omega_h \geq 0.05$	$0.21+1.0\omega_h \leq 0.35$	
		$2.5 \leq a < 3$	$\omega_h < 0.05$	$0.08+3.0\omega_h \leq 0.35$	
			$\omega_h \geq 0.05$	$0.16+1.4\omega_h \leq 0.35$	
		$a > 3$	-	ACI 318 ($V_n = V_c + V_s \leq V_{n,max}$)	
	Inelastic web crushing strength $V_n = V_{wc} + V_b = 0.5kf_c'l_e t_w + V_b$	Shear span ratio		k values	V_b
		$\alpha_v \leq 1$		$\dfrac{1.8}{\psi(520 + 48a - 320\alpha_v)\delta} \leq 0.3$	$\dfrac{2(1-\alpha_v)M_{bp}}{l_e}$
		$\alpha_v > 1$		$\dfrac{1.8}{170\delta} \leq 0.3$	0

Note: design k for elastic web crushing strength is valid only when $\omega_h \leq 1.0$; and k ($\alpha_v \leq 1$) for inelastic web crushing strength is valid only when $a \leq 3.0$ (for $a > 3.0$, k is calculated as the same as that for $a = 3.0$).

Table 7-3 Deformation capacity for design

Conditions		Equations	
		Overall drift ratio	Drift ratio at plastic hinge zone
Yield		$\delta_y = \frac{\phi_y l_s}{3}$	-
Post-yield shear failure	$\alpha_v \leq 1$	$\delta_u = \frac{6}{\psi(520 + 48a - 320\alpha_v)C_v}$	$\delta_{pu} = \left(\frac{\psi a - k_\alpha}{2(a-0.5)} + k_\alpha\right)\delta_u$
	$\alpha_v > 1$	$\delta_u = \frac{6}{170C_v}$	

Note: $\phi_y = 2\varepsilon_y/l_w$; $C_v = \frac{V_f - V_b}{V_{wc,m}}$; $V_{wc,m} = 0.15 f_c' t_w l_e$; $\psi = 1.15 - 0.15\alpha \geq 0.85$; k_α is calculated from Eq. (6-41) or (6-43); and when $a > 3$, δ_u and δ_{pu} are the same as the values corresponding to $a = 3$, respectively.

7.2.5 Comparison to test results

Fig. 7-24 compares the tested lateral load-drift ratio relationships with the strength and deformation capacity calculated by the proposed design method. Here, the drift ratio indicates the lateral displacement measured at the top of the test specimens. The flexural strength M_n of the test specimens was calculated according to ACI 318 (2019) (see Section 7.2.2). That is, in calculating M_n, the effect of the confinement and strain hardening was neglected. Thus, the shear demand V_f was calculated by multiplying M_n by the over-strength factor of Ω = 1.1, according to Section 7.2.2. In general, the proposed design method safely predicts the strength and deformation capacity at shear failure (denoted as point A). Only in **CF2.5** (**Fig. 7-24**(a)), the predicted deformation capacity (δ_u = 5.7%) was greater than the test result (δ_u = 3.7%), because the tested deformation capacity was limited by the premature weld-fracture of the boundary steel U-section, without web crushing.

On the other hand, **Fig. 7-25** compares the test results and the prediction in terms of normalized plastic hinge deformation. In the figure, the yield drift ratio δ_{py} for the plastic hinge zone was assumed to be the same as the overall yield drift ratio δ_y, for simplicity. The plastic hinge deformation capacity calculated from Eq. (7-35) reasonably predicts the test results.

Despite the good agreement with the test results, for reliable design of SUB-C walls, the proposed design method should be verified on the walls with various design parameters. In particular, in the walls subjected to high axial force, other post-yield failure modes, such as flexural compression failure, may occur, which limits the deformation capacity. The relevant discussion is presented in Section 6.7.

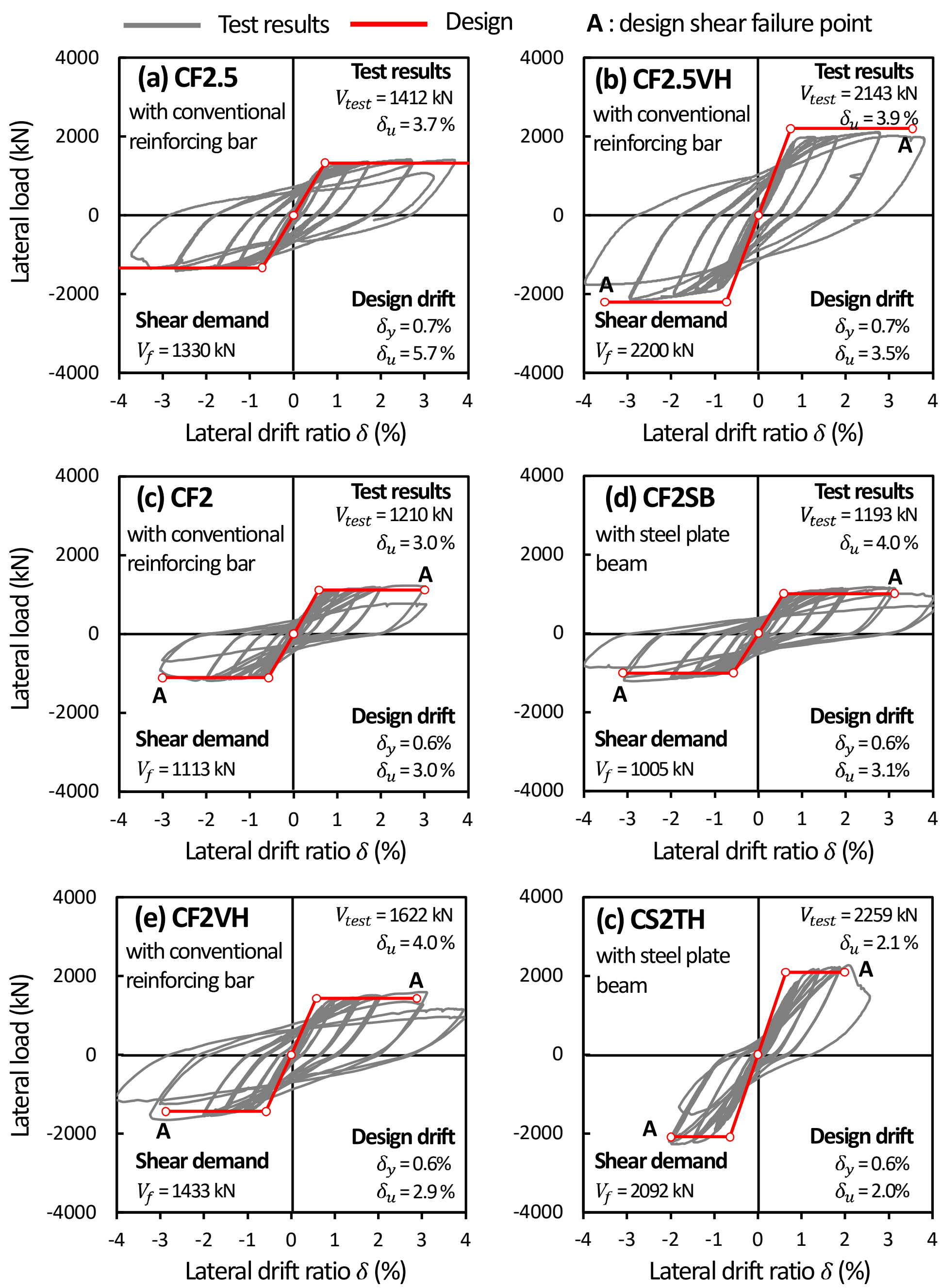

Fig. 7-24 Comparison of design strength and deformation capacity to tested lateral load-drift ratio relationship.

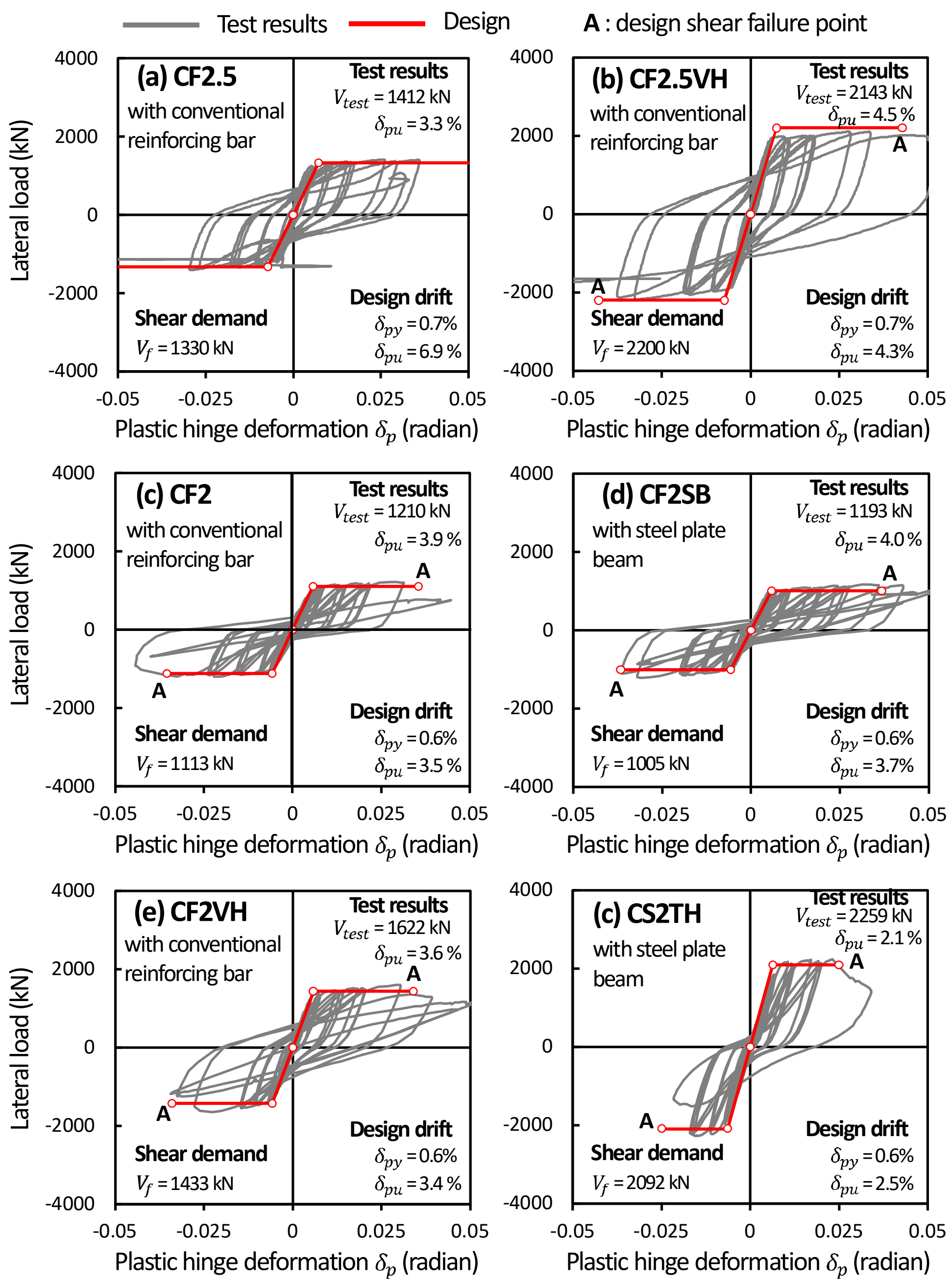

Fig. 7-25 Comparison of design strength and deformation capacity to tested lateral load-plastic hinge deformation relationship.

7.3 Materials and Detailing Recommendations

The detailing requirements for lateral load design of SUB-C walls were developed based on the experimental test results and existing design methods. The proposed design strengths are valid only when the proposed detailing requirements are satisfied. For this reason, the detailing methods outside the scope of this experimental study should be applied after in-depth verification through additional experimental and analytical studies.

7.3.1 Material strengths

Table 7-4 shows the allowable material strengths for design of SUB-C walls. Some are based on the test results, others are based on existing design provisions.

1) Steel plate

For use in boundary element, the yield strength of steel plates, F_y, is limited depending on the governing failure mode of walls. For flexure-controlled walls, the yield strength shall not be less than 350 MPa nor more than 450 MPa. For shear-controlled walls, the yield strength shall not be less than 350 MPa nor more than 600 MPa. These limitations were based on the design provisions (Appendix N9: Steel-plate composite walls) of AISC N 690 (2018) and the tested strengths of the steel U-sections: F_y values were between 379 MPa and 404 MPa for flexural yielding specimens, and those were between 444 MPa and 596 MPa for shear-failure specimens. The limitation for flexure-controlled walls is to avoid the use of extremely thin or slender plates that are susceptible to buckling and fracture, and to avoid the development of large flexural strength of walls that are susceptible to premature shear failure due to the increased shear demand. For shear-controlled walls, greater yield strength is allowed because the strain levels of steel plates is relatively limited and resulting instability due to inelastic buckling is decreased.

Table 7-4 Recommended material strengths

		Yield strength f_y or F_y [MPa]	
		Min	Max
Steel			
boundary element	Flexure-controlled	350	450
	Shear-controlled	350	600
Reinforcement	plate beams	350	450
	faceplates	350	450
	Deformed bar	-	700
Concrete		35	70
Shear connector		400	650

For use in shear (web) reinforcement, such as steel plate beams and steel faceplates, the tested yield strengths were F_y = 321 MP (for steel plate beams) and 456 MPa (for steel faceplates) only. For this reason, the allowable yield strength (= 350 MPa $\leq F_y \leq$ 450 MPa) is provide according to the existing design provisions of AISC N 690 (2018). Considering construction quality, the weldable structural steel (KS D 3515, ASTM A36/A36M) shall be used.

2) Reinforcing bar

The tested strengths of reinforcing bars that used for web reinforcement ranged 445 MPa and 514 MPa, which belongs the normal-strength steel. Due to the lack of test data, only the maximum limit for yield strength of f_y = 700 MPa is provided according to the seismic provisions of ACI 318 (2019).

3) Concrete

The concrete strengths measured from the cylinder tests ranged 44.7 MPa – 68.3 MPa, which is greater than the minimum requirement of 35 MPa for special structural walls in ACI 318 (2019). However, for the concrete confined by steel U-sections, the shear connectors in the steel plates should be anchored well by the confined concrete, which limits the use of concrete strengths higher than 70 MPa (ACI 318). Thus, the allowable concrete strengths for the reliable design of SUB-C walls shall be 35 MPa $\leq f_c' \leq$ 70 MPa.

4) Steel anchors

In the present study, steel anchors (headed stud and lateral tie bar) with nominal tensile strength of 500 MPa were for steel U-sections. To ensure quality for strength and weldability, steel headed stud anchors or lateral ties shall conform to the requirements of national design codes: e.g., the Structural Welding Code—Steel (AWS D1.1/D1.1M) for U.S.; Headed Studs (KS B 1062) for South Korea.

7.3.2 Boundary element

1) Details of steel U-section

The use of steel U-sections significantly improves the flexural performance of walls, due to the large steel area at the boundary zone, and confinement effect to the infilled concrete. Thus, the proposed SUB-C walls can be used for buildings or structures in high seismic zone, as an alternative to ductile RC walls (i.e., special structural walls, ACI 318, 2019). Further, by using the steel U-section, strict detailing requirements for boundary elements (lateral confining reinforcements) can be attenuated, which increases overall constructability. For use in ductile walls, the following details are required for steel U-sections.

The length l_{be} of the web plates in a steel U-section shall not be less than the greater of (**Fig. 7-26**(a)):

(a) $0.15l_w$

(b) $0.15c$

(c) $c-0.1l_w$

The first requirement was based on the tested geometry of steel U-sections, to ensure the tested shear resistance and frame action (flexural resistance) of the steel U-section; shorter length of the web plates does not provide proper contribution to the shear strength of walls. The last two requirements were based on the requirements for special structural walls in ACI 318 (2019). Here, the depth c of the compression zone is calculated assuming the extreme compression fiber strain of 0.003. Further, it is recommended that l_{be} be less than $0.25l_w$, reflecting the maximum length of the web plates in the test specimens.

On the basis of the test results and the proposed shear strength model, the mechanical vertical steel ratio ρ_m $(=\ \rho_s F_y/f_c')$ shall have a maximum value of 1.0 and a minimum value of 0.15.

$$0.15 \le \rho_m \le 1.0 \tag{7-36}$$

However, for shear-controlled SUB-C walls, ρ_m shall be greater than 0.5, to develop the proposed elastic web crushing strength. Otherwise, the shear strength design should follow the existing RC design methods. Such limitation is based on the test results of shear failure-mode specimens where $0.42 \le \rho_m \le 0.9$.

Steel U-sections are anchored to concrete using steel anchors, ties, or a combination thereof. The width-to-thickness ratio of the flange and web plates in a steel U-section should satisfy the following requirements, to minimize inelastic buckling of the steel U-section (**Fig. 7-26**(b)).

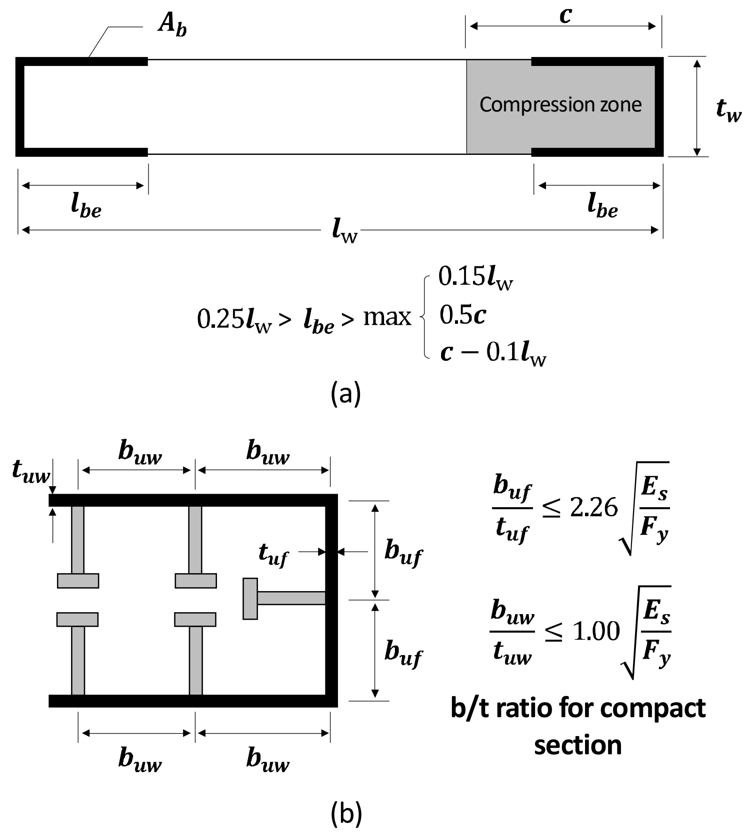

Fig. 7-26 Recommended details of steel U-section.

$$\frac{b_{uf}}{t_{uf}} \leq 2.26\sqrt{\frac{E_s}{F_y}} \qquad \text{for flange} \qquad (7\text{-}37a)$$

$$\frac{b_{uw}}{t_{uw}} \leq 1.00\sqrt{\frac{E_s}{F_y}} \qquad \text{for web} \qquad (7\text{-}37b)$$

where, b_{uf} and b_{uw} = largest unsupported length of the flange and web plates between steel anchors or between steel anchors and the plate edge (**Fig. 26**(b)); t_{uf} and t_{uw} = thickness of the flange and web plates, respectively. Eq. (7-37a) refers to the design code of concrete-filled steel columns subjected to compression (AISC 360, 2016). On the other hand, Eq. (7-37b) refers to the requirement of steel plate composite walls in AISC N690 (2018), because the web plates not only resist shear but also flexural moments.

2) Spacing of steel anchors

In the tests, the steel U-sections showed significant yielding and adequate composite action with the infilled concrete, by satisfying the following requirements. **Fig. 7-27** shows the recommended arrangement of headed studs and lateral ties between the web plates in a steel U-section.

The steel anchors (e.g., headed studs and lateral ties) in a steel U-sections shall be spaced not to exceed the following requirement, to develop the yield strength of the steel U-section.

$$s_c \leq \sqrt{\frac{Q_{cv} l_{dp}}{T_p}} \qquad (7\text{-}38)$$

where,

$$Q_{cv} = 0.5A_{sc1}\sqrt{f_c' E_c} \leq 0.75A_{sc1}F_{u,sc} \qquad (7\text{-}39)$$

where, s_c = spacing of shear connectors in a steel U-section for both vertical and horizontal directions; Q_{cv} = shear strength of shear connectors; l_{dp} = development length of the steel U-section,($\approx$ $3t_w$); T_p = $F_y t_{uf}$ for flange plate and $F_y t_{uw}$ for web plate; A_{sc1} = area of a steel connector; and $F_{u,sc}$ = tensile strength of shear connector. Eq. (7-38) refers to the requirement for steel plate composite walls in AISC N 690 (2018). Eq. (7-39) refers to AISC 360 (2016), where the coefficients of R_g and R_g, representing the arrangement method and type of connected elements, were determined as 1.0 and 0.75, respectively.

3) Arrangement of steel anchors

In SUB-C walls, headed studs shall be placed in a steel U-section: In the steel U-section with headed studs, bearing stress fields are formed by the tension force of the studs, which provides lateral restraint for the steel U-section and composite action between the steel U-section and infilled concrete. **Fig. 7-27**(a) shows the flexural critical zone of SUB-C walls, which shall be defined to be greater than the wall length l_w (ACI 318, 2019). In the steel U-section outside the critical zone, the headed studs can be placed without overlapping between any studs in the steel U-section. That is, it allows independent bond failure of each studs due to concrete crushing (see the failure plane for a headed stud in Fig. **7-27**(b)).

On the other hand, in the critical zone, such arrangement for headed studs shall not be used for the following reason: the steel U-section at large plastic deformation is no longer effective because the concrete at boundaries, subjected to a high level of stress, crushes and each headed studs will lose their stiffness and strength and then the steel U-section becomes prone to buckle. Further, the out of plane action of the two web plates in the steel U-section cannot resist against the Poison effect of the infilled concrete subjected to a high level of axial stress. To prevent early buckling and failure of the steel U-sections at wall boundaries, it is necessary to use through-thickness lateral ties to directly connect the two web plates of the steel U-section together and provide better confinement to concrete at boundaries. When headed studs are used only, the studs shall be placed so that they overlap each other and the tension force of the studs can be transferred through the compression zone formed between the bearing stress fields (act as struts, see **Fig. 7-27**(b)) (Yan et al. 2018). Here, the inclination angle of the bearing stress fields are assumed as 45 degrees (ACI 318, 2019).

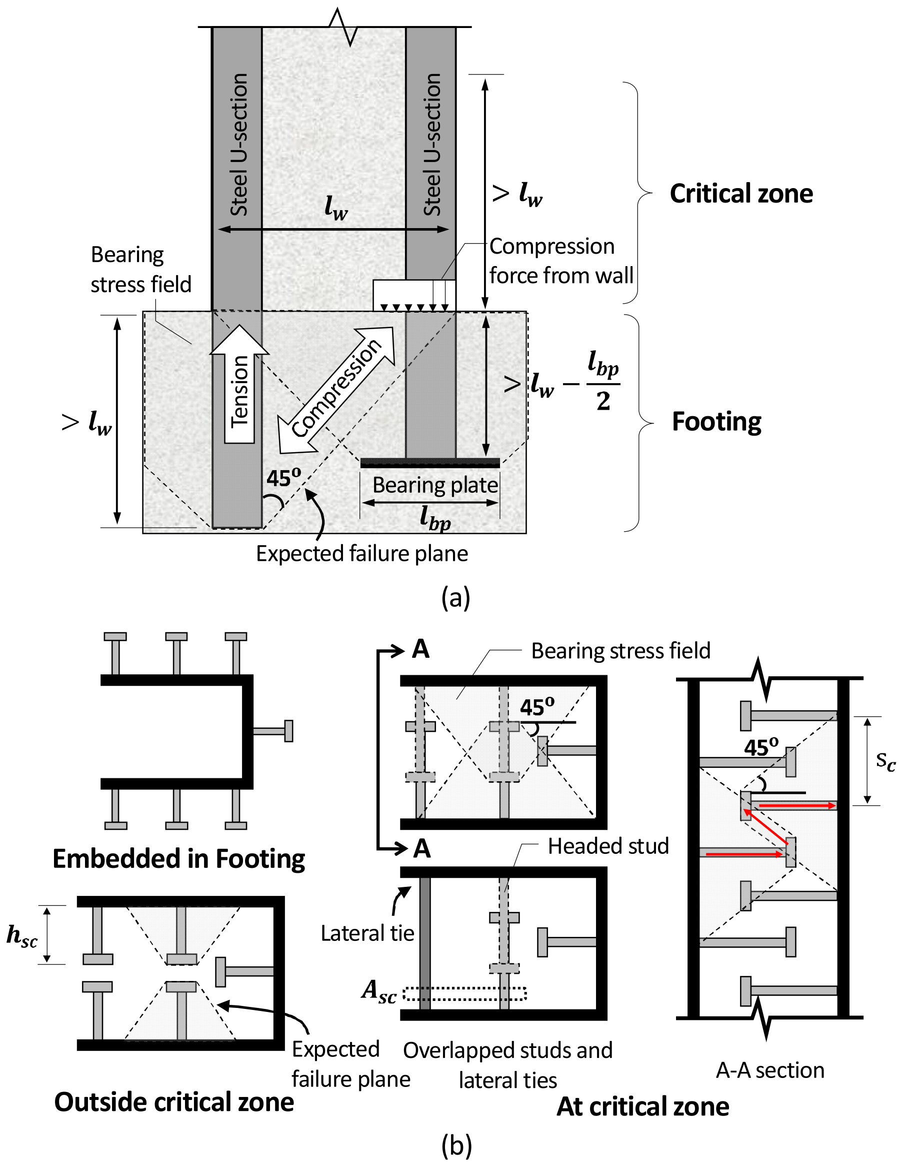

Fig. 7-27 Recommended details of (a) anchorage; and (b) steel anchors of steel U-sections.

The required area ratio ρ_c (= confinement ratio) of the lateral ties and headed studs in the critical zone shall be calculated as follows:

$$\rho_c = \frac{A_{sc}}{b_c s_c} \geq 0.12 \frac{f_c'}{F_{u,sc}} \tag{7-40}$$

where, A_{sc} = total cross-sectional area of headed studs and tie bars within their vertical spacing (= s_c) in a web plate (see **Fig. 7-27**(b)); and b_c = boundary zone length (= l_{be}). In test specimen **CF2.5VH**, the steel U-sections showed stable stress-strain behavior even at large plastic deformation, even though the confinement ratio ρ_c (= 0.89%) was designed to be less than the requirement (= 1.34%) for rectilinear confining reinforcement of special structural walls (see Section 3.4.7). This result indicates that the steel U-sections with headed studs provided better confinement to the concrete, despite their open section. Thus, the minimum requirement for ρ_c is slightly attenuated by adopting the requirement for circular confining reinforcement of special structural walls in ACI 318 (2019).

Note that, in the critical zone, the required amount of headed studs shall be determined from the greater of Eq. (7-38) and (7-40).

4) Anchorage

Fig. 7-27(a) also shows anchorage details of the steel U-sections embedded in footing. The required number and spacing of shear connectors shall be calculated by Eq. (7-38). However, to ensure shear transfer to the footing, the shear connectors shall be placed outside the steel U-sections. Further, due to the large area of the steel U-sections, large flexural tension force is concentrated at a small area of the boundary zone, which is transferred to the footing. For this reason, the footing is susceptible to concrete breakout failure along the expected failure plane inclined at 45 degrees. Therefore, the anchorage length for the steel U-section shall be greater than the wall length l_w, so that the pullout mechanism of the concrete can be restrained by the compression force of walls. The anchorage length can be reduced by using the bearing plates at the end of the steel U-section.

In this case, the required anchorage length shall be greater than $l_w - 0.5l_{bp}$, in which l_{bp} is the length of the bearing plates (see **Fig. 7-27**(a)). A further study is required to validate such failure mechanism and to provide a relevant strength equation.

7.3.3 Web reinforcement

1) Horizontal reinforcement

In SUB-C walls, horizontal reinforcement provides adequate shear strength to the walls, where the horizontal reinforcement can be designed using conventional reinforcing bars or steel plate beams. For the reinforcing bars, existing RC design methods can be used to determine their minimum spacing and relevant details for development. The present study adopted the design provisions of ACI 318 (2019).

The spacing s_h of horizontal reinforcing bars shall not exceed the lesser of:

(a) $3h$

(b) 450 mm

(c) $0.2l_w$

Fig. 7-28 shows possible anchorage details for horizontal deformed bars in tension, for the boundary zone of SUB-C walls: straight, headed, hooked bars, or a combination thereof. The bar yield strength shall be developed on each side of the bar by the following embedment lengths.

$$l_d = \left(\frac{3\psi_s f_{yh}}{40\sqrt{f_c'}}\right) d_b \tag{7-41}$$

$$l_{dt} = \left(\frac{f_{yh}}{75\sqrt{f_c'}}\right) d_b^{1.5} \tag{7-42}$$

$$l_{dh} = \left(\frac{f_{yh}}{55\sqrt{f_c'}}\right) d_b^{1.5} \tag{7-43}$$

where, l_d, l_{dt}, and l_{dh} = required embedment lengths for straight, headed, and hooked deformed bars, respectively. ψ_s= modification factor to consider the effect of bar diameter d_b on the development length (= 1.0 for $d_b \geq$ 22 mm, and 0.8 for $d_b \leq$ 19 mm). Eq. (7-41), (7-42), and (7-43) refer to ACI 318 (2019).

Fig. 7-29 shows the minimum ratio $\rho_{h,min}$ of horizontal shear reinforcement, to ensure the proposed shear strength of SUB-C walls: The elastic web crushing strength decreases as the shear span ratio increases, due to the increased horizontal elongation; increased truss action of horizontal shear reinforcement. Therefore, the minimum shear reinforcement ratio was defined according to the shear span ratio, based on the tested shear reinforcement ratio.

$$
\begin{aligned}
\rho_{h,min} &= 0.002 && \text{for } l_s/l_w < 1 \\
\rho_{h,min} &= 0.00133\frac{l_s}{l_w} + 0.000667 && \text{for } 1 \le l_s/l_w < 2.5 \\
\rho_{h,min} &= 0.004 && \text{for } l_s/l_w > 2.5
\end{aligned}
\tag{7-44}
$$

However, for steel plate beams, their minimum reinforcement ratio shall be twice the ratio of Eq. (7-44), to avoid the use of extremely thin plates that are susceptible to tensile fracture or connection (weld) failure at the ends of the plate beams subjected to large flexural moments.

On the basis of the test results, the mechanical shear reinforcement ratio ω_h ($= \rho_h f_{yh}/f_c'$) shall not be less than 0.02.

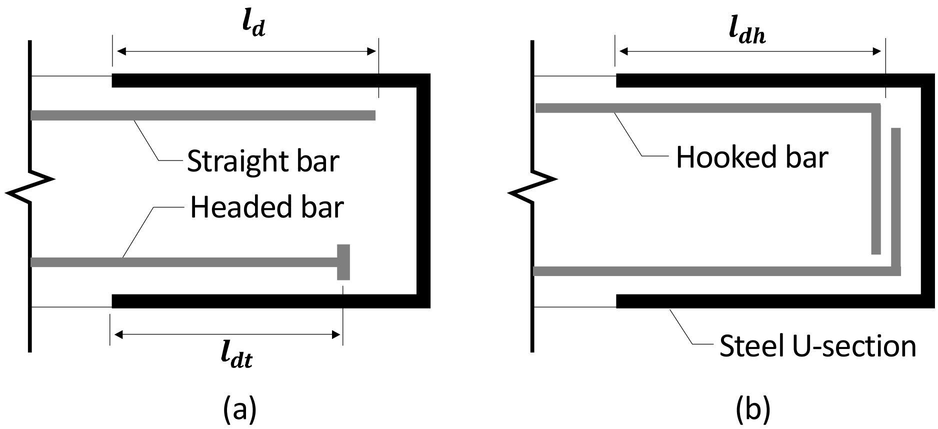

Fig. 7-28 Anchorage details for horizontal deformed bars.

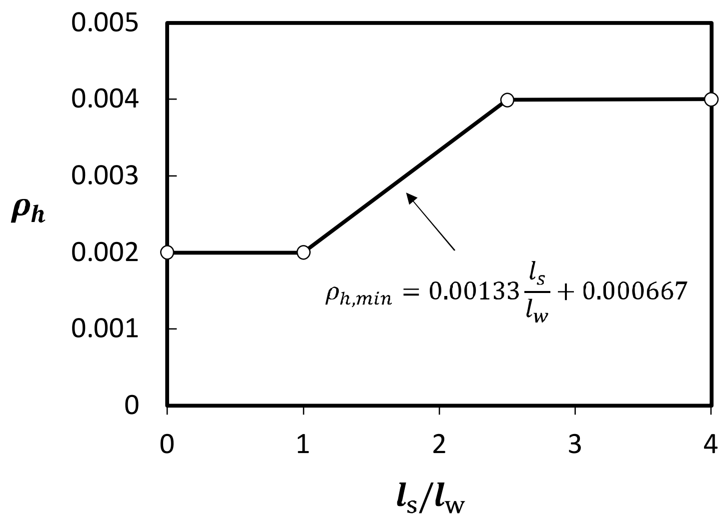

Fig. 7-29 Minimum ratio of horizontal shear reinforcement.

2) Vertical reinforcement

In SUB-C walls, the applied flexural moments are resisted primarily by the boundary steel U-sections with relatively large area. Nevertheless, vertical reinforcement is required in the web to control cracking and long-term effect of concrete, such as creep and shrinkage. The present study adopted the design provisions of ACI 318 (2019).

The spacing s_v of vertical reinforcing bars shall not exceed the lesser of:

(a) $3h$

(b) 450 mm

(c) $l_w/3$

The minimum reinforcement ratio $\rho_{v,min}$ of vertical reinforcing bars is calculated as follows:

$$\rho_{v,min} = 0.0025 + 0.5\left(2.5 - \frac{l_s}{l_w}\right)\left(\rho_h - \rho_{h,min}\right) \geq 0.0025 \qquad (7\text{-}45)$$

The requirements for anchorage and development of vertical reinforcement are the same as those of horizontal reinforcement.

7.4 Summary

In this chapter, the equivalent elastic analysis (EEA) method was developed to obtain more accurate and economic design of the elastic web crushing strength of SUB-C walls. Secondly, the deformation-based design method for SUB-C walls was developed based on the proposed shear strength model. Lastly, based on the tested properties and existing design methods, allowable material strengths and several detailing rules for SUB-C walls are recommended. The major conclusions drawn are summarized as follows:

1) In the proposed EAA, the structural response of SUB-C walls is evaluated using a strip model. The nonlinearity from yielding of shear reinforcement is considered by adopting the equivalent elastic stiffness of the horizontal ties corresponding to the maximum horizontal elongation. The adequacy of the proposed EEA was verified by comparing the calculated shear strengths with the test results. The proposed EEA better predicted the shear strength of SUB-C walls than the proposed shear strength model of Eq. (6-12), showing a prediction error of 4% only (Eq. (6-12) showed the error of 12%).

2) The proposed deformation-based design method reasonably predicted the lateral load-displacement relationship of the test specimens. The deformation capacity, in terms of overall drift ratio and plastic hinge drift ratio, was defined at the intersection point between the shear demand and inelastic web crushing strength.

3) The proposed design strengths are valid only when the proposed design recommendations are followed. The detailing methods outside the scope of the recommendations should be applied after in-depth verification through additional experimental and analytical studies.

Chapter 8. Conclusions

For high structural performance and constructability, a steel-concrete composite wall with boundary elements of steel U-sections was developed. Experimental and analytical studies were performed to investigate the in-plane flexural and shear performances of the proposed SUB-C walls, and to verify the research hypotheses described in Section 2.4. Based on the test and analysis results, an analytical model to predict the shear strength (elastic web crushing strength) and post-yield shear strength (inelastic web crushing strength) of SUB-C walls was developed, and the deformation-based design method was established. Finally, the design recommendations for materials and detailing were provided.

The general conclusions for the research hypotheses are presented as follows:

The use of boundary steel U-sections with large area (boundary reinforcement ratio = 9.3%–19.0%) provided high lateral confinement to the boundary concrete, without plate buckling, which prevented crushing of the boundary concrete even at large plastic deformation. Further, the steel U-sections resisted shear transferred from the diagonal struts, restraining shear cracking and sliding. Therefore, the flexural and shear performances of SUB-C walls were greater than those of equivalent RC walls with the same amount of steel materials, which validates the applicability of SUB-C walls for high-performance walls. However, for reliable use of SUB-C walls, a further study is required for SUB-C walls subjected to high axial force and cyclic lateral loading.

Specifically, for the flexural performance of SUB-C walls, the following conclusions are drawn:

1) In RC specimens with highly confined boundary elements (boundary

reinforcement ratio = 9.6%, lateral confinement ratio = 1.34%), the inelastic deformation capacity was limited by shear sliding at the wall bottom, even though the shear demand (i.e., flexural strength) was significantly less than the nominal shear-friction strength. In the proposed composite walls with steel U-sections, such shear sliding was restrained. However, the composite walls failed due to crushing of the web concrete (i.e., post-yield shear failure) in the plastic hinge zone, without failure of the steel U-sections. The steel U-sections restrained diagonal cracking of the web concrete and crushing of the boundary concrete.

2) The flexural strength of the SUB-C wall was 37% greater than that of the counterpart RC wall. This is because the steel U-sections experienced large strain hardening stress by restraining shear sliding, diagonal cracking of the web concrete, and crushing and spalling of the boundary concrete. For the same reason, the deformation capacity and energy dissipation were increased by 38%-53% and 99%-173%, respectively. When steel U-sections with greater area were used, such advantages were more pronounced.

3) In the SUB-C wall with steel plate beams, the plate beams provided adequate shear resistance without conventional shear reinforcing bars. Further, diagonal cracking and spalling of web concrete were better restrained, despite the absence of reinforcing bars. Thus, the deformation capacity and energy dissipation were 33% and 52% greater than those of the SUB-C wall without steel plate beams, respectively.

4) In the SUB-C wall with steel faceplates (web steel ratio = 4.0%), the flexural strength and lateral stiffness were increased by 36% and 18%, respectively, even though the web faceplates were not connected to boundary steel elements. However, local buckling was initiated at the free edges of the faceplates, followed by the crushing of web concrete, and eventually, strength degradation. For better ductility, vertical connections

between the web plates and boundary steel sections are required in the plastic hinge zone.

5) The nominal flexural strengths based on strain compatibility and plastic stress distribution underestimated the test results of the SUB-C walls, neglecting the lateral confinement (to infill concrete), and strain hardening of the steel U-sections. The over-strength ratio was 7%–31% for strain compatibility method, and 10%–34% for plastic stress distribution method.

6) In the comparison of the present test results and those of existing the composite walls, the normalized flexural strength and ductility of SUB-C walls were greater than those of the existing composite specimens, even with low mechanical steel ratio (= $\rho_s F_y / f_c'$): the flexural strength efficiency of the SUB-C walls was better.

For the shear performance of SUB-C walls, the following conclusions are drawn:

1) The RC walls with heavily reinforced boundary elements (boundary reinforcement ratio = 11.6%–19.0%) showed diagonal tension failure (full penetration of diagonal cracks across the cross section, and tensile yielding of shear reinforcement), and subsequent web concrete spalling. On the other hand, SUB-C walls showed web crushing, without diagonal tension failure. This is because the steel U-sections restrained diagonal cracking and protected the boundary zone (i.e., full crack penetration was prevented).

2) The shear strength of the SUB-C walls was 13%–54% greater than that of the counterpart RC walls, due to the contribution of boundary steel U-sections (23%–45% of the shear strength for the inclined crack plane): The steel U-sections resisted shear transferred from the diagonal strut. As the steel plate area increased, the contribution of steel U-sections increased.

3) In the SUB-C wall with steel plate beams, the plate beams acted as shear

reinforcement, providing adequate shear resistance. Further, the shear failure mode was less brittle, as the diagonal cracking and spalling of web concrete were better restrained by the plate beams. As the vertical spacing of steel plate beams decreased, the shear strength of SUB-C walls increased, due to the increased contribution of steel plate beams.

4) In the SUB-C walls with steel web faceplates (steel ratio = 4.0%), shear yielding of the faceplates occurred, though the faceplates and boundary steel U-sections were not connected. Further, as the faceplates and steel U-sections confined the concrete subjected to flexural compression, the shear strength contribution of concrete increased. Thus, the shear strength was 13%–54% greater than that of the SUB-C walls without faceplates. The shear strength of SUB-C walls with faceplates can be predicted according to AISC N690 (2018).

5) Existing RC design methods underestimated the shear strengths of SUB-C walls, neglecting the contribution of steel U-sections. On the other hand, JGJ 318 (2016) provided better accuracy, by including the contribution of steel boundary elements. For design of composite walls, the steel plate beams and steel faceplates can be regarded as horizontal reinforcement.

From the nonlinear finite element (FE) analysis, the following conclusions are drawn:

1) The FE analysis confirms that the web crushing before flexural yielding is primarily due to large horizontal tensile deformation (i.e., horizontal elongation) in the mid-height panel zone. In the lower panel zone (near the wall base), the horizontal elongation decreased due to the steel U-section with high stiffness.

2) The FE analysis confirms that diagonal tension failure is prevented as the steel U-sections protect the boundary zone. Thus, the shear strength is increased until web crushing occurs. Here, the increase in shear strength is

attributed to the shear strength contribution of the steel U-sections and the increased contribution of concrete.

3) For various design parameters (mechanical shear reinforcement ratio, mechanical vertical steel ratio, and aspect ratio), the contribution of boundary steel U-sections (calculated for the wall cross section) to the web crushing strength ranges 10%–23%. That is, the shear contribution ratio of the steel U-section is much less than that of the RC wall, and its variation is not significant.

4) From the parametric analysis, the maximum horizontal elongation at web crushing is 0.6 – 4.51 times the yield strain of shear reinforcement. The horizontal elongation increases in proportion to aspect ratio and inversely proportional to mechanical shear reinforcement ratio ($\rho_h f_{yh}/f_c'$). However, the horizontal elongation is independent of the boundary steel area. From the regression analysis, an empirical equation to predict the horizontal elongation was proposed. In general, the calculated horizontal elongation agrees with the prediction of FE analysis.

For the proposed shear strength model, the following conclusions are drawn:

1) The shear strength model of SUB-C walls was developed modifying the traditional truss analogy. The shear resistance of boundary steel U-sections was incorporated into the truss model by replacing the vertical compression and tension truss elements with beam-column elements (Truss-beam model). Based on the test results, two failure mechanisms were defined: elastic and inelastic web crushing failures. The shear strength degradation of the web concrete was determined from the effective average strength of the diagonal concrete struts: effective average strength factor k

2) For the elastic web crushing strength, k was defined based on the horizontal elongation mechanism; the elastic web crushing strength decreases as the horizontal elongation increases. Based on the FE analysis results, the

contribution of the steel U-sections was neglected, for simplicity in design. Nevertheless, the proposed model reasonably predicted the elastic web crushing strength of the test specimens, except for a slight conservatism shown in the walls with aspect ratio of 1.0. The proposed elastic web crushing strength is valid only if the steel U-sections remain elastic at web crushing (i.e., if flexural yielding of walls is prevented).

3) The inelastic web crushing strength was defined as the sum of the contributions of the concrete and boundary steel U-sections in the plastic hinge zone. The concrete contribution was defined as a function of the deformation demand, based on the vertical elongation mechanism. The contribution of the steel U-section was determined from its axial-flexural capacity, assuming frame behavior. The proposed strength model agreed with the test results, in terms of the tested strength, failure mode, and deformation capacity.

For the proposed equivalent elastic analysis (EEA) method, deformation-based design method, and design recommendations, the following conclusions are drawn:

1) The equivalent elastic analysis (EEA) method was developed to achieve more accurate and economic design of the elastic web crushing strength of SUB-C walls. In the proposed EAA, the structural response of SUB-C walls was simulated using a strip model. The nonlinearity from yielding of shear reinforcement was idealized using the equivalent elastic stiffness of the horizontal ties corresponding to the maximum horizontal elongation. The adequacy of the proposed EEA was validated from the comparison with the test results. The proposed EEA better predicted the shear strength of SUB-C walls than the proposed shear strength model of Eq. (6-12).

2) The deformation-based design method reasonably predicted the lateral load-displacement relationship of the test specimens. The deformation capacity, in terms of overall drift ratio and plastic hinge drift ratio, was

defined at the intersection point between the shear demand and inelastic web crushing strength.

3) The proposed design strengths are valid only when the proposed design recommendations are satisfied. The detailing methods outside the scope of the recommendations should be applied after in-depth verification through additional experimental and analytical studies.

References

[1] ACI (2019). "Building code requirements for structural concrete (ACI 318-19) and commentary." American Concrete Institute.

[2] Adebar, P., Ibrahim, A. M., and Bryson, M. (2007). "Test of high-rise core wall: effective stiffness for seismic analysis." ACI Structural Journal, 104(5), 549.

[3] American Welding Society (2010). "Structural Welding Code–Steel: AWS D1. 1/D1. 1M."

[4] ANSI (2016). "Specification for structural steel buildings (AISC 360-16)." American Institute of Steel Construction, Chicago, IL, USA.

[5] ANSI/AISC (2016). "Seismic provisions for structural steel buildings (AISC 341-16)." American Institute of Steel Construction, Chicago, IL.

[6] ANSI/AISC (2018). "Specification for Safety-Related Steel Structures for Nuclear Facilities (ANSI/AISC N690)." American Institute of Steel Construction (AISC), Chicago, Illinois.

[7] ASCE/SEI (2019). "ASCE/SEI 43-19: Seismic Design Criteria for Structures, Systems, and Components in Nuclear Facilities." American Society of Civil Engineers, Reston, Virginia, USA.

[8] ASTM (2019). "A36/A36M-19: Standard Specification for Carbon Structural Steel "Pennsylvania, USA.

[9] Bachmann, H. (2004). "Neue Tendenzen im

Erdbebeningenieurwesen." Beton-und Stahlbetonbau, 99(5), 356-371.

[10] Bentz, E. C., Vecchio, F. J., and Collins, M. P. (2006). "Simplified modified compression field theory for calculating shear strength of reinforced concrete elements." ACI Materials Journal, 103(4), 614.

[11] Bohl, A., and Adebar, P. (2011). "Plastic hinge lengths in high-rise concrete shear walls." ACI Structural Journal, 108(2), 148.

[12] Booth, P. N., Bhardwaj, S. R., Tseng, T.-C., Seo, J., and Varma, A. H. (2020). "Ultimate shear strength of steel-plate composite (SC) walls with boundary elements." Journal of Constructional Steel Research, 165, 105810.

[13] Calvi, G., Priestley, M., and Kowalsky, M. (2007). "Displacement–based seismic design of structures." Earthquake spectra, 24(2), 1-24.

[14] Carrillo, J., and Alcocer, S. M. (2012). "Backbone model for performance-based seismic design of RC walls for low-rise housing." Earthquake Spectra, 28(3), 943-964.

[15] CEB-FIP (2013). "fib model code for concrete structures 2010." Wilhelm Ernst & Sohn, Verlag für Architektur und technische Wissenschaften GmbH & Co. KG, Berlin, Germany.

[16] CEN (2004). "Eurocode 2: Design of concrete structures-Part 1-1: General rules and rules for buildings." European Committee for Standardization, Brussels.

[17] CEN (2004). "Eurocode 8: Design of structures for earthquake resistance Part 1: General rules, seismic actions and rules for buildings." European Committee for Standardization, Brussels, 1998-1991.

[18] Chen, L., Mahmoud, H., Tong, S.-M., and Zhou, Y. (2015). "Seismic behavior of double steel plate–HSC composite walls." Engineering Structures, 102, 1-12.

[19] Chen, W.-F., and Saleeb, A. F. (2013). Constitutive equations for engineering materials: Elasticity and modeling, Elsevier.

[20] Choi, K.-K., Kim, J.-C., and Park, H.-G. (2016). "Shear Strength Model of Concrete Beams Based on Compression Zone Failure Mechanism." ACI Structural Journal, 113(5).

[21] Dan, D., Fabian, A., and Stoian, V. (2011). "Theoretical and experimental study on composite steel–concrete shear walls with vertical steel encased profiles." Journal of Constructional Steel Research, 67(5), 800-813.

[22] Dan, D., Fabian, A., and Stoian, V. J. E. S. (2011). "Nonlinear behavior of composite shear walls with vertical steel encased profiles." 33(10), 2794-2804.

[23] Duffey, T., Farrar, C., and Goldman, A. (1994). "Low-rise shear wall ultimate drift limits." Earthquake Spectra, 10(4), 655-674.

[24] Eom, T.-S., and Park, H.-G. (2010). "Elongation of reinforced concrete members subjected to cyclic loading." Journal of structural engineering, 136(9), 1044-1054.

[25] Eom, T.-S., Park, H.-G., Kim, J.-Y., and Lee, H.-S. (2013). "Web crushing and deformation capacity of low-rise walls subjected to cyclic loading." ACI Structural Journal, 110(4), 575.

[26] Eom, T.-S., Park, H.-G., Lee, C.-H., Kim, J.-H., and Chang, I.-H.

(2009). "Behavior of double skin composite wall subjected to in-plane cyclic loading." Journal of structural engineering, 135(10), 1239-1249.

[27] Epackachi, S., Nguyen, N. H., Kurt, E. G., Whittaker, A. S., and Varma, A. H. (2015). "In-plane seismic behavior of rectangular steel-plate composite wall piers." Journal of Structural Engineering, 141(7), 04014176.

[28] Epackachi, S., Sharma, N., Whittaker, A., Hamburger, R. O., and Hortacsu, A. (2019). "A cyclic backbone curve for shear-critical reinforced concrete walls." Journal of Structural Engineering(4), 04019006.

[29] Foster, S. J., and Gilbert, R. I. (1996). "The design of nonflexural members with normal and high-strength concretes." ACI Structural Journal, 93(1), 3-10.

[30] Greaves, G. N., Greer, A., Lakes, R. S., and Rouxel, T. (2011). "Poisson's ratio and modern materials." Nature materials, 10(11), 823-837.

[31] Gulec, C. K., and Whittaker, A. S. (2011). "Empirical Equations for Peak Shear Strength of Low Aspect Ratio Reinforced Concrete Walls." ACI Structural Journal, 108(1).

[32] Hidalgo, P., and Jordan, R. "Strength and energy dissipation characteristics of reinforced concrete walls under shear failure." Proc., The 11th World Conf. on Earthquake Engineering.

[33] Hines, E. M., and Seible, F. (2004). "Web crushing capacity of hollow rectangular bridge piers." ACI Structural Journal, 101(4), 569-579.

[34] Hu, H.-S., Nie, J.-G., Fan, J.-S., Tao, M.-X., Wang, Y.-H., and Li, S.-Y. (2016). "Seismic behavior of CFST-enhanced steel plate-reinforced concrete shear walls." J Journal of Constructional Steel Research, 119, 176-189.

[35] Hwang, S.-J., Fang, W.-H., Lee, H.-J., and Yu, H.-W. (2001). "Analytical model for predicting shear strengthof squat walls." Journal of Structural Engineering, 127(1), 43-50.

[36] Ji, X., Jiang, F., and Qian, J. (2013). "Seismic behavior of steel tube–double steel plate–concrete composite walls: experimental tests." Journal of Constructional Steel Research, 86, 17-30.

[37] Ji, X., Sun, Y., Qian, J., and Lu, X. (2015). "Seismic behavior and modeling of steel reinforced concrete (SRC) walls." Earthquake Engineering Structural Dynamics, 44(6), 955-972.

[38] Jiang, D., Xiao, C., Chen, T., and Zhang, Y. (2019). "Experimental Study of High-Strength Concrete-Steel Plate Composite Shear Walls." Applied Sciences, 9(14), 2820.

[39] Kim, H.-J., and Park, H.-G. (2022). "Cyclic Loading Test for Composite Walls with U-Shaped Steel Boundary Elements." Journal of Structural Engineering, 148(1), 04021241.

[40] KS (2018). "Rolled steels for welded structures." Korean Agency for Technology and Standards, Eumseong-gun, Chungcheongbuk-do, Korea.

[41] KS (2020). "Headed studs." Korean Agency for Technology and Standards, Eumseong-gun, Chungcheongbuk-do, Korea.

[42] Kuyt, B. (1972). "A method for ultimate strength design of

rectangular reinforced concrete beams in combined torsion, bending and shear." Magazine of Concrete Research, 24(78), 15-24.

[43] Lee, J.-Y., and Watanabe, F. (2003). "Shear deterioration of reinforced concrete beams subjected to reversed cyclic loading." ACI Structural Journal, 100(4), 480-489.

[44] Ma, K., Ma, Y., and Liu, B. (2019). "Quasistatic cyclic tests and finite element analysis of low-aspect ratio double steel concrete composite walls." Advances in Civil Engineering, 2019.

[45] Massone, L. M., and Wallace, J. W. (2004). "Load-deformation responses of slender reinforced concrete walls." ACI Structural Journal, 101(1), 103-113.

[46] Menetrey, P., and Willam, K. (1995). "Triaxial failure criterion for concrete and its generalization." J Structural Journal, 92(3), 311-318.

[47] MIDAS (2021). "GEN 2021." MIDAS IT, Pankyo, Sungnam, South Korea.

[48] Oesterle, R., Aristizabal-Ochoa, J., Fiorato, A., Russell, H., and Corley, W. (1979). "Earthquake resistant structural walls-tests of isolated walls-phase II." Construction Technology Laboratories, Portland Cement Association.

[49] Oesterle, R., Aristizabal-Ochoa, J., Shiu, K., and Corley, W. (1984). "Web crushing of reinforced concrete structural walls." ACI Journal, 81(3), 231-241.

[50] Ozaki, M., Akita, S., Niwa, N., Matsuo, I., and Usami, S. (2001). "Study on steel plate reinforced concrete bearing wall for nuclear power

plants part1; shear and bending loading tests of SC walls."

[51] Ozaki, M., Akita, S., Osuga, H., Nakayama, T., Adachi, N. J. N. E., and Design (2004). "Study on steel plate reinforced concrete panels subjected to cyclic in-plane shear." 228(1-3), 225-244.

[52] Paulay, T., and Priestley, M. N. (1992). "Seismic design of reinforced concrete and masonry buildings."

[53] Qian, J., Jiang, Z., and Ji, X. (2012). "Behavior of steel tube-reinforced concrete composite walls subjected to high axial force and cyclic loading." Engineering structures, 36, 173-184.

[54] Sánchez-Alejandre, A., and Alcocer, S. M. (2010). "Shear strength of squat reinforced concrete walls subjected to earthquake loading—trends and models." Engineering Structures, 32(8), 2466-2476.

[55] Sittipunt, C., Wood, S. L., Lukkunaprasit, P., and Pattararattanakul, P. (2001). "Cyclic behavior of reinforced concrete structural walls with diagonal web reinforcement." ACI Structural Journal, 98(4), 554-562.

[56] Thorburn, L. J., Montgomery, C., and Kulak, G. L. (1983). "Analysis of steel plate shear walls." Department of civil engineering, University of Alberta, Edmonton, Alberta, Canada.

[57] Vallenas, J. M., Bertero, V. V., and Popov, E. P. (1979). "Hysteric behavior of reinforced concrete structural walls." NASA STI/Recon Technical Report N, 80, 27533.

[58] Van Mier, J. G. (1986). "Multiaxial strain-softening of concrete." J Materials structures, 19(3), 190-200.

[59] Vecchio, F. J., and Collins, M. P. (1986). "The modified compression-field theory for reinforced concrete elements subjected to shear." ACI Journal, 83(2), 219-231.

[60] Vladimír Červenka, J. Č., Zdeněk Janda, and Dobromil Pryl (2017). "ATENA." Cervenka Consulting, Na Hrebenkach 55/2667, 150 00 Prague, Czech Republic.

[61] Wang, W., Wang, Y., and Lu, Z. (2018). "Experimental study on seismic behavior of steel plate reinforced concrete composite shear wall." Engineering Structures, 160, 281-292.

[62] Wood, S. L. (1990). "Shear strength of low-rise reinforced concrete walls." ACI Structural Journal, 87(1), 99-107.

[63] Xiao, C., Tian, C., Chen, T., and Jiang, D. "Compression-bending behavior of steel plate reinforced concrete shear walls with high axial compression ratio." Proc., Proceedings of the 15th World Conference on Earthquake Engineering, Lisbon, Portugal, 24-28.

[64] Yan, J.-B., Li, Z.-X., and Wang, T. (2018). "Seismic behaviour of double skin composite shear walls with overlapped headed studs." Construction and Building Materials, 191, 590-607.

[65] Zhang, J., Li, X., Yu, C., and Cao, W. (2021). "Cyclic behavior of high-strength concrete shear walls with high-strength reinforcements and boundary CFST columns." Journal of Constructional Steel Research, 182, 106692.

[66] Zhang, W., Wang, K., Chen, Y., and Ding, Y. (2019). "Experimental study on the seismic behaviour of composite shear walls with stiffened

steel plates and infilled concrete." Thin-Walled Structures, 144, 106279.

[67] Zhao, Q., Li, Y., and Tian, Y. (2020). "Cyclic behavior of double-skin composite walls with flat and corrugated faceplates." Engineering Structures, 220, 111013.

Appendix I: Calculations of Displacement Contributions

To measure flexural deformation in the lower part of walls (with aspect ratios of 2.5 and 2.0), two consecutive rotations θ_{f1} and θ_{f2} were obtained from two pairs of vertical LVDTs located at wall boundaries, as follows (**Fig. 3-18**):

$$\theta_{f1} = (r_1 - r_3)/b_f \tag{A-1a}$$

$$\theta_{f2} = (r_2 - r_4)/b_f \tag{A-1b}$$

where, θ_{f1} and θ_{f2} = rotations over the two consecutive panels (with a height of h_f = 800 mm) at the wall bottom, respectively; r_1, r_2, r_3, and r_4 = displacements measured from the vertical LVDTs of R1, R2, R3, and R4; and b_f = distance between the vertical LVDTs. In flexure-mode walls, curvature distribution varies in the plastic hinge zones. Thus, multiple LVDTS (more than four pairs) may be required to accurately measure the curvature distribution. In the present study, following the study of Massone and Wallace (2004), the center of the rotation based on the inelastic curvature distribution was assumed to be located at 2/3 of the distance from the wall base. Based on this assumption, the displacement contribution of the rotations $\Delta_{f,L}$ in the lower part of walls was calculated from two pairs of LVDTs, as follows (see shaded area in the rotation profile in **Fig. 3-18**):

$$\Delta_{f,L} = \frac{2}{3}(\theta_{f1} + \theta_{f2})h_f + \theta_{f1}(l_s - h_f) + \theta_{f2}(l_s - 2h_f) \tag{A-2}$$

Eq. (A-2) is applied to the specimens with aspect ratios of 2.5 and 2.0. On the other hand, in the specimens with aspect ratio of 1.0, only a pair of LVDTs was used (see Fig. 4-6). Thus, for calculating $\Delta_{f,L}$, Eq. (A-2) is modified as follows:

$$\Delta_{f,L} = \frac{2}{3}\theta_{f1}h_f + \theta_{f1}(l_s - h_f) \qquad \text{(A-3)}$$

The lateral displacement $\Delta_{f,U}$ contributed by flexural deformation in the upper part (height = $L_s - 2h_f$) was calculated based on elastic theory, as follows:

$$\Delta_{f,U} = \frac{V(l_s - l_p)^3}{3(EI)_{eff}} \qquad \text{(A-4)}$$

The lateral displacement $\Delta_{s,1}$, $\Delta_{s,2}$, or $\Delta_{s,3}$ contributed by shear deformation at each shear panel in **Fig. 3-18** was calculated from the measurement according to Sittipunt et al. (2001), as follows:

$$\Delta_{s,j} = h_s \gamma_{s,j} \qquad \text{(A-5)}$$

Where,

$$\gamma_{s,j} = \frac{d_o}{2b_s h_s}[(d_{2j} - d_o) - (d_{2j-1} - d_o)] \qquad \text{(A-6)}$$

where, b_s, h_s and d_o = original lengths of width, height, and diagonals of a shear panel ($b_s = h_s$ = 1,400 mm and d_o = 1,980 mm for the walls with aspect ratio of 2.5; and $b_s = h_s$ = 1,300 mm and d_o = 1,690 mm for the walls with aspect ratios of 2.0 and 1.0); and d_{2j-1} and d_{2j} = deformed lengths of diagonal LVDTs at j^{th} shear panel (j = index number of shear panels = 1, 2, 3).

Appendix II: Summary of Existing SC Composite Wall Specimens

Appendix II: Summary of Existing SC Composite Wall Specimens

Table A. Summary of existing SC composite wall specimens

Researcher	Specimen ID	Wall Type	$\frac{l_s}{l_w}$	ρ_{be} [%]	ρ_w [%]	ρ_h [%]	f_c' [MPa]	F_{yb} [MPa]	F_{yw} [MPa]	f_{yh} [MPa]	$\frac{N}{A_g f_c'}$	V_f [kN]	V_{test} [kN]	Δ_y [mm]	Δ_u [mm]	μ
Eom et al. (2009)	DSCW1N[a]	CFSP	3.85	25.0	16.7	0.0	40	383	383	0	0.00	707	667	0	0	0.0
	DSCW1H[a]	CFSP	3.85	25.0	16.7	0.0	40	383	383	0	0.00	707	765	0	0	0.0
	DSCW1C[a]	CFSP	3.85	25.0	16.7	0.0	40	383	383	0	0.00	707	869	34	97	2.9
	DSCW2[a]	CFSP	3.85	25.0	16.7	0.0	40	383	383	0	0.00	707	809	35	273	7.8
Epackachi et al. (2014)	SC1[a]	CFSP	1.00	3.1	3.1	0.0	31	262	262	0	0.00	1,547	1,417	9	36	3.9
	SC2[a]	CFSP	1.00	3.1	3.1	0.0	31	262	262	0	0.00	1,547	1,408	11	25	2.2
	SC3[a]	CFSP	1.00	4.2	4.2	0.0	37	262	262	0	0.00	1,520	1,201	10	27	2.7
	SC4[a]	CFSP	1.00	4.2	4.2	0.0	37	262	262	0	0.00	1,520	1,212	10	32	3.3
Takeuchi et al. (1998)	H10T05[b]	CFSP	1.16	16.1	4.0	0.0	30	286	286	0	0.00	4,370	2,630	-	-	-
	H10T10[b]	CFSP	1.09	10.9	2.0	0.0	33	286	286	0	0.00	5,697	4,130	-	-	-
	H10T10V[b]	CFSP	1.09	10.9	2.0	0.0	33	286	286	0	0.09	6,484	4,980	-	-	-
	H10T15[b]	CFSP	1.03	9.1	1.3	0.0	30	286	286	0	0.00	7,137	6,700	-	-	-
	H07T10[b]	CFSP	0.87	10.9	2.0	0.0	30	286	286	0	0.00	7,112	4,710	-	-	-
	H15T10[b]	CFSP	1.53	10.9	2.0	0.0	33	286	286	0	0.00	4,047	4,000	-	-	-

Note: ρ_w = area rato of web steel section to the web section; F_{yb} = yield strength of boundary steel section; F_{yw} = yield strength of web steel section; Δ_y = yield displacement; Δ_u = ultimate displacement.
[a]boundary element type = No boundary element.
[b]boundary element type = Flange wall.

Table A. Summary of existing SC composite wall specimens (Continued)

Researcher	Specimen ID	Wall Type	$\frac{l_s}{l_w}$	ρ_{be} [%]	ρ_w [%]	ρ_h [%]	f_c' [MPa]	F_{yb} [MPa]	F_{yw} [MPa]	f_{yh} [MPa]	$\frac{N}{A_g f_c'}$	V_f [kN]	V_{test} [kN]	Δ_y [mm]	Δ_u [mm]	μ
Ozaki et al. 2001	BS70T05[b]	CFSP	0.70	15.4	3.9	0.0	34	353	353	0	0.00	11,083	7,370	-	-	-
	BS70T10[b]	CFSP	0.70	15.4	2.0	0.0	34	389	389	0	0.00	10,751	5,730	-	-	-
	BS70T14[b]	CFSP	0.70	15.4	1.4	0.0	36	448	448	0	0.00	11,713	5,410	-	-	-
	BS50T10[b]	CFSP	0.50	15.4	2.0	0.0	36	389	389	0	0.00	15,249	6,570	-	-	-
	BS85T10[b]	CFSP	0.85	15.4	2.0	0.0	34	389	389	0	0.00	8,851	5,450	-	-	-
	No.1[b]	CFSP	0.85	9.0	2.0	0.0	34	402	400	0	0.00	5,990	4,180	-	-	-
	No.2[b]	CFSP	0.70	10.5	2.0	0.0	34	477	400	0	0.00	9,382	5,080	-	-	-
	No.3[b]	CFSP	0.70	10.5	2.0	0.0	34	477	400	0	0.00	9,382	5,300	-	-	-
	No.4[b]	CFSP	0.70	10.5	2.0	0.0	41	477	400	0	0.00	9,363	5,430	-	-	-
Ji et al. 2017	DSCW1[b]	CFSP	1.21	16.4	6.7	0.0	36	302	341	0	0.20	3,060	2,212	3	15	4.5
	DSCW2[b]	CFSP	1.21	16.4	6.7	0.0	40	302	341	0	0.35	3,181	2,306	4	13	3.7
	DSCW3[b]	CFSP	1.21	16.4	6.7	0.0	38	302	341	0	0.37	3,146	2,387	5	32	6.3

Note: ρ_w = area rato of web steel section to the web section; F_{yb} = yield strength of boundary steel section; F_{yw} = yield strength of web steel section; Δ_y = yield displacement; Δ_u = ultimate displacement.
[a]boundary element type = No boundary element.
[b]boundary element type = CFSP Flange wall.

Appendix II: Summary of Existing SC Composite Wall Specimens

Table A. Summary of existing SC composite wall specimens (Continued)

Researcher	Specimen ID	Wall Type	$\frac{l_s}{l_w}$	ρ_{be} [%]	ρ_w [%]	ρ_h [%]	f_c' [MPa]	F_{yb} [MPa]	F_{yw} [MPa]	f_{yh} [MPa]	$\frac{N}{A_g f_c'}$	V_f [kN]	V_{test} [kN]	Δ_y [mm]	Δ_u [mm]	μ
Chen et al. 2015	DSHCW1[a]	CFSP	2.61	10.7	6.0	0.0	84	292	283	271	0.11	509	584	32	99	3.1
	DSHCW2[a]	CFSP	2.61	10.7	6.0	0.0	84	292	283	271	0.00	406	446	29	99	3.4
	DSHCW3[a]	CFSP	2.61	10.7	6.0	0.0	84	292	283	271	0.11	509	584	42	115	2.8
Cheng et al. 2014	SCW1-1a[a]	CFSP	1.00	8.0	4.0	0.0	29	330	330	0	0.34	1,195	1,782	-	-	-
	SCW1-1b[a]	CFSP	1.00	8.0	4.0	0.0	29	330	330	0	0.34	1,195	1,612	-	-	-
	SCW1-2a[a]	CFSP	1.50	8.0	4.0	0.0	29	330	330	0	0.34	797	1,035	-	-	-
	SCW1-2b[a]	CFSP	1.50	8.0	4.0	0.0	29	330	330	0	0.34	797	954	-	-	-
	SCW1-3[a]	CFSP	2.00	8.0	4.0	0.0	29	330	330	0	0.34	597	604	-	-	-
	SCW1-4[a]	CFSP	1.00	5.3	2.7	0.0	29	307	307	0	0.28	891	962	-	-	-
	SCW1-5[a]	CFSP	1.00	10.7	5.3	0.0	29	361	361	0	0.40	1,545	1,972	-	-	-
	SCW1-6[a]	CFSP	1.00	8.0	4.0	0.0	29	330	330	0	0.34	1,195	1,568	-	-	-
	SCW1-7[a]	CFSP	1.00	8.0	4.0	0.0	29	330	330	0	0.34	1,195	1,659	-	-	-

Note: ρ_w = area rato of web steel section to the web section; F_{yb} = yield strength of boundary steel section; F_{yw} = yield strength of web steel section; Δ_y = yield displacement; Δ_u = ultimate displacement.
[a]boundary element type = CFT column.

Table A. Summary of existing SC composite wall specimens (Continued)

Researcher	Specimen ID	Wall Type	$\frac{l_s}{l_w}$	ρ_{be} [%]	ρ_w [%]	ρ_h [%]	f_c' [MPa]	F_{yb} [MPa]	F_{yw} [MPa]	f_{yh} [MPa]	$\frac{N}{A_g f_c'}$	V_f [kN]	V_{test} [kN]	Δ_y [mm]	Δ_u [mm]	μ
Nie et al. 2013	CFSCW-1[a]	CFSP	2.00	11.2	5.6	0.0	88	306	306	0	0.31	2,126	2,647	19	45	2.3
	CFSCW-2[a]	CFSP	2.00	11.2	5.6	0.0	86	306	306	0	0.31	2,109	2,539	17	41	2.4
	CFSCW-3[a]	CFSP	2.00	11.2	5.6	0.0	86	306	306	0	0.31	2,109	2,697	21	39	1.9
	CFSCW-4[a]	CFSP	2.00	7.5	3.7	0.0	90	351	351	0	0.31	1,936	2,198	15	41	2.7
	CFSCW-5[a]	CFSP	2.00	5.6	2.8	0.0	88	443	443	0	0.31	1,874	2,120	16	43	2.8
	CFSCW-6[a]	CFSP	2.00	9.3	4.7	0.0	65	306	306	0	0.33	1,680	2,357	19	37	2.0
	CFSCW-7[a]	CFSP	2.00	9.3	4.7	0.0	103	306	306	0	0.28	2,130	2,666	19	38	2.0
	CFSCW-8[a]	CFSP	2.00	11.2	3.7	0.0	88	363	351	0	0.32	2,211	2,438	21	45	2.1
	CFSCW-9[a]	CFSP	2.00	9.3	4.7	0.4	83	306	306	327.4	0.32	1,949	2,607	18	36	2.0
	CFSCW-10[a]	CFSP	2.00	9.6	4.8	0.0	84	443	443	0	0.35	797	1,117	8	23	2.8
	CFSCW-11[a]	CFSP	1.50	9.6	4.8	0.0	81	443	443	0	0.36	1,045	1,365	6	16	2.4
	CFSCW-12[a]	CFSP	1.00	9.6	4.8	0.0	88	443	443	0	0.34	1,630	2,018	5	14	2.9

Note: ρ_w = area rato of web steel section to the web section; F_{yb} = yield strength of boundary steel section; F_{yw} = yield strength of web steel section; Δ_y = yield displacement; Δ_u = ultimate displacement.
[a]boundary element type = CFT column.

Appendix II: Summary of Existing SC Composite Wall Specimens

Table A. Summary of existing SC composite wall specimens (Continued)

Researcher	Specimen ID	Wall Type	$\frac{l_s}{l_w}$	ρ_{be} [%]	ρ_w [%]	ρ_h [%]	f_c' [MPa]	F_{yb} [MPa]	F_{yw} [MPa]	f_{yh} [MPa]	$\frac{N}{A_g f_c'}$	V_f [kN]	V_{test} [kN]	Δ_y [mm]	Δ_u [mm]	μ
Nie et al. 2014	CSW-1[a]	CFSP	2.00	11.0	6.7	0.0	36	306	306	0	0.21	415	554	10	26	2.7
	CSW-2[a]	CFSP	1.50	11.0	6.7	0.0	39	306	306	0	0.21	564	737	8	17	2.0
	CSW-3[a]	CFSP	1.50	11.0	6.7	0.0	35	306	306	0	0.29	557	764	8	18	2.3
	CSW-4[a]	CFSP	1.50	11.0	6.7	0.0	36	306	306	0	0.36	573	757	7	15	2.2
	CSW-5[a]	CFSP	1.50	11.0	6.7	0.0	28	306	306	0	0.20	766	1,000	5	13	2.5
	CSW-6[a]	CFSP	1.00	11.0	6.7	0.0	25	306	306	0	0.23	756	971	5	15	2.7
	CSW-7[a]	CFSP	1.00	11.0	6.7	0.0	30	306	306	0	0.16	774	979	6	17	3.0
	CSW-8[a]	CFSP	1.00	11.0	6.7	0.0	28	306	306	0	0.20	772	994	6	13	2.4
	CSW-9[a]	CFSP	1.00	11.0	6.7	0.0	26	306	306	0	0.28	771	965	5	15	3.1
Ji et al. 2013	SW1[a]	CFSP	2.50	16.4	4.3	0.0	33	299	434	0	0.25	712	814	18	56	3.2
	SW2[a]	CFSP	2.50	12.5	4.3	0.0	31	299	434	0	0.24	673	809	23	79	3.5
	SW3[a]	CFSP	2.50	10.2	2.9	0.0	31	322	441	0	0.20	585	669	16	76	4.8
	SW4[a]	CFSP	2.50	12.5	2.9	0.0	33	299	441	0	0.20	644	799	18	70	4.0
	SW5[a]	CFSP	2.50	9.4	4.3	0.0	31	299	434	0	0.20	574	698	17	76	4.5

Note: ρ_w = area rato of web steel section to the web section; F_{yb} = yield strength of boundary steel section; F_{yw} = yield strength of web steel section; Δ_y = yield displacement; Δ_u = ultimate displacement.
[a]boundary element type = CFT column.

Table A. Summary of existing SC composite wall specimens (Continued)

Researcher	Specimen ID	Wall Type	$\frac{l_s}{l_w}$	ρ_{be} [%]	ρ_w [%]	ρ_h [%]	f_c' [MPa]	F_{yb} [MPa]	F_{yw} [MPa]	f_{yh} [MPa]	$\frac{N}{A_g f_c'}$	V_f [kN]	V_{test} [kN]	Δ_y [mm]	Δ_u [mm]	μ
Yan et al. 2018	W1[a]	CFSP	2.00	11.2	7.4	0.0	27	235	235	0	0.42	466	615	18	51	2.9
	W2[a]	CFSP	2.00	11.2	7.4	0.0	27	235	235	0	0.42	466	611	22	64	2.8
	W3[a]	CFSP	2.00	11.2	7.4	0.0	27	235	235	0	0.42	466	613	22	53	2.4
	W4[a]	CFSP	2.00	11.2	7.4	0.0	27	235	235	0	0.42	466	606	21	68	3.3
	W5[a]	CFSP	2.00	11.2	7.4	0.0	27	235	235	0	0.59	458	636	19	49	2.6
	W6[a]	CFSP	2.00	8.6	7.4	0.0	27	235	235	0	0.39	413	560	22	48	2.2
	W7[a]	CFSP	1.00	11.2	7.4	0.0	27	235	235	0	0.42	933	1,188	12	47	3.9
Zhang et al. 2019	CWSC-1a[a]	CFSP	0.75	8.4	5.0	0.0	28	467	467	0	0.50	1,318	888	7	14	1.9
	CWSC-1b[a]	CFSP	0.75	8.4	5.0	0.0	28	467	467	0	0.50	1,318	1,257	11	37	3.4
	CWSC-1c[a]	CFSP	0.75	8.4	5.0	0.0	28	467	467	0	0.50	1,318	1,258	12	37	3.0
	CWSC-2a[a]	CFSP	0.75	7.6	5.0	0.0	28	467	467	0	0.50	1,284	1,102	7	16	2.2
	CWSC-2b[a]	CFSP	0.75	7.6	5.0	0.0	28	467	467	0	0.50	1,284	1,258	11	27	2.5
	CWSC-2c[a]	CFSP	0.75	7.6	5.0	0.0	28	467	467	0	0.50	1,284	1,052	9	18	2.0
	CWSC-3a[a]	CFSP	0.75	9.3	5.0	0.0	28	467	467	0	0.50	1,338	911	9	23	2.6

Note: ρ_w = area rato of web steel section to the web section; F_{yb} = yield strength of boundary steel section; F_{yw} = yield strength of web steel section; Δ_y = yield displacement; Δ_u = ultimate displacement.
[a]boundary element type = CFT column.

Appendix II: Summary of Existing SC Composite Wall Specimens

Table A. Summary of existing SC composite wall specimens (Continued)

Researcher	Specimen ID	Wall Type	$\frac{l_s}{l_w}$	ρ_{be} [%]	ρ_w [%]	ρ_h [%]	f_c' [MPa]	F_{yb} [MPa]	F_{yw} [MPa]	f_{yh} [MPa]	$\frac{N}{A_g f_c'}$	V_f [kN]	V_{test} [kN]	Δ_y [mm]	Δ_u [mm]	μ
Zhang et al. 2019	CWSC-3b[a]	CFSP	0.75	9.3	5.0	0.0	28	467	467	0	0.50	1,338	1,085	8	23	2.8
	CWSC-3c[a]	CFSP	0.75	9.3	5.0	0.0	28	467	467	0	0.50	1,338	1,272	15	48	3.2
	CWSC-4a[a]	CFSP	0.75	9.1	5.7	0.0	28	467	467	0	0.50	1,232	1,163	12	28	2.3
	CWSC-4b[a]	CFSP	0.75	9.1	5.7	0.0	28	467	467	0	0.50	1,232	1,223	12	31	2.6
	CWSC-4c[a]	CFSP	0.75	9.1	5.7	0.0	28	467	467	0	0.50	1,232	1,011	9	18	2.0
	CWSC-5a[a]	CFSP	0.75	7.9	4.4	0.0	28	467	467	0	0.50	1,404	1,018	7	15	2.1
	CWSC-5b[a]	CFSP	0.75	7.9	4.4	0.0	28	467	467	0	0.50	1,404	1,289	10	35	3.6
	CWSC-5c[a]	CFSP	0.75	7.9	4.4	0.0	28	467	467	0	0.50	1,404	1,083	9	21	2.3
Zhao et al. 2020	CW-F1[a]	CFSP	1.50	11.7	6.0	0.0	51	306	305	0	0.22	945	1,060	27	52	1.9
	CW-F2[a]	CFSP	1.50	9.3	6.0	0.0	34	314	307	0	0.33	767	884	13	37	2.8
	CW-C1[a]	CFSP	1.50	11.7	6.0	0.0	52	306	305	0	0.21	948	1,131	19	46	2.4
	CW-C2[a]	CFSP	1.50	11.7	6.0	0.0	53	306	305	0	0.21	951	1,082	23	54	2.4

Note: ρ_w = area rato of web steel section to the web section; F_{yb} = yield strength of boundary steel section; F_{yw} = yield strength of web steel section; Δ_y = yield displacement; Δ_u = ultimate displacement.
[a]boundary element type = CFT column.

Table A. Summary of existing SC composite wall specimens (Continued)

Researcher	Specimen ID	Wall Type	$\frac{l_s}{l_w}$	ρ_{be} [%]	ρ_w [%]	ρ_h [%]	f_c' [MPa]	F_{yb} [MPa]	F_{yw} [MPa]	f_{yh} [MPa]	$\frac{N}{A_g f_c'}$	V_f [kN]	V_{test} [kN]	Δ_y [mm]	Δ_u [mm]	μ
Ma et al. 2019	DSCW-1[a]	CFSP	1.00	10.0	5.0	0.0	54	323	323	0	0.13	703	711	4	13	2.9
	DSCW-2[a]	CFSP	1.00	12.0	6.0	0.0	54	334	334	0	0.13	821	801	4	15	3.3
	DSCW-3[a]	CFSP	1.00	12.0	6.0	0.0	54	334	334	0	0.26	891	864	6	13	2.2
Hu et al. 2016	SRCW-1[a]	CESP	2.00	13.0	4.7	0.4	67	306	432	327.4	0.35	2,052	2,552	22	46	2.1
	SRCW-2[a]	CESP	2.00	13.0	4.7	0.4	88	306	432	327.4	0.33	2,324	2,729	20	46	2.3
	SRCW-3[a]	CESP	2.00	7.8	2.8	0.4	83	443	363	327.4	0.31	1,978	2,317	17	40	2.4
Jiang et al. 2019	SPRCW1-a[b]	CESP	2.25	4.0	3.3	0.5	48	353	353	368.6	0.18	418	396	12	35	3.0
	SPRCW2-a[b]	CESP	2.25	4.0	3.3	0.5	48	353	353	368.6	0.22	434	426	9	34	3.7
	SPRCW3-a[b]	CESP	2.25	4.0	3.3	0.5	48	353	353	368.6	0.25	447	428	12	34	2.8
	SPRCW1-b[b]	CESP	2.70	4.3	3.3	0.7	84	334	310	291.2	0.20	509	639	8	33	3.9
	SPRCW2-b[b]	CESP	2.70	4.3	3.3	0.7	84	334	310	291.2	0.24	538	660	7	26	3.8
	SPRCW3-b[b]	CESP	2.70	4.3	3.3	0.7	84	334	310	291.2	0.28	561	688	8	20	2.4

Note: ρ_w = area rato of web steel section to the web section; F_{yb} = yield strength of boundary steel section; F_{yw} = yield strength of web steel section; Δ_y = yield displacement; Δ_u = ultimate displacement.

[a]boundary element type = CFT column.

[b]boundary element type = CES column.

Appendix II: Summary of Existing SC Composite Wall Specimens

Table A. Summary of existing SC composite wall specimens (Continued)

Researcher	Specimen ID	Wall Type	$\frac{l_s}{l_w}$	ρ_{be} [%]	ρ_w [%]	ρ_h [%]	f_c' [MPa]	F_{yb} [MPa]	F_{yw} [MPa]	f_{yh} [MPa]	$\frac{N}{A_g f_c'}$	V_f [kN]	V_{test} [kN]	Δ_y [mm]	Δ_u [mm]	μ
Xiao et al. 2012	SPRCW1-a[a]	CESP	2.25	4.0	3.3	0.5	48	353	353	368.6	0.18	418	396	12	35	3.0
	SPRCW2-a[a]	CESP	2.25	4.0	3.3	0.5	48	353	353	368.6	0.22	434	426	9	34	3.7
	SPRCW3-a[a]	CESP	2.25	4.0	3.3	0.5	48	353	353	368.6	0.25	447	428	12	34	2.8
	SPRCW1-b[a]	CESP	2.70	4.3	3.3	0.7	84	334	310	291.2	0.20	509	639	8	33	3.9
	SPRCW2-b[a]	CESP	2.70	4.3	3.3	0.7	84	334	310	291.2	0.24	538	660	7	26	3.8
	SPRCW3-b[a]	CESP	2.70	4.3	3.3	0.7	84	334	310	291.2	0.28	561	688	8	20	2.4
Wang et al. 2018	SRPW1[a]	CESP	2.00	3.6	3.2	0.3	35	313	302	347.8	0.50	402	437	14	26	1.8
	SPRW2[a]	CESP	2.00	3.6	4.8	0.3	35	313	313	347.8	0.40	436	450	22	36	1.7
	SPRW3[a]	CESP	2.00	3.6	3.2	0.3	51	313	302	347.8	0.30	492	439	25	56	2.3
	SPRW4[a]	CESP	2.00	3.6	3.2	0.3	51	313	302	347.8	0.30	492	471	20	59	3.0
	SPRW5[a]	CESP	2.00	3.6	3.2	0.3	51	313	302	347.8	0.30	492	473	25	56	2.2
	SPRW6[a]	CESP	2.00	2.7	3.0	0.2	51	313	313	347.8	0.40	766	585	24	53	2.2
	SPRW7[a]	CESP	2.00	2.7	2.0	0.2	35	313	302	347.8	0.40	567	581	17	49	2.9
	SPRW8[a]	CESP	2.00	2.7	2.0	0.2	51	313	302	347.8	0.30	702	601	52	45	1.0

Note: ρ_w = area rato of web steel section to the web section; F_{yb} = yield strength of boundary steel section; F_{yw} = yield strength of web steel section; Δ_y = yield displacement; Δ_u = ultimate displacement.
[a]boundary element type = CES column.

Table A. Summary of existing SC composite wall specimens (Continued)

Researcher	Specimen ID	Wall Type	$\frac{l_s}{l_w}$	ρ_{be} [%]	ρ_w [%]	ρ_h [%]	f_c' [MPa]	F_{yb} [MPa]	F_{yw} [MPa]	f_{yh} [MPa]	$\frac{N}{A_g f_c'}$	V_f [kN]	V_{test} [kN]	Δ_y [mm]	Δ_u [mm]	μ
Wang et al. 2018	SPRW9[a]	CESP	1.50	3.6	3.2	0.3	35	313	302	347.8	0.40	541	593	24	20	1.0
	SPRW10[a]	CESP	1.50	3.6	4.8	0.3	17	313	313	347.8	0.40	404	537	10	29	2.8
	SPRW1[a]	CESP	1.50	3.6	3.2	0.3	24	313	302	347.8	0.30	447	567	8	30	3.7
	SPRW12[a]	CESP	1.50	4.3	3.2	0.3	24	313	302	347.8	0.30	477	625	12	35	2.9
	SPRW13[a]	CESP	1.50	3.6	3.2	0.3	24	313	302	347.8	0.30	447	531	8	39	4.9
	SPRW14[a]	CESP	1.50	2.7	3.0	0.2	17	313	313	347.8	0.40	526	698	13	34	2.7
	SPRW15[a]	CESP	1.50	2.7	2.0	0.2	17	313	302	347.8	0.40	491	693	12	35	2.9
	SPRW16[a]	CESP	1.50	2.7	2.0	0.2	24	313	302	347.8	0.30	602	727	13	38	3.0
Dan et al. 2011	CSRCW-1[a]	RC	2.60	8.6	0.0	0.7	55	342	0	479	0.02	306	354	38	124	3.3
	CSRCW-2[a]	RC	2.60	9.2	0.0	0.7	46	328	0	479	0.02	308	311	37	119	3.2
	CSRCW-4[a]	RC	2.60	9.2	0.0	0.7	62	328	0	479	0.02	317	325	36	125	3.5
	CSRCW-5[a]	RC	2.60	8.5	0.0	0.7	66	328	0	479	0.02	326	357	36	123	3.4

Note: ρ_w = area rato of web steel section to the web section; F_{yb} = yield strength of boundary steel section; F_{yw} = yield strength of web steel section; Δ_y = yield displacement; Δ_u = ultimate displacement.
[a]boundary element type = CES column.

Appendix II: Summary of Existing SC Composite Wall Specimens

Table A. Summary of existing SC composite wall specimens (Continued)

Researcher	Specimen ID	Wall Type	$\frac{l_s}{l_w}$	ρ_{be} [%]	ρ_w [%]	ρ_h [%]	f_c' [MPa]	F_{yb} [MPa]	F_{yw} [MPa]	f_{yh} [MPa]	$\frac{N}{A_g f_c'}$	V_f [kN]	V_{test} [kN]	Δ_y [mm]	Δ_u [mm]	μ
Ji et al. 2014	SRCW1[a]	RC	2.43	5.8	0.0	0.9	43	282	0	334.8	0.32	493	541	10	38	3.8
	SRCW2[a]	RC	2.43	4.8	0.0	0.7	43	383	0	334.8	0.32	488	510	10	37	3.5
	SRCW3[a]	RC	2.43	3.9	0.0	0.7	45	426	0	334.8	0.32	472	515	10	39	3.8
	SRCW4[a]	RC	2.43	4.5	0.0	0.9	41	337	0	334.8	0.34	461	518	11	36	3.3
	SRCW5[a]	RC	2.43	5.0	0.0	0.9	37	311	0	334.8	0.32	439	481	11	43	3.9
Qian et al. 2012	SW2[a]	RC	2.27	4.5	0.0	0.8	44	369	0	344	0.18	617	718	8	35	4.2
	SW3[a]	RC	2.27	4.5	0.0	1.2	41	369	0	344	0.11	621	738	9	35	3.9
	SW4[a]	RC	2.27	4.5	0.0	1.2	40	369	0	344	0.12	648	771	8	26	3.3
	SW5[a]	RC	2.27	4.0	0.0	0.8	47	356	0	344	0.14	636	719	8	26	3.3
	SW6[a]	RC	2.27	6.3	0.0	0.8	50	356	0	344	0.13	791	851	10	37	3.9
	SW7[a]	RC	2.27	2.3	0.0	1.6	47	356	0	344	0.16	634	721	7	55	7.5
Bryce Tupper 1999	W1[b]	RC	3.75	19.1	0.0	0.6	26	377	0	487.8	0.11	338	324	37	101	2.8
	W2[b]	RC	3.75	15.8	0.0	0.5	38	402	0	402	0.11	313	344	34	104	3.1
Ren et al. 2018	CFST-W[c]	RC	2.05	6.7	0.0	0.6	31	342	0	312	0.30	543	603	14	60	4.3
	DCFST-W[c]	RC	2.05	12.1	0.0	0.6	31	342	0	312	0.35	793	798	15	60	4.1

Note: ρ_w = area rato of web steel section to the web section; F_{yb} = yield strength of boundary steel section; F_{yw} = yield strength of web steel section; Δ_y = yield displacement; Δ_u = ultimate displacement.

[a]boundary element type = CES column.

[b]boundary element type = HSS (Hollow steel section) column.

[c]boundary element type = CFT column.

초 록

U형 강재단부요소를 지닌 합성벽체에 대한 반복가력실험 및 강도예측모델

김 현 진

서울대학교 건축학과 대학원

고층건물과 대규모 산업건물(공장, 발전소 등)에서는 높은 안전성과 사용성(예, 층류비, 바닥진동)을 만족시키기 위해 상당한 구조성능이 요구된다. 이러한 높은 구조성능을 만족시키기 위해 강철 U-단면의 경계요소가 있는 강철-콘크리트 복합 벽체(SUB-C 벽체)가 개발되었다. 제안된 방법에서는 휨강도 및 강성을 최대화하고 강재 접합부와 용접 길이를 최소화하기 위해 강재면적을 벽체 양 단부에 집중배치하였다. U자형 강재요소의 열린 단면으로 인하여, 콘크리트 타설시 단부 강재요소와 철근콘크리트가 일반 전단연결재를 사용하여 간단히 일체화되므로 구조적 건전성 및 시공성을 크게 향상시킬 수 있다. 또한 U자형 요소는 벽체 단부영역에 횡구속을 제공하고 벽의 전단강도를 증가시키므로 수직보강 및 횡보강 철근공사를 최소화할 수 있다.

휨전단 성능을 조사하기 위해 제안된 벽체에 대한 반복 횡가력 실험을 수행했다. U형 형강이 단부콘크리트에 높은 구속력을 제공함에 따라 단부콘크리트의 압괴가 억제되어 인장측 U형 형강의 변형 경화가 발생했다. 따라서 SUB-C 벽의 휨강도는 RC 벽의 휨강도보다

37% 더 큰 것으로 나타났다. 또한, U-형강은 복부영역에서 전단균열 및 전단미끄러짐을 억제했다. 따라서 변형 능력과 에너지 소산은 각각 38–53 % 및 99–173 % 증가했다. SUB-C 벽은 3% 이상의 극한 변형능력을 보였고 결과적으로 소성힌지 영역에서 복부압괴로 인해 강도가 저하되었다(휨항복 후 전단 파괴). SUB-C 벽의 전단강도는 RC 벽의 전단강도보다 13–54 % 더 큰 것으로 나타났다. 이는 U형강이 대각스트럿에서 전달되는 전단력에 저항할 뿐만 아니라 대각 인장균열을 억제하고 경계부를 보호하기 때문이다. 이러한 이유로, SUB-C 벽체의 전단강도는 사인장 전단파괴 등 다른 파괴유형 없이 모두 복부압괴에 의해 결정되었다.

탄성복부압괴(휨항복 이전)로 파괴된 벽체실험체에 대해 비선형 유한 요소 해석을 수행하였다. 해석결과, 벽체 중앙높이에서 나타난 큰 수평인장영역으로 인해, 대각스트럿의 압축강도가 현저히 저하되어 복부압괴에 이르는 것으로 나타났다. 이러한 파괴메커니즘을 "수평 연신" 이라 명명하였고, 매개변수 분석을 기반으로 수평 연신율을 예측하는 경험식을 개발하였다. 수평 연신율은 벽체의 전단보강비와 종횡비에 의해 크게 영향을 받는다. 그러나 경계 보강비 (단부 U형 형강의 단면적)는 수평 연신율에 거의 영향을 미치지 않았다.

전단강도모델 개발을 위해 “탄성 및 비탄성 복부 압괴” 두 가지 전단파괴 메커니즘이 정의되었다. 이러한 메커니즘은 전통적인 트러스모델 방식으로 구현하였으며, SUB-C 벽체의 특성을 고려하여 모델을 개선하였다. 탄성 및 비탄성 복부압괴강도(휨항복 이후 전단강도)는 각각 수평연신 및 수직연신 메커니즘을 고려하였으며, 비탄성 복부압괴강도의 경우 소성힌지영역에서 경계요소의 골조 작용을 추가적으로 고려하였다. 특히, 수직연신은 벽체변형의 함수로 정의되므로 벽체의 휨항복 이후 모든 변형수준에서 전단강도 평가가

가능하였다. 제안된 모델의 정확도는 실험결과와의 비교를 통해 검증되었다. 보다 정밀한 탄성 복부압괴강도 예측을 위하여 상용 해석프로그램을 이용한 등가탄성해석법을 개발하였다.

SUB-C 벽체의 변형기반 설계방법은 제안된 전단강도 모델을 사용하여 개발되었다. 설계변형능력은 요구전단력과 비탄성 복부압괴강도가 교차하는 점에서 정의되었다. 일반적으로, 예측된 벽체 최상부 및 소성힌지부 변형능력은 실험결과와 일치하였다.

실험결과 및 기존 설계방법을 기반으로 SUB-C 벽에 대한 허용 재료강도와 상세설계 요구사항을 정리하였다. 제안된 설계강도는 설계요구사항이 충족되는 경우에만 유효하며, 요구사항 범위를 벗어난 상세설계방법은 추가 실험 및 분석 연구를 통해 심층 검증 후 적용되어야 한다.

주제어 : 강-콘크리트 합성벽, 합성단부요소, U형 단부강판, 휨강도, 복부압괴전단강도, 수직연신, 수평연신, 휨 항복 후 전단강도.

학 번 : 2014-22627